Spatiotemporal Regulation of Plant Plasma Membrane Proteins at the Nanoscale: Advancements in and Applications of sptPALM and FRET-FLIM Techniques for Integrated Analyses

Dissertation

der Mathematisch-Naturwissenschaftlichen Fakultät

der Eberhard Karls Universität Tübingen

zur Erlangung des Grades eines

Doktors der Naturwissenschaften

(Dr. rer. nat.)

vorgelegt von

M.Sc. Leander Karl Wilhelm Rohr

aus Karlsruhe

Tübingen

2024

Gedruckt mit Genehmigung der Mathematisch-Naturwissenschaftlichen Fakultät der Eberhard Karls Universität Tübingen.

Tag der mündlichen Qualifikation:	18.02.2025
Dekan:	Prof. Dr. Thilo Stehle
1. Berichterstatter/-in:	Prof. Dr. Klaus Harter
2. Berichterstatter/-in:	Prof. Dr. Claudia Oecking
3. Berichterstatter/-in:	Prof. Dr. Kay Schneitz

Acknowledgements

During the laboratory work and the writing process, many people gave advice and support to me. To find the right words, I will switch to my mother tongue for the following acknowledgements.

Zunächst möchte ich meinem Doktorvater Prof. Dr. Klaus Harter herzlich danken. Nicht nur dein wissenschaftlicher Rat hat mir stets geholfen, diese Arbeit in der vorliegenden Form fertig zu stellen, auch das ein oder andere von mir heraufbeschworene Datentief hast du durch deine stets optimistische Art in neue Motivation transformiert. Nicht zuletzt ist es auch deiner Neugierde und Offenheit für interdisziplinäre Zusammenarbeiten zu verdanken, dass wir hier am ZMBP an spannenden Themen wie der Einzelmolekülverfolgung arbeiten und im speziellen Ich daran forschen durfte. Vielen Dank!

Ich möchte auch Prof. Dr. Claudia Oecking danken, welche sich, ohne zu zögern bereit erklärt hat, als Zweitgutachterin zu fungieren. Deine gezielten Nachfragen zu Aspekten der sptPALM Methode haben mir nochmals sehr geholfen, einige Erkenntnisse genauer zu hinterfragen.

Ein herzliches Dankeschön auch an Prof. Dr. Kay Schneitz für das Erstellen des dritten Gutachtens.

Einen weiteren Dank möchte ich den Mitgliedern meines *Thesis Advisory Committee* aussprechen. Sei es Prof. Dr. Julien Gronnier, Prof. Dr. Sabine Müller oder Prof. Dr. Sebastian Wolf, ihr alle habt stets hilfreiche Diskussionen für das Voranbringen des Projekts mit mir geführt.

Insbesondere Dir, Sabine, möchte ich an dieser Stelle nochmals gesondert danken, da du mir 2015 die Möglichkeit gegeben hast, in deinem Labor erste Erfahrungen im molekularbiologischen Arbeiten zu sammeln. Gerne erinnere ich mich an diese großartige Zeit zurück – Arvid, Steffi und Co., ihr wart hervorragende Lehrmeister.

In diesem Zuge möchte ich auch Dr. Friederike Wanke danken! Fredi, du warst es dann, die mich bei Klaus unter ihre Fittiche nahm. Mit dir war jede Menge Spaß im Labor garantiert, und noch heute, wenn komplizierte Experimente nicht so funktionieren wie sie sollen, bemühe ich „Fredi-Methoden“ aus meinen Notizen. Es freut mich sehr, dass wir uns immer noch regelmäßig sehen!

Geht es um besonderen Dank im Kontext meiner Arbeit, darf eine Person nicht vergessen werden: Dr. Sven zur Oven-Krockhaus. Ohne Zweifel kann ich sagen, dass dieses Projekt in seiner Form ohne dein Zutun nicht möglich gewesen wäre. Dein unfassbares Know-how und deine Bereitschaft, dich in jedes Detail zu stürzen, haben die uns zur Verfügung stehende Mikroskopie Plattform zu einem Angebot gemacht, welches ihresgleichen sucht. Vielen Dank auch für alle Anpassungen im Setup und in der Software, deine unglaubliche Geduld im Erläutern verschiedenster Sachverhalte und deine ausführlichen Korrekturen – sie waren immer sehr hilfreich!

Danken möchte ich auch allen Co-Autoren und Kooperationspartnern, die in welcher Form auch immer an verschiedensten Projekten meiner Doktorarbeit beteiligt waren. Besonderer Dank gilt dabei Dr. Nina Glöckner Burmeister und Dr. Alexandra Ehinger. Liebe Nina, bereits während meiner Masterstudien hast du mir einige Methoden im Labor nahegebracht und mich nicht zuletzt davon überzeugt, dein Projekt fortzuführen. Auch wenn das Suchen spezifischer Punkte in deinen Notizen mich manchmal durch hunderte Seiten Laborbuch geleitet hat, hast du mir doch ein hervorragendes Fundament zur Weiterführung deiner Arbeit hinterlassen. Vielen Dank auch, Luiselotte Rausch. Viele lustige Momente im Labor und wissenschaftliche Diskussionen rund um das Thema *single-particle tracking* haben den Arbeitsalltag erheblich bereichert.

Danke auch allen aktuellen sowie ehemaligen Mitgliedern des Arbeitskreises Harter. Seien es die Mittagspausen, Retreats oder eure stetige Hilfsbereitschaft in sämtlichen Aspekten des Laboralltags, aber auch im Privaten; Ihr macht den Arbeitskreis zu dem, was er ist:
Einem großartigen Ort für Forschung ohne das Vergessen von Spaß!

Nicht versäumen möchte ich auch, allen Praktikanten und Hilfswissenschaftlern, welche in den vergangenen Jahren Beiträge zu dieser Arbeit geleistet haben, zu danken. Ich konnte mich stets auf euch verlassen.

Besonders wichtig ist es mir auch, die Arbeit der Zentralen Bereiche am ZMBP hervorzuheben. Im Besonderen gilt mein Dank dem Team des Gewächshauses. Besuche bei euch waren mir stets eine Freude. Speziell vielen Dank an dich, Sofia, wenn du mal wieder die ein oder anderen Arbeiten für mich in meiner Abwesenheit übernommen hast oder mich zum Oster-Umtrunk mit Martin eingeladen hast.

Danken möchte ich auch meinen Freunden, seien es all die lieben Menschen in Tübingen oder der „HARTE KERN“ zuhause. Vielen Dank für eure Unterstützung und eure Freundschaft in den letzten Jahren und Jahrzehnten!

Liebe Mama: Einfach, danke für alles! Du weißt, wir sind die Meister der wenigen Worte, und daher soll es auch kurz blieben. Vielen Dank für Deine Unterstützung in all den Jahren. Du hast mir so einiges gelehrt, vor allem, dass es immer weitergeht! Wie passend, dass mit der Abgabe meiner Arbeit auch du es ab Oktober, etwas geruhsamer angehen kannst!

Leticia: Auch an dich, vielen Dank für deine Unterstützung und Verlässlichkeit. Auch wenn wir uns gar nicht mehr so häufig sehen, kann ich mir Deiner bedingungslosen Hilfe immer sicher sein.

Liebe Madeleine, vielen Dank für deine Liebe, deine Unterstützung und vor allem dein Verständnis. Wenn ich mal wieder die „sausenden Augen“ hatte, hast du immer die richtigen Worte gefunden, um mich zu beruhigen und mich weiter zu motivieren. Unser Zusammensein macht mich glücklich!

Die meisten kennen mich als stets entspannt und relaxed, aber so eine Arbeit kann auch mal die tiefenentspanntesten Personen kurzzeitig unsicher und nervös machen – daher an all die Genannten und auch an all die potenziell Vergessenen: **Danke für Alles!**

Content

Abbreviations

A. thaliana	*Arabidopsis thaliana*
AHA1/2	Plasma membrane *Arabidopsis* H^+-ATPase isoform 1/2
BAK1	BRI1-ASSOCIATED RECEPTOR KINASE 1
BES1	BRI1-EMS-SUPPRESSOR 1
BIK1	BOTRYTIS-INDUCED KINASE 1
BIN2	BRASSINOSTEROID INSENSITIVE 2
BIR3	BAK1-INTERACTING RECEPTOR-LIKE KINASE 3
BKI1	BRI1 KINASE INHIBITOR 1
BL	Brassinolide
BR	Brassinosteroid
BRI1	BRASSINOSTEROID INSENSITIVE 1
BZR1	BRASSINAZOLE-RESISTANT 1
CESAs	CELLULOSE SYNTHASE GENES
CNGC10/17	CYCLIC NUCLEOTIDE GATED CHANNEL 10/17
Co-IP	Co-immunoprecipitation
CRISPR	Clustered regularly interspaced short palindromic repeats
DBSCAN	Density-based spatial clustering of applications with noise
DOI	Digital object identifier
EZ	Elongation zone
FAIR	Findable, Accessible, Interoperable, Reusable
flg22	Flagellin 22
FLIM	Fluorescence Lifetime Imaging Microscopy
FLS2	FLAGELLIN-SENSITIVE 2
FLT	Fluorescence lifetime
FP	Fluorescent protein

FRET	Förster Resonance Energy Transfer
GFP	Green Fluorescent Protein
GPU	Graphics processing unit
HA	Hemagglutinin
HILO	Highly inclined and laminated optical sheet
IC	Internal conversion
LRR	Leucin-rich-repeat
LTi6a	Low temperature inducible 6a
LYK3	LYSINE MOTIF KINASE 3
LysM	Lysin motif
MDP40	MICROTUBULE DESTABILIZING PROTEIN 40
mRFP	Monomeric RFP
MSD	Mean square displacement
mTRQ2	Monomeric Turquoise 2
mVEN	Monomeric Venus
MZ	Meristematic zone
N. benthamiana	*Nicotiana benthamiana*
NASTIC	Nanoscale spatiotemporal indexing clustering
NRT1.1/2.1	NITRATE TRANSPORTER 1.1/2.1
PA	Photoactivatable
PALM	Photoactivated localization microscopy
PEP7	ELICITOR PEPTIDE 7
PHS1ΔP	Truncated version of PROPYZAMIDE HYPERSENSITIVE 1
PIP2;1/2;4/2A	PLASMA MEMBRANE INTRINSIC PROTEIN 2;1/2;4/2A
PM	Plasma membrane
PPI	Protein-protein interaction

PSF	Point spread function
PSK	Phytosulfokine
PSKR1/2	PHYTOSULFOKINE RECEPTOR 1/2
QSK1	QIAN SHOU KINASE 1
R_0	Förster distance
REM	REMORIN
REM-CA	REMORIN C-terminal Anchor
RLK	Receptor-like kinase
RLP	Receptor-like protein
ROP6	RHO OF PLANTS 6
SA	Salicylic acid
sCMOS	Scientific complementary metal-oxide semiconductor
SEC-MS	Size-exclusion-chromatography coupled to mass spectrometry
SIRK1	SUCROSE-INDUCED RECEPTOR KINASE 1
SPFH	Stomatin/prohibitin/flotillin/HflK/C
spt	Single-particle tracking
SpvB	*Salmonella* virulence plasmid B protein
TIRF	Total internal reflection fluorescence
TZ	Transition zone
VAEM	Variable-angle epifluorescence microscopy
VR	Vibrational Relaxation

Deutsche Zusammenfassung

Proteine in der pflanzlichen Plasmamembran (PM) sind nicht homogen verteilt, sondern vielmehr in verschiedenen Domänen im Nanomaßstab organisiert, welche molekulare Knotenpunkte bilden können. Während einige Aspekte dieser Komplexe, wie zum Beispiel Protein-Protein-Wechselwirkungen oder die Auswirkungen ihrer Signalkaskaden, häufig bereits bekannt sind, wurde ihrer räumlich-zeitlichen Regulierung bisher vergleichsweise wenig Aufmerksamkeit geschenkt. Allerdings legen Studien eine zentrale Rolle dieser Regulation in verschiedenen Signalkaskaden nahe, sodass es von besonderem Interesse ist, auch diese Prozesse im Detail zu untersuchen.

Die Einzelpartikelverfolgung in Kombination mit der photoaktivierten Lokalisationsmikroskopie (*sptPALM*) liefert räumlich-zeitliche Informationen über Proteine mit hoher Präzision. Während die Methode in nichtpflanzlichen Systemen bereits länger etabliert ist, hat sich die Technik in der Pflanzenforschung erst kürzlich verbreitet und befindet sich noch unter ständiger Verbesserung und Weiterentwicklung. Dabei haben wir zwei große Herausforderungen identifiziert: (i) Die Analyse der Daten wird durch mehrstufige Auswertungsprozesse erschwert, wofür spezifische Softwarelösungen verwendet werden müssen. (ii) Um physiologische Prozesse besser zu verstehen, ist die raum-zeitliche Untersuchung von mehr als einem Protein zeitglich besonders wichtig; dies war jedoch bisher mit *sptPALM* in Pflanzen nicht möglich. Neben diesen technischen Aspekten waren wir auch daran interessiert, inwieweit verschiedene Komponenten der pflanzlichen Zelle, im speziellen das Zytoskelett, die Organisation von PM-Proteinen beeinflussen.

In dieser Arbeit stellen wir eine universelle Softwarelösung vor, welche intuitiv ist und den Anwender durch alle Analyseschritte führt. Wir haben ihre Funktionalität demonstriert, indem wir Proteine mit publizierten raum-zeitlichen Daten sowie weitere gut charakterisierte pflanzliche PM-Proteine analysiert haben, welche bisher nicht Gegenstand von *sptPALM*-Studien waren. Unsere Ergebnisse weisen zudem auf organspezifische Effekte und einen Einfluss des Entwicklungsstadiums der Pflanze auf den Diffusionskoeffizienten hin – Aspekte, die bisher in keinen anderen Untersuchungen berücksichtigt wurden.

Darüber hinaus haben wir zum ersten Mal die generelle Verwendbarkeit von zwei fluoreszierenden Proteinen (FP) gezeigt –photoaktivierbares (PA)-GFP und PATagRFP – welche simultane zweifarbige *sptPALM*-Studien in Pflanzen ermöglichen könnten. Anschließend haben wir ihre tatsächliche Anwendung in einer *Proof-of-Principle*-Studie nachgewiesen, in der wir die Proteindynamik von zwei unterschiedlich markierten Proteinen gleichzeitig analysiert haben. Dies erweitert nicht nur das Portfolio verfügbarer FP, sondern ermöglicht es Forschern in Zukunft auch, beispielsweise die Wirkung externer Stimuli auf verschiedene Proteine gleichzeitig zu untersuchen.

In Folge der Untersuchungen, wie das Zytoskelett die pflanzliche PM und die darin lokalisierten Proteine reguliert, konnten wir gegenläufige Effekte von Aktinfilamenten und Mikrotubuli zeigen. Die Störung von Aktinfilamenten führt in erster Linie zu verringerten Diffusionskoeffizienten, größeren Proteinclustern und eingeschränkteren Bewegungen, während die Manipulation von Mikrotubuli zu erhöhten Diffusionskoeffizienten, vermehrter ungehinderter Diffusion und verringerten Clustergrößen führt. Mit diesen Ergebnissen unterstreichen wir die potenziell spezifischen regulatorischen Funktionen dieser unterschiedlichen Zytoskelett-Komponenten. Infolgedessen schlagen wir einen veränderten Mechanismus für die Zytoskelett-vermittelte Kompartimentierung der PM im Vergleich zum *picket fence model* der tierischen Zellen vor.

Außerdem habe ich Forscher bei Förster-Resonanzenergietransfer (FRET)-Messungen in Kombination mit Fluoreszenz-Lebensdauer-Imaging-Mikroskopie (FLIM; FRET-FLIM) unterstützt, um verschiedene Signalwege genauer zu verstehen. Erneut konnten wir demonstrieren, dass FRET-FLIM Experimente hervorragend geeignet sind, um Ergebnisse anderer Protein-Protein-Interaktionsmethoden zu unterstützen oder zu bestätigen sowie um aktuelle Arbeitsmodelle um neue Erkenntnisse zu erweitern. Zum Beispiel deuten unsere Ergebnisse darauf hin, dass die SUCROSE-INDUCED RECEPTOR KINASE 1 (SIRK1), QIAN SHOU KINASE 1 (QSK1) und das PLASMA MEMBRANE INTRINSIC PROTEIN 2;4 (PIP2;4) in präformierten Proteinclustern vorhanden sein könnten; eine Hypothese, welche wir aktuell weiterverfolgen.

Schließlich habe ich an zwei Projekten mitgewirkt, bei welchen wir eine FRET-FLIM-Methode zur Untersuchung von tripartiten Komplexen in lebenden Zellen vorgestellt haben und bei welchen wir klassische Laborexperimente mit computergestützten Modellierungen kombiniert haben um das Verständnis des Brassinosteroid-Signalnetzwerks zu verbessern. Dadurch konnten wir beispielsweise CYCLIC NUCLEOTIDE GATED CHANNEL 10 (CNGC10) als eine neue Komponente dieses Signalwegs identifizieren.

Zusammenfassend stellt diese Arbeit wesentliche methodische und technische Fortschritte sowie Anwendungen vor, die es Pflanzenwissenschaftlern erleichtern werden, die räumlich-zeitliche Organisation von PM-Proteinen effektiver zu erforschen.

Summary

Proteins within the plasma membrane (PM) of plants are not homogenously distributed; rather, they are organized in diverse domains at the nanoscale, which may form molecular nodes. While some aspects of these complexes, such as within protein-protein interactions (PPI) or signaling outputs, are often already known, their spatiotemporal regulation has received comparatively little attention. However, given that studies implicate a pivotal role of these regulations in various signaling cascades, it is of special interest to study these processes in detail, too.

Single-particle tracking (spt) in combination with photoactivated localization microscopy (PALM) provides spatiotemporal information about proteins with high precision. Being well established in non-plant systems, sptPALM has only recently become an emerging technique in plant research and is still under constant improvement and development. We identified two major challenges: (i) The analysis is complicated by multi-step evaluation processes that are carried out by individual software solutions. (ii) The spatiotemporal examination of more than one protein at a time is highly important to understand physiological processes but has so far not been possible using sptPALM in plants. Besides these technical issues, we were also interested in how distinct components of the plant cell influence the organization of PM proteins, namely the cytoskeleton.

In this work, we present an all-in-one software solution that is intuitive and guides the user through all analysis steps. We demonstrated its usability by analyzing a set of proteins with available spatiotemporal information as well as a set of other well-characterized plant PM proteins that were so far not subjected to sptPALM studies. During these studies, the results indicate organ-specific effects and an influence of the plant developmental stage on the diffusion coefficient - aspects that were not yet considered in any other study.

Furthermore, we showed the general usability of two fluorescent proteins (FPs) that would allow for simultaneous dual-color sptPALM studies in plants, namely photoactivatable (PA)-GFP and PATagRFP for the first time.
Next, we proved their actual application in a proof-of-principle study where we analyzed the protein dynamics of two differentially labeled proteins simultaneously. This not only expands the portfolio of available FPs but also allows researchers in the future to, for example, analyze the effect of external stimuli on various protein species at a time.

By studying how the cytoskeleton regulates the plant PM and proteins localized within it, we showed contrary effects of actin filaments and microtubules. The disintegration of actin filaments predominantly results in decreased diffusion coefficients, enlarged protein clusters, and more restricted motion patterns, whereas the manipulation of microtubules leads to increased diffusion,

more unconstrained diffusive behavior, and decreased cluster sizes. With these results, we emphasize the potential unique regulatory function of these distinct cytoskeleton components in plants and thus suggest an altered mechanism for the cytoskeleton-mediated compartmentalization compared to the picket fence model of the animal cell system.

Additionally, I supported researchers in Förster Resonance Energy Transfer (FRET)-Fluorescence Lifetime Imaging Microscopy (FLIM) experiments to understand several signaling pathways. Once more, we show that FRET-FLIM experiments are excellently suited to support and confirm results of other PPI methods and to expand current working models with new insights. Our results suggested, for example, that SUCROSE-INDUCED RECEPTOR KINASE 1 (SIRK1), QIAN SHOU KINASE 1 (QSK1), and the PLASMA MEMBRANE INTRINSIC PROTEIN 2;4 (PIP2;4) may be present in the PM in pre-formed protein clusters; a hypothesis we currently pursue.

Lastly, I contributed to two projects where we established a FRET-FLIM method to study tripartite complexes in vivo and where we combined classic “wetlab” experiments with computational modeling to enhance the understanding of the brassinosteroid signaling network. By doing so, we, for example, identified CYCLIC NUCLEOTIDE GATED CHANNEL 10 (CNGC10) as a new component of this signaling pathway.

Overall, this work presents notable method- and technique-based advancements as well as applications that facilitate molecular plant scientists to explore the spatiotemporal organization of PM proteins more effectively.

List of Publications

Plasma Membrane Protein Dynamics and Nanoscale Organization

Accepted

1. **Rohr et al., 2024**: OneFlowTraX: a user-friendly software for super-resolution analysis of single-molecule dynamics and nanoscale organization. *Frontiers in Plant Science*.
   doi: https://doi.org/10.3389/fpls.2024.1358935

Submitted

2. **Rohr et al., 2024**: Simultaneous and Dynamic Super-Resolution Imaging of Two Proteins in *Arabidopsis thaliana* using dual-color sptPALM. *Preprint on bioRxiv*.
   doi: https://doi.org/10.1101/2024.03.13.584811
3. **Rohr et al., 2024**: Contrasting Effects of Cytoskeleton Disruption on Plasma Membrane Receptor Dynamics: Insights from Single-Molecule Analyses. *Preprint on bioRxiv*.
   doi: https://doi.org/10.1101/2024.09.09.612020

FRET-FLIM for Analyzing Complex Composition and Function

Accepted

4. **Gilbert et al., 2021**: Comparison of path-based centrality measures in protein-protein interaction networks revealed proteins with phenotypic relevance during adaptation to changing nitrogen environments. *Journal of Proteomics*.
   doi: https://doi.org/10.1016/j.jprot.2021.104114
5. **Wang et al., 2022**: PEP7 acts as a peptide ligand for the receptor kinase SIRK1 to regulate aquaporin-mediated water influx and lateral root growth. *Molecular Plant.*
   doi: https://doi.org/10.1016/j.molp.2022.09.016

Others

Accepted

6. **Glöckner et al., 2022**: Three-Fluorophore FRET Enables the Analysis of Ternary Protein Association in Living Plant Cells. *Plants (Basel)*.
   doi: https://doi.org/10.3390%2Fplants11192630

7. **Großeholz et al., 2022**: Computational modeling and quantitative physiology reveal central parameters for brassinosteroid-regulated early cell physiological processes linked to elongation growth of the *Arabidopsis* root. *Elife*.
   doi: https://doi.org/10.7554/elife.73031

Scientific Contributions

1. **<u>Rohr L.</u>, Ehinger A., Rausch L., Glöckner Burmeister N., Meixner A. J., Gronnier J., Harter K., Kemmerling B., zur Oven-Krockhaus S. (2024)**

   I conducted most of the construct cloning and generated the majority of the plant lines used in this study. I performed most of the sptPALM measurements and all subsequent analyses. Throughout the project, I designed and executed several experimental setups. Additionally, I wrote the original draft and was involved in the reviewing and editing process. I also designed and generated the figures representing the measurements. The curation of biological data was under my responsibility. Other resources were generated or provided by Dr. Alexandra Ehinger and Dr. Nina Glöckner Burmeister. Luiselotte Rausch conducted a few measurements and performed their subsequent formal analysis. Dr. Sven zur Oven-Krockhaus designed and programmed the OneFlowTraX software and was responsible for the microscope setup. He also conceptualized the project, conducted a few measurements, and created the figures related to the software and setup.

2. **<u>Rohr L.</u>, Ehinger A., Glöckner Burmeister N., Meixner A. J., Kemmerling B., Harter K., zur Oven-Krockhaus S. (2024)**

   I was responsible for the majority of the construct cloning and the generation of all plant lines utilized in this study. I established the functional use of the two novel fluorescent proteins (PA-GFP and PATagRFP) for simultaneous sptPALM measurements in *Arabidopsis thaliana*, including several optimization steps throughout the project. I conducted the majority of the measurements, analyzed the data, and generated the respective figure. Dr. Alexandra Ehinger and Dr. Nina Glöckner Burmeister provided or generated a few constructs and resources, and also performed initial experiments and tests. Dr. Sven zur Oven-Krockhaus carried out some replicate measurements and designed the research setup and provided the microscope environment. The original manuscript draft was written by me, Dr. Sven zur Oven-Krockhaus and Prof. Dr. Klaus Harter.

3. **<u>Rohr L.</u>, Rausch L., Harter K. and zur Oven-Krockhaus S. (2024)**

   I was responsible for most of the construct cloning required for the expression of the respective mEos3.2 fusion proteins. I generated and designed all genetically encoded enzymatic tools for the destruction of cytoskeleton components, based on templates provided by Prof. Dr. Alexis Maizel (COS Heidelberg). I confirmed the functionality of these constructs using confocal laser scanning microscopy. I designed the experimental setup for the sptPALM experiments and conducted the majority of the measurements and all data analyses. I also wrote R scripts used in addition to available software solutions. The original draft was written by Prof. Dr. Klaus Harter, Dr. Sven zur Oven-Krockhaus and me. I created all figures. Luiselotte Rausch performed some construct cloning and a few sptPALM measurements. Dr. Sven zur Oven-Krockhaus provided the microscope setup, the software and conducted a few sptPALM measurements.

4. **Gilbert M., Li Z., Wu X. N., <u>Rohr L.</u>, Gombos S., Harter K., Schulze W. X. (2021)**

   I generated the constructs used for the FRET-FLIM experiments, which were performed by me. I also analyzed the FRET-FLIM data and interpreted the results with Prof. Dr. Klaus Harter. Based on these analyses, I created the corresponding figure. Both, Prof. Dr. Klaus Harter and I provided input for the respective manuscript sections and participated in proofreading. The study was conceived by Prof. Dr. Waltraud Schulze.

   Dr. Max Gilbert and co-authors conducted the proteomics experiments, performed their analysis, and generated the network.

5. **Wang J., Xi L., Wu X. N., König S., Rohr L., Neumann T., Weber J., Harter K., Schulze W. X. (2022)**
   I performed the FRET-FLIM experiments with the from Dr. Lin Xi provided constructs (University of Hohenheim). I also analyzed the data and performed preliminary test that are not shown in the publication, such as the evaluation of different light conditions and the application of another non-binding ligand (i.e., PEP6).

6. **Glöckner N., zur Oven-Krockhaus S., Rohr L., Wackenhut F., Burmeister M., Wanke F., Holzwart E., Meixner A. J., Wolf S., Harter K. (2022)**
   Based on the original draft from Dr. Nina Glöckner Burmeister, I collected together already compiled data, re-evaluated them and designed and generated most of the figures. Additionally, I conducted the mathematical and statistical analyses. Together with Dr. Nina Glöckner Burmeister, Dr. Sven zur Oven-Krockhaus and Prof. Dr. Klaus Harter, I wrote the paper.

7. **Großeholz R., Wanke F., Rohr L., Glöckner N., Rausch L., Scholl S., Scacchi E., Spazierer A.-J., Shabala L., Shabala S., Schumacher K., Kummer U., Harter K. (2022)**
   Based on the original draft by Dr. Nina Glöckner Burmeister and Dr. Ruth Großeholz, I was involved in the reviewing and editing process of the final manuscript. I re-evaluated previously compiled data from Dr. Nina Glöckner Burmeister and performed the statistical analyses for all experiments. With the help of Dr. Thomas Denyer (University of Tübingen), I analyzed the developmental trajectories of AHA1, AHA2, BIR3, and BRI1 (i.e., their relative expression against pseudotime). Additionally, I conducted the mating-based split ubiquitin assay and analyzed the results. I also assessed the localization patterns of AHA2-GFP, BIR3-GFP, and BRI1-GFP using confocal laser scanning microscopy. I generated the majority of figures, with the exception of those describing the computational modeling approach. The conceptualization of the modeling approach was conducted by Dr. Ruth Großeholz and other co-authors from Bioquant, Heidelberg.

1 Introduction

Internal and external signaling cues and their integration are essential for all living organisms. This is particularly important for plants, as they cannot avoid unfavorable conditions due to their sessile lifestyle. In this context, a delicate balance between, for instance, defense and developmental (growth) mechanisms is important, which is often facilitated by plasma membrane (PM)-localized receptors that frequently share mutual components [1]. Considering that diverse receptors promote distinct signaling outputs by interacting with a limited subset of co-receptors and other associated proteins, the question of specificity becomes paramount. Although great efforts have been made in recent years and many aspects have been examined, the mechanism is yet not conclusively clarified.

1.1 Cell Surface Receptors Regulate Diverse Functions in Plants

To cope with the diverse demands, plants such as *Arabidopsis thaliana* (*A. thaliana)* make use of more than 600 receptor-like kinases (RLKs) [2] and 60 receptor-like proteins (RLPs) [3-5]. Both types consist of an ectodomain, usually responsible for ligand binding or pattern recognition, a transmembrane domain, and a cytoplasmic part, which is either equipped with a kinase function (RLKs) or not (RLPs). The composition of the ectodomain is very diverse in general, including but not limited to leucin-rich-repeats (LRR), G- or L-lectin, Lysin motifs (LysM), or Malectin in the context of RLKs. RLPs, however, are restricted to the LRR and LysM domains [4]. With more than 200 members, LRR-RLKs are by far the largest subfamily of plant RLKs and therefore the subject of many studies [6]. This also applies to RLPs, where 57 out of 60 identified RLPs belong to LRR-RLPs [3-5].

In the last decades, more and more LRR receptors were characterized and their ligands identified; among them are famous examples such as FLAGELLIN-SENSITIVE 2 (FLS2) or BRASSINOSTEROID INSENSITIVE 1 (BRI1), the receptors for flagellin 22 (flg22) and brassinosteroids (BRs), respectively.

1.1.1 Classical Brassinosteroid Signaling

With the identification of BRI1 nearly 25 years ago, it stands out as one of the best characterized RLKs to date [7] (Figure 1). The BR signaling is initiated when brassinolide (BL) or any other active BR ligand binds to the island domain of BRI1 (or its paralogues BRI1-LIKE1 and BRI1-LIKE3 [8]; not considered in this introduction). This creates a binding interface with its co-receptor BRI1-ASSOCIATED RECEPTOR KINASE 1 (BAK1), and the heterodimer formation between receptor and co-receptor leads to the juxtaposition of the intracellular kinase domains and the initiation of trans- and autophosphorylation events [9, 10]. Additionally, inhibitory factors dissociate from the involved components upon phosphorylation. Among those, the BRI1 KINASE

INHIBITOR 1 (BKI1) [11] and BOTRYTIS-INDUCED KINASE 1 (BIK1) [12], as well as the BAK1-interacting receptor like kinase 3 (BIR3) [13], play crucial roles. While BKI1 and BIK1 negatively regulate BRI1 in the absence of a ligand, during the inactivity of the BR pathway, BIR3 sequesters BAK1 away from BRI1, preventing the complex formation of BRI1 and BAK1 in the absence of BRs. With ligand binding, the affinity of BAK1 is shifted towards BRI1 and enables complex activation. Interestingly, BIR3 not exclusively binds to BAK1 but also to BRI1, suggesting the existence of additional BIR3-dependent regulatory mechanisms [13, 14] (Figure 1B).

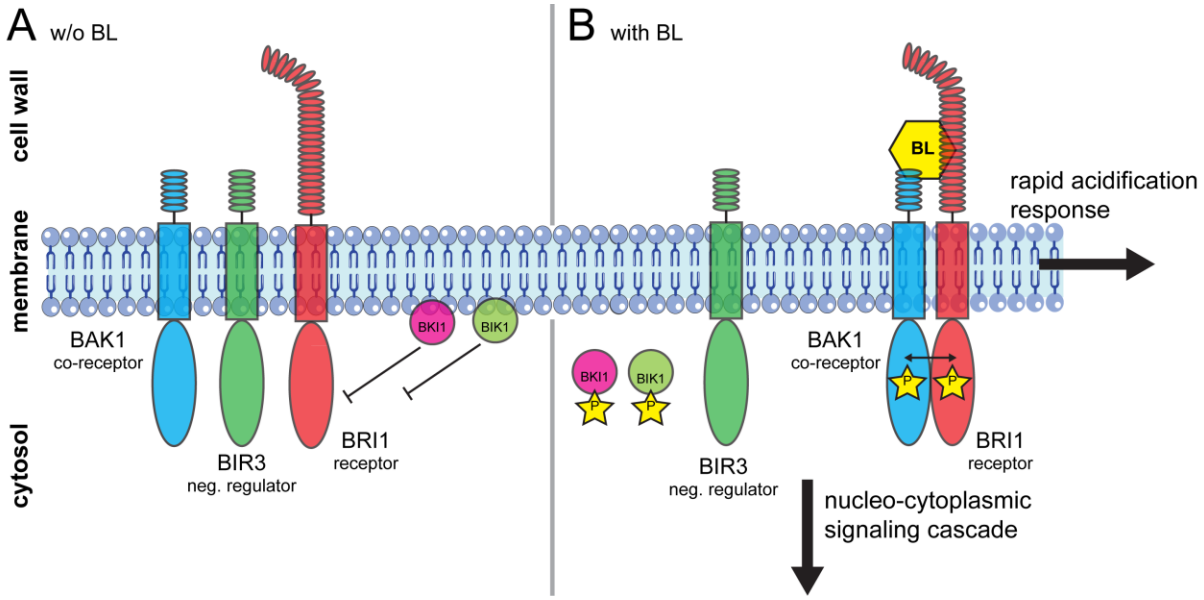

Figure 1 | Schematic overview of the key components and processes during the initiation of brassinosteroid signaling.
(A) Inactive state: In the absence of an active ligand, the components co-localize in a preformed nano-organized complex at the PM. The co-receptor BAK1 is sequestered away from BRI1 by BIR3 which prevents interaction. The activity of BRI1 is negatively regulated by numerous protein partners, such as BIK1 or BKI1, which all interact with BRI1 when the BR pathway is not active. **(B)** Active state: Upon the binding of BL (or any other active ligand) to the island domain of BRI1, BIR3 releases BAK1, and BKI1 and BIK1 are phosphorylated (i.e., losing their inhibitor function), resulting in active BRI1-BAK1 heterodimers. This leads to the juxtaposition of their intracellular domains and trans- and autophosphorylation events. An active BRI1-BAK1 complex fulfills several functions. The canonical functions can be divided into two main responses: (i) a nucleo-cytoplasmic singling cascade (Figure 2A) and (ii) a rapid acidification at the PM (Figure 2B).

Adapted from [15]

The canonical functions of BRI1 can be divided into two main responses: (i) differential regulation of BR responsive genes via a nucleo-cytoplasmic signaling cascade [16-19] (Figure 2A) and (ii) a rapid acidification response of the apoplast that includes, among others, the activation of PM-resident P-type proton pumps [20, 21] (Figure 2B).

During the nucleo-cytoplasmic signaling cascade, the negative regulator BRASSINOSTEROID INSENSITIVE 2 (BIN2) is inactivated and degraded, preventing it to phosphorylate BR-responsive transcription factors such as BRASSINAZOLE-RESISTANT 1 (BZR1) and BRI1-EMS-

SUPPRESSOR 1 (BES1). As a consequence, the transcription factors undergo dephosphorylation, leading to their release from cytosolic sequestration, a process orchestrated by 14-3-3 proteins. Subsequently, BES1 and BZR1 translocate to the nucleus, where they modify the expression of BR-responsive genes about 30 minutes after exogenous BR application (Figure 2A).
Both have a large number of direct target genes in the *Arabidopsis* genome, including over 3000 high-confidence BZR1 targets and over 1000 putative BES1 targets [22, 23]. Among those genes, CELLULOSE SYNTHASE GENES (CESAs) are one of the most famous examples [24]; but also, less prominent components, such as MICROTUBULE DESTABILIZING PROTEIN 40 (MDP40), are regulated via BZR1 to regulate BR-dependent hypocotyl cell elongation [25].

In contrast to the relatively slow transcriptional regulation, the apoplast's rapid acidification response is also regulated by BRs [20, 21] (Figure 2B). The initial steps are comparable to those previously described. However, the formation of the active BRI1-BAK1 complex facilitates the activity of the PM proton ATPases (e.g., PM *Arabidopsis* H^+-ATPase isoform 1 (AHA1) and AHA2), resulting in apoplast acidification, PM hyperpolarization, cell wall swelling and subsequent cell elongation [20, 26, 27]. In a recent study [15], this response module was expanded by the addition of another component from the cyclic nucleotide-gated channel (CNGC) family, which is discussed in greater detail in chapter 3.3.2.

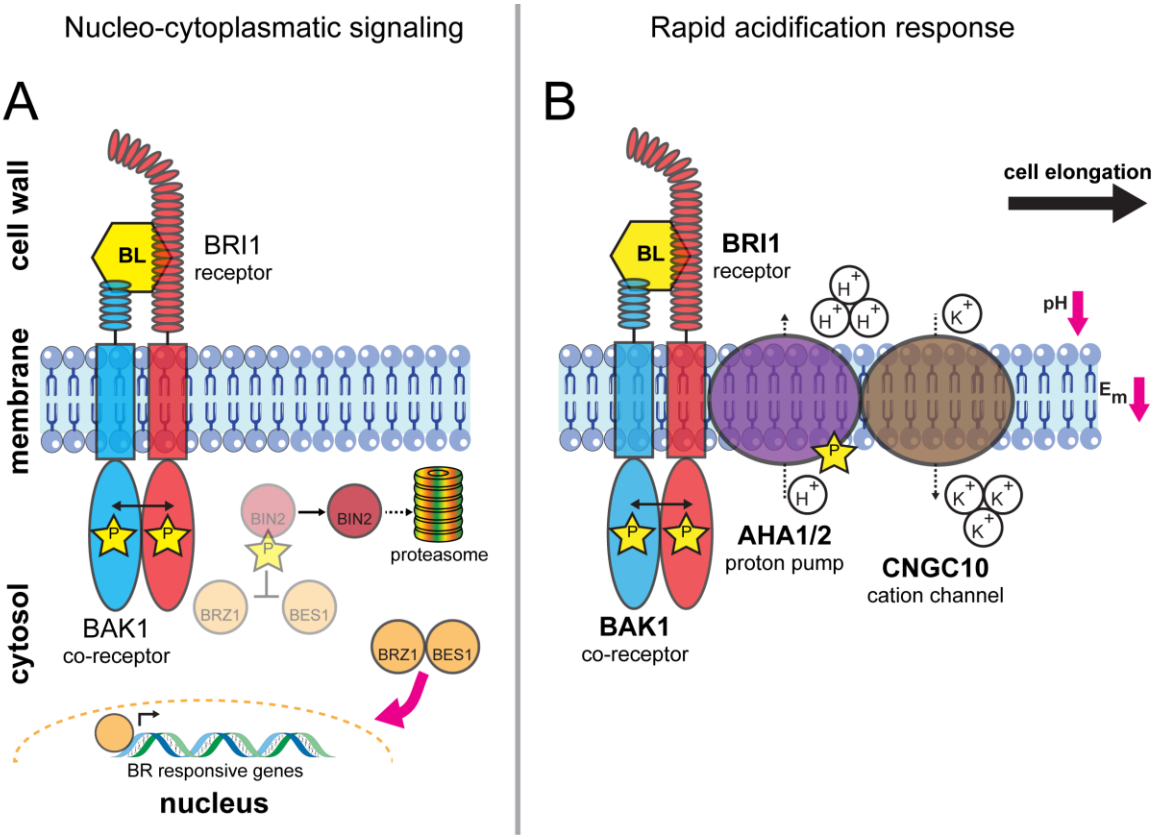

Figure 2 | Main responses of the canonical functions of the brassinosteroid signaling pathway.
(A) Nucleo-cytoplasmic signaling cascade after brassinosteroid perception. After the activation of the BRI1-BAK1 complex (Figure 1), BIN2, another negative regulator, is degraded by the proteasome. In the absence of a ligand, BIN2 is phosphorylated and keeps BR responsive transcription factors, such as BZR1 or BES1, inactive in the cytosol. Consequently, upon the degradation of BIN2, the transcription factors can be dephosphorylated and are released from their cytosolic sequestration, translocating into the nucleus, where they facilitate the expression of BR-responsive genes. **(B)** Rapid acidification response. With the receptor complex activated, it can furthermore facilitate the activity of the PM proton ATPases (AHA1/2), likely by phosphorylation. This in turn induces the acidification (i.e., decrease in pH) of the apoplastic space by the export of protons and leads to the hyperpolarization of the PM's membrane potential that becomes more negative. This allows for cell wall swelling and cell elongation, according to the acid-growth theory. Recently, CNGC10 was identified to compensate for positive charges when protons are transported towards extracellular spaces. The process is fast since cell wall swelling occurs within 10 minutes after BR application.

1.1.2 Non-Canonical Brassinosteroid Signaling and Integration of Other Pathways

In addition to the classical functions (see chapter 1.1.1), more and more non-canonical connections of BR signaling to other signaling pathways have become the focus of recent studies. For example, it was shown that BRI1 is involved in sensing cell wall integrity [28] and that this process is regulated via an additional component, namely RLP44 [29]. The exact mechanism is not fully understood, but RLP44 might occupy pectate (i.e., demethylesterified pectin), which is limited under certain conditions. As a consequence of its limitation, RLP44 is released and freely available to interact with its downstream components, such as BRI1 [30]. Nevertheless, it cannot be entirely excluded that RLP44 itself may be a downstream component of a cell wall integrity response module, with sensing occurring via other elements [29]. In both cases, cell wall cues are sensed by

RLP44 or another factor, which results in the activation of a compensatory BR signaling pathway [28]. In this cascade, RLP44 can interact directly with both BRI1 and its co-receptor BAK1, likely stabilizing this complex and acting as a scaffold [31, 32]. With an elegant approach, we showed in Glöckner*, et al.* [31] that BRI1, BAK1 and RLP44 form a tripartite protein complex. The approach and the resulting findings are presented and discussed in detail in chapter 3.3.1.
However, RLP44's role in interacting with BRI1 is not only restricted to cell wall integrity; it also controls vascular cell fate in the *Arabidopsis* root through its interplay with phytosulfokine (PSK) signaling [32]. Phytosulfokines are small plant peptide hormones [33] and are recognized by LRR-RLKs, namely PHYTOSULFOKINE RECEPTOR 1 (PSKR1) and PSKR2 [34, 35], which show high structural similarity to BRI1 and use BAK1 as co-receptor, too [36]. Comparable to BRI1's fast response module, PSKR1 interacts with P-type proton pumps and activates CNGC17, which lead to cell swelling and expansion [36]. In addition, the PSK receptors are involved in defense responses, as mutants exhibit antagonistic effects to bacterial and necrotrophic fungal infections. Independent loss-of-function mutants show increased resistance to biotrophic bacteria but are more susceptible to necrotrophic fungal infection [37, 38].
One of the most recent findings is the involvement of RLP44 in the maintenance of procambial cell identity [32]. It was shown that PSK signaling is necessary for xylem cell fate, with this process being controlled by RLP44. Interestingly, RLP44 promotes the complex formation of PSKR1 and BRI1 with their co-receptor BAK1, suggesting that RLP44 might act as a scaffold in this context. Additionally, RLP44 can interact with PSKR1, too. While the BRI1-RLP44 interaction might not be necessary for cell fate determination, BRI1 transcriptionally controls the RLP44 amount and, thus, is required for PSK signaling that maintains the procambial cell fate.

1.2 Signaling Components are Organized in Nanodomains

A plant mesophyll cell contains approximately 25 billion protein molecules, with approximately 200 millions of these located in the PM [39]. These impressive numbers, together with the above-shown sceneries, where distinct pathways share common components, highlight the requirement of a mechanism that ensures quick, efficient, precise, and specific signal transduction from the PM to the nucleus. Advanced imaging techniques revealed that plant membrane proteins are actually located into nanodomains [40-44]. This suggestion is derived from several models originated from other non-plant model organisms, with the famous "fluid mosaic model" being the initial concept [45]. The model assumes that proteins can laterally diffuse within the membrane without major restrictions. However, this would result in uniformly distributed membrane-embedded receptors independent of the entire PM proteome, which is a clear contradiction to the observed data. An expansion of this model was introduced by Simons and Ikonen [46], who proposed the existence of "lipid rafts" that contain high levels of cholesterol and sphingolipids and serve as platforms with a high molecular order of proteins and lipids. Originating from the mammalian

field, the model later found acceptance in plant science as well [47-51]. These studies revealed that membranes are partitioned binarily into detergent-resistant and detergent-sensitive fractions and that their protein profiles are distinct. However, the isolation of detergent-resistant fractions and the detergents themselves may induce changes in the PM properties and results derived from the application of newer techniques question whether detergent-resistant membranes indeed define functional "membrane rafts". To decipher the nature of compartmentalization, the further development of modern imaging techniques enabled a more detailed view. It was shown that plant and fungal membrane microdomains are quite stable in location; thus, concerns were expressed about defining those regions as "lipid rafts". This is based on the fact that rafts, after all, are supposed to be moving. In consequence, such regions are now referred to as "micro- or nanodomains" [40, 41, 52-54]. While there is no commonly accepted definition of nanodomains, Ott [52] proposed the following concept for plants: Nanodomains are small protein- and/or lipid-based assemblies in the sub-micrometer range that consist of homomeric or heteromeric protein complexes. These nanodomains can serve as functional nodes for higher-order protein complexes and are dynamic in their structure. They can either move over time or be subject to a permanent protein turnover in which new proteins are recruited into the nanodomains. Proteins within nanodomains exhibit longer residence times, while proteins that are not within nanodomains presumably demonstrate increased lateral mobility.

1.2.1 Nanodomains are Organized by Several Factors

Several factors are thought to be important to organize and maintain nanodomains in plants.
Two groups of proteins are hypothesized to function as scaffolds for receptor complexes at the PM, namely SPFH (stomatin/prohibitin/flotillin/HflK/C) domain proteins and remorins (REMs) [55]. REMs are plant-specific proteins that are recruited to the PM and attached to its inner leaflet, mainly mediated by the REMORIN C-terminal Anchor (REM-CA) [56-58]. For REM1.3 from *Solanum tuberosum*, it was shown that those anchors are necessary to segregate the remorins into nanodomains. Their properties, such as the degree of segregation within the membrane, can be altered by mutations in the REM-CA domain [57]. The actual involvement in the recruitment of receptors to nanodomains by REMs was demonstrated in *Oryza sativa*. The ligand-induced phosphorylation of *Os*REM4.1 by *Os*BRI1 causes the dissociation of *Os*REM4.1 and *Os*SERK1, which allows the receptor to be recruited into *Os*BRI1/*Os*SERK1 signaling complexes [41, 59]. Additionally, REMs also play roles in plant defense, hormone signaling, and developmental processes [60].

The other major group of scaffolding membrane organizing proteins are SPHF-domain containing proteins. In contrast to the plant specific REMs, SPFH-domain-containing proteins are conserved in other taxa as well [61]. In *Arabidopsis*, five groups can be distinguished, which are all

hypothesized to be involved in the regulation and assembly of signaling hubs such as nanodomains [62, 63]. However, it remains elusive how SPFH proteins are targeted to the membrane and how they are recruited into nanodomains [60]. In some cases, members of the REM family mutually act with SPFH proteins. For instance, it was shown that FLOTILLIN 4 recruits REM1 into nanodomains during LYSINE MOTIF KINASE 3 (LYK3) complex formation in *Medicago truncatula* [64].

Another important factor for PM compartmentalization and organization is its lipid composition, as lipids are not uniformly distributed in the PM [41]. The outer membrane leaflet is enriched with plant sphingolipids [65], while the inner leaflet contains mainly phospholipids [66]. Due to these anionic lipids, there is a strong electronegative charge on the inner surface of the PM. This contributes to the specific functional properties of the PM and enables the recruitment of numerous soluble or lipid-anchored proteins [67-69].
Additionally, the lateral separation of PM components within each leaflet plays a crucial role, too. This is reminiscent of the “lipid raft” hypothesis from Kusumi*, et al.* [70], where liquid-ordered phases (enriched in sterols and glycosphingolipids) and disordered phases are present. Recently, it was shown that liquid-ordered phases are relevant for protein localization, as they colocalize with *St*REM1.3. Furthermore, the organization of *St*REM1.3 into nanodomains is dependent on sterols, as such domains are sensitive to the PM sterol composition [57]. This indirectly indicates that sterols participate in the formation of liquid-ordered membrane domains. The molecular basis of the lipid raft hypothesis is complicated by the fact that proteins themselves highly influence the lateral sorting of lipids [71, 72]. Consequently, several questions remain unanswered, and the full extent of lipid segregation in nanodomains remains unknown.

The research on PMs is particularly driven by the development and testing of specialized models, which are crucial for understanding the complex mechanisms and dynamics of this structure. This resulted in the idea of another regulatory mechanism that considers the cytoskeleton as a key organizer, referred to as the picket fence model [70]. Originating from the animal field, the model is suggested to be true for plant cells as well, with minor adjustments (Figure 3). While animals do not possess cortical microtubules, this structure needs to be additionally considered for plant cells. It is suggested that, together with cortical actin filaments, the microtubules define membrane domains that are 40-300 nm in size by acting as a “fence”. The model also postulates the presence of "pickets", which are formed by transmembrane proteins. These are anchored either by the cytoskeleton in the cytosol or in the extracellular matrix. Due to the large number of proteins with an extracellular domain in plants, all of which can act as "pickets," the functional role of specific "pickets" may be overestimated [41].
Several plant PM-localized nanodomain resident proteins are known to directly or indirectly associate with the cytoskeleton, such as FLS2 or BRI1 [40, 73]. Although a global effect and thus a

comparable consequence on all membrane proteins is expected when cytoskeleton components are manipulated, no consistent understanding is available currently.

For example, McKenna, *et al.* [74] showed an impact of the cytoskeleton on the lateral diffusion of some but not all proteins in the PM. Moreover, additional studies revealed a change in or loss of nanodomain organization of proteins after cytoskeleton disruption, again for some but not for all tested proteins [40, 42, 63, 75-78]. Despite these contrary effects, there is strong evidence that the cytoskeleton is involved in the dynamics and spatial organization of PM nanodomains, possibly with a less prominent role than in animal cells [41].

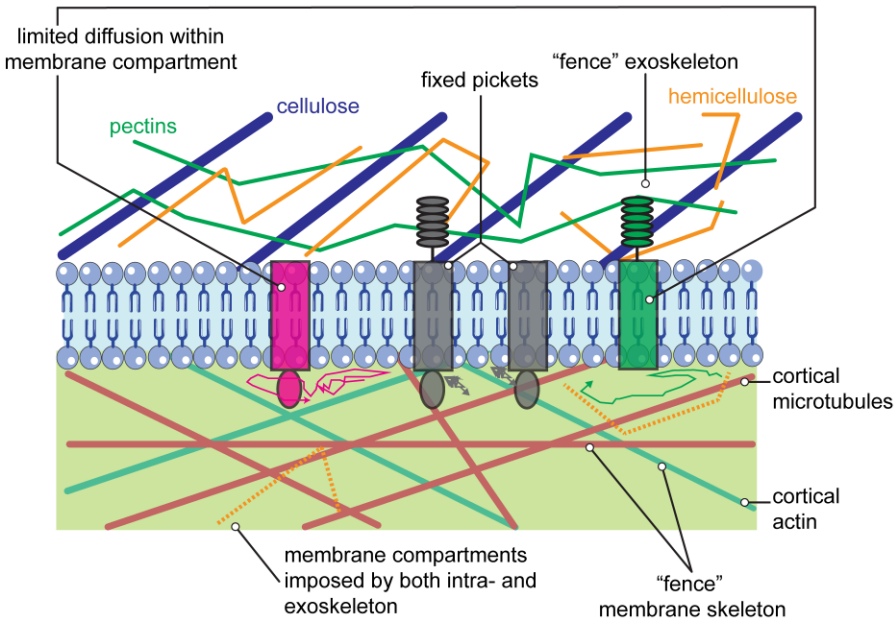

Figure 3 | Schematic overview of the possible revision of the picket fence model in plants.
The picket fence model in plants is likely to involve, besides cortical actin filaments, microtubules as well, both acting as a membrane skeleton "fence". In addition, an exoskeleton "fence" consisting of cell wall components (pectins, cellulose, hemicellulose) is proposed, which may also compartmentalize the membrane (indicated with dashed orange areas). This could explain the limited diffusion of PM proteins. Lines with arrowheads indicate examples of diffusion trajectories of respective PM proteins influenced by several barriers. Transmembrane proteins act as fixed pickets. They are thought to either be anchored by the cytoskeleton in the cytosol or the extracellular matrix. The diffusion of other components (such as lipids) could thus be hindered by the pickets

Adapted from [41]

While the cytoskeleton is proposed to be an important regulator intracellularly, the key component for the extracellular space can be the cell wall. The exceptionally high turgor pressure in plant cells presses the PM to the rigid cell wall, which strongly influences lipid and protein dynamics at the PM-cell wall interface. It was shown that receptors with an extracellular domain display limited lateral diffusion [74, 79] compared to faster diffusing proteins that associate with the inner leaflet of the PM [79]. The essentially immobile nature of plant PM proteins with an extracellular domain is a property that is rarely seen in animal cells and could point to a highly important role

of the plant cell wall regarding the protein diffusion processes in the PM. Undoubtedly, a variety of different approaches in recent publications showed that the manipulation of the PM-cell wall continuum has an impact on protein dynamics and the formation of nanodomains [63, 74, 79].

1.3 Advanced Spectroscopy and Microscopy Techniques Unravel the Spatial, Temporal and Compositional Properties of Proteins and their Complexes

As described above, proteins, their interactors and their behavior are regulated at the nanoscale. To study these processes in detail, appropriate techniques are necessary. In general, microscopy and spectroscopy methods are regarded as distinct disciplines. In classical microscopy, the detected light intensity serves as the main source of information. However, already early developments, such as the use of polarization in microscopy nearly 200 years ago [80], showed that the utilization of other photophysical properties is indispensable for further developments. These properties can be accessed with the help of spectroscopy, which describes the analysis of light-matter interactions. Thus, the combination of spectroscopy and microscopy ("spectromicroscopy") allows for deeper spatiotemporal insights into complex biological processes.

1.3.1 General Concepts of Fluorescent Microscopy and its Background

Humankind is fascinated by things we cannot see with the naked eye. Thus, the development of microscopes was a significant contribution to better understand processes that were previously inaccessible. Moreover, to enhance image quality, it is crucial to distinguish between the signal and the background. One possibility to achieve this is the use of fluorescence microscopy. Here, only certain objects are made visible against an otherwise dark background by labeling them with fluorophores. The following section will introduce the basic concepts of absorption and fluorescence as well as related processes that form the basis for the advanced microscopy methods presented in the subsequent chapters.

Fluorescence refers to the inherent property of molecules to absorb light at a certain wavelength and then emit light at a longer wavelength after a very short time interval. The delay between absorbance and emission is referred to as the fluorescence lifetime (FLT). Most molecules exist in the electronic single ground state S_0 at room temperature. Upon absorbing a photon, the molecule enters an excited state, for example, a vibrational level of the first excited singlet state S_1. However, molecules rapidly relax to lower energy states through various pathways, including internal conversion (IC) and vibrational relaxation (VR). A detailed description of these processes is beyond the scope of this thesis but is explained comprehensively in the literature [81, 82].
In the context of the mentioned processes, fluorescence can be considered the reversal of absorption, whereby the molecule returns to the ground state S_0 by emitting a photon. Non-radiative and

non-coherent VR and IC processes are fast compared to fluorescence and are, in general, already completed before fluorescence occurs within a nanosecond time delay after the absorption. Consequently, fluorescence emission occurs almost exclusively from the lowest vibrational level of S_1, regardless of the energy originally used for excitation, which is also known as Kasha's rule [83]. Conversely, this means that the emission spectra are commonly independent of the excitation wavelength (see Kasha–Vavilov rule; [84]). The spectral red-shift that is observable between the excitation and the emission spectra is due to an energy loss caused by VR after excitation and is commonly known as the Stokes shift [85]. This characteristic is used by spectroscopy techniques that separate the excitation from the emission light with the help of color filters.

1.3.2 Determination of Interactions and Distances by Förster Resonance Energy Transfer and Fluorescence Lifetime Imaging Microscopy

Förster Resonance Energy Transfer (FRET) is a physical concept that, in an interplay with fluorescence microscopy, can give information about distances and interactions/associations between molecules with impressive spatial resolution. FRET describes the energy transfer from a donor fluorophore to an acceptor fluorophore without the emission of a photon. This effect depends on the following three factors: (i) A spectral overlap between the donor emission and the acceptor absorbance spectra, (ii) the distance between donor and acceptor as well as (iii) the relative orientation of their transition dipole moments (Figure 4A). The transfer of energy from the donor to the acceptor can be characterized by the FRET efficiency, which is defined as the proportion of the donor molecules that have transferred their excited state energy to the acceptor molecules. The efficiency increases with the presence of a large spectral overlap described in (i), decreasing intermolecular distance (typically below 10 nm) and is highest for parallel or antiparallel orientation of the transition dipole moments. In this context, the Förster distance (R_0) is the distance between donor and acceptor, where the probability of energy transfer is 50 % (Figure 4A). When the donor transfers energy to the acceptor, the fluorescence intensity of the donor decreases, while the acceptor itself can emit a photon that can be recognized as an increase in fluorescence intensity at a higher wavelength compared to the one from the donor, a property that is made use of during intensity-based FRET assays [86, 87]. A schematic overview of the energy processes is depicted by the Jabłoński diagram in Figure 4B.

In the past decades, concepts have been presented that use FRET as an in vivo concept to study fundamental biological processes [88]. The ability to interact with or associate with other structures is an important feature of proteins from all organisms to fulfill diverse biological functions. With FRET and FRET-related approaches, interactions or associations can be evaluated when proteins of interest are fused to fluorescent markers, such as genetically encoded fluorophores [89]. As described above, intensity-based FRET assays can then be used since FRET only occurs at small distances, which indirectly suggests an interaction or association. However, intensity-based FRET

approaches may not be ideal for biological live-cell applications since the detection of fluorophore intensities is influenced by several factors, such as the excitation power, detection sensitivities, chromophore concentrations, their quantum yields or saturation effects [90, 91]. Thus, precise calibrations and the control of the above-mentioned parameters are necessary, which can be problematic in biological systems where, for example, chromophore concentrations are dependent on the expression levels of the respective fusion proteins.

To overcome these limitations, FRET-FLIM (Fluorescence Lifetime Imaging Microscopy) has emerged as a robust alternative since the approach is not affected by the aforementioned caveats. By measuring the FLT of the donor fluorophore, FRET-FLIM provides a more direct and reliable readout of molecular interactions.

In the presence of an acceptor that offers an alternative relaxation path from the donor to an acceptor, FRET decreases the radiative decay rate of the donor, which can be quantified as an apparently reduced FLT [87, 92] (Figure 4B). Typically, FRET-FLIM experiments are designed as follows: (i) The donor fluorophore fused to a protein of interest is initially evaluated alone. Without the presence of a FRET partner here, the evaluated FLT reflects a control situation. (ii) The same protein-donor fluorophore fusion is co-expressed with a protein-acceptor fluorophore fusion that may be closely associated with the protein fused to the donor. In the case of an interaction or spatial proximity, FRET occurs, which can be read out as a decrease in the FLT of the donor (Figure 4B). In contrast, comparable FLTs to (i) can be observed when no close association (i.e., no FRET) is present.

(iii) As a negative control, the protein-donor fluorophore fusion is co-expressed with a known non-associating protein-acceptor fluorophore fusion. In consequence, no change in the FLT is expected, comparable with (i). Decreased FLTs in (ii) that significantly differ from the control situation in (i) indicate an association between the proteins. However, in general, caution is advised, as an association based on reduced FLTs do not necessarily confirm an interaction, necessitating additional validation methods.

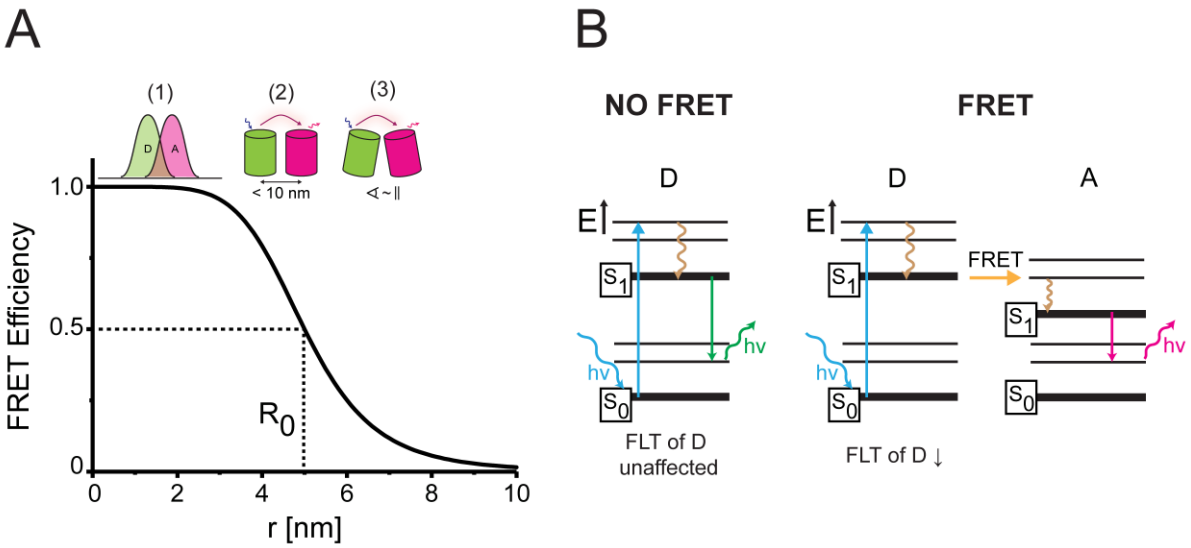

Figure 4 | Schematic overview of FRET-(FLIM) principles and criteria.
(A) Shown is the FRET efficiency plotted against the distance *r* (in nm) between the donor (D) and acceptor (A) molecules. The distance at which the probability of energy transfer is 50 % is defined as the Förster distance R_0 (here: 5 nm). The FRET efficiency mainly depends on three factors: (i) The spectral overlap between donor emission and acceptor excitation, (ii) the distance between D and A, typically below 10 nm, and (iii) the relative orientations of the respective dipoles of D and A. The more optimal these factors are, the higher the FRET efficiency.
(B) Schematic depictions of the energy flow in the absence or presence of FRET, illustrated by Jabłoński diagrams. Left: Energy flow in the absence of FRET. Upon the absorption of a photon (*hv*), the donor molecule enters an excited state (blue arrow, S_1) and relaxes relatively fast by vibrational relaxation (VR, brown arrow). Subsequently, the molecule can return to its ground state (S_0) by fluorescence (green arrow), emitting a photon (*hv*). The fluorescence lifetime (FLT) of the donor is unaffected. Right: Energy flow in the presence of FRET with the same color code. In the presence of an acceptor, the donor transfers energy to the acceptor instead of emitting a photon. The acceptor then becomes excited and can then return to its ground state by fluorescence (red arrow), emitting a photon (*hv*). The process influences the FLT of the donor by decreasing it.

A striking advantage of FRET-FLIM studies compared to other interaction assays is their ability to uncover both steady-state and dynamic interaction processes of protein complexes [93, 94]. Cell structures, such as the PM, do not show a homogenous distribution of components; thus, it is evident that not every investigated protein has access to its putative interaction partner. In consequence, mixtures of donor subpopulations will appear with different FLTs, indicating that the donor is present in differently composed complexes. For the analysis process, several proprietary software solutions are available to extract the FLT. However, the processes behind the software calculations (i.e., from raw data to FLTs) are beyond the scope of this thesis. They are discussed in detail in the literature [95, 96].

In plant science, FRET, FRET-FLIM and related approaches have emerged relatively recently, with increasing numbers of publications in the late 2000s (see Web of Science keyword search, April 2024 [97]). In addition, the method was designed for bipartite protein interactions. This however, exacerbates to account for actual biological processes, which require the involvement of more than two proteins [98]. While an adequate approach was already introduced in the animal field in 2010 [99], the delay of integrating novel technologies into plant science was present here

as well [100] until a triple FRET method was presented [31], which is discussed in detail in chapter 3.3.1

1.3.3 Plasma Membrane Protein Dynamics and Nanoscale Organization

The plant PM serves as the interface between intracellular and extracellular signals, enabling highly dynamic processes that are primarily regulated by heterogeneously distributed membrane-localized or associated proteins (see chapter 1.1). In order to elucidate the underlying processes, the time-dependent analysis of individual molecules (proteins) is essential. This can be achieved with a concept named single-particle tracking (spt). Here, the precise localization of single fluorescent molecule fusions is highly important. Due to the diffraction limit, a point source of light (e.g., a single emitter fluorophore) in the sample plane will appear much larger in the image plane in a lens-based microscope, which is described by the point spread function (PSF). The resulting pattern, known as Airy pattern, is characterized by a central peak of typically 200 nm in width, which represents the limit of resolving two neighboring points or structures. Nevertheless, single emitters can be localized with much higher precision up to 20 nm as long as overlap with neighboring PSFs is avoided [101]. This can be done, for example, with the help of special fluorophores, an approach that is described in detail in chapter 1.3.3.1. The spatial isolation of emitters with non-overlapping PSFs then allows for the single-molecule detection and their localization with high spatial precision, which is performed computationally. For successful detection, a high signal-to-noise ratio is crucial so that algorithms can differentiate between pixel regions with potential fluorescence emitters and background noise. In the localization step, the pixel regions determined before are analyzed further to compute the subpixel coordinates of each molecule [102-104]. The detailed processes are beyond the scope of this thesis but are introduced comprehensively in the literature [102, 105-107].

The concept of spt can be combined with photoactivated localization microscopy (PALM) [108], referred to as sptPALM [109]. The next chapters will first introduce special fluorophores that are used in sptPALM approaches to ensure the separation of emitters in time and secondly, the technique itself will be discussed in detail, including application possibilities and examples with a focus on plant cell science.

1.3.3.1 Special Fluorophores with Different Optical States Enable Single-Molecule Detection

To achieve the requirements of spatially separate emitters, special fluorophores are used. Although these fluorophores can also be organic dyes, the following sections will focus on fluorescent proteins (FPs), since the investigation of plants precludes the usage of organic dyes that are applied in other systems [102, 110]. This is mainly due to the presence of the cell wall, which hinders the reliable uptake of synthetic dyes by plant cells [111].

The Green Fluorescent Protein (GFP) has been one of the most widely used FPs in life science since its discovery [112] and its successful demonstration as a genetically encodable fluorescent marker was one of the most striking developments in the last decades [113]. However, with the advent of new technologies, these more conventional fluorophores are no longer optimal for advanced techniques such as sptPALM. Among other factors, this is due to the property that all illuminated FPs are active simultaneously, resulting in the generation of overlapping signals. In consequence, the detection of single molecules is hindered.

An elegant solution is the application of fluorophores with different optical states, which can be categorized by their mode of action: (i) Photoswitchable FPs, (ii) Photoconvertible FPs and (iii) Photoactivatable (PA) -FPs. While the reactions of (i) are reversible, those of (ii) and (iii) are irreversible. They all change their chromophore configuration in response to light of a specific wavelength, resulting in a fluorescent state or a shift in the emission spectrum (Figure 5). With the help of this stochastic transition process, the FP pool can be separated into a subset that can be imaged (i.e., is active) and a subset that is inactive or in a state that is not excited by the wavelength used for imaging [114].

Dronpa [115] and Skylan-NS [116] are two prominent examples of reversible photoswitchable fluorophores. Their native, non-fluorescent state can be converted into a fluorescent active state by irradiation with light of a wavelength of around 400 nm. Additionally, the FPs can be reverted to their dark state. This switching can be performed several times.

One of the most widely applied photoconvertible FPs are mEos variants, such as mEos3.2 [117]. Photoconvertible FPs in general are present in two spectrally different states; in the case of mEos3.2, a native green and a photoconverted red variant. The switch from the green to the red variant is irreversible and performed by irradiation with a 405 nm laser. Thus, the spatial separation is achieved by imaging only the photoconverted red variant. This is possible due to the fact that mEos is predominantly present in the native green variant, so in consequence, the density of the red variant is easier to control.

PA-FPs are naturally in a dark state and are irreversibly converted into an active fluorescent state by illumination with UV light. PA-GFP was identified by screening for amino acid substitutions in GFP that would result in a PA version [118]. The fluorescent active version can then be imaged with properties comparable to classic GFP. Another example is PATagRFP. Its fluorescent active

state exhibits an excitation maximum at 562 nm, comparable to classic RFP. Indeed, a combination of PA-GFP and PATagRFP seems ideal for the simultaneous observations of two proteins with super-resolution microscopy, a topic that is further discussed in chapter 3.1.2.

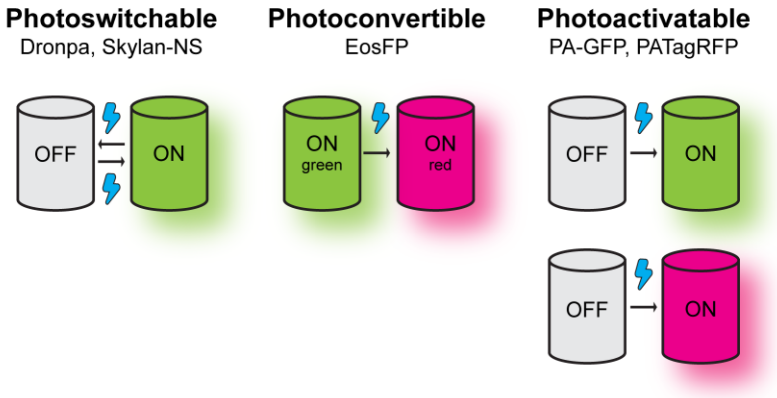

Figure 5 | Schematic overview of different types of fluorescent proteins used in super-resolution microscopy. Grey barrels indicate FPs in their non-emitting "off" state. Green and magenta barrels represent FPs emitting light in the respective colors. Blue flashes illustrate the application of light to switch, convert or activate the different fluorescent states. Photoswitchable FPs, such as Dronpa or Sklyan-NS exist in a native non-fluorescent state and can be converted to an active state. This process is reversible. Photoconvertible FPs like EosFP exist in a native green variant and a red variant. The conversion is initiated by the irradiation of the molecules with light at 405 nm. The process is irreversible. PA-GFP and PATagRFP are two examples for photoactivatable FPs. They naturally exist in a dark state and can be activated by the use of light at 405 nm to obtain their fluorescent active versions.

New fluorophores are constantly being developed for super-resolution microscopy [114, 119]. This, in particular, is advantageous for transferring methods to other organisms or tissues, as this often requires adaptions such as distinct pH optima or specific spectral properties. The challenge of incorporating two fluorophores for super-resolution microscopy in plants is thoroughly examined in chapter 3.1.2.

1.3.3.2 Single-Particle Tracking with PALM (sptPALM) Enables the Investigation of Dynamics and the Spatiotemporal Organization of Single Proteins

The combination of spt with PALM (i.e., sptPALM) was first introduced by Manley*, et al.* [109] and has been widely used ever since. In this approach, a single molecule (e.g., a protein) fused to a fluorophore is tracked for as long as possible, allowing researchers to follow its movement with high spatial (below 100 nm) and temporal (in the range of milliseconds) resolution. As a result, valuable information about the diffusion coefficient and type of movement can be obtained.
For the successful realization of sptPALM experiments, two requirements (among others) are especially important: (i) The application of special fluorophores (see chapter 1.3.3.1). This is of particular interest as PM proteins are very densely packed. In this context, it is important to finely control the proportion of active fluorophores to enable precise localization and tracking. To ensure the longest possible tracking time, relatively low excitation intensities are used to avoid premature photobleaching. Consequently, the resulting low signal intensity must be compensated for by the use of superior detection systems. Furthermore, high frame rates are essential to capture fast, dynamic processes [120]. (ii) High image contrast is also crucial for the detection and precise localization of single emitters. Consequently, sptPALM setups utilize total internal reflection fluorescence (TIRF) microscopy [121, 122]. Unlike epifluorescence microscopy, where light passes through the sample, TIRF reflects light at the coverslip/sample interface. The collimated laser beam, focused off-axis onto the objective's back focal plane, strikes the interface at a critical angle of incidence, causing total reflection and generating an evanescent wave that penetrates the sample, typically between 50 nm and 150 nm in depth. This excites only fluorophores in the vicinity of the interface, reducing out-of-focus light and enhancing image contrast. This approach is optimal for the study of animal cells because they can be grown directly on coverslips, facilitating access to near-surface structures such as the cortical cytoskeleton or PM [123]. However, plant cells are surrounded by walls that keep these structures more than 200 nm away from the interface [124]. To overcome this, experimenters adjust the angle of incidence for optimal contrast. Techniques such as highly inclined and laminated optical sheet (HILO) microscopy [125] and variable-angle epifluorescence microscopy (VAEM) [126] use this principle to achieve higher contrast than classical epifluorescence microscopy, although still less than TIRF microscopy.

If the aforementioned requirements are met, sptPALM experiments can be conducted, and their analysis is typically divided into three principal processes: (i) Localization, (ii) tracking, and (iii) the calculation of motion and diffusion parameters. Furthermore, other types of analysis can be carried out, such as the analysis of the properties of clusters/nanodomains and/or their patterns based on (i) or (ii) [109].

After the acquisition of time-series images, the usual format of sptPALM raw data, further analysis steps are computationally performed by diverse algorithms, presented in the following as a short procedural overview with references to state-of-the-art publications. First, the fluorophore-tagged molecules are localized in each image frame with high spatial precision [127]. In the next step, a tracking algorithm is applied. With this, localizations that were detected and that belong to the same molecule can be connected to form a trajectory [127-129]. Once the tracks are generated, movement and diffusion parameters can be calculated. The mean square displacement (MSD) analysis is currently the most widely used method to extract diffusion coefficients and motion patterns for this type of data [103]. The details of the calculation are discussed in the literature, for example in Saxton and Jacobson [130].

In short, assuming Brownian motion (unrestricted diffusion), the molecule tracks are used for the calculations of the MSD for each time interval that can be applied to the trajectories as follows:

$$MSD\left(t_{lag} = m\Delta t\right) = \frac{1}{N-m}\sum_{i=1}^{N-m}\left[x_j(t_i + m\Delta t) - x_j(t_i)\right]^2$$

In this formula, x_j is the position of the respective molecule j that is sampled at N discrete times at different timepoints t_i. The values for t_{lag} are defined as interval distance (m) multiplied with Δt, which describes the smallest time difference between two localizations, thus the acquisition time of a recorded movie. In consequence, the start of the track and its end determine the largest possible interval. The MSD is typically plotted versus t_{lag} on either a linear-linear or log-log scale [103].

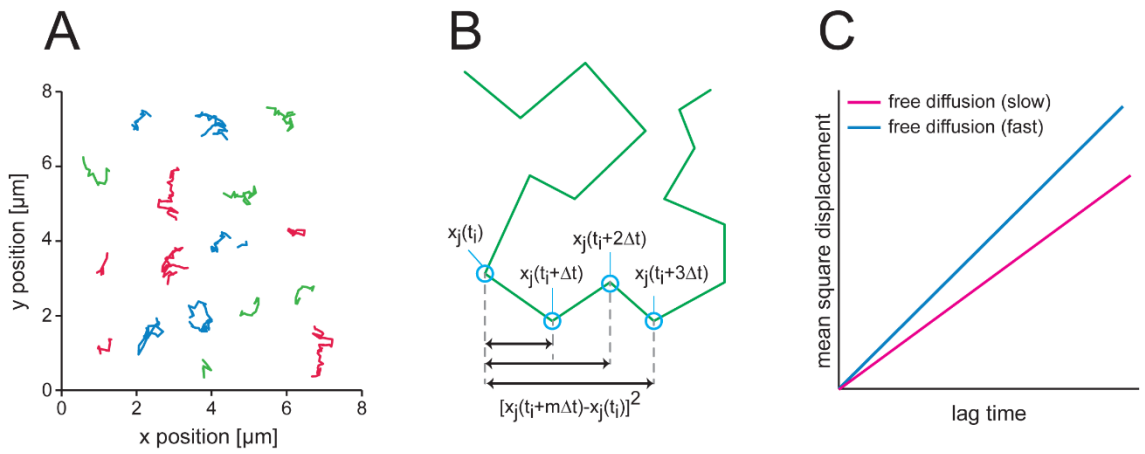

Figure 6 | Molecule trajectory analysis and mean square displacement (MSD) plot.
(A) Exemplary depiction of particle tracks recorded from single fluorescent-tagged proteins moving in a live cell membrane. The tracks are colored randomly. **(B)** Calculation of MSD values for a single molecule trajectory (green) as described in the equation above. **(C)** Exemplary MSD plots of Brownian movement (free diffusion) showing on curve representing slow diffusion (magenta) and one illustrating fast diffusion (blue).

Adapted from [103]

The PM needs to be considered as a two-dimensional structure that restricts, due to its heterogeneous environment, the free diffusion of molecules. Based on this, the diffusion coefficient (D) that is directly linked to the slope of the MSD can be estimated directly by the following formula:

$$MSD\left(t_{lag}\right) = 4Dt_{lag}{}^{\alpha}$$

The introduction of the power law with α, the so-called anomalous exponent, allows for the description of biological systems. Active transport or flow gradients result in $\alpha > 1$, as the molecule is pulled in a certain direction, while $\alpha < 1$ indicates restricted or confined motion, for example, due to the trapping of a protein in membrane subdomains. However, using the MSD-derived anomalous exponent to classify the motion behavior may be challenging. For example most of the MSD-based methods are not able to detect switches from one motion type to another within the same trajectory, although this is a core biological characteristic [131, 132]. Yet, more and more methods and algorithms are developed to overcome this issue [133-137].

Another interesting feature of proteins is their ability to associate into clusters, a process that can be studied by sptPALM-based experiments as well. This has one major advantage, since by doing so, previously recorded mobility data can be directly correlated with their spatial organization and allow for a mutual interpretation. Again, numerous sophisticated algorithms are available for these processes [138]. The following section will provide only a brief overview and will instead refer to the original references and practical applications.

For the determination of plant PM protein clusters, one method has almost exclusively been applied in recent years, namely segmentation via Voronoi diagrams [57, 139, 140]. Two

commonly applied software solutions make use of this approach: (i) SR-Tesseler [141] and (ii) ClusterViSu [142]. Despite their frequent use, the exact selection of parameter values to execute the analyses often remains elusive. Recently, Wallis*, et al.* [143] introduced a different approach. While the majority of other methods are restricted to the centroids or molecule positions, Nanoscale spatiotemporal indexing clustering (NASTIC) specifically uses the complete track as a source for clustering information. So far, the method has not been tested specifically with plant cells, but a proof-of-principle study showed its applicability [144]. It is important to highlight that all methods are based on user-defined parameters that can strongly influence the result. For this reason, when working with these methods, it is generally advisable not to report absolute values for any evaluated parameters but rather relative changes with respect to different treatments or conditions. In addition, all methods require further care since the algorithms tend to overestimate the presence of clusters, even in simulated datasets with high localization density. This phenomenon often occurs imperceptibly, as there is a deficiency in quality control measures to detect it [138, 145].

While live-cell sptPALM measurements in the mammalian field were already performed by Manley*, et al.* [109], the first applications in plant science by Hosy*, et al.* [146] were conducted later. In their proof-of-principle study using mEos2, they investigated the dynamics of different membrane proteins and revealed that they are characterized by distinct dynamic properties. After the publication of these initial studies, the number of sptPALM approaches in the plant field rose in recent years. Among those, Gronnier*, et al.* [57] showed that mutations in the C-terminal domain of REM1.3 alters its mobility and organization in domains, thus being critical for immunity. McKenna*, et al.* [74] investigated the roles of the cell wall and the cytoskeleton on PM protein dynamics and domain organization. Additionally, studies also investigated the influence of external applications of substances, such as auxin. It was shown that the Rho GTPase RHO OF PLANTS 6 (ROP6) is rather mobile under control conditions and changes its behavior upon the addition of auxin, becoming immobile [147]. Very recently, the successful application of sptPALM to proteins localized in the membrane of the endoplasmic reticulum was shown by Pain*, et al.* [148]. These examples clearly demonstrate the role of sptPALM as an emerging technique in plant science. However, during the establishment of the method over the last years in our lab, we faced two major challenges:

(i) As described in detail, the analysis process of sptPALM data is a multi-step process that is based on several distinct methods and algorithms and requires experience and expertise. However, the individual steps of the process have so far been carried out by individual software solutions, including SMAP by Ries [149], TrackMate by Tinevez*, et al.* [129], and sptPALM_viewer by Bayle*, et al.* [120]. The availability of internal laboratory solutions in addition to the programs mentioned above makes it difficult to transfer the data from one step to another. This may

exacerbate to follow the FAIR (Findable, Accessible, Interoperable, Reusable) principle [150], as during import and export processes, data integrity and storage are often problematic. In recent years, this topic has received more and more attention, both in general and in particular with regard to plant science [151] and software design [152]. In order to address the specific needs of sptPALM data evaluation and management, Hugelier*, et al.* [153] identified a significant gap that needs to be filled. They emphasized the importance of creating an open-source tool that brings together algorithms to standardize and simplify evaluation processes. Additionally, they suggested integrating an active feedback system into the pipeline, aiding users in understanding the reliability and robustness of both data and results. This would also lower the threshold for non-experts and improve the reproducibility of the experimental outcome. We developed an all-in-one software that incidentally follows most of the colleagues' suggestions above. The software is discussed in detail in chapter 3.1.1 and led to the publication of OneFlowTraX (see [144]).

(ii) A challenge specific to plant science has been that all previous studies have observed the mobility behavior of only one protein at the single-molecule level at a time. However, as described before, interactions or the complex formation of more than one protein is a main mechanism to achieve and regulate biological processes; thus tracking at least two proteins simultaneously at once via sptPALM is of particular interest. However, the dependence on genetically encoded FP for sptPALM experiments in plants is the main reason why this objective has not yet been achieved. In contrast to other cell systems, synthetically produced organic dyes cannot be used in plant cells [102, 110, 111]. A development of such a dual-color sptPALM for plants will give novel mechanistic insights into the dynamic molecular processes of membrane organizations, e.g., the influence of ligands on receptor/co-receptor pairs. The implementation of two plant codon-optimized FPs for dual-color sptPALM and their successful application are discussed in detail in chapter 3.1.2 and are based on the preprint from Rohr*, et al.* [154].

2 Aim of the Thesis

In recent years, several studies have revealed that plant-PM proteins are heterogeneously distributed and organized in nanodomains. While the members, interactions, and signaling outputs of these complexes are often well described, the spatiotemporal regulation of complex members at the nanoscale may also be of great importance. These modulations can be analyzed using advanced microscopy techniques, such as sptPALM, which provides these spatiotemporal information about proteins with high precision. Although well established in non-plant systems, sptPALM has only recently become an emerging technique in plant research. Consequently, the method is still under constant improvement and development.

My studies aimed to continue the establishment of sptPALM in our research group and to refine and develop further sophisticated aspects. To achieve this, I collaborated with Dr. Sven zur Oven-Krockhaus from the Institute of Physical and Theoretical Chemistry at the University of Tübingen. Two major challenges were identified: (i) The analysis is complicated by being a multi-step process involving several distinct methods that are carried out by individual software solutions. (ii) In plants, observing protein mobility at the single-molecule level has been restricted to one protein at a time. However, understanding physiological processes in detail requires the analysis of more than one protein simultaneously.

The first goal was to develop an all-in-one software solution. The design and programming were executed by Dr. Sven zur Oven-Krockhaus, while the applicability to plant PM proteins was my scientific task. Secondly, the objective was to extend the portfolio of usable FPs for plant sptPALM studies, laying the foundation for dual-color single-molecule observations.

Furthermore, I sought to gain a deeper understanding of the regulation of PM protein dynamics and their organization in nanodomain-like structures. Given the numerous factors that influence this process, I aimed to focus my attention on the role of the cytoskeleton.

PPI studies and the analysis of protein association are powerful methods for understanding signaling pathways. FRET-FLIM approaches enable live-cell observations and are often used to substantiate results obtained by ex vivo methods. With my expertise in plant FRET-FLIM experiments, I aimed to provide support to Dr. Max Gilbert from the University of Hohenheim in validating protein associations predictions made by his path-based centrality measures. Furthermore, I aimed to provide support to Dr. Lin Xi (University of Hohenheim) with FRET-FLIM studies to better understand the processes of SUCROSE-INDUCED RECEPTOR KINASE 1 (SIRK1)-regulated aquaporin-mediated water influx.

In addition, I contributed to two projects that aimed to establish a triple FRET-FLIM method in plant cells and to elucidate the brassinosteroid-regulated rapid cell elongation response. These projects sought to enhance our understanding of brassinosteroid signaling and to introduce a method for studying tripartite protein complexes in general.

3 Results and Discussion

3.1 Plasma Membrane Protein Dynamics and Nanoscale Organization

The regulation of molecular dynamics at the nanoscale is crucial for maintaining accurate biological processes in all living cells. Investigating the underlying functional mechanisms at the molecular level with high spatiotemporal resolution necessitates specialized methods, a challenge further compounded when studying plants. However, recent advancements in microscopy techniques, such as sptPALM, have revolutionized cell biology and now enable the evaluation of such processes [120]. Nevertheless, we identified two major hurdles during our establishment of the sptPALM method:
(i) The post-acquisition analysis is often complex and time-consuming and yet depended on several software solutions [120, 129, 149]. (ii) Previous studies observed the mobility of only one protein at the single-molecule level at a time. However, interactions or complex formations with more than one protein are highly important. To observe such processes, the labeling of proteins with different fluorophores is necessary (e.g., for dual-color sptPALM). Due to the presence of a wall surrounding plant cells, organic dyes that are often applied in other cell systems cannot be used here [102, 110, 111]. Instead, genetically encoded FPs with specific properties need to be used but are, due to their limited number, the bottleneck for the establishment of such a method.

In this section, three publications are introduced. In two of them, I present results obtained by me and my co-workers to solve the above-mentioned hurdles, while the third publication illustrates an application of the sptPALM technique to explore the influence of the cytoskeleton on protein dynamics and nanoscale organization.

3.1.1 OneFlowTraX is a User-Friendly All-In-One Software Solution for the Analysis of Single-Molecule Dynamics and Nanoscale Organization

The following chapter is based on **(1) Rohr et al., 2024:** OneFlowTraX: a user-friendly software for super-resolution analysis of single-molecule dynamics and nanoscale organization (see - 2 -)

Frontiers in Plant Science

More information about my scientific contribution can be found in the respective section (see XIII).

As sptPALM approaches in plant science are still an emerging field, the software was designed, on the one hand, as a user-friendly interface for unexperienced users but also for experts who can modify the source code for their specific requirements.

The software consists of four main tabs: (i) Localization, (ii) Tracking (with mobility analysis), (iii) Cluster Analysis and (iv) Batch Analysis. The first three tabs focus on parameter optimization, quality assessment, and outlier identification, while batch analysis is recommended for large datasets, utilizing pre-determined parameters that were tested in the aforementioned tabs.

For localization and tracking, algorithms that are well accepted in the respective research area were applied and adapted [149, 155]. The localization algorithm is accelerated by employing a graphics processing unit (GPU). However, personal computers, which do not comprise such a unit, can also execute the calculations, albeit with decreased speed. For localization and tracking, OneFlowTraX provides pre-defined parameters that can be used as a starting point without the need for extensive expertise. In addition, OneFlowTraX generates histograms and other visualizations that help the user adjust their parameters to find ideal values or to exclude raw data that may be responsible for significant outliers. A detailed description of the parameters and expected outputs is summarized in the software manual and example datasets are available online.

For the evaluation of the diffusion coefficient based on the track data, OneFlowTraX offers several options: Firstly, the mean MSD over all tracks is calculated and the diffusion coefficient is estimated by a linear fit. Usually, this rather averaged analysis is used as a first impression. A more detailed analysis is provided by a second approach, where the diffusion coefficients are calculated for the MSD curves of all individual tracks and plotted as a histogram distribution. This reveals the possible presence of multiple populations that would remain hidden in the mean MSD plot. Goodness-of-fit thresholds reject inconclusive results, and the final report includes both peak diffusion coefficients and the proportion of multiple populations.

The Cluster Analysis tab allows the spatial organization of molecules to be investigated from single-molecule data. Here, OneFlowTraX provides a variety of available methods that are commonly used in the field, including Voronoi tessellation [141, 142], density-based spatial clustering of applications with noise (DBSCAN) [156] and the recently published NASTIC [143].

The last tab comprises batch analysis, which is the core of OneFlowTraX. This tab allows large datasets to be evaluated quickly (around seven seconds per file with around 30,000 localizations each). For the batch analysis, it is possible to load settings for the parameters previously tested and saved in the other three tabs. After the batch analysis, the results file includes the list of parameters according to the FAIR principles and the results themselves.

While the coding and the design of the software were done by Dr. Sven zur Oven-Krockhaus, I provided the biological material and conducted the measurements to prove the applicability of OneFlowTraX.

To do so, we used protein fusions with FP that are codon-optimized for their application in plants, namely mEos3.2, PA-GFP and PATagRFP. While PA-GFP as well as mEos3.2 and its variants were

used before in plants for sptPALM measurements [57, 74, 146, 157], PATagRFP has not been applied so far. With the successful demonstration of the individual usability of PA-GFP and PATagRFP, we laid the foundation for subsequent dual-color experiments, described in chapter 3.1.2.

In short, we generated constructs with well-characterized PM-localized proteins, such as BRI1 and RLP44, which are expressed under the control of their native promoter. For a quick evaluation, transient expression of the BRI1 fusion proteins in epidermal cells of *Nicotiana benthamiana* (*N. benthamiana*) was used, which resulted in similar outcomes for the tested fluorophores after undergoing the aforementioned analysis steps for the diffusion coefficient. Moreover, stable transgenic *A. thaliana* lines were generated harboring RLP44 fusions with the respective fluorophores. The measurements were performed on epidermal hypocotyl cells. All the analysis steps were completed successfully and resulted in comparable diffusion coefficients. For both plant systems, mEos3.2 had the best signal-to-noise ratio. The general applicability of carrying out cluster analyses was demonstrated by using the NASTIC algorithm.

While the above-described results confirmed the general usability of the FPs and OneFlowTraX, we reproduced observations for Low temperature inducible 6a (LTi6a)-mEos3.2 and PLASMA MEMBRANE INTRINSIC PROTEIN 2;1 (PIP2;1)-mEos3.2 from Hosy*, et al.* [146] to validate the reliability of the software. We additionally showed that differences in the diffusion coefficient between LTi6a and PIP2;1 are more pronounced in epidermal hypocotyl cells than root cells. Moreover, the mobility of LTi6a was significantly higher in the PM of epidermal hypocotyl cells than in epidermal cells of the root. This observation indicates organ-specific differences in protein dynamics that were never addressed before.

Furthermore, we evaluated the impact of light conditions during growth on the diffusion coefficient to examine whether the developmental stage of *A. thaliana* affects protein dynamics. Our results showed that RLP44-mEos3.2 moves significantly faster in the PM of cells located in the upper part of hypocotyls of dark-grown seedlings compared to those in the lower part. The diffusion coefficients obtained in the upper part of the hypocotyls of light-grown seedlings were similar to those obtained from the lower part of the etiolated hypocotyl. This may explain the high data variability we observed when using light-grown seedlings, as accessing specific positions is technically difficult due to the short hypocotyl. Consequently, these findings emphasize the significance of considering the position of measurement, particularly for physiological inquiries.

Exploring dynamic changes following treatments is one major objective of sptPALM studies. To test for the ability of OneFlowTraX to detect such changes, we subjected RLP44-mEos3.2-expressing seedlings to sorbitol, which is known to induce concentration-dependent changes in the diffusion coefficient [44, 146]. Indeed, we were able to reproduce the published findings that increasing plasmolysis enhances the dynamics of PM proteins quantitatively for RLP44-mEos3.2 as well.

In consequence, we demonstrated that OneFlowTraX is able to resolve dynamic changes between treatments.

In summary, with OneFlowTraX, we presented an all-in-one software solution for the evaluation of sptPALM data. The establishment of our software incidentally followed the suggestions from Hugelier, *et al.* [153]. The authors emphasized the need for an open-source tool that combines all the needed algorithms to simplify the data evaluation process and suggested the integration of a feedback system to allow the user to interpret intermediate data.
While the initial focus was on plant PM proteins, OneFlowTraX is usable for various applications, including post-acquisition processing of non-plasma membrane-related processes in both prokaryotic and eukaryotic cells. In addition, we laid the foundation for dual-color sptPALM in plants with the introduction of a compatible FP-pair, namely PA-GFP and PATagRFP.

The successful proof-of-principle implementation of a dual-color approach is described in the following section.

3.1.2 Dual-Color sptPALM Opens New Possibilities to Study the Dynamics of Two Proteins Simultaneously in *A. thaliana*

The following chapter summarizes and discusses **(2) Rohr et al., 2024**: Simultaneous and Dynamic Super-Resolution Imaging of Two Proteins in *Arabidopsis thaliana* using dual-color sptPALM (see - 17 -)

Preprint on bioRxiv

More information about my scientific contribution can be found in the respective section (see XIII).

Previous investigations focusing on the dynamics and sub-compartmentalization of two proteins used classical fluorophores, such as GFP and RFP/mCherry [40, 158]. However, this approach is not ideal for single-molecule analyses, as using these fluorophores can result in the illumination of protein congregations, leading to the observation of homomultimers instead of single-molecules.

In Rohr, *et al.* [144] (see chapter 3.1.1), we introduced PATagRFP as a red-spectrum PA-FP that is spectrally well distinguishable from PA-GFP. The single application of PATagRFP and PA-GFP in *N. benthamiana* and *A. thaliana* was shown, too. Although their general usability expands the available portfolio, the main research interest lies in their simultaneous use. This is because spatiotemporal observation of two or more differentially labeled proteins is of great interest in understanding the dynamics within membrane nanodomains and the nanoscale reorganization of receptor complexes upon ligand perception.

Within the here-described publication, we confirm that PA-GFP and PATagRFP behave identically when acquired in the same *A. thaliana* cell. For this proof-of-principle study, we selected a plant line that was created by crossing pRLP44::RLP44-PA-GFP and pRLP44::RLP44-PATagRFP. The measurements were conducted using light-grown epidermal hypocotyl cells from seven-day-old seedlings grown on ½ Murashige and Skoog media supplemented with 1% sucrose. The specimen's signal was split into two optical paths (green and red) by a dichroic beam splitter and then projected side-by-side onto a single scientific complementary metal-oxide semiconductor (sCMOS) camera chip. The provided movies were pre-processed for OneFlowTraX analysis and separated into two files, representing the green and red channels, respectively. The super-resolved trajectories of the corresponding fusion proteins were generated using files containing over 1,500 frames each, recorded at 20 Hz and analyzed by applying filtering thresholds commonly used in the field [120, 144, 146]. As a result, we observed tracks with similar heterogenous spatial patterns within the PM for both fusions, as is characteristic for numerous proteins [41, 144]. The diffusion coefficients were extracted based on the MSD. We observed a bell-shaped distribution of the decadic logarithm of the diffusion coefficients for both simultaneously recorded fusion proteins, suggesting singular RLP44 populations. The distribution of track data was analyzed using a normal distribution to extract the absolute values of the diffusion coefficient (in $\mu m^2/s$) for each cell, as previously described [144, 146]. We observed no significant differences (Mann-Whitney-U-Test, $p = 0.8282$) for the diffusion coefficients, with means (± standard deviation) of 0.0203 ± 0.00617 $\mu m^2/s$ for RLP44-PA-GFP and 0.0205 ± 0.00587 $\mu m^2/s$ for RLP44-PATagRFP. Consequently, the selected FPs are an excellent choice for dual-color sptPALM since the behavior of the protein is not affected by the FP, and they can be interchanged without altering the diffusion behavior of the fusion proteins. Our results demonstrate that PA-GFP and PATagRFP offer high image contrast during data acquisition, enabling precise detection and localization. Their photophysical properties, such as photostability, allow for the recording of tracks with sufficient length for statistical analysis. Their spectral separability makes the implementation of live-cell dual-color sptPALM feasible, opening up new possibilities for the simultaneous study of two proteins in one and the same living plant cells. This will broaden the understanding of molecule dynamics within the plant plasma membrane.

The following parenthesis was not part of the discussed preprint. However, recently acquired data give interesting insights into the future direction of the dual-color approach and potential refinements.

We showed in the meantime that the presented proof-of-principle study can be extended to other proteins as well (data not shown). We were able to simultaneously observe BRI1-PA-GFP and

RLP44-PATagRFP, where significant differences in mobility were detected, as previously shown for these proteins, albeit fused to mEos3.2 [144].
Despite the evaluation of the mobility of certain proteins, their aggregation in clusters is of great interest, too. By using protein fusions that are known to interact with each other, it is expected that a majority of the detected clusters from both channels show high co-localization rates. We generated cluster maps from both channels for all recorded movies (data not shown) and overlaid them. Contrary to our expectations, we observed sparse co-localization and a shift of red clusters to the right-hand side. We assume that this is a technical issue caused by illumination problems rather than a biological one due to its consistent appearance. Therefore, this obstacle will be one of the highest-priority problems for the future to solve. Based on a recent publication from the Ries Lab [159], adaptations of the microscope setup are planned to homogenize the illumination. In addition, the observation of cluster co-localization may be affected by the recording time. Initially, we decided on 1,500 frames due to several technical and biological obstacles as well as for memory-saving reasons. However, by now, after optimization processes, longer recording times may be feasible. As sptPALM experiments are based on the stochastic activation of FPs, the recording time can significantly affect the robustness of cluster detection via the algorithms. Thus, longer recording times are likely to result in the detection of more co-localizing clusters, as a short recording time may not activate enough FPs in both channels in the same area. Therefore, in addition to minor setup changes, a prolonged recording time can be tested.

In summary, with the successful implementation of a dual-color sptPALM approach in plants, we have provided a technique that allows the simultaneous observation of the mobility dynamics of two proteins within the same plant cell, a technique that was previously limited to non-plant organisms. With further adjustments to the optical system, we believe that multi-channel cluster analysis, which is currently aggravated, may be feasible.

3.1.3 Single-Molecule Analyses Reveal Insights About the Contrasting Effects of Cytoskeleton Disruption on Plasma Membrane Receptor Dynamics

The following chapter is based on **(3) Rohr et al., 2024:** Contrasting Effects of Cytoskeleton Disruption on Plasma Membrane Receptor Dynamics: Insights from Single Molecule Analyses (see - 31 -)

Preprint on bioRxiv

More information about my scientific contribution can be found in the respective section (see XIV).

While chapter 3.1.1 and chapter 3.1.2 introduced method-based publications, the following section summarizes and discusses the application of sptPALM to a specific research question.

In this publication, we characterized the influence of the cytoskeleton on the dynamics and nanoscale organization of proteins in the PM of plant cells using several sptPALM-based analysis methods.

The PM, together with the cell wall, is the first selective barrier between the cell and the environment and has a fundamental function during diverse processes. The organization of the PM is influenced by several factors, such as scaffolding proteins, lipids, the cell wall, or the cytoskeleton. All of those are proposed to be involved in the regulation of nanodomains, structures that can serve as functional nodes for higher-order protein complexes [41, 160].

Here, we focused our research on the cytoskeleton, which is considered a key PM organizer. The so-called picket fence model [70] was originally postulated for the animal field, and it is discussed whether it is a viable model for plant cells as well [41].

In short, it is suggested that cortical actin filaments together with cortical microtubules define PM domains that are 40-300 nm in size by acting as “fences”. The model also suggests the presence of “pickets”, which are formed by transmembrane proteins. In consequence, it is assumed that membrane proteins are constrained in their motion by the presence of such “fences” and “pickets”.

To test whether the picket fence model is transferable to the plant cell system as well, we made use of genetically encoded enzymatic tools that can manipulate actin and microtubule integrity, namely the *Salmonella enterica* effector *Salmonella* virulence plasmid B protein (SpvB) (for actin) and a truncated version of the atypical tubulin kinase PROPYZAMIDE HYPERSENSITIVE 1 (PHS1ΔP) (for microtubules) [161-163], and we evaluated three parameters based on sptPALM experiments. More specifically, we tested the impact of the cytoskeleton destruction on: (i) The protein diffusion, (ii) cluster sizes and (iii) the motion behavior. To do so, we used a set of different PM receptor proteins: RLP44, BRI1, PSKR1, FLS2, and BAK1 (all fused to mEos3.2). The data were acquired in *N. benthamiana* epidermal leaf cells three days post-infiltration.

Apart from BAK1, all fusion proteins showed a bell-shaped distribution of the diffusion coefficient, independent of whether the co-expressed enzymatic tool was present or not. BAK1 showed two populations of mobility: one slower population and a faster one. The presence of such subpopulations usually indicates diverse molecular states of the protein, such as a bound state and a free-moving fraction [164].

After the disintegration of actin filaments, we observed a decrease in the diffusion coefficient for RLP44-, BRI1-, PSKR1-mEos3.2, and the fast fraction of BAK1-mEos3.2, while FLS2-mEos3.2 diffusion was unaffected. Additionally, we also evaluated the protein cluster sizes. Here, we observed an increase in the cluster diameter for BRI1-, PSKR1-, FLS2-, and BAK1-mEos3.2. The clusters of RLP44-mEos3.2 showed a tendency to increase as well.

As a third parameter, we classified the molecular movements of the proteins and studied their transient movement types to analyze whether there is a change upon the disintegration of the cytoskeleton. According to Vega*, et al.* [136], we classified the protein tracks into four different

motion types: (i) free diffusion, (ii) confined diffusion, (iii) immobility, and (iv) directed diffusion. In response to the actin disintegration by SpvB, we observed a similar shift in the motion patterns for RLP44-, BRI1-, and PSKR1-mEos3.2: Free diffusion was decreased, while immobility and confined movements increased. Compared to RLP44- and PSKR1-mEos3.2, the effects on BRI1-mEos3.2 were less pronounced. FLS2-mEos3.2, however, showed opposing effects. Here, less immobility and increased free diffusion were observable. BAK1-mEos3.2 exhibited a minor effect in response to actin filament disintegration, suggesting a less eminent role of actin filaments on this aspect.

After the disintegration of microtubules, we observed results opposite to the data obtained after the destruction of actin filaments. The manipulation of cortical microtubules resulted in significantly increased diffusion of RLP44-, PSKR1- and the less mobile BAK1-mEos3.2 fraction. Although BRI1-mEos3.2 showed a trend of increasing diffusion as well, the changes were not significant. In contrast, the mobility of FLS2-mEos3.2 remained nearly unaffected. For the cluster diameters, we observed a decrease in size for RLP44-, BRI1-, PSKR1-, and BAK1-mEos3.2. The observed increase for FLS2 was statistically not significant. Again, the disintegration of microtubules resulted in contrary results compared to actin destruction in the context of the proteins' motion behaviors. In the absence of intact microtubules, RLP44-mEos3.2 spent more time in a free diffusive state, while confined and immobile behavior was less present. A comparable effect was present for PSKR1-mEos3.2, as well. FLS2-mEos3.2 showed a decrease in immobility in the absence of microtubules and minor increasing effects on the free diffusive and confined proportion. As with actin disintegration, microtubule disruption did not substantially affect the movement patterns of BAK1-mEos3.2 or those of BRI1-mEos3.2.

It is worth mentioning that none of the tested fusion proteins showed substantial directed motion. This suggests that the studied proteins are not regulated by direct transport processes via the cytoskeleton.

In summary, we showed contrary effects of actin and microtubule disintegration on three tested parameters, namely (i) the diffusion coefficient, (ii) the organization in nano-sized clusters, and (iii) the motion behavior. While some results of actin or microtubule disintegration match with the picket fence model, others do not, such as, for example, the decreased cluster sizes in the absence of microtubules. Based on these results, the model cannot be directly transferred from the animal cell system to plant science. We hypothesize that this might be tied to the presence of cortical actin and cortical microtubule filaments in plants, contrary to animal cells, where microtubules arise from centrosomes and do not have a pivotal role in the regulation of PM organization [165]. To decipher a potential compensatory effect, the depletion of both structures will be of great interest in the future, especially in *A. thaliana,* which also allows for a more background-free observation of the effects. Although decreased diffusion coefficients after the disintegration of actin filaments, i.e., in the absence of "fences", seem counterintuitive, a recent

publication showed that the destruction of actin leads to increased salicylic acid (SA) levels and that the external application of SA results in a constrained diffusion of a PM protein and enlarges their clusters [166-169]. Whether this process reflects a rather general and global concept that applies to a variety of proteins needs to be confirmed by experiments in the future. To this end, the application of SA to test the dynamics and organization of our proteins at the nanoscale should be carried out. In addition to the proposed experiments, we plan to intensify our computational modeling approach, which we started recently. There, we used Smoldyn, a particle-based spatial simulation software [170] to model the dynamics and nanoscale organization of membrane proteins, based on a simplified reaction environment. Recently, we identified new components of the fast brassinosteroid pathway in cooperation with modeling experts from the Bioquant, Heidelberg [15]. Although comparative approaches for membrane dynamics in plants are still lacking, which is a common phenomenon for computational modeling in plant science in general [171], we believe that we might reveal so-far hidden aspects in the regulation of the cytoskeleton together with our cooperation partners.

3.2 FRET-FLIM for Analyzing Complex Composition and Function

The identification of essential players and their interaction partners is crucial for comprehending biochemical processes at the molecular level. A complex network of protein-protein interactions (PPI) executes many, if not all, cellular functions. Historically, the increasing number of available techniques to detect such interactions highlights the need for diverse methods to meet specific research needs. In the realm of plant science, it is crucial to consider various factors before deciding whether to use a heterologous system (e.g., yeast two-hybrid) or an in situ method (e.g., co-immunoprecipitation; Co-IP). Additionally, interaction dynamics must be considered, as PPIs can be weak or strong and either transient or stable in the context of time. Each property may be better suited to a specific technique [172]. FRET-FLIM applications can be carried out in living plant cells and enable the observation of rapid molecular events [173].

In this section, two publications are introduced where I substantiated the work with FRET-FLIM measurements to confirm findings obtained through other techniques. To provide a framework, only a summary of each publication's results is presented here.

3.2.1 FRET-FLIM Approach Confirms Interactions Predicted by Path-Based Centrality Measures

The following chapter is based on **(4) Gilbert et al., 2021:** Comparison of path-based centrality measures in protein-protein interaction networks revealed proteins with phenotypic relevance during adaptation to changing nitrogen environments (see - 63 -)

Journal of Proteomics

More information about my scientific contribution can be found in the respective section (see XIV).

The authors, including me, investigated the dynamic assembly and disassembly of PPIs triggered by external stimuli. Such phenomena are observed in response to, for example, nutrient changes, such as nitrogen availability, in plants. However, these highly dynamic assemblies are difficult to capture. The PPI network of plants grown under full nutrition was compared to plants exposed to nitrogen starvation using a size-exclusion-chromatography coupled to mass spectrometry (SEC-MS) approach [174]. The proteins identified with this approach and their interactomes under different nutrient conditions were analyzed using the concept of Betweenness Centrality. This parameter describes the frequency at which a given node occurs among all possible shortest paths. The following proteins were defined as nodes (i.e., key roles in the regulation of information flow): PM *Arabidopsis* H^+-ATPase isoform 2 (AHA2), QIAN SHOU KINASE 1 (QSK1), BAK1, NITRATE TRANSPORTER 1.1 (NRT1.1), NRT2.1 and *At*5g49770. Notably, a nitrogen starvation-induced interaction was proposed between *At*5g49770 and QSK1. High-confidence interactions were predicted for QSK1 with NRT1.1 and BAK1. An interaction of QSK1 with AHA2 was considered a low-confidence interaction under full nutrition, and an interaction of *At*5g49770 with BAK1 was found to be a low-confidence interaction at nitrate starvation. Co-Ips validated the proposed interactions, confirming the associations of QSK1 with *At*5g49770, NTR1.1, AHA2, and BAK1.

Subsequently, FRET-FLIM experiments were carried out to examine the association between QSK1 and BAK1 and between QSK1 and AHA2. For the proposed QSK1-BAK1 interaction, the FRET-FLIM approach revealed a strong association. In contrast, the interaction between QSK1 and AHA2, predicted as a low-confidence interaction, resulted in no significant associations detectable by FRET-FLIM. The *At*5g49770-AHA2 pair served as a negative control since the predicted network did not indicate a direct interaction. No association was observed in the FRET-FLIM approach for them. The results presented here, obtained through FRET-FLIM measurements, accurately reflect the interactions proposed by the SEC-MS workflow.

Once again, the results highlight the importance of combining diverse interaction methods, such as FRET-FLIM and Co-IP. While the Co-IP was not able to distinguish between the low- and the

high-confidence interactions, the FRET-FLIM approach did not detect an association for the low-confidence pair QSK1-AHA2 pair. This effect could be explained by the fact that results obtained by Co-IP may be a consequence of bridged interactions. This means that the interaction is not taking place directly but via a third protein connecting QSK1 and AHA2. However, for FRET-FLIM, the distances produced by a third protein could be too large to fulfill the demands of efficient FRET, which would result in decreased FLTs. A further advantage of FRET-FLIM is that the interaction is observed in real-time in vivo in the plant cell compartment, while for Co-IP experiments, tissue material is extracted and solubilized to perform the pull-down. This can lead to artificial interactions, even between proteins that would not meet under native conditions. Although the results shown here are very convincing, the experimental setup should be improved for future evaluations. Instead of *N. benthamiana* transient expression, stably transformed *A. thaliana* lines should be used. This will enable the analysis of the proteins in their homologous plant background. Moreover, these plants can be exposed to different nitrogen supplies to reflect the situations used in the SEC-MS experiments.

3.2.2 FRET-FLIM Approach Supports SIRK1-QSK1 Interaction and Proposes the Presence of Pre-Formed Nanodomains

The following chapter summarizes and discusses **(5) Wang et al., 2022:** PEP7 acts as a peptide ligand for the receptor kinase SIRK1 to regulate aquaporin-mediated water influx and lateral root growth (see - 76 -)

Molecular Plant

More information about my scientific contribution can be found in the respective section (see XV).

In this publication, we characterize the previously identified receptor/co-receptor pair SIRK1-QSK1 [175, 176], which regulates aquaporins in response to sucrose-induced osmotic conditions. However, the ligand of the receptor pair has been unknown so far. This study uncovers ELICITOR PEPTIDE 7 (PEP7) as the ligand of the receptor kinase SIRK1 that binds to its extracellular domain. PEP7 is secreted to the apoplast specifically in response to sucrose treatments. Biochemically stable interactions between SIRK1 and QSK1 were detectable only after PEP7 treatment. Activation of SIRK1 by PEP7 involved transphosphorylation of QSK1 and aquaporins, akin to sucrose-induced processes reported by the authors in previous studies [175, 176]. The concept of phosphorylation events to ensure signaling upon the binding of ligands is common for many receptor/co-receptor pairs, such as BRI1-BAK1 or FLS2-BAK1 [40]. In the here-discussed publication, it was confirmed that instead of sucrose, PEP7 can induce phosphorylation of QSK1 and aquaporins as well.

Experiments with several mutants pointed out that SIKR1 is the responsible kinase and that in the absence of both SIRK1 and native PEP7, sucrose and external PEP7 cannot induce phosphorylation of QSK1 and aquaporins. Interestingly, the quantified phosphopeptides of aquaporins correspond to known phosphorylation sites for pore-gating in PIP2A from *Spinacia 34eplete34*, suggesting that PEP7 induces the phosphorylation-dependent opening of aquaporin pores.

To further evaluate the impact of PEP7 on the associations between SIRK1 and QSK1, I conducted FRET-FLIM measurements using transiently transformed *N. benthamiana* epidermal leaf cells. Our findings demonstrated that QSK1 and SIRK1 associate and potentially interact with each other. Interestingly, upon the application of PEP7, there was no change in the FRET efficiency between SIRK1 and QSK1. To exclude the possibility that native PEP7 may mask the effects of the applied PEP7 on the QSK1-SIRK1 association, the protease inhibitor leupeptin was used. Leupeptin acts as an inhibitor of metacaspase [177], which facilitates PEP7 release from its precursor [178]. However, after the leupeptin supply, QSK1 still associates with SIRK1, regardless of the presence of PEP7. This indicates that SIRK1 and QSK1 associate in pre-formed nano-structured membrane domains in the absence of PEP7. This phenomenon is observable for other complexes as well, like the RLP44-BRI1-BAK1 module, where the application of the ligand does not alter the receptors interaction behavior [31]. Restricted to the receptor/co-receptor interaction of BRI1-BAK1, Bücherl*, et al.* [179] demonstrated that heterooligomers of BRI1-BAK1 are observed despite the 34epleteon of endogenous BL. The external application of BL increases the number of heterooligomers. This suggests that there is a subset of (pre-existing) complexes whose number increases after applying the ligand. Observations from the animal cell systems support all the aforementioned results and hypotheses derived from plant-specific research. Pre-formed receptor complexes have been identified that may enhance the affinity for the ligand, prolong the half-life of the complex, expedite signal transduction, and encourage lateral signal propagation [180-182]. Bücherl*, et al.* [179], like us, observed a discrepancy between the results obtained from the FRET-FLIM and Co-IP experiments. They found a significant increase in the number of heterooligomers upon ligand application after Co-IP compared with the FRET-FLIM data. The authors attributed this difference to several technique-related limitations, such as variations in protein extraction during Co-IP experiments. They hypothesized that fluorescence microscopy captures the entirety of tagged proteins, whereas biochemical methods such as Co-IP only capture a subset.

For future experiments and in light of the aforementioned findings, the use of the parameter "interaction pixels", according to Bücherl*, et al.* [179], should be considered as well. With this approach, the FLT is not reported as a single averaged value over a larger region of interest (e.g., the PM), but instead the values of each image pixel can be evaluated. By applying this method, it will be possible to determine whether PEP7 increases the number of heterooligomers

based on FLT. Additionally, it would be prudent to assess results in stably transformed *A. thaliana* plants, utilizing mutant lines like *pep7* knockouts. This may present a more reliable approach than the external depletion of endogenous PEP7. With our recent advances in super-resolution techniques [144, 154], we will be able to investigate the dynamics of SIRK1 and QSK1 in response to PEP7 in various genetic backgrounds. By utilizing dual-color methods along with advanced algorithms to evaluate the formation of nanoscale clusters, it may be feasible to examine their composition and how they are altered following the application of PEP7 with regards to size, density, and additional characteristics.

3.3 Others

The primary drivers of research have consistently been the development of new techniques and the integration of advanced, contemporary methods.

In this section, two publications are introduced. In the first, we developed a new method to evaluate tripartite protein interactions. Alongside the re-evaluation processes, I supported the authors with mathematical and statistical analyses. In the second publication, we combined several "wet lab" approaches with computational modeling and predicted a new component of the rapid BRI1 response pathway. In particular, the use of computational modeling represents an approach in plant science that has been so far underrepresented.

3.3.1 Three-Fluorophore FRET-FLIM is a New Method to Study and Assess Ternary Protein Complexes in Living Plant Cells

The following chapter is based on **(6) Glöckner et al., 2022:** Three-Fluorophore FRET Enables the Analysis of Ternary Protein Association in Living Plant Cells (see - 103 -)

Plants (Basel)

More information about my scientific contribution can be found in the respective section (see XV).

FRET-FLIM has emerged as a commonly utilized technique to investigate protein-protein association and complex composition. Nevertheless, in plants, it is limited to pairs of proteins, which does not accurately represent reality given that most processes necessitate the involvement of more than two proteins [98]. Here, a new three-fluorophore FRET-FLIM approach is introduced that exemplary shows that BRI1, BAK1 and RLP44 form a trimeric complex, spatially separated from other BAK1-containing complexes, such as FLS2-BAK1. All experiments conducted for this proof-of-principle study were performed in transiently transformed epidermal leaf cells of *N. benthamiana*.

The selection of appropriate fluorophores is of great importance for successful FRET approaches. Our screening procedure resulted in the choice of three monomeric fluorophores: monomeric Turqoise 2 (mTRQ2), monomeric Venus (mVEN) and mRFP. Their monomeric properties reduce false-positive results from unspecific aggregation. Moreover, the overlap in their donor fluorescence emission and acceptor absorbance spectra made these fluorophores ideal for our approach. Among them, mTRQ2 was chosen as the first donor due to its long, monoexponential FLT [183]. As the first acceptor (and second donor), we chose mVEN. mRFP was selected as the second acceptor.

To study the theoretical assumptions, R_0 (i.e., Förster distances) and the distances corresponding to 10 % FRET efficiency were calculated. This efficiency value was chosen because it is at the lower detection limit for FRET. For a donor-acceptor ratio of 1:1, comparable values below 8.5 nm for mTRQ2-mVEN, mVEN-mRFP and mTRQ2-mRFP were obtained for $r_{10\%}$. For large distances between mTRQ2 and mRFP, no direct FRET is expected to be possible. However, the introduction of the intermediate acceptor mVEN could increase the dynamic range between mTRQ2 and mRFP. Since neither the geometry nor the exact positions of the attached fluorophores are known in multimeric protein complexes, randomly placed positions were evaluated, which resulted in a distance of 11.1 nm. This is large enough to detect long-range associations with the proposed three-fluorophore FRET approach.

For latter biological applications, it is important to consider the dimensions of the proteins, too. Thus, further assumptions and calculations were carried out with the following fusions: RLP44-mTRQ2, BRI1-mVEN and BAK1-mRFP. The information about the dimensions were based on freely available structural data or models. The calculated $r_{10\%}$ values from the approach above, can span the distance of two kinase domains, which have diameters of about 4.8 nm. However, RLP44-mTRQ2 and BAK1-mRFP are too far apart for direct FRET, when BRI1-mVEN is positioned in between. In contrast, three-fluorophore FRET from RLP44-mTRQ2 via BRI1-mVEN to BAK1-mRFP can span this distance. The same is expected for a RLP44-mTRQ2/BAK1-mVEN/BRI1-mRFP arrangement.

Especially intensity-based, spectral FRET approaches are highly influenced by several factors. To address possible issues of cross-excitation and bleed-trough, simulations of emission spectra with various intermolecular distances and different stoichiometric ratios were conducted. Interestingly, a ratio of 1:2 between mTRQ2 and mVEN during the absence of FRET resulted in a peak of fluorescence intensity that was even higher than the one observed between the fluorophores during the occurrence of FRET. This shows that bleed-through and cross-excitation effects can have a greater impact on the apparent mVEN signal than FRET itself, emphasizing the need for careful calibrations of fusion protein amounts.

Before the final establishment of the triple-FRET approach, intensity-based, spectral FRET analyses for dual protein-protein association were tested. To do so, RLP44-mTRQ2/BRI1-mVEN were

used as a positive control and RLP44-mTRQ2/FLS2-mVEN were used as a pair where no association was expected [184]. The possible issues caused by stoichiometric differences prompted us to determine the levels for each experiment by combining spectral unmixing information with sequential excitation acquisitions for each spectrum separately. Both combinations showed a comparable donor-acceptor ratio (1:4). We observed that the peak intensity at approximately 525 nm (i.e., mVEN emission) was significantly higher in the RLP44-mTRQ2/BRI1-mVEN combination than in the RLP44-mTRQ2/FLS2-mVEN sample. In conclusion, FRET from RLP44-mTRQ2 to BRI1-mVEN was observed when compared with the RLP44-mTRQ2/FLS2-mVEN control pair. An equivalent approach, evaluating the emission at 610 nm (i.e., mRFP emission), was conducted to confirm the energy transfer from mTRQ2-fusions to mRFP-fusions.

Finally, the three-fluorophore approach was performed based on the previous theoretical considerations. Here, the distance between RLP44 and BAK1 might be altered by the presence of BRI1, for example, when BRI1 is located between them. Thus, a non-fluorescent, hemagglutinin (HA)-tagged version of BRI1 was employed to test for this. Its co-expression with RLP44-mTRQ2 and BAK1-mRFP did not lead to any emission peak at 610 nm in the spectrum. In contrast, replacing the non-fluorescent BRI1 with FLS2-mVEN, which is known not to interact with RLP44, retained the intensity peak at around 610 nm. This indicates that BRI1-HA enlarges the distance, as other reasons such as stoichiometric changes were excluded. Upon substituting BRI1-HA with BRI1-mVEN, the emission peak around 610 nm reappeared. Simultaneously, the RLP44-mTRQ2/BRI1-mVEN/BAK1-mRFP sample exhibited an energy transfer from mVEN to mRFP. This was evident by the significant decrease in the mVEN emission peak at 525 nm compared with the RLP44-mTRQ2/BRI1-mVEN sample. Importantly, this effect was absent in the RLP44-mTRQ2/FLS2-mVEN/FLS2-mRFP control samples. The emission peak at approximately 610 nm with a coinciding reduction in emission at about 525 nm fulfills the criteria for three-chromophore FRET from RLP44-mTRQ2 via BRI1-mVEN to BAK1-mRFP.

As highlighted, intensity-based FRET approaches are relatively time-consuming, require expertise and are influenced by several factors, such as the stoichiometry of the proteins that necessitate labor-intensive calibrations.

To overcome these limitations, FRET-FLIM has emerged as a powerful alternative. With this method, the reduction of the donor FLT provides a direct measure for the presence of FRET. Subsequently, we conducted FRET-FLIM experiments to test the usability with the chosen three fluorophores. In this approach, changes in the FLT of mTRQ2 were monitored. The co-expression of RLP44-mTRQ2 with either BRI1-mVEN, BRI1-mRFP or BAK1-mRFP resulted in a significant decrease in the donor FLT, indicating that FRET occurs from mTRQ2 to mVEN and mRFP. In contrast, using FLS2 as an acceptor (i.e., as control; fused to mVEN or mRFP) did not result in a decrease.

The presence of RLP44-mTRQ2, BRI1-mVEN and BAK1-mRFP simultaneously caused an enhanced decrease in the FLT of mTRQ2 compared to the aforementioned bipartite tests. Such an enhanced reduction can only be explained by the existence of an additional FRET pathway that is available when RLP44, BAK1 and BRI1 have formed a ternary complex. The absence of the effect was observed when FLS2-mRFP replaced BAK1-mRFP. Importantly, in line with previous reports [95], we confirmed that the amount of the fluorophore-tagged proteins (i.e., expression proportions) does not affect the FLT.

In summary, we offer with this approach a new possibility to verify and assess ternary complexes. While intensity-based FRET approaches are labor-intensive and vulnerable to false-positive results, the more elegant, fast, and robust way is to use FRET-FLIM, instead. We clearly showed that although FLS2 interacts with BAK1, this interaction occurs at least 11.1 nm away from the BRI1-BAK1-RLP44 complex. In the future, it will be interesting to combine these approaches with other advanced techniques, such as sptPALM, to increase not only the spatial but also the temporal resolution.

3.3.2 A Combination of Computational Modeling and Quantitative Physiology Reveals Central Parameters for the Brassinosteroid-Regulated Rapid Cell Elongation Response

The following chapter summarizes and discusses **(7) Großeholz et al., 2022:** Computational modeling and quantitative physiology reveal central parameters for brassinosteroid-regulated early cell physiological processes linked to elongation growth of the *Arabidopsis* root (see - 139 -)

Elife

More information about my scientific contribution can be found in the respective section (see XV).

In this publication, we combined results from “wet lab” experiments with a computational modeling approach. With this, we identified central parameters and new components for the brassinosteroid-regulated rapid acidification response of the apoplast, which finally results in the elongation growth of root cells. While the constitution of the signaling hub and the involved proteins are qualitatively well described (see chapter 1.1.1), detailed quantitative data were lacking. With our approach, we provided substantial insights into the quantitative understanding of the process.

Our experimental and computational concepts used cells from the root tip of *A. thaliana*, where they undergo a phase of cell division in the meristematic zone (MZ), followed by a phase of growth in the elongation zone (EZ). In a first step, Dr. Ruth Großeholz and other collaboration partners from Bioquant Heidelberg generated a model employing ordinary differential equations.

Our model considered four compartments, namely the cytosol, the cell wall, the vacuole and the PM. Their sizes were set according to van Esse*, et al.* [185]. The model was generated with freely available information, such as, for example, the specific capacitance of the PM [186]. Additionally, all essential activities, such as the inhibitory effect of BIR3 or the basal activity of the proton ATPase, were considered.

To refine the model, we decided to quantify the key components, namely BRI1, BAK1, BIR3 and the proton ATPases in the PM of epidermal cells of the root tip. First, high-throughput single-cell RNA-sequencing data [187] revealed that BRI1 and BIR3 transcripts accumulate evenly in all cell types of the root and did not alter much in their amount during cell development along the root axis. In contrast, the AHA2 transcript showed a strong increase in the cortex and epidermal cells of the transition zone (TZ) and EZ. Based on this data, we then focused on protein quantifications. BRI1-GFP and BAK1-GFP amounts were quantified before by confocal laser scanning microscopy in the EZ [185]. In addition, all key components, namely BRI1, BIR3, BAK1 and AHA2, were quantified in all respective root zones. The measured intensities were set in relation to the BRI1-GFP intensity, for which absolute values for the receptor density were reported by van Esse*, et al.* [185].

BRI1, BIR3 and BAK1 showed homogenous distributions along the root axis. In contrast, AHA2 had a notable gradient, with a relatively low amount in the MZ compared to the EZ. This indicates a regulatory correlation between AHA2 accumulation and BR-regulated root growth along the root axis, which is supported by findings that AHA2 physically interacts with BRI1 and BAK1 and is phosphorylated within five minutes upon BR treatment in vivo [20, 27, 36, 188].

To test this hypothesis, we decided to characterize the functional role of AHA in the context of BR-regulated signaling, both experimentally and with the computational model.

As a quantitative readout, we used the apoplastic pH by applying a non-PM-penetrating dye that incorporates into the plant cell wall [189]. We conducted dose-response measurements and time-course experiments. Our results in the EZ revealed a significant decrease in the apoplastic pH already at a BL concentration of 0.1 nM that continued up to concentrations of 10 nM. Additionally, the time-course experiment showed rapid acidification within ten minutes after hormone application, which was maintained for the entire time span. Both experimental results were reproduced by our computational model.

With our model, we then analyzed the importance and impact of individual components on cell wall acidification after five minutes of BL application. To do so, we calculated their scaled sensitivities. Here, it was clearly visible that factors such as the initial concentrations of BRI1 and AHA2, the degree of inhibition and the pump activity of the ATPases strongly control the early BR responses. Similar calculations for the acidification taking place 60 min after BL application revealed a greater significance of down-regulating elements, although the amount and activity of

the proton pumps remained important. The model's predictions supported the hypothesis that proton pumps are the key elements that control BR-regulated elongation growth.
In consequence, it was assumed that cells in the MZ have a higher starting pH and react less strongly to BR stimulation due to reduced AHA2 expression levels evaluated before.
To test this, we adapted our model and parameters to reflect the behavior of the MZ. Indeed, a higher starting pH and a reduced BR-sensitivity were predicted by the model. The data were confirmed by experimental pH measurements.
Finally, we assessed that this regulation via BL is triggered by BRI1. To do so, we used the *bri1-301* mutant, which exhibits reduced BRI1-kinase activity [190]. Indeed, a less pronounced reduction after the addition of BL was present, indicating that the described processes are initiated by BRI1.

The great value of computational modeling becomes obvious when it can be used to predict new components. We calculated the membrane potential derived from our pH value changes in the apoplastic cell space and compared it to data from Caesar*, et al.* [20]. Our model predicted much stronger values than those measured. However, the incorporation of monovalent cation import, such as potassium, into the model rectified this discrepancy. An extensive literature research taking several criteria into account, pointed to CNGC10 as a potential candidate for this cation import. By integrating its molecular properties into the model, the discrepancy was resolved, and the membrane potential was accurately predicted as experimentally measured.
We performed interaction studies to unravel whether CNGC10 interacts with the components of the BRI1 signaling complex. The results obtained by FRET-FLIM and a mating-based split ubiquitin assay suggested a spatial association or even physical interaction of CNGC10 with BAK1, AHA2 and BRI1, respectively. The direct involvement of CNGC10 in the fast BR response pathway was analyzed by pH measurements using two independent *Arabidopsis cngc10* loss-of-function lines [191, 192]. In contrast to the corresponding wild type, *cngc10-1* and *cngc10-2* did not acidify the apoplast upon BL application, suggesting that CNGC10 serves as the primary cation channel (i.e., for potassium) that regulates membrane potential homeostasis during BL-induced apoplastic acidification.

In summary, we have presented an elegant combination of experimental data and computational modeling that objectively highlights the specific role of proton pump activity for apoplastic acidification and reveals a new component of the fast BR pathway, namely CNGC10. The amount and activity of AHA2 appear to be the rate-limiting factor for the cells' ability to elongate in response to BL. It is suggested that the signaling components could potentially be arranged differentially in pre-existing nanoclusters along the root axis, analogous to the BRI1-BAK1-RLP44 complex [31]. Based on our model, the proportion of associated AHA2 molecules should increase in BRI1 clusters along the root axis, being low in the MZ and high in the TZ and the EZ. This hypothesis can be verified with FRET-FLIM experiments using transgenic *Arabidopsis* seedlings in the future that not

only consider the overall association but also the number of associating pixels that correlate with the number of associating molecules [179].

Recent improvements in cloning technologies make it now possible to apply cell-, tissue- or organ-specific knockouts via clustered regularly interspaced short palindromic repeats (CRISPR) without effecting the expression on a global level [193]. The approach and its usefulness were recently demonstrated using BRI1-CRISPR knockouts [194]. For our requirements, promoters specifically active in the meristematic or early elongation zone are needed. By utilizing this approach, it will be feasible to precisely regulate protein amounts (such as BRI1, AHA2 and CNGC10) in the relevant areas crucial for the rapid BR response. The experimental output can then be compared to the model's predictions. Furthermore, developments in super-resolution microscopy can link the presented results with spatiotemporal information, such as assessing whether the absence of CNGC10 affects the mobility or nanoscale organization of BRI1. Subsequently, these data can be used to improve and refine the model. With more data, an extension of the model to ideally the entire root tip will be likely, taking anisotropic elongation growth into account as well [195].

References

1. Gou, X.; Li, J. Paired Receptor and Coreceptor Kinases Perceive Extracellular Signals to Control Plant Development. *Plant Physiol* **2020**, *182*, 1667-1681 doi: https://doi.org/10.1104/pp.19.01343.

2. Shiu, S.H.; Karlowski, W.M.; Pan, R.; Tzeng, Y.H.; Mayer, K.F.; Li, W.H. Comparative analysis of the receptor-like kinase family in Arabidopsis and rice. *Plant Cell* **2004**, *16*, 1220-1234 doi: https://doi.org/10.1105/tpc.020834.

3. Jamieson, P.A.; Shan, L.; He, P. Plant cell surface molecular cypher: Receptor-like proteins and their roles in immunity and development. *Plant Sci* **2018**, *274*, 242-251 doi: https://doi.org/10.1016/j.plantsci.2018.05.030.

4. Ngou, B.P.M.; Wyler, M.; Schmid, M.W.; Kadota, Y.; Shirasu, K. Evolutionary trajectory of pattern recognition receptors in plants. *Nat Commun* **2024**, *15*, 308 doi: https://doi.org/10.1038/s41467-023-44408-3.

5. Steidele, C.E.; Stam, R. Multi-omics approach highlights differences between RLP classes in Arabidopsis thaliana. *BMC Genomics* **2021**, *22*, 557 doi: https://doi.org/10.1186/s12864-021-07855-0.

6. Torii, K.U. Leucine-rich repeat receptor kinases in plants: structure, function, and signal transduction pathways. *Int Rev Cytol* **2004**, *234*, 1-46 doi: https://doi.org/10.1016/s0074-7696(04)34001-5.

7. Friedrichsen, D.M.; Joazeiro, C.A.; Li, J.; Hunter, T.; Chory, J. Brassinosteroid-insensitive-1 is a ubiquitously expressed leucine-rich repeat receptor serine/threonine kinase. *Plant Physiol* **2000**, *123*, 1247-1256 doi: https://doi.org/10.1104/pp.123.4.1247.

8. Cano-Delgado, A.; Yin, Y.; Yu, C.; Vafeados, D.; Mora-Garcia, S.; Cheng, J.C.; Nam, K.H.; Li, J.; Chory, J. BRL1 and BRL3 are novel brassinosteroid receptors that function in vascular differentiation in Arabidopsis. *Development* **2004**, *131*, 5341-5351 doi: https://doi.org/10.1242/dev.01403.

9. Hohmann, U.; Santiago, J.; Nicolet, J.; Olsson, V.; Spiga, F.M.; Hothorn, L.A.; Butenko, M.A.; Hothorn, M. Mechanistic basis for the activation of plant membrane receptor kinases by SERK-family coreceptors. *Proc Natl Acad Sci U S A* **2018**, *115*, 3488-3493 doi: https://doi.org/10.1073/pnas.1714972115.

10. Wang, G.; Ellendorff, U.; Kemp, B.; Mansfield, J.W.; Forsyth, A.; Mitchell, K.; Bastas, K.; Liu, C.M.; Woods-Tor, A.; Zipfel, C.; de Wit, P.J.; Jones, J.D.; Tor, M.; Thomma, B.P. A genome-wide functional investigation into the roles of receptor-like proteins in Arabidopsis. *Plant Physiol* **2008**, *147*, 503-517 doi: https://doi.org/10.1104/pp.108.119487.

11. Wang, X.; Chory, J. Brassinosteroids regulate dissociation of BKI1, a negative regulator of BRI1 signaling, from the plasma membrane. *Science* **2006**, *313*, 1118-1122 doi: https://doi.org/10.1126/science.1127593.

12. Lin, W.; Lu, D.; Gao, X.; Jiang, S.; Ma, X.; Wang, Z.; Mengiste, T.; He, P.; Shan, L. Inverse modulation of plant immune and brassinosteroid signaling pathways by the receptor-like cytoplasmic kinase BIK1. *Proc Natl Acad Sci U S A* **2013**, *110*, 12114-12119 doi: https://doi.org/10.1073/pnas.1302154110.

13. Imkampe, J.; Halter, T.; Huang, S.; Schulze, S.; Mazzotta, S.; Schmidt, N.; Manstretta, R.; Postel, S.; Wierzba, M.; Yang, Y.; van Dongen, W.; Stahl, M.; Zipfel, C.; Goshe, M.B.; Clouse, S.; de Vries, S.C.; Tax, F.; Wang, X.; Kemmerling, B. The Arabidopsis Leucine-Rich Repeat Receptor Kinase BIR3 Negatively Regulates BAK1 Receptor Complex Formation and Stabilizes BAK1. *Plant Cell* **2017**, *29*, 2285-2303
doi: https://doi.org/10.1105/tpc.17.00376.

14. Grosseholz, R.; Feldman-Salit, A.; Wanke, F.; Schulze, S.; Glöckner, N.; Kemmerling, B.; Harter, K.; Kummer, U. Specifying the role of BAK1-interacting receptor-like kinase 3 in brassinosteroid signaling. *J Integr Plant Biol* **2020**, *62*, 456-469
doi: https://doi.org/10.1111/jipb.12803.

15. Grosseholz, R.; Wanke, F.; Rohr, L.; Glöckner, N.; Rausch, L.; Scholl, S.; Scacchi, E.; Spazierer, A.J.; Shabala, L.; Shabala, S.; Schumacher, K.; Kummer, U.; Harter, K. Computational modeling and quantitative physiology reveal central parameters for brassinosteroid-regulated early cell physiological processes linked to elongation growth of the Arabidopsis root. *Elife* **2022**, *11*, e73031
doi: https://doi.org/10.7554/eLife.73031.

16. Mora-Garcia, S.; Vert, G.; Yin, Y.; Cano-Delgado, A.; Cheong, H.; Chory, J. Nuclear protein phosphatases with Kelch-repeat domains modulate the response to brassinosteroids in Arabidopsis. *Genes Dev* **2004**, *18*, 448-460
doi: https://doi.org/10.1101/gad.1174204.

17. Vert, G.; Chory, J. Downstream nuclear events in brassinosteroid signalling. *Nature* **2006**, *441*, 96-100
doi: https://doi.org/10.1038/nature04681.

18. Yin, Y.; Vafeados, D.; Tao, Y.; Yoshida, S.; Asami, T.; Chory, J. A new class of transcription factors mediates brassinosteroid-regulated gene expression in Arabidopsis. *Cell* **2005**, *120*, 249-259
doi: https://doi.org/10.1016/j.cell.2004.11.044.

19. Zhu, J.Y.; Li, Y.; Cao, D.M.; Yang, H.; Oh, E.; Bi, Y.; Zhu, S.; Wang, Z.Y. The F-box Protein KIB1 Mediates Brassinosteroid-Induced Inactivation and Degradation of GSK3-like Kinases in Arabidopsis. *Mol Cell* **2017**, *66*, 648-657
doi: https://doi.org/10.1016/j.molcel.2017.05.012.

20. Caesar, K.; Elgass, K.; Chen, Z.; Huppenberger, P.; Witthoft, J.; Schleifenbaum, F.; Blatt, M.R.; Oecking, C.; Harter, K. A fast brassinolide-regulated response pathway in the plasma membrane of Arabidopsis thaliana. *Plant J* **2011**, *66*, 528-540
doi: https://doi.org/10.1111/j.1365-313X.2011.04510.x.

21. Witthoft, J.; Caesar, K.; Elgass, K.; Huppenberger, P.; Kilian, J.; Schleifenbaum, F.; Oecking, C.; Harter, K. The activation of the Arabidopsis P-ATPase 1 by the brassinosteroid receptor BRI1 is independent of threonine 948 phosphorylation. *Plant Signal Behav* **2011**, *6*, 1063-1066
doi: https://doi.org/10.4161/psb.6.7.15650.

22. Sun, Y.; Fan, X.Y.; Cao, D.M.; Tang, W.; He, K.; Zhu, J.Y.; He, J.X.; Bai, M.Y.; Zhu, S.; Oh, E.; Patil, S.; Kim, T.W.; Ji, H.; Wong, W.H.; Rhee, S.Y.; Wang, Z.Y. Integration of brassinosteroid signal transduction with the transcription network for plant growth regulation in Arabidopsis. *Dev Cell* **2010**, *19*, 765-777
doi: https://doi.org/10.1016%2Fj.devcel.2010.10.010.

23. Yu, X.; Li, L.; Zola, J.; Aluru, M.; Ye, H.; Foudree, A.; Guo, H.; Anderson, S.; Aluru, S.; Liu, P.; Rodermel, S.; Yin, Y. A brassinosteroid transcriptional network revealed by genome-wide identification of BESI target genes in Arabidopsis thaliana. *Plant J* **2011**, *65*, 634-646 doi: https://doi.org/10.1111/j.1365-313X.2010.04449.x.

24. Xie, L.; Yang, C.; Wang, X. Brassinosteroids can regulate cellulose biosynthesis by controlling the expression of CESA genes in Arabidopsis. *J Exp Bot* **2011**, *62*, 4495-4506 doi: https://doi.org/10.1093/jxb/err164.

25. Wang, X.; Zhang, J.; Yuan, M.; Ehrhardt, D.W.; Wang, Z.; Mao, T. Arabidopsis microtubule destabilizing protein40 is involved in brassinosteroid regulation of hypocotyl elongation. *Plant Cell* **2012**, *24*, 4012-4025 doi: https://doi.org/10.1105/tpc.112.103838.

26. Elgass, K.; Caesar, K.; Schleifenbaum, F.; Stierhof, Y.D.; Meixner, A.J.; Harter, K. Novel application of fluorescence lifetime and fluorescence microscopy enables quantitative access to subcellular dynamics in plant cells. *PLoS One* **2009**, *4*, e5716 doi: https://doi.org/10.1371/journal.pone.0005716.

27. Lin, L.L.; Hsu, C.L.; Hu, C.W.; Ko, S.Y.; Hsieh, H.L.; Huang, H.C.; Juan, H.F. Integrating Phosphoproteomics and Bioinformatics to Study Brassinosteroid-Regulated Phosphorylation Dynamics in Arabidopsis. *BMC Genomics* **2015**, *16*, 533 doi: https://doi.org/10.1186/s12864-015-1753-4.

28. Wolf, S.; Mravec, J.; Greiner, S.; Mouille, G.; Hofte, H. Plant cell wall homeostasis is mediated by brassinosteroid feedback signaling. *Curr Biol* **2012**, *22*, 1732-1737 doi: https://doi.org/10.1016/j.cub.2012.07.036.

29. Wolf, S.; van der Does, D.; Ladwig, F.; Sticht, C.; Kolbeck, A.; Schurholz, A.K.; Augustin, S.; Keinath, N.; Rausch, T.; Greiner, S.; Schumacher, K.; Harter, K.; Zipfel, C.; Hofte, H. A receptor-like protein mediates the response to pectin modification by activating brassinosteroid signaling. *Proc Natl Acad Sci U S A* **2014**, *111*, 15261-15266 doi: https://doi.org/10.1073/pnas.1322979111.

30. Wolf, S. Cell Wall Signaling in Plant Development and Defense. *Annu Rev Plant Biol* **2022**, *73*, 323-353 doi: https://doi.org/10.1146/annurev-arplant-102820-095312.

31. Glöckner, N.; Zur Oven-Krockhaus, S.; Rohr, L.; Wackenhut, F.; Burmeister, M.; Wanke, F.; Holzwart, E.; Meixner, A.J.; Wolf, S.; Harter, K. Three-Fluorophore FRET Enables the Analysis of Ternary Protein Association in Living Plant Cells. *Plants (Basel)* **2022**, *11*, 2630 doi: https://doi.org/10.3390/plants11192630.

32. Holzwart, E.; Huerta, A.I.; Glöckner, N.; Garnelo Gomez, B.; Wanke, F.; Augustin, S.; Askani, J.C.; Schurholz, A.K.; Harter, K.; Wolf, S. BRI1 controls vascular cell fate in the Arabidopsis root through RLP44 and phytosulfokine signaling. *Proc Natl Acad Sci U S A* **2018**, *115*, 11838-11843 doi: https://doi.org/10.1073/pnas.1814434115.

33. Matsubayashi, Y.; Sakagami, Y. Phytosulfokine, sulfated peptides that induce the proliferation of single mesophyll cells of Asparagus officinalis L. *Proc Natl Acad Sci U S A* **1996**, *93*, 7623-7627 doi: https://doi.org/10.1073/pnas.93.15.7623.

34. Amano, Y.; Tsubouchi, H.; Shinohara, H.; Ogawa, M.; Matsubayashi, Y. Tyrosine-sulfated glycopeptide involved in cellular proliferation and expansion in Arabidopsis. *Proc Natl Acad Sci U S A* **2007**, *104*, 18333-18338
doi: https://doi.org/10.1073/pnas.0706403104.

35. Matsubayashi, Y.; Ogawa, M.; Kihara, H.; Niwa, M.; Sakagami, Y. Disruption and overexpression of Arabidopsis phytosulfokine receptor gene affects cellular longevity and potential for growth. *Plant Physiol* **2006**, *142*, 45-53
doi: https://doi.org/10.1104/pp.106.081109.

36. Ladwig, F.; Dahlke, R.I.; Stuhrwohldt, N.; Hartmann, J.; Harter, K.; Sauter, M. Phytosulfokine Regulates Growth in Arabidopsis through a Response Module at the Plasma Membrane That Includes CYCLIC NUCLEOTIDE-GATED CHANNEL17, H+-ATPase, and BAK1. *Plant Cell* **2015**, *27*, 1718-1729
doi: https://doi.org/10.1105/tpc.15.00306.

37. Igarashi, D.; Tsuda, K.; Katagiri, F. The peptide growth factor, phytosulfokine, attenuates pattern-triggered immunity. *Plant J* **2012**, *71*, 194-204
doi: https://doi.org/10.1111/j.1365-313X.2012.04950.x.

38. Mosher, S.; Seybold, H.; Rodriguez, P.; Stahl, M.; Davies, K.A.; Dayaratne, S.; Morillo, S.A.; Wierzba, M.; Favery, B.; Keller, H.; Tax, F.E.; Kemmerling, B. The tyrosine-sulfated peptide receptors PSKR1 and PSY1R modify the immunity of Arabidopsis to biotrophic and necrotrophic pathogens in an antagonistic manner. *Plant J* **2013**, *73*, 469-482
doi: https://doi.org/10.1111/tpj.12050.

39. Heinemann, B.; Kunzler, P.; Eubel, H.; Braun, H.P.; Hildebrandt, T.M. Estimating the number of protein molecules in a plant cell: protein and amino acid homeostasis during drought. *Plant Physiol* **2021**, *185*, 385-404
doi: https://doi.org/10.1093/plphys/kiaa050.

40. Bücherl, C.A.; Jarsch, I.K.; Schudoma, C.; Segonzac, C.; Mbengue, M.; Robatzek, S.; MacLean, D.; Ott, T.; Zipfel, C. Plant immune and growth receptors share common signalling components but localise to distinct plasma membrane nanodomains. *Elife* **2017**, *6*, e25114
doi: https://doi.org/10.7554/eLife.25114.

41. Jaillais, Y.; Ott, T. The Nanoscale Organization of the Plasma Membrane and Its Importance in Signaling: A Proteolipid Perspective. *Plant Physiol* **2020**, *182*, 1682-1696
doi: https://doi.org/10.1104/pp.19.01349.

42. Jarsch, I.K.; Konrad, S.S.; Stratil, T.F.; Urbanus, S.L.; Szymanski, W.; Braun, P.; Braun, K.H.; Ott, T. Plasma Membranes Are Subcompartmentalized into a Plethora of Coexisting and Diverse Microdomains in Arabidopsis and Nicotiana benthamiana. *Plant Cell* **2014**, *26*, 1698-1711
doi: https://doi.org/10.1105/tpc.114.124446.

43. Kleine-Vehn, J.; Wabnik, K.; Martiniere, A.; Langowski, L.; Willig, K.; Naramoto, S.; Leitner, J.; Tanaka, H.; Jakobs, S.; Robert, S.; Luschnig, C.; Govaerts, W.; Hell, S.W.; Runions, J.; Friml, J. Recycling, clustering, and endocytosis jointly maintain PIN auxin carrier polarity at the plasma membrane. *Mol Syst Biol* **2011**, *7*, 540
doi: https://doi.org/10.1038/msb.2011.72.

44. Martiniere, A.; Fiche, J.B.; Smokvarska, M.; Mari, S.; Alcon, C.; Dumont, X.; Hematy, K.; Jaillais, Y.; Nollmann, M.; Maurel, C. Osmotic Stress Activates Two Reactive Oxygen Species Pathways with Distinct Effects on Protein Nanodomains and Diffusion. *Plant Physiol* **2019**, *179*, 1581-1593
doi: https://doi.org/10.1104/pp.18.01065.

45. Singer, S.J.; Nicolson, G.L. The fluid mosaic model of the structure of cell membranes. *Science* **1972**, *175*, 720-731
doi: https://doi.org/10.1126/science.175.4023.720.

46. Simons, K.; Ikonen, E. Functional rafts in cell membranes. *Nature* **1997**, *387*, 569-572
doi: https://doi.org/10.1038/42408.

47. Borner, G.H.; Sherrier, D.J.; Weimar, T.; Michaelson, L.V.; Hawkins, N.D.; Macaskill, A.; Napier, J.A.; Beale, M.H.; Lilley, K.S.; Dupree, P. Analysis of detergent-resistant membranes in Arabidopsis. Evidence for plasma membrane lipid rafts. *Plant Physiol* **2005**, *137*, 104-116
doi: https://doi.org/10.1104/pp.104.053041.

48. Laloi, M.; Perret, A.M.; Chatre, L.; Melser, S.; Cantrel, C.; Vaultier, M.N.; Zachowski, A.; Bathany, K.; Schmitter, J.M.; Vallet, M.; Lessire, R.; Hartmann, M.A.; Moreau, P. Insights into the role of specific lipids in the formation and delivery of lipid microdomains to the plasma membrane of plant cells. *Plant Physiol* **2007**, *143*, 461-472
doi: https://doi.org/10.1104/pp.106.091496.

49. Lefebvre, B.; Furt, F.; Hartmann, M.A.; Michaelson, L.V.; Carde, J.P.; Sargueil-Boiron, F.; Rossignol, M.; Napier, J.A.; Cullimore, J.; Bessoule, J.J.; Mongrand, S. Characterization of lipid rafts from Medicago truncatula root plasma membranes: a proteomic study reveals the presence of a raft-associated redox system. *Plant Physiol* **2007**, *144*, 402-418
doi: https://doi.org/10.1104/pp.106.094102.

50. Mongrand, S.; Morel, J.; Laroche, J.; Claverol, S.; Carde, J.P.; Hartmann, M.A.; Bonneu, M.; Simon-Plas, F.; Lessire, R.; Bessoule, J.J. Lipid rafts in higher plant cells: purification and characterization of Triton X-100-insoluble microdomains from tobacco plasma membrane. *J Biol Chem* **2004**, *279*, 36277-36286
doi: https://doi.org/10.1074/jbc.M403440200.

51. Morel, J.; Claverol, S.; Mongrand, S.; Furt, F.; Fromentin, J.; Bessoule, J.J.; Blein, J.P.; Simon-Plas, F. Proteomics of plant detergent-resistant membranes. *Mol Cell Proteomics* **2006**, *5*, 1396-1411
doi: https://doi.org/10.1074/mcp.M600044-MCP200.

52. Ott, T. Membrane nanodomains and microdomains in plant-microbe interactions. *Curr Opin Plant Biol* **2017**, *40*, 82-88
doi: https://doi.org/10.1016/j.pbi.2017.08.008.

53. Tanner, W.; Malinsky, J.; Opekarova, M. In plant and animal cells, detergent-resistant membranes do not define functional membrane rafts. *Plant Cell* **2011**, *23*, 1191-1193
doi: https://doi.org/10.1105/tpc.111.086249.

54. Tapken, W.; Murphy, A.S. Membrane nanodomains in plants: capturing form, function, and movement. *J Exp Bot* **2015**, *66*, 1573-1586
doi: https://doi.org/10.1093/jxb/erv054.

55. Yu, M.; Cui, Y.; Zhang, X.; Li, R.; Lin, J. Organization and dynamics of functional plant membrane microdomains. *Cell Mol Life Sci* **2020**, *77*, 275-287
doi: https://doi.org/10.1007/s00018-019-03270-7.

56. Gouguet, P.; Gronnier, J.; Legrand, A.; Perraki, A.; Jolivet, M.D.; Deroubaix, A.F.; German-Retana, S.; Boudsocq, M.; Habenstein, B.; Mongrand, S.; Germain, V. Connecting the dots: from nanodomains to physiological functions of REMORINs. *Plant Physiol* **2021**, *185*, 632-649
doi: https://doi.org/10.1093/plphys/kiaa063.

57. Gronnier, J.; Crowet, J.M.; Habenstein, B.; Nasir, M.N.; Bayle, V.; Hosy, E.; Platre, M.P.; Gouguet, P.; Raffaele, S.; Martinez, D.; Grelard, A.; Loquet, A.; Simon-Plas, F.; Gerbeau-Pissot, P.; Der, C.; Bayer, E.M.; Jaillais, Y.; Deleu, M.; Germain, V.; Lins, L.; Mongrand, S. Structural basis for plant plasma membrane protein dynamics and organization into functional nanodomains. *Elife* **2017**, *6*, e26404
doi: https://doi.org/10.7554/eLife.26404.

58. Raffaele, S.; Mongrand, S.; Gamas, P.; Niebel, A.; Ott, T. Genome-wide annotation of remorins, a plant-specific protein family: evolutionary and functional perspectives. *Plant Physiol* **2007**, *145*, 593-600
doi: https://doi.org/10.1104/pp.107.108639.

59. Gui, J.; Zheng, S.; Liu, C.; Shen, J.; Li, J.; Li, L. OsREM4.1 Interacts with OsSERK1 to Coordinate the Interlinking between Abscisic Acid and Brassinosteroid Signaling in Rice. *Dev Cell* **2016**, *38*, 201-213
doi: https://doi.org/10.1016/j.devcel.2016.06.011.

60. Martiniere, A.; Zelazny, E. Membrane nanodomains and transport functions in plant. *Plant Physiol* **2021**, *187*, 1839-1855
doi: https://doi.org/10.1093/plphys/kiab312.

61. Rivera-Milla, E.; Stuermer, C.A.; Malaga-Trillo, E. Ancient origin of reggie (flotillin), reggie-like, and other lipid-raft proteins: convergent evolution of the SPFH domain. *Cell Mol Life Sci* **2006**, *63*, 343-357
doi: https://doi.org/10.1007/s00018-005-5434-3.

62. Browman, D.T.; Hoegg, M.B.; Robbins, S.M. The SPFH domain-containing proteins: more than lipid raft markers. *Trends Cell Biol* **2007**, *17*, 394-402
doi: https://doi.org/10.1016/j.tcb.2007.06.005.

63. Danek, M.; Angelini, J.; Malinska, K.; Andrejch, J.; Amlerova, Z.; Kocourkova, D.; Brouzdova, J.; Valentova, O.; Martinec, J.; Petrasek, J. Cell wall contributes to the stability of plasma membrane nanodomain organization of Arabidopsis thaliana FLOTILLIN2 and HYPERSENSITIVE INDUCED REACTION1 proteins. *Plant J* **2020**, *101*, 619-636
doi: https://doi.org/10.1111/tpj.14566.

64. Liang, P.; Stratil, T.F.; Popp, C.; Marin, M.; Folgmann, J.; Mysore, K.S.; Wen, J.; Ott, T. Symbiotic root infections in Medicago truncatula require remorin-mediated receptor stabilization in membrane nanodomains. *Proc Natl Acad Sci U S A* **2018**, *115*, 5289-5294
doi: https://doi.org/10.1073/pnas.1721868115.

65. Cacas, J.L.; Bure, C.; Grosjean, K.; Gerbeau-Pissot, P.; Lherminier, J.; Rombouts, Y.; Maes, E.; Bossard, C.; Gronnier, J.; Furt, F.; Fouillen, L.; Germain, V.; Bayer, E.; Cluzet, S.; Robert, F.; Schmitter, J.M.; Deleu, M.; Lins, L.; Simon-Plas, F.; Mongrand, S. Revisiting Plant Plasma Membrane Lipids in Tobacco: A Focus on Sphingolipids. *Plant Physiol* **2016**, *170*, 367-384
doi: https://doi.org/10.1104/pp.15.00564.

66. Colin, L.A.; Jaillais, Y. Phospholipids across scales: lipid patterns and plant development. *Curr Opin Plant Biol* **2020**, *53*, 1-9
doi: https://doi.org/10.1016/j.pbi.2019.08.007.

67. Noack, L.C.; Jaillais, Y. Precision targeting by phosphoinositides: how PIs direct endomembrane trafficking in plants. *Curr Opin Plant Biol* **2017**, *40*, 22-33
doi: https://doi.org/10.1016/j.pbi.2017.06.017.

68. Platre, M.P.; Noack, L.C.; Doumane, M.; Bayle, V.; Simon, M.L.A.; Maneta-Peyret, L.; Fouillen, L.; Stanislas, T.; Armengot, L.; Pejchar, P.; Caillaud, M.C.; Potocky, M.; Copic, A.; Moreau, P.; Jaillais, Y. A Combinatorial Lipid Code Shapes the Electrostatic Landscape of Plant Endomembranes. *Dev Cell* **2018**, *45*, 465-480
doi: https://doi.org/10.1016/j.devcel.2018.04.011.

69. Simon, M.L.; Platre, M.P.; Marques-Bueno, M.M.; Armengot, L.; Stanislas, T.; Bayle, V.; Caillaud, M.C.; Jaillais, Y. A PtdIns(4)P-driven electrostatic field controls cell membrane identity and signalling in plants. *Nat Plants* **2016**, *2*, 16089
doi: https://doi.org/10.1038/nplants.2016.89.

70. Kusumi, A.; Fujiwara, T.K.; Chadda, R.; Xie, M.; Tsunoyama, T.A.; Kalay, Z.; Kasai, R.S.; Suzuki, K.G. Dynamic organizing principles of the plasma membrane that regulate signal transduction: commemorating the fortieth anniversary of Singer and Nicolson's fluid-mosaic model. *Annu Rev Cell Dev Biol* **2012**, *28*, 215-250
doi: https://doi.org/10.1146/annurev-cellbio-100809-151736.

71. Huang, D.; Sun, Y.; Ma, Z.; Ke, M.; Cui, Y.; Chen, Z.; Chen, C.; Ji, C.; Tran, T.M.; Yang, L.; Lam, S.M.; Han, Y.; Shu, G.; Friml, J.; Miao, Y.; Jiang, L.; Chen, X. Salicylic acid-mediated plasmodesmal closure via Remorin-dependent lipid organization. *Proc Natl Acad Sci U S A* **2019**, *116*, 21274-21284
doi: https://doi.org/10.1073/pnas.1911892116.

72. Legrand, A.; Martinez, D.; Grelard, A.; Berbon, M.; Morvan, E.; Tawani, A.; Loquet, A.; Mongrand, S.; Habenstein, B. Nanodomain Clustering of the Plant Protein Remorin by Solid-State NMR. *Front Mol Biosci* **2019**, *6*, 107
doi: https://doi.org/10.3389/fmolb.2019.00107.

73. Bhandari, D.D.; Brandizzi, F. Plant endomembranes and cytoskeleton: moving targets in immunity. *Curr Opin Plant Biol* **2020**, *58*, 8-16
doi: https://doi.org/10.1016/j.pbi.2020.09.003.

74. McKenna, J.F.; Rolfe, D.J.; Webb, S.E.D.; Tolmie, A.F.; Botchway, S.W.; Martin-Fernandez, M.L.; Hawes, C.; Runions, J. The cell wall regulates dynamics and size of plasma-membrane nanodomains in Arabidopsis. *Proc Natl Acad Sci U S A* **2019**, *116*, 12857-12862
doi: https://doi.org/10.1073/pnas.1819077116.

75. Konrad, S.S.; Popp, C.; Stratil, T.F.; Jarsch, I.K.; Thallmair, V.; Folgmann, J.; Marin, M.; Ott, T. S-acylation anchors remorin proteins to the plasma membrane but does not primarily determine their localization in membrane microdomains. *New Phytol* **2014**, *203*, 758-769
doi: https://doi.org/10.1111/nph.12867.

76. Lv, X.; Jing, Y.; Xiao, J.; Zhang, Y.; Zhu, Y.; Julian, R.; Lin, J. Membrane microdomains and the cytoskeleton constrain AtHIR1 dynamics and facilitate the formation of an AtHIR1-associated immune complex. *Plant J* **2017**, *90*, 3-16
doi: https://doi.org/10.1111/tpj.13480.

77. Raffaele, S.; Vailleau, F.; Leger, A.; Joubes, J.; Miersch, O.; Huard, C.; Blee, E.; Mongrand, S.; Domergue, F.; Roby, D. A MYB transcription factor regulates very-long-chain fatty acid biosynthesis for activation of the hypersensitive cell death response in Arabidopsis. *Plant Cell* **2008**, *20*, 752-767
doi: https://doi.org/10.1105/tpc.107.054858.

78. Szymanski, W.G.; Zauber, H.; Erban, A.; Gorka, M.; Wu, X.N.; Schulze, W.X. Cytoskeletal Components Define Protein Location to Membrane Microdomains. *Mol Cell Proteomics* **2015**, *14*, 2493-2509
doi: https://doi.org/10.1074/mcp.M114.046904.

79. Martiniere, A.; Lavagi, I.; Nageswaran, G.; Rolfe, D.J.; Maneta-Peyret, L.; Luu, D.T.; Botchway, S.W.; Webb, S.E.; Mongrand, S.; Maurel, C.; Martin-Fernandez, M.L.; Kleine-Vehn, J.; Friml, J.; Moreau, P.; Runions, J. Cell wall constrains lateral diffusion of plant plasma-membrane proteins. *Proc Natl Acad Sci U S A* **2012**, *109*, 12805-12810
doi: https://doi.org/10.1073/pnas.1202040109.

80. Talbot, H.F. XLIV. Experiments on light. *The London, Edinburgh, and Dublin Philosophical Magazine and Journal of Science* **1834**, *5*, 321-334
doi: https://doi.org/10.1080/14786443408648474.

81. Limpouchová, Z.; Procházka, K. Theoretical principles of fluorescence spectroscopy. *Fluorescence studies of polymer containing systems* **2016**, 91-149
doi: https://doi.org/10.1007/978-3-319-26788-3_4.

82. So, P.T.; Dong, C.Y. Fluorescence spectrophotometry. *e LS* **2001**,
doi: https://doi.org/10.1038/npg.els.0002978.

83. Kasha, M. Characterization of electronic transitions in complex molecules. *Discussions of the Faraday society* **1950**, *9*, 14-19
doi: https://doi.org/10.1039/DF9500900014.

84. Verhoeven, J. Glossary of terms used in photochemistry (IUPAC Recommendations 1996). *Pure and Applied Chemistry* **1996**, *68*, 2223-2286
doi: https://doi.org/10.1351/pac199668122223.

85. Stokes, G.G. XXX. On the change of refrangibility of light. *Philosophical transactions of the Royal Society of London* **1852**, 463-562
doi: https://doi.org/10.1098/rstl.1852.0022.

86. Förster, T. Zwischenmolekulare Energiewanderung und Fluoreszenz. *Annalen der Physik* **2006**, *437*, 55-75
doi: https://doi.org/10.1002/andp.19484370105.

87. Medintz, I.L.; Hildebrandt, N. *FRET-Förster Resonance Energy Transfer: From Theory to Applications*; John Wiley & Sons: 2013.

88. Chen, Y.; Mills, J.D.; Periasamy, A. Protein localization in living cells and tissues using FRET and FLIM. *Differentiation* **2003**, *71*, 528-541
doi: https://doi.org/10.1111/j.1432-0436.2003.07109007.x.

89. Margineanu, A.; Chan, J.J.; Kelly, D.J.; Warren, S.C.; Flatters, D.; Kumar, S.; Katan, M.; Dunsby, C.W.; French, P.M. Screening for protein-protein interactions using Forster resonance energy transfer (FRET) and fluorescence lifetime imaging microscopy (FLIM). *Sci Rep* **2016**, *6*, 28186
doi: https://doi.org/10.1038/srep28186.

90. Chen, H.; Puhl, H.L., 3rd; Koushik, S.V.; Vogel, S.S.; Ikeda, S.R. Measurement of FRET efficiency and ratio of donor to acceptor concentration in living cells. *Biophys J* **2006**, *91*, 39-41
doi: https://doi.org/10.1529/biophysj.106.088773.

91. Hoppe, A.; Christensen, K.; Swanson, J.A. Fluorescence resonance energy transfer-based stoichiometry in living cells. *Biophysical journal* **2002**, *83*, 3652-3664
doi: https://doi.org/10.1016/s0006-3495(02)75365-4.

92. Noomnarm, U.; Clegg, R.M. Fluorescence lifetimes: fundamentals and interpretations. *Photosynth Res* **2009**, *101*, 181-194
doi: https://doi.org/10.1007/s11120-009-9457-8.

93. Lakowicz, J.R. *Principles of fluorescence spectroscopy*; Springer: 2006.

94. Valeur, B.; Berberan-Santos, M.N. *Molecular fluorescence: principles and applications*; John Wiley & Sons: 2013.

95. Becker, W. Fluorescence lifetime imaging--techniques and applications. *J Microsc* **2012**, *247*, 119-136
doi: https://doi.org/10.1111/j.1365-2818.2012.03618.x.

96. Warren, S.C.; Margineanu, A.; Alibhai, D.; Kelly, D.J.; Talbot, C.; Alexandrov, Y.; Munro, I.; Katan, M.; Dunsby, C.; French, P.M. Rapid global fitting of large fluorescence lifetime imaging microscopy datasets. *PLoS One* **2013**, *8*, e70687
doi: https://doi.org/10.1371/journal.pone.0070687.

97. Clarivate. Web of Science Available online: https://www.webofscience.com/wos/woscc/analyze-results/b6373be7-7334-48d4-9300-b52b75f92593-01047f20aa (accessed on 10.04.2024).

98. McWhite, C.D.; Papoulas, O.; Drew, K.; Cox, R.M.; June, V.; Dong, O.X.; Kwon, T.; Wan, C.; Salmi, M.L.; Roux, S.J.; Browning, K.S.; Chen, Z.J.; Ronald, P.C.; Marcotte, E.M. A Pan-plant Protein Complex Map Reveals Deep Conservation and Novel Assemblies. *Cell* **2020**, *181*, 460-474
doi: https://doi.org/10.1016/j.cell.2020.02.049.

99. Sun, Y.; Wallrabe, H.; Booker, C.F.; Day, R.N.; Periasamy, A. Three-color spectral FRET microscopy localizes three interacting proteins in living cells. *Biophys J* **2010**, *99*, 1274-1283
doi: https://doi.org/10.1016/j.bpj.2010.06.004.

100. Ehrhardt, D.W.; Frommer, W.B. New technologies for 21st century plant science. *Plant Cell* **2012**, *24*, 374-394
doi: https://doi.org/10.1105/tpc.111.093302.

101. Clarke, D.T.; Martin-Fernandez, M.L. A Brief History of Single-Particle Tracking of the Epidermal Growth Factor Receptor. *Methods Protoc* **2019**, *2*
doi: https://doi.org/10.3390/mps2010012.

102. Lelek, M.; Gyparaki, M.T.; Beliu, G.; Schueder, F.; Griffie, J.; Manley, S.; Jungmann, R.; Sauer, M.; Lakadamyali, M.; Zimmer, C. Single-molecule localization microscopy. *Nat Rev Methods Primers* **2021**, *1*, 39
doi: https://doi.org/10.1038/s43586-021-00038-x.

103. Manzo, C.; Garcia-Parajo, M.F. A review of progress in single particle tracking: from methods to biophysical insights. *Rep Prog Phys* **2015**, *78*, 124601
doi: https://doi.org/10.1088/0034-4885/78/12/124601.

104. Shen, H.; Tauzin, L.J.; Baiyasi, R.; Wang, W.; Moringo, N.; Shuang, B.; Landes, C.F. Single Particle Tracking: From Theory to Biophysical Applications. *Chem Rev* **2017**, *117*, 7331-7376
doi: https://doi.org/10.1021/acs.chemrev.6b00815.

105. Cheng, C.-Y.; Hsieh, C.-L. Background Estimation and Correction for High-Precision Localization Microscopy. *ACS Photonics* **2017**, *4*, 1730-1739
doi: https://doi.org/10.1021/acsphotonics.7b00238.

106. Mortensen, K.I.; Churchman, L.S.; Spudich, J.A.; Flyvbjerg, H. Optimized localization analysis for single-molecule tracking and super-resolution microscopy. *Nat Methods* **2010**, *7*, 377-381
doi: https://doi.org/10.1038/nmeth.1447.

107. Ober, R.J.; Ram, S.; Ward, E.S. Localization accuracy in single-molecule microscopy. *Biophysical journal* **2004**, *86*, 1185-1200
doi: https://doi.org/10.1016%2FS0006-3495(04)74193-4.

108. Betzig, E.; Patterson, G.H.; Sougrat, R.; Lindwasser, O.W.; Olenych, S.; Bonifacino, J.S.; Davidson, M.W.; Lippincott-Schwartz, J.; Hess, H.F. Imaging intracellular fluorescent proteins at nanometer resolution. *Science* **2006**, *313*, 1642-1645
doi: https://doi.org/10.1126/science.1127344.

109. Manley, S.; Gillette, J.M.; Patterson, G.H.; Shroff, H.; Hess, H.F.; Betzig, E.; Lippincott-Schwartz, J. High-density mapping of single-molecule trajectories with photoactivated localization microscopy. *Nat Methods* **2008**, *5*, 155-157
doi: https://doi.org/10.1038/nmeth.1176.

110. Magrassi, R.; Scalisi, S.; Cella Zanacchi, F. Single-molecule localization to study cytoskeletal structures, membrane complexes, and mechanosensors. *Biophys Rev* **2019**, *11*, 745-756
doi: https://doi.org/10.1007/s12551-019-00595-2.

111. Iwatate, R.J.; Yoshinari, A.; Yagi, N.; Grzybowski, M.; Ogasawara, H.; Kamiya, M.; Komatsu, T.; Taki, M.; Yamaguchi, S.; Frommer, W.B.; Nakamura, M. Covalent Self-Labeling of Tagged Proteins with Chemical Fluorescent Dyes in BY-2 Cells and Arabidopsis Seedlings. *Plant Cell* **2020**, *32*, 3081-3094
doi: https://doi.org/10.1105/tpc.20.00439.

112. Shimomura, O.; Johnson, F.H.; Saiga, Y. Extraction, purification and properties of aequorin, a bioluminescent protein from the luminous hydromedusan, Aequorea. *J Cell Comp Physiol* **1962**, *59*, 223-239
doi: https://doi.org/10.1002/jcp.1030590302.

113. Chalfie, M.; Tu, Y.; Euskirchen, G.; Ward, W.W.; Prasher, D.C. Green fluorescent protein as a marker for gene expression. *Science* **1994**, *263*, 802-805
doi: https://doi.org/10.1126/science.8303295.

114. Shcherbakova, D.M.; Sengupta, P.; Lippincott-Schwartz, J.; Verkhusha, V.V. Photocontrollable fluorescent proteins for superresolution imaging. *Annu Rev Biophys* **2014**, *43*, 303-329
doi: https://doi.org/10.1146/annurev-biophys-051013-022836.

115. Ando, R.; Mizuno, H.; Miyawaki, A. Regulated fast nucleocytoplasmic shuttling observed by reversible protein highlighting. *Science* **2004**, *306*, 1370-1373
doi: https://doi.org/10.1126/science.1102506.

116. Zhang, X.; Zhang, M.; Li, D.; He, W.; Peng, J.; Betzig, E.; Xu, P. Highly photostable, reversibly photoswitchable fluorescent protein with high contrast ratio for live-cell superresolution microscopy. *Proc Natl Acad Sci U S A* **2016**, *113*, 10364-10369
doi: https://doi.org/10.1073/pnas.1611038113.

117. Zhang, M.; Chang, H.; Zhang, Y.; Yu, J.; Wu, L.; Ji, W.; Chen, J.; Liu, B.; Lu, J.; Liu, Y.; Zhang, J.; Xu, P.; Xu, T. Rational design of true monomeric and bright photoactivatable fluorescent proteins. *Nat Methods* **2012**, *9*, 727-729
doi: https://doi.org/10.1038/nmeth.2021.

118. Patterson, G.H.; Lippincott-Schwartz, J. A photoactivatable GFP for selective photolabeling of proteins and cells. *Science* **2002**, *297*, 1873-1877
doi: https://doi.org/10.1126/science.1074952.

119. Gaytan, P.; Roldan-Salgado, A. Photoactivatable Blue Fluorescent Protein. *ACS Omega* **2024**, *9*, 28577-28582
doi: https://doi.org/10.1021/acsomega.4c02603.

120. Bayle, V.; Fiche, J.B.; Burny, C.; Platre, M.P.; Nollmann, M.; Martiniere, A.; Jaillais, Y. Single-particle tracking photoactivated localization microscopy of membrane proteins in living plant tissues. *Nat Protoc* **2021**, *16*, 1600-1628
doi: https://doi.org/10.1038/s41596-020-00471-4.

121. Ambrose, E. A surface contact microscope for the study of cell movements. *Nature* **1956**, *178*, 1194-1194
doi: https://doi.org/10.1038/1781194a0.

122. Axelrod, D. Cell-substrate contacts illuminated by total internal reflection fluorescence. *The Journal of cell biology* **1981**, *89*, 141-145
doi: https://doi.org/10.1083/jcb.89.1.141.

123. Trache, A.; Meininger, G.A. Total internal reflection fluorescence (TIRF) microscopy. *Curr Protoc Microbiol* **2008**, *Chapter 2*
doi: https://doi.org/10.1002/9780471729259.mc02a02s10.

124. Langhans, M.; Meckel, T. Single-molecule detection and tracking in plants. *Protoplasma* **2014**, *251*, 277-291
doi: https://doi.org/10.1007/s00709-013-0601-0.

125. Tokunaga, M.; Imamoto, N.; Sakata-Sogawa, K. Highly inclined thin illumination enables clear single-molecule imaging in cells. *Nat Methods* **2008**, *5*, 159-161
doi: https://doi.org/10.1038/nmeth1171.

126. Konopka, C.A.; Bednarek, S.Y. Variable-angle epifluorescence microscopy: a new way to look at protein dynamics in the plant cell cortex. *Plant J* **2008**, *53*, 186-196
doi: https://doi.org/10.1111/j.1365-313X.2007.03306.x.

127. Manley, S.; Gillette, J.M.; Lippincott-Schwartz, J. Single-particle tracking photoactivated localization microscopy for mapping single-molecule dynamics. *Methods Enzymol* **2010**, *475*, 109-120
doi: https://doi.org/10.1016/S0076-6879(10)75005-9.

128. Kalaidzidis, Y. Multiple objects tracking in fluorescence microscopy. *J Math Biol* **2009**, *58*, 57-80
doi: https://doi.org/10.1007/s00285-008-0180-4.

129. Tinevez, J.Y.; Perry, N.; Schindelin, J.; Hoopes, G.M.; Reynolds, G.D.; Laplantine, E.; Bednarek, S.Y.; Shorte, S.L.; Eliceiri, K.W. TrackMate: An open and extensible platform for single-particle tracking. *Methods* **2017**, *115*, 80-90
doi: https://doi.org/10.1016/j.ymeth.2016.09.016.

130. Saxton, M.J.; Jacobson, K. Single-particle tracking: applications to membrane dynamics. *Annual review of biophysics and biomolecular structure* **1997**, *26*, 373-399
doi: https://doi.org/10.1146/annurev.biophys.26.1.373.

131. Arts, M.; Smal, I.; Paul, M.W.; Wyman, C.; Meijering, E. Particle Mobility Analysis Using Deep Learning and the Moment Scaling Spectrum. *Sci Rep* **2019**, *9*, 17160
doi: https://doi.org/10.1038/s41598-019-53663-8.

132. Munoz-Gil, G.; Volpe, G.; Garcia-March, M.A.; Aghion, E.; Argun, A.; Hong, C.B.; Bland, T.; Bo, S.; Conejero, J.A.; Firbas, N.; Garibo, I.O.O.; Gentili, A.; Huang, Z.; Jeon, J.H.; Kabbech, H.; Kim, Y.; Kowalek, P.; Krapf, D.; Loch-Olszewska, H.; Lomholt, M.A.; Masson, J.B.; Meyer, P.G.; Park, S.; Requena, B.; Smal, I.; Song, T.; Szwabinski, J.; Thapa, S.; Verdier, H.; Volpe, G.; Widera, A.; Lewenstein, M.; Metzler, R.; Manzo, C. Objective comparison of methods to decode anomalous diffusion. *Nat Commun* **2021**, *12*, 6253
doi: https://doi.org/10.1038/s41467-021-26320-w.

133. Das, R.; Cairo, C.W.; Coombs, D. A hidden Markov model for single particle tracks quantifies dynamic interactions between LFA-1 and the actin cytoskeleton. *PLoS Comput Biol* **2009**, *5*, e1000556
doi: https://doi.org/10.1371/journal.pcbi.1000556.

134. Helmuth, J.A.; Burckhardt, C.J.; Koumoutsakos, P.; Greber, U.F.; Sbalzarini, I.F. A novel supervised trajectory segmentation algorithm identifies distinct types of human adenovirus motion in host cells. *J Struct Biol* **2007**, *159*, 347-358
doi: https://doi.org/10.1016/j.jsb.2007.04.003.

135. Persson, F.; Linden, M.; Unoson, C.; Elf, J. Extracting intracellular diffusive states and transition rates from single-molecule tracking data. *Nat Methods* **2013**, *10*, 265-269
doi: https://doi.org/10.1038/nmeth.2367.

136. Vega, A.R.; Freeman, S.A.; Grinstein, S.; Jaqaman, K. Multistep Track Segmentation and Motion Classification for Transient Mobility Analysis. *Biophys J* **2018**, *114*, 1018-1025
doi: https://doi.org/10.1016/j.bpj.2018.01.012.

137. Wagner, T.; Kroll, A.; Haramagatti, C.R.; Lipinski, H.G.; Wiemann, M. Classification and Segmentation of Nanoparticle Diffusion Trajectories in Cellular Micro Environments. *PLoS One* **2017**, *12*, e0170165
doi: https://doi.org/10.1371/journal.pone.0170165.

138. Khater, I.M.; Nabi, I.R.; Hamarneh, G. A Review of Super-Resolution Single-Molecule Localization Microscopy Cluster Analysis and Quantification Methods. *Patterns (N Y)* **2020**, *1*, 100038
doi: https://doi.org/10.1016/j.patter.2020.100038.

139. Perraki, A.; Gronnier, J.; Gouguet, P.; Boudsocq, M.; Deroubaix, A.F.; Simon, V.; German-Retana, S.; Legrand, A.; Habenstein, B.; Zipfel, C.; Bayer, E.; Mongrand, S.; Germain, V. REM1.3's phospho-status defines its plasma membrane nanodomain organization and activity in restricting PVX cell-to-cell movement. *PLoS Pathog* **2018**, *14*, e1007378 doi: https://doi.org/10.1371/journal.ppat.1007378.

140. Smokvarska, M.; Francis, C.; Platre, M.P.; Fiche, J.B.; Alcon, C.; Dumont, X.; Nacry, P.; Bayle, V.; Nollmann, M.; Maurel, C.; Jaillais, Y.; Martiniere, A. A Plasma Membrane Nanodomain Ensures Signal Specificity during Osmotic Signaling in Plants. *Curr Biol* **2020**, *30*, 4654-4664 doi: https://doi.org/10.1016/j.cub.2020.09.013.

141. Levet, F.; Hosy, E.; Kechkar, A.; Butler, C.; Beghin, A.; Choquet, D.; Sibarita, J.B. SR-Tesseler: a method to segment and quantify localization-based super-resolution microscopy data. *Nat Methods* **2015**, *12*, 1065-1071 doi: https://doi.org/10.1038/nmeth.3579.

142. Andronov, L.; Orlov, I.; Lutz, Y.; Vonesch, J.L.; Klaholz, B.P. ClusterViSu, a method for clustering of protein complexes by Voronoi tessellation in super-resolution microscopy. *Sci Rep* **2016**, *6*, 24084 doi: https://doi.org/10.1038/srep24084.

143. Wallis, T.P.; Jiang, A.; Young, K.; Hou, H.; Kudo, K.; McCann, A.J.; Durisic, N.; Joensuu, M.; Oelz, D.; Nguyen, H.; Gormal, R.S.; Meunier, F.A. Super-resolved trajectory-derived nanoclustering analysis using spatiotemporal indexing. *Nat Commun* **2023**, *14*, 3353 doi: https://doi.org/10.1038/s41467-023-38866-y.

144. Rohr, L.; Ehinger, A.; Rausch, L.; Glöckner Burmeister, N.; Meixner, A.J.; Gronnier, J.; Harter, K.; Kemmerling, B.; Zur Oven-Krockhaus, S. OneFlowTraX: a user-friendly software for super-resolution analysis of single-molecule dynamics and nanoscale organization. *Front Plant Sci* **2024**, *15*, 1358935 doi: https://doi.org/10.3389/fpls.2024.1358935.

145. Martens, K.J.A.; Turkowyd, B.; Endesfelder, U. Raw Data to Results: A Hands-On Introduction and Overview of Computational Analysis for Single-Molecule Localization Microscopy. *Front Bioinform* **2021**, *1*, 817254 doi: https://doi.org/10.3389/fbinf.2021.817254.

146. Hosy, E.; Martiniere, A.; Choquet, D.; Maurel, C.; Luu, D.T. Super-resolved and dynamic imaging of membrane proteins in plant cells reveal contrasting kinetic profiles and multiple confinement mechanisms. *Mol Plant* **2015**, *8*, 339-342 doi: https://doi.org/10.1016/j.molp.2014.10.006.

147. Platre, M.P.; Bayle, V.; Armengot, L.; Bareille, J.; Marques-Bueno, M.d.M.; Creff, A.; Maneta-Peyret, L.; Fiche, J.-B.; Nollmann, M.; Miège, C. Developmental control of plant Rho GTPase nano-organization by the lipid phosphatidylserine. *Science* **2019**, *364*, 57-62 doi: https://doi.org/10.1126/science.aav9959.

148. Pain, C.; Tynan, C.; Botchway, S.W.; Kriechbaumer, V. Variable-Angle Epifluorescence Microscopy for Single-Particle Tracking in the Plant ER. *Methods Mol Biol* **2024**, *2772*, 273-283 doi: https://doi.org/10.1007/978-1-0716-3710-4_20.

149. Ries, J. SMAP: a modular super-resolution microscopy analysis platform for SMLM data. *Nat Methods* **2020**, *17*, 870-872 doi: https://doi.org/10.1038/s41592-020-0938-1.

150. Wilkinson, M.D.; Dumontier, M.; Aalbersberg, I.J.; Appleton, G.; Axton, M.; Baak, A.; Blomberg, N.; Boiten, J.W.; da Silva Santos, L.B.; Bourne, P.E.; Bouwman, J.; Brookes, A.J.; Clark, T.; Crosas, M.; Dillo, I.; Dumon, O.; Edmunds, S.; Evelo, C.T.; Finkers, R.; Gonzalez-Beltran, A.; Gray, A.J.; Groth, P.; Goble, C.; Grethe, J.S.; Heringa, J.; t Hoen, P.A.; Hooft, R.; Kuhn, T.; Kok, R.; Kok, J.; Lusher, S.J.; Martone, M.E.; Mons, A.; Packer, A.L.; Persson, B.; Rocca-Serra, P.; Roos, M.; van Schaik, R.; Sansone, S.A.; Schultes, E.; Sengstag, T.; Slater, T.; Strawn, G.; Swertz, M.A.; Thompson, M.; van der Lei, J.; van Mulligen, E.; Velterop, J.; Waagmeester, A.; Wittenburg, P.; Wolstencroft, K.; Zhao, J.; Mons, B. The FAIR Guiding Principles for scientific data management and stewardship. *Sci Data* **2016**, *3*, 160018 doi: https://doi.org/10.1038/sdata.2016.18.

151. Weil, H.L.; Schneider, K.; Tschope, M.; Bauer, J.; Maus, O.; Frey, K.; Brilhaus, D.; Martins Rodrigues, C.; Doniparthi, G.; Wetzels, F.; Lukasczyk, J.; Kranz, A.; Gruning, B.; Zimmer, D.; Dessloch, S.; von Suchodoletz, D.; Usadel, B.; Garth, C.; Muhlhaus, T. PLANTdataHUB: a collaborative platform for continuous FAIR data sharing in plant research. *Plant J* **2023**, *116*, 974-988 doi: https://doi.org/10.1111/tpj.16474.

152. Barker, M.; Chue Hong, N.P.; Katz, D.S.; Lamprecht, A.L.; Martinez-Ortiz, C.; Psomopoulos, F.; Harrow, J.; Castro, L.J.; Gruenpeter, M.; Martinez, P.A.; Honeyman, T. Introducing the FAIR Principles for research software. *Sci Data* **2022**, *9*, 622 doi: https://doi.org/10.1038/s41597-022-01710-x.

153. Hugelier, S.; Colosi, P.L.; Lakadamyali, M. Quantitative Single-Molecule Localization Microscopy. *Annu Rev Biophys* **2023**, *52*, 139-160 doi: https://doi.org/10.1146/annurev-biophys-111622-091212.

154. Rohr, L.; Ehinger, A.; Burmeister, N.G.; Meixner, A.J.; Kemmerling, B.; Harter, K.; zur Oven-Krockhaus, S. Simultaneous and Dynamic Super-Resolution Imaging of Two Proteins in Arabidopsis thaliana using dual-color sptPALM. *bioRxiv* **2024**, doi: https://doi.org/10.1101/2024.03.13.584811.

155. Tinevez, J.-Y. simpletracker (GitHub). Available online: https://github.com/tinevez/simpletracker (accessed on 28.08.2024).

156. Ester, M.; Kriegel, H.-P.; Sander, J.; Xu, X. A density-based algorithm for discovering clusters in large spatial databases with noise. In Proceedings of the kdd, 1996; pp. 226-231.

157. Jolivet, M.-D.; Deroubaix, A.-F.; Boudsocq, M.; Abel, N.B.; Rocher, M.; Robbe, T.; Wattelet-Boyer, V.; Huard, J.; Lefebvre, D.; Lu, Y.-J. Interdependence of a kinase and its cognate substrate plasma membrane nanoscale dynamics underlies Arabidopsis response to viral infection. *bioRxiv* **2023**, doi: https://doi.org/10.1101/2023.07.31.551174.

158. Gronnier, J.; Franck, C.M.; Stegmann, M.; DeFalco, T.A.; Abarca, A.; von Arx, M.; Dunser, K.; Lin, W.; Yang, Z.; Kleine-Vehn, J.; Ringli, C.; Zipfel, C. Regulation of immune receptor kinase plasma membrane nanoscale organization by a plant peptide hormone and its receptors. *Elife* **2022**, *11*, e74162 doi: https://doi.org/10.7554/eLife.74162.

159. Power, R.M.; Tschanz, A.; Zimmermann, T.; Ries, J. Build and operation of a custom 3D, multicolor, single-molecule localization microscope. *Nat Protoc* **2024**, doi: https://doi.org/10.1038/s41596-024-00989-x.

160. Gronnier, J.; Gerbeau-Pissot, P.; Germain, V.; Mongrand, S.; Simon-Plas, F. Divide and Rule: Plant Plasma Membrane Organization. *Trends Plant Sci* **2018**, *23*, 899-917
doi: https://doi.org/10.1016/j.tplants.2018.07.007.

161. Fujita, S.; Pytela, J.; Hotta, T.; Kato, T.; Hamada, T.; Akamatsu, R.; Ishida, Y.; Kutsuna, N.; Hasezawa, S.; Nomura, Y.; Nakagami, H.; Hashimoto, T. An atypical tubulin kinase mediates stress-induced microtubule depolymerization in Arabidopsis. *Curr Biol* **2013**, *23*, 1969-1978
doi: https://doi.org/10.1016/j.cub.2013.08.006.

162. Harterink, M.; da Silva, M.E.; Will, L.; Turan, J.; Ibrahim, A.; Lang, A.E.; van Battum, E.Y.; Pasterkamp, R.J.; Kapitein, L.C.; Kudryashov, D.; Barres, B.A.; Hoogenraad, C.C.; Zuchero, J.B. DeActs: genetically encoded tools for perturbing the actin cytoskeleton in single cells. *Nat Methods* **2017**, *14*, 479-482
doi: https://doi.org/10.1038/nmeth.4257.

163. Vilches Barro, A.; Stockle, D.; Thellmann, M.; Ruiz-Duarte, P.; Bald, L.; Louveaux, M.; von Born, P.; Denninger, P.; Goh, T.; Fukaki, H.; Vermeer, J.E.M.; Maizel, A. Cytoskeleton Dynamics Are Necessary for Early Events of Lateral Root Initiation in Arabidopsis. *Curr Biol* **2019**, *29*, 2443-2454
doi: https://doi.org/10.1016/j.cub.2019.06.039.

164. Hansen, A.S.; Woringer, M.; Grimm, J.B.; Lavis, L.D.; Tjian, R.; Darzacq, X. Robust model-based analysis of single-particle tracking experiments with Spot-On. *Elife* **2018**, *7*, e33125
doi: https://doi.org/10.7554/eLife.33125.

165. Farquharson, K.L. On the origin of cortical microtubules. *Plant Cell* **2009**, *21*, 2193
doi: https://doi.org/10.1105/tpc.109.210812.

166. Kalachova, T.; Leontovyčová, H.; Iakovenko, O.; Pospíchalová, R.; Maršík, P.; Klouček, P.; Janda, M.; Valentová, O.; Kocourková, D.; Martinec, J.; Burketová, L.; Ruelland, E. Interplay between phosphoinositides and actin cytoskeleton in the regulation of immunity related responses in Arabidopsis thaliana seedlings. *Environmental and Experimental Botany* **2019**, *167*, 103867
doi: https://doi.org/10.1016/j.envexpbot.2019.103867.

167. Ke, M.; Ma, Z.; Wang, D.; Sun, Y.; Wen, C.; Huang, D.; Chen, Z.; Yang, L.; Tan, S.; Li, R.; Friml, J.; Miao, Y.; Chen, X. Salicylic acid regulates PIN2 auxin transporter hyperclustering and root gravitropic growth via Remorin-dependent lipid nanodomain organisation in Arabidopsis thaliana. *New Phytol* **2021**, *229*, 963-978
doi: https://doi.org/10.1111/nph.16915.

168. Leontovycova, H.; Kalachova, T.; Trda, L.; Pospichalova, R.; Lamparova, L.; Dobrev, P.I.; Malinska, K.; Burketova, L.; Valentova, O.; Janda, M. Actin depolymerization is able to increase plant resistance against pathogens via activation of salicylic acid signalling pathway. *Sci Rep* **2019**, *9*, 10397
doi: https://doi.org/10.1038/s41598-019-46465-5.

169. Matouskova, J.; Janda, M.; Fiser, R.; Sasek, V.; Kocourkova, D.; Burketova, L.; Duskova, J.; Martinec, J.; Valentova, O. Changes in actin dynamics are involved in salicylic acid signaling pathway. *Plant Sci* **2014**, *223*, 36-44
doi: https://doi.org/10.1016/j.plantsci.2014.03.002.

170. Andrews, S.S. Accurate particle-based simulation of adsorption, desorption and partial transmission. *Phys Biol* **2009**, *6*, 046015
doi: https://doi.org/10.1088/1478-3975/6/4/046015.

171. Dale, R.; Oswald, S.; Jalihal, A.; LaPorte, M.F.; Fletcher, D.M.; Hubbard, A.; Shiu, S.H.; Nelson, A.D.L.; Bucksch, A. Overcoming the Challenges to Enhancing Experimental Plant Biology With Computational Modeling. *Front Plant Sci* **2021**, *12*, 687652
doi: https://doi.org/10.3389/fpls.2021.687652.

172. Xing, S.; Wallmeroth, N.; Berendzen, K.W.; Grefen, C. Techniques for the Analysis of Protein-Protein Interactions in Vivo. *Plant Physiol* **2016**, *171*, 727-758
doi: https://doi.org/10.1104/pp.16.00470.

173. Bajar, B.T.; Wang, E.S.; Zhang, S.; Lin, M.Z.; Chu, J. A Guide to Fluorescent Protein FRET Pairs. *Sensors (Basel)* **2016**, *16*, 1488
doi: https://doi.org/10.3390/s16091488.

174. Gilbert, M.; Schulze, W.X. Global Identification of Protein Complexes within the Membrane Proteome of Arabidopsis Roots Using a SEC-MS Approach. *J Proteome Res* **2019**, *18*, 107-119
doi: https://doi.org/10.1021/acs.jproteome.8b00382.

175. Wu, X.N.; Chu, L.; Xi, L.; Pertl-Obermeyer, H.; Li, Z.; Sklodowski, K.; Sanchez-Rodriguez, C.; Obermeyer, G.; Schulze, W.X. Sucrose-induced Receptor Kinase 1 is Modulated by an Interacting Kinase with Short Extracellular Domain. *Mol Cell Proteomics* **2019**, *18*, 1556-1571
doi: https://doi.org/10.1074/mcp.RA119.001336.

176. Wu, X.N.; Sanchez Rodriguez, C.; Pertl-Obermeyer, H.; Obermeyer, G.; Schulze, W.X. Sucrose-induced receptor kinase SIRK1 regulates a plasma membrane aquaporin in Arabidopsis. *Mol Cell Proteomics* **2013**, *12*, 2856-2873
doi: https://doi.org/10.1074/mcp.M113.029579.

177. Vercammen, D.; van de Cotte, B.; De Jaeger, G.; Eeckhout, D.; Casteels, P.; Vandepoele, K.; Vandenberghe, I.; Van Beeumen, J.; Inze, D.; Van Breusegem, F. Type II metacaspases Atmc4 and Atmc9 of Arabidopsis thaliana cleave substrates after arginine and lysine. *J Biol Chem* **2004**, *279*, 45329-45336
doi: https://doi.org/10.1074/jbc.M406329200.

178. Moussu, S.; Broyart, C.; Santos-Fernandez, G.; Augustin, S.; Wehrle, S.; Grossniklaus, U.; Santiago, J. Structural basis for recognition of RALF peptides by LRX proteins during pollen tube growth. *Proc Natl Acad Sci U S A* **2020**, *117*, 7494-7503
doi: https://doi.org/10.1073/pnas.2000100117.

179. Bücherl, C.A.; van Esse, G.W.; Kruis, A.; Luchtenberg, J.; Westphal, A.H.; Aker, J.; van Hoek, A.; Albrecht, C.; Borst, J.W.; de Vries, S.C. Visualization of BRI1 and BAK1(SERK3) membrane receptor heterooligomers during brassinosteroid signaling. *Plant Physiol* **2013**, *162*, 1911-1925
doi: https://doi.org/10.1104/pp.113.220152.

180. Bader, A.N.; Hoetzl, S.; Hofman, E.G.; Voortman, J.; van Bergen en Henegouwen, P.M.; van Meer, G.; Gerritsen, H.C. Homo-FRET imaging as a tool to quantify protein and lipid clustering. *Chemphyschem* **2011**, *12*, 475-483
doi: https://doi.org/10.1002/cphc.201000801.

181. Martin-Fernandez, M.; Clarke, D.T.; Tobin, M.J.; Jones, S.V.; Jones, G.R. Preformed oligomeric epidermal growth factor receptors undergo an ectodomain structure change during signaling. *Biophysical journal* **2002**, *82*, 2415-2427
doi: https://doi.org/10.1016%2FS0006-3495(02)75585-9.

182. Yu, X.; Sharma, K.D.; Takahashi, T.; Iwamoto, R.; Mekada, E. Ligand-independent dimer formation of epidermal growth factor receptor (EGFR) is a step separable from ligand-induced EGFR signaling. *Mol Biol Cell* **2002**, *13*, 2547-2557
doi: https://doi.org/10.1091/mbc.01-08-0411.

183. Goedhart, J.; von Stetten, D.; Noirclerc-Savoye, M.; Lelimousin, M.; Joosen, L.; Hink, M.A.; van Weeren, L.; Gadella, T.W., Jr.; Royant, A. Structure-guided evolution of cyan fluorescent proteins towards a quantum yield of 93%. *Nat Commun* **2012**, *3*, 751
doi: https://doi.org/10.1038/ncomms1738.

184. Garnelo Gomez, B.; Holzwart, E.; Shi, C.; Lozano-Duran, R.; Wolf, S. Phosphorylation-dependent routing of RLP44 towards brassinosteroid or phytosulfokine signalling. *J Cell Sci* **2021**, *134*, 259134
doi: https://doi.org/10.1242/jcs.259134.

185. van Esse, W.G.; Westphal, A.H.; Surendran, R.P.; Albrecht, C.; van Veen, B.; Borst, J.W.; de Vries, S.C. Quantification of the brassinosteroid insensitive1 receptor in planta. *Plant Physiol* **2011**, *156*, 1691-1700
doi: https://doi.org/10.1104/pp.111.179309.

186. White, P.J.; Biskup, B.; Elzenga, J.T.M.; Homann, U.; Thiel, G.; Wissing, F.; Maathuis, F.J.M. Advanced patch-clamp techniques and single-channel analysis. *J Exp Bot* **1999**, *50*, 1037-1054
doi: https://doi.org/10.1093/jxb/50.Special_Issue.1037.

187. Denyer, T.; Ma, X.; Klesen, S.; Scacchi, E.; Nieselt, K.; Timmermans, M.C.P. Spatiotemporal Developmental Trajectories in the Arabidopsis Root Revealed Using High-Throughput Single-Cell RNA Sequencing. *Dev Cell* **2019**, *48*, 840-852
doi: https://doi.org/10.1016/j.devcel.2019.02.022.

188. Yuan, W.; Li, Y.; Li, L.; Siao, W.; Zhang, Q.; Zhang, Y.; Liu, J.; Xu, W.; Miao, R. BR-INSENSITIVE1 regulates hydrotropic response by interacting with plasma membrane H(+)-ATPases in Arabidopsis. *Plant Signal Behav* **2018**, *13*, e1486147
doi: https://doi.org/10.1080/15592324.2018.1486147.

189. Barbez, E.; Dunser, K.; Gaidora, A.; Lendl, T.; Busch, W. Auxin steers root cell expansion via apoplastic pH regulation in Arabidopsis thaliana. *Proc Natl Acad Sci U S A* **2017**, *114*, E4884-E4893
doi: https://doi.org/10.1073/pnas.1613499114.

190. Xu, W.; Huang, J.; Li, B.; Li, J.; Wang, Y. Is kinase activity essential for biological functions of BRI1? *Cell Res* **2008**, *18*, 472-478
doi: https://doi.org/10.1038/cr.2008.36.

191. Borsics, T.; Webb, D.; Andeme-Ondzighi, C.; Staehelin, L.A.; Christopher, D.A. The cyclic nucleotide-gated calmodulin-binding channel AtCNGC10 localizes to the plasma membrane and influences numerous growth responses and starch accumulation in Arabidopsis thaliana. *Planta* **2007**, *225*, 563-573
doi: https://doi.org/10.1007/s00425-006-0372-3.

192. Jin, Y.; Jing, W.; Zhang, Q.; Zhang, W. Cyclic nucleotide gated channel 10 negatively regulates salt tolerance by mediating Na+ transport in Arabidopsis. *J Plant Res* **2015**, *128*, 211-220
doi: https://doi.org/10.1007/s10265-014-0679-2.

193. Decaestecker, W.; Buono, R.A.; Pfeiffer, M.L.; Vangheluwe, N.; Jourquin, J.; Karimi, M.; Van Isterdael, G.; Beeckman, T.; Nowack, M.K.; Jacobs, T.B. CRISPR-TSKO: A Technique for Efficient Mutagenesis in Specific Cell Types, Tissues, or Organs in Arabidopsis. *Plant Cell* **2019**, *31*, 2868-2887 doi: https://doi.org/10.1105/tpc.19.00454.

194. Nolan, T.M.; Vukasinovic, N.; Hsu, C.W.; Zhang, J.; Vanhoutte, I.; Shahan, R.; Taylor, I.W.; Greenstreet, L.; Heitz, M.; Afanassiev, A.; Wang, P.; Szekely, P.; Brosnan, A.; Yin, Y.; Schiebinger, G.; Ohler, U.; Russinova, E.; Benfey, P.N. Brassinosteroid gene regulatory networks at cellular resolution in the Arabidopsis root. *Science* **2023**, *379*, eadf4721 doi: https://doi.org/10.1126/science.adf4721.

195. Fridman, Y.; Strauss, S.; Horev, G.; Ackerman-Lavert, M.; Reiner-Benaim, A.; Lane, B.; Smith, R.S.; Savaldi-Goldstein, S. The root meristem is shaped by brassinosteroid control of cell geometry. *Nat Plants* **2021**, *7*, 1475-1484 doi: https://doi.org/10.1038/s41477-021-01014-9.

List of Figures

Appendix

The sections below comprise the peer-reviewed papers and preprints to which I contributed (see XIII).

Please note that the attached documents were created as JPEG files for improved accessibility. The supplementary materials were only inserted here, when they were present as condensed files. Expending separate supplemental objects, such as data tables have been excluded from this appendix and can be accessed instead via the published original versions.

The original publications, as long as they are available online, can be accessed using the provided unique digital object identifier (DOI) name.

OneFlowTraX: a user-friendly software for super-resolution analysis of single-molecule dynamics and nanoscale organization

by Rohr L., Ehinger A., Rausch L., Glöckner Burmeister N., Meixner A. J., Gronnier J., Harter K., Kemmerling B., zur Oven Krockhaus S. (2024)

in *Frontiers in Plant Science*

doi: https://doi.org/10.3389/fpls.2024.1358935

Accepted

frontiers | Frontiers in Plant Science

TYPE Technology and Code
PUBLISHED 19 April 2024
DOI 10.3389/fpls.2024.1358935

OPEN ACCESS

EDITED BY
Barbara Hinterstoisser,
University of Natural Resources and Life Sciences Vienna, Austria

REVIEWED BY
Verena Kriechbaumer,
Oxford Brookes University, United Kingdom
Matthieu Platre,
Salk Institute for Biological Studies, United States

*CORRESPONDENCE
Sven zur Oven-Krockhaus
sven.zur-oven-krockhaus@uni-tuebingen.de

RECEIVED 20 December 2023
ACCEPTED 01 April 2024
PUBLISHED 19 April 2024

CITATION
Rohr L, Ehinger A, Rausch L, Glöckner Burmeister N, Meixner AJ, Gronnier J, Harter K, Kemmerling B and zur Oven-Krockhaus S (2024) OneFlowTraX: a user-friendly software for super-resolution analysis of single-molecule dynamics and nanoscale organization.
Front. Plant Sci. 15:1358935.
doi: 10.3389/fpls.2024.1358935

OneFlowTraX: a user-friendly software for super-resolution analysis of single-molecule dynamics and nanoscale organization

Leander Rohr[1], Alexandra Ehinger[1], Luiselotte Rausch[1], Nina Glöckner Burmeister[2], Alfred J. Meixner[3], Julien Gronnier[1], Klaus Harter[1], Birgit Kemmerling[1] and Sven zur Oven-Krockhaus[1,3]*

[1]Center for Plant Molecular Biology (ZMBP), University of Tübingen, Tübingen, Germany, [2]Department of Biomedicine, Aarhus University, Aarhus, Denmark, [3]Institute for Physical and Theoretical Chemistry, University of Tübingen, Tübingen, Germany

Super-resolution microscopy (SRM) approaches revolutionize cell biology by providing insights into the nanoscale organization and dynamics of macromolecular assemblies and single molecules in living cells. A major hurdle limiting SRM democratization is post-acquisition data analysis which is often complex and time-consuming. Here, we present OneFlowTraX, a user-friendly and open-source software dedicated to the analysis of single-molecule localization microscopy (SMLM) approaches such as single-particle tracking photoactivated localization microscopy (sptPALM). Through an intuitive graphical user interface, OneFlowTraX provides an automated all-in-one solution for single-molecule localization, tracking, as well as mobility and clustering analyses. OneFlowTraX allows the extraction of diffusion and clustering parameters of millions of molecules in a few minutes. Finally, OneFlowTraX greatly simplifies data management following the FAIR (Findable, Accessible, Interoperable, Reusable) principles. We provide a detailed step-by-step manual and guidelines to assess the quality of single-molecule analyses. Applying different fluorophores including mEos3.2, PA-GFP, and PATagRFP, we exemplarily used OneFlowTraX to analyze the dynamics of plant plasma membrane-localized proteins including an aquaporin, the brassinosteroid receptor Brassinosteroid Insensitive 1 (BRI1) and the Receptor-Like Protein 44 (RLP44).

KEYWORDS

super-resolution microscopy, localization, single-particle tracking PALM, photoconvertible/-activatable fluorophores, cluster analysis, plasma membrane, BRI1, RLP44

1 Introduction

All living cells regulate the dynamics and organization of molecules at the nanoscale to control their biological processes. Accordingly, appropriate methods are needed to elucidate the underlying mechanisms and functions at the molecular level. In recent years, there has been a significant focus on the plasma membrane (PM) due to its crucial role in important functions such as homeostasis and mass transport, and its primary role as a mediator of signals into and out of the cell. However, only a few techniques allow the *in vivo* analysis of molecules with high spatiotemporal resolution. Suitable microscopy techniques include fluorescence recovery after bleaching (FRAP) (Peters et al., 1974; Axelrod et al., 1976), fluorescence correlation spectroscopy (FCS) (Magde et al., 1972), and single-particle tracking (spt) (Manzo and Garcia-Parajo, 2015) of labeled molecules, the latter being mainly driven by the advent of super-resolution technologies such as photoactivated localization microscopy (PALM) (Betzig et al., 2006; Hess et al., 2006; Manley et al., 2008).

Imaging of single molecules in living cells is usually performed under total internal reflection (TIRF) illumination, which provides greatly enhanced contrast for a thin layer of the biological sample due to its small penetration depth of around 150 nm beyond the coverslip. However, due to the relatively thick cell wall of plant cells, their compartments, such as the PM, are not in the optimal range for TIRF. Therefore, alternative illumination methods such as highly inclined thin illumination (HiLo) (Tokunaga et al., 2008), also known as variable angle epifluorescence microscopy (VAEM) (Konopka and Bednarek, 2008), are widely used for plants. Moreover, due to the limited permeability of the cell wall, plant cell biologists cannot use organic dyes common in the animal or human field (Lelek et al., 2021) for live cell imaging but must rely on a limited selection of genetically encoded fluorophores fused to the gene of interest (Hosy et al., 2015; McKenna et al., 2019; Jolivet et al., 2023).

These technical difficulties have contributed to the fact that dynamic analysis of proteins in plant cells at very high resolution has only recently taken off. The improvement of technical possibilities in microscopy and other methods, such as single-molecule tracking and cluster analysis, now offers data on dynamic parameters, including diffusion coefficients and nanoscale organization, especially for membrane proteins (Gronnier et al., 2017; Perraki et al., 2018; McKenna et al., 2019; Platre et al., 2019; Smokvarska et al., 2020; Platre et al., 2022; Smokvarska et al., 2023; Pain et al., 2024).

Despite the progress made in recent years, the analysis of single-molecule localization microscopy (SMLM) data remains a complicated, multistep process. First, the positions of the individual labeled membrane proteins in each image must be determined with high precision (localization), followed by the assignment of localizations across multiple images to trajectories (tracking). The mobilities or proportions of mobile/immobile proteins are then calculated from the analysis of these trajectories. Subsequently, a map of all observed single molecules localizations can be reconstituted to analyze the nanoscale organization of molecules (e.g., cluster analysis). Each of these steps has been implemented over the years with dedicated analysis software (Chenouard et al., 2014; Sage et al., 2019). Localization depends on physical camera parameters and localization algorithms that must incorporate noise statistics for the low photon counts typical of single-molecule microscopy. Tracking can be performed with a variety of algorithms, and the chosen parameters have a large impact on the data evaluation, representation and thus their interpretation. Mobility analysis is initially performed using mean square displacement (MSD) plots (Qian et al., 1991). Still, this method is not always applicable and is highly sensitive to the parameters used. Combining sptPALM data with cluster analysis is a relatively recent development; several methods have advantages and disadvantages, leading to different data evaluation, representation and interpretation. This procedural complexity and challenges prevent broader application of SMLM techniques such as sptPALM especially in plant cell biology.

Although practical guides have been published recently (Bayle et al., 2021), there is still a lack of software packages that guide the user through all analyses without excessive computational knowledge. The available software is usually limited to or specializes in only one of the above sub-steps, with compatibility problems between the different solutions.

In this work we present a comprehensive, all-in-one open-source, time-saving software package, named OneFlowTraX, guiding the scientist through the steps of SMLM-based localization, tracking, mobility- and cluster analyses of molecules in living cells, which we apply to plant cells. Moreover, the storage of the SMLM data and metadata follow FAIR (Findable, Accessible, Interoperable and Reusable) principles (Wilkinson et al., 2016) for scientific data management and stewardship. We explored three genetically encoded fluorophores (mEos3.2, PA-GFP and PATagRFP) of different photophysical characteristics, suitable for sptPALM studies in living plant cells, exemplified by the temporal and spatial analysis of four different plant plasma membrane proteins. The PA-GFP and PATagRFP pair will also enable dual-color sptPALM applications in the future.

2 Method

2.1 Design and properties of OneFlowTraX

2.1.1 Purpose and workflow

OneFlowTraX runs as an executable program or as an application in MATLAB (Mathworks). The user is guided through several steps, including the localization of single molecules, the reconstruction of single-molecule trajectories, the calculation of mobility parameters, and cluster analyses based on molecule or trajectory positions. The easily scriptable and customizable code is available on GitHub (https://github.com/svenzok/OneFlowTraX), accompanied by a user guide that answers all analysis-specific questions. For each main analysis step (localization, tracking, mobility and cluster analysis), extensive literature research was conducted to select the most suitable method or algorithm for OneFlowTraX. Published codes

were partially adapted to meet the requirements of OneFlowTraX; alternatively, new software code was written to provide a robust and efficient all-in-one analysis pipeline for state-of-the-art single-molecule imaging analyses. This eliminates the need for the user to convert analysis data from one specialized software solution to another, which both saves time and reduces the complexity of these consecutive analysis steps. Some combinations, such as the generation and use of track data for cluster analysis (see below), are particularly important for the evaluation of single-molecule tracking experiments and were not previously available in an integrated software pipeline. The individual steps are discussed in more detail in the following sections.

2.1.2 Localization

The sptPALM raw data (Figure 1A) usually consists of time series images that are saved as TIFF image stacks. Typical formats in our experiments are 100x100 to 400x400 pixels (corresponding to 10x10 to 40x40 µm) with 2 000 to 10 000 images taken at a frame rate between 20 and 50 Hz. These parameters can vary depending on the specific experiment but are mainly governed by the optimal magnification of the imaging system for single-molecule detection, the choice of the frame rate that achieves sufficient contrast, the size of the imaged PM region of interest, and the photophysical characteristics of the chosen fluorophore.

In the first step, the fluorophore-tagged molecules are localized in each image with high precision using algorithms developed for super-resolution microscopy. Bright pixels indicate possible detected single molecules, and larger sections around these pixels are fitted with a two-dimensional Gaussian (Figure 1A). This results not only in the position but also the PSF size, the number of photons and the subsequently calculated localization accuracy, which are stored for each localized single molecule (Figure 1B). For this purpose, we adapted the core of the SMAP software (Ries, 2020). Its algorithm for determining single-molecule positions uses a robust maximum likelihood estimation (MLE) of Gaussian point spread function (PSF) models, which was shown to be very accurate (Sage et al., 2019). Furthermore, it can make use of a graphic processing unit (GPU) that massively accelerates image processing speed. In addition, the fitter can also account for the pixel-specific noise of commonly used complementary metal-oxide semiconductor (CMOS) cameras. In OneFlowTraX, this process can be started for a list of files using default parameters (Figure 1C). An auxiliary window can be opened to check the performance of the algorithm on selected single images and adjust the parameters (see the user guide that is provided with the software for detailed information) if necessary. At the end of the localization process, three histograms show (i) the PSF sizes, (ii) photons and (iii) localization accuracy for all detected and fitted molecules. These histograms can be used to check the quality of the raw data and exclude outliers from further analysis, for example, localizations with unusually large PSFs due to poor focusing or aggregation artifacts. After review, the molecule positions can be used to define single-molecule trajectories.

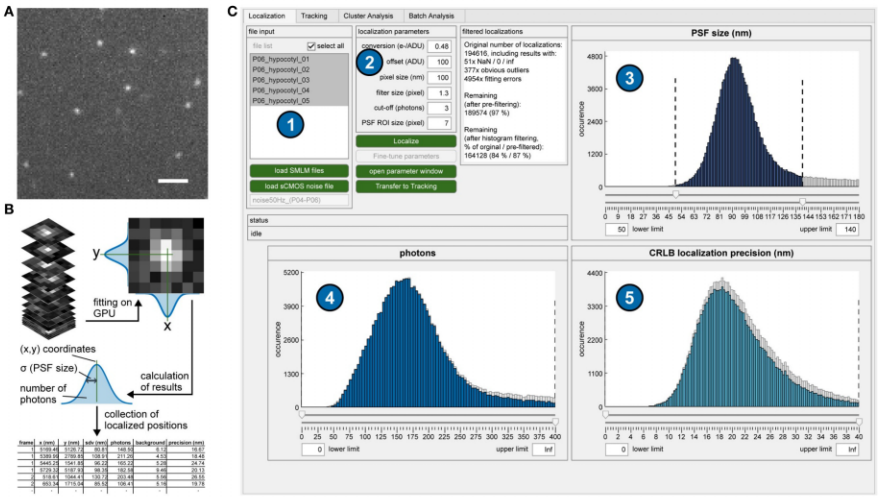

FIGURE 1
Single-molecule localization procedure. **(A)** Single frame of a typical sptPALM image stack. Scale bar = 2 µm. **(B)** Localization process. Each putative single molecule position is cut out as a larger section and fitted with a two-dimensional Gaussian function. The fitting results (most importantly, the coordinates) for each detected single molecule are stored as lists. **(C)** Graphical user interface (GUI) of OneFlowTraX for the localization step. After loading in the sptPALM files (1), the localization procedure is executed based on user-defined parameters (2), with its results visualized as three histograms (PSF sizes (3), photon numbers (4) and localization precision (5) for all detected and fitted fluorescence spots. This serves as quality control and allows the user to filter out, e.g., badly localized single-molecule positions.

2.1.3 Tracking

The generally low localization density in sptPALM data allows for a simple but very fast tracking algorithm. A trajectory is formed from all those molecule positions that do not exceed a maximum distance from each other in successive images (Figure 2A). In addition, short sequences are bridged in which a molecule was temporarily undetectable (gap closing), which is typical of the blinking behavior of fluorophores observed in single-molecule microscopy. The corresponding code for this algorithm was adapted from a MATLAB program published by Jean-Yves Tinevez (Tinevez, 2011). The underlying Linear Assignment Problem (LAP) tracker (Jaqaman et al., 2008) is also part of the widely used software TrackMate (Tinevez et al., 2017). After performing the tracking in OneFlowTraX, the resulting trajectories can be visualized (Figure 2B, upper right), and colored according to their duration, displacement, mobility and other characteristics. In case of obvious connection errors (see the user guide for examples), the tracking can be repeated with adjusted track-building parameters.

2.1.4 Mobility analysis

The mean square displacement (MSD) analysis is currently the most widely used method for extracting diffusion coefficients and motion patterns for this type of data (Manzo and Garcia-Parajo, 2015). Therefore, the distances a molecule has traveled in certain time intervals is assessed to calculate mobility metrics like the diffusion coefficient (Figure 2A). A more detailed description of this method was described previously (Saxton and Jacobson, 1997). Only selected tracks with a certain minimum length (typically eight or more localized positions) are used for further analyses, removing short track artifacts that may originate from background signals. The mean MSD over all tracks is calculated and the diffusion coefficient is estimated via a linear fit (Figure 2B, lower left plot) that commonly only includes the first few points of an MSD curve. While this averaged analysis gives a first impression of protein mobility, a more detailed analysis is possible by estimating individual diffusion coefficients for the MSD curves of each track. Their distribution can then be plotted as a histogram (Figure 2B, lower right plot), revealing the potential existence of nonuniform mobility distributions that would remain hidden in the mean MSD plot. Due to the small number of data points for individual tracks, a goodness-of-fit threshold value (the adjusted R^2) can be specified for the linear fit to reject inconclusive results. In addition to storing the peak log(D) value for each file examined, the relative proportion of multiple populations can also be estimated. Performing the MSD analysis adds new options to the tracking images, such as coloring tracks based on their mobility or splitting them visually into mobile and immobile tracks (for more details refer to the user guide).

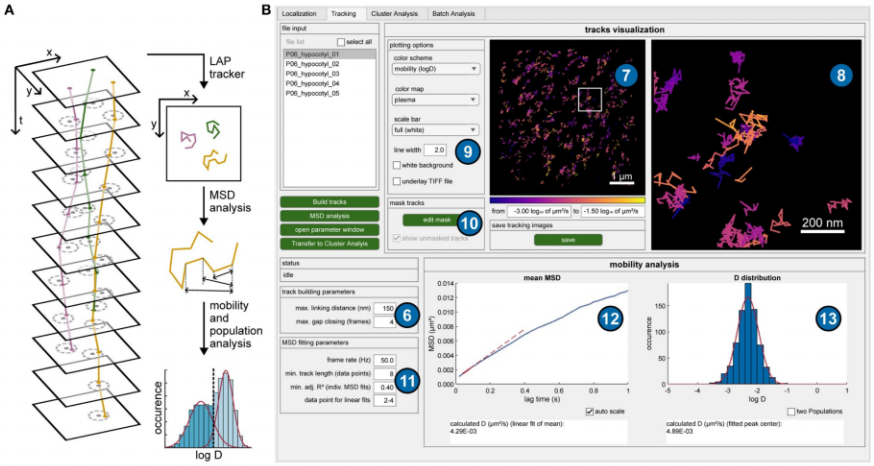

FIGURE 2
Tracking procedure and mobility analysis. **(A)** Schematic overview of the tracking procedure and subsequent analyses. Single-molecule positions are connected to trajectories when they do not exceed a maximum distance (dashed circles) in subsequent frames. The Linear Assignment Problem (LAP) tracker uses a global optimization and can also deal with detection gaps. All tracks then undergo mean square displacement (MSD) analysis based on averaged traveled distances for certain time intervals, offering mobility metrics like diffusion coefficients and more extensive evaluations such as population analyses. **(B)** GUI of OneFlowTraX for the tracking step, including mobility analysis. The track building algorithm uses the specified parameters (6) to connect the detected localization to trajectories, which are displayed in the overview image (7) and a user-defined magnified view (8). Different layers and visualization options can be chosen (9), and the resulting images stored as vector graphics. A binary mask can be defined for each file (10) to exclude tracks (for example, extracellular areas) from further analysis. The mobility analysis via MSD plots is performed based on user-specified parameters (11) and visualized as the mean MSD plot (12), containing the averaged MSD data of the selected file(s). Additionally, the distribution of logarithmized, individual diffusion coefficients (13) is shown, based on the collection of derived diffusion coefficients from fitting the MSD curves of each individual track.

2.1.5 Cluster analysis

While mobility analysis provides information about the dynamics of membrane proteins, their spatial nanoscale organization can also be obtained by cluster analysis based on the single-molecule data using OneFlowTraX, which implements several current state-of-the-art methods. Our analysis pipeline includes Voronoi tessellation (Levet et al., 2015; Andronov et al., 2016), density-based spatial clustering of applications with noise (DBSCAN) (Ester et al., 1996) and the recently introduced nanoscale spatiotemporal indexing clustering (NASTIC) (Wallis et al., 2023) (Figure 3A). A detailed description of these methods can also be found in the user guide.

When applying the different clustering methods, the user can base the analysis in OneFlowTraX (Figure 3B) on two different data sets: (i) all localized fluorophore positions in the sample or (ii) the centroids of the assembled tracks. Option (i) disregards the assignment of localizations to individual membrane proteins, which can result in varying numbers of cluster points for each protein, while option (ii) assigns each detected membrane protein to one cluster point, at the expense of a smaller set of points (also compare Figure 3A). This choice largely depends on the available data quantity, but option (ii) should be generally preferred for its more consistent assignment. Only the NASTIC method is based solely on the protein tracks themselves, since their spatial overlap is used for cluster analysis. OneFlowTraX implements all the above algorithms, so the users can follow their preferences or compare different algorithms. This use of calculated track data for cluster analysis in a single pipeline has, to our knowledge, not been available before. It can therefore greatly benefit the data analysis of single particle tracking experiments, not only in terms of processing speed, but also by providing control and knowledge of upstream analysis step parameters that could influence the cluster analysis results. Finally, all applied analyses are visualized and can be color-coded with different settings and exported.

2.1.6 Batch processing

The batch analysis, outlined schematically in Figure 4A, automatically processes the raw sptPALM data selected by the user and then stores all analysis results in a consistent format. It allows the evaluation of big datasets, including all the above analysis steps, in a very short time (about seven seconds per file with approximately 30 000 localizations each). A summary of all parameters used for the individual steps in the analysis of the membrane protein of interest is listed in an intuitive selection structure (Figure 4B). If necessary, parameters can still be changed here, and the subsequent batch analysis is performed based on these parameters collectively for all analysis steps (localization, tracking, mobility and cluster analysis). The parameter list is also attached to the collected results so that all steps and settings can be traced back according to the FAIR principle.

2.2 Fluorophores for in planta sptPALM analysis

In plant cells, the rather impenetrable cell wall largely precludes dye- or quantum dot based single molecule tracking approaches, so that sptPALM with genetically encoded fluorescent proteins (FPs) must be used, which are fused translationally to the protein of

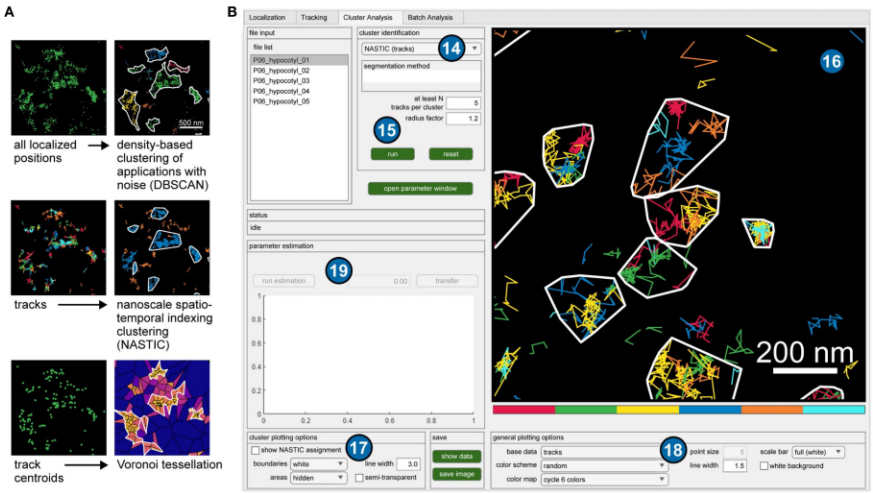

FIGURE 3
Application of clustering algorithms. **(A)** Different representations of the same exemplary data set (all localized positions, tracks and track centroids), and visualized results of implemented clustering algorithms. **(B)** GUI of OneFlowTraX for the cluster analysis. The user can choose from several clustering algorithms (14) and set their specific parameters (15). The visualization of the results (16) depends on the chosen method and can be adjusted with several options (17), (18). For some algorithms, parameter estimates can be calculated (19) based on the chosen data.

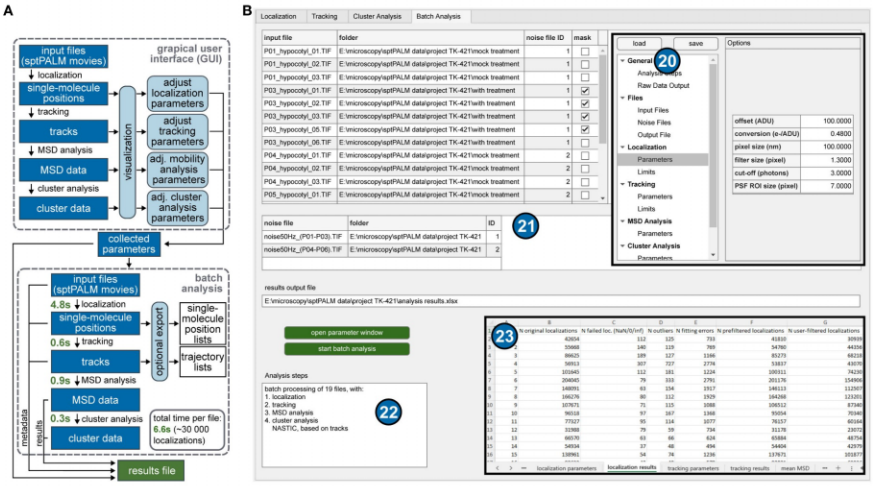

FIGURE 4
Workflow and batch processing. **(A)** Schematic overview of the workflow steps in the GUI of the software and the batch analysis. The GUI is intended to find a suitable set of parameters for all analysis steps, supported by the visualization of intermediate results. The collected parameters can then be used in the batch analysis, which quickly performs all analysis steps for each input file and saves all relevant data in one comprehensive results file. The measured fitting times per file were achieved using an AMD Ryzen 5 4500 CPU and a GTX 960 consumer graphics card. **(B)** GUI of OneFlowTraX for the batch analysis. All user-specified parameters from all previous tabs are stored in a systematic overview window (20) that can be opened from any tab. Input files for batch processing are also added here and are shown as tables (21) for inspection and the assignment of noise files and masks. The entire file list can then be automatically processed, beginning with the localization procedure and may include tracking, mobility and cluster analysis as chosen by the user, summarized in (22). All parameters and results are stored in a spreadsheet file, a section of which is shown as the inset (23).

interest. Conversely, FPs exhibit comparatively low photostability and brightness. Moreover, sptPALM analyses of proteins require photoactivatable or -convertible FP variants, where the density of visible fluorophores per image is controlled by an additional activation laser, further limiting the pool of applicable FPs. Genetic constructs encoding photoconvertible mEos2 fusions have been useful for sptPALM-based analyses of membrane proteins in plant cells (Hosy et al., 2015; Gronnier et al., 2017; Platre et al., 2019; Smokvarska et al., 2020; Platre et al., 2022; Smokvarska et al., 2023). However, it was shown previously that mEos2 tends to form oligomers and aggregates in animal cells, especially when fused to membrane proteins (Zhang et al., 2012). We therefore recommend to prefer the improved version mEos3.2 that is monomeric and also works in plants (Jolivet et al., 2023). As with mEos2, the native green form of mEos3.2 can be converted to a red form using light of ~400 nm wavelength, allowing to adjust the density of the visible fluorophores in the red imaging channel. However, as mEos3.2 occupies both the green and red parts of the spectrum, it is not compatible to combine it with other FPs for potential dual-color applications. Based on their photophysical characteristics (Supplementary Table 1), we propose the use of photoactivatable (PA-) GFP (Patterson and Lippincott-Schwartz, 2002) and PATagRFP (Subach et al., 2010) as additional fluorophores for sptPALM applications in plant cells. Both PA FPs are non-fluorescent in their respective native forms and can be converted to their spectrally distinct fluorescent forms with light of ~400 nm, enabling simultaneous imaging of differently labeled proteins in two color channels. The three fluorophore coding sequences were codon-optimized for their use in plant cells (Supplementary Table 2).

3 Results

3.1 PM proteins used for proof-of-principle sptPALM analyses

In order to demonstrate the applicability of OneFlowTraX for sptPALM analyses with focus on plant cells, well-described *A. thaliana* membrane proteins were used, namely BRI1, RLP44, LTi6a and the aquaporin PIP2;1. LTi6a-mEos2 and PIP2;1-mEos2 *A. thaliana* transgenic lines (Hosy et al., 2015) are under the control of the *PIP2;1* promoter (*pPIP2;1*). BRI1 and RLP44 were expressed as mEos3.2, PA-GFP and PATagRFP fusions under the control of the respective native promoter (*pBRI1*, *pRLP44*).

The aquaporin PIP2;1 is a large six transmembrane domains-containing, tetrameric water and hydrogen peroxide permeable pore (Dynowski et al., 2008), whereas LTi6a is a small two- transmembrane-domains-containing intrinsic PM protein of yet unclear function (Kim et al., 2021). BRI1 initiates well-understood signaling pathways in plant cells. Upon binding of BR to BRI1's extracellular domain, its interaction with the co-receptor BRI1-ASSOCIATED KINASE 1 (BAK1) is

enhanced. This leads to a re-arrangement of proteins within the complex, eventually resulting in auto- and transphosphorylation of their kinase domains and its full signaling activity (Gou and Li, 2020; Wolf, 2020). The outcomes of BR activation of the BRI1/BAK1 complex are on the one hand the differential regulation of BR-responsive genes via a nucleo-cytoplasmic signaling cascade (Mora-Garcia et al., 2004; Yin et al., 2005; Vert and Chory, 2006; Zhu et al., 2017) and on the other hand a rapid acidification of the apoplast via the activation of PM-resident P-type proton pumps (Caesar et al., 2011; Witthöft et al., 2011; Grosseholz et al., 2022)

RLP44 is proposed to be a cell wall integrity sensor that controls cell wall homeostasis by interplay with BRI1 and BAK1 (Wolf et al., 2012, 2014). In fact, we were recently able to demonstrate the existence of a ternary RLP44/BRI1/BAK1 complex in the PM of living plant cells using a spectral Förster resonance energy transfer (FRET) and FRET-Fluorescence-lifetime imaging microscopy (FLIM) approach (Glöckner et al., 2022). Additionally, RLP44 has been linked to phytosulfokine signaling. The corresponding receptor Phytosulfokine Receptor 1 (PSKR1) is also proposed to form a complex with RLP44 and BAK1 (Holzwart et al., 2018; Gomez et al., 2021).

3.2 OneFlowTraX analysis of BRI1 and RLP44 dynamics and nano-structured organization in the *Nicotiana benthamiana* transient expression system and transgenic *Arabidopsis* seedlings

For initial assessment, mEos3.2, PA-GFP and PATagRFP-tagged BRI1 fusion proteins were transiently expressed in *Nicotiana benthamiana* (*N. benthamiana*) epidermal leaf cells. Such transient expression setups provide a fast and convenient way to test the functionality of protein fusions with photoswitchable/photoconvertible fluorophores (Gronnier et al., 2017; Perraki et al., 2018). For the transgenic approach in *A. thaliana*, the mEos3.2, PA-GFP and PATagRFP-tagged fusions of RLP44 were chosen.

The density of the single fusion proteins after photoconversion or –activation was optimal (Figure 5A) for a comprehensive evaluation of sptPALM data (Bayle et al., 2021).

Using OneFlowTraX (for detailed parameters see Supplementary Table 3), the data were processed, and single-molecule trajectories were generated (Figure 5B). After MSD analysis, the diffusion coefficients were calculated (Figure 5C).

Although the three fluorophores are sptPALM-optimized versions of different precursors from various marine organisms, the BRI1 fusion proteins showed comparable diffusion coefficients in *N. benthamiana* epidermal leaf cells (Figure 5C, left panel). The same was observed for the RLP44 fusion proteins in transgenic *Arabidopsis* epidermal hypocotyl cells (Figure 5C, right panel). This demonstrates that all three fluorophores can be reliably used for sptPALM studies in different plant cell systems. The best signal-to-noise ratio was obtained with mEos3.2, due to its excellent photophysical properties (Supplementary Table 1). On the other hand, PA-GFP and PATagRFP can be combined - due to their non-overlapping spectra - for dual-color sptPALM experiments.

Moreover, as shown in Figure 5D, OneFlowTraX allows the use of sptPALM single-molecule track data to show that the BRI1-mEos3.2 and RLP44-mEos3.2 fusion proteins are partially organized in clusters.

3.3 OneFlowTraX application examples to detect changes in protein mobility

To validate the usefulness of OneFlowTraX, we first analyzed the dynamics of LTi6a-mEos2 and PIP2;1-mEos2 (Hosy et al., 2015) in the PM of epidermal root tip and epidermal hypocotyl cells of transgenic *A. thaliana* seedlings. In accordance with their previous results, we observed that LTi6a exhibited a significantly higher mobility than PIP2;1 in the PM of root epidermal cells (Figure 6A, left). We found that this difference was even more pronounced in the PM of epidermal hypocotyl cells (Figure 6A, right). Moreover, the mobility of LTi6a was significantly higher in the PM of epidermal hypocotyl cells than in epidermal cells of the root. In contrast, we observed no difference for PIP2;1 (Figure 6A).

We then conducted OneFlowTraX analysis of the RLP44-mEos3.2 dynamics in transgenic *A. thaliana* seedlings grown either in white light or darkness in order to determine whether the developmental state (photomorphogenic versus skotomorphogenic) influences the fusion protein's dynamics. Firstly, as shown in Figure 6B, RLP44-mEos3.2 moved significantly faster in the PM of cells of the upper part of dark-grown hypocotyls compared to the lower part. The diffusion coefficient of RLP44-mEos3.2 in the PM of hypocotyl cells of light-grown seedlings, where a differentiation of different cell types along the axis is hardly possible, was similar to the diffusion coefficients gained from the lower part of the etiolated hypocotyl. These in planta generated results show that positional and developmental differences in the RLP44-mEos3.2 dynamics can be detected by sptPALM-based OneFlowTraX analysis.

The effect of other environmental factors on protein mobility can also be evaluated by OneFlowTraX. Here we chose the hyper-osmotic stress response of plant cells after addition of sorbitol, a non-toxic, widely used, non-metabolic osmolyte already applied for sptPALM (Hosy et al., 2015). Sorbitol induces a cell volume loss (plasmolysis) when used at a concentration of 300 mM. Under milder hyper-osmotic conditions (100 mM), the cells experience a reduction in turgor without major changes in their volume (Martinière et al., 2019). Thus, the increasing concentration of sorbitol from 100 to 300 mM induces a progressive separation of the PM from the cell wall which enhanced the dynamics of almost all intrinsic PM proteins (Hosy et al., 2015). Based on this knowledge, treatments with 100 mM and 300 mM sorbitol or mock treatment (all applied for 20 min) were performed with light-grown and dark-grown seedlings expressing RLP44-mEos3.2. Then, the sptPALM data were measured in epidermal hypocotyl cells of light-grown seedlings and epidermal cells of the upper hypocotyl part of dark-grown seedlings and analyzed using OneFlowTraX. Whereas the concentration of 100 mM sorbitol did not significantly affect the diffusion coefficient of RLP44-mEos3.2 compared to the mock

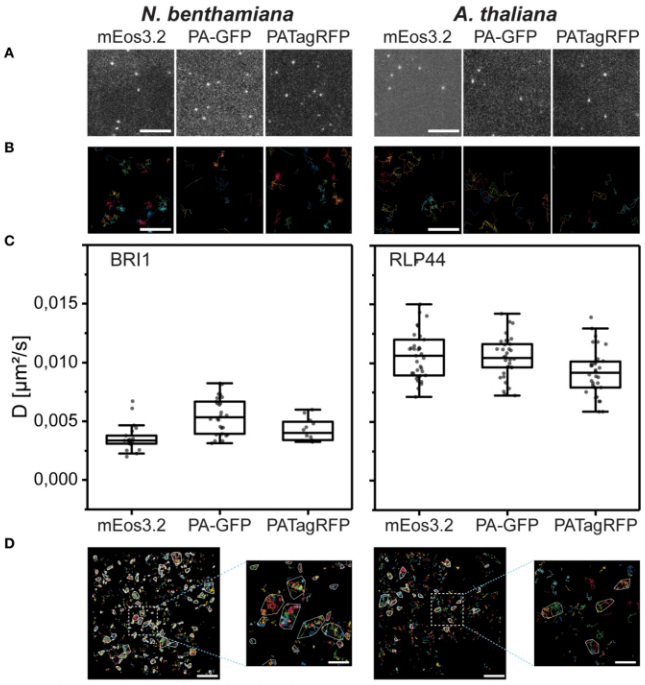

FIGURE 5
BRI1 and RLP44 FP fusions accumulate in the PM of transiently transformed *N. benthamiana* epidermal leaf cells or transgenic *A. thaliana* epidermal hypocotyl cells, respectively, and their nanoscale organization can be evaluated by OneFlowTraX. **(A)** Representative images from sptPALM movies, showing, from left to right, single mEos3.2, PA-GFP and PATagRFP of BRI1 in transiently transformed *N. benthamiana* leaf epidermal cells and of RLP44 in light-grown transgenic *A. thaliana* hypocotyl epidermal cells. The BRI1 and RLP44 fusion proteins were expressed via their native promoters (*pBRI1, pRLP44*). Scale bar = 1 µM. **(B)** Representative magnifications of areas containing tracks generated by OneFlowTraX (random coloring per track) after localization of the BRI1 and RLP44 fusion proteins, with panels ordered as above. Scale bar = 100 nm. **(C)** Diffusion coefficients for the indicated BRI1 and RLP44 fusion proteins in the PM obtained with OneFlowTraX. For statistical evaluation, the data were checked for normal distribution and unequal variances and then analyzed applying the Kruskal-Wallis test followed by the Steel-Dwass *post-hoc* test, with $n \geq 12$ for each fusion protein derived from at least five plants, measured on at least three different days. Whiskers show the data range excluding outliers, while the boxes represent the 25-75 percentile. For detailed statistics see Supplementary Table 3. **(D)** The track data was used for cluster analysis in OneFlowTraX, exemplified for BRI1-mEos3.2 and RLP44-mEos3.2 clusters that were assigned using the NASTIC algorithm. The images represent one cell with random coloring per track and cluster boundaries highlighted in white. Scale bar = 2 µm (500 nm for the magnified view).

treatment (0 mM), 300 mM sorbitol significantly increased the protein mobility in all measured cells (Figure 6C).

These examples represent "blueprints" for the analyses of sptPALM data in plant research and demonstrate the applicability of OneFlowTraX, as it was used to perform all evaluation steps, including localization, tracking, protein mobility and cluster analysis.

4 Discussion

4.1 OneFlowTraX is an all-in-one software package for SMLM data processing and analysis

With OneFlowTraX, we provide a unique, user-friendly open-source software package that guides users through the steps of localization, tracking, analysis of mobility and nanoscale organization of single molecules based on SMLM data. OneFlowTraX facilitates the previously very time-consuming and cumbersome post-acquisition processing of SMLM data. Although OneFlowTraX is tailored for use by cell biologists, who want to perform sptPALM analyses in the PM of plant cells, it also offers the possibility of post-acquisition data processing for other non-PM bound processes in any prokaryotic and eukaryotic cells. For instance, the software could be used to analyze the spatial organization of chromosomes into topologically associating domains (Wang et al., 2016).

In plants, due to the cell wall, only regions close to the microscope slide can be analyzed such as the PM and PM-associated molecules. OneFlowTraX provides a default set of analysis parameters that are well suited for plant PM molecules located in a 2D environment. However, as described in the provided

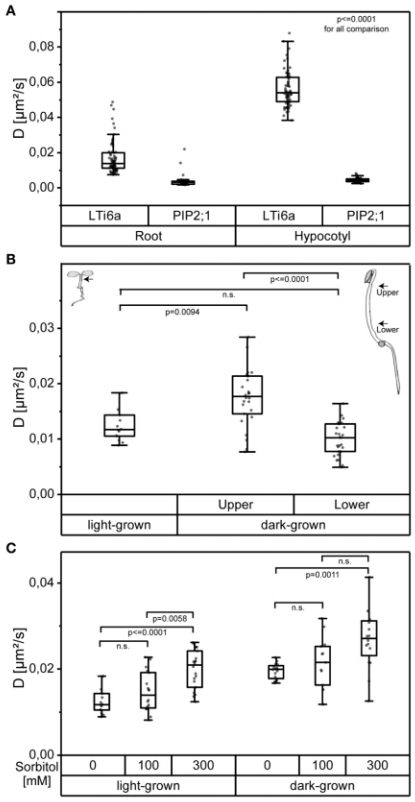

FIGURE 6
OneFlowTraX analysis of sptPALM data reveals organ- and position-specific as well as environmentally caused differences in the dynamics of the indicated FP fusion proteins in epidermal cells of *A. thaliana*. **(A)** Diffusion coefficients of *pPIP2;1* expressed LTi6a-mEos2 and PIP2;1-mEos2 in epidermal root and hypocotyl cells of light-grown *A. thaliana* seedlings. For statistical evaluation, the data were checked for normal distribution and unequal variances and then analyzed applying the Kruskal-Wallis test followed by the Steel-Dwass *post-hoc* test, with n ≥ 37 for each fusion protein derived from at least six plants, measured on at least four different days. Whiskers show the data range excluding outliers, while the boxes represent the 25-75 percentile. For detailed statistics see Supplementary Table 3. **(B)** Diffusion coefficients of *pRLP44* expressed RLP44-mEos3.2 in epidermal hypocotyl cells of light-grown and dark-grown *A. thaliana* seedlings. The locations of the recorded measurements are indicated by arrows in the corresponding seedling sketches. For dark-grown seedlings, the center of the distance from the apical hook to the seed was used as the reference point. Based on this, the centers to the apical hook and to the seed were used as selected regions, named 'upper' and 'lower', respectively. Statistical evaluation was performed as described in **(A)** with n ≥ 14, from at least three plants. For detailed statistics see Supplementary Table 3. **(C)** Diffusion coefficients of *pRLP44* expressed RLP44-mEos3.2 recorded from epidermal hypocotyl cells of light-grown or dark-grown *A. thaliana* seedlings after 20 min treatment with sorbitol solution of 100 mM or 300 mM or after mock-treatment (0 mM). For the recording of the data in the dark-grown seedlings the upper part of the hypocotyl cells was chosen (see **B**). Statistical evaluation was performed as described in **(A)**, with n ≥ 13, from three different plants. For detailed statistics see Supplementary Table 3.

manual, all settings can be adjusted by the user to their specific experimental requirements for the SMLM analysis of any process of interest independent of the organism.

The primary objective of OneFlowTraX is to integrate established algorithms from the community into a pipeline and to optimize data flow. We have successfully combined approaches from specialized software that, for example, either focuses on single-molecule localization or tracking. Our integrated solution also enables the utilization of track data for cluster analyses, which is particularly important in single-molecule tracking experiments. OneFlowTraX includes comprehensive batch analysis, with detailed parameter and data output for all analysis paths, a feature that was previously missing from many analysis tools. This not only saves the user time, but also maintains the consistency of the single-molecule data with the calculated results, making it easier to apply the FAIR principle. The detailed but clearly structured parameter organization also provides a method to evaluate the reliability of the analyses: running multiple batch analyses with different parameters will show the impact of individual parameters in the overall analysis process on the results.

OneFlowTraX was programmed in MATLAB, a software language that is easy to work with and widely used in academia. The code has been designed in a clear and concise manner, with comments provided to aid in the insertion of changes or extensions. This could also make OneFlowTraX of interest to scientists working with animal or human cells.

4.2 PATagRFP, PA-GFP and mEos3.2 are suitable FPs for sptPALM analyses in living plant cells

Especially plant scientists rely on genetically encoded photoactivatable or photoconvertible FPs fused to the protein of interest as the cell wall is impenetrable for dyes applied from the outside. With mEos3.2, PA-GFP and PATagRFP, three different FPs are now available that do not tend to aggregate, deliver satisfactory signal-to-noise ratios during imaging and are therefore applicable for sptPALM applications both in a transient transformation system (*N. benthamiana*) and in stably transformed *A. thaliana* plants. We expect that these fluorophores will also work in other plant species. Of particular interest is the combination of PA-GFP and PATagRFP, which will enable dual-color sptPALM in the future for simultaneous recording and spatiotemporal analysis of two different fusion proteins. Because of its superior photophysical properties, we recommend the use of mEos3.2 for single FP fusion protein analyses. Especially when analyzing the mobility of PM proteins in living plant cells, the sptPALM technology shows its superiority in terms of spatiotemporal resolution compared with other methods such as FRAP and FCS (Bayle et al., 2021).

4.3 OneFlowTraX allows the rapid *in vivo* analysis of PM proteins in transiently and stably transformed plant cells

We used two functionally well-studied PM proteins, namely BRI1 and RLP44, for our proof-of-principle experiments regarding the usability of the three FPs and the applicability of OneFlowTraX. Both proteins were evaluated in either transiently transformed *N. benthamiana* epidermal leaf cells or the epidermis of the hypocotyl of stable transgenic *A. thaliana* seedlings. The accumulation of the BRI1 and RLP44 fusion proteins was driven by the respective endogenous promoters. In our experience, strong over-accumulation of the fusion proteins driven by constitutively active promoters can sometimes lead to overcrowded sptPALM movies in both plant systems, even before photoconversion. Analysis of these movies results in misconnected tracks that affect the entire OneFlowTraX analysis causing inadequate results in subsequent steps. If it is not possible to control the visible fluorophore density with 405 nm illumination, we therefore suggest using weaker promoters when possible.

While OneFlowTraX further demonstrated its utility through the replication of LTi6a-mEos2 and PIP2;1-mEos2 sptPALM-derived findings in the roots of light-grown *A. thaliana* seedlings (Hosy et al., 2015), we were additionally able to observe that the PM dynamics of both mEos2 fusions differ between epidermal cells of the root and hypocotyl. This suggests that the organ context of a tissue has an influence on PM protein dynamics in plant cells. Although our root measurements for PIP2;1 (0.0032 $\mu m^2/s$) and LTi6b (0.0139 $\mu m^2/s$) do not exactly match the data reported previously (Hosy et al., 2015) (0.0047 $\mu m^2/s$ and 0.077 $\mu m^2/s$, respectively), we confirmed the high mobility of LTi6a in contrast to the confined behavior of PIP2;1.

During our OneFlowTraX analysis of the RLP44-mEos3.2 dynamics in epidermal cells of light-grown *Arabidopsis* hypocotyls, we observed high data variability. This led to the hypothesis that cell-specific effects depending on the cell's position in the organ, i.e., on its physiological state, interfere with the membrane dynamics of the fusion protein to be investigated. This hypothesis was substantiated by the technically easier access to the potential positional effects in the dynamics of RLP44-mEos3.2 in epidermal cells along the hypocotyl axis of dark-grown seedlings: The diffusion coefficient of RLP44-mEos3.2 is significantly higher in the epidermal cells of the upper part than in those of the lower part of the dark-grown hypocotyl. Furthermore, the diffusion coefficient in the lower part is similar to that found in the epidermal cells of light-grown hypocotyls. We suspect that the observed discrepancies mentioned above can be explained by presumably different measurement locations within the root as well as external factors such as temperature. Another group (Martinière et al., 2019) also observed variations, while maintaining the general characteristics of PIP2;1 and, in their case, LTi6b. OneFlowTraX can easily capture these differences in dynamics, allowing SMLM in different cells and tissues that may vary in their membrane properties.

As shown previously (Hosy et al., 2015; Martinière et al., 2019), the treatment of *A. thaliana* root cells with increasing concentration of the osmolyte sorbitol increases the diffusion coefficient of membrane proteins such as the aquaporin PIP2;1. Using OneFlowTraX, we could substantiate these findings for the RLP44-mEos3.2 fusion and demonstrated potential effects of the differentiation states of the analyzed tissue. This shows that reproducible and robust SMLM data analysis is provided by OneFlowTraX.

In addition to the analysis of protein dynamics, OneFlowTraX also offers different algorithms (Voronoi tessellation, DBSCAN, NASTIC) for the analysis of the nanoscale organization of a given membrane protein. For sptPALM data, we recommend the NASTIC algorithm as it is specifically designed to work with track data. Because of the sensitivity to parameter changes, care must be taken when regarding the results of the nanoscale evaluation output by all of these algorithms as absolute values. However, relative comparisons of the nanoscale organization for a given membrane protein are possible if there are no changes in the parameter settings between the experiments.

In summary, SMLM data acquisition such as that from sptPALM becomes more easily accessible and faster analyzable with OneFlowTraX. The fluorophores mEos3.2, PA-GFP and PATagRFP have proven to be suitable for SMLM in planta and allow analysis of membrane proteins in transient expression systems as well as in stable transformed plants. The respective FP

fusions are suitable for the analysis of protein dynamics in epidermal cells of different organs and at different developmental or physiological stages as well as in response to environmental factors. Therefore, OneFlowTraX will greatly facilitate the comprehensive investigation of the dynamics and nanoscale organization of single molecules in the future.

5 Materials and methods

5.1 Plasmid construction

All expression clones were constructed using GoldenGate assembly with BB10 as the vector (Binder et al., 2014). Promoter sequences were obtained with the help of the Integrated Genome Browser (Freese et al., 2016). Level I modules were generated by PCR amplification of the desired sequences and then blunt-end cloned into pJET1.2 (Thermo Fisher Scientific). Fluorophores were designed as C-terminal fusions (D-E module) using either a glycine/serine or a glycine/alanine-rich linker. The coding sequences of BRI1 and RLP44 were constructed as B-D modules, eliminating the need for a B-C dummy module. A full list of used constructs can be found in Supplementary Table 5. The correctness of Level I constructs was confirmed by Sanger sequencing. Cut-ligations for the Level II generation were performed with 40 cycles, without using bovine serum albumin as described before (Binder et al., 2014). Reactions were transformed into TOP10 cells (Thermo Fisher Scientific), and colony correctness was verified via restriction enzyme analysis and partial Sanger sequencing.

5.2 Plant material and growth conditions

The transgenic *A. thaliana* lines generated for this study were all in the Columbia (Col-0) background. The respective stable lines were created using the Floral dip method (Zhang et al., 2006). For the reproduction of LTi6a and PIP2;1 results, seeds of the corresponding lines were provided by Dr. Doan-Trung Luu. Transgenic seeds were propagated either based on the presence of the pFAST marker by binocular visual inspection or by selection of survivors on ½ Murashige and Skoog (MS) plates containing 1% (w/v) sucrose and 0.8% (w/v) phytoagar supplemented with 25 µM hygromycin. For sptPALM measurements, seeds were sterilized with a solution of 70% ethanol (v/v) and 0.05% Triton X-100 for 30 minutes followed by a 10-minute treatment with absolute ethanol. Seeds were sown on ½ MS plates (+1% sucrose and 0.8% phytoagar) and stratified at 4°C for at least 24 hours. For measurements of dark-grown seedlings, seeds were exposed to light from the growth chamber for two hours before being wrapped in aluminum foil until the day of measurement. Light-grown seedlings were cultivated in growth chambers at 20°C under long-day conditions (16 hours light/8 hours dark). The duration of growth is indicated in the respective figures. The *N. benthamiana* plants used in this study were cultivated under controlled greenhouse conditions. Proteins were transiently expressed using the AGL1 *Agrobacterium tumefaciens* strain (Lifeasible), as previously described (Hecker et al., 2015; Ladwig et al., 2015), without the washing step with sterile water. The plants were infiltrated with the respective construct at an OD600 of 0.1, in a ratio of 1:1 with the silencing inhibitor p19. After watering, the plants were kept in ambient conditions and were imaged three days after infiltration.

5.3 Sample preparation and movie acquisition

All sptPALM measurements with transiently transformed *N. benthamiana* were performed three days after infiltration. A small leaf area was cut out, excluding veins, and placed between two coverslips (Epredia 24x50 mm #1 or equivalent) with a drop of water. This "coverslip sandwich" was then placed on the specimen stage, lightly weighted down by a brass ring to help flatten the uneven cell layers, especially in *N. benthamiana*. Seven-day-old *A. thaliana* seedlings were used to acquire data from stable *Arabidopsis* lines. Depending on the experiment, either light-grown or dark-grown plants were used. For sorbitol (obtained by Roth) treatments, seedlings were pre-incubated with the appropriate concentration in 12-well plates for five minutes (Hosy et al., 2015). Afterwards, the seedlings were transferred to the coverslip and imaged in the respective incubation solution as mounting medium for up to 20 minutes. Similar to the handling of *N. benthamiana* leaf discs, the seedlings were placed between coverslips and brass rings.

The custom-built microscope platform for sptPALM acquisition is described in detail in Supplementary Materials and Methods. Briefly, lasers of different wavelengths and their intensities are controlled by an acousto-optic transmission filter. A laterally translatable lens in the excitation beam path allows to adjust the VAEM illumination of the sample utilizing a high NA objective. The emitted light from the sample is separated from the excitation light by a multi-band beam splitter and is detected by an sCMOS camera. Depending on the fluorophore fusion, the following filters were inserted into the emission beam path: (i) mEos3.2: 568 LP Edge Basic Longpass Filter, 584/40 ET Bandpass; (ii) PA-GFP: 488 LP Edge Basic Longpass Filter, 525/50 BrightLine HC; (iii) PATagRFP: 568 LP Edge Basic Longpass Filter, 600/52 BrightLine HC (all AHF analysentechnik AG). The excitation power arriving at the sample was measured (PM100D with S120C, Thorlabs) in epifluorescence mode after the objective to keep it constant for the respective experiment sets. If necessary, photoconversion or photoactivation was performed using 405 nm excitation at varying low intensities (for detailed acquisition parameters see Supplementary Table 4). The magnification of the optical system was adjusted so that the length of one camera pixel corresponds to 100 nm in the sample plane. Viable regions of interest were screened in a larger area of 51.2 x 51.2 µm by adjusting the focal plane and the VAEM angle with a frame rate of 10 Hz, while recording was performed with 12.8 x 12.8 µm and frame rates

between 20 and 50 Hz, recording between 2 500 and 5 000 frames per movie (see Supplementary Table 4). For each measurement day, noise files (a series of dark images) were recorded with the corresponding frame rates.

5.4 Raw data processing and analysis with OneFlowTraX

Subsets of each experimental data set were loaded into OneFlowTraX to inspect the quality of the data and to find appropriate parameters for each analysis step as described above. On the Batch Analysis tab, all sptPALM raw data files that share the same parameter set were processed together (see Supplementary Table 4 for a detailed list of applied analysis parameters). Samples that showed significantly low numbers of localizations or tracks compared to others in the same batch were discarded.

Data availability statement

The OneFlowTraX software is freely available for non-commercial users on GitHub (https://github.com/svenzok/OneFlowTraX). This includes a user manual and generated result files, which form the basis for Figure 5C and Figure 6. To test the software, sample raw data and noise files are available at https://drive.google.com/drive/folders/12FSUjpxNaUjJI9i2XCgpqXz_B-BYsNJS?usp=sharing.

Author contributions

LRo: Data curation, Formal analysis, Investigation, Visualization, Writing – original draft, Writing – review & editing. AE: Resources, Writing – review & editing. LRa: Data curation, Investigation, Writing – review & editing. NG: Resources, Writing – review & editing. AM: Conceptualization, Funding acquisition, Resources, Supervision, Writing – review & editing. JG: Supervision, Writing – review & editing. KH: Conceptualization, Funding acquisition, Supervision, Writing – original draft, Writing – review & editing. BK: Conceptualization, Funding acquisition, Supervision, Writing – review & editing. SO-K: Conceptualization, Data curation, Formal analysis, Investigation, Methodology, Software, Visualization, Writing – original draft, Writing – review & editing.

Funding

The author(s) declare financial support was received for the research, authorship, and/or publication of this article. Our research was supported by the German Research Foundation (DFG) via the CRC grant 1101 (project A09, D02, D03, Z02), the TRR grant 356 (project B01, B02) and individual grants to KH (HA 2146/22, HA 2146/23). We also thank the DFG for grants for scientific equipment (FUGG: INST 37/991-1, INST 37/992-1, INST 37/819-1, INST 37/965-1). We acknowledge support from the Open Access Publication Fund of the University of Tübingen.

Acknowledgments

We would like to thank Dr. Andrea Gust for providing us with the pFAST construct. We would also like to thank Dr. Doan-Trung Luu for providing seeds of the LTi6a-mEos2 and PIP2;1-mEos2 transgenic *A. thaliana* lines.

Conflict of interest

The authors declare that the research was conducted in the absence of any commercial or financial relationships that could be construed as a potential conflict of interest.

The author(s) declared that they were an editorial board member of Frontiers, at the time of submission. This had no impact on the peer review process and the final decision.

Publisher's note

Supplementary material

The Supplementary Material for this article can be found online at: https://www.frontiersin.org/articles/10.3389/fpls.2024.1358935/full#supplementary-material

References

Andronov, L., Orlov, I., Lutz, Y., Vonesch, J. L., and Klaholz, B. P. (2016). ClusterViSu, a method for clustering of protein complexes by Voronoi tessellation in super-resolution microscopy. *Sci. Rep.* 6, 24084. doi: 10.1038/srep24084

Axelrod, D., Koppel, D. E., Schlessinger, J., Elson, E., and Webb, W. W. (1976). Mobility measurement by analysis of fluorescence photobleaching recovery kinetics. *Biophys. J.* 16, 1055–1069. doi: 10.1016/S0006-3495(76)85755-4

Bayle, V., Fiche, J. B., Burny, C., Platre, M. P., Nollmann, M., Martiniere, A., et al. (2021). Single-particle tracking photoactivated localization microscopy of membrane proteins in living plant tissues. *Nat. Protoc.* 16, 1600–1628. doi: 10.1038/s41596-020-00471-4

Betzig, E., Patterson, G. H., Sougrat, R., Lindwasser, O. W., Olenych, S., Bonifacino, J. S., et al. (2006). Imaging intracellular fluorescent proteins at nanometer resolution. *Science* 313, 1642–1645. doi: 10.1126/science.1127344

Binder, A., Lambert, J., Morbitzer, R., Popp, C., Ott, T., Lahaye, T., et al. (2014). A modular plasmid assembly kit for multigene expression, gene silencing and silencing rescue in plants. *PloS One* 9, e88218. doi: 10.1371/journal.pone.0088218

Caesar, K., Elgass, K., Chen, Z., Huppenberger, P., Witthoft, J., Schleifenbaum, F., et al. (2011). A fast brassinolide-regulated response pathway in the plasma membrane of Arabidopsis thaliana. *Plant J.* 66, 528–540. doi: 10.1111/j.1365-313X.2011.04510.x

Chenouard, N., Smal, I., de Chaumont, F., Maska, M., Sbalzarini, I. F., Gong, Y. H., et al. (2014). Objective comparison of particle tracking methods. *Nat. Methods* 11, 281–289. doi: 10.1038/nmeth.2808

Dynowski, M., Schaaf, G., Loque, D., Moran, O., and Ludewig, U. (2008). Plant plasma membrane water channels conduct the signalling molecule H2O2. *Biochem. J.* 414, 53–61. doi: 10.1042/Bj20080287

Ester, M., Kriegel, H.-P., Sander, J., and Xu, X. (1996). "A density-based algorithm for discovering clusters in large spatial databases with noise," in *KDD'96: Proceedings of the Second International Conference on Knowledge Discovery and Data Mining*. Washington D.C (USA): AAAI Press, 226–231. doi: 10.5555/3001460

Freese, N. H., Norris, D. C., and Loraine, A. E. (2016). Integrated genome browser: visual analytics platform for genomics. *Bioinformatics* 32, 2089–2095. doi: 10.1093/bioinformatics/btw069

Glöckner, N., zur Oven-Krockhaus, S., Rohr, L., Wackenhut, F., Burmeister, M., Wanke, F., et al. (2022). Three-fluorophore FRET enables the analysis of ternary protein association in living plant cells. *Plants* 11, 2630. doi: 10.3390/plants11192630

Gomez, B. G., Holzwart, E., Shi, C., Lozano-Duran, R., and Wolf, S. (2021). Phosphorylation-dependent routing of RLP44 towards brassinosteroid or phytosulfokine signalling. *J. Cell Sci.* 134, jcs259134. doi: 10.1242/jcs.259134

Gou, X., and Li, J. (2020). Paired receptor and coreceptor kinases perceive extracellular signals to control plant development. *Plant Physiol.* 182, 1667–1681. doi: 10.1104/pp.19.01343

Gronnier, J., Crowet, J. M., Habenstein, B., Nasir, M. N., Bayle, V., Hosy, E., et al. (2017). Structural basis for plant plasma membrane protein dynamics and organization into functional nanodomains. *eLife* 6, e26404. doi: 10.7554/eLife.26404

Grosseholz, R., Wanke, F., Rohr, L., Glöckner, N., Rausch, L., Scholl, S., et al. (2022). Computational modeling and quantitative physiology reveal central parameters for brassinosteroid-regulated early cell physiological processes linked to elongation growth of the Arabidopsis root. *eLife* 11, 73031. doi: 10.7554/eLife.73031

Hecker, A., Brand, L. H., Peter, S., Simoncello, N., Kilian, J., Harter, K., et al. (2015). The arabidopsis GAGA-binding factor BASIC PENTACYSTEINE6 recruits the POLYCOMB-REPRESSIVE COMPLEX1 component LIKE HETEROCHROMATIN PROTEIN1 to GAGA DNA motifs. *Plant Physiol.* 168, 1013–1024. doi: 10.1104/pp.15.00409

Hess, S. T., Girirajan, T. P. K., and Mason, M. D. (2006). Ultra-high resolution imaging by fluorescence photoactivation localization microscopy. *Biophys. J.* 91, 4258–4272. doi: 10.1529/biophysj.106.091116

Holzwart, E., Huerta, A. I., Glockner, N., Garnelo Gomez, B., Wanke, F., Augustin, S., et al. (2018). BRI1 controls vascular cell fate in the Arabidopsis root through RLP44 and phytosulfokine signaling. *Proc. Natl. Acad. Sci. U.S.A.* 115, 11838–11843. doi: 10.1073/pnas.1814434115

Hosy, E., Martiniere, A., Choquet, D., Maurel, C., and Luu, D. T. (2015). Super-resolved and dynamic imaging of membrane proteins in plant cells reveal contrasting kinetic profiles and multiple confinement mechanisms. *Mol. Plant* 8, 339–342. doi: 10.1016/j.molp.2014.10.006

Jaqaman, K., Loerke, D., Mettlen, M., Kuwata, H., Grinstein, S., Schmid, S. L., et al. (2008). Robust single-particle tracking in live-cell time-lapse sequences. *Nat. Methods* 5, 695–702. doi: 10.1038/nmeth.1237

Jolivet, M. D., Deroubaix, A. F., Boudsocq, M., Abel, N. B., Rocher, M., Robbe, T., et al. (2023). Interdependence of a kinase and its cognate substrate plasma membrane nanoscale dynamics underlies Arabidopsis response to viral infection. *bioRxiv*. 2023.07.31.551174. doi: 10.1101/2023.07.31.551174

Kim, H. S., Park, W., Lee, H. S., Shin, J. H., and Ahn, S. J. (2021). Subcellular journey of rare cold inducible 2 protein in plant under stressful condition. *Front. Plant Sci.* 11. doi: 10.3389/fpls.2020.610251

Konopka, C. A., and Bednarek, S. Y. (2008). Variable-angle epifluorescence microscopy: a new way to look at protein dynamics in the plant cell cortex. *Plant J.* 53, 186–196. doi: 10.1111/j.1365-313X.2007.03306.x

Ladwig, F., Dahlke, R. I., Stuhrwohldt, N., Hartmann, J., Harter, K., and Sauter, M. (2015). Phytosulfokine Regulates Growth in Arabidopsis through a Response Module at the Plasma Membrane That Includes CYCLIC NUCLEOTIDE-GATED CHANNEL17, H+-ATPase, and BAK1. *Plant Cell* 27, 1718–1729. doi: 10.1105/tpc.15.00306

Lelek, M., Gyparaki, M. T., Beliu, G., Schueder, F., Griffie, J., Manley, S., et al. (2021). Single-molecule localization microscopy. *Nat. Rev. Methods Prim.* 1, 39. doi: 10.1038/s43586-021-00038-x

Levet, F., Hosy, E., Kechkar, A., Butler, C., Beghin, A., Choquet, D., et al. (2015). SR-Tesseler: a method to segment and quantify localization-based super-resolution microscopy data. *Nat. Methods* 12, 1065–1071. doi: 10.1038/nmeth.3579

Magde, D., Webb, W. W., and Elson, E. (1972). Thermodynamic fluctuations in a reacting system - measurement by fluorescence correlation spectroscopy. *Phys. Rev. Lett.* 29, 705–708. doi: 10.1103/PhysRevLett.29.705

Manley, S., Gillette, J. M., Patterson, G. H., Shroff, H., Hess, H. F., Betzig, E., et al. (2008). High-density mapping of single-molecule trajectories with photoactivated localization microscopy. *Nat. Methods* 5, 155–157. doi: 10.1038/Nmeth.1176

Manzo, C., and Garcia-Parajo, M. F. (2015). A review of progress in single particle tracking: from methods to biophysical insights. *Rep. Prog. Phys.* 78, 124601. doi: 10.1088/0034-4885/78/12/124601

Martinière, A., Fiche, J. B., Smokvarska, M., Mari, S., Alcon, C., Dumont, X., et al. (2019). Osmotic stress activates two reactive oxygen species pathways with distinct effects on protein nanodomains and diffusion. *Plant Physiol.* 179, 1581–1593. doi: 10.1104/pp.18.01065

McKenna, J. F., Rolfe, D. J., Webb, S. E. D., Tolmie, A. F., Botchway, S. W., Martin-Fernandez, M. L., et al. (2019). The cell wall regulates dynamics and size of plasma-membrane nanodomains in Arabidopsis. *Proc. Natl. Acad. Sci. U.S.A.* 116, 12857–12862. doi: 10.1073/pnas.1819077116

Mora-Garcia, S., Vert, G., Yin, Y., Cano-Delgado, A., Cheong, H., and Chory, J. (2004). Nuclear protein phosphatases with Kelch-repeat domains modulate the response to brassinosteroids in Arabidopsis. *Genes Dev.* 18, 448–460. doi: 10.1101/gad.1174204

Pain, C., Tynan, C., Botchway, S. W., and Kriechbaumer, V. (2024). Variable-angle epifluorescence microscopy for single-particle tracking in the plant ER. *Methods Mol. Biol.* 2772, 273–283. doi: 10.1007/978-1-0716-3710-4_20

Patterson, G. H., and Lippincott-Schwartz, J. (2002). A photoactivatable GFP for selective photolabeling of proteins and cells. *Science* 297, 1873–1877. doi: 10.1126/science.1074952

Perraki, A., Gronnier, J., Gouguet, P., Boudsocq, M., Deroubaix, A. F., Simon, V., et al. (2018). REM1.3's phospho-status defines its plasma membrane nanodomain organization and activity in restricting PVX cell-to-cell movement. *PloS Pathog.* 14, e1007378. doi: 10.1371/journal.ppat.1007378

Peters, R., Peters, J., and Tews, K. H. (1974). Microfluorimetric studies on translational diffusion of proteins in erythrocyte-membrane. *Pflugers Arch. - Eur. J. Physiol.* 347, R36–R36. doi: 10.1016/0005-2736(74)90085-6

Platre, M. P., Bayle, V., Armengot, L., Bareille, J., Marquès-Bueno, M. D., Creff, A., et al. (2019). Developmental control of plant Rho GTPase nano-organization by the lipid phosphatidylserine. *Science* 364, 57–62. doi: 10.1126/science.aav9959

Platre, M. P., Gleason, M. F., Brent, L., Cao, M., Zhang, L., Satbhai, S. B., et al. (2022). Ubiquitination steers SRF3 plasma membrane nano-organization to specify signaling outputs. *bioRxiv*. 2022.10.28.514292. doi: 10.1101/2022.10.28.514292

Qian, H., Sheetz, M. P., and Elson, E. L. (1991). Single-particle tracking - analysis of diffusion and flow in 2-dimensional systems. *Biophys. J.* 60, 910–921. doi: 10.1016/S0006-3495(91)82125-7

Ries, J. (2020). SMAP: a modular super-resolution microscopy analysis platform for SMLM data. *Nat. Methods* 17, 870–872. doi: 10.1038/s41592-020-0938-1

Sage, D., Pham, T. A., Babcock, H., Lukes, T., Pengo, T., Chao, J., et al. (2019). Super-resolution fight club: assessment of 2D and 3D single-molecule localization microscopy software. *Nat. Methods* 16, 387–395. doi: 10.1038/s41592-019-0364-4

Saxton, M. J., and Jacobson, K. (1997). Single-particle tracking: Applications to membrane dynamics. *Annu. Rev. Biophys. Biomol. Struct.* 26, 373–399. doi: 10.1146/annurev.biophys.26.1.373

Smokvarska, M., Bayle, V., Maneta-Peyret, L., Fouillen, L., Poitout, A., Dongois, A., et al. (2023). The receptor kinase FERONIA regulates phosphatidylserine localization at the cell surface to modulate ROP signaling. *Sci. Adv.* 9, eadd4791. doi: 10.1126/sciadv.add4791

Smokvarska, M., Francis, C., Platre, M. P., Fiche, J. B., Alcon, C., Dumont, X., et al. (2020). A plasma membrane nanodomain ensures signal specificity during osmotic signaling in plants. *Curr. Biol.* 30, 4654–4664. doi: 10.1016/j.cub.2020.09.013

Subach, F. V., Patterson, G. H., Renz, M., Lippincott-Schwartz, J., and Verkhusha, V. V. (2010). Bright monomeric photoactivatable red fluorescent protein for two-color super-resolution sptPALM of live cells. *J. Am. Chem. Soc* 132, 6481–6491. doi: 10.1021/ja100906g

Tinevez, J.-Y. (2011). *simpletracker* (GitHub). Available at: https://github.com/tinevez/simpletracke.

Tinevez, J. Y., Perry, N., Schindelin, J., Hoopes, G. M., Reynolds, G. D., Laplantine, E., et al. (2017). TrackMate: An open and extensible platform for single-particle tracking. *Methods* 115, 80–90. doi: 10.1016/j.ymeth.2016.09.016

Tokunaga, M., Imamoto, N., and Sakata-Sogawa, K. (2008). Highly inclined thin illumination enables clear single-molecule imaging in cells. *Nat. Methods* 5, 455–455. doi: 10.1038/nmeth0508-455

Vert, G., and Chory, J. (2006). Downstream nuclear events in brassinosteroid signalling. *Nature* 441, 96–100. doi: 10.1038/nature04681

Wallis, T. P., Jiang, A., Young, K., Hou, H., Kudo, K., McCann, A. J., et al. (2023). Super-resolved trajectory-derived nanoclustering analysis using spatiotemporal indexing. *Nat. Commun.* 14, 3353. doi: 10.1038/s41467-023-38866-y

Wang, S. Y., Su, J. H., Beliveau, B. J., Bintu, B., Moffitt, J. R., Wu, C. T., et al. (2016). Spatial organization of chromatin domains and compartments in single chromosomes. *Science* 353, 598–602. doi: 10.1126/science.aaf8084

Wilkinson, M. D., Dumontier, M., Aalbersberg, I. J., Appleton, G., Axton, M., Baak, A., et al. (2016). Comment: The FAIR Guiding Principles for scientific data management and stewardship. *Sci. Data* 3, 160018. doi: 10.1038/sdata.2016.18

Witthöft, J., Caesar, K., Elgass, K., Huppenberger, P., Kilian, J., Schleifenbaum, F., et al. (2011). The activation of the Arabidopsis P-ATPase 1 by the brassinosteroid receptor BRI1 is independent of threonine 948 phosphorylation. *Plant Signaling Behav.* 6, 1063–1066. doi: 10.4161/psb.6.7.15650

Wolf, S. (2020). Deviating from the beaten track: new twists in brassinosteroid receptor function. *Int. J. Mol. Sci.* 21, 1561. doi: 10.3390/ijms21051561

Wolf, S., Mravec, J., Greiner, S., Mouille, G., and Hofte, H. (2012). Plant cell wall homeostasis is mediated by brassinosteroid feedback signaling. *Curr. Biol.* 22, 1732–1737. doi: 10.1016/j.cub.2012.07.036

Wolf, S., van der Does, D., Ladwig, F., Sticht, C., Kolbeck, A., Schurholz, A. K., et al. (2014). A receptor-like protein mediates the response to pectin modification by activating brassinosteroid signaling. *Proc. Natl. Acad. Sci. U.S.A.* 111, 15261–15266. doi: 10.1073/pnas.1322979111

Yin, Y., Vafeados, D., Tao, Y., Yoshida, S., Asami, T., and Chory, J. (2005). A new class of transcription factors mediates brassinosteroid-regulated gene expression in Arabidopsis. *Cell* 120, 249–259. doi: 10.1016/j.cell.2004.11.044

Zhang, M. S., Chang, H., Zhang, Y. D., Yu, J. W., Wu, L. J., Ji, W., et al. (2012). Rational design of true monomeric and bright photoactivatable fluorescent proteins. *Nat. Methods* 9, 727–729. doi: 10.1038/Nmeth.2021

Zhang, X., Henriques, R., Lin, S. S., Niu, Q. W., and Chua, N. H. (2006). Agrobacterium-mediated transformation of Arabidopsis thaliana using the floral dip method. *Nat. Protoc.* 1, 641–646. doi: 10.1038/nprot.2006.97

Zhu, J. Y., Li, Y., Cao, D. M., Yang, H., Oh, E., Bi, Y., et al. (2017). The F-box protein KIB1 mediates brassinosteroid-induced inactivation and degradation of GSK3-like kinases in arabidopsis. *Mol. Cell* 66, 648–657.e644. doi: 10.1016/j.molcel.2017.05.012

Simultaneous and Dynamic Super-Resolution Imaging of Two Proteins in *Arabidopsis thaliana* using dual-color sptPALM

by Rohr L., Ehinger A., Glöckner Burmeister N., Meixner A. J., Kemmerling B., Harter K., zur Oven-Krockhaus S. (2024)

available as preprint on *bioRxiv*

doi: https://doi.org/10.1101/2024.03.13.584811

Submitted

Simultaneous and Dynamic Super-Resolution Imaging of Two Proteins in *Arabidopsis thaliana* using dual-color sptPALM

Leander Rohr[1], Alexandra Ehinger[1], Nina Glöckner Burmeister[2], Alfred J. Meixner[3], Birgit Kemmerling[1], Klaus Harter[1] and Sven zur Oven-Krockhaus[1, 3]

1 Center for Plant Molecular Biology (ZMBP), University of Tübingen, Tübingen, Germany

2 Department of Biomedicine, Aarhus University, Aarhus, Denmark

3 Institute for Physical and Theoretical Chemistry, University of Tübingen, Tübingen, Germany

Corresponding author:
Sven zur Oven-Krockhaus, sven.zur-oven-krockhaus@uni-tuebingen.de

Keywords: Plant membrane proteins, super-resolution microscopy, dual-color, single-particle tracking, PA-GFP, PATagRFP

ABSTRACT

Super-resolution microscopy techniques have revolutionized cell biology by providing insights into the dynamics of single molecules and nanoscale organization within living cells. However, the application of dynamic live-cell methods in plants has been limited by the lack of suitable fluorophores for simultaneous visualization of multiple proteins. To address this challenge, we implemented a two-color sptPALM approach using codon-optimized photoactivatable fluorescent proteins PA-GFP and PATagRFP. Recently, we showed their individual usability in single-color experiments in *Nicotiana benthamiana* and *Arabidopsis thaliana* cells. Here, we now demonstrate the suitability of these fluorophores and their combined use for dual-color sptPALM for the simultaneous observation of two different protein fusions in the same plant cell.

MAIN

Imaging techniques such as super-resolution microscopy (SRM) provide insights into the dynamics of single molecules and the nanoscale organization of molecular assemblies in living cells and therefore have revolutionized cell biology in recent years (Schermelleh et al., 2019). While live-cell single-particle tracking photoactivated localization microscopy (sptPALM) measurements in the mammalian field were already performed by Manley et al. (2008), the first application in plants was introduced by Hosy et al. (2015). Studies in plants are restricted to a limited number of genetically encoded

fluorophores (FPs) fused to the gene of interest. Externally added organic dyes that are regularly applied for animal cells are not viable for plant cells as the plant cell wall prevents their entry (Hosy et al., 2015; McKenna et al., 2019; Lelek et al., 2021; Jolivet et al., 2023). This drawback made it impossible to simultaneously visualize and track two distinct proteins within the same plant cell as spectrally compatible genetically encoded photoswitchable or activatable FPs for sptPALM were missing. Nevertheless, the simultaneous spatiotemporal observation of two (or more) differentially labelled proteins is of great interest to understand the dynamics of proteins within membrane nanodomains and the nanoscale (re-)organization of, e.g., receptor complexes upon ligand perception. For single-color approaches in plants, mEos and its variants proved to be effective (Rohr et al., 2023). However, mEos-derived FPs are unsuitable for dual-color measurements as its native and photoconverted form occupy both the green and red part of the spectrum (Wiedenmann et al., 2004).

To identify suitable FP pairs for a dual-color approach, extensive literature research and pilot tests were performed to find candidates with appropriate spectral properties, sufficient brightness, an adequate maturation time, photostability and low inherent blinking activity (Shcherbakova et al., 2014). Eventually, codon-optimized PA-GFP and PATagRFP (Supplementary Material and Methods; Supplementary Table 1) proved suitable to express corresponding fusion proteins separately in transiently transformed *Nicotiana benthamiana* (*N.* benthamiana) cells as well as in stably transformed *Arabidopsis thaliana* (*A. thaliana*) plants. We recorded single-molecule tracks of these fusions in live cell-imaging, analyzed their mobility, and found that both chromophores are functional for single-color sptPALM in plant cells (Rohr et al., 2023). Their combined (dual-color) use now enables the simultaneous spatiotemporal observation of two different protein fusions within the same plant cell.

For the proof of concept of dual-color sptPALM, we selected the plasma membrane-integral receptor-like protein 44 (RLP44) (Wolf et al., 2014). As shown previously, PA-GFP-, PATagRFP- and mEos3.2-tagged versions of RLP44 show comparable diffusion coefficients when expressed individually under the control of the native *RLP44* promoter in independent transgenic Ar*abidopsis* lines (Rohr et al., 2023). The transgenic *Arabidopsis* line used in this work, expressing RLP44-PA-GFP and RLP44-PATagRFP simultaneously, was obtained by crossing the previously characterized individual lines (Supplementary Table 2).

Measurements were performed in epidermal hypocotyl cells of seven-day-old seedlings grown in light on ½ Murashige and Skoog (MS) media supplemented with 1 % sucrose. The imaging procedure was carried out according to Rohr et al. (2023), with the following minor adjustments:

The specimen's signal was separated into two channels (green and red) with the help of a dichroic beam splitter and redirected to a 768 x 384 px section of one single sCMOS (scientific complementary

metal-oxide-semiconductor) camera. Following this, the files were preprocessed, and sample areas for each channel were extracted for subsequent analysis steps (Figure 1 A, B, left panel; Supplementary Figure 1).

Using the recently released OneFlowTraX software package (Rohr et al., 2023), we generated super-resolved trajectories of the corresponding fusion proteins, which were obtained evaluating sptPALM movies with over 1,500 frames each, recorded at a rate of 20 Hz. To exclude potential tracking artifacts, data were filtered according to previously reported procedures (Hosy et al., 2015; Bayle et al., 2021; Rohr et al., 2023), i.e., setting the maximum linking distance (here: 200 nm), which is the upper distance limit between two fluorophore positions in two consecutive frames to be assigned to the same track and the maximum gap closing (here: 4) that defines the maximum allowed number of successive frames without detected localizations. Applying those, tracks showed a similar heterogeneous spatial pattern within the plasma membrane for both fusion proteins (Figure 1 A, B, right panel). Similar localization patterns are commonly observed for numerous proteins (Jaillais and Ott, 2020) and were previously also shown for RLP44-mEos3.2 fusions (Rohr et al., 2023). To calculate the mean square displacement (MSD), which is currently the most widely used method to extract diffusion coefficients and motion patterns for sptPALM data (Manzo and Garcia-Parajo, 2015), selected tracks with a minimum length of eight localized positions were considered for further analyses. This removes short tracks that cannot be reliably statistically analyzed, as well as track artifacts that originate from short-lived autofluorescent molecules in the background. Following the calculation of the tracks, the diffusion coefficient (D) was estimated via a linear fit using points two to four of the MSD curve, as outlined in (Rohr et al., 2023).

As shown in Figure 1 C, the decadic logarithm of the diffusion coefficients for simultaneously recorded RLP44-PA-GFP and RLP44-PATagRFP fusions proteins displayed a bell-shaped distribution, suggesting singular RLP44 populations. To obtain the absolute value of D (in $\mu m^2/s$) for each cell, the track data distributions were fitted with normal distributions, and the peak value was extracted, as previously described (Figure 1 D; (Hosy et al., 2015; Rohr et al., 2023)). The mean D (± standard deviation) was $0.0203 \pm 0.00617\ \mu m^2/s$ for RLP44-PA-GFP and $0.0205 \pm 0.00587\ \mu m^2/s$ for RLP44-PATagRFP. Statistical analyses revealed no significant difference between the two fusion proteins (Mann-Whitney-U-Test, $p = 0.8282$). Thus, the selected FPs are an excellent choice for dual-color sptPALM as they do not affect the behavior of the proteins and could be interchanged without altering their diffusion behavior. They offer high image contrast during data acquisition for detection and localization, and their photostability allows for the recording of long tracks suitable for statistical analysis. Additionally, their spectral separability makes them well suited for dual-color microscopy setups.

The successful implementation of live-cell dual-color sptPALM in plants, utilizing the two codon-optimized FPs PA-GFP and PATagRFP, opens up new possibilities for studying two proteins simultaneously in living plant cells. This will widen the understanding of the dynamics of molecules within the plant plasma membrane.

ACKNOWLEDGMENTS AND FUNDING

This research was supported by the German Research Foundation (DFG) via the CRC 1101 to A.J.M., B.K., K.H. and S.z.O.-K., and by individual DFG grants to K.H. (HA 2146/22, HA 2146/23). We also thank the DFG for grants for scientific equipment (FUGG: INST 37/991-1, INST 37/992-1, INST 37/819-1, INST 37/965-1). Furthermore, we would like to thank Dr. Andrea Gust for providing us with the pFAST construct, Jutta Keicher for her help with generating the crossed plant lines, and Luiselotte Rausch for the fruitful discussions of the manuscript.

AUTHOR CONTRIBUTIONS

A.J.M., B.K., K.H., and S.z.O.-K. designed the research. L.R. and S.z.O.-K. performed research. A.E. and N.G.B. contributed resources and performed preliminary tests. L.R. and S.z.O.-K. analyzed data. L.R., K.H. and S.z.O.-K. wrote the paper.

FIGURE LEGENDS

Figure 1: Dual-colour sptPALM of RLP44 fused to PA-GFP or PATagRFP in living *A. thaliana* hypocotyl cells

(A,B) Single frame of an sptPALM movie (left; scale bar = 5 µm) showing RLP44-PA-GFP (A) and RLP44-PATagRFP (B) fusion proteins that are expressed under control of their native promoter, visible as diffraction-limited spots at the plasma membrane. Trajectories of individual molecules over time (right; scale bar = 500 nm) were generated by OneFlowTrax (Rohr et al., 2023). **(C)** Distribution of D represented as $\log_{10}$(D) for RLP44-PA-GFP (green) and RLP44-PATagRFP (magenta) including n=99 cells from six plants for each fusion protein. **(D)** Peak D values of individual cells with RLP44-PA-GFP in green and RLP44-PATagRFP in magenta, obtained by normal fits of distributions for individual cells. For statistical analysis, data were tested for normal distribution, and a consecutive Mann-Whitney-U-Test revealed no significant differences between the groups. Whiskers show the data range excluding outliers, while the boxes represent the 25-75 percentiles.

REFERENCES

Bayle V, Fiche JB, Burny C, Platre MP, Nollmann M, Martiniere A, Jaillais Y (2021) Single-particle tracking photoactivated localization microscopy of membrane proteins in living plant tissues. Nat Protoc **16:** 1600-1628

Hosy E, Martiniere A, Choquet D, Maurel C, Luu DT (2015) Super-resolved and dynamic imaging of membrane proteins in plant cells reveal contrasting kinetic profiles and multiple confinement mechanisms. Mol Plant **8:** 339-342

Jaillais Y, Ott T (2020) The Nanoscale Organization of the Plasma Membrane and Its Importance in Signaling: A Proteolipid Perspective. Plant Physiol **182:** 1682-1696

Jolivet M-D, Deroubaix A-F, Boudsocq M, Abel NB, Rocher M, Robbe T, Wattelet-Boyer V, Huard J, Lefebvre D, Lu Y-J, Day B, Saias G, Ahmed J, Cotelle V, Giovinazzo N, Gallois J-L, Yamaji Y, German-Retana S, Gronnier J, Ott T, Mongrand S, Germain V (2023) Interdependence of a kinase and its cognate substrate plasma membrane nanoscale dynamics underlies *Arabidopsis* response to viral infection. eLife **12:** RP90309

Lelek M, Gyparaki MT, Beliu G, Schueder F, Griffie J, Manley S, Jungmann R, Sauer M, Lakadamyali M, Zimmer C (2021) Single-molecule localization microscopy. Nat Rev Methods Primers **1:** 39

Manley S, Gillette JM, Patterson GH, Shroff H, Hess HF, Betzig E, Lippincott-Schwartz J (2008) High-density mapping of single-molecule trajectories with photoactivated localization microscopy. Nat Methods **5:** 155-157

Manzo C, Garcia-Parajo MF (2015) A review of progress in single particle tracking: from methods to biophysical insights. Rep Prog Phys **78:** 124601

McKenna JF, Rolfe DJ, Webb SED, Tolmie AF, Botchway SW, Martin-Fernandez ML, Hawes C, Runions J (2019) The cell wall regulates dynamics and size of plasma-membrane nanodomains in Arabidopsis. Proc Natl Acad Sci U S A **116:** 12857-12862

Rohr L, Ehinger A, Rausch L, Glöckner Burmeister N, Meixner AJ, Gronnier J, Harter K, Kemmerling B, zur Oven-Krockhaus S (2023) OneFlowTraX: A User-Friendly Software for Super-Resolution Analysis of Single-Molecule Dynamics and Nanoscale Organization. bioRxiv**:** 2023.2008.2010.552827

Schermelleh L, Ferrand A, Huser T, Eggeling C, Sauer M, Biehlmaier O, Drummen GPC (2019) Super-resolution microscopy demystified. Nat Cell Biol **21:** 72-84

Shcherbakova DM, Sengupta P, Lippincott-Schwartz J, Verkhusha VV (2014) Photocontrollable fluorescent proteins for superresolution imaging. Annu Rev Biophys **43:** 303-329

Wiedenmann J, Ivanchenko S, Oswald F, Schmitt F, Röcker C, Salih A, Spindler K-D, Nienhaus GU (2004) EosFP, a fluorescent marker protein with UV-inducible green-to-red fluorescence conversion. Proceedings of the National Academy of Sciences **101:** 15905-15910

Wolf S, van der Does D, Ladwig F, Sticht C, Kolbeck A, Schurholz AK, Augustin S, Keinath N, Rausch T, Greiner S, Schumacher K, Harter K, Zipfel C, Hofte H (2014) A receptor-like protein mediates the response to pectin modification by activating brassinosteroid signaling. Proc Natl Acad Sci U S A **111:** 15261-15266

175 FIGURES

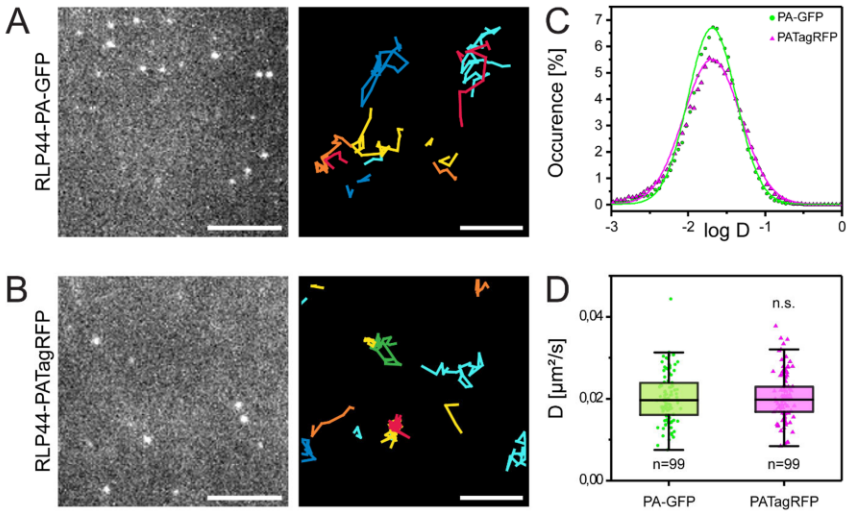

176

177 **Figure 1 | Dual-colour sptPALM of RLP44 fused to PA-GFP or PATagRFP in living A. thaliana hypocotyl cells**
178 **(A,B)** Single frame of an sptPALM movie (left; scale bar = 5 µm) showing RLP44-PA-GFP (A) and RLP44-PATagRFP (B) fusion
179 proteins that are expressed under control of their native promoter, visible as diffraction-limited spots at the plasma
180 membrane. Trajectories of individual molecules over time (right; scale bar = 500 nm) were generated by OneFlowTrax (Rohr
181 et al., 2023). **(C)** Distribution of D represented as $\log_{10}$(D) for RLP44-PA-GFP (green) and RLP44-PATagRFP (magenta) including
182 n=99 cells from six plants for each fusion protein. **(D)** Peak D values of individual cells with RLP44 PA GFP in green and RLP44
183 PATagRFP in magenta, obtained by normal fits of distributions for individual cells. For statistical analysis, data were tested
184 for normal distribution, and a consecutive Mann-Whitney-U-Test revealed no significant differences between the groups.
185 Whiskers show the data range excluding outliers, while the boxes represent the 25-75 percentiles.

SUPPLEMENTAL MATERIAL AND METHODS

Simultaneous and Dynamic Super-Resolution Imaging of Two Proteins in *Arabidopsis thaliana* using dual-color sptPALM

Leander Rohr[1], Alexandra Ehinger[1], Nina Glöckner Burmeister[2], Alfred J. Meixner[3], Birgit Kemmerling[1], Klaus Harter[1] and Sven zur Oven-Krockhaus[1, 3]

1 Center for Plant Molecular Biology (ZMBP), University of Tübingen, 72076 Tübingen, Germany

2 Department of Biomedicine, Aarhus University, Aarhus, Denmark

3 Institute for Physical and Theoretical Chemistry, University of Tübingen, Tübingen, Germany

Corresponding author:
Sven zur Oven-Krockhaus, sven.zur-oven-krockhaus@uni-tuebingen.de

PLASMID CONSTRUCTION

All expression clones were constructed using GoldenGate assembly with BB10 as the vector (Binder et al., 2014). The promoter sequence of RLP44 was obtained with the help of the Integrated Genome Browser (Freese et al., 2016). Level I modules were generated by PCR amplification of the desired sequences and then blunt-end cloned into pJET1.2 (Thermo Fisher Scientific) or ready-to-use obtained by others, such as the pFAST module from Dr. Andrea Gust and the hygromycin resistance module (Binder et al., 2014). Fluorophores were designed as C-terminal fusions (D-E module) using a glycine/alanine-rich linker. The coding sequence of RLP44 was constructed as B-D module, eliminating the need for a B-C dummy module. The further procedure was performed as described in Rohr et al. (2023). A full list of used constructs can be found in Supplementary Table 2.

PLANT MATERIAL AND GROWTH CONDITIONS

The transgenic *A. thaliana* lines generated for this study were all in the Columbia (Col-0) background. The respective stable lines expressing one individual fusion protein were created using the Floral dip method according to Zhang et al. (2006) and were already described in Rohr et al. (2023). The plant line utilized in this study was generated through the crossing of RLP44-PA-GFP-pFAST as the maternal parent and RLP44-PATagRFP-Hygromycin, which provided the pollen. The seeds resulting from the crossings were propagated via the presence of the pFAST marker by binocular visual inspection and

by selection of survivors on ½ Murashige and Skoog (MS) plates containing 1 % (w/v) sucrose and 0.8 % (w/v) phytoagar supplemented with 25 µM hygromycin. For the presented experiments, a line homozygous for both transgenes was used. For sptPALM measurements, seeds were sterilized with a solution of 70 % ethanol (v/v) and 0.05 % Triton X 100 for 30 minutes followed by a 10-minute treatment with absolute ethanol. Seeds were sown on ½ MS plates (+1 % sucrose and 0.8 % phytoagar) and stratified at 4 °C for at least 24 hours. The light-grown seedlings were cultivated for seven days in growth chambers at 20 °C under long-day conditions (16 hours light / 8 hours dark).

SAMPLE PREPARATION AND MOVIE ACQUISITION

For a sptPALM measurement, a seven-day old seedling was placed between two coverslips (Epredia 24x50 mm #1 or equivalent) with a drop of water. This "coverslip sandwich" was then placed on the specimen stage, lightly weighted down by a brass ring.

For the sptPALM acquisition, a custom-built microscope platform was used that is described in detail in Rohr et al. (2023), with the following customization to enable dual-colour imaging: a dichroic beam splitter (Laser Beamsplitter H 560 LPXR superflat, AHF analysentechnik AG) was introduced into the emission beam path to separate the signal from PA-GFP and PATagRFP. The filtered (488 LP Edge Basic Longpass Filter and 525/50 BrightLine HC for PA-GFP; 568 LP Edge Basic Longpass Filter and 600/52 BrightLine HC for PATagRFP; all AHF analysentechnik AG) emission signals were then focused onto an sCMOS camera chip with the aid of individual lenses and a D-shaped mirror, which introduced a lateral offset between both colour channels. The further procedure was performed according to the protocol described by Rohr et al. (2023) with minor adjustments. The recording was performed with a section of 76.8 x 38.4 µm and a frame rate of 20 Hz, recording 1 500 frames per movie. The output power of the 488 nm laser was adjusted to 1 200 µW. For each measurement day, noise files (a series of dark images) were recorded with the corresponding frame rates.

RAW DATA PROCESSING AND ANALYSIS WITH ONEFLOWTRAX

Recorded TIFF files were pre-processed by a custom-built MATLAB application to store the PA-GFP and PATagRFP channel as separate files, which were then loaded into OneFlowTraX to inspect the quality of the data and to confirm the applicability of previous used parameters for each analysis step (Rohr et al., 2023). If necessary, regions of interest (ROIs; also referred to as masks) were defined. We observed that the same parameters used before for one-color approaches are applicable for dual-color experiments, as well (Rohr et al., 2023). The final analysis was then performed by using the "Batch analysis" option of OneFlowTraX.

Supplementary Table 1 | Nucleotide sequences of the codon-optimized fluorophores PA-GFP and PATagRFP
Shown are the codon optimized nucleotide sequences of the fluorophores PA-GFP and PATagRFP and the respective position. Genes were synthesized by Invitrogen's GeneArt services (Thermo Fisher Scientific)

PA-GFP

```
1       ATG GTG AGC AAG GGC GAA GAG TTG TTC ACT GGT GTT GTT CCT ATC CTC GTT
52      GAG CTT GAC GGT GAT GTG AAC GGG CAT AAG TTC TCC GTT TCT GGT GAA GGT
103     GAG GGT GAT GCT ACT TAC GGA AAG CTC ACC CTC AAG TTC ATC TGT ACC ACT
154     GGA AAG CTC CCT GTG CCT TGG CCT ACT CTC GTT ACC ACT TTC TCT TAC GGG
205     GTG CAA TGC TTC AGC AGA TAC CCT GAT CAT ATG AAG CAG CAC GAC TTC TTC
256     AAG AGC GCT ATG CCT GAG GGA TAC GTG CAA GAG AGA ACC ATT TTC TTC AAG
307     GAC GAC GGG AAC TAC AAG ACC AGA GCT GAG GTT AAG TTC GAA GGT GAC ACC
358     CTC GTG AAC AGG ATC GAG CTT AAG GGC ATC GAC TTC AAA GAG GAC GGA AAC
409     ATC CTC GGG CAC AAG TTG GAG TAC AAC TAC AAC AGC CAC AAC GTG TAC ATC
460     ATG GCC GAC AAG CAG AAG AAC GGC ATC AAG GCC AAC TTC AAG ATC AGG CAC
511     AAC ATC GAG GAT GGC TCT GTT CAG CTC GCT GAT CAT TAC CAG CAG AAC ACC
562     CCT ATT GGA GAT GGA CCT GTT CTT CTC CCT GAC AAC CAC TAC CTT AGC CAC
613     CAG AGC AAG TTG AGC AAG GAC CCT AAT GAG AAG AGG GAC CAC ATG GTG CTC
664     TTG GAG TTT GTT ACT GCT GCT GGA ATC ACC CTC GGA ATG GAC GAG CTT TAC
715     AAG TGA
```

PATagRFP

```
1      ATG GAA CTC ATC AAA GAA AAC ATG CAC ATG AAG CTC TAC ATG GAA GGG ACC
52     GTG AAC AAC CAC CAT TTC AAG TGC ACA AGC GAA GGT GAG GGA AAG CCT TAC
103    GAG GGA ACT CAG ACC ATG AGA ATC AAG GTG GTG GAA GGT GGA CCT CTT CCT
154    TTC GCC TTC GAT ATT CTC GCC ACC TCC TTC ATG TAC GGG TCC TCT ACT TTC
205    ATC AAC CAC ACT CAG GGA ATC CCG GAC TTC TGG AAG CAA TCT TTT CCA GAG
256    GGA TTC ACC TGG GAG AGA GTG ACT ACT TAC GAG GAT GGT GGT GTG CTC ACT
307    GCT ACT CAG GAT ACT TCT CTT CAG GAC GGC TGC CTC ATC TAC AAC GTG AAG
358    ATC AGA GGT GTG AAC TTC CCG TCT AAC GGA CCG GTG ATG AAG AAA AAG ACT
409    CTC GGA TGG GAG CCG TCT ACC GAG AAA CTT AAG CCT GCT GAT GGT GGA CTT
460    GAG GGA AGA GTT GAC ATG GCT CTT AAG CTC GTT GGA GGT GGA CAT CTC ATC
511    TGC AAC TTC AAG ACC ACC TAC AGG TCT AAG AAG CCG GCC AAG AAC CTT AAG
562    ATG CCT GGG GTT TAC TAC GTG GAC AGG CGT CTT GAG ATT ATC AAA GAG GCC
613    GAC AAA GAG ACT TAC TGG GAG CAG CAT GAA GTG GCT GTG GCT AGG TAT TCT
664    GAC CTT CCA TCT AAG CTC GGG CAC AAG CTC AAT TGA
```

Supplementary Table 2 | List of constructs and used plant lines
All used constructs (top) and plant lines (bottom) are listed with our internal numbering, their name, their purpose and source.

Internal #	Name	Purpose	Source
4390	pJET1.2_pRLP44	LI A-B Module	this study
4401	pJET1.2_cRLP44	LI B-D Module	this study
4437	pJET1.2_(GA)PA-GFP	LI D-E Module (with Gly/Ala Linker)	this study
4438	pJET1.2_(GA)PATagRFP	LI D-E Module (with Gly/Ala Linker)	this study
4398	pUC57_nosTerm	LI E-F Module	(Binder et al., 2014)
4400	pGEM-T_pFAST	LI F-G Module	this study
4503	pUC57_Hygromycin	LI F-G Module	(Binder et al., 2014)
4479	BB10 -- pRLP44:cRLP44-(GA)PA-GFP-nosTerm-pFast -- BB10	LII; Expression in *A. thaliana*	this study
4494	BB10 -- pRLP44:cRLP44-(GA)PATagRFP-nosTerm-Hygromycin -- BB10	LII; Expression in *A. thaliana*	this study
AtLR185	pRLP44:cRLP44-(GA)PA-GFP-nosTerm-pFast (in Col-0)	Crossing with AtLR226	this study
AtLR226	pRLP44:cRLP44-(GA)PATagRFP-nosTerm-Hygromycin (in Col-0)	Crossing with AtLR185	this study
AtLR371	♀ pRLP44:cRLP44-(GA)PA-GFP x ♂ pRLP44:cRLP44-(GA)PATagRFP	in planta sptPALM	this study

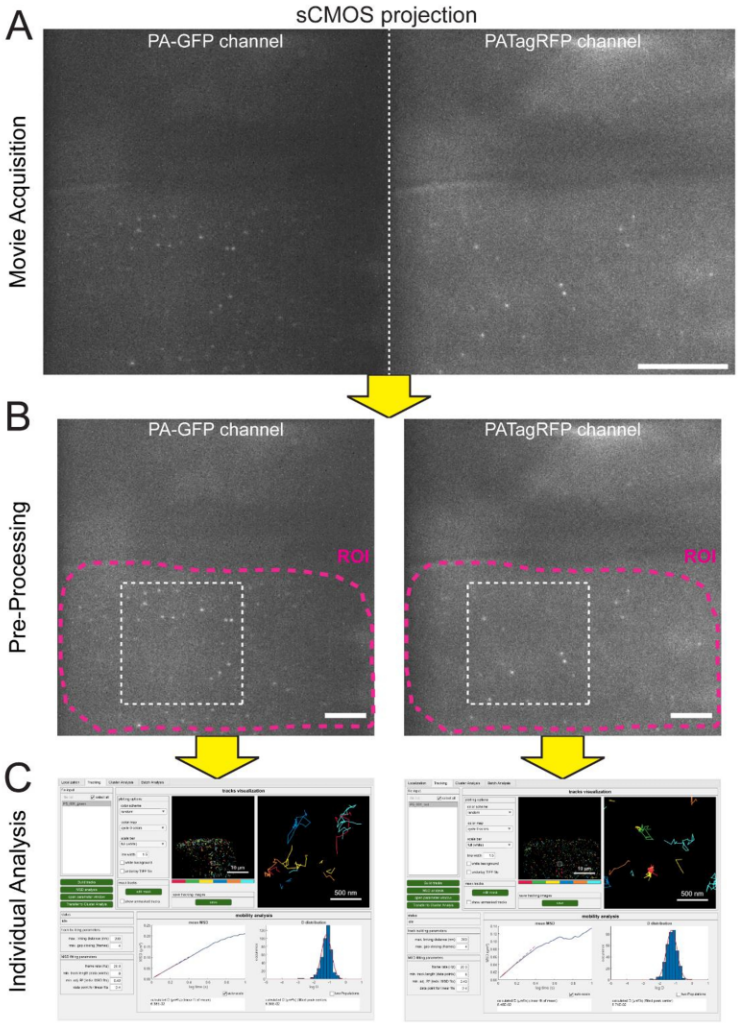

Supplementary Figure 1 | Acquisition and analysis workflow for dual-color sptPALM
(A) Representative image of one frame during movie acquisition. Shown is the full projection of the sCMOS camera, with the PA-GFP channel on the left and the PATagRFP channel on the right. For the simplification of the separation the white dashed line was inserted for this visualization (scale bar = 10 µm). **(B)** Pre-processing of the recorded movies. Shown are the distinct channels (PA-GFP left and PATagRFP right) from the representative movie from (A) after it was split by an in-house Matlab application at the position of the white dashed line from (A). Dashed magenta lines define the region of interest (ROI) that can be generated by OneFlowTrax (Rohr et al., 2023) and that represents one cell in this depiction, enabling the analysis of one specific cell exclusively, without signals from outside. The white dashed square defines the area that is illustrated in main text Figure 1 A and B, left panel (scale bar = 5 µm). **(C)** Exemplary visualizations of the individual analysis of distinct channels. Show are screenshots of the "Tracking" option from OneFlowTraX (Rohr et al., 2023) that enables the generation of tracks and subsequently MSD analysis. Distinct channels are analysed separately and results are combined afterwards.

REFERENCES

Binder A, Lambert J, Morbitzer R, Popp C, Ott T, Lahaye T, Parniske M (2014) A modular plasmid assembly kit for multigene expression, gene silencing and silencing rescue in plants. PLoS One **9:** e88218. https://doi.org/10.1371/journal.pone.0088218

Freese NH, Norris DC, Loraine AE (2016) Integrated genome browser: visual analytics platform for genomics. Bioinformatics **32:** 2089-2095. https://doi.org/10.1093/bioinformatics/btw069

Rohr L, Ehinger A, Rausch L, Glöckner Burmeister N, Meixner AJ, Gronnier J, Harter K, Kemmerling B, zur Oven-Krockhaus S (2023) OneFlowTraX: A User-Friendly Software for Super-Resolution Analysis of Single-Molecule Dynamics and Nanoscale Organization. bioRxiv. 2023.2008.2010.552827. https://doi.org/10.1101/2023.08.10.552827

Zhang X, Henriques R, Lin SS, Niu QW, Chua NH (2006) Agrobacterium-mediated transformation of Arabidopsis thaliana using the floral dip method. Nat Protoc **1:** 641-646. https://doi.org/10.1038/nprot.2006.97

Contrasting Effects of Cytoskeleton Disruption on Plasma Membrane Receptor Dynamics: Insights from Single-Molecule Analyses

by Rohr L., Rausch L., Harter, K., zur Oven-Krockhaus S. (2024)

available as preprint on *bioRxiv*

doi: https://doi.org/10.1101/2024.09.09.612020

Submitted

Contrasting Effects of Cytoskeleton Disruption on Plasma Membrane Receptor Dynamics: Insights from Single-Molecule Analyses

Leander Rohr[1], Luiselotte Rausch[1], Klaus Harter[1] and Sven zur Oven-Krockhaus[1, 2]

1 Center for Plant Molecular Biology (ZMBP), University of Tübingen, Tübingen, Germany

2 Institute for Physical and Theoretical Chemistry, University of Tübingen, Tübingen, Germany

Corresponding author:
Sven zur Oven-Krockhaus, sven.zur-oven-krockhaus@uni-tuebingen.de

Keywords: cytoskeleton, actin filaments, microtubules, plant membrane protein dynamics, super-resolution microscopy, motion classification, sptPALM, NASTIC, DC-MSS

Abstract

Traditional models such as the fluid mosaic model or the lipid raft hypothesis have shaped our understanding of plasma membrane (PM) organization. However, recent discoveries have extended these paradigms by pointing to the existence of micro- and nanodomains. Here, we investigated the role of the cytoskeleton in general and whether the picket fence model, established in animal cells, is transferable to the plant cell system. By using single-particle tracking photoactivated localization microscopy (sptPALM) in combination with genetically encoded enzymatic tools for the targeted disruption of the cytoskeleton, we studied the dynamics and nanoscale organization of a selection of PM receptor-like kinases (RLKs) and receptor-like proteins (RLPs). Our findings show that the disintegration of actin filaments leads to decreased diffusion, more restrictive motion patterns, and enlarged clusters, whereas the disintegration of microtubules results in increased diffusion, more unconstrained diffusive behavior, and decreased cluster sizes of the tested RLKs and RLPs. These results underscore the potential unique regulatory functions of cytoskeleton components in plants and suggest an altered mechanism compared to the picket fence model of the animal cell system. Our qualitative data can serve as the foundation for further investigations aimed at developing a comprehensive and refined model of protein dynamics and organization in plant cells.

Introduction

The plasma membrane (PM), together with the cell wall, functions as the first selective barrier between the cell and the environment (Gronnier et al., 2018; Jaillais and Ott, 2020). Singer and Nicolson (1972) emphasized the fundamental significance of biological membranes and their organization in general and proposed the widely known fluid mosaic model. Their assumption was that proteins can laterally diffuse within the membrane without major restrictions. However, this would result in uniformly distributed membrane-embedded proteins such as receptors, independent of the entire PM proteome, which is unequivocally not the case. One significant expansion of the model was the introduction of the "lipid raft" hypothesis, which suggests that lipid rafts, containing high levels of cholesterol and sphingolipids, serve as platforms with a high molecular order of proteins and lipids. These platforms facilitate, for instance, selective interactions between signaling proteins and effector molecules (Simons and Ikonen, 1997). The hypothesis found support in results from the mammalian field, which indicated a binary characteristic of membranes that are partitioned into detergent-resistant and detergent-sensitive fractions (Brown and Rose, 1992; Yu et al., 1973). Similar research was later conducted in plants, delivering comparable results (Borner et al., 2005; Laloi et al., 2007; Lefebvre et al., 2007; Mongrand et al., 2004; Morel et al., 2006). These studies showed that the detergent-resistant membrane protein profile is distinct from that of the whole PM. However, the isolation of detergent-resistant fractions and the detergents used may cause changes in the PM itself. Moreover, results derived from the application of newer methods, such as fluorescent microscopy techniques, raised the question of whether detergent-resistant membrane areas indeed define functional membrane rafts (Kusumi et al., 2005; Raffaele et al., 2009; Tanner et al., 2011). Although the existence of "lipid rafts" in plants, now referred to as "micro- or nanodomains", is undoubtedly accepted, their dynamics, organization and regulation still require further research.

Besides the plant-specific family of remorin proteins serving as scaffolding factors (Jarsch and Ott, 2011; Raffaele et al., 2009), the asymmetric localization and order of lipids within the PM (Gronnier et al., 2018), as well as the cell wall-PM continuum (Martiniere et al., 2012), the cytoskeleton is believed to play a vital regulatory role in the organization of plant PMs (Jaillais and Ott, 2020). This hypothesis is based on the so-called picket fence model from the mammalian field (Kusumi et al., 2012). In this model, the cortical cytoskeleton, composed of actin filaments in mammalian cells, defines membrane domains by acting as a fence that restricts the lateral diffusion of lipids and proteins within these domains. The model postulates additional pickets, which are represented by transmembrane proteins that are anchored either by the cytoskeleton in the cytosol or the extracellular matrix. However, it is important to note that the model, as being based on animal cells, does not include specific properties of plants, such as the existence of cortical microtubules that could act as an additional fence (Jaillais

and Ott, 2020). McKenna et al. (2019) demonstrated an impact of actin and microtubules on the diffusion of some but not all proteins in the PM. Moreover, additional studies revealed a change in or loss of nanodomain organization of proteins after cytoskeleton disruption, again for some but not for all tested proteins (Bücherl et al., 2017; Danek et al., 2020; Jarsch et al., 2014; Konrad et al., 2014; Lv et al., 2017; Raffaele et al., 2008; Szymanski et al., 2015). Chemicals such as latrunculin or oryzalin were used in these studies to disintegrate either the actin or the microtubule cytoskeleton. However, these chemicals are difficult to fine-tune in terms of their tissue-specific activity and concentration. In contrast, we utilized recently developed genetically encoded, enzymatic tools that mimic the function of those chemicals. Specifically, we employed the *Salmonella enterica* effector SpvB for actin cytoskeleton disintegration (Harterink et al., 2017; Vilches Barro et al., 2019) and a phosphatase-inactive variant of the atypical tubulin kinase PROPYZAMIDE-HYPERSENSITIVE 1 (PHS1ΔP) for microtubule cytoskeleton disintegration (Fujita et al., 2013; Vilches Barro et al., 2019).

To address the question of how the cytoskeleton may interfere with the dynamics and organization of plant PM proteins, we focused on a group of proteins associated with signaling mechanisms, namely the receptor-like kinases (RLKs) BRASSINOSTEROID INSENSITIVE 1 (BRI1), PHYTOSULFOKIN RECEPTOR 1 (PSKR1), FLAGELLIN-SENSITIVE 2 (FLS2) and BRI1-ASSOCIATED RECEPTOR KINASE (BAK1), along with the RECEPTOR-LIKE PROTEIN 44 (RLP44). RLP44 is proposed to be a cell wall integrity sensor that controls cell wall homeostasis through an interplay with BRI1 and its co-receptor BAK1. The three proteins form a ternary receptor complex in the PM of plant cells (Glöckner et al., 2022). Additionally, RLP44 has been associated with phytosulfokine signaling, as it forms a complex with the corresponding PSKR1 receptor and its co-receptor BAK1 (Garnelo Gomez et al., 2021; Holzwart et al., 2018). FLS2 was chosen as a protein that is not connected to RLP44. Although FLS2 interacts with BAK1, it has been demonstrated that this interaction takes place at a minimum distance of 11.1 nm from the BRI1-BAK1-RLP44 complexes (Glöckner et al., 2022).

We used SpvB and PHS1ΔP to analyze the cytoskeleton influence on the dynamic properties of the four above-mentioned PM receptors using single-particle tracking with photoactivated localization microscopy (sptPALM) in a transient *Nicotiana benthamiana* system. To gain insight into the underlying mechanisms, we focused our investigation on three key parameters: (i) The diffusion coefficients, (ii) the organization of the respective receptors into nanoscale-like protein clusters, and (iii) the classification of molecular movement into transient movement types. It is worth mentioning that the three parameters are not inherently linked, for example, a reduced diffusion coefficient does not necessarily result in larger nanoscale protein clusters and/or immobile movement patterns. Consequently, their separate evaluation can give insights into different regulatory mechanisms.

We were able to show a clear link between manipulated microtubule formation, reflected by an increase in the diffusion coefficient for most of the tested proteins. Conversely, disintegration of actin filaments predominantly led to reduced diffusion coefficients. We furthermore demonstrated that destroyed microtubules predominantly led to decreased cluster sizes of the analyzed proteins clusters, while actin destruction resulted in increased cluster sizes.
Additionally, the classification of the protein tracks into the motion types (i) free diffusion, (ii) confined diffusion, (iii) immobility and (iv) directed diffusion revealed another influence of the cytoskeleton. Our data show that proteins spend more time in free diffusion states in the absence of microtubules. Conversely, disintegration of actin filaments resulted in an overall more confined behavior.

The opposing effects on diffusion, cluster sizes and motion patterns demonstrate the potentially unique regulatory functions of cytoskeletal components in plants and suggest that the picket fence model is not directly transferable to plant systems. However, our research may provide a basis for further investigation to translate these findings into an extended or revised functional model.

Results

Genetically encoded, enzymatic tools for cytoskeleton disruption are functional

Initially, SpvB and PHS1ΔP (Vilches Barro et al., 2019) were modified for our needs to be applied in sptPALM experiments. To avoid potential compatibility problems with the used sptPALM fluorophores, we decided to generate versions of the genetically encoded enzymatic tools without fluorescent tags but instead with a hemagglutinin (HA) tag. In addition, the expression of SpvB and PHS1ΔP was designed to be under the control of constitutive promoters (Figure 1C and F). The modified protein tools were tested for their ability to destroy the integrity of the cytoskeleton by co-expressing them with corresponding marker proteins in *N. benthamiana*. To label actin filaments, we used actin-binding domain 2 (ABD2) of *Arabidopsis* fimbrin 1 fused to GFP at the C- and N- terminus (Wang et al., 2008). To test the state of the microtubules, we applied the MICROTUBULE-ASSOCIATED PROTEIN 65-8 (MAP65-8) fused to RFP, which is known to bind cortical microtubules (Smertenko et al., 2008). Epidermal cells of *N. benthamiana* leaves were investigated under the confocal microscope three days post infiltration (dpi) with the constructs-containing *Agrobacteria*. The clear actin filament and microtubule cytoskeleton disassembly was observed in the presence of the corresponding genetically encoded, enzymatic tool (Figure 1B and E), proving their applicability as disintegration tools in epidermal *N. benthamiana* leaf cells.

Disintegration of actin filaments predominantly leads to reduced protein mobility in the PM

To determine the influence of the actin cytoskeleton on the dynamics and the nanoscale organization of RLP44, BRI1, PSKR1, FLS2 and BAK1, we first expressed corresponding mEos3.2-tagged versions under the control of their native promoter in the absence or presence of HA-SpvB in *N. benthamiana* epidermal leaf cells. Subsequently, we used sptPALM and used the recently introduced OneFlowTraX software package for the analysis of protein dynamics and complex organization (Rohr et al., 2024). Independent of the co-expression with HA-SpvB, some general findings are worth mentioning: While the mEos3.2 fusions of RLP44, BRI1, PSKR1 and FLS2 showed one population of mobility each, BAK1-mEos3.2 presents a more confined and a more mobile variety (Figure 2A). The diffusion coefficients of RLP44-mEos3.2, BRI1-mEos3.2, PSKR1-mEos3.2 and FLS2-mEos3.2, as well as the one of the slower population of BAK1-mEos3.2, were comparable with other confined receptor proteins such as the PM intrinsic protein (PIP) 2;1 (D = 0,0047 µm²/s) reported before (Bayle et al., 2021; Hosy et al., 2015). In contrast, the more mobile variety of BAK1-mEos3.2 showed a diffusion coefficient about ten times higher than the other proteins (Figure 2B).

In the presence of HA-SpvB, we observed a significant reduction of the diffusion coefficient for RLP44-mEos3.2, PSKR1-mEos3.2, BRI1-mEos3.2 and the mobile population of BAK1-Eos3.2. In contrast, actin disruption did not affect FLS2-mEos3.2 dynamics. Moreover, the less mobile population of BAK1-mEos3.2 tended to have an even more reduced mobility. Additionally, the bimodal mobility distribution of BAK1-mEos3.2 shifted overall when the actin cytoskeleton was destroyed with HA-SpvB, increasing the fraction of the more restricted variant of BAK1-mEos3.2 compared to control cells.

Disintegration of the microtubule cytoskeleton predominantly leads to enhanced protein mobility in the PM

While microtubules arise from centrosomes in animal cells, plants possess cortical microtubules (Farquharson, 2009). Their presence needs to be considered when a putative effect of the "membrane skeleton" on protein dynamics is investigated. Therefore, the identical set of RLK fusion proteins used for the actin approach (see above) were co-expressed with PHS1ΔP-HA, which specifically causes depolymerization of cortical microtubules (Fujita et al., 2013). While the mEos3.2-fusions of RLP44, BRI1, PSKR1 and FLS2 displayed one population for the diffusion coefficient, BAK1-mEos3.2 again showed two populations of different mobility, independent of the absence or presence of PHS1ΔP-HA (Figure 3A). In contrast to the data obtained after the destruction of actin filaments, the manipulation of cortical microtubules caused an increased diffusion of RLP44-mEos3.2

and PSKR1-mEos3.2. However, the mobility of BRI1-mEos3.2 and FLS2-mEos3.2 remained nearly unaffected in the presence of PHS1ΔP-HA (although a trend of increased diffusion was present for BRI1-mEos3.2). For BAK1-mEos3.2 a significant increase in the mobility was solely observed for the less mobile population (Figure 3B). Additionally, in the absence of polymerized microtubules, there was a slight shift in the BAK1 distribution between the two populations: More BAK1-mEos3.2 was present in the faster fraction and less in the slower one compared to the measurements where PHS1ΔP-HA was not present.

The nanoscale organization of most PM proteins is changed by cytoskeleton disintegration

By manipulating the cytoskeleton structures, it is of great interest to know whether the nanoscale organization of protein clusters, commonly referred to as nanodomains, is affected as well (Jaillais and Ott, 2020; McKenna et al., 2019). To determine the cluster properties on the basis of spt data, several algorithms are available, such as Voronoi tessellation (Andronov et al., 2016; Levet et al., 2015), density-based spatial clustering of applications with noise (DBSCAN) (Ester et al., 1996) and the recently introduced nanoscale spatiotemporal indexing clustering (NASTIC) (Wallis et al., 2023). For our studies, we decided to apply the NASTIC algorithm since its approach is the least influenced by user-defined parameters and exclusively deals with track data as a whole (Rohr *et al.*, 2024; Wallis et al., 2023). However, it is, like all the other algorithms, partly influenced by the set parameters and the raw data quality. Thus, we want to emphasize that only the relative changes in the nanoscale organization of clusters should be considered rather than absolute values.

Applying the NASTIC algorithm (see Material and Methods) to our tracking data in the absence or presence of actin-disintegrating SpvB, a predominantly decreased cluster diameter was observed for all tested PM proteins, with the exception of RLP44-mEos3.2 and FLS2-mEos3.2 (Figure 4A). In contrast, improper polymerization of cortical microtubules predominantly led to enlarged cluster diameters for all tested protein fusions, except for FLS2-mEos3.2, where the cluster size remained unaffected (Figure 4B).

In summary, the destruction of the actin filaments predominantly led to reduced mobility and smaller clusters, while the disintegration of the microtubule cytoskeleton resulted in higher mobility and enlarged clusters of most of the tested PM proteins.

Classification of motion behavior reveals changes upon the disintegration of cytoskeleton components

In typical sptPALM experiments, the so-called short-range diffusion coefficient is extracted from molecular trajectories to obtain a value that is as independent as possible of directional motion, obstacles and boundaries (Saxton, 1997). Consequently, transient interactions of a diffusing protein with structural elements such as the cytoskeleton are not necessarily detectable by the diffusion coefficient alone. However, the long-term temporal evolution of these trajectories can be used to classify the type of movement (e.g., confined, directed, or free movement). For this purpose, several freely available software solutions and algorithms can be used (Das et al., 2009; Helmuth et al., 2007; Persson et al., 2013; Wagner et al., 2017).

Vega et al. (2018) introduced an efficient transient mobility analysis framework called "divide and conquer moment scaling spectrum" (DC-MSS), which was used to analyze the spatiotemporal organization of cell surface receptors and proved to be a suitable tool to analyze our data as well.

We focused on four major motion types of proteins, which are commonly used for studying biological systems. Proteins can (i) diffuse freely, for example in large unilamellar vesicles and in membrane blebs (Jaqaman and Grinstein, 2012; Kusumi et al., 2005), (ii) or become confined within structural corrals (Fujiwara et al., 2016). Furthermore, they can get (iii) anchored or immobilized when they bind to static components (Komura et al., 2016) or (iv) exhibit directed motion, for example, by transport processes via cytoskeleton components (Serge et al., 2003). Importantly, a protein may switch between different motion types during its lifespan. This was also suggested previously for plant PM proteins, such as PIP2,1 (Li et al., 2011).

In our analysis pipeline, the motion type classification was based on the same track data that were used before to evaluate the diffusion coefficients and cluster sizes. Individual tracks were classified with DC-MSS, and motion types were assigned either to entire tracks or track segments if the protein changed its motion type during the recording time. This allowed for an overall analysis of the relative time proteins spent in the following states: immobility, confined diffusion, free diffusion, and directed diffusion (Figure 5). A negligible number of tracks or track segments could not be classified (< 0.5 %) and were therefore excluded from the calculations.

Under control conditions, RLP44-mEos3.2 mostly exhibited confined (49 %) and free behavior (37 %). In the presence of SpvB, i.e., in the absence of actin filaments, there was a decrease in the free diffusive behavior (- 11 %) while immobile and confined movement increased (+ 5 % and + 6 %, respectively). A comparable effect was observable for PSKR1-mEos3.2: Confined behavior represented the majority (50 %) under control conditions, and the disintegration of actin filaments by

SpvB led to a shift in the motion patterns: The free diffusive motions decreased (- 18 %) while immobility and confined movement increased (+ 12 % and + 6 % respectively). These observations hold true for BRI1-mEos3.2 as well, although with less pronounced shifts as compared to RLP44 mEos3.2 and PSKR1-mEos3.2. In contrast, the consequences of actin disintegration on FLS2-mEos3.2 were contrary to those of the mEos3.2-fusions of BRI1, PSKR1 and RLP44. Here, a decrease in the immobile proportion (- 11 %) and an increase in the free diffusive behavior (+ 9 %) were detectable. Finally, BAK1-mEos3.2 exhibited a minor effect in response to actin filament disintegration, with shifts smaller than 2 %, suggesting a less eminent role of actin filaments on the motion behavior of BAK1 (Figure 5A and B).

As shown for the analysis of the diffusion coefficient and the cluster sizes, the disintegration of actin filaments and microtubules had contrary effects. This was also the case when evaluating the motion patterns.

In the presence of intact microtubules, RLP44-mEos3.2 mostly exhibited free diffusive or confined behavior (approx. 44 % each). However, with disintegrated microtubules, RLP44-mEos3.2 spent more time in a free diffusive state (+ 12 %) while confined and immobile behavior was less present (- 8 % and - 4 %, respectively). A comparable trend was observable for PSKR1-mEos3.2, where, under control conditions, confined motions represented the majority with 50 % followed by free diffusion (27 %). Again, with the co-expression of PHS1ΔP, there was in an increase in free diffusive behavior (+ 8 %), while immobile (- 5 %) and confined states (- 3 %) decreased. The relative changes for FLS2-mEos3.2 showed a decrease of immobility (- 5 %) in the absence of microtubules, a slight increase in the free diffusive proportion (+ 3 %) and a negligible effect on the confined behavior (+ 2 %). Compared to the strength of the shifts that RLP44-, PSKR1- and FLS2-mEos3.2 showed, BRI1's changes were less pronounced, indicating a minor role of microtubules on the motion behavior of BRI1. This holds true as well for BAK1-mEos3.2, which exhibits shifts in the motion patterns below 1 % for all mobility classes (Figure 5C and D). All studied protein did not display substantial directed diffusive behavior, which suggests that the cytoskeleton components may not play a major role in transport processes (Figure 5).

In summary, we evaluated three parameters that gave insights into the organizational function of the cytoskeleton on PM proteins. Interestingly, diffusion coefficients, cluster sizes and motion classes were influenced in an opposite manner by the disintegration of actin filaments and microtubules. While the disintegration of actin filaments resulted predominantly in decreased diffusion but bigger clusters, the absence of microtubules increased the diffusion and led to smaller clusters. Concerning the motion classes, actin disruption predominantly caused a shift to more immobility and confined movement, while free diffusive behavior was reduced. Contrarily, the disintegration of microtubules

resulted in increased free diffusive behavior, while immobility and the time proteins spent in confined states decreased. For BRI1 and BAK1, a less pronounced effect of the cytoskeleton on the motion behavior can be assumed, as the shifts between control conditions and the absence of actin filaments or microtubules were relatively low compared to the other PM proteins.

Discussion

The PM plays a vital role for cell properties and a variety of biological processes. Its organization and associated functions have been the subject of several theories and considerations (Simons and Ikonen, 1997; Singer and Nicolson, 1972). Among them, the picket fence hypothesis is one of the most recent models that was initially studied in animal cells. Mainly due to the dynamic nature of the submembrane actin meshwork, no tractable experimental model for the mechanistic investigation of the fence or picket model is available. However, recently it was shown that actin rings in neurons compartmentalize the PM, acting as fences and confining membrane proteins (Rentsch et al., 2024). The direct transfer of the picket fence model from animal to plant cell biology is challenging since plant-specific properties need to be considered, such as the presence of cortical microtubules (Farquharson, 2009). Nevertheless, the model has also been tested and discussed as important for the dynamics and organization of plant PM protein dynamics and organization in several research articles and reviews (Jaillais and Ott, 2020; Martiniere et al., 2012; McKenna et al., 2019).

By applying genetically encoded enzymatic tools, we investigated the influence of the actin and microtubule cytoskeleton disintegration on the dynamics (i.e., via the diffusion coefficient and motion classification) and nanoscale organization of selected plant PM integral protein fusions, namely RLP44-mEos3.2, BRI1-mEos3.2, PSKR1-mEos3.2, FLS2-mEos3.2 and BAK1-mEos3.2, in the tobacco epidermal leaf cell system (Fujita et al., 2013; Harterink et al., 2017; Vilches Barro et al., 2019).

After the disintegration of the actin cytoskeleton by SpvB, we observed a decreased diffusion coefficient for all proteins, except for FLS2-mEos3.2. Furthermore, we exclusively detected two protein populations with different mobilities for BAK1-mEos3.2. The presence of such subpopulations usually indicates diverse molecular states of the protein. For instance, the subpopulation with lower mobility could be bound to cellular structures or other molecules, while the second one moves more freely. This may subsequently provide information about the biological roles of the protein (Hansen et al., 2018). Here, we speculate that the slow subpopulation of BAK1-mEos3.2 may be involved in signaling processes in restricted nanodomains, while the faster subpopulation is freely available for possible other interaction partners. Interestingly, the two subpopulations responded differently to actin filament disintegration via SpvB. Whereas no significant change was observed for the

slower-moving BAK1-mEos3.2 population, the faster one showed a decreased diffusion comparable to the one of the other analyzed fusion proteins.

Furthermore, we observed that in the presence of intact actin filaments, the overall mobility distribution of BAK1 mEos3.2 features a higher fraction of the more mobile variant. The destruction of actin increases the relative amount of slower BAK1-mEos3.2, resulting in comparably equal amounts for both populations. Evidently, the functional meaning of these changes requires future experiments.

We additionally observed an increase in the cluster sizes for all tested proteins, except for RLP44-mEos3.2, after SpvB-mediated actin filament disintegration. This observation is in line with the picket fence model. In addition, the results can be integrated into a broader context: Recently, it was shown that the chemical destruction of actin leads to an increase in salicylic acid (SA) levels and the activation of SA-responsive genes in *A. thaliana* (Kalachova et al., 2019; Leontovycova et al., 2019; Matouskova et al., 2014). Moreover, the external application of SA constrained the diffusion of the PM auxin efflux carrier PIN-FORMED 2 (PIN2), followed by its condensation into PIN2 hyperclusters; a process mediated by remorins (Ke et al., 2021). We observed the same phenomenon for our fusion proteins: reduced diffusion with enlarged clusters. Whether these changes in the dynamics and nanoscale organization are related to SA requires further study.

However, so far, none of the available studies have shown a decrease in PM protein diffusion as a direct consequence of actin cytoskeleton disintegration (Hosy et al., 2015; McKenna et al., 2019).

For BRI1 and RLP44, no experiments have been published yet that tested the influence of the actin cytoskeleton on their dynamics. Interestingly, according to Lanza et al. (2012), brassinosteroid application modifies the actin cytoskeleton in an auxin-like manner by unbundling actin filaments. This implicates a contribution of BR signaling to the reorganization of the actin cytoskeleton. Moreover, a link between BR signaling and the actin cytoskeleton is further substantiated by the observation that the root-waving phenotype of the *Arabidopsis act2-5* mutant copies that of wildtype *Arabidopsis* seedlings treated with brassinolide (Lanza et al., 2012).

In contrast, the application of flg22, being the ligand of FLS2, increased the formation of actin filaments within three hours. This process is proposed to be the result of a well-orchestrated signaling cascade that (i) triggers the local high-order assembly of remorins that (ii) recruit formins, components comparable to mammalian integrins, which finally (iii) results in increased actin polymerization (Ma et al., 2021; Ma et al., 2022; Ma et al., 2023)

A long-standing paradigm that was still recently under debate was the direct involvement of actin during clathrin-mediated endocytosis. For example, it has been reported that FLS2 internalization depends on actin directly (Beck et al., 2012). However, Narasimhan et al. (2020) showed that actin is

neither involved in membrane bending and scission nor in the initiation of endocytic processes. Rather, it is only required to transport endocytic vesicles after vesicle scission. Although this perspective seems to be acknowledged in the scientific community now (Kraus et al., 2024), current publications still refer to the old paradigm (Lu et al., 2023), stifling the debate. Whether the changed mobility and nanoscale organization of our tested proteins are a result of disturbed transport after vesicle scission due to actin filament disintegration requires further investigation.

In contrast to our results, McKenna et al. (2019) reported that the mobility of FLS2-GFP in epidermal hypocotyl cells of *A. thaliana* is enhanced after latrunculin treatment. However, we used SpvB, a bacterial effector from *Salmonella enterica,* as an actin disintegration tool. Although both latrunculin and SpvB are thought to specifically address actin, their modes of action differ: While SpvB acts almost exclusively on G actin by ADP-ribosylation (Hochmann et al., 2006), more recent publications indicate that latrunculin functions via direct binding to G actin (Spector et al., 1999) and can also affect F actin (Fujiwara et al., 2018). In addition, tool-specific, pleiotropic effects on cell physiology cannot be excluded. Both different modes of action and tool-specific site effects may have an impact on FLS2 dynamics. Another aspect that should be considered is that our experimental setup investigates proteins from *A. thaliana* in the heterologous cell environment of *N. benthamiana*. Therefore, the transfer of our results to cells of transgenic *A. thaliana* plants is not possible on a one-to-one basis, because the physiological, cellular and biochemical contexts of the *N. benthamiana* and *A. thaliana* cells are certainly not identical.

Besides studying the dynamics of the tested proteins via the diffusion coefficient, we analyzed their motion classes, too. We observed that all proteins show predominantly confined behavior under control conditions as well as in situations where the actin filaments were disintegrated. However, there was a substantial shift in the proportions of the motion classes for some but not all fusion proteins. In the absence of actin filaments, RLP44-mEos3.2 showed increased immobility and confined behavior, while free motion was reduced. The same holds true for PSKR1-mEos3.2 and BRI1-mEos3.2, although the effect on BRI1-mEos3.2 was less pronounced. In contrast, FLS2-mEos3.2 showed less immobile behavior but increased free motion in the absence of actin filaments. BAK1-mEos3.2 was nearly unaffected in its diffusive behavior when actin was disrupted.

In consideration of the combined results of the actin disintegration within the framework of the picket fence model, a direct transfer from the animal to the plant cell system does not appear to be possible without the inclusion of further aspects.

Due to the lack of actin filaments, an increase in the diffusion coefficient accompanied by enlarged nano-sized cluster structures and less confined and/or immobile behavior is expected (Fujiwara et al., 2002; Fujiwara et al., 2016; Jaqaman and Grinstein, 2012). However, our data prompt for a more

sophisticated mechanism, as exclusively FLS2's increase in cluster sizes and motion behavior in the absence of actin fits into the picket fence model. As actin is involved in a variety of processes, such as cell growth, cell division, cytokinesis, and various intracellular trafficking events (Szymanski and Staiger, 2018), pleiotropic effects cannot be excluded that are not linked to the role of actin in membrane organization. Additionally, in the absence of actin, a compensatory cytoskeletal interaction could take place through increased microtubule associations that would trap the proteins in confined corrals. Thus, a combined disruption of actin and microtubules will be of special interest in the future. So far, in the presented study, we focused on individual manipulations.

Through the disintegration of microtubules via PHS1ΔP (Fujita et al., 2013; Vilches Barro et al., 2019), we observed a contrary effect compared to that of the actin cytoskeleton disturbance: With the exception of BRI1-mEos3.2 and FLS2-mEos3.2, a significant increase in the diffusion coefficient was observed for the tested fusion proteins. Furthermore, reduced cluster sizes were observed for all tested receptors, again apart from FLS2-mEos3.2. Interestingly, for BAK1-mEos3.2, the significantly changed diffusion coefficient was this time observable for the slower subpopulation, while the faster one remained unaffected. This suggests a stronger connection between microtubules and the slower subpopulation of BAK1 than for the faster subpopulation.

Additionally, we analyzed the motion patterns of the fusion proteins. In the absence of microtubules, RLP44-mEos3.2, PSKR1-mEos3.2 and FLS2-mEos3.2 showed more free diffusive behavior, while BRI1-mEos3.2 and BAK1-mEos3.2 were barely affected.

In particular, the increased diffusion coefficients after microtubule destruction as well as the shift to more mobile motion patterns in combination with decreased immobility and confined motion are in good agreement with the picket fence model.

However, considering that the absence of physical barriers in the form of microtubules enables a less restricted motion of the fusion proteins, the decrease in cluster sizes after microtubule disintegration is difficult to interpret. Again, this change in nanoscale organization might be an indirect pleiotropic effect, as microtubules participate in a variety of processes in plant cells, such as the guidance of the cellulose synthase complexes to the PM (Paredez et al., 2006) or the maintenance of pavement cell morphogenesis (Belteton et al., 2018). Thus, alterations in the microtubule cytoskeleton organization may change the properties at the cell wall-PM interface that interfere with the dimension of the PM protein clusters.

Additionally, McKenna et al. (2019) showed that FLS2-GFP exhibits an enhanced diffusion coefficient after the disintegration of microtubules by oryzalin. In general, these observations are confirmed by our data, although in our case, the increase was less pronounced.

In summary, we studied three parameters that changed upon the disintegration of actin filaments and microtubules. Interestingly, the manipulated cytoskeleton components influenced the studied proteins in a contrary manner and resulted in distinct trends for diffusion coefficients, cluster sizes and motion patterns. While some aspects of either the actin or microtubule disruption match the picket fence model, others do not. Consequently, the model cannot be directly transferred from the animal field to the plant cell system. We conclude that this might be caused by the regulatory and functional responsibility of two cortical components, namely actin and microtubules, instead of cortical actin exclusively in animal cells. To further unravel a potential compensatory effect, the depletion of both structures will be a main task in the future. Additionally, studies in *A. thaliana* with inducible manipulations of the cytoskeleton will enable more background-free observation in the native organism.

We also started integrating our experimental data into a computational model generated by Smoldyn, a particle-based spatial simulation software (Andrews, 2009). Although modeling approaches have the potential to advance plant science to a great extent, the biggest challenge is still its underutilization in plant biology and thus the lack of comparative approaches (Dale et al., 2021). Recently, we predicted a new component of the fast brassinosteroid signaling pathway by computational modeling and emphasized its strengths in combination with wetlab experiments (Grosseholz et al., 2022). Based on our experience, we believe that the modeling of spatiotemporal dynamics may also reveal so-far hidden aspects in its regulation by the cytoskeleton.

Material and Methods

Plasmid construction

The genetically encoded enzymatic tools for the cytoskeleton manipulation, namely SpvB and PHS1ΔP, were provided by Prof. Alexis Maizel (COS Heidelberg) (Vilches Barro et al., 2019). For the generation of the expression constructs, the desired plasmid DNA was first amplified by PCR and then either a BP reaction into pDONR207 (for SpvB) or a blunt-end cloning reaction into pJET1.2 (Thermo Fisher Scientific) (for PHS1ΔP) was performed. Subsequently, an LR reaction was performed according to the manufacturer's manual for SpvB into pEG201 (Earley et al., 2006) and cut-ligations with the needed Level I constructs into BB10 (Binder et al., 2014) were executed for PHS1ΔP. While SpvB cloning resulted in an N-terminally HA-tagged version under the control of the 35S promoter, PHS1ΔP is controlled by a 2x 35Sω promoter and C-terminally HA-tagged (Figure 1C and F). The BRI1-mEos3.2 and RLP44-mEos3.2 constructs are described in Rohr et al. (2024) and the construction of PSKR1-mEos3.2 was performed according to their protocol. BAK1-mEos3.2 and FLS2-mEos3.2 were

425 provided by Dr. Birgit Kemmerling (ZMBP, Tübingen). The cytoskeleton markers GFP-ABD2-GFP and
426 MAP65-8-RFP were kindly provided by Dr. Pantelis Livanos (FAU Erlangen).

427 ## Plant material and growth conditions

428 All experiments conducted in this study were performed in transiently transformed *N. benthamiana*
429 plants, cultivated under controlled greenhouse conditions. The desired proteins were transiently
430 expressed using the AGL1 *Agrobacterium tumefaciens* strain (Lifeasible), as previously
431 described (Hecker et al., 2015; Ladwig et al., 2015), without the washing step with sterile water. The
432 plants were infiltrated with the respective constructs at an OD600 of 0.1 in a ratio of 1:1 or 1:1:1 with
433 the silencing inhibitor p19. After watering, the plants were kept in ambient conditions and were
434 imaged three days after infiltration.

435 ## Confocal imaging

436 To confirm the functionality of the genetically encoded enzymatic tools for the cytoskeleton
437 manipulation, the constructs were co-expressed with corresponding markers, namely
438 GFP-ABD2-GFP (for actin) and MAP65-8-RFP (for microtubules). Subsequently, their localization inside
439 epidermal leaf cells of *N. benthamiana* was investigated using confocal laser scanning microscopy on
440 a SP8 laser scanning microscope (Leica Microsystems GmbH) with HyD detectors and a HC PL APOCS2
441 63 x/1.20 WATER objective three days post infiltration. For detection of the GFP signal, a 488 nm argon
442 laser was used. The detection range was set to 500 nm – 550 nm. The images in Figure 1 are maximum
443 projections that covered a z range of ~ 15 µm obtained with a step size of 1 µm. The resulting images
444 were processed with the help of the Leica Application Suite X (Version 3.3.0.16x). The detection of the
445 RFP signal was performed as described above, using a detection range from 600 nm – 650 nm and a
446 561 nm diode pumped solid state laser.

447 ## Sample preparation and movie acquisition for sptPALM measurements

448 All sptPALM measurements with transiently transformed *N. benthamiana* were performed three days
449 post infiltration. For the acquisition, a small leaf area was cut out, excluding veins, and was placed
450 between two coverslips (Epredia 24x50 mm #1 or equivalent) with a drop of water. The
451 "coverslip sandwich" was then placed on the specimen stage, lightly weighted down by a brass ring to
452 help flatten uneven cell layers. The composition of the custom-built microscope platform is described
453 in detail in Rohr et al. (2024). For our purposes, the following filters for mEos3.2 were inserted into
454 the emission beam path: 568 LP Edge Basic Longpass Filter, 584/40 ET Bandpass. The excitation power
455 arriving at the sample was quantified (PM100D with S120C, Thorlabs) in epifluorescence mode after
456 the objective to maintain consistency across experimental sets. Photoconversion of mEos3.2 was

457 executed by applying moderate low intensities using 405 nm excitation. The signal of the red version
458 of mEos3.2 was then obtained by excitation at 561 nm with 1800 µW. The magnification of the optical
459 system was adjusted so that the length of one camera pixel corresponds to 100 nm in the sample
460 plane. To identify feasible regions, larger areas of 51.2 x 51.2 µm were utilized by adjusting the focal
461 plane and the VAEM angle with a frame rate of 10 Hz. In contrast, the recording was conducted in
462 smaller regions of 12.8 x 12.8 µm and frame rates of 20 Hz by streaming between 2,500 and 5,000
463 frames per movie. A series of dark images were recorded at the same frame rate as the corresponding
464 movies to correct for noise in data processing.

465 ## Raw data processing and analysis of sptPALM movies

466 The experimental data sets were imported into OneFlowTraX (Rohr et al., 2024) to assess their quality.
467 Samples exhibiting obvious outliers during the quality assessment were excluded from further
468 analysis. The remaining files were analyzed using the "Batch Analysis" function of OneFlowTraX,
469 according to the settings introduced by Rohr et al. (2024) for localization, tracking, and mobility
470 analysis. The diffusion coefficients were calculated for all samples except BAK1 by fitting the data
471 distribution with a Gaussian function and subsequently extracting the average diffusion coefficient
472 from its peak center. For BAK1, two populations were clearly visible, necessitating the use of a
473 two-component Gaussian mixture model to estimate their respective diffusion coefficients and
474 relative fractions. The nanoscale organization of protein clusters was investigated using the NASTIC
475 algorithm from Wallis et al. (2023) (also available in OneFlowTraX) with the following parameters:
476 radius factor: 1.2 and at least three tracks per cluster. For the comparisons between the different
477 cytoskeleton disintegration scenarios, the cluster diameter (nm) was used. This is calculated by
478 treating the localizations in a cluster as a point cloud that is fitted by a two-dimensional Gaussian
479 function. Its full width at half maximum (FWHM) values for x and y are then averaged to provide one
480 value that is defined as the cluster's diameter. The subsequent analysis steps were processed with
481 custom-built R applications. Clusters with diameters greater than 2,500 nm were excluded from
482 further analysis. Given that cluster data are log-normally distributed, specific statistical tests were
483 employed to identify significant differences (Zhou et al., 1997). The respective figure (Figure 4) report
484 the corrected, transformed mean as recommended by the aforementioned study.

485

Motion classification with DC-MSS

The motion classification of individual (sub-)trajectories was conducted using the "divide-and-conquer moment scaling spectrum" (DC-MSS) algorithm (Vega et al., 2018). In short, trajectories that consist of at least 20 localizations are initially divided into segments of potentially disparate motion classes based on the extent of molecular movement. Subsequently, a movement scaling spectrum analysis is employed for the classification of these segments, utilizing threshold values to minimize the probability of misclassification among adjacent motion types. Intermediate refining steps are incorporated to enhance the confidence of both the trajectory segmentation and their classification.

Acknowledgments and Funding

Our research was supported by the German Research Foundation (DFG) via the CRC 1101 (projects D02 and Z02) to S.z.O.-K and K.H. and by individual DFG grants to K.H. (HA 2146/22, HA 2146/23 We also thank the DFG for grants for scientific equipment (FUGG: INST 37/991-1, INST 37/992-1, INST 37/819-1, INST 37/965-1).

Author contributions

Conceptualization, L.R. (Leander Rohr), K.H. and S.z.O.-K.; Data curation, L.R. and Ll.R. (Luiselotte Rausch); Formal Analysis, L.R. and Ll.R.; Funding acquisition, K.H.; Investigation, L.R. and Ll.R.; Methodology, S.z.O.-K.; Project administration, L.R., K.H. and S.z.O.-K.; Resources, Ll.R. and S.z.O.-K.; Software, S.z.O.-K.; Supervision, K.H.; Visualization, L.R.; Writing – original draft, L.R., K.H and S.z.O.-K.; Writing – review & editing, L.R., Ll.R., K.H and S.z.O.-K.

Figure legends

Figure 1 | Overview of genetically encoded, enzymatic tools for cytoskeleton disintegration.

(A) Exemplary confocal microscopy image of epidermal leaf cells of *Nicotiana benthamiana* (*N. benthamiana*) expressing the actin marker GFP-ABD2-GFP with the GFP channel on the left and the corresponding transmission light channel on the right. Intact actin filaments are clearly visible. Scale bar = 10 µm **(B)** Exemplary image of the co-expression of the disruption tool HA-SpvB and the actin marker GFP-ABD2-GFP in the GFP channel (left) and the corresponding transmission light channel (right). The co-expression with the disruption tool leads to removal of F-actin cables in all cells as shown before (Vilches Barro et al., 2019). Scale bar = 10 µm. **(C)** Schematic plasmid structure of the genetically encoded SpvB tool: By Gateway® technology SpvB was inserted into the pEG201 backbone (Earley et al., 2006) which contains a 35S promoter and an N-terminal HA-tag. **(D)** Exemplary confocal microscopy image of epidermal leaf cells of *N. benthamiana* expressing the microtubules marker MAP65-8-RFP with the RFP channel on the left and the corresponding transmission light channel on the right. Intact microtubules are observable. Scale bar = 10 µm. **(E)** Exemplary image of the co-expression of the disruption tool PHS1ΔP-HA and the microtubules marker MAP65-8-RFP in the RFP channel (left) and the corresponding transmission light channel (right). The co-expression with the disruption tool leads to the destabilization of cortical microtubules. Scale bar = 10 µm. **(F)** Schematic plasmid structure of the genetically encoded PHS1ΔP tool: The plasmid was generated by GoldenGate cloning (Binder et al., 2014) using Level I modules which were subsequently assembled in the Level II backbone of BB10. PHS1ΔP is under the control of a 2x 35Sω promoter module and fused C-terminally to an HA-tag. For the generation of higher order assemblies, BB10 contains Bpi I recognition sites.

Figure 2 | Disintegration of actin filaments primarily results in reduced protein dynamics in the plasma membrane.

(A) Distribution of diffusion coefficients (D) represented as log(D) and plotted against their occurrence [%] over all quantified cells for RLP44-, BRI1-, PSKR1-, FLS2- and BAK1-mEos3.2. For each protein fusion, two distributions are shown: (i) In black, values obtained from epidermal *N. benthamiana* leaf cells expressing the respective fusion alone (- SpvB) and (ii) in blue values from the co-expression of the respective protein fusions with the genetically encoded, enzymatic tool SpvB (+ SpvB). For RLP44-, BRI1- and PSKR1-mEos3.2 a slight shift to lower log(D) values is observable, when SpvB is co-expressed. The effect is barely visible for FLS2-mEos3.2 and BAK1-mEos3.2. All measurements were performed three days post infiltration. Please note that all protein fusions show a bell-shape distribution (i.e., one mobility population), except for BAK1-mEos3.2 that presents a slower and a faster variety (two Gaussian fit). When co-expressed with SpvB, the slow fraction of BAK1-mEos3.2 is increased. **(B)** Representation of the peak D values of RLP44-, BRI1-, PSKR1-, FLS2- and BAK1-mEos3.2. with same color code as in (A). The peak values of individual cells (illustrated as single dots or triangles; $n \geq 17$) were obtained by normal fits of distributions comparable to (A) expect of BAK1-mEos3.2 where a two-component Gaussian mixture model was applied (see Material *and Methods*). The separation of the BAK1 fractions was done according to this model with the peaks of the first maxima representing the slow fraction and the peaks of the second maxima the fast fraction, respectively. In the absence of intact actin filaments (blue; +SpvB) the diffusion coefficient is significantly decreased for the RLP44-, BRI1- and PSKR1-mEos3.2 fusions, while the reduction for FLS2-mEos3.2 is not significant. For BAK1-mEos3.2, only a decrease in the fast fraction is observable. For statistical evaluation, the data were checked for normal distribution and unequal variances and then analyzed according to the results of the test by applying either a Mann-Whitney U test or a One-way ANOVA. Whiskers show the data range excluding outliers, while the boxes represent the 25-75 percentile. $p \leq 0.001$ (***); $p \leq 0.01$ (**); $p \leq 0.05$ (*); $p > 0.05$ (n.s.). All statistical analyses were performed with custom-made R scripts.

Figure 3 | Disintegration of microtubule filaments primarily results in increased protein dynamics in the plasma membrane.

(A) Distribution of diffusion coefficients (D) represented as log(D) and plotted against their occurrence [%] over all quantified cells for RLP44-, BRI1-, PSKR1-, FLS2- and BAK1-mEos3.2. For each protein fusion, two distributions are shown: (i) In black, values obtained from epidermal *N. benthamiana* leaf cells expressing the respective fusion alone (- PHS1ΔP) and (ii) in blue values from the co-expression of the respective protein fusions with the genetically encoded, enzymatic tool PHS1ΔP (+ PHS1ΔP). RLP44, PSKR1, and BAK1-mEos3.2 show a slight shift to higher log(D) values when co-expressed with PHS1ΔP. The effect is barely visible for the other protein fusions. Measurement conditions are as described in Figure 2. Again, all protein fusions show a bell-shape distribution (i.e., one mobility population), except for BAK1-mEos3.2 that presents a slower and a faster variety (two Gaussian fit). When co-expressed with PHS1ΔP, the fast fraction of BAK1-mEos3.2 is increased. **(B)** Representation of the peak D values of RLP44-, BRI1-, PSKR1-, FLS2- and BAK1-mEos3.2. with same color code as in (A) and obtained by n ≥ 25 cells. The evaluation was performed as described for Figure 2. In the absence of intact microtubules (blue; + PHS1ΔP) the diffusion coefficient is significantly increased for the RLP44- and PSKR1-mEos3.2 fusions as well as for the slow fraction of BAK1-mEos3.2, without a significant effect on the fast variety. Although BRI1- and FLS2-mEos3.2, as well as the fast variety of BAK1-mEos3.2, show no significant effect, a trend of increasing diffusion coefficients after microtubule disintegration is observable. Statistical analyses were conducted as in Figure 2, with the same box representation. $p \leq 0.001$ (***); $p \leq 0.01$ (**); $p \leq 0.05$ (*); $p > 0.05$ (n.s.).

Figure 4 | Actin and microtubules disintegration lead to opposing effects on nanocluster sizes.

(A) Representation of corrected, transformed means of nanocluster diameter sizes (nm) of the tested protein fusions based on the track trajectories, also used for Figure 2 and Figure 3. The sizes were either determined for the protein fusions expressed alone (- SpvB, black) or together with the genetically encoded disruption tool for actin, SpvB (+ SpvB, blue). The analyses were performed by applying the NASTIC algorithm (Wallis et al., 2023) available in OneFlowTraX (Rohr et al., 2024) with a radius factor of 1.3 and at least three tracks per cluster. The corrected, transformed means are based on the log-normal distribution of all determined clusters among all evaluated cells (n as in Figure 2 and Figure 3), not considering clusters larger than 2,500 nm in diameter (≥ 1630). Except for RLP44-mEos3.2, all other tested fusions proteins show significantly increased cluster sizes upon the disintegration of actin filaments. Statistical analyses were performed according to Zhou et al. (1997). **(B)** Representation of corrected, transformed means of nanocluster diameter sizes (nm) as in (A) but here either with intact microtubules (i.e., expressed alone; - PHS1ΔP, black) or upon microtubules disintegration (+ PHS1ΔP, blue). Parameters and filtering as in (A) with ≥ 4356 evaluated cluster. Except for FLS2-mEos3.2, all other tested fusions proteins show significantly decreased cluster sizes upon the disintegration of microtubules filaments. Statistical analyses were performed as in (A). $p \leq 0.001$ (***); $p \leq 0.01$ (**); $p \leq 0.05$ (*); $p > 0.05$ (n.s.).

Figure 5 | Classification of segment motion patterns depending on the cytoskeleton integrity.

(A) Proportion of motion behavior (in percent) depending on the status of the actin cytoskeleton (either intact (- SpvB) or disintegrated (+ SpvB)), namely, directed (magenta), free (grey), confined (yellow) and immobile (blue). All studied proteins reveal primarily confined behavior, independent of the actin integrity. Immobility and free diffusive behavior are present in varying amounts amongst the proteins. Directed movement is barely present. The classification was performed according to Vega et al. (2018). **(B)** Relative shifts in the motion patterns in the absence of actin filaments with the same color code as in (A). RLP44-, BRI1- and PSKR1-mEos3.2 show a clear decrease in free diffusive behavior, while immobility and confined behavior (not for BRI1-mEos3.2) increases. However, FLS2-mEos3.2 shows a contrary effect by a decrease in immobility and an increase in free diffusive behavior. BAK1-mEos3.2 is nearly unaffected by the manipulation of the actin cytoskeleton. **(C)** Proportion of motion behavior (in percent) depending on the status of the microtubule cytoskeleton (either intact (- PHS1ΔP) or disintegrated (+ PHS1ΔP) with same behavior classes and color code as in (A) and (B). Again, all studied proteins reveal primarily confined behavior, independent of the microtubule disintegration except for RLP44-mEos3.2 (+ PHS1ΔP) that shows mostly free diffusive behavior. Immobility and free diffusive behavior are present again with varying amounts amongst the proteins, with distinct differences between RLP44-mEos3.2 (+ PHS1ΔP) and the other fusion proteins under manipulated conditions. Again, directed movement is barely present. **(D)** Relative shifts in the motion patterns in the absence of the microtubule cytoskeleton with the same color code as before. RLP44- and PSKR1-mEos3.2 show comparable effects with increased free diffusive behavior as well as with decreased confined movement and immobility. BRI1-mEos3.2 exhibits only minor changes while FLS2-mEos3.2 shows a slight increase in free and confined motion, while immobility is decreased, too. BAK1 is barely affected.

References

Andrews, S.S. (2009). Accurate particle-based simulation of adsorption, desorption and partial transmission. Phys Biol **6**:046015.
DOI: https://doi.org/10.1088/1478-3975/6/4/046015

Andronov, L., Orlov, I., Lutz, Y., Vonesch, J.L., and Klaholz, B.P. (2016). ClusterViSu, a method for clustering of protein complexes by Voronoi tessellation in super-resolution microscopy. Sci Rep **6**:24084.
DOI: https://doi.org/10.1038/srep24084

Bayle, V., Fiche, J.B., Burny, C., Platre, M.P., Nollmann, M., Martiniere, A., and Jaillais, Y. (2021). Single-particle tracking photoactivated localization microscopy of membrane proteins in living plant tissues. Nat Protoc **16**:1600-1628.
DOI: https://doi.org/10.1038/s41596-020-00471-4

Beck, M., Zhou, J., Faulkner, C., MacLean, D., and Robatzek, S. (2012). Spatio-temporal cellular dynamics of the Arabidopsis flagellin receptor reveal activation status-dependent endosomal sorting. Plant Cell **24**:4205-4219.
DOI: https://doi.org/10.1105/tpc.112.100263

Belteton, S.A., Sawchuk, M.G., Donohoe, B.S., Scarpella, E., and Szymanski, D.B. (2018). Reassessing the Roles of PIN Proteins and Anticlinal Microtubules during Pavement Cell Morphogenesis. Plant Physiol **176**:432-449.
DOI: https://doi.org/10.1104/pp.17.01554

Binder, A., Lambert, J., Morbitzer, R., Popp, C., Ott, T., Lahaye, T., and Parniske, M. (2014). A modular plasmid assembly kit for multigene expression, gene silencing and silencing rescue in plants. PLoS One **9**:e88218.
DOI: https://doi.org/10.1371/journal.pone.0088218

Borner, G.H., Sherrier, D.J., Weimar, T., Michaelson, L.V., Hawkins, N.D., Macaskill, A., Napier, J.A., Beale, M.H., Lilley, K.S., and Dupree, P. (2005). Analysis of detergent-resistant membranes in Arabidopsis. Evidence for plasma membrane lipid rafts. Plant Physiol **137**:104-116.
DOI: https://doi.org/10.1104/pp.104.053041

Brown, D.A., and Rose, J.K. (1992). Sorting of GPI-anchored proteins to glycolipid-enriched membrane subdomains during transport to the apical cell surface. Cell **68**:533-544.
DOI: https://doi.org/10.1016/0092-8674(92)90189-j

Bücherl, C.A., Jarsch, I.K., Schudoma, C., Segonzac, C., Mbengue, M., Robatzek, S., MacLean, D., Ott, T., and Zipfel, C. (2017). Plant immune and growth receptors share common signalling components but localise to distinct plasma membrane nanodomains. Elife **6**:e25114.
DOI: https://doi.org/10.7554/eLife.25114

Dale, R., Oswald, S., Jalihal, A., LaPorte, M.F., Fletcher, D.M., Hubbard, A., Shiu, S.H., Nelson, A.D.L., and Bucksch, A. (2021). Overcoming the Challenges to Enhancing Experimental Plant Biology With Computational Modeling. Front Plant Sci **12**:687652.
DOI: https://doi.org/10.3389/fpls.2021.687652

649 **Danek, M., Angelini, J., Malinska, K., Andrejch, J., Amlerova, Z., Kocourkova, D., Brouzdova, J.,**
650 **Valentova, O., Martinec, J., and Petrasek, J.** (2020). Cell wall contributes to the stability of plasma
651 membrane nanodomain organization of Arabidopsis thaliana FLOTILLIN2 and HYPERSENSITIVE
652 INDUCED REACTION1 proteins. Plant J **101**:619-636.
653 DOI: https://doi.org/10.1111/tpj.14566
654
655 **Das, R., Cairo, C.W., and Coombs, D.** (2009). A hidden Markov model for single particle tracks
656 quantifies dynamic interactions between LFA-1 and the actin cytoskeleton. PLoS Comput Biol
657 **5**:e1000556.
658 DOI: https://doi.org/10.1371/journal.pcbi.1000556
659
660 **Earley, K.W., Haag, J.R., Pontes, O., Opper, K., Juehne, T., Song, K., and Pikaard, C.S.** (2006).
661 Gateway-compatible vectors for plant functional genomics and proteomics. Plant J **45**:616-629.
662 DOI: https://doi.org/10.1111/j.1365-313X.2005.02617.x
663
664 **Ester, M., Kriegel, H.-P., Sander, J., and Xu, X.** (1996). A density-based algorithm for discovering
665 clusters in large spatial databases with noise. Proceedings of the Second International Conference on
666 Knowledge Discovery and Data Mining. AAAI Press.
667
668 **Farquharson, K.L.** (2009). On the origin of cortical microtubules. Plant Cell **21**:2193.
669 DOI: https://doi.org/10.1105/tpc.109.210812
670
671 **Fujita, S., Pytela, J., Hotta, T., Kato, T., Hamada, T., Akamatsu, R., Ishida, Y., Kutsuna, N.,**
672 **Hasezawa, S., Nomura, Y., et al.** (2013). An atypical tubulin kinase mediates stress-induced
673 microtubule depolymerization in Arabidopsis. Curr Biol **23**:1969-1978.
674 DOI: https://doi.org/10.1016/j.cub.2013.08.006
675
676 **Fujiwara, I., Zweifel, M.E., Courtemanche, N., and Pollard, T.D.** (2018). Latrunculin A Accelerates
677 Actin Filament Depolymerization in Addition to Sequestering Actin Monomers. Curr Biol **28**:3183-
678 3192.
679 DOI: https://doi.org/10.1016/j.cub.2018.07.082
680
681 **Fujiwara, T., Ritchie, K., Murakoshi, H., Jacobson, K., and Kusumi, A.** (2002). Phospholipids undergo
682 hop diffusion in compartmentalized cell membrane. J Cell Biol **157**:1071-1081.
683 DOI: https://doi.org/10.1083/jcb.200202050
684
685 **Fujiwara, T.K., Iwasawa, K., Kalay, Z., Tsunoyama, T.A., Watanabe, Y., Umemura, Y.M., Murakoshi,**
686 **H., Suzuki, K.G., Nemoto, Y.L., Morone, N., et al.** (2016). Confined diffusion of transmembrane
687 proteins and lipids induced by the same actin meshwork lining the plasma membrane. Mol Biol Cell
688 **27**:1101-1119.
689 DOI: https://doi.org/10.1091/mbc.E15-04-0186
690
691 **Garnelo Gomez, B., Holzwart, E., Shi, C., Lozano-Duran, R., and Wolf, S.** (2021). Phosphorylation-
692 dependent routing of RLP44 towards brassinosteroid or phytosulfokine signalling. J Cell Sci
693 **134**:jcs259134.
694 DOI: https://doi.org/10.1242/jcs.259134
695
696 **Glöckner, N., Zur Oven-Krockhaus, S., Rohr, L., Wackenhut, F., Burmeister, M., Wanke, F.,**
697 **Holzwart, E., Meixner, A.J., Wolf, S., and Harter, K.** (2022). Three-Fluorophore FRET Enables the
698 Analysis of Ternary Protein Association in Living Plant Cells. Plants (Basel) **11**:2630.
699 DOI: https://doi.org/10.3390/plants11192630

Gronnier, J., Gerbeau-Pissot, P., Germain, V., Mongrand, S., and Simon-Plas, F. (2018). Divide and Rule: Plant Plasma Membrane Organization. Trends Plant Sci **23**:899-917.
DOI: https://doi.org/10.1016/j.tplants.2018.07.007

Grosseholz, R., Wanke, F., Rohr, L., Glöckner, N., Rausch, L., Scholl, S., Scacchi, E., Spazierer, A.J., Shabala, L., Shabala, S., et al. (2022). Computational modeling and quantitative physiology reveal central parameters for brassinosteroid-regulated early cell physiological processes linked to elongation growth of the Arabidopsis root. Elife **11**:e73031.
DOI: https://doi.org/10.7554/eLife.73031

Hansen, A.S., Woringer, M., Grimm, J.B., Lavis, L.D., Tjian, R., and Darzacq, X. (2018). Robust model-based analysis of single-particle tracking experiments with Spot-On. Elife **7**:e33125.
DOI: https://doi.org/10.7554/eLife.33125

Harterink, M., da Silva, M.E., Will, L., Turan, J., Ibrahim, A., Lang, A.E., van Battum, E.Y., Pasterkamp, R.J., Kapitein, L.C., Kudryashov, D., et al. (2017). DeActs: genetically encoded tools for perturbing the actin cytoskeleton in single cells. Nat Methods **14**:479-482.
DOI: https://doi.org/10.1038/nmeth.4257

Hecker, A., Brand, L.H., Peter, S., Simoncello, N., Kilian, J., Harter, K., Gaudin, V., and Wanke, D. (2015). The Arabidopsis GAGA-Binding Factor BASIC PENTACYSTEINE6 Recruits the POLYCOMB-REPRESSIVE COMPLEX1 Component LIKE HETEROCHROMATIN PROTEIN1 to GAGA DNA Motifs. Plant Physiol **168**:1013-1024.
DOI: https://doi.org/10.1104/pp.15.00409

Helmuth, J.A., Burckhardt, C.J., Koumoutsakos, P., Greber, U.F., and Sbalzarini, I.F. (2007). A novel supervised trajectory segmentation algorithm identifies distinct types of human adenovirus motion in host cells. J Struct Biol **159**:347-358.
DOI: https://doi.org/10.1016/j.jsb.2007.04.003

Hochmann, H., Pust, S., von Figura, G., Aktories, K., and Barth, H. (2006). Salmonella enterica SpvB ADP-ribosylates actin at position arginine-177-characterization of the catalytic domain within the SpvB protein and a comparison to binary clostridial actin-ADP-ribosylating toxins. Biochemistry **45**:1271-1277.
DOI: https://doi.org/10.1021/bi051810w

Holzwart, E., Huerta, A.I., Glöckner, N., Garnelo Gomez, B., Wanke, F., Augustin, S., Askani, J.C., Schurholz, A.K., Harter, K., and Wolf, S. (2018). BRI1 controls vascular cell fate in the Arabidopsis root through RLP44 and phytosulfokine signaling. Proc Natl Acad Sci U S A **115**:11838-11843.
DOI: https://doi.org/10.1073/pnas.1814434115

Hosy, E., Martiniere, A., Choquet, D., Maurel, C., and Luu, D.T. (2015). Super-resolved and dynamic imaging of membrane proteins in plant cells reveal contrasting kinetic profiles and multiple confinement mechanisms. Mol Plant **8**:339-342.
DOI: https://doi.org/10.1016/j.molp.2014.10.006

Jaillais, Y., and Ott, T. (2020). The Nanoscale Organization of the Plasma Membrane and Its Importance in Signaling: A Proteolipid Perspective. Plant Physiol **182**:1682-1696.
DOI: https://doi.org/10.1104/pp.19.01349

751 **Jaqaman, K., and Grinstein, S.** (2012). Regulation from within: the cytoskeleton in transmembrane
752 signaling. Trends Cell Biol **22**:515-526.
753 DOI: https://doi.org/10.1016/j.tcb.2012.07.006
754
755 **Jarsch, I.K., and Ott, T.** (2011). Perspectives on remorin proteins, membrane rafts, and their role
756 during plant-microbe interactions. Mol Plant Microbe Interact **24**:7-12.
757 DOI: https://doi.org/10.1094/mpmi-07-10-0166
758
759 **Jarsch, I.K., Konrad, S.S., Stratil, T.F., Urbanus, S.L., Szymanski, W., Braun, P., Braun, K.H., and Ott,**
760 **T.** (2014). Plasma Membranes Are Subcompartmentalized into a Plethora of Coexisting and Diverse
761 Microdomains in Arabidopsis and Nicotiana benthamiana. Plant Cell **26**:1698-1711.
762 DOI: https://doi.org/10.1105/tpc.114.124446
763
764 **Kalachova, T., Leontovyčová, H., Iakovenko, O., Pospíchalová, R., Maršík, P., Klouček, P., Janda, M.,**
765 **Valentová, O., Kocourková, D., Martinec, J., et al.** (2019). Interplay between phosphoinositides and
766 actin cytoskeleton in the regulation of immunity related responses in Arabidopsis thaliana seedlings.
767 Environmental and Experimental Botany **167**:103867.
768 DOI: https://doi.org/10.1016/j.envexpbot.2019.103867
769
770 **Ke, M., Ma, Z., Wang, D., Sun, Y., Wen, C., Huang, D., Chen, Z., Yang, L., Tan, S., Li, R., et al.** (2021).
771 Salicylic acid regulates PIN2 auxin transporter hyperclustering and root gravitropic growth via
772 Remorin-dependent lipid nanodomain organisation in Arabidopsis thaliana. New Phytol **229**:963-
773 978.
774 DOI: https://doi.org/10.1111/nph.16915
775
776 **Komura, N., Suzuki, K.G., Ando, H., Konishi, M., Koikeda, M., Imamura, A., Chadda, R., Fujiwara,**
777 **T.K., Tsuboi, H., Sheng, R., et al.** (2016). Raft-based interactions of gangliosides with a GPI-anchored
778 receptor. Nat Chem Biol **12**:402-410.
779 DOI: https://doi.org/10.1038/nchembio.2059
780
781 **Konrad, S.S., Popp, C., Stratil, T.F., Jarsch, I.K., Thallmair, V., Folgmann, J., Marin, M., and Ott, T.**
782 (2014). S-acylation anchors remorin proteins to the plasma membrane but does not primarily
783 determine their localization in membrane microdomains. New Phytol **203**:758-769.
784 DOI: https://doi.org/10.1111/nph.12867
785
786 **Kraus, M., Pleskot, R., and Van Damme, D.** (2024). Structural and Evolutionary Aspects of Plant
787 Endocytosis. Annu Rev Plant Biol:521-550.
788 DOI: https://doi.org/10.1146/annurev-arplant-070122-023455
789
790 **Kusumi, A., Fujiwara, T.K., Chadda, R., Xie, M., Tsunoyama, T.A., Kalay, Z., Kasai, R.S., and Suzuki,**
791 **K.G.** (2012). Dynamic organizing principles of the plasma membrane that regulate signal
792 transduction: commemorating the fortieth anniversary of Singer and Nicolson's fluid-mosaic model.
793 Annu Rev Cell Dev Biol **28**:215-250.
794 DOI: https://doi.org/10.1146/annurev-cellbio-100809-151736
795
796 **Kusumi, A., Nakada, C., Ritchie, K., Murase, K., Suzuki, K., Murakoshi, H., Kasai, R.S., Kondo, J., and**
797 **Fujiwara, T.** (2005). Paradigm shift of the plasma membrane concept from the two-dimensional
798 continuum fluid to the partitioned fluid: high-speed single-molecule tracking of membrane
799 molecules. Annu Rev Biophys Biomol Struct **34**:351-378.
800 DOI: https://doi.org/10.1146/annurev.biophys.34.040204.144637
801

Ladwig, F., Dahlke, R.I., Stuhrwohldt, N., Hartmann, J., Harter, K., and Sauter, M. (2015). Phytosulfokine Regulates Growth in Arabidopsis through a Response Module at the Plasma Membrane That Includes CYCLIC NUCLEOTIDE-GATED CHANNEL17, H+-ATPase, and BAK1. Plant Cell **27**:1718-1729.
DOI: https://doi.org/10.1105/tpc.15.00306

Laloi, M., Perret, A.M., Chatre, L., Melser, S., Cantrel, C., Vaultier, M.N., Zachowski, A., Bathany, K., Schmitter, J.M., Vallet, M., et al. (2007). Insights into the role of specific lipids in the formation and delivery of lipid microdomains to the plasma membrane of plant cells. Plant Physiol **143**:461-472.
DOI: https://doi.org/10.1104/pp.106.091496

Lanza, M., Garcia-Ponce, B., Castrillo, G., Catarecha, P., Sauer, M., Rodriguez-Serrano, M., Paez-Garcia, A., Sanchez-Bermejo, E., T, C.M., Leo del Puerto, Y., et al. (2012). Role of actin cytoskeleton in brassinosteroid signaling and in its integration with the auxin response in plants. Dev Cell **22**:1275-1285.
DOI: https://doi.org/10.1016/j.devcel.2012.04.008

Lefebvre, B., Furt, F., Hartmann, M.A., Michaelson, L.V., Carde, J.P., Sargueil-Boiron, F., Rossignol, M., Napier, J.A., Cullimore, J., Bessoule, J.J., et al. (2007). Characterization of lipid rafts from Medicago truncatula root plasma membranes: a proteomic study reveals the presence of a raft-associated redox system. Plant Physiol **144**:402-418.
DOI: https://doi.org/10.1104/pp.106.094102

Leontovycova, H., Kalachova, T., Trda, L., Pospichalova, R., Lamparova, L., Dobrev, P.I., Malinska, K., Burketova, L., Valentova, O., and Janda, M. (2019). Actin depolymerization is able to increase plant resistance against pathogens via activation of salicylic acid signalling pathway. Sci Rep **9**:10397.
DOI: https://doi.org/10.1038/s41598-019-46465-5

Levet, F., Hosy, E., Kechkar, A., Butler, C., Beghin, A., Choquet, D., and Sibarita, J.B. (2015). SR-Tesseler: a method to segment and quantify localization-based super-resolution microscopy data. Nat Methods **12**:1065-1071.
DOI: https://doi.org/10.1038/nmeth.3579

Li, X., Wang, X., Yang, Y., Li, R., He, Q., Fang, X., Luu, D.T., Maurel, C., and Lin, J. (2011). Single-molecule analysis of PIP2;1 dynamics and partitioning reveals multiple modes of Arabidopsis plasma membrane aquaporin regulation. Plant Cell **23**:3780-3797.
DOI: https://doi.org/10.1105/tpc.111.091454

Lu, Y., Zhang, Y., Lian, N., and Li, X. (2023). Membrane Dynamics Regulated by Cytoskeleton in Plant Immunity. Int J Mol Sci **24**:6059.
DOI: https://doi.org/10.3390/ijms24076059

Lv, X., Jing, Y., Xiao, J., Zhang, Y., Zhu, Y., Julian, R., and Lin, J. (2017). Membrane microdomains and the cytoskeleton constrain AtHIR1 dynamics and facilitate the formation of an AtHIR1-associated immune complex. Plant J **90**:3-16.
DOI: https://doi.org/10.1111/tpj.13480

Ma, Z., Zhu, K., Gao, Y.G., Tan, S.M., and Miao, Y. (2023). Molecular condensation and mechanoregulation of plant class I formin, an integrin-like actin nucleator. FEBS J **290**:3336-3354.
DOI: https://doi.org/10.1111/febs.16571

Ma, Z., Sun, Y., Zhu, X., Yang, L., Chen, X., and Miao, Y. (2022). Membrane nanodomains modulate formin condensation for actin remodeling in Arabidopsis innate immune responses. Plant Cell **34**:374-394.
DOI: https://doi.org/10.1093/plcell/koab261

Ma, Z., Liu, X., Nath, S., Sun, H., Tran, T.M., Yang, L., Mayor, S., and Miao, Y. (2021). Formin nanoclustering-mediated actin assembly during plant flagellin and DSF signaling. Cell Rep **34**:108884.
DOI: https://doi.org/10.1016/j.celrep.2021.108884

Martiniere, A., Lavagi, I., Nageswaran, G., Rolfe, D.J., Maneta-Peyret, L., Luu, D.T., Botchway, S.W., Webb, S.E., Mongrand, S., Maurel, C., et al. (2012). Cell wall constrains lateral diffusion of plant plasma-membrane proteins. Proc Natl Acad Sci U S A **109**:12805-12810.
DOI: https://doi.org/10.1073/pnas.1202040109

Matouskova, J., Janda, M., Fiser, R., Sasek, V., Kocourkova, D., Burketova, L., Duskova, J., Martinec, J., and Valentova, O. (2014). Changes in actin dynamics are involved in salicylic acid signaling pathway. Plant Sci **223**:36-44.
DOI: https://doi.org/10.1016/j.plantsci.2014.03.002

McKenna, J.F., Rolfe, D.J., Webb, S.E.D., Tolmie, A.F., Botchway, S.W., Martin-Fernandez, M.L., Hawes, C., and Runions, J. (2019). The cell wall regulates dynamics and size of plasma-membrane nanodomains in Arabidopsis. Proc Natl Acad Sci U S A **116**:12857-12862.
DOI: https://doi.org/10.1073/pnas.1819077116

Mongrand, S., Morel, J., Laroche, J., Claverol, S., Carde, J.P., Hartmann, M.A., Bonneu, M., Simon-Plas, F., Lessire, R., and Bessoule, J.J. (2004). Lipid rafts in higher plant cells: purification and characterization of Triton X-100-insoluble microdomains from tobacco plasma membrane. J Biol Chem **279**:36277-32686.
DOI: https://doi.org/10.1074/jbc.M403440200

Morel, J., Claverol, S., Mongrand, S., Furt, F., Fromentin, J., Bessoule, J.J., Blein, J.P., and Simon-Plas, F. (2006). Proteomics of plant detergent-resistant membranes. Mol Cell Proteomics **5**:1396-1411.
DOI: https://doi.org/10.1074/mcp.M600044-MCP200

Narasimhan, M., Johnson, A., Prizak, R., Kaufmann, W.A., Tan, S., Casillas-Perez, B., and Friml, J. (2020). Evolutionarily unique mechanistic framework of clathrin-mediated endocytosis in plants. Elife **9**:eLife.52067.
DOI: https://doi.org/10.7554/eLife.52067

Paredez, A.R., Somerville, C.R., and Ehrhardt, D.W. (2006). Visualization of cellulose synthase demonstrates functional association with microtubules. Science **312**:1491-1495.
DOI: https://doi.org/10.1126/science.1126551

Persson, F., Linden, M., Unoson, C., and Elf, J. (2013). Extracting intracellular diffusive states and transition rates from single-molecule tracking data. Nat Methods **10**:265-269.
DOI: https://doi.org/10.1038/nmeth.2367

Raffaele, S., Vailleau, F., Leger, A., Joubes, J., Miersch, O., Huard, C., Blee, E., Mongrand, S., Domergue, F., and Roby, D. (2008). A MYB transcription factor regulates very-long-chain fatty acid

biosynthesis for activation of the hypersensitive cell death response in Arabidopsis. Plant Cell **20**:752-767.
DOI: https://doi.org/10.1105/tpc.107.054858

Raffaele, S., Bayer, E., Lafarge, D., Cluzet, S., German Retana, S., Boubekeur, T., Leborgne-Castel, N., Carde, J.P., Lherminier, J., Noirot, E., et al. (2009). Remorin, a solanaceae protein resident in membrane rafts and plasmodesmata, impairs potato virus X movement. Plant Cell **21**:1541-1555.
DOI: https://doi.org/10.1105/tpc.108.064279

Rentsch, J., Bandstra, S., Sezen, B., Sigrist, P., Bottanelli, F., Schmerl, B., Shoichet, S., Noe, F., Sadeghi, M., and Ewers, H. (2024). Sub-membrane actin rings compartmentalize the plasma membrane. J Cell Biol **223**:e202310138.
DOI: https://doi.org/10.1083/jcb.202310138

Rohr, L., Ehinger, A., Rausch, L., Glöckner Burmeister, N., Meixner, A.J., Gronnier, J., Harter, K., Kemmerling, B., and Zur Oven-Krockhaus, S. (2024). OneFlowTraX: a user-friendly software for super-resolution analysis of single-molecule dynamics and nanoscale organization. Front Plant Sci **15**:1358935.
DOI: https://doi.org/10.3389/fpls.2024.1358935

Saxton, M.J. (1997). Single-particle tracking: the distribution of diffusion coefficients. Biophys J **72**:1744-1753.
DOI: https://doi.org/10.1016/s0006-3495(97)78820-9

Serge, A., Fourgeaud, L., Hemar, A., and Choquet, D. (2003). Active surface transport of metabotropic glutamate receptors through binding to microtubules and actin flow. J Cell Sci **116**:5015-5022.
DOI: https://doi.org/10.1242/jcs.00822

Simons, K., and Ikonen, E. (1997). Functional rafts in cell membranes. Nature **387**:569-572.
DOI: https://doi.org/10.1038/42408

Singer, S.J., and Nicolson, G.L. (1972). The fluid mosaic model of the structure of cell membranes. Science **175**:720-731.
DOI: https://doi.org/10.1126/science.175.4023.720

Smertenko, A.P., Kaloriti, D., Chang, H.Y., Fiserova, J., Opatrny, Z., and Hussey, P.J. (2008). The C-terminal variable region specifies the dynamic properties of Arabidopsis microtubule-associated protein MAP65 isotypes. Plant Cell **20**:3346-3358.
DOI: https://doi.org/10.1105/tpc.108.063362

Spector, I., Braet, F., Shochet, N.R., and Bubb, M.R. (1999). New anti-actin drugs in the study of the organization and function of the actin cytoskeleton. Microscopy Research and Technique **47**:18-37.
DOI: https://doi.org/10.1002/(sici)1097-0029(19991001)47:1%3C18::aid-jemt3%3E3.0.co;2-e

Szymanski, D., and Staiger, C.J. (2018). The Actin Cytoskeleton: Functional Arrays for Cytoplasmic Organization and Cell Shape Control. Plant Physiol **176**:106-118.
DOI: https://doi.org/10.1104/pp.17.01519

Szymanski, W.G., Zauber, H., Erban, A., Gorka, M., Wu, X.N., and Schulze, W.X. (2015). Cytoskeletal Components Define Protein Location to Membrane Microdomains. Mol Cell Proteomics **14**:2493-2509.
DOI: https://doi.org/10.1074/mcp.M114.046904

Tanner, W., Malinsky, J., and Opekarova, M. (2011). In plant and animal cells, detergent-resistant membranes do not define functional membrane rafts. Plant Cell **23**:1191-1193.
DOI: https://doi.org/10.1105/tpc.111.086249

Vega, A.R., Freeman, S.A., Grinstein, S., and Jaqaman, K. (2018). Multistep Track Segmentation and Motion Classification for Transient Mobility Analysis. Biophys J **114**:1018-1025.
DOI: https://doi.org/10.1016/j.bpj.2018.01.012

Vilches Barro, A., Stockle, D., Thellmann, M., Ruiz-Duarte, P., Bald, L., Louveaux, M., von Born, P., Denninger, P., Goh, T., Fukaki, H., et al. (2019). Cytoskeleton Dynamics Are Necessary for Early Events of Lateral Root Initiation in Arabidopsis. Curr Biol **29**:2443-2454.
DOI: https://doi.org/10.1016/j.cub.2019.06.039

Wagner, T., Kroll, A., Haramagatti, C.R., Lipinski, H.G., and Wiemann, M. (2017). Classification and Segmentation of Nanoparticle Diffusion Trajectories in Cellular Micro Environments. PLoS One **12**:e0170165.
DOI: https://doi.org/10.1371/journal.pone.0170165

Wallis, T.P., Jiang, A., Young, K., Hou, H., Kudo, K., McCann, A.J., Durisic, N., Joensuu, M., Oelz, D., Nguyen, H., et al. (2023). Super-resolved trajectory-derived nanoclustering analysis using spatiotemporal indexing. Nat Commun **14**:3353.
DOI: https://doi.org/10.1038/s41467-023-38866-y

Wang, Y.S., Yoo, C.M., and Blancaflor, E.B. (2008). Improved imaging of actin filaments in transgenic Arabidopsis plants expressing a green fluorescent protein fusion to the C- and N-termini of the fimbrin actin-binding domain 2. New Phytol **177**:525-536.
DOI: https://doi.org/10.1111/j.1469-8137.2007.02261.x

Yu, J., Fischman, D.A., and Steck, T.L. (1973). Selective solubilization of proteins and phospholipids from red blood cell membranes by nonionic detergents. J Supramol Struct **1**:233-248.
DOI: https://doi.org/10.1002/jss.400010308

Zhou, X.-H., Gao, S., and Hui, S.L. (1997). Methods for Comparing the Means of Two Independent Log-Normal Samples. Biometrics **53**:1129-1135.
DOI: https://doi.org/10.2307/2533570

Figures

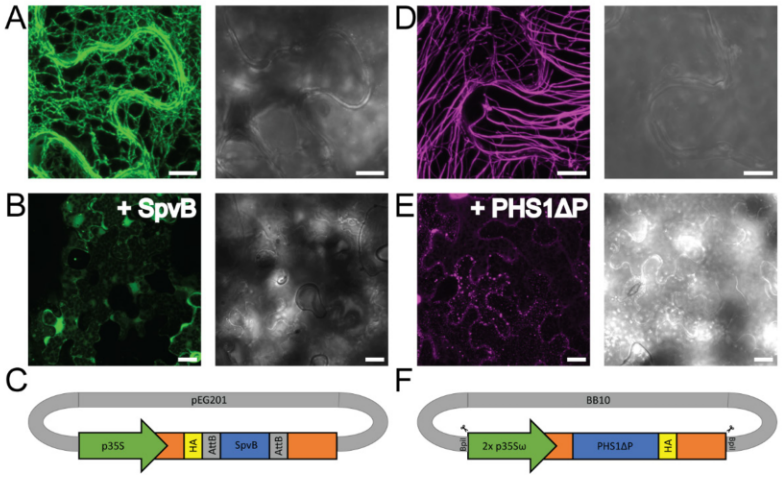

Figure 1 | Overview of genetically encoded, enzymatic tools for cytoskeleton disintegration.

(A) Exemplary confocal microscopy image of epidermal leaf cells of *Nicotiana benthamiana* (*N. benthamiana*) expressing the actin marker GFP-ABD2-GFP with the GFP channel on the left and the corresponding transmission light channel on the right. Intact actin filaments are clearly visible. Scale bar = 10 µm **(B)** Exemplary image of the co-expression of the disruption tool HA-SpvB and the actin marker GFP-ABD2-GFP in the GFP channel (left) and the corresponding transmission light channel (right). The co-expression with the disruption tool leads to removal of F-actin cables in all cells as shown before (Vilches Barro et al., 2019). Scale bar = 10 µm. **(C)** Schematic plasmid structure of the genetically encoded SpvB tool: By Gateway® technology SpvB was inserted into the pEG201 backbone (Earley et al., 2006) which contains a 35S promoter and an N-terminal HA-tag. **(D)** Exemplary confocal microscopy image of epidermal leaf cells of *N. benthamiana* expressing the microtubules marker MAP65-8-RFP with the RFP channel on the left and the corresponding transmission light channel on the right. Intact microtubules are observable. Scale bar = 10 µm. **(E)** Exemplary image of the co-expression of the disruption tool PHS1ΔP-HA and the microtubules marker MAP65-8-RFP in the RFP channel (left) and the corresponding transmission light channel (right). The co-expression with the disruption tool leads to the destabilization of cortical microtubules. Scale bar = 10 µm. **(F)** Schematic plasmid structure of the genetically encoded PHS1ΔP tool: The plasmid was generated by GoldenGate cloning (Binder et al., 2014) using Level I modules which were subsequently assembled in the Level II backbone of BB10. PHS1ΔP is under the control of a 2x 35Sω promoter module and fused C-terminally to an HA-tag. For the generation of higher order assemblies, BB10 contains Bpi I recognition sites.

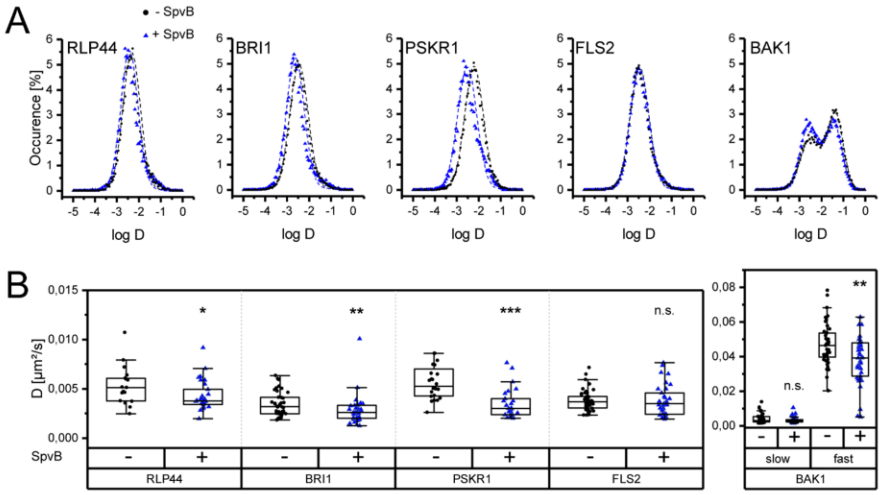

Figure 2 | Disintegration of actin filaments primarily results in reduced protein dynamics in the plasma membrane.

(A) Distribution of diffusion coefficients (D) represented as log(D) and plotted against their occurrence [%] over all quantified cells for RLP44-, BRI1-, PSKR1-, FLS2- and BAK1-mEos3.2. For each protein fusion, two distributions are shown: (i) In black, values obtained from epidermal *N. benthamiana* leaf cells expressing the respective fusion alone (- SpvB) and (ii) in blue values from the co-expression of the respective protein fusions with the genetically encoded, enzymatic tool SpvB (+ SpvB). For RLP44-, BRI1- and PSKR1-mEos3.2 a slight shift to lower log(D) values is observable, when SpvB is co-expressed. The effect is barely visible for FLS2-mEos3.2 and BAK1-mEos3.2. All measurements were performed three days post infiltration. Please note that all protein fusions show a bell-shape distribution (i.e., one mobility population), except for BAK1-mEos3.2 that presents a slower and a faster variety (two Gaussian fit). When co-expressed with SpvB, the slow fraction of BAK1-mEos3.2 is increased. **(B)** Representation of the peak D values of RLP44-, BRI1-, PSKR1-, FLS2- and BAK1-mEos3.2. with same color code as in (A). The peak values of individual cells (illustrated as single dots or triangles; $n \geq 17$) were obtained by normal fits of distributions comparable to (A) expect of BAK1-mEos3.2 where a two-component Gaussian mixture model was applied (see Material *and Methods*). The separation of the BAK1 fractions was done according to this model with the peaks of the first maxima representing the slow fraction and the peaks of the second maxima the fast fraction, respectively. In the absence of intact actin filaments (blue; +SpvB) the diffusion coefficient is significantly decreased for the RLP44-, BRI1- and PSKR1-mEos3.2 fusions, while the reduction for FLS2-mEos3.2 is not significant. For BAK1-mEos3.2, only a decrease in the fast fraction is observable. For statistical evaluation, the data were checked for normal distribution and unequal variances and then analyzed according to the results of the test by applying either a Mann-Whitney U test or a One-way ANOVA. Whiskers show the data range excluding outliers, while the boxes represent the 25-75 percentile. $p \leq 0.001$ (***); $p \leq 0.01$ (**); $p \leq 0.05$ (*); $p > 0.05$ (n.s.). All statistical analyses were performed with custom-made R scripts.

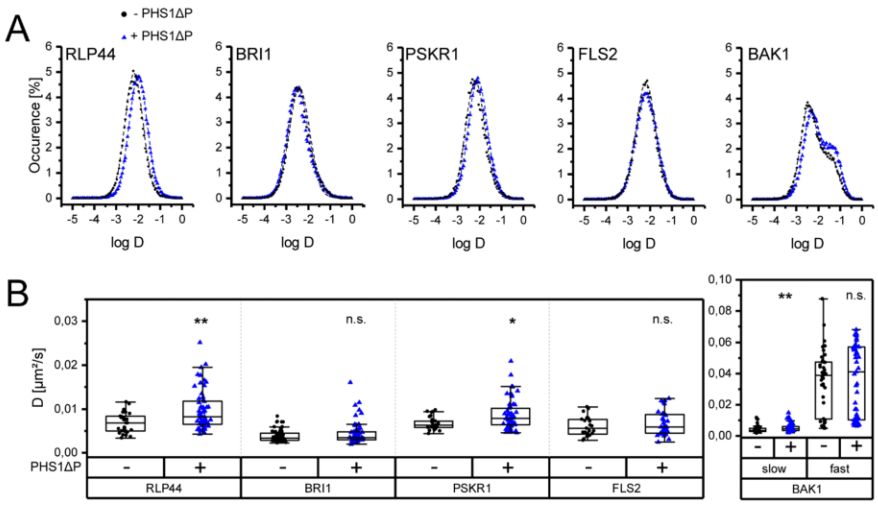

Figure 3 | Disintegration of microtubule filaments primarily results in increased protein dynamics in the plasma membrane.

(A) Distribution of diffusion coefficients (D) represented as log(D) and plotted against their occurrence [%] over all quantified cells for RLP44-, BRI1-, PSKR1-, FLS2- and BAK1-mEos3.2. For each protein fusion, two distributions are shown: (i) In black, values obtained from epidermal *N. benthamiana* leaf cells expressing the respective fusion alone (- PHS1ΔP) and (ii) in blue values from the co-expression of the respective protein fusions with the genetically encoded, enzymatic tool PHS1ΔP (+ PHS1ΔP). RLP44, PSKR1, and BAK1-mEos3.2 show a slight shift to higher log(D) values when co-expressed with PHS1ΔP. The effect is barely visible for the other protein fusions. Measurement conditions are as described in Figure 2. Again, all protein fusions show a bell-shape distribution (i.e., one mobility population), except for BAK1-mEos3.2 that presents a slower and a faster variety (two Gaussian fit). When co-expressed with PHS1ΔP, the fast fraction of BAK1-mEos3.2 is increased. **(B)** Representation of the peak D values of RLP44-, BRI1-, PSKR1-, FLS2- and BAK1-mEos3.2. with same color code as in (A) and obtained by n ≥ 25 cells. The evaluation was performed as described for Figure 2. In the absence of intact microtubules (blue; + PHS1ΔP) the diffusion coefficient is significantly increased for the RLP44- and PSKR1-mEos3.2 fusions as well as for the slow fraction of BAK1-mEos3.2, without a significant effect on the fast variety. Although BRI1- and FLS2-mEos3.2, as well as the fast variety of BAK1-mEos3.2, show no significant effect, a trend of increasing diffusion coefficients after microtubule disintegration is observable. Statistical analyses were conducted as in Figure 2, with the same box representation. $p \leq 0.001$ (***); $p \leq 0.01$ (**); $p \leq 0.05$ (*); $p > 0.05$ (n.s.).

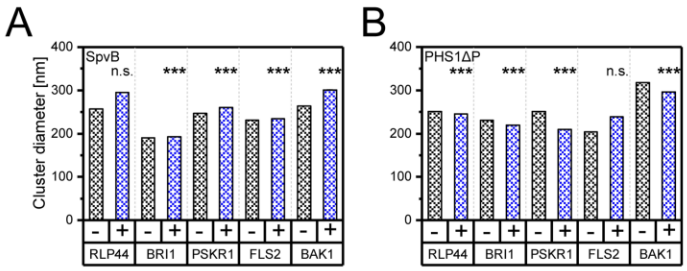

Figure 4 | Actin and microtubules disintegration lead to opposing effects on nanocluster sizes.

(A) Representation of corrected, transformed means of nanocluster diameter sizes (nm) of the tested protein fusions based on the track trajectories, also used for Figure 2 and Figure 3. The sizes were either determined for the protein fusions expressed alone (- SpvB, black) or together with the genetically encoded disruption tool for actin, SpvB (+ SpvB, blue). The analyses were performed by applying the NASTIC algorithm (Wallis et al., 2023) available in OneFlowTraX (Rohr et al., 2024) with a radius factor of 1.3 and at least three tracks per cluster. The corrected, transformed means are based on the log-normal distribution of all determined clusters among all evaluated cells (n as in Figure 2 and Figure 3), not considering clusters larger than 2,500 nm in diameter (≥ 1630). Except for RLP44-mEos3.2, all other tested fusions proteins show significantly increased cluster sizes upon the disintegration of actin filaments. Statistical analyses were performed according to Zhou et al. (1997). **(B)** Representation of corrected, transformed means of nanocluster diameter sizes (nm) as in (A) but here either with intact microtubules (i.e., expressed alone; - PHS1ΔP, black) or upon microtubules disintegration (+ PHS1ΔP, blue). Parameters and filtering as in (A) with ≥ 4356 evaluated cluster. Except for FLS2-mEos3.2, all other tested fusions proteins show significantly decreased cluster sizes upon the disintegration of microtubules filaments. Statistical analyses were performed as in (A). $p \leq 0.001$ (***); $p \leq 0.01$ (**); $p \leq 0.05$ (*); $p > 0.05$ (n.s.).

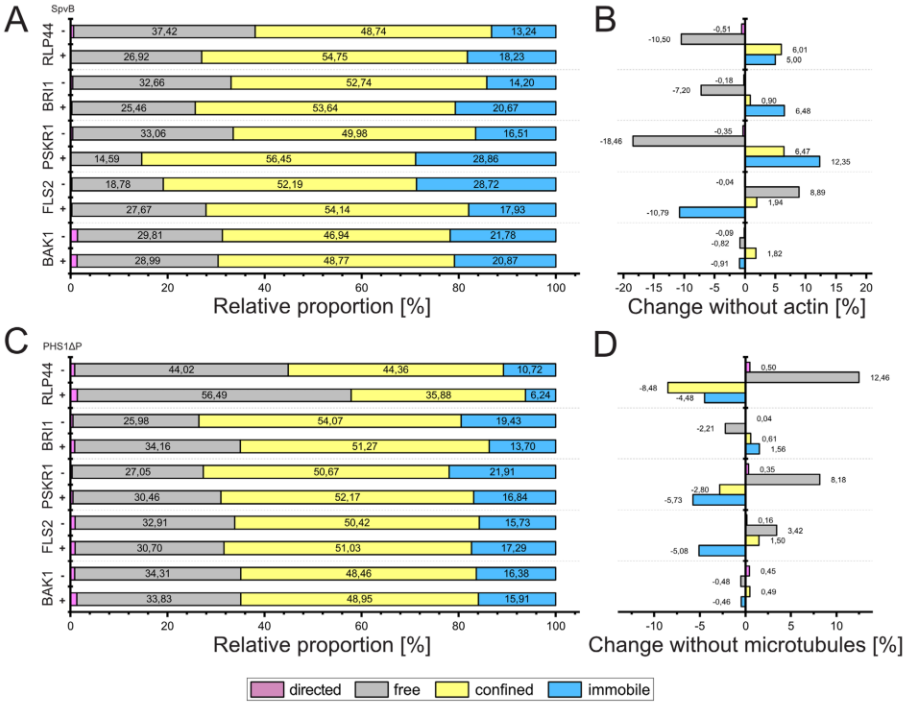

Figure 5 | Classification of segment motion patterns depending on the cytoskeleton integrity.

(A) Proportion of motion behavior (in percent) depending on the status of the actin cytoskeleton (either intact (- SpvB) or disintegrated (+ SpvB)), namely, directed (magenta), free (grey), confined (yellow) and immobile (blue). All studied proteins reveal primarily confined behavior, independent of the actin integrity. Immobility and free diffusive behavior are present in varying amounts amongst the proteins. Directed movement is barely present. The classification was performed according to Vega et al. (2018). **(B)** Relative shifts in the motion patterns in the absence of actin filaments with the same color code as in (A). RLP44-, BRI1- and PSKR1-mEos3.2 show a clear decrease in free diffusive behavior, while immobility and confined behavior (not for BRI1-mEos3.2) increases. However, FLS2-mEos3.2 shows a contrary effect by a decrease in immobility and an increase in free diffusive behavior. BAK1-mEos3.2 is nearly unaffected by the manipulation of the actin cytoskeleton. **(C)** Proportion of motion behavior (in percent) depending on the status of the microtubule cytoskeleton (either intact (- PHS1ΔP) or disintegrated (+ PHS1ΔP) with same behavior classes and color code as in (A) and (B). Again, all studied proteins reveal primarily confined behavior, independent of the microtubule disintegration except for RLP44-mEos3.2 (+ PHS1ΔP) that shows mostly free diffusive behavior. Immobility and free diffusive behavior are present again with varying amounts amongst the proteins, with distinct differences between RLP44-mEos3.2 (+ PHS1ΔP) and the other fusion proteins under manipulated conditions. Again, directed movement is barely present. **(D)** Relative shifts in the motion patterns in the absence of the microtubule cytoskeleton with the same color code as before. RLP44- and PSKR1-mEos3.2 show comparable effects with increased free diffusive behavior as well as with decreased confined movement and immobility. BRI1-mEos3.2 exhibits only minor changes while FLS2-mEos3.2 shows a slight increase in free and confined motion, while immobility is decreased, too. BAK1 is barely affected.

Comparison of path-based centrality measures in protein-protein interaction networks revealed proteins with phenotypic relevance during adaptation to changing nitrogen environments

by Gilbert M., Li Z., Wu X. N., Rohr L., Gombos S., Harter K., Schulze W. X. (2021)

in *Journal of Proteomics*

doi: https://doi.org/10.1016/j.jprot.2021.104114

Accepted

Journal of Proteomics 235 (2021) 104114

Contents lists available at ScienceDirect

Journal of Proteomics

journal homepage: www.elsevier.com/locate/jprot

Comparison of path-based centrality measures in protein-protein interaction networks revealed proteins with phenotypic relevance during adaptation to changing nitrogen environments

Max Gilbert [a], Zhi Li [a], Xu Na Wu [c], Leander Rohr [b], Sven Gombos [a], Klaus Harter [b], Waltraud X. Schulze [a,*]

[a] Department of Plant Systems Biology, University of Hohenheim, 70593 Stuttgart, Germany
[b] Center for Plant Molecular Biology, University of Tübingen, 72076 Tübingen, Germany
[c] School of Life Science, Yunnan University, 650091 Kunming, China

ARTICLE INFO

Keywords:
Dynamic protein complexes
Network path analysis
Nitrate starvation

ABSTRACT

Plants must rapidly adapt to changes in nutrient conditions. Especially adaptations to changing nitrogen environments are very complex involving also major adjustments on the protein level. Here, we used a size-exclusion chromatography-coupled to mass spectrometry approach to study the dynamics of protein-protein interactions induced by transition from full nutrition to nitrogen starvation. Comparison of interaction networks established for each nutrient condition revealed a large overlap of proteins which were part of the protein-protein interaction network, but that same set of proteins underwent different interactions at each treatment. Network topology parameter betweenness centrality (BC) was found to best reflect the relevance of individual proteins in the information flow within each network. Changes in BC for individual proteins may therefore indicate their involvement in the cellular adjustments to the new condition. Based on this analysis, a set of proteins was identified showing high nitrogen-dependent changes in their BC values: The receptor kinase AT5G49770, co-receptor QSK1, and proton-ATPase AHA2. Mutants of those proteins showed a nitrate-dependent root growth phenotype. Individual interactions within the reconstructed network were tested using FRET-FLIM technology. Taken together, we present a systematic strategy comparing dynamic changes in protein-protein interaction networks based on their network parameters to identify regulatory nodes.

Significance: Protein-protein interactions are known to be important in cellular signaling events, but the dynamic changes in interaction networks induced by external stimuli are still rarely studied. We systematically analyzed how changes in the nutrient environment induced a rewiring of protein-protein interactions in roots. We observed small changes in overall protein abundances, but instead a rewiring of pairwise protein-protein interactions. Betweenness centrality was found to be the optimal network topology parameter to identify protein candidates with high relevance to the information flow in the (dynamic) network. Predicted interactions of those relevant nodes were confirmed in FLIM/FRET experiments and in phenotypic analysis. The network approach described here may be a useful application in dynamic network analysis more generally.

1. Introduction

The dynamic assembly and disassembly of protein-protein interactions upon external and internal signals is a well-conceived concept. However, it is much more difficult to gain experimental evidence. Over the past decades the dynamic nature of individual protein-protein interactions has been elucidated. Especially transporters in the plasma membrane, which are involved in the flow of nutrients and ions across the cellular barrier, undergo condition-dependent protein-protein interactions with regulatory proteins such as kinases and phosphatases. Well studied examples are the ion channel SLAH3, which was described to interact with an activating kinase CPK21 upon stimulation with the phytohormone abscisic acid, but in absence of the hormone forms an interaction with a phosphatase [1]. Also the plasma membrane ATPase AHA2 is known to interact with different kinases under different conditions to be phosphorylated at activating or inhibiting phosphorylation

* Corresponding author.
E-mail address: wschulze@uni-hohenheim.de (W.X. Schulze).

https://doi.org/10.1016/j.jprot.2021.104114
Received 20 October 2020; Received in revised form 21 December 2020; Accepted 6 January 2021
Available online 14 January 2021

sites [2]. AHA2 is one of the most abundant proteins within the plasma membrane of roots and essential in control of the membrane potential and a proton gradient for nutrient uptake. Activating interactions include the interaction with receptor kinase PSKR1, which activates the proton pump in presence of the hormone phytosulfokine [3]. By contrast, interaction of AHA2 with FERONIA results in phosphorylation at an inhibitory serine and inactivation of the pump [4].

Two of the most prominent and widely used techniques for the systematic and targeted identification of protein interaction partners are the yeast-two-hybrid system and the affinity purification of proteins. Both methods [5,6] are now widely used in large-scale biology. However, the dynamic nature of protein-protein interactions *in planta* cannot be addressed using heterologous expression systems of the two-hybrid systems. Thus, researchers identify interaction partners to selected target proteins by affinity purification combined with quantitative mass spectrometry. By this method, for example, conditional interaction partners to receptor kinase SIRK1 were identified [7], or conditional interactors of cell cycle components were characterized [8]. The interactome of aquaporins was recently studied by enrichment of protein complexes from plants grown at different stresses, proposing new candidate proteins for regulation of the water channels [9]. However, the system-wide, *in planta* study of the dynamic nature of protein-protein interaction has not been widely addressed so far.

Dynamic re-arrangements of protein-protein interactions are especially to be expected when plants are exposed to a change in nutrient conditions, for example nitrogen. Nitrogen, as a component of protein, nucleic acids and thousands of metabolites, is an essential macronutrient for plants and is mainly taken up in the form of nitrate. The cellular responses to nitrate starvation or to the resupply of nitrate to starved plants was in the past especially well studied at the gene transcriptional level [10,11]. At the protein level, the change of phosphorylation status was quantified in nitrate starvation-resupply experiments [12], and in response to nitrate starvation [13]. However, global insights into dynamic changes at the level of protein-protein interactions are still missing. Therefore, in this work, we apply a recently published size-exclusion-chromatography coupled to mass spectrometry (SEC-MS) approach [14] to compare the protein-protein interaction network of plants grown under full nutrition and plants exposed to nitrogen starvation. We here aim to (i) define a workflow of comparing interaction networks and (ii) develop measures to identify key proteins involved in regulation of nitrogen starvation response.

2. Materials and methods

Plant growth conditions – All experiments were done using *Arabidopsis thaliana* (Col-0). Plant seedlings were grown in a hydroponic system [15]. Plants under full nutrition were grown in liquid half-strength Murashige and Skoog (½ MS) growth medium with 0.5% sucrose for three weeks before harvesting the full nutrition sample. Plants for nitrogen starvation were firstly grown in half-strength Murashige and Skoog growth medium supplemented with 2 mM KNO_3 for 14 days, and then transferred to 1 mM KNO_3 for 7 days. After three weeks of growth on nitrate supplemented medium, plants were then transferred to nitrogen-free half-strength MS-medium for two days before harvesting the N-starvation sample. For the nitrogen resupply condition, plants were firstly starved for nitrogen as described. Then after two days of starvation, nitrate was resupplied to a final concentration of 2 mM KNO_3 directly into the nitrogen-free growth medium for 15 min prior to harvest. In all conditions, the growth medium was supplemented with 0.5% sucrose.

Experimental design and statistical rationale – Two data sets were analyzed, acquired under full nutrition or nitrate starvation. Each data set consisted of two biological replicates of size exclusion chromatography followed by mass spectrometry analysis of the acquired fractions as described [14]. Only those proteins consistently identified in both replicates were considered for comparisons between conditions. A third experimental condition, in which nitrate was resupplied to nitrate starved plants was included with one biological replicate. Statistical comparisons were carried out by pairwise *t*-tests (two sample comparisons) or ONEWAY ANOVA (multiple sample comparisons). We used the MaxQuant / Perseus data analysis platform for quantitative analysis in all proteomics experiments.

Microsomal protein enrichment – A total of 1 to 1.5 g of roots (fresh weight) was homogenized in 10 ml ice-cold extraction buffer (330 mM sucrose, 100 mM KCl, 1.5 mM EDTA, 50 mM Tris-MES, fresh 5 mM DTT, and 1 mM phenylmethylsulfonylfluoride, pH 7.5) [16] in the presence of 0.5% *v*/v proteinase inhibitor mixture (Sigma-Aldrich, Germany) and phosphatase inhibitors (50 mM NaF, 1 mM Na3VO4, 1 mM benzamidin, 4 μM proteinase inhibitor leupeptin). The homogenate was centrifuged for 15 min at 7500 ×*g* at 4 °C. The pellet was discarded, and the supernatant was centrifuged for 75 min at 48,000 ×*g* at 4 °C. Microsomal pellets were stored at −80 °C until further processing. The microsomal pellet was resuspended in 100 μl of membrane buffer (137 mM NaCl, 2.7 mM KCL, 10 mM Na2HPO4, 1.8 mM KH2PO4; pH = 7.4, 0.1% n-Dodecylmaltodise) or UTU (6 M urea, 2 M thiourea, pH 8) supplemented with 0.1% n-Dodecyl β-D-maltoside (DDM). Insolubilized membrane fragments were pelleted before further processing of solubilized membrane proteins.

For isolating membrane proteins in their native form, it is important to isolate membranes as intact vesicles. Sonication, French-Press or similar methods for plant-protein-purification use brute force to disrupt the cell wall and membranes to gain access to soluble proteins. This often results in a poor yield of membrane proteins as they are dependent of their membrane environment. This problem was avoided by using a Glass/PTFE Potter Elvehjem Tissue Grinder. Through careful grinding of the plant material, small membrane-vesicles form up which can be purified by differential centrifugation as described [17,18]. The use of DDM in solubilization of the membrane pellet was essential for the experiment as it was shown that DDM enhances stability and preserves activity of membrane-proteins during purification [19,20].

Size-exclusion chromatography followed by mass spectrometry – Protein-protein interactions were defined using a SEC-MS approach as described [14]. A total amount of 1 mg microsomal extract was run on an Enrich SEC650 (BioRad) column using 1 column volume of phosphate buffered saline (PBS). Eluting protein fractions were collected in 50 dynamic fractions. The volume of earlier fractions was 25 μL and 50 μL for later fractions to maximize functional chromatographic resolution and to correct for higher protein content in earlier fractions [14]. Equal protein amount from each fraction was digested by LysC/trypsin and desalted over C18 as described [7].

LC-MS/MS analysis of peptides – Peptides mixtures were analyzed by nanoflow Easy-nLC (Thermo Scientific) and Orbitrap hybrid mass spectrometer (Q-exactive, Thermo Scientific). Peptides were eluted from a 75 μm × 50 cm analytical C_{18} column (PepMan, Thermo Scientific) on a linear gradient running from 4% to 64% acetonitrile over 135 min. Proteins were identified based on the information-dependent acquisition of fragmentation spectra of multiple charged peptides. Up to twelve data-dependent MS/MS spectra were acquired in the linear ion trap for each full-scan spectrum acquired at 70,000 full-width half-maximum (FWHM) resolution.

Protein identification and label-free quantitation – MaxQuant version 1.5.3.8 [21] was used for raw file peak extraction and protein identification against the Arabidopsis proteome (TAIR10, 35,386 entries). Protein quantification was performed in MaxQuant using the label free quantification (LFQ) algorithm [22]. The following parameters were applied: trypsin as cleaving enzyme; minimum peptide length of seven amino acids; maximal two missed cleavages; carbamidomethylation of cysteine as a fixed modification; N-terminal protein acetylation, oxidation of methionine as variable modifications. Peptide mass tolerance (4.5 ppm) and MS/MS tolerance (20 ppm) were used according to the standard settings in MaxQuant. Further settings were: “label-free quantification” marked, multiplicity set to 1; “match between runs”

marked with time window 2 min; peptide and protein false discovery rates (FDR) set to 0.01; common contaminants (trypsin, keratin, etc.) excluded. Label-free protein quantitation [22] was applies using the software Perseus and based on the "proteingroups.txt" output table of MaxQuant. The mass spectrometry proteomics data have been deposited to the ProteomeXchange Consortium via the PRIDE [23] partner repository with the dataset identifier PXD009511 for the full-nutrition data set, PXD015841 for the nitrate starvation and resupply data. Protein identification information is listed in Supporting Table S6.

Definition of protein-protein interactions – Interacting protein pairs were defined as described [14]. Briefly, proteins exhibiting an earlier-than expected retention pattern of at least six fractions during SEC-chromatography were defined as nodes in the protein-protein interaction network. Interaction partners to those node proteins were defined by pair-wise correlation of elution profiles among the node proteins. Thus, the edges in the protein-protein interaction networks were defined by pairwise comparison of elution profiles and the requirements for co-elution same fraction. We used publicly available databases STRING [24] and MIND [25] of confirmed protein-protein interactions to define optimal filtering criteria and cutoff scores. High confidence interactions were defined as those the interaction pairs which eluted with less than one fraction difference and stricter correlation score cutoff [14].

Protein abundance quantitation –LFQ-values [22] across multiple samples were used to compare protein abundance between different experiments. We normalize the data as follows: Firstly, within each replicate the relative abundance (relLFQ, Eq. [1]) for each protein was obtained by dividing the summarized protein LFQ-values by the total LFQ-sum of that replicate.

$$relLFQ_{Protein} = \frac{LFQ_{Protein\ Sum}}{LFQ_{Experiment\ Sum}} \quad (1)$$

Secondly, relative protein abundances were weighted against the respective protein mass in Dalton. This was done to compensate for differing identification probabilities due to different protein sizes (Eq. [2]).

$$\mathrm{Abundance_{weighted}} = \frac{\mathrm{relLFQ_{Protein}}}{\mathrm{Molecular\ Weight\ [Dalton]}} \quad (2)$$

Thirdly, proteins were sorted according to their weighted abundances (AW_{LFQ}) and proteins were divided into 100 dynamic abundance categories (AC_{LFQ}) for each experiment to account for different numbers of proteins identified in different replicates. Category size depended on the total number of proteins in each replicate. By binning all proteins into a fixed number of abundance categories enabled the observation of protein abundance changes across experiments.

Network topology analysis – Networks were constructed with Cytoscape 3.7.1 and evaluated with the Cytoscape network analyzer tool regarding node parameters degree, betweenness centrality, closeness centrality, stress. Introduced in 1950 [26], Closeness Centrality (CC, Eq. [3]) can be used to describe the efficiency of a node for distributing information to other members of the network. It is defined as the reciprocal of the average shortest path length (σ) for a node i to all other nodes j, where n is the total number of nodes:

$$CC(i) = \frac{1}{\sum_{j \neq i}^{n} \sigma_{ij}} \quad (3)$$

Since CC scales with the total number of nodes, it was normalized by using the average length of the shortest paths instead of their sum (Eq. [4]):

$$\mathrm{CC(i)'} = \frac{1}{\mathrm{average}\left(\sum_{j \neq i}^{n} \sigma_{ij,}\right)} \quad (4)$$

While a high CC is a good indicator for a node that has broad access to all other nodes, it cannot be used to describe the potential influence on the flow of information. For that purpose, Stress Centrality can be used. It is defined as the number of shortest paths passing through a node i (Eq. [5]). By this definition, a node gains importance if it is facilitating the flow of information between other nodes. This parameter can only be defined for networks without multiple edges like protein-interaction networks.

$$\mathrm{SC(i)} = \sum_{s \neq i \neq t} \sigma_{st}(i) \quad (5)$$

Betweenness Centrality (BC) [27] also assigns importance to nodes that are in the path of other nodes, by describing each node's power over the flow of information. It builds on the definition of Stress Centrality and is defined as the sum of all shortest paths (σ) between nodes j and t passing through node i ($\sigma_{jt}(i)$) divided by all possible shortest paths σ_{jt} (Eq. [6]).

$$\mathrm{BC(i)} = \sum_{j \neq i \neq t} \frac{\sigma_{st}(i)}{\sigma_{st}} \quad (6)$$

BC also scales linearly with network size. To account for scaling, the BC values can be normalized by dividing through the maximum value of a given network. For an undirected network with the size n, the division is further multiplied by the factor 2 (Eq. [7]):

$$\mathrm{BC(i)'} = \frac{2 \sum_{s \neq i \neq t} \frac{\sigma_{st}(i)}{\sigma_{st}}}{(n-1)(n-2)} \quad (7)$$

A high BC value is usually assigned to nodes that connect different network communities. In this way, BC offers more unique and sensitive information about local network topology than focusing on degree based metrics alone.

A metric to describe modular organization is the clustering coefficient [28]. For undirected networks, it is defined as the number of connected pairs between all neighbors of a node i, where e_n is the number of connected pairs and k_n is the number of neighbors (Eq. [8]).

$$\mathrm{C(n)} = \frac{2\,e_n}{(k_n(k_n-1))} \quad (8)$$

Random networks – Random networks were generated containing the same numbers of nodes and edges as respective protein-protein interaction networks. Edges were randomly assigned between the nodes.

Root growth assay – Primary root length and lateral root density of wildtype and mutant plants were assessed by growth of seedlings on vertical plates of MES-buffered ½ MS-Agar (0.25 gl^{-1} MES, 0.39 gl^{-1} N-Free MS, 0.5% Sucrose, 8 gl^{-1} agar, supplemented with KNO_3 when needed). All plates were supplemented with 30 mM sucrose. After sterilization (incubation in 2% Sodium-Hypochlorite solution for 12 min and subsequent washing), the seeds (5 seeds per plate) were spread on ½ MS-agar plates and incubated for 2 days at 6 °C for vernalization. After vernalization, the seeds were germinated for 4 days at room temperature after which they were transferred to the treatment plates (5 mM KNO_3, 0.3 mM KNO_3, 0 mM KNO_3). Each plate was scanned with a desktop office scanner (600dpi) at the start of the treatment phase and after 5 days of growth. Images were evaluated with the ImageJ software v.1.52a (imagej.nih.gov/ij).

Pull-downs of GFP-tagged SIRK1 and QSK1 – Root microsomal proteins (150 μg) isolated as described above was incubated with 25 μl of anti-GFP agarose beads (Chromotek, Germany) for two hours on a rotating wheel at 4 °C [29]. After incubation, the beads were collected by centrifugation and washed two times with 500 μl wash buffer (10 mM Tris/HCl pH 7.5, 150 mM NaCl, 0.5 mM EDTA, 0.01% IGEPAL). For protein–protein interaction assays, the proteins were eluted from the beads with 100 μl UTU (6 M urea, 2 M thiourea), pH 8, before in-solution tryptic digestion.

FLIM/FRET – For FRET-FLIM analysis, the coding sequences of BAK1

and AHA2 as well as of QSK1 and At5g49770 were expressed as C-terminal fluorophore fusions in 2in1 vectors, namely pFRETcg-2in1-CC [30]. To obtain GFP-donor only controls, a coding sequence of gentamycin fused to mCherry was used. The binary vectors and p19 as gene silencing suppressor were transformed into *Agrobacterium tumefaciens* strain *GV3101* and infiltrated into *Nicotiana benthamiana* leaves. The measurements were performed two to three days after infiltration using a SP8 laser scanning microscope (Leica Microsystems) with LAS AF and SymPhoTime software as described [31]. Before performing the FRET-FLIM measurement, the presence of the fluorophores was detected by using the 488 or 561 nm lasers for GFP or mCherry excitation, respectively. The fluorescence lifetime in nanoseconds of either the donor only expressing cells or the cells expressing the indicated combinations was measured with a pulsed laser as an excitation light source of 470 nm and a repetition rate of 40 MHz (PicoQuant Sepia Multichannel Picosecond Diode Laser, PicoQuant Timeharp 300 TCSPC Module and Picosecond Event Timer). The acquisition was performed until 500 photons in the brightest pixel were reached. To obtain the GFP fluorescence lifetime, data processing was performed with SymPhoTime software and bi-exponential curve fitting as well as correction for the instrument response function. A total range of 23 ns was evaluated. Statistical analysis was carried out with JMP 14. To test for homogeneity of variance, a Brown-Forsythe test was applied. As the variances are unequal, a Kruskal-Wallis test followed by Dunn's post-hoc test were performed.

Public resources – Functional classification of proteins was done based on MAPMAN [32]. Information about subcellular location was derived from SUBA3 [33]. Detailed protein function was manually updated with the support of TAIR [34].

Data visualization – Functional classification of proteins was done based on MAPMAN [32]. Information about subcellular location was derived from SUBA3 [33]. Detailed protein function was manually updated with the support of TAIR [34]. Other statistical analyses were carried out with Sigma Plot (version 11.0) and Excel (Microsoft, 2013). Over-representation analysis was done via Fisher's exact test, p values were adjusted using Bonferroni correction. Networks were visualized using Cytoscape [35].

3. Results

3.1. Protein abundance dynamics

Different growth conditions can not only induce dynamics in protein-protein interactions, but can affect overall protein abundance. To address this, we used normalized LFQ-values to describe protein abundance changes. The normalized LFQ values were weighted by protein molecular weight, allowing abundance ranking of all proteins (weighted abundance, AW_{LFQ}). To be able to compare the different data sets and replicates which contained different total numbers of proteins, we defined 100 dynamic abundance categories (AC_{LFQ}) within each replicate. Each abundance category contained different numbers of proteins, but reflected the same relative abundance within the sample. For example: category 1 contained the 1% most abundant proteins, and this category contained 35 proteins in the full nutrition data set, and 22 proteins in the nitrogen starvation data set. To compare relative protein abundance changes between the two conditions, the change in AC_{LFQ} for each protein was taken as a readout.

Most proteins identified in two biological replicates of the same nutrient condition showed an abundance category variation of up to 10 categories, and over 80% of the proteins showed between replicate variations of less than 20 categories, independently of the nutrient condition (Fig. 1A). Based on this observation, we only considered those proteins that showed a change of less than 20 abundance categories between replicates for further comparison between conditions. In general, ribosomal proteins were among the most abundant proteins identified under both nutrient conditions (Supporting Table 1). The most abundant 10% of proteins were furthermore highly enriched for

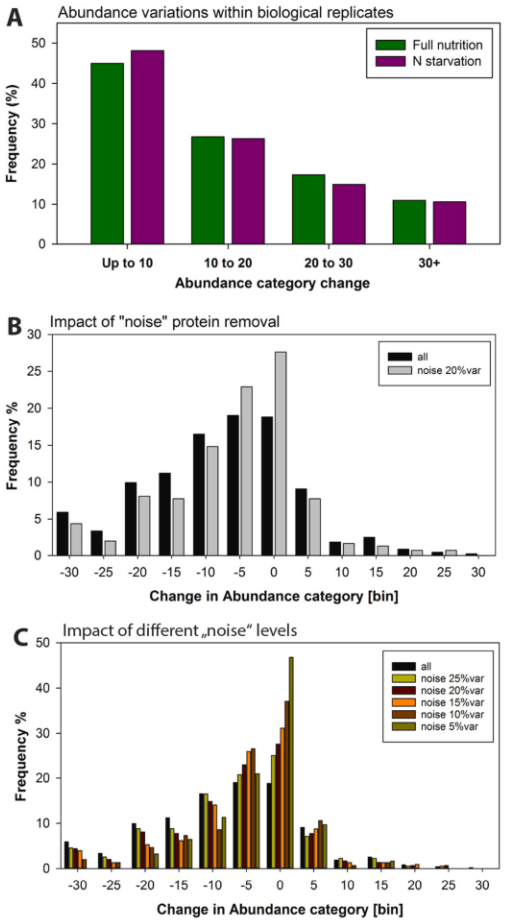

Fig. 1. Protein abundance in replicates. (**A**) Abundance variation within two biological replicates of each treatment, full nutrition and nitrogen starvation. Abundance variations of more than to 20% were considered "noise". (**B**) Changes in abundance category upon nitrogen starvation. Black bars represent the full data set, gray bars represent the data set corrected for those proteins with more than 20% variation between replicates ("noise"). (**C**) Changes in abundance category upon nitrogen starvation at different levels of variation between replicates ("noise").

transporters ($p < 2.3*10^{-7}$, Fisher Exact Test), particularly aquaporins, and the plasma membrane H^+-ATPases. The least abundant 10% of proteins were enriched for signaling proteins ($4.4*10^{-7}$, Fisher Exact Test), transporters, among them nitrate and ammonium transporters ($8.74*10^{-6}$, Fisher Exact Test), and proteins involved in cell organization ($2.53*10^{-3}$, Fisher Exact Test). Fig. 1:

In general, nitrogen starvation resulted in a decrease in protein abundance compared to full nutrition (Fig. 1B). Based on the MAPMAN [32] annotation categories (="bins"), nitrogen starvation led to an increased abundance category for proteins of the "protein" bin (neogenesis, degradation and modification), and "RNA"-bins, while "stress"-, "signaling"- and "transport"- associated bins decreased in abundance categories. Excluding those proteins with change in abundance

categories between biological replicates of greater than 20 emphasized the skewed pattern of protein abundance changes under nitrogen starvation (Fig. 1B). Proteins with strongest change in abundance category (more than 30 abundance categories) upon nitrogen starvation were some transporters, and many other receptor kinases, among them FERONIA (FER, AT3G51550). Despite the tendency for reduced protein abundances under nitrate starvation, the abundance category of the majority of proteins remained unaltered. However, filtering the data set from proteins with abundance category changes of more than 20 categories between replicates ("noise") reduced the total number of proteins with observed abundance change from 473 to 297 shared candidate proteins.

If the stringency of the "noise"-filter was increased (Fig. 1C), it became obvious that proteins with highly consistent abundance categories between replicates (i.e. change of less than 5 categories between replicates), were also those proteins that remained stable in their abundance category upon nitrogen starvation (Fig. 1C). Among this group we found many constituents of the ribosomes, essential proton-transporting ATPases (AHA2, AAC1/2), porins (e.g. PIP2B, VDAC3), and members of the mitochondrial electron transport chain (e.g. ATP Synthase, Cytochrome C Oxidase).

3.2. *Protein-protein interaction networks under full nutrition and nitrogen starvation*

Under full nutrition, 3520 proteins were identified in both replicates, and under nitrogen starvation 2280 proteins were found in both replicates (Fig. 2). Indeed, there was even a very high overlap of identified proteins in the two nutrient conditions. 90% of the proteins identified in the nitrogen starvation data set were also identified under full nutrition. After application of quality filter criteria and the quantitation workflow described previously [14], 965 and 677 proteins were proposed as nodes of the protein-protein interaction network under full nutrition and nitrogen starvation, respectively. Fig. 2:

These nodes were those proteins, which based on their elution properties in the SEC-MS experiments, displayed higher than expected apparent mass and thus were considered to undergo an interaction. We show a high reproducibility of retention time shifts of individual proteins in the two biological replicates (Supporting Fig. S1 A,B) for full nutrition condition [14], as well as for nitrogen starvation condition. Since the definition of nodes in the interaction network was based on higher than expected retention times, the reproducible retention time shifts indicate robust detection of interaction nodes. Correlation analysis [14] revealed 1752 high confidence protein-protein interactions at full nutrition and 1375 interactions under nitrogen starvation. However, the overlap of identified high confidence interactions was rather low (7 to 9%) between the two nutrient conditions, while we found an overlap of identified interactions between biological replicates of up to 25% [14]. Rather, each condition showed a high number of exclusive interactions, the majority of which were not found in the other condition (Fig. 2). Thus, the same proteins (nodes) seemed to undergo different interaction (edges) in each of the nutritional environments. Overlapping high-confidence interactions were few, but well-characterized. These high-confidence interactions might therefore be an indicator for well-characterized very stable interactions, which were unaffected by the treatment (Supporting Table 2). Those known and stable interactions mainly related to larger protein complexes, such as ribosomes, or protein complexes of the mitochondrial respiration chain. Specifically, the interactions not affected by the nutrient conditions included constituents of the mitochondrial ATP synthase, chaperonin complexes, ion transporters (mitochondrial ADP/ATP carrier AAC2, AT5G13490 and Voltage Dependent Anion Channel 2, VDAC2, AT5G67500) and redox systems (Cytochrome C1 and FRO1, AT1G01590). Since these interactions were detected independently of the treatment, they are likely to have been previously found in other experiments (i.e. confirmed by previous publications). By contrast, examples for novel (i.e. yet unconfirmed) high confidence interactions were among several LRR-receptor kinases and their substrates. Among these were co-receptor QIAN SHOU KINASE, QSK1 with CHITIN ELICITOR RECEPTOR KINASE 1 (CERK1, AT3G21630) or ABC-Transporter PEN3, AT1G59870. Since interactions of these proteins were found only under specific conditions, it is unlikely these interactions were described previously (i.e. they were

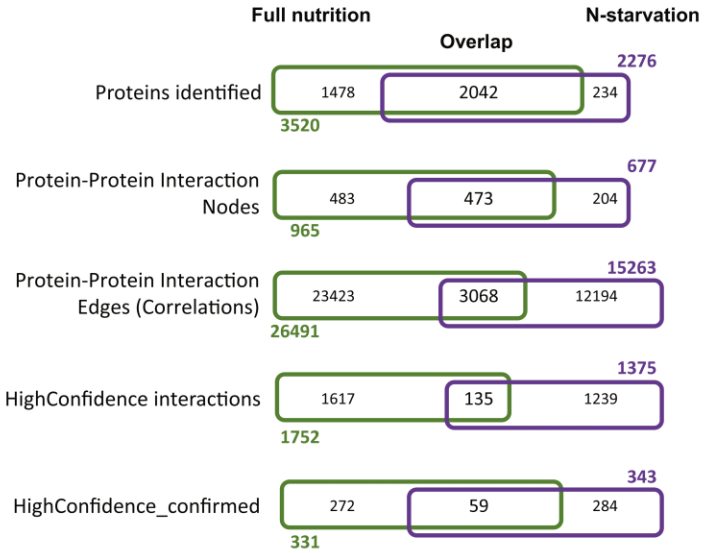

Fig. 2. Overlap of proteins identified and those considered as nodes of protein-protein interaction networks, as well as an overview of their edges in full nutrition and nitrogen starvation.

classified as unconfirmed). We conclude that high-confidence reproducible protein-protein interactions tend to depict those stable protein-protein interactions of larger protein complexes, while dynamic and conditional protein-protein interactions showed a tendency to affect the cellular signaling in pairwise interactions and smaller complexes. The detection of stable and reproducible protein-protein interactions can be seen as an indication that the cell is able to maintain basic functions, such as protein synthesis, photosynthesis and respiration, or ion homeostasis also under unfavorable conditions of nitrogen starvation. Our results indicate that dynamic interaction rewiring upon nitrogen

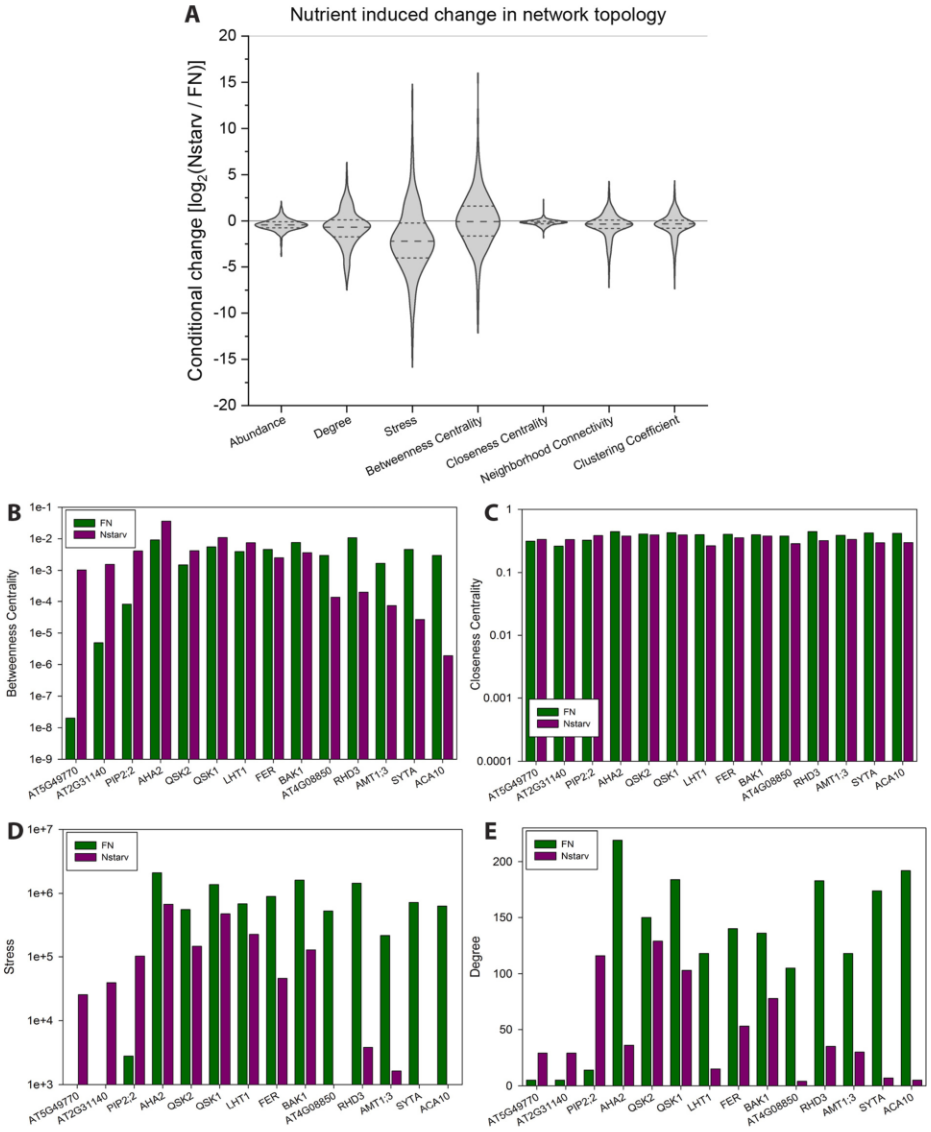

Fig. 3. Network dynamics full nutrition and nitrogen starvation. (**A**) Violin plots of nitrogen starvation-induced changes of network parameters. Each parameter is displayed as $\log_2$ ratio of the parameter in the nitrogen-starvation network to the parameter in the full nutrition network. For display of abundances, abundance categories (AC_{LFQ}) were inverse, since higher AC_{LFQ} indicates lower abundance. All network parameters beside Degree and Stress are normalized. Selected network parameters are displayed for individual proteins: (**B**) Betweenness Centrality, (**C**) Closeness Centrality, (**D**) Stresslevel, (**E**) Degree. Each parameters is displayed for the full nutrition network (green) and the nitrogen starvation network (purple). (For interpretation of the references to color in this figure legend, the reader is referred to the web version of this article.)

starvation seemed to more frequently affect interactions of proteins with signaling functions (MAPMAN [32] annotation category 'bin' 30) with proteins of cell organization (bin 31), within proteins of signaling functions (bin 30), within transporters (bin 34) and within protein of functions in protein modification, biosynthesis and degradation (bin 29) (Supporting Table S2). As expected, degree distribution of reconstructed protein-protein interaction networks under full nutrition as well as under nitrogen starvation followed a truncated power law [36] (Supporting Fig. S1C). Proteins of these stable complexes of respiratory chain and ribosomes were the proteins with highest degree in the protein-protein interaction network. (Supplementary Fig. S1)

3.3. Network dynamics induced by nitrogen starvation

As indicated above, the nodes of the protein-protein interaction network were defined based on their shifted retention behavior in the size-exclusion chromatography, and edges of the interaction network were derived from (i) pairwise correlations of elution profiles acquired by mass spectrometry and (ii) the requirement of being identified within a narrow window of neighboring elution fractions [37]. Application of this workflow to the full nutrition and nitrogen starvation data set resulted in a protein-protein interaction network in which nodes represent the proteins found with larger apparent size and edges indicate interactions present either at full nutrient supply (Supporting Fig. S2A, green edges) or at nitrogen starvation (Supporting Fig. S2A, purple edges). The network contains two large interaction domains, one dominated by plasma membrane proteins and the other dominated by proteins of cytosolic location. Interactions between proteins of the mitochondrial respiratory chain grouped more distantly from the plasma membrane and cytosolic proteins as revealed by the Mcode algorithm [38].

Examples for proteins with highly dynamic interaction partners are co-receptor SERK3/BAK1 (AT4G33430) (Supporting Fig. S2B), which was found to interact with receptor kinase FER under full nutrition, but under nitrogen starvation switched to an interaction preference with BAK1-Interacting Receptor Kinase 2 (BIR2, AT3G28450), Impaired Oomycete Susceptibility 1 (IOS1, AT1G51800) and AT5G49760. (Supplementary Fig. S2)

To obtain a more unbiased view of the dynamic processes induced by nitrogen starvation, we specifically compared network topology parameters. Degree describes the number of interactions of each node. Average Shortest Path describes the average number of steps along the shortest paths for all possible pairs of each node. Closeness Centrality is a measure of centrality of a node within a network and Betweenness Centrality describes the frequency at which a given node occurs among all the possible shortest paths. Stresslevel describes the number of shortest paths leading through a given node. Comparing the nitrogen starvation network with the full nutrition network, it became apparent that nitrogen starvation induced large overall changes in Degree and Stresslevel, indicating a change in overall network size (Fig. 3A). Stresslevel and Betweenness Centrality were the two paramters with largest scatter in the magnitudes of changes induced by nitrogen starvation (Fig. 3A). This indicates that nitrogen starvation induced changes in the utilization of distinct paths during information flow through the network. Among the proteins with strongest increase in Betweenness Centrality in response to nitrogen starvation were protein kinase AT5G49770, a peptidase AT3G55600, respiratory burst oxidase RbohD (AT5G47910), aquaporin PIP2;2 (AT2G37170), and plasma membrane ATPase AHA2 (AT4G30190) (Fig. 3B). Proteins with a strong decrease in Betweenness Centrality upon nitrogen starvation were calcium ATPase ACA10 (AT4G29900), a synaptogamin SYTA (AT2G20990), ammonium transporter AMT1;3 (AT3G24300), GTP binding protein Root Hair Deficient (RHD3, AT3G13870), and receptor kinase MDIS1-Interacting Receptor Like Kinase 2 (MIK2, AT4G08850) (Supporting Table 3). As already indicated above, Closeness Centrality was unaffected by the nutrient condition (Fig. 3C). Stresslevel was correlated with Betweenness Centrality, thus proteins with a strong change in Betweenness Centrality also displayed an equally strong increase or decrease in Stresslevel (Fig. 3D). A strong decrease in degree was particularly observed for proteins which showed a decreased Betweenness Centrality upon nitrogen starvation, particularly ammonium transporter AMT1;3, Synaptogamin A (SYTA), and calcium ATPase ACA10 (Fig. 3E). Fig. 3:

To test the hypothesis of dynamic adjustments in cellular networks by interaction rewiring and altered path utilization, we analyzed the protein-protein interaction network of nitrogen starved roots re-supplied with 2 mM nitrate. By nitrogen re-supply, the network status is expected to restore similarly to the status found under full nutrition. Upon nitrate resupply, we identified 1746 nodes of the protein-protein interaction network. Interestingly, resupply of 2 mM nitrate (Supporting Table 4) to the roots of nitrate starved plants indeed resulted in partial recovery of the interaction network after 15 min. The overall pattern of protein-protein interactions and network parameters was again shifted towards the status at full nutrition. For example, there was a higher overlap of high-confidence interactions predicted for nitrogen resupply with interactions predicted for full nutrition than for interactions predicted under nitrogen resupply with interactions predicted at nitrogen starvation (Fig. 4A). On a more global scale, proteins with increased BC values under N-starvation were enriched for signaling proteins ($p = 0.023$), transport proteins ($p = 9.3*10^{-3}$), lipid metabolism ($p = 0.041$) and proteins in TCA cycle ($p = 2.08*10^{-3}$). Signaling proteins were also enriched ($p = 2.5*10^{-3}$) in proteins with decreased BC valued upon nitrogen starvation, suggesting that indeed signaling proteins are frequently involved in rewiring of information flow in biological networks. Fig. 4:

Moreover, changes in betweenness centrality (BC) induced by nitrogen starvation were inversely proportional to changes induced by nitrate resupply (Fig. 4B). Thus, for a large number of proteins, opposite changes in network path utilization were induced by nitrogen starvation and nitrate resupply. Specifically, these changes affected vesicle trafficking processes, transporters and signaling proteins: For example, the interaction of different SNARE proteins with transporters, such as Early Response To Dehydration 6 (AT1G08930, ERD6) or Sugar Transporter 1 (AT1G11260, STP1), the coatomer complex, or the confirmed interaction of two glutamine synthase proteins GSR2 (AT1G66200) and GLN1.3 (AT3G17820) (Supporting Table 4).

We used randomly generated networks of the same size as the full nutrition interaction network and nitrogen starvation network (Supporting Fig. S3A) to confirm that changes in BC induced by nitrogen starvation or resupply were due to non-random biological effects. In the random network the variation of BC values across proteins was far lower than in the biological network (Supporting Fig. S3B). We conclude that strong changes in BC for individual proteins, such as AT5G49770, were indeed due to different path usage and not due to random effects. (Supplementary Fig. S3)

In our analysis, the nitrate transporters NRT1.1 (AT1G12110) and NRT2.1 (AT1G08090) were among those proteins which were identified with low reproducibility between replicates, and were thus excluded from the large-scale comparative network analysis of centrality indices. NRT1.1 was found as a protein-protein interaction node in two replicates in the full nutrition data set, while NRT2.1 was found as a protein-protein interaction node only in one replicate under nitrate starvation. Nevertheless, nitrate transporters connected to the cellular network, for example through a high confidence interaction found between QSK1 and NRT1.1, or between PERK1 and NRT2.1 (Fig. 4C).

3.4. Specific nitrogen-starvation-induced regulatory modules

Receptor kinase AT5G49770 showed strongest changes in BC-values upon nitrogen starvation (Fig. 3B) and this was reverted upon nitrate resupply. Therefore, we hypothesized that this kinase could have a key role in the adjustment of cellular networks in the response to nitrogen

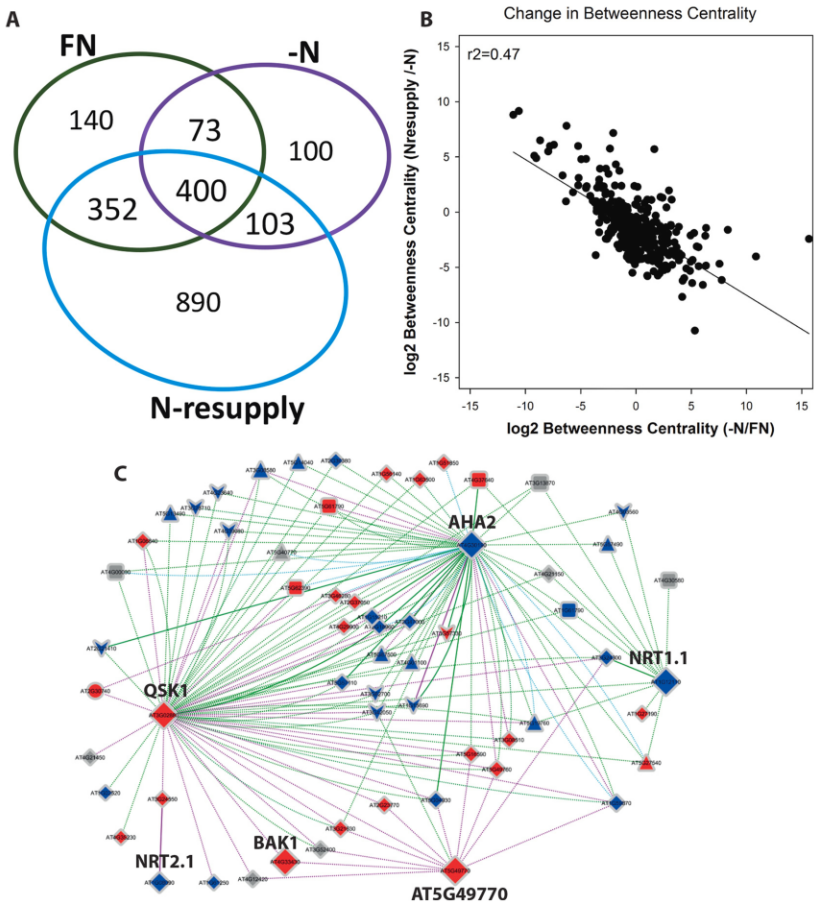

Fig. 4. Network dynamics in response to nutrient conditions. (**A**) Overlap of protein complex candidates predicted for the three nutrient conditions. In full nutrition (FN) and nitrogen starvation (—N) the complex candidates were derived from the overlap of two biological replicates, for N-resupply only one replicate was considered. (**B**) Change in Betweenness Centrality upon nitrogen starvation and nitrogen resupply. (**C**) Detailed network dynamics of nodes AHA2 (AT4G30190), receptor kinase AT5G49770, co-receptor QSK1 (AT3G02880) and nitrate transporters NRT1.1 and NRT2.1. Edge color represents nutrient status: green, full nutrition; purple, nitrogen starvation; cyan; nitrate resupply after starvation. Solid edges represent confirmed interactions based on public literature, dotted edges represent unconfirmed interactions. Node color represents protein function: blue, transporters; red, signaling proteins. Node size reflects betweenness centrality value changes. (For interpretation of the references to color in this figure legend, the reader is referred to the web version of this article.)

starvation. The reconstructed interaction networks proposed an interaction of AT5G49770 with a co-receptor QSK1 (AT3G02880) specifically under nitrogen starvation. The plasma membrane ATPase AHA2 (AT4G30190), which is well known to be activated under nitrogen starvation to allow enhanced uptake of nitrate ions, was also connected to the two kinases AT5G49770 and QSK1 (Fig. 4C, Supporting Table 5). QSK1 as a coreceptor in the reconstructed networks showed direct high-confidence interactions with receptor kinase AT5G49770, NRT1.1, and BAK1. The interaction of QSK1 with AHA2 was considered as low-confidence interaction under full nutrition and the interaction of AT5G49770 with BAK1 as found as low-confidence interaction at nitrate starvation (Fig. 4C).

We next confirmed selected pairs of these proposed interactions in the network by co-immunoprecipitation or FLIM-FRET experiments. Firstly, pull-downs of QSK1-GFP in comparison to GFP only at re-supply of 0.2 mM nitrate after nitrogen starvation revealed high-confidence interactions of QSK1 with AT5G49770, NRT1.1 and BAK1, but also with AHA2 (Fig. 5A). Secondly, FLIM-FRET experiments were performed to test interaction of QSK1 with AHA2 and BAK1, as well as of AT5G49770 with AHA2 (Fig. 5B, Supplementary Fig. S4:). In cases where no interactions should take place (donor-GFP alone controls), the fluorescent lifetime is expected to be higher than for those protein pairs which show an interaction (Fig. 5B). QSK1 and BAK1 were found to interact with significant difference to the respective control, while for low-confidence interaction of QSK1 with AHA2, the fluorescent lifetime was found in between the control and the high-confidence interactor. The interaction of AT5G49770 with AHA2, which was not proposed as direct interaction in the network reconstruction, was used as a control of a negative interaction with fluorescent lifetime values not different from the respective control (Fig. 5B). The FLIM-FRET experiments very well

reflected the interactions proposed by our SEC-MS analytical workflow: QSK1, BAK1 and AT5G49770 show strong correlations in their elution profiles (Supplementary Fig. S5), while plasma membrane ATPase AHA2 showed a different elution profile which did not suggest direct interaction with QSK1 or AT5G49770. Fig. 5:

We next confirmed selected pairs of these proposed interactions in the network by co-immunoprecipitation or FLIM-FRET experiments. Firstly, pull-downs of QSK1-GFP in comparison to GFP only at re-supply of 0.2 mM nitrate after nitrogen starvation revealed high-confidence interactions of QSK1 with AT5G49770, NRT1.1 and BAK1, but also with AHA2 (Fig. 5A). Secondly, FLIM-FRET experiments were performed to test interaction of QSK1 with AHA2 and BAK1, as well as of AT5G49770 with AHA2 (Fig. 5B, Supplementary Fig. S4). In cases where no interactions should take place (donor-GFP alone controls), the fluorescent lifetime is expected to be higher than for those protein pairs which show an interaction (Fig. 5B). QSK1 and BAK1 were found to interact with significant difference to the respective control, while for low-confidence interaction of QSK1 with AHA2, the fluorescent lifetime was found in between the control and the high-confidence interactor. The interaction of AT5G49770 with AHA2, which was not proposed as direct interaction in the network reconstruction, was used as a control of a negative interaction with fluorescent lifetime values not different from the respective control (Fig. 5B). The FLIM-FRET experiments very well reflected the interactions proposed by our SEC-MS analytical workflow: QSK1, BAK1 and AT5G49770 show strong correlations in their elution profiles (Supplementary Fig. S5), while plasma membrane ATPase AHA2 showed a different elution profile which did not suggest direct interaction with QSK1 or AT5G49770. Fig. 5:

Based on their strong N-starvation induced changes betweenness centrality, we propose receptor kinase AT5G49770, and to some extent also co-receptor QSK1, and proton ATPase AHA2 to be directly or indirectly involved in rewiring of the cellular signaling network in response to nitrogen starvation. Therefore, we studied the knock-out mutants of these genes for nitrogen related root growth phenotypes. Knock-out mutants of high-affinity nitrate transporter *NRT2.1* and dual-affinity transporter *NRT1.1* were used as controls. Primary root growth and lateral root density was observed on growth assay under nitrogen starvation (0 mM KNO_3), low nitrate supply (0.3 mM KNO_3) or high nitrate supply (5 mM KNO_3).

As expected, primary root growth in wild type was reduced by nitrate starvation and low nitrate supply (Fig. 6A). The nitrate transporter mutants *nrt1.1* and *nrt2.1* showed higher than wild type root growth under nitrate starvation and significantly lower than wild type primary root growth at high nitrate supply. The general pattern of higher than wild type primary root growth at nitrate starvation and lower than wild type primary root growth at high nitrate supply was observed also in knock-out mutants of receptor kinase *at5g40770* and co-receptor *qsk1*. By contrast, *aha2* knock-out mutants had lower than wild type primary root growth under all conditions (Fig. 6B). Fig. 6:

For lateral roots, in wild type an increased lateral root density was found at low nitrate supply and lower lateral root densities were observed under nitrate starvation and high nitrate (Fig. 6C). The *nrt2.1* mutant displayed very high lateral root density at low nitrate supply and low lateral root density at high nitrate supply. This is in agreement with literature, at least when sucrose is supplied to the agar plates [39]. Mutants of receptor kinase *at5g40770* and co-receptor *qsk1* also regarding lateral root density resembled the phenotype of *nrt2.1* suggesting involvement in regulation of nitrate uptake through NRT2.1 (Fig. 6D). Mutants of *aha2* had lower than wild type lateral root density especially at high nitrate supply. These root growth experiments suggest, that although AT5G49770 can interact with QSK1 and BAK1, and co-receptor QSK1 can interact with AHA2 (Fig. 5A), the specific roles of the three proteins in nitrate responses may be quite different. We propose At5G40770 to act together with QSK1 and BAK1, possibly as receptor-co-receptor pairs to regulate nitrate uptake through NRT2.1 and NRT1.1, and to regulate proton export necessary for nitrate uptake

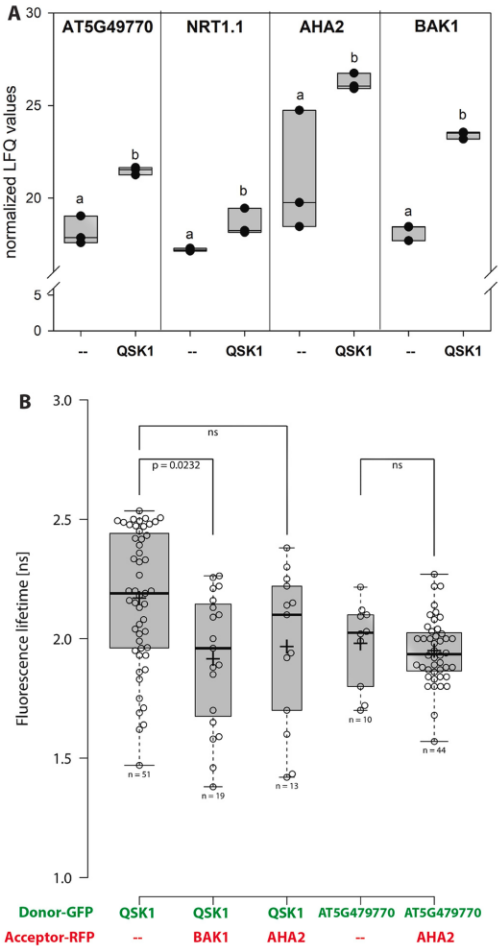

Fig. 5. Confirmation of proposed interaction pairs. (**A**) Pulldowns of bait QSK1 (QSK1-GFP) identified AT5G49770, NRT1.1, AHA2 and BAK1 as interactors to QSK1 compared to pulldowns with GFP alone (--). Small letters indicate significant differences ($p < 0.05$) of protein LFQ values in pulldowns with QSK1-GFP compared to GFP-only control. Boxplots of three independent experiments are shown, individual LFQ-values of three replicates are shown as black dots. (**B**) FRET-FLIM experiments for selected protein pairs. Box plots of fluorescent lifetime for each donor-GFP and acceptor-RFP pair are shown. Donor-GFP constructs without acceptor-RFP (--) were used as negative controls.

through AHA2. However, root growth in general is a complex trait involving not only direct responses to nutrients and the respective signaling pathways, but also proton pump activity [40] and gating of water channels [41]. Thus, it is to no surprise that the knock-out mutant of the most abundant H^+-ATPase in roots, *aha2*, shows a more severe root growth phenotype irrespective of the nitrate environment.

4. Discussion

We studied the response of cellular protein-protein interaction networks to changes in nitrogen availability, regarding protein abundance

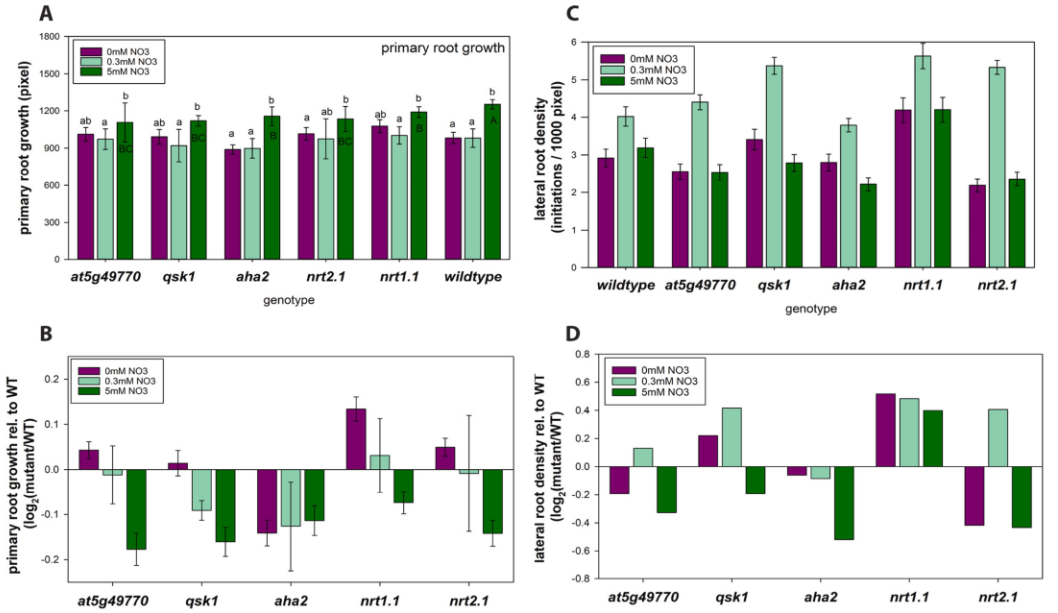

Fig. 6. Root growth phenotypes of selected mutants based on their betweenness centrality value changes upon nitrogen starvation. (**A**) Primary root growth, (**B**) Primary root growth relative to wild type, (**C**) Lateral root growth, (**D**) Lateral root growth relative to wild type. Seedlings were grown on agar plates without nitrate for one week and transferred to new plates without nitrogen (0 mM, nitrogen starvation), low nitrate (0.3 mM) or high nitrate (5 mM). All plates contained 30 mM sucrose. Averages of at least 40 seedlings are shown with standard deviations. For ratios, standard deviations were obtained by 10 bootstrapping iterations of random ratios.

as well as rewiring of protein-protein interactions. We used network topology parameters to define the most relevant proteins within the interaction network governing these changes.

4.1. Protein abundances and their variation

Abundance variations of proteins were thoroughly investigated regarding technical and biological variations, confirmed substantial quantitative variability for some proteins [42]. However, variability in protein abundance between biological replicates has been described to be slightly lower than variations introduced by the technical component, and the majority of proteins was not affected by treatments [42]. In our experiments, for most proteins nitrogen starvation induced a reduction in protein abundance category, even when considering only those proteins with low variability between replicates. This is to be expected from generally lower protein content in nitrate starved plants [43,44]. We observed that proteins with highly reproducible abundance levels between biological replicates were also those proteins which showed no strong abundance changes upon nitrogen starvation. It must be kept in mind that we compare changes in abundance categories. Thus, it can happen that a protein remains within the same abundance category, despite its actual change in abundance. In turn, proteins may change their abundance category mainly due to large abundance changes of other proteins.

Thus, the requirement for reproducibility between biological replicates filtered for those proteins, which seemed to have stable abundances under different cellular conditions. In turn, proteins with showed stronger abundance variability between replicates were tentatively filtered out as “non-reproducible”. However, these “variable” proteins were also those, which showed high response to the nitrogen starvation treatment. This indicates that the cellular protein network indeed is in a dynamic equilibrium of protein abundances and their interactions. Environmental changes – such as nitrogen starvation – can push the system into a new equilibrium, in which protein abundances and their interactions are adjusted to the new conditions. Since these adjustments are a constant process depending on external and internal status of the plant, regulatory proteins showed a tendency to be among the more variable proteins also in comparisons between biological replicates. Protein abundances were also previously reported to respond to nitrate starvation to a similar magnitude as transcriptional changes [13].

4.2. Network topology parameters to identify key nodes in network rewiring

Following workflows established in social sciences [45,46], we used network topology parameters to identify nodes which could have a key role in regulation of information flow within the networks. In network analysis, certain parameters emerged aiming to describe overall network structure (e.g. modularity or clusters) and functional relevance of nodes and edges. These network parameters are based on intuitive conceptions of node connectivity, since the influence of each node is mainly defined by the direct or indirect neighborhood. The general assumption then is that a node, which lies within the center of a network, is also of high relevance to network structure and/or information flow.

To describe node centrality, different centrality indices have been introduced for the use in biological networks [47], which are mainly distinguished by their metric. Neighborhood based centralities such as “Degree Centrality” or “Clustering Centrality” are based on the degree of a node. Other measures of centrality like “Closeness Centrality” or “Betweenness Centrality” are path-based metrics, which rely on the

distances of nodes. Identifying vital nodes of the network largely depends on the criteria that are used to define "importance". In biological networks, signaling pathways contain key regulator proteins which control signal transduction processes. Therefore, we decided to focus mainly on path-based centrality measures since they can be used to define the ability of each node to exert influence on the flow of information. However, the original definition of centrality measures have some shortcomings when trying to apply these principles to biological networks. Mainly, in biological networks, there might be some hubs or sub-networks that are not connected to each other. In this case, CC cannot be calculated, since $\sigma_{ij} = \infty$. These separated hubs can occur as a result of biological relevance (e.g. multiple self-sufficient protein-protein interaction complexes) or missing data. In addition, because BC is sensitive towards local topology, BC is more affected by missing data or random errors in edge-distribution than degree-based centrality measures [48]. On the other hand, because of its sensitivity, BC is most suited to observe true changes in network connectivity and node importance. Although the centrality indices like closeness centrality and betweenness centrality are prone to systematical error, the actual performance is also dependent on the underlying dataset. In direct comparison, CC and BC are quite robust in randomly generated ("sampled") and perturbed networks, while the variability is higher in real life networks with randomly introduced errors [49]. This can be explained by the fact that perturbations of network topology have far more influences on CC and BC than sampling level alone. In consequence, performance is quite robust in real life networks which only showed errors in randomly selected sub-samples. In our experiments, the "true" networks show clear non-random changes in BC upon changes of nitrogen conditions (Supporting Fig. S3).

This indicates that network properties can still be used to describe dynamic processes in networks, even if there are inaccuracies in the data or general variability between samples exists [49,50]. We here used BC as a measure of the relevance of nodes in network rewiring induced by nitrate starvation or nitrate resupply. A member of the LRR receptor kinase family (AT5G49770) was identified as a candidate key regulator at low nitrate supply and nitrate starvation. Nitrate-dependent root growth analysis confirmed the involvement of AT5G49770 in nitrate-related processes. In that regards, it is important to note that nitrate resupply for 15 min did not fully recover the proteome status to the full nutrition condition. In general, based on previous nitrogen starvation experiments, despite a large overlap of responsive (phospho)proteins, the response to nitrate starvation was not found fully opposite to the response to nitrate resupply after starvation [13].

Furthermore, our data suggest a close connection between protein function and protein interaction stability. Stable and reproducible protein-interactions found in several experimental conditions seemed biased towards proteins that were not associated to the specific stress response but had basic homeostatic functions in processes such as protein synthesis, photosynthesis and respiration. Proteins associated to signaling and cellular organization showed higher variability in their interactions. One possible explanation could be that proteins associated with basic cellular function are often stable also regarding long term gene expression homeostasis which is why they are often used as reference genes/proteins ("house-keeping genes"). Signaling processes on protein level are more short lived and dynamic protein interactions, and their abundance is often also subject to control by gene expression.

In conclusion, we here present a strategy involving path-based centrality measures to describe dynamic rewiring of cellular protein-protein interaction networks in response to external stimuli. This approach identified AT5G49770 as a novel player in nitrate-induced responses, which was corroborated by phenotypic analysis. We expect the use of path-based centrality measures to be a powerful strategy also in the analysis of dynamic responses of cellular networks to other stresses and stimuli.

Supplementary data to this article can be found online at https://doi.org/10.1016/j.jprot.2021.104114.

Data availability

Data has been made available in public repositories mentioned in the methods section

Acknowledgements

Research in our laboratories was supported by the German Research Foundation (DFG) with grants to MG, WS and KH (HA 2146/23-1 and SCHU1533/11-1).

Author contributions

MG performed the proteomics experiments, data analysis, and network analysis, and wrote the manuscript. **ZL** contributed unpublished materials (constructs). **XNW** contributed pull-down data sets. **LR** perfomed FRET/FLIM experiments. **SG** performed root growth assays. **KH** interpreted the FRET/FLIM experiments and participated in writing of the manuscript. **WXS** conceived the study, was involved in data interpretation and wrote the manuscript.

References

[1] F. Demir, C. Hontrich, J.O. Blachutzik, S. Scherzer, Y. Reinders, S. Kierszniowska, et al., Arabidopsis nanodomain-delimited ABA signaling pathway regulates the anion channel SLAH3, Proc. Natl. Acad. Sci. U. S. A. 110 (2013) 8296–8301.
[2] M. Haruta, W.M. Gray, M.R. Sussman, Regulation of the plasma membrane proton pump (H-ATPase) by phosphorylation, Curr. Opin. Plant Biol. 28 (2015) 68–75.
[3] A.T. Fuglsang, A. Kristensen, T. Cuin, W.X. Schulze, J. Persson, K.H. Thuesen, et al., Receptor kinase mediated control of primary active proton pumping at the plasma membrane, Plant J. 80 (2014) 951–964.
[4] M. Haruta, G. Sabat, K. Stecker, B.B. Minkoff, M.R. Sussman, A peptide hormone and its receptor protein kinase regulates plant cell expansion, Science. 343 (2014) 408–411.
[5] S. Fields, O. Song, A novel genetic system to detect protein-protein interactions, Nature. 340 (1989) 245–246.
[6] M.O. Collins, J.S. Choudhary, Mapping multiprotein complexes by affinity purification and mass spectrometry, Curr Opin Biotech. 19 (2008) 324–330.
[7] X.N. Wu, L. Chu, L. Xi, H. Pertl-Obermeyer, Z. Li, K. Sklodowski, et al., Sucrose-induced receptor kinase 1 is modulated by an interacting kinase with short extracellular domain, Molecular & cellular proteomics : MCP. 18 (2019) 1556–1571.
[8] J. Van Leene, H. Stals, D. Eeckhout, G. Persiau, E. Van Slijke, G. Van Isterdael, et al., A tandem affinity purification-based technology platform to study the cell cycle interactome in Arabidopsis thaliana, Mol. Cell. Proteomics 6 (2007) 1226–1238.
[9] J. Bellati, C. Champeyroux, S. Hem, V. Rofidal, G. Krouk, C. Maurel, et al., Novel aquaporin regulatory mechanisms revealed by Interactomics, Molecular & cellular proteomics : MCP. 15 (2016) 3473–3487.
[10] W.R. Scheible, R. Morcuende, T. Czechowski, C. Fritz, D. Osuna, N. Palacios-Rojas, et al., Genome-wide reprogramming of primary and secondary metabolism, protein synthesis, cellular growth processes, and the regulatory infrastructure of Arabidopsis in response to nitrogen, Plant Physiol. 136 (2004) 2483–2499.
[11] G. Krouk, P. Mirowski, Y. LeCun, D.E. Shasha, G.M. Coruzzi, Predictive network modeling of the high-resolution dynamic plant transcriptome in response to nitrate, Genome Biol. 11 (2010) R123.
[12] W.R. Engelsberger, W.X. Schulze, Nitrate and ammonium lead to distinct global dynamic phosphorylation patterns when resupplied to nitrogen starved Arabidopsis seedlings, Plant J. 69 (2012) 978–995.
[13] J. Menz, Z. Li, W. Schulze, U. Ludewig, Early nitrogen-deprivation responses in Arabidopsis roots reveal distinct differences on transcriptome and (phospho-) proteome levels between nitrate and ammonium nutrition, Plant J. 88 (2016) 717–734.
[14] M. Gilbert, W.X. Schulze, Global identification of protein complexes within the membrane proteome of Arabidopsis roots using a SEC-MS approach, J. Proteome Res. 18 (2019) 107–119.
[15] B. Schlesier, A. Berna, F. Bernier, H.P. Mock, Proteome analysis differentiates between two highly homologues germin-like proteins in Arabidopsis thaliana ecotype Col-0 and Ws-2, Phytochem. 65 (2004) 1565–1574.
[16] H. Pertl, M. Himly, R. Gehwolf, R. Kriechbaumer, D. Strasser, W. Michalke, et al., Molecular and physiological characterisation of a 14-3-3 protein from lily pollen grains regulating the activity of the plasma membrane H+ ATPase during pollen grain germination and tube growth, Planta. 213 (2001) 132–141.
[17] H. Pertl-Obermeyer, O. Trentmann, K. Duscha, H.E. Neuhaus, W.X. Schulze, Quantitation of vacuolar sugar transporter abundance changes using QconCAT Synthtetic peptides, Front. Plant Sci. 7 (2016) 411.
[18] X.N. Wu, W.X. Schulze, Phosphopeptide profiling of receptor kinase mutants, Methods Mol. Biol. 1306 (2015) 71–79.
[19] T. Arnold, D. Linke, The use of detergents to purify membrane proteins, Current protocols in protein science 53 (2008) 4.8.1–4.8.30.

[20] A.M. Seddon, P. Curnow, P.J. Booth, Membrane proteins, lipids and detergents: not just a soap opera, Biochim. Biophys. Acta 2004 (1666) 105–117.
[21] J. Cox, M. Mann, MaxQuant enables high peptide identification rates, individualized p.p.b.-range mass accuracies and proteome-wide protein quantification, Nature Biotechnol. 26 (2008) 1367–1372.
[22] J. Cox, M.Y. Hein, C.A. Luber, I. Paron, N. Nagaraj, M. Mann, Accurate proteome-wide label-free quantification by delayed normalization and maximal peptide ratio extraction, termed MaxLFQ, Mol. Cell. Proteomics 13 (2014) 2513–2526.
[23] J.A. Vizcaíno, R.G. Côté, A. Csordas, J.A. Dianes, A. Fabregat, J.M. Foster, et al., The PRoteomics IDEntifications (PRIDE) database and associated tools: status in 2013, Nucleic Acids Res. 41 (2013). D1063-D9.
[24] D. Szklarczyk, J.H. Morris, H. Cook, M. Kuhn, S. Wyder, M. Simonovic, et al., The STRING database in 2017: quality-controlled protein-protein association networks, made broadly accessible, Nucleic Acids Res. 45 (2017). D362-D8.
[25] A.M. Jones, Y. Xuan, M. Xu, R.-S. Wang, C.H. Ho, S. Lalonde, et al., Border control - a membrane-linked interactome of Arabidopsis, Science. 344 (2014) 711–716.
[26] A. Bavelas, Communication patterns in task-oriented groups, The Journal of the Acoustical Society of America. 22 (1950) 725–730.
[27] L.C. Freeman, Centrality in social networks conceptual clarification, Soc. Networks 1 (1978) 215–239.
[28] E. Ravasz, A.L. Somera, D.A. Mongru, Z.N. Oltvai, A.L. Barabasi, Hierarchical organization of modularity in metabolic networks, Science. 297 (2002) 1551–1555.
[29] X. Wu, C. Sanchez-Rodriguez, H. Pertl-Obermeyer, G. Obermeyer, W.X. Schulze, Sucrose-induced receptor kinase SIRK1 regulates a plasma membrane aquaporin in Arabidopsis, Mol. Cell. Proteomics 12 (2013) 2856–2873.
[30] A. Hecker, N. Wallmeroth, S. Peter, M.R. Blatt, K. Harter, C. Grefen, Binary 2in1 vectors improve in planta (co)localization and dynamic protein interaction studies, Plant Physiol. 168 (2015) 776–787.
[31] M. Veerabagu, K. Elgass, T. Kirchler, P. Huppenberger, K. Harter, C. Chaban, et al., The Arabidopsis B-type response regulator 18 homomerizes and positively regulates cytokinin responses, The Plant journal : for cell and molecular biology. 72 (2012) 721–731.
[32] O. Thimm, O. Bläsing, Y. Gibon, A. Nagel, S. Meyer, P. Kruger, et al., MAPMAN: a user-driven tool to display genomics data sets onto diagrams of metabolic pathways and other biological processes, Plant J. 37 (2004) 914–939.
[33] S.K. Tanz, I. Castleden, C.M. Hooper, M. Vacher, I. Small, H.A. Millar, SUBA3: a database for integrating experimentation and prediction to define the SUBcellular location of proteins in Arabidopsis, Nucleic Acids Res. 41 (2013) D1185–D1191.
[34] R.L. Poole, The TAIR database, Methods Mol. Biol. 406 (2007) 179–212.
[35] P. Shannon, A. Markiel, O. Ozier, N.S. Baliga, J.T. Wang, D. Ramage, et al., Cytoscape: a software environment for integrated models of biomolecular interaction networks, Genome Res. 13 (2003) 2498–2504.
[36] J. Alstott, E. Bullmore, D. Plenz, Powerlaw: a Python package for analysis of heavy-tailed distributions, PLoS One 9 (2014), e85777.
[37] G.A. Gilbert, M.V. Gadush, C. Wilson, M.A. Madore, Amino acid accumulation in sink and source tissues of *Coleus blumei* Benth. During salinity stress, J. Exp. Bot. 49 (1998) 107–114.
[38] G.D. Bader, C.W. Hogue, An automated method for finding molecular complexes in large protein interaction networks, BMC Bioinformatics. 4 (2003) 2.
[39] D.Y. Little, H. Rao, S. Oliva, F. Daniel-Vedele, A. Krapp, J.E. Malamy, The putative high-affinity nitrate transporter NRT2.1 represses lateral root initiation in response to nutritional cues, in: Proceedings of the National Academy of Sciences of the United States of America 102, 2005, pp. 13693–13698.
[40] E. Mlodzinska, G. Klobus, M.D. Christensen, A.T. Fuglsang, The plasma membrane H(+) -ATPase AHA2 contributes to the root architecture in response to different nitrogen supply, Physiol. Plant. 154 (2015) 270–282.
[41] B. Péret, G. Li, J. Zhao, L.R. Band, U. Voß, O. Postaire, et al., Auxin regulates aquaporin function to facilitate lateral root emergence, Nat. Cell Biol. 14 (2012) 991–998.
[42] M.R. Al Shweiki, S. Monchgesang, P. Majovsky, D. Thieme, D. Trutschel, W. Hoehenwarter, Assessment of label-free quantification in discovery proteomics and impact of technological factors and natural variability of protein abundance, J. Proteome Res. 16 (2017) 1410–1424.
[43] G. Krouk, N.M. Crawford, G.M. Coruzzi, Y.F. Tsay, Nitrate signaling: adaptation to fluctuating environments, Curr. Opin. Plant Biol. 13 (2010) 266–273.
[44] A. Melzer, G. Gebauer, H. Rehder, Nitrate content and nitrate reductase activity in *Rumex obtusifolius* L. II. Responses to nitrate starvation and nitrogen fertilization, Oecologia. 63 (1984) 380–385.
[45] M.E. Sardiu, J.M. Gilmore, B. Groppe, L. Florens, M.P. Washburn, Identification of topological network modules in perturbed protein interaction networks, Sci. Rep. 7 (2017) 43845.
[46] M.E. Sardiu, J.M. Gilmore, B.D. Groppe, A. Dutta, L. Florens, M.P. Washburn, Topological scoring of protein interaction networks, Nat. Commun. 10 (2019) 1118.
[47] M. Jalili, A. Salehzadeh-Yazdi, S. Gupta, O. Wolkenhauer, M. Yaghmaie, O. Resendis-Antonio, et al., Evolution of centrality measurements for the detection of essential proteins in biological networks, Front. Physiol. 7 (2016) 375.
[48] J.M. Bolland, Sorting out centrality: an analysis of the performance of four centrality models in real and simulated networks, Soc. Networks 10 (1988) 233–253.
[49] E. Costenbader, T.W. Valente, The stability of centrality measures when networks are sampled, Soc. Networks 25 (2003) 283–307.
[50] Q. Niu, A. Zeng, Y. Fan, Z. Di, Robustness of centrality measures against network manipulation, Physica A: Statistical Mechanics and its Applications. 438 (2015) 124–131.

PEP7 acts as a peptide ligand for the receptor kinase SIRK1 to regulate aquaporin-mediated water influx and lateral root growth

by Wang J., Xi L., Wu X. N., König S., Rohr L., Neumann T., Weber J., Harter K., Schulze W. X. (2022)

in *Molecular Plant*

doi: https://doi.org/10.1016/j.molp.2022.09.016

Accepted

Molecular Plant
Research Article

CellPress
Partner Journal

PEP7 acts as a peptide ligand for the receptor kinase SIRK1 to regulate aquaporin-mediated water influx and lateral root growth

Jiahui Wang[1,4], Lin Xi[1,4], Xu Na Wu[1,2], Stefanie König[1], Leander Rohr[3], Theresia Neumann[1], Jan Weber[1], Klaus Harter[3] and Waltraud X. Schulze[1,*]

[1]Department of Plant Systems Biology, University of Hohenheim, 70593 Stuttgart, Germany

[2]School of Life Science, Center for Life Sciences, Yunnan University, 650091 Kunming, People's Republic of China

[3]Center for Plant Molecular Biology, University of Tübingen, 72076 Tübingen, Germany

[4]These authors contributed equally to this article.

***Correspondence: Waltraud X. Schulze (wschulze@uni-hohenheim.de)**

https://doi.org/10.1016/j.molp.2022.09.016

ABSTRACT

Plant receptors constitute a large protein family that regulates various aspects of development and responses to external cues. Functional characterization of this protein family and the identification of their ligands remain major challenges in plant biology. Previously, we identified plasma membrane-intrinsic sucrose-induced receptor kinase 1 (SIRK1) and Qian Shou kinase 1 (QSK1) as receptor/co-receptor pair involved in the regulation of aquaporins in response to osmotic conditions induced by sucrose. In this study, we identified a member of the elicitor peptide (PEP) family, namely PEP7, as the specific ligand of th receptor kinase SIRK1. PEP7 binds to the extracellular domain of SIRK1 with a binding constant of 1.44 ± 0.79 μM and is secreted to the apoplasm specifically in response to sucrose treatment. Stabilization of a signaling complex involving SIRK1, QSK1, and aquaporins as substrates is mediated by alterations in the external sucrose concentration or by PEP7 application. Moreover, the presence of PEP7 induces the phosphorylation of aquaporins *in vivo* and enhances water influx into protoplasts. Disturbed water influx, in turn, led to delayed lateral root development in the *pep7* mutant. The loss-of-function mutant of SIRK1 is not responsive to external PEP7 treatment regarding kinase activity, aquaporin phosphorylation, water influx activity, and lateral root development. Taken together, our data indicate that the PEP7/SIRK1/QSK1 complex represents a crucial perception and response module that mediates sucrose-controlled water flux in plants and lateral root development.

Key words: receptor kinase, peptide signaling, receptor-ligand pair, sugar signaling, regulation of water influx

Wang J., Xi L., Wu X.N., König S., Rohr L., Neumann T., Weber J., Harter K., and Schulze W.X. (2022). PEP7 acts as a peptide ligand for the receptor kinase SIRK1 to regulate aquaporin-mediated water influx and lateral root growth. Mol. Plant. **15**, 1615–1631.

INTRODUCTION

Plants as sessile organisms must be able to rapidly adapt to altering environmental conditions throughout the diurnal cycle and during their life span. This requires precise integration of extracellular information with intracellular (metabolic) signals. This integration of environmental and developmental signals in plants is often controlled by small peptides that then activate signaling cascades through receptor kinases. Receptor kinases constitute the biggest subclade within the plant kinome (Zulawski et al., 2014). The plant receptor kinases are involved in plant developmental processes as well as in responses to biotic and abiotic cues (Osakabe et al., 2013).

The first peptide with signaling function discovered in plants was systemin (Pearce et al., 1991), which at that time was postulated to be perceived by a leucine-rich repeat (LRR)-family receptor kinase (Scheer and Ryan, 2002), and for which in 2018 indeed an LRR receptor kinase was identified as its receptor (Wang et al., 2018). Since then, more and more signaling peptides were discovered, which are involved in cell-to-cell communication, developmental processes, and stress responses (Matsubayashi, 2014; Tavormina et al., 2015;

Published by the Molecular Plant Shanghai Editorial Office in association with Cell Press, an imprint of Elsevier Inc., on behalf of CSPB and CEMPS, CAS.

Olsson et al., 2019). It is a characteristic of the small signaling peptides that they are mobile between cells. Thus, the site of their secretion may be different from the site of their perception. For example, peptide CLAVATA3 is recognized by an LRR-receptor kinase expressed in neighboring cell files (Clark et al., 1997). The peptides can even be translocated throughout the plant, as exemplified by the C-terminally encoded peptide family peptides, which are secreted by nitrogen-starved roots, but their receptors are located in the shoot (Tabata et al., 2014).

The biologically active peptides are defined as being smaller than 100 amino acids and usually undergo a process of maturation from larger precursor proteins (Tavormina et al., 2015; Olsson et al., 2019). Thus, the final active peptide is matured from its preproprotein through proteolytic processing by specific peptidases (Schaller et al., 2018). In many cases, this involves two steps: firstly, the cleavage of an N-terminal signal sequence necessary for secretion of the protein to the apoplasm, and secondly, release of the active peptide by cleavage of the prodomains. The peptides themselves are frequently subject to posttranslational modifications such as sulfatation, modification with sugar residues or hydroxyprolines (Matsubayashi, 2014). Formation of secondary structures through intramolecular disulfide bridges is a characteristic feature of cysteine-rich peptides, such as the rapid alkalinization factor (RALF) family (Moussu et al., 2020; Abarca et al., 2021). The process of peptide maturation has moved a variety of peptidase families into the focus of attention in the context of plant signaling pathways (Rautengarten et al., 2005). Subtilases were shown to be involved during maturation of the IDA peptide (Schardon et al., 2016), during biogenesis of TWS1 (Abarca et al., 2021), and also in phytosulfokine processing (Stührwohldt et al., 2021). Although it is apparent that receptor kinases are primary candidates for the recognition of a variety of biologically active peptides with signaling functions, for most of the receptor kinases, the precise ligand remains unknown. In turn, also for many biologically active peptides, the receptors remain to be identified (Matsubayashi, 2003). Thus, for a more complete understanding of the functional implications of plant receptor kinases, it is of high interest to identify and characterize ligand–receptor pairs.

In the past, our group has studied sucrose-induced protein phosphorylation in a time course experiment resupplying sucrose to sucrose-starved *Arabidopsis* seedlings (Niittylä et al., 2007). Based on this time course information, sucrose-dependent regulation of an aquaporin and sucrose-induced phosphorylation of the sucrose exporter SWEET11 by a protein complex involving sucrose-induced receptor kinase SIRK1 was discovered (Wu et al., 2013). As a follow up to this work, we recently showed that the SIRK1 signaling complex is stabilized by the co-receptor QSK1 (Wu et al., 2019b). Together, SIRK1 and QSK1 regulate aquaporins through phosphorylation. Since aquaporin phosphorylation status was shown to correlate with the plant hydraulic status (di Pietro et al., 2013), the SIRIK1 complex may affect water balance of root cells. However, the ligand of this SIRK1–QSK1 receptor complex remained unknown. We therefore conducted a series of biochemical and physiological experiments to identify PEP7 as the specific ligand of receptor kinase SIRK1.

RESULTS

Sucrose-induced receptor kinase (SIRK1) belongs to the LRR-receptor kinases (Zulawski et al., 2014). SIRK1 was found to be activated by an external supply of sucrose (Wu et al., 2013). It interacts with co-receptor Qian Shou kinase (QSK1) and, in the active state, regulates the opening status of aquaporins (Wu et al., 2019b). The majority of the LRR-receptor kinases for which a ligand is known so far were found to bind small peptide ligands. Therefore, we followed the hypothesis that also SIRK1 could bind a small peptide ligand.

Identification of SIRK1 ligand candidates

To systematically screen for a putative peptide ligand to SIRK1, we prepared apoplasmic protein extracts derived from wild-type liquid-grown *Arabidopsis* seedling cultures. Apoplasmic proteins were ultrafiltrated to exclude all protein components larger than 1 kDa and then separated into different fractions by reversed-phase chromatography (Figure 1A). Each fraction was tested for its ability to *in vitro* induce the kinase activity of SIRK1-GFP, which was enriched from root tissue of hydroponic cultures 2 days after sucrose starvation (Figure 1A). Kinase-active SIRK1–GFP (SIRK1–GFP_{suc}), which also contains interacting co-receptor QSK1 (Wu et al., 2019b), was enriched from sucrose-stimulated hydroponic cultures (Wu et al., 2013) and used as a positive control (Figure 1B). Exposure of sucrose alone to SIRK1–GFP enriched from sucrose starved plants (SIRK1–GFP_{starv}) was not able to induce SIRK1 activity (Figure 1B). By contrast, SIRK1–GFP_{stav} activity was highly induced after exposure to protein fraction F2 and, to a lesser extent, to protein fraction F1. Kinase activity was lowest upon exposure of SIRK1–GFP_{starv} to protein fraction F3 (Figure 1B). An aliquot of each fraction was analyzed by mass spectrometry. We performed two runs in parallel—one with standard protocol including trypsin digestion, and one without prior tryptic digestion—in case the ligand candidates would not yield suitable tryptic peptides. Altogether, in fraction F1, we identified 1531 proteins, in fraction F2 4106 proteins, and in fraction F3 440 proteins. Among the identified proteins, we then selected those candidate proteins that were present with spectral counts higher than three in fractions F1 and F2 and that were not present (no spectra) in fraction F3. A total of 30 identified proteins were predicted to be secreted proteins, and 14 of these met the requirements of high abundance in fractions F1 and F2 but not in fraction F3 (Figure 1C). Two of these candidate proteins were also identified in the non-tryptic samples, namely RALF1 (AT1G02900) and PEP7 (AT5G09978). All tryptic and non-tryptic RALF1 and PEP7 peptides covered the C-terminal parts of the respective propeptides, which constitutes the biologically active RALF1 or PEP7 versions, respectively. Other RALF peptides such as RALF22, RALF23, and RALF33 were also identified in the fractions F1, F2, and F3 but did not strictly meet the criteria set for putative ligands as described above (supplemental Table 1).

We next used synthetic peptides of RALF1, RALF22, RALF32, and RALF33 at different concentrations to test for their ability to induce the kinase activity of SIRK1–GFP_{starv} (supplemental Figure 1). Independently of the concentrations used, neither

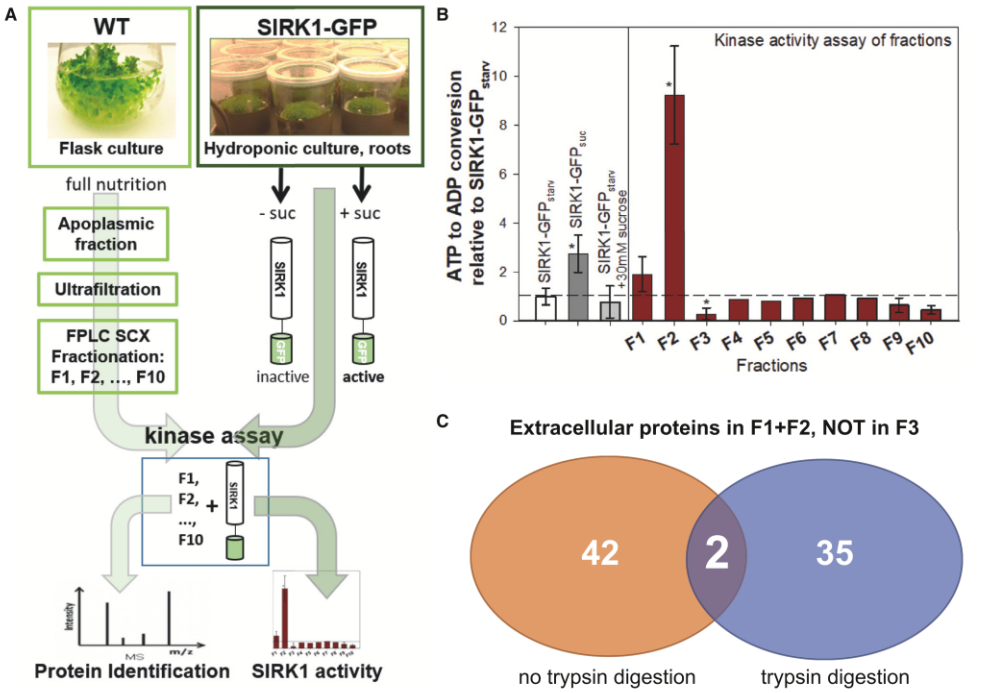

Figure 1. The screen for peptide ligands.

(A) Workflow involving apoplasmic protein fractions exposed to SIRK1–GFP enriched from hydroponic culture without sucrose stimulation and SIRK1–GFP from hydroponic culture stimulated by sucrose served as positive control.

(B) Kinase activity of SIRK1–GFP purified from sucrose-starved plants exposed to different fractions of apoplasmic proteins to test for SIRK1 activation. Asterisks indicate significant differences to SIRK1–GFP isolated from sucrose starved cultures (SIRK1–GFP_{starv}) without additional activation. For fractions F4 to F8, only one fraction was analyzed; all other fractions were tested in three independent replicates.

(C) Summary of the number of proteins with predicted extracellular location identified in fractions F1 and F2 but not F3. Fractions were analyzed after trypsin digestion and without trypsin digestion.

the RALF peptides nor the non-related reference peptides IDA and CLE were able to induce SIRK1–GFP_{starv} kinase activity above background level (supplemental Figure 1). By contrast, with the exception of RALF1, the application of these peptides even reduced SIRK1–GFP_{starv} kinase activity compared with the control conditions (supplemental Figure 1). Inhibition of complex formation between receptor and co-receptor by RALF23 has been described for the FLS2/EFR–BAK1 complex (Stegmann et al., 2017). In addition, recently it was shown that RALFs require internal disulfide bonding to acquire the required structure for receptor binding (Moussu et al., 2020). This may affect the performance of synthesized RALF peptides in this kinase assay.

PEP7 can bind to SIRK1 in biochemical and biophysical assays

The abundance of the signaling peptide PEP7 increased in the apoplasm of liquid-grown seedlings when resupplied with 30 mM sucrose after starvation (Figure 2A) but not when the sucrose-starved seedlings were supplied with related disaccharides such as sucralose or trehalose or the monosaccharide glucose. Thus, the observed PEP7 accumulation was specific for sucrose-supplemented seedlings. To test, whether PEP7 influences SIRK1–GFP_{starv} kinase activity, we performed an *in vitro* dose-response assay. Increasing concentrations of synthetic PEP7 enhanced SIRK1–GFP_{starv} kinase activity, which reached saturation at PEP7 concentrations above 1 μM (Figure 2B). We then tested whether PEP7 can directly bind to SIRK1–GFP. SIRK1–GFP, immobilized on anti-GFP magnetic beads (supplemental Figure 2A), was exposed to 1 μM PEP7. After washing and elution, association of the putative ligand with SIRK1–GFP was detected by mass spectrometry. Indeed, SIKR1–GFP captured PEP7 from the solution (Figure 2C). Next, we performed a series of co-immunoprecipitation experiments to test for binding of PEP7 to the extracellular domain of SIRK1 (SIRK1–ECD). Firstly, StrepII-tagged SIRK1–ECD was purified after transient expression in *Nicotiana benthamiana* leaves

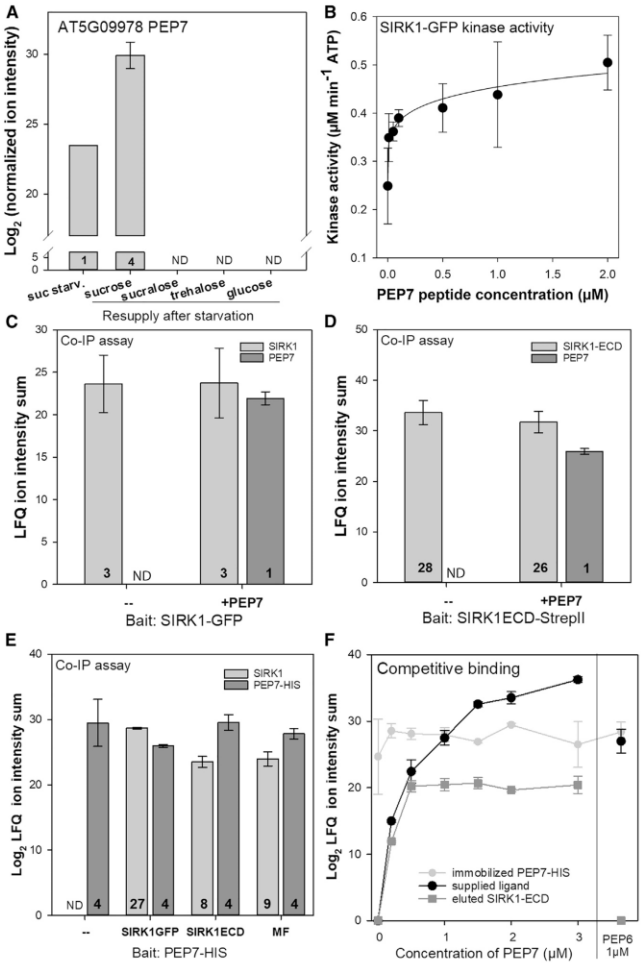

Figure 2. Characterization of PEP7 as a ligand candidate of SIRK1.

(A) Normalized ion intensity of PEP7 in apoplasmic fractions in response to sucrose resupply or supply of other sugars.

(B) Kinase activity of SIRK1–GFP induced by different concentrations of PEP7.

(C) Normalized ion intensity (label-free quantification [LFQ] values) of SIRK1 and PEP7 in co-immunoprecipitation assays with SIRK1–GFP with or without the supply of PEP7.

(D) Normalized ion intensity (LFQ values) of SIRK1–ECD–HA and PEP7 in co-immunoprecipitation assays with SIRK1–ECD–HA with or without the supply of PEP7. Averages of at least three biological replicates are displayed with standard deviations. In bar charts, numbers indicate the number of peptides identified.

(E) Normalized LFQ intensities of PEP7–HIS and SIRK1 in pull-downs with PEP7–HIS as a bait.

(F) Competitive elution of SIRK1–ECD from pre-bound complexes with immobilized PEP7–HIS with different concentrations of PEP7. PEP6 was used as a control.

In all panels, averages of at least three biological replicates are displayed with standard deviations. In bar charts, numbers indicate the number of peptides identified.

(supplemental Figure 2B) and was then immobilized to streptavidin beads and exposed to PEP7 at a concentration of 1 µM. Again, PEP7 was detected by mass spectrometry among the eluted proteins that were bound to the SIRK1–ECD bait (Figure 2D). In a reverse co-immunoprecipitation experiment, synthetic $(His)_6$-tagged PEP7 was immobilized to Ni-NTA magnetic beads (supplemental Figure 2C) and exposed either to 50 µg SIRK1–GFP, 20 µg SIRK1–ECD purified from *N. benthamiana* leaves after transient expression, or to root microsomal membrane preparations, which are expected to contain native full-length SIRK1 (Figure 2E). Indeed, in all three approaches, PEP7–$(His)_6$ was found to capture SIRK1–GFP, StrepII-tagged SIRK1–ECD, or root-derived SIRK1 from the solutions. Next, we tested whether binding of SIRK1–ECD to immobilized PEP7–$(His)_6$ can be competitively released by addition of free, non-tagged PEP7. We detected a release of SIRK1–ECD from the PEP7–$(His)_6$ beads with increasing concentrations of free PEP7 (Figure 2F). Saturation was reached at PEP7 concentrations above 1 µM. When free PEP6 (1 µM) was used to elute SIRK1–ECD from the PEP7–$(His)_6$ beads, no release of SIRK1–ECD was observed. These experiments suggest that indeed PEP7 associates with SIRK1 via its ECD.

We used microscale thermophoresis to obtain more quantitative data with respect to the binding of PEP7 to SIRK1–ECD. StrepII-tagged SIRK1–ECD was purified (supplemental Figure 3) and labeled with fluorescent dye RED-NHS. Incubation of different concentrations of PEP7 with SIRK1–ECD resulted in a sigmoidal binding curve, allowing the calculation of the binding constant (K_d value) of 1.4 ± 0.79 µM PEP7 (range: 1–1.8 µM) based on three assays from independent protein isolations (Figure 3). Adding an approximate amount of co-receptor QSK1–ECD as a third component to the binding assay reduced the binding constant to a K_d of 57.0 ± 22.2 nM (range: 33.9–80 nM). When PEP4 or PEP6 instead of PEP7 was used as a putative ligand in the microscale thermophoresis assay, no sigmoidal dose-response curve could be obtained, and the signal-to-noise ratio (around 1.4) was too small to calculate a K_d value. Thus, experimental evidence from the different association assays and from microscale thermophoresis point to PEP7 being able to physically bind to SIRK1–ECD.

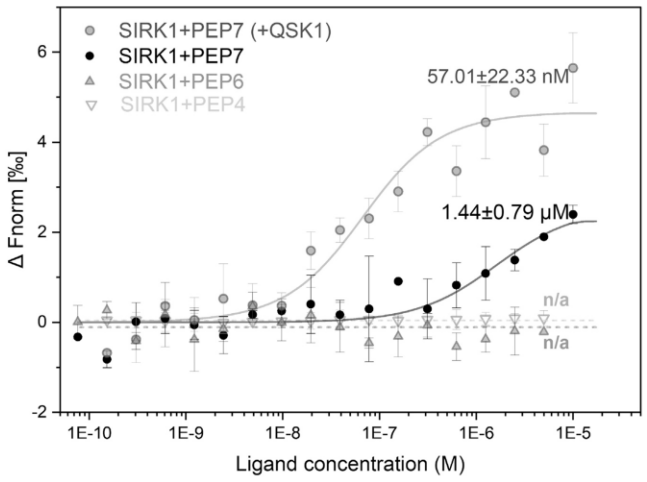

Figure 3. Microscale thermophoresis assay with SIRK1–ECD and PEP7 or PEP6 as putative ligands.
In affinity measurement of SIRK1–ECD and PEP7 in the presence of QSK1–ECD, 20 nM QSK1–ECD was applied. A signal-to-noise ratio of 8 was achieved in assays for PEP7 as the ligand, while the signal-to-noise ratio was 1.4 for PEP6 as the control. K_d values are as indicated. Each dot represents an average of at least three independent measurements. Error bars indicate SD. Fitting of the dose-response curve was performed by the instrument software.

QSK1–ECD could increase the binding affinity of SIRK1–ECD and PEP7, as expected from QSK1 function as a co-receptor. Thus, PEP7 is a strong candidate to be the specific ligand of SIRK1.

PEP7 induces the formation of SIRK1 signaling complex and phosphorylation of SIRK1 substrates

SIRK1–GFP fusion expressed in the *sirk1* and *pep7* background was used to determine the interactome of SIRK1 after addition of sucrose, PEP7, or mock treatment following an established affinity purification protocols (Wu et al., 2019b) (supplemental Table 2). Protein abundances were normalized to the protein abundance of the bait SIRK1–GFP (Figure 4A). Protein abundance ratios were calculated as $\log_2$ ratios of treatment (sucrose or PEP7) versus mock treatment (Figure 4B). Proteins, which showed a positive $\log_2$-fold change in their abundance, were considered to be recruited as interactors of SIRK1 in response to the respective treatment. Generally, there was a large overlap of induced $\log_2$ fold changes upon sucrose or PEP7 treatment (Figure 4C), and we found a correlation of $\log_2$ fold changes in prey protein abundances upon treatments with sucrose and PEP7 (Figure 4D). The known co-receptor QSK1 and its homolog QSK2 were found to be among the recruited interaction partners of SIRK1 in both treatments (Figure 4E). Also, aquaporins were identified to be associated with SIRK1, again confirming earlier observations that SIRK1 interacts with aquaporins upon sucrose supply and that aquaporins are substrates for the SIRK1/QSK1 signaling complex (Wu et al., 2013, 2019b). (Figure 4F). Furthermore, PEP7 induced a comparable change of aquaporin abundance in the SIRK1-GFP pull-downs as did sucrose (Figure 4F). We conclude that PEP7 induced the formation of a highly similar interactome of SIRK1 as was observed after treatment with external sucrose.

As shown previously, the activation of SIRK1 by external sucrose supply (Wu et al., 2013, 2019b) involved the *trans*-phosphorylation of QSK1 and the phosphorylation of aquaporins (Figure 5A). In those experiments, hydroponic cultures of *Arabidopsis* plants where starved for sucrose and resupplied with 30 mM sucrose solution for 5 min prior to harvesting of tissue and analysis of protein phosphorylation (Wu et al., 2013, 2019b). Here, we show that in the wild type, an external supply of PEP7 (instead of sucrose) also resulted in increased phosphorylation of QSK1/QSK2 and aquaporins (Figure 5B). The sucrose-induced phosphorylation of QSK1/QSK2 and aquaporins was reduced in the previously described *sirk1* loss-of-function mutant (Figure 5B). The external supply of PEP7 instead of sucrose to *sirk1* seedlings resulted in an even lower phosphorylation of QSK1/QSK2 and aquaporins compared with wild type. Moreover, the phosphorylation of aquaporins and QSK1/QSK2 was not observed in the *pep7* mutant upon sucrose supply. However, the increased phosphorylation of QSK1/QSK2 and aquaporins in *pep7* was restored by external supply of PEP7. In the *sirk1;pep7* double mutant, the phosphorylation of QSK1/QSK2 and aquaporins was neither induced by sucrose nor rescued by an external supply of PEP7. Importantly, the quantified phosphopeptides of aquaporins (supplemental Table 3) corresponded to the known pore-gating phosphorylation sites from SoPIP2A (Figure 5C), suggesting that, indeed, PEP7 induced pore-opening phosphorylations of aquaporins, similar to the treatment with external sucrose (Figure 5D).

PEP7 may stabilize *in vivo* association of SIRK1 and QSK1 for forming active complexes

To investigate potential effect of PEP7 on SIRK1 and QSK1 associations, we measured their spatial proximity *in vivo* by Förster resonance energy transfer by fluorescence lifetime (FLT) imaging (FRET–FLIM). In transiently transformed *N. benthamiana* epidermal leaf cells, QSK1–GFP and SIRK1–mCherry co-localize in the plasma membrane with or without the supply of PEP7 (supplemental Figures 4A and 4B). To determine the background FRET–FLIM values, the FRET donor QSK1–GFP was expressed alone, and the FLT was measured. In all cases, where QSK1–GFP and SIRK1–mCherry (FRET acceptor) were co-expressed, a reduction in FLT was observed, indicating a close spatial proximity (less than 10 nm; Glöckner et al., 2019) of the two proteins. There was no significant further reduction in FLT when PEP7 was applied compared with mock treatment

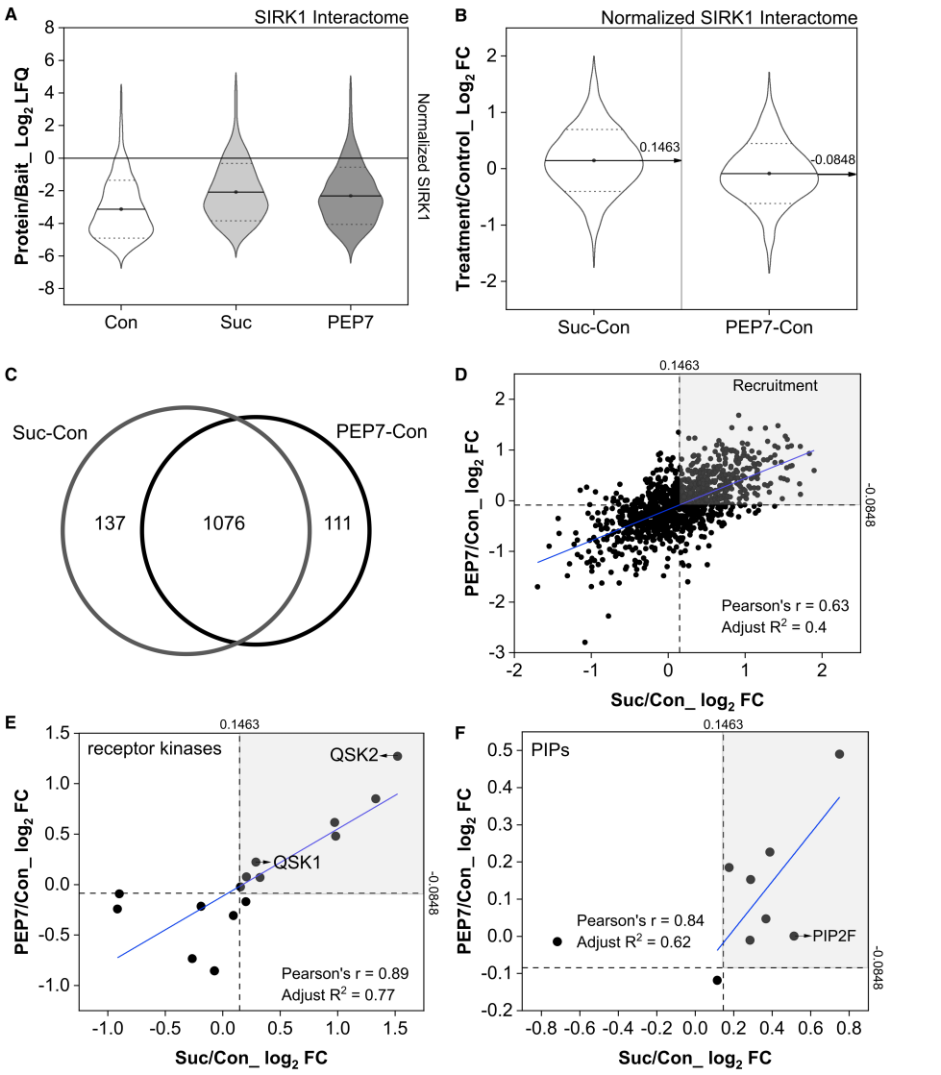

Figure 4. Interactome of SIRK1 induced by PEP7 and sucrose.

(A) Protein abundance distribution normalized to bait (SIRK1) abundance. LFQ values were taken as measure of protein abundance.

(B) Distribution of treatment/control comparisons centered on median values. The two median values within each comparison are shown in the violin plot, respectively.

(C) Venn diagram of responding proteins upon sucrose or PEP7 treatment.

(D) Correlation analysis of all protein comparisons under two treatments. Proteins with values greater than the median were considered to be recruited by SIRK1 under both treatments.

(E) Correlation analysis of only receptor kinases.

(F) Correlation analysis of only PIPs under two treatments.

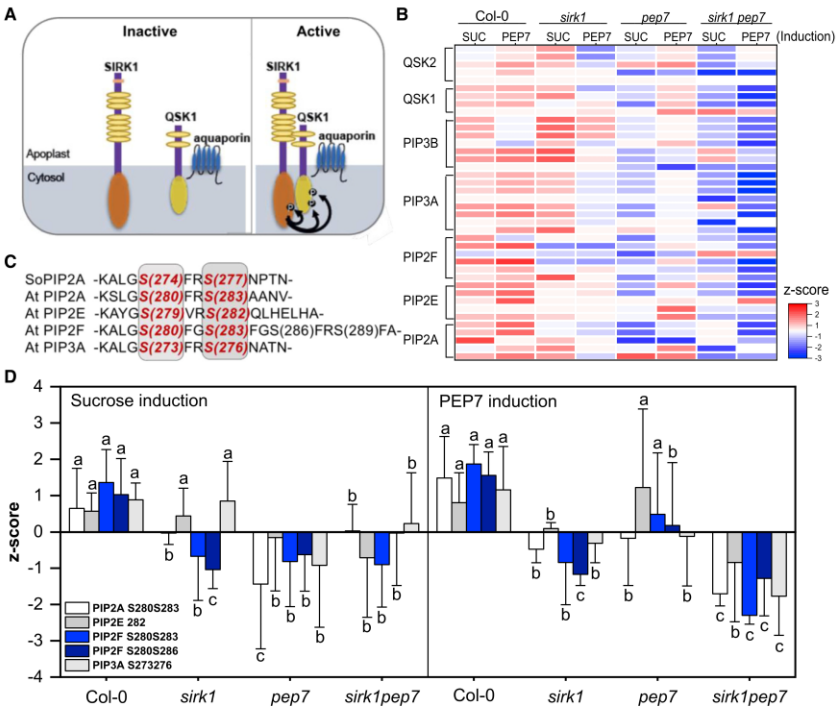

Figure 5. PEP7-induced changes of phosphorylation levels of SIRK1 substrates.
(A) SIRK1 signaling scheme highlighting substrates that presented previously.
(B) Heatmap of means of *Z* scored phosphosite intensities of different phosphopeptides identified for known members of the SIRK1 signaling pathway. Each row represents one phosphopeptide.
(C) Sequence alignment of C-terminal phosphorylated plant aquaporins. Gray area indicates the conserved residues that can be phosphorylated.
(D) *Z* scored phosphorylation levels of conserved residues of PIPs that correspond to the pore gating that induced by sucrose and PEP7. Small letters indicate significant differences ($p < 0.05$; pairwise *t*-test) for each phosphopeptide between genotypes.

(supplemental Figure 4B). To exclude the possibility that endogenous PEP7 may mask the effects of externally applied PEP7 on QSK1–GFP/SIRK1–mCherry association, we performed the FRET–FLIM experiments in the presence of the protease inhibitor leupeptin. Leupeptin inhibits the metacaspase 4 (MC4) (Vercammen et al., 2004), which releases PEP7 from its propeptide (Moussu et al., 2020). After treatment with leupeptin, the FLT of QSK1–GFP in the donor-only control was reduced in response to PEP7 addition (supplemental Figure 4B). However, the FLT of QSK1–GFP in presence of SIRK1–mCherry was not significantly altered in response to PEP7 application even after treatment with leupeptin (supplemental Figure 4B). Likely, SIRK1 and QSK1 are associated in preformed nano-structured membrane domains in the absence of PEP7 as was described for several other LRR–RK complexes (Bucherl et al., 2017; Glöckner et al., 2019; Gronnier et al., 2022). Therefore, PEP7 may act as a stabilizing factor of the QSK1/SIRK1 association, thereby transforming the preformed inactive complexes into active ones. Indeed, when the SIRK1–QSK1 complex was activated by sucrose or PEP7 treatment, SIRK1 was reliably detected in pull-downs of QSK1–GFP (supplemental Figure 4C). Moreover, when the QSK1 complex was fixed in the active state (e.g., by mutation of the phosphorylated serines of QSK1 to aspartates), SIRK1 was also detected in pull-downs under non-stimulated conditions (supplemental Figure 4C).

PEP7 affects water influx to protoplasts via receptor kinase SIRK1

Sucrose as an osmotic agent was previously shown to induce water influx into protoplasts, and this sucrose-induced water influx was significantly reduced in the *sirk1* mutant (Wu et al., 2013). We performed protoplast swelling assays with wild type and *sirk1* and *pep7* single mutants as well as the *sirk1;pep7* double mutant to test if supply of PEP7 was also able to induce water influx and whether this was dependent on the presence of SIRK1 receptor kinase. In wild type, mannitol and sucrose induced water influx density (Figures 6A and 6B). An external

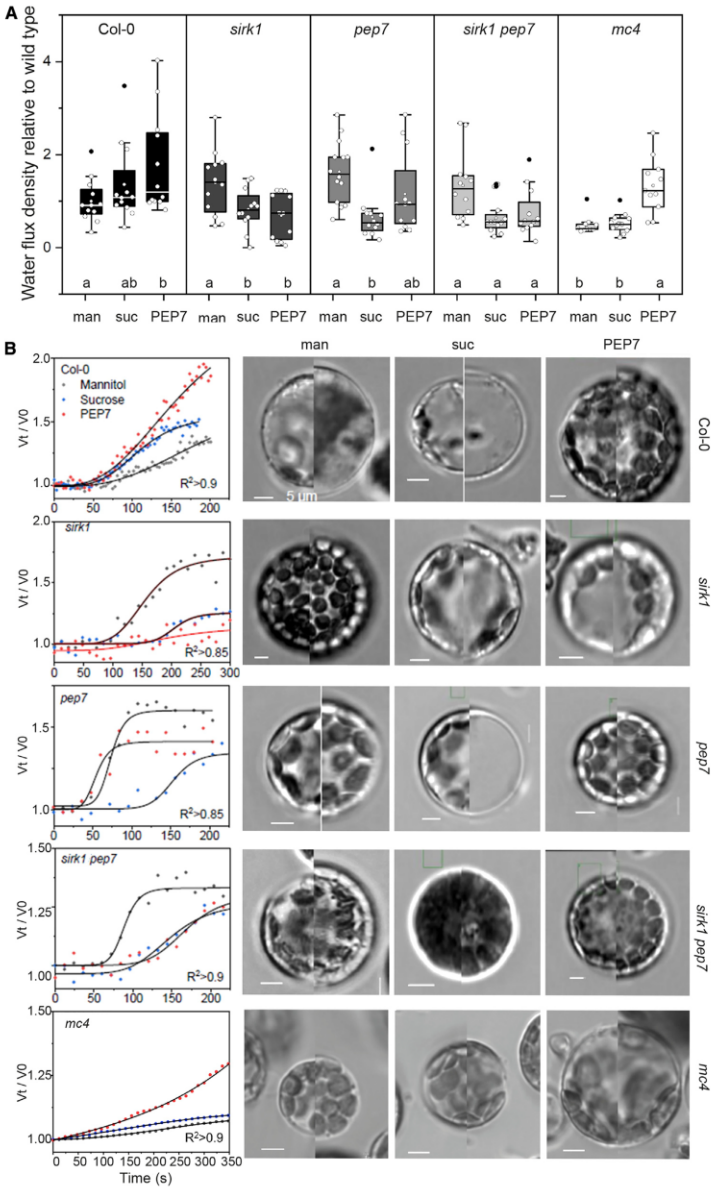

Figure 6. Water influx density of protoplasts induced by osmotic changes through mannitol, sucrose, or by the supply of PEP7 in the wild type (Col-0), *sirk1*, *pep7*, the double mutant *sirk1pep7*, and *mc4*.

(A) Boxplots show the water flux density relative to wild type. The average of Col-0 under mannitol treatment was used as the control and set to 1. Vertical lines in the boxes indicate the median and upper/lower borders represent the 25th percentile. White dots represent individual

(legend continued on next page)

supply of PEP7 in wild type significantly further increased water influx density compared with mannitol or as observed in presence of sucrose. In the *sirk1* mutant, mannitol induced water influx density, but sucrose treatment did not. Supply of PEP7 to *sirk1* mutant did not increase water influx density (Figures 6A and 6B), which remained low, similar to water flux density observed in *sirk1* with sucrose treatment. In the *pep7* mutant, mannitol induced water influx, but sucrose treatment resulted in low water influx density, similar as in the *sirk1* mutant. Strikingly, external supply of PEP7 to the *pep7* mutant restored water influx densities to higher values statistically not different from wild type under mannitol treatment (Figures 6A and 6B). In the *sirk1;pep7* double mutant, neither sucrose nor PEP7 treatment resulted in enhanced water influx densities, suggesting that SIRK1 is required for the protoplast swelling response.

Recently, the MC4 was identified to be involved in PEP7 maturation (Moussu et al., 2020). Interestingly, water influx rates of the *mc4* loss-of function mutant resembled the water influx rates of the *pep7* mutant. In *mc4*, as in *pep7*, sucrose did not induce water influx, but PEP7, also in *mc4,* was able to restore water influx to the protoplasts (Figures 6A and 6B). This further supports our conclusion of PEP7, as being produced by MC4 activity, to be involved in regulation of water influx.

We then tested whether other members of the PEP family were able to affect water influx to protoplasts in a similar way. PEP4 and PEP6 were used since they were also found to be expressed in root tissue (Shulse et al., 2019). Water influx densities in wild type were not significantly affected by the presence of PEP4 or PEP6. When the receptor kinase SIRK1 was absent (*sirk1* mutant), water influx densities in the presence of PEP4 or PEP6 were not different from wild type, suggesting that PEP4 and PEP6 did not require the presence of receptor kinase SIRK1 (supplemental Figure 5A). In the *pep7* mutant, no difference in water influx densities compared with wild type was observed when PEP4 or PEP6 was supplied externally (supplemental Figure 5A). To differentiate the effects of SIRK1 from other known PEP-family receptors, we performed protoplast swelling assays using *pepr1* and *pepr2* mutants. PEPR1 and PEPR2 are known receptors to PEP1 (Bartels et al., 2013). Although *pepr1* and *pepr2* showed an increased water influx density in response to mannitol compared with wild type, PEP7 was still able to increase water influx density similarly as in wild type, suggesting that PEPR1 and PEPR2 are not involved in the PEP7 pathway (supplemental Figure 5B).

Lateral root growth mediated by PEP7 requires SIRK1

Next, we explored the role of the PEP7/SIRK1 signaling pathway on the organ level of roots. We hypothesize that particularly lateral root growth, which relies on sucrose supply as carbon source and water transport for turgor buildup (Péret et al., 2012), may—in addition to auxin—be affected by the SIRK1/QSK1/PEP7 signaling module. In wild type, PEP7 treatment resulted in lateral root primordia (LRP) being more frequently found at later developmental stages (stages VI + VII, VIII) (Figure 7) compared with untreated plants. In the *sirk1* mutant, LRP were equally distributed across stages, and no effect of PEP7 treatment was observed, suggesting a generally delayed lateral root development in the *sirk1* mutant, and this was not affected by PEP7 treatment. In the *pep7* mutant under control conditions, most LRP were observed at early stages II + III. PEP7 supply significantly decreased LRP at early stages, and we found a significant increase of LRP frequency at stages VI + VII and VIII (Figure 7). This may indicate that PEP7 contributes to progressing LRP from early stages (I to III) to later stages (VI + VII and VIII). In the *sirk1;pep7* mutants, LRP distribution under control conditions was similar to the distribution observed in the *pep7* mutant, with low frequency of LRP at stages IV + V. PEP7 treatment resulted in a similar distribution of LRP stages as in the *sirk1* mutant, lacking a significant progression of LRP stages to later developmental stages.

In general, it must be kept in mind that root growth and lateral root development are complex traits affected by multiple signaling pathways over a more long-term time scale. In previous work, LRP emergence was shown to be affected by aquaporin activity, which was in turn affected by auxin (Péret et al., 2012). Thus, the observed low numbers at stages IV and V in in *pep7* and *sirk1;pep7* may be attributed to complex interactions of multiple signaling pathways (e.g., auxin signaling) affecting aquaporin activities, and these may still be active even in the absence of SIRK1. Also, the more long-term time scale compared with other biochemical process, such as protein phosphorylation and protoplast swelling assays, must be considered. However, our data clearly show a contribution of PEP7 and SIRK1 to the complex trait of LRP emergence.

DISCUSSION

PEP7 (AT5G09978) belongs to a family of "danger signaling peptides" consisting of eight family members (Zhang et al., 2016a). Out of this family, PEP1 was shown to be recognized by receptors PEPR1 (AT1G73080) and PEPR2 (AT1G17750) (Krol et al., 2010; Yamaguchi et al., 2010), but very little is known about the other PEP-family members. Here, we point to a signaling pathway for PEP7. Based on the sequences of the active peptides, PEP6 shows strongest similarity to PEP7 and therefore was used as a control. PEP4, although its propeptide shares expression with PEP7 in root tissue, shows the strongest dissimilarity to PEP7 and was used as a second negative control (Zhang et al., 2016a).

PROPEP7 was found by single-cell sequencing of root cells, clustering with marker genes of mature root hairs (Ryu et al., 2019). In the same study, PROPEP6 was found in a gene cluster with marker genes of the endocortex, while other members of the

measurements. Small letters indicate significant differences ($p < 0.05$) between treatments as determined by one-way ANOVA with Holm-Sidak correction.

(B) Volume change of protoplasts over time under induced by mannitol only, in the presence of sucrose, or in the presence of PEP7, and representative images of protoplasts at high and low osmolarity conditions. Scale bar, 5 μm. man, mannitol; suc, sucrose.

PEP family or the respective PEPR receptors were not found. Most interestingly, in another single-cell sequencing study of root cells (Shulse et al., 2019), expression of PROPEP7 was induced by external sucrose supply, while expression of PROPEP6 and PROPEP4 were not induced by sucrose (Shulse et al., 2019). Thus, members of the PEP family are involved in other signaling pathways besides biotic stress responses and were shown to be released also upon changes in plant central carbon metabolism (e.g., sucrose). Our research points to an involvement of PEP7 in regulatory processes induced by osmotic imbalances in sucrose availability.

Processing of PEP7

Recently, type II metacaspases were found to be involved in processing of the plant elicitor peptides (Moussu et al., 2020), specifically MC4 (AT1G79340) was able to process also PROPEP7 by releasing the active peptide from the C terminus of the propeptide by cleavage after arginine or lysine. The processing of PEPs was induced by calcium signals (Hander et al., 2019) and required intramolecular proteolysis even of the metacaspase. The mRNA of MC4 was shown to be cell-to-cell mobile (Thieme et al., 2015). Little is known about further requirements for processing of the PEP precursors. Our work supports that MC4 may indeed be involved in PEP7 maturation as concluded from the protoplast swelling assays of the *mc4* mutant with supply of external PEP7 and/or sucrose (Figure 6).

The signaling pathway of PEP7

The expression pattern of PROPEP7 does not show overlaps with expression of the known PEP receptors PEPR1 and PEPR2 (Bartels et al., 2013), suggesting a different perception pathway for PEP7. Also, SIRK1 shows unique expression patterns compared with PEPR1 and PEPR2, especially in sink tissues of shoot and root (Winter et al., 2007). Distinct signaling pathways for SIRK1 and PEPR1/2 were also concluded here, since *pepr1* and *pepr2* mutants remained responsive to PEP7 treatment in protoplast swelling assays (supplemental Figure 5B). However, the SIRK1 signaling pathway is linked with components of PEPR1 and PEPR2 signaling through common interaction partners. For instance, BAK1, two HERK2 paralogs, and QSK1—all classified as co-receptors (Xi et al., 2019)—are suggested as common interaction partners for all three receptors (PEPR1, PEPR2, SIRK1) (Arabidopsis Interactome Mapping Consortium, 2011; Jones et al., 2014).

One important function of co-receptors is in the stabilization of the interaction of the receptor with the ligand. The co-receptor contributes as a shape-complementary component and, by interaction with the receptor, holds the ligand in place (Sun et al., 2013a, 2013b; Santiago et al., 2013; Zhang et al., 2016b, 2016c). Our biochemical assays and the proteomics study of protein complexes and their phosphorylation, as well as the cellular and whole-plant responses, support PEP7 as a ligand to receptor kinase SIRK1. QSK1 was previously proposed to have a role in stabilization of the activated SIRK1 complex (Wu et al., 2019b; supplemental Figure 6C). It may even be speculated that QSK1 could also function as co-receptor with other receptor kinases, possibly also involving other PEPs as ligands. A ligand-stabilizing function was clearly also demonstrated for co-receptor BAK1, in which different regions of the ECD are involved in interaction with different ligands (Sun et al., 2013a, 2013b; Santiago et al., 2013).

Receptor-ligand binding and preformed complexes of SIRK1 and QSK1

Receptor kinases are known to have strong binding affinities for their ligands. Brassinolide binds to the BRI1 receptor with a K_d of 15 nM as determined by immunoprecipitation assays (Wang et al., 2001). Scatchard plots suggested the K_d of Clavata3 binding to its receptor Clavata1 at 17 nM (Ogawa et al., 2008). The binding of CLE41/44 to receptor PXY with a K_d of 33 nM was detected by using isothermal titration calorimetry (Zhang et al., 2016b). The binding of RALF to its receptor Feronia with a K_d of around 1 μM was determined by microscale thermophoresis. Interestingly, far higher binding constants were found for binding of the peptide IDA to its receptor Hasea with a K_d of 20 μM using isothermal titration calorimetry (Santiago et al., 2016). The higher K_d values, as in the case of IDA, were obtained under conditions in which the co-receptor (SERK1) was not present. In that regard, the K_d values obtained here for the binding of PEP7 to receptor SIRK1 are within this range at around 1 μM. Strikingly, by adding the co-receptor QSK1 to the binding assay, a significantly higher binding affinity for PEP7 was observed (K_d = 57.01 ± 22.3 nM). We use the approximated same amount of QSK1–ECD as the SIRK1–ECD in the binding assays, but it is not yet known if different ratios of receptor and co-receptor could result in different K_d of SIRK1 binding PEP7.

Apparently, PEP7 is produced under conditions of changed sucrose supply (Shulse et al., 2019). According to our biochemical data, the ligand PEP7 would induce the formation of the SIRK1 signaling complex. However, our attempts to visualize the recruitment of co-receptor QSK1 to ligand-activated SIRK1 using FLIM/FRET experiments revealed no clear differences between treatments with PEP7 and controls. This supports the hypothesis that receptor and co-receptor are arranged in preformed complexes within nano-domains (Bucherl et al., 2017; Gronnier et al., 2022) and that these complexes are likely stabilized or rearranged by the ligand to reveal their full activity. This was already observed for other receptor/co-receptor pairs (Caesar et al., 2011; Ladwig et al., 2015).

We found biochemically stable interactions between SIRK1 and QSK1 only after treatment with PEP7 (Figure 4). This supports the view that the complex is stabilized so that it can be detected after biochemical purification. The phosphorylation of scaffold proteins may be important in formation and rearrangement of such preformed signaling domains (Perraki et al., 2018). In any case, we here could show that binding of PEP7 to the SIRK1–QSK1 protein complex leads to the activation of a downstream signaling cascade involving activation of aquaporins and subsequent changes in water influx to the cell.

PEP7 and the response to sucrose

Our findings strongly point to a receptor/co-receptor signaling pathway of SIRK1/QSK1 that is activated by the elicitor peptide PEP7 and results in the opening of aquaporins by

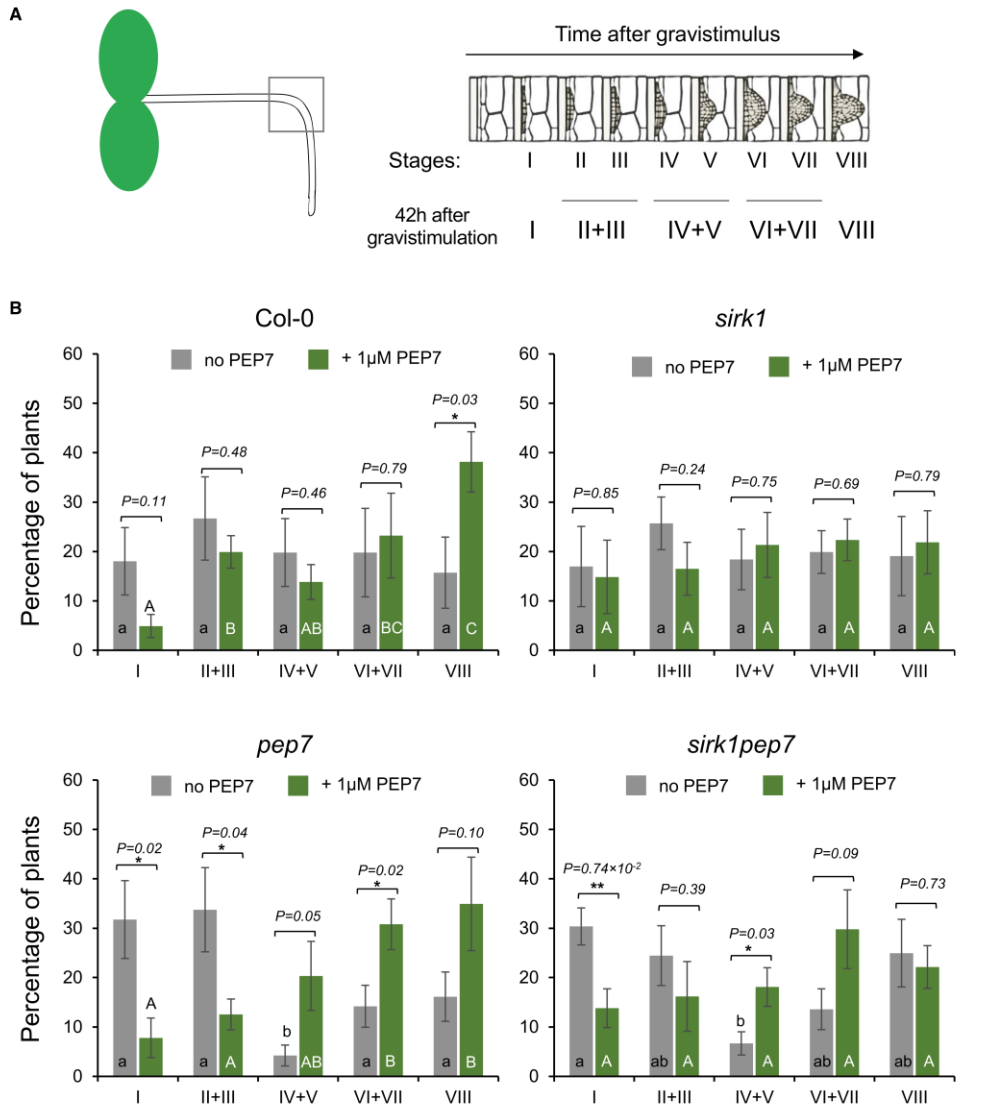

Figure 7. Lateral root development in the wild type (Col-0), *sirk1*, *pep7*, and *sirk1;pep7*.
(A) Experimental setup and definition of stages as described (Péret et al., 2012).
(B) Percentage of the plants on different lateral root developmental stage sections, without PEP7 (gray) and with 1 μM PEP7 supply (green) in wild type and mutants. Data are shown as mean values ± SEM (n = 27–30). Small letters indicate significant differences of lateral root primordia frequencies within one genotype without PEP7 supply. Capital letters indicate significant differences of lateral root primordia frequencies within one genotype under 1 μM PEP7 supply. Asterisks mark the statistical comparisons between no PEP7 and with 1 μM PEP7 supply at each stage section (Student's *t*-test, *p < 0.05 and **p < 0.01).

SIRK1-dependent phosphorylation. The opening status of aquaporins was shown to also have effects on lateral root emergence (Péret et al., 2012) via auxin signaling, and root hydraulic conductivity is affected by aquaporin abundance, even in response to signals from the shoot (Vandeleur et al., 2014). Thus, effects of the SIRK1/QSK1/PEP7 signaling pathway on lateral root development may also be indirect through reduced cell expansion in mutants where aquaporin activation is impaired. In general, the SIRK1/QSK1/PEP7 signaling pathway could have biological functions during sucrose allocation within the plant and/or during response to osmotic stresses and drought.

We here show that PEP7 is secreted in response to external sucrose supply. Thus, activation of SIRK1 by sucrose, as studied in previous work (Wu et al., 2013, 2019a), requires sensing of sucrose status and maturation of PEP7 before the receptor SIRK1 is activated. A challenging question remains for further study as to whether external sucrose triggers the PEP7 maturation or whether sucrose acts after uptake into the cells.

MATERIALS AND METHODS

Plant materials

Arabidopsis seeds of wild type (col-0), *sirk1* (SALK_125543), *qsk1* (SALK_019840), *pep7* (SALK_025824), *pep6* (SALK_141703), and *mc4* (SAIL_856_D05) were used. Double mutants *sirk1;pep7* and *sirk1;qsk1* were obtained by crossings of the respective single mutants. Furthermore, we overexpressed of SIRK1 (*35 S::SIRK1-GFP*) in the background of *sirk1* and *pep7*. Homozygous T-DNA insertional mutants *sirk1* and double mutant *sirk1;qsk1* were confirmed via PCR amplification as reported previously (Wu et al., 2019b). Mutants of *pep7* and *sirk1;pep7* were confirmed via PCR amplification using T-DNA border primer LBb1.3 (5′-ATTTTGCC GATTTCGGAAC-3′) and gene-specific primers (PEP7-RP: 5′- GGA AGGTGCCTAGTTGGTACC -3′, PEP7-LP: 5′-GTTTTCACGTTTCAAAT TCGG-3'; SIRK1-RP: 5′-TTTCCAGCATTTCCAACACTC-3′, SIRK1-LP: 5′-CACTAAGCTTGTTGAGGTCGC-3′) (supplemental Figure S6).

Hydroponic cultures, treatments, and phenotyping

Plants were germinated and grown under 16/8 day/night (22°C, 120 μE/s·m^2) in $^1/_2$MS medium plus 0.5% sucrose in a hydroponic cultivation system (Schlesier et al., 2003). Whole seedling cultures were grown in 50 ml $^1/_2$MS medium with 0.5% sucrose as described (Niittylä et al., 2007). Sucrose starvation–resupply experiments were performed as described (Niittylä et al., 2007). Plant material was collected after sucrose starvation (no resupply), after sucrose treatment (1% sucrose for 5 min), or after PEP7 treatment (1 μM PEP7 for 5 min). Addition of glucose (33 mM), sucralose (30 mM), and trehalose (40 mM) with the same osmolarity (Vapro 5600, Wescor Biomedical Systems) as the 30 mM sucrose solution were used as control treatments in some experiments. For lateral root growth phenotypical analysis, lateral root induction was performed on 5-day-old seedlings grown on $^1/_2$MS plates with or without 1 μM PEP7 by rotating the plates at 90° (Péret et al., 2012).

Protein extraction and ultrafiltration

At harvesting, tissue was flash frozen in liquid nitrogen. After breaking 300 g of frozen tissue to coarse pieces, the frozen tissue was transferred to a glass grinder (GLASS/PTFE Potter Elvehjem Tissue Grinder 30 ml), and 0.1% trifluoroacetic acid (TFA) was added to a volume of about 30 ml per sample. After tissue homogenization, the solution was filtered through four layers of gaze (Miracloth, Merck Millipore). Remaining cell debris was pelleted at 4°C and 10 000 × *g* for 15 min. The supernatant was used for further ultrafiltration and fractionation. The protein extract was firstly filtered through a 0.45 μm filter to get rid of any insolubilized material. Afterward, the protein extract was concentrated over a tangential flow filtration (Minimate Tangantial Flow Filtration Systems, Pall Corporation) using a molecular weight cutoff of 1 kDa (i.e., retaining anything larger than 1 kDa).

Fractionation by size-exclusion chromatography

The ultrafiltrate was fractioned by fast protein liquid chromatography (NGC chromatography systems, BioRad) reverse-phase chromatography using a Bio-scale MT column (2 ml, BioRad). The column was packed with Macro-Prep t-Butyl and Methyl Hydrophobic Interaction Chromatography Media. Before fractionation, the fast protein liquid chromatography system was washed with 20% ethanol using a flowrate of 10 ml·min^{-1} (50% pump A/50% pump B). The system was then washed with 2.5 ml H_2O at a speed of 0.5 ml min^{-1} for 5 min. The column was equilibrated with 6 ml 2% acetonitrile and 0.1% TFA (8.57 min × 0.7 ml·min^{-1}), and a 500 μl sample was loaded to the column. A linear elution gradient was run from 100% pump A to 100% pump B. Pump A was supplied with 2% acetonitrile with 0.1% TFA and pump B with 50% acetonitrile with 0.1% TFA. The gradient was run for 28 min, of which the last 3 min were 100% pump B. The fractioned solution was collected with a fraction collector (BioFrac Fraction Collector, BioRad) in 10 2 ml fractions.

Transient expression of recombinant SIRK1 in *N. benthamiana*

Agrobacterium tumefaciens GV3101 strain harboring the relevant constructs and strain C58C1 (pBinG1 vector with P19 gene) were grown in liquid LB medium (10 gl^{-1} Tryptone, 5 gl^{-1} yeast extract, and 10 gl^{-1} NaCl) at 28°C with appropriate antibiotics. For infiltration, *Agrobacterium* culture was adjusted to final OD_{600} 0.5 for GV3101 and 0.25 for strain C58C1 in a mixture using infiltration buffer 10 mM MES-KOH (pH 5.6), 200 μM Acetosyringon, and 10 mM $MgCl_2$. Three- to four-week-old *N. benthamiana* leaves were syringe infiltrated and harvested after 48 h. The harvested leaves were flash frozen in liquid nitrogen before protein extraction and purification. SIRK1–ECD and QSK1–ECD were expressed as C-terminal fusion with an HA and StrepII tag using the pXCS vector series in GV3101::pMP90RK strain (Witte et al., 2004).

Protein extraction and strep-tag purification

N. benthamiana leaf material harboring SIRK1–ECD or QSK1–ECD was ground in liquid nitrogen (Witte et al., 2004) and thawed in 100 mM Tris-HCl (pH 8.0), 150 mM NaCl, 1 mM EDTA, 2% w/v PVPP, 0.5% Triton X-100, 1 mM PMSF, and 5 mM DTT. The mixture was incubated at 4°C for 2 h under constant shaking. After centrifugation (14 000 RPM, 10 min, 4°C), the supernatant was subjected into an equilibrated Strep-Tactin column (2-4013-001, IBA GmbH) according to the manufacturer's tutorial. The StrepII-tagged protein was eluted with 50 mM biotin, 100 mM Tris-HCl (pH 8.0), 150 mM NaCl, and 1 mM EDTA. Eluates were passed through a Macrosep Advance Centrifugal Devices with Omega Membrane 10K (MAP010C36, Pall Corporation) to get rid of the biotin contamination in the eluate. The target protein (SIRK1–ECD and QSK1–ECD) was collected from the sample reservoir.

Microsomal membrane preparation

Microsomal membranes were enriched by differential centrifugation as described (Pertl et al., 2001; Wu et al., 2013, 2019a). 1.5 g fresh tissue was homogenized in 10 ml ice-cold 330 mM mannitol, 100 mM KCl, 1 mM EDTA, 50 mM Tris-MES (pH 7.5), 5 mM DTT, 1 mM PMSF, and 0.5% v/v Protease inhibitor cocktail (P9599, Sigma-Aldrich) and phosphatase inhibitors (25 mM NaF, 1 mM Na_3VO_4, 1 mM benzamidin, 3 μM leupeptin). The homogenate was centrifuged for 15 min at 7500 × *g* at 4°C. The supernatant was centrifuged again for 75 min at 48 000 × *g* at 4°C, resulting in the microsomal membrane pellet.

Pull-downs of GFP-tagged SIRK1

Microsomal proteins (100 μg) resuspended in 330 mM mannitol, 25 mM Tris-MES (pH 7.5), and 0.5 mM DTT was incubated with 25 μl anti-GFP agarose beads (Chromotek) (Wu et al., 2013). After incubation, beads were collected and washed twice with 500 μl 10 mM Tris-HCl (pH 7.5), 150 mM NaCl, 0.5 mM EDTA, and 0.01% IGEPAL. For protein–protein interaction assays, the proteins were eluted from the beads with 100 μl buffer (10 mM Tris-HCl [pH 8.0], 6 M urea, 2 M thiourea). For kinase activity assays, three more washing steps were carried out, once with 10 mM Tris-HCl (pH 7.5), 300 mM NaCl, and 0.5 mM EDTA and twice with 40 mM Tris-HCl (pH 7.5), 10 mM $MgCl_2$, 0.1% BSA, and 2 mM DTT.

Kinase activity assay

SIRK1–GFP fusion proteins were affinity purified over anti-GFP beads (see above). A luciferase-based kinase activity assay was performed as described (Wu et al., 2013). The agarose beads with GFP-tagged proteins were resuspended in 30 μl kinase reaction buffer with ATP and the generic kinase substrate myelin basic protein (40 mM Tris-HCl [pH 7.5], 10 mM $MgCl_2$, 0.1% BSA, 2 mM DTT, 100 μM ATP, 0.4 μg μL^{-1} myelin basic protein). After incubation, 30 μl ADP-GLO Reagents (Promega) was added. Then, kinase detection reagents were added and incubated for another hour. Luminescence as a measure of ATP conversion from ADP was recorded with a luminometer (TecanM200Pro). Proteins from three independent protein isolations were averaged.

Binding assays of PEP7–HIS to immobilized SIRK1

The C-terminal HIS-tagged PEP7 (Pepmic) was used as bait. 20 μl HisPur Ni-NTA Magnetic Beads (Thermo Fisher Scientific) were equilibrated with 100 mM NaH_2PO_4/Na_2HPO_4, 600 mM NaCl, 0.05% Tween-20, and 30 mM imidazole (pH 8.0), and the beads were collected by a magnet. The mixture of 100 μl equilibration buffer containing final concentration 1 μM PEP7–HIS was incubated with beads for 1 h at 4°C. After incubation, the beads were washed three times with 100 mM NaH_2PO_4/Na_2HPO_4, 600 mM NaCl, 0.05% Tween-20 Detergent, and 50 mM imidazole (pH 8.0). SIRK1 full-length GFP protein extract from *N. benthamiana* (50 μg), SIRK1 full-length GFP from microsomal fraction of SIRK1–GFP overexpression line (50 μg), or purified SIRK1ECD–HA–StrepII (20 μg) was added as prey protein. Formed complexes were enriched on a magnet and eluted with 40 μl 100 mM NaH_2PO_4/Na_2HPO_4, 600 mM NaCl, and 250 mM imidazole (pH 8.0). Ten μg of the eluate were vacuum dried and stored for further use.

Binding assays of SIRK1 to immobilized PEP7–HIS

SIRK1 full-length GFP protein obtained from membrane fraction and SIRK1–ECD–HA–StrepII protein obtained from transient expression in *N. benthamiana* were used as bait to capture PEP7. For binding assay of SIRK1 full-length GFP with PEP7, 100 μg SIRK1–GFP protein extract was prebound to GFP-Traps-MA beads (Chromotek) for 2 h under rotation at 4°C. The slurry was separated with a magnet, the supernatant was discarded, and the beads were washed three times with 500 μl 10 mM Tris-HCl (pH 7.5), 150 mM NaCl, and 0.5 mM EDTA. Then, prey PEP7 (1 μM) was added to the beads for 1 h at 4°C. Beads were washed three more times, and proteins were eluted with 60 μl 6 M urea and 2 M thiourea. For the binding assay of SIRK1–ECD to PEP7, 200 μg SIRK1–ECD protein extracted from *N. benthamiana* was prebound to Strep-tagII beads (Thermo Fisher Scientific) for 2 h under rotation at 4°C. The beads were collected by centrifugation and washed three times in 100 mM HEPES (pH 8.0), 100 mM NaCl, 0.5 mM EDTA, 0.05% Triton X-100, and 2 mM DTT. PEP7 was added, and bead slurry was eluted with 100 μl 100 mM HEPES (pH 8.0), 100 mM NaCl, 0.5 mM EDTA, 0.05% Triton X-100, 2 mM DTT, and 10 mM biotin (Witte et al., 2004). Ten μg of the eluates were vacuum dried and stored for further use.

Competitive binding assay

All buffers used were identical to those described for the PEP7–HIS pull-down assay described above. PEP7–HIS (final concentration 1 μM) was firstly immobilized on 20 μl HisPur Ni-NTA Magnetic Beads, and subsequently 100 μg purified protein SIRK1ECD–HA–StrepII was bound to the immobilized PEP7–HIS. Different concentrations of untagged PEP7 (100 μl ddH_2O containing 0, 0.2, 0.5, 1, 1.5, 2, or 3 μM PEP7) was added to elute the SIRK1–ECD from the immobilized PEP7–HIS. The remaining SIRK1–ECD that was not eluted by PEP7 was then eluted with HIS–beads elution buffer (100 mM NaH_2PO_4/Na_2HPO_4 [pH 8.0], 600 mM NaCl, 250 mM imidazole).

Microscale thermophoresis

A buffer exchange column was firstly applied to purified SIRK1–ECD protein to remove any unfavorable reagents. Concentration of purified ECDs was measured by BCA assay. The RED-NHS 2nd generation amine reactive dye (MO-L011, NanoTemper Technologies) was used to label the purified SIRK1–ECD (2 μM) with a 5:1 dye:protein ratio for 30 min at room temperature in the dark. Column B was employed to remove the excess of dye and produced the labeled protein in PBST buffer (20 mM NaH_2PO_4/Na_2HPO_4, 100 mM NaCl [pH 7.5], 0.05% (v/v) Tween 20). Labeled SIRK1–ECD was adjusted to a final concentration of about 20 nM in PBST buffer and then titrated with serial (1:1) dilutions of PEP7 (starting at 0.5 mM), PEP6, or PEP4 (all peptides obtained from Pepmic). The complex was allowed to establish for 10 min at room temperature before the samples were loaded into the capillaries (MO-K025, NanoTemper Technologies). Binding was detected by a Monolith NT.115 instrument (NanoTemper Technologies) at 24°C with 80% excitation power and 40% MST power, and a dose-response curve was generated. QSK1–ECD with a final concentration 20 nM was applied for triple binding affinity estimation. All experiments were repeated at least three times. Raw data were analyzed by MO Affinity Analysis software (v.2.2.4) and OriginPro software.

Protoplast swelling assays

Surface-sterilized seeds after vernalization for 48 h were germinated and grown vertically on sucrose-starved medium ($^1/_2$MS solid medium with 0.02% sucrose). Approximately 30 seedlings were cut into small pieces, and cell walls were digested in 300 mM mannitol, 10 mM MES-KOH (pH 5.8), 10 mM $CaCl_2$, 10 mM KCl containing 1% (w/v) cellulase Onozuka R10 (Duchefa), and 1% (w/v) macerozyme R10 (Duchefa). After 3 h of gentle shaking in the dark at room temperature, the protoplasts were prepared via a 50 μm nylon mesh filter. Protoplasts were then enriched by centrifugation at 80 × *g* at 4°C for 10 min and washed three times with ice-cold wash buffer (300 mM mannitol, 10 mM MES-KOH [pH 5.8], 10 mM $CaCl_2$, 10 mM KCl). The protoplasts were finally resuspended in 150 μL wash buffer and stored in the dark on ice for at least 30 min before an experiment was started. In principle, protoplast swelling experiments were performed as described earlier (Sommer et al., 2007; Wu et al., 2013). Approximately 20 μl of the protoplast suspension were pipetted to 200 μL high osmolarity solution (supplemental Table 4) in a perfusion chamber mounted on the stage of an inverted microscope (DMi8, Leica). Protoplasts were allowed to settle down for 5 min. The chamber was perfused with 3 ml of high osmolarity solution to select protoplasts sticking well to the glass bottom of the chamber, then the chamber was perfused with low osmolarity solution. Solution change in the chamber took about 15 s. A video was recorded for 5 min to capture the dynamic change of the protoplasts with the time interval of 3 s. Buffers with 30 mM sucrose and/or 1 μM PEP7 are described in supplemental Table 4. The diameter of the protoplasts was measured directly by using the Leica software LAS X Core, followed by the calculation of volume and surface area at each time point. A regression curve was fitted to the volume change, and the maximal slope was obtained from the first derivative of the curve. The maximal water flux density that corresponds to aquaporin activity thus was determined by the maximal slope divided by the protoplast surface area at the corresponding time point.

Curve fitting and derivative calculation were performed with OriginPro software.

FLIM–FRET analysis

The coding sequences of SIRK1 and QSK1 were expressed as C-terminal fluorophore fusions in 2in1 vectors, namely pFRETcg-2in1-CC (Hecker et al., 2015). To obtain GFF-donor-only controls, a coding sequence of gentamycin fused to mCherry was used. The binary vectors and p19 as gene silencing suppressor were introduced into *GV3101* and infiltrated into 3- to 4-week-old *N. benthamiana* leaves. After infiltration, the plants were put in darkness for 2 days. Then, 1 μM PEP7 or water was added to the system by infiltration into the leaves right before the measurement. In some experiments, the proteinase inhibitor leupeptin was infiltrated directly with the constructs at a concentration of 10 μM. The measurements were performed for a maximum time of 10 min based on a modified protocol (Glöckner et al., 2019) with a SP8 confocal laser scanning microscope (Leica Microsystems) equipped with Leica Microsystems Application Suite software and a FastFLIM upgrade from PicoQuant consisting of Sepia Multichannel Picosecond Diode Laser, PicoQuant Timeharp 260, TCSPC Module, and Picosecond Event Timer (Picoquant). Imaging was done by using a 63×/1.20 water-immersion objective and focusing on the plasma membrane of the abaxial epidermal cells. The presence of the fluorophores was detected by excitation with 488 or 561 nm and 500–500 or 600–650 nm detection range for GFP or mCherry, respectively. Co-localization was demonstrated by reading out signal intensities over the plasma membrane. GFP FLT in nanoseconds of either donor-only-expressing cells or cells expressing the indicated combinations was measured with a pulsed laser as an excitation light source of 470 nm and a repetition rate of 40 MHz. The acquisition was performed until 500 photons in the brightest pixel were reached at a resolution of 256 × 256 pixels. For data processing, a region of interest at the plasma membrane was defined in the SymPhoTime software, and bi-exponential curve fitting as well as correction for the instrument response function was applied. A total range of 23 ns was evaluated. Statistical analysis was carried out with JMP 14 and OriginPro software.

Trypsin digestion and phosphopeptide enrichment

Protein pellets were solubilized in 10 mM Tris-HCl (pH 8.0), 6 M urea, and 2 M thiourea and by subjecting the protein solution to ultrasonic bath for 10 min. In-solution trypsin digestion was carried out as described (Wu et al., 2017). Digested peptides were resuspended in 1 M glycolic acid, 80% v/v Acetonitrile, and 6% v/v TFA 80%. Phosphopeptides were enriched by TiO_2 beads (Titansphere, 5 μm, GL Sciences) as described (Wu et al., 2017).

Liquid chromatography–tandem mass spectrometry analysis of peptides and phosphopeptides

Peptides mixtures were analyzed by nanoflow Easy-nLC (Thermo Fisher Scientific) and Orbitrap hybrid mass spectrometer (Q-exactive HF, Thermo Fisher Scientific). Peptides were eluted from a 75 μm × 25 cm analytical C_{18} column (PepMan, Thermo Fisher Scientific) on a linear gradient running from 4% to 64% acetonitrile over 135 min. Proteins were identified based on the information-dependent acquisition of fragmentation spectra of multiple charged peptides. Up to 12 data-dependent tandem mass spectrometry spectra were acquired for each full-scan spectrum acquired at 60 000 full-width half-maximum resolution.

Peptide and protein identification

Protein identification and ion intensity quantitation was carried out by MaxQuant v.1.5.3.8 (Cox and Mann, 2008). Spectra were matched against the *Arabidopsis* proteome (TAIR10, 35 386 entries) using Andromeda (Cox et al., 2011). Thereby, carbamidomethylation of cysteine was set as a fixed modification; oxidation of methionine as well as phosphorylation of serine, threonine, and tyrosine were set as variable modifications. Mass tolerance for the database search was set to 20 ppm on full scans and 0.5 Da for fragment ions. Multiplicity was set to 1. For label-free quantitation, retention time matching between runs was chosen within a time window of 2 min. Peptide false discovery rate (FDR) and protein FDR were set to 0.01, while site FDR was set to 0.05. Hits to contaminants (e.g., keratins) and reverse hits identified by MaxQuant were excluded from further analysis. The mass spectrometry proteomics data have been deposited to the ProteomeXchange Consortium via the PRIDE (Deutsch et al., 2017) partner repository with the dataset identifiers PXD029498 (affinity purification combined with mass spectrometry experiments), PXD029050 (binding assays), and PXD029509 (phosphoproteomics).

Label-free peptide and protein quantitation

We followed a label-free quantitation approach bases on the label-free quantification (LFQ) values as quantitative information obtained from MaxQuant (Cox et al., 2014). For protein identification and quantitation, protein groups information (protein groups.txt) was used. For quantitation of phosphopeptides, the phosphosite data (Phospho(STY)Sites.txt) were used as they were written by MaxQuant. Data analysis and multivariate statistics were performed by Perseus (Tyanova et al., 2016).

Statistical analyses and data visualization

Functional classification of proteins was done based on MapMan (Thimm et al., 2004). Subcellular location information was derived from SUBA (Tanz et al., 2013). Protein function was manually updated with TAIR (Poole, 2007). Other statistical analyses were carried out with SigmaPlot (v.11.0) and Excel (Microsoft, 2013).

SUPPLEMENTAL INFORMATION

Supplemental information is available at *Molecular Plant Online*.

FUNDING

We thank Julian Ams and Sonja Pressmar for their work on apoplasmic proteomes. We thank Prof. Gerhard Obermeyer and Prof. Heidi-Pertl Obermeyer for advice on establishing the protoplast swelling assay system and Sandra Herold for her assistance during the revision process. Research in our laboratories was supported by the German Research Foundation (DFG) with grants to W.X.S. (SCHU1533/10-1 and SCHU1533/11-1) and to K.H. (CRC 1101-D02, HA 2146/22-2, and HA 2146/23-1) and a grant for scientific equipment (INST 37/819-1 FUGG).

AUTHOR CONTRIBUTIONS

J.W. and L.X., performed experiments, analyzed data, and wrote manuscript; X.N.W., S.K., L.R., T.N., and J.W., performed experiments and analyzed data; K.H. and W.X.S., analyzed data and wrote manuscript.

ACKNOWLEDGMENTS

No conflict of interest is declared.

Received: April 5, 2022
Revised: July 11, 2022
Accepted: September 19, 2022
Published: September 20, 2022

REFERENCES

Abarca, A., Franck, C.M., and Zipfel, C. (2021). Family-wide evaluation of RAPID ALKALINIZATION FACTOR peptides. Plant Physiol. **187**:996–1010.

Arabidopsis Interactome Mapping Consortium, T. (2011). Evidence for network evolution in an Arabidopsis interactome map. Science **333**:601–607.

Bartels, S., Lori, M., Mbengue, M., van Verk, M., Klauser, D., Hander, T., Böni, R., Robatzek, S., and Boller, T. (2013). The family of Peps and their precursors in Arabidopsis: differential expression and localization but similar induction of pattern-triggered immune responses. J. Exp. Bot. **64**:5309–5321.

Bücherl, C.A., Jarsch, I.K., Schudoma, C., Segonzac, C., Mbengue, M., Robatzek, S., MacLean, D., Ott, T., and Zipfel, C. (2017). Plant immune and growth receptors share common signalling components but localise to distinct plasma membrane nanodomains. Elife **6**:e25114.

Caesar, K., Elgass, K., Chen, Z., Huppenberger, P., Witthöft, J., Schleifenbaum, F., Blatt, M.R., Oecking, C., and Harter, K. (2011). A fast brassinolide-regulated response pathway in the plasma membrane of Arabidopsis thaliana. Plant J. **66**:528–540.

Clark, S.E., Williams, R.W., and Meyerowitz, E.M. (1997). The CLAVATA1 gene encodes a putative receptor kinase that controls shoot and floral meristem size in Arabidopsis. Cell **89**:575–585.

Cox, J., Hein, M.Y., Luber, C.A., Paron, I., Nagaraj, N., and Mann, M. (2014). Accurate proteome-wide label-free quantification by delayed normalization and maximal peptide ratio extraction, termed MaxLFQ. Mol. Cell. Proteomics **13**:2513–2526.

Cox, J., and Mann, M. (2008). MaxQuant enables high peptide identification rates, individualized p.p.b.-range mass accuracies and proteome-wide protein quantification. Nat. Biotechnol. **26**:1367–1372.

Cox, J., Neuhauser, N., Michalski, A., Scheltema, R.A., Olsen, J.V., and Mann, M. (2011). Andromeda: a peptide search engine integrated into the MaxQuant environment. J. Proteome Res. **10**:1794–1805.

Deutsch, E.W., Csordas, A., Sun, Z., Jarnuczak, A., Perez-Riverol, Y., Ternent, T., Campbell, D.S., Bernal-Llinares, M., Okuda, S., Kawano, S., et al. (2017). The ProteomeXchange consortium in 2017: supporting the cultural change in proteomics public data deposition. Nucleic Acids Res. **45**:D1100–D1106.

di Pietro, M., Vialaret, J., Li, G.W., Hem, S., Prado, K., Rossignol, M., Maurel, C., and Santoni, V. (2013). Coordinated post-translational responses of aquaporins to abiotic and nutritional stimuli in Arabidopsis roots. Mol. Cell. Proteomics **12**:3886–3897.

Glöckner, N., zur Oven-Krockhaus, S., Wackenhut, F., Burmeister, M., Wanke, F., Holzwart, E., Meixner, A.J., Wolf, S., and Harter, K. (2019). Three-fluorophore FRET-FLIM enables the study of trimeric protein interactions and complex formation with nanoscale resolution in living plant cells. Preprint at bioRxiv. https://doi.org/10.1101/722124.

Gronnier, J., Franck, C.M., Stegmann, M., DeFalco, T.A., Abarca, A., Von Arx, M., Dünser, K., Lin, W., Yang, Z., Kleine-Vehn, J., et al. (2022). Regulation of immune receptor kinase plasma membrane nanoscale organization by a plant peptide hormone and its receptors. Elife **11**:e74162.

Hander, T., Fernández-Fernández, Á.D., Kumpf, R.P., Willems, P., Schatowitz, H., Rombaut, D., Staes, A., Nolf, J., Pottie, R., Yao, P., et al. (2019). Damage on plants activates Ca(2+)-dependent metacaspases for release of immunomodulatory peptides. Science **363**:eaar7486.

Hecker, A., Wallmeroth, N., Peter, S., Blatt, M.R., Harter, K., and Grefen, C. (2015). Binary 2in1 vectors improve in planta (Co) localization and dynamic protein interaction studies. Plant Physiol. **168**:776–787.

Jones, A.M., Xuan, Y., Xu, M., Wang, R.-S., Ho, C.H., Lalonde, S., You, C.H., Sardi, M.I., Parsa, S.A., Smith-Valle, E., et al. (2014). Border control - a membrane-linked interactome of Arabidopsis. Science **344**:711–716.

Krol, E., Mentzel, T., Chinchilla, D., Boller, T., Felix, G., Kemmerling, B., Postel, S., Arents, M., Jeworutzki, E., Al-Rasheid, K.A.S., et al. (2010). Perception of the Arabidopsis danger signal peptide 1 involves the pattern recognition receptor AtPEPR1 and its close homologue AtPEPR2. J. Biol. Chem. **285**:13471–13479.

Ladwig, F., Dahlke, R.I., Stührwohldt, N., Hartmann, J., Harter, K., and Sauter, M. (2015). Phytosulfokine regulates growth in Arabidopsis through a response module at the plasma membrane that includes CYCLIC NUCLEOTIDE-GATED CHANNEL17, H+-ATPase, and BAK1. Plant Cell **27**:1718–1729.

Matsubayashi, Y. (2003). Ligand-receptor pairs in plant peptide signaling. J. Cell Sci. **116**:3863–3870.

Matsubayashi, Y. (2014). Posttranslationally modified small-peptide signals in plants. Annu. Rev. Plant Biol. **65**:385–413.

Moussu, S., Broyart, C., Santos-Fernandez, G., Augustin, S., Wehrle, S., Grossniklaus, U., and Santiago, J. (2020). Structural basis for recognition of RALF peptides by LRX proteins during pollen tube growth. Proc. Natl. Acad. Sci. **117**:7494–7503.

Niittylä, T., Fuglsang, A.T., Palmgren, M.G., Frommer, W.B., and Schulze, W.X. (2007). Temporal analysis of sucrose-induced phosphorylation changes in plasma membrane proteins of Arabidopsis. Mol. Cell. Proteomics **6**:1711–1726.

Ogawa, M., Shinohara, H., Sakagami, Y., and Matsubayashi, Y. (2008). Arabidopsis CLV3 peptide directly binds CLV1 ectodomain. Science **319**:294.

Olsson, V., Joos, L., Zhu, S., Gevaert, K., Butenko, M.A., and De Smet, I. (2019). Look closely, the beautiful may Be small: precursor-derived peptides in plants. Annu. Rev. Plant Biol. **70**:153–186.

Osakabe, Y., Yamaguchi-Shinozaki, K., Shinozaki, K., and Tran, L.S.P. (2013). Sensing the environment: key roles of membrane-localized kinases in plant perception and response to abiotic stress. J. Exp. Bot. **64**:445–458.

Pearce, G., Strydom, D., Johnson, S., and Ryan, C.A. (1991). A polypeptide from tomato leaves induces wound-inducible proteinase inhibitor proteins. Science **253**:895–897.

Péret, B., Li, G., Zhao, J., Band, L.R., Voß, U., Postaire, O., Luu, D.T., Da Ines, O., Casimiro, I., Lucas, M., et al. (2012). Auxin regulates aquaporin function to facilitate lateral root emergence. Nat. Cell Biol. **14**:991–998.

Perraki, A., DeFalco, T.A., Derbyshire, P., Avila, J., Séré, D., Sklenar, J., Qi, X., Stransfeld, L., Schwessinger, B., Kadota, Y., et al. (2018). Phosphocode-dependent functional dichotomy of a common co-receptor in plant signalling. Nature **561**:248–252.

Pertl, H., Himly, M., Gehwolf, R., Kriechbaumer, R., Strasser, D., Michalke, W., Richter, K., Ferreira, F., and Obermeyer, G. (2001). Molecular and physiological characterisation of a 14-3-3 protein from lily pollen grains regulating the activity of the plasma membrane H+ ATPase during pollen grain germination and tube growth. Planta **213**:132–141.

Poole, R.L. (2007). The TAIR database. Methods Mol. Biol. **406**:179–212.

Rautengarten, C., Steinhauser, D., Büssis, D., Stintzi, A., Schaller, A., Kopka, J., and Altmann, T. (2005). Inferring hypotheses on functional relationships of genes: analysis of the Arabidopsis thaliana subtilase gene family. PLoS Comput. Biol. **1**:e40.

Ryu, K.H., Huang, L., Kang, H.M., and Schiefelbein, J. (2019). Single-cell RNA sequencing resolves molecular relationships among individual plant cells. Plant Physiol. **179**:1444–1456.

Santiago, J., Brandt, B., Wildhagen, M., Hohmann, U., Hothorn, L.A., Butenko, M.A., and Hothorn, M. (2016). Mechanistic insight into a peptide hormone signaling complex mediating floral organ abscission. Elife **5**:e15075.

Santiago, J., Henzler, C., and Hothorn, M. (2013). Molecular mechanism for plant steroid receptor activation by somatic embryogenesis co-receptor kinases. Science **341**:889–892.

Schaller, A., Stintzi, A., Rivas, S., Serrano, I., Chichkova, N.V., Vartapetian, A.B., Martínez, D., Guiamét, J.J., Sueldo, D.J., van der Hoorn, R.A.L., et al. (2018). From structure to function - a family portrait of plant subtilases. New Phytol. **218**:901–915.

Schardon, K., Hohl, M., Graff, L., Pfannstiel, J., Schulze, W., Stintzi, A., and Schaller, A. (2016). Precursor processing for plant peptide hormone maturation by subtilisin-like serine proteinases. Science **354**:1594–1597.

Scheer, J.M., and Ryan, C.A. (2002). The systemin receptor SR160 from *Lycopersicon peruvianum* is a member of the LRR receptor kinase family. Proc. Natl. Acad. Sci. **99**:9585–9590.

Schlesier, B., Bréton, F., and Mock, H.P. (2003). A hydroponic culture system for growing Arabidopsis thaliana plantlets under sterile conditions. Plant Mol. Biol. Rep. **21**:449–456.

Shulse, C.N., Cole, B.J., Ciobanu, D., Lin, J., Yoshinaga, Y., Gouran, M., Turco, G.M., Zhu, Y., O'Malley, R.C., Brady, S.M., et al. (2019). High-throughput single-cell transcriptome profiling of plant cell types. Cell Rep. **27**:2241–2247.e4.

Sommer, A., Mahlknecht, G., and Obermeyer, G. (2007). Measuring the osmotic water permeability of the plant protoplast plasma membrane: implication of the nonosmotic volume. J. Membr. Biol. **215**:111–123.

Stegmann, M., Monaghan, J., Smakowska-Luzan, E., Rovenich, H., Lehner, A., Holton, N., Belkhadir, Y., and Zipfel, C. (2017). The receptor kinase FER is a RALF-regulated scaffold controlling plant immune signaling. Science **355**:287–289.

Stührwohldt, N., Bühler, E., Sauter, M., and Schaller, A. (2021). Phytosulfokine (PSK) precursor processing by subtilase SBT3.8 and PSK signaling improve drought stress tolerance in Arabidopsis. J. Exp. Bot. **72**:3427–3440.

Sun, Y., Han, Z., Tang, J., Hu, Z., Chai, C., Zhou, B., and Chai, J. (2013a). Structure reveals that BAK1 as a co-receptor recognizes the BRI1-bound brassinolide. Cell Res. **23**:1326–1329.

Sun, Y., Li, L., Macho, A.P., Han, Z., Hu, Z., Zipfel, C., Zhou, J.M., and Chai, J. (2013b). Structural basis for flg22-induced activation of the Arabidopsis FLS2-BAK1 immune complex. Science **342**:624–628.

Tabata, R., Sumida, K., Yoshii, T., Ohyama, K., Shinohara, H., and Matsubayashi, Y. (2014). Perception of root-derived peptides by shoot LRR-RKs mediates systemic N-demand signaling. Science **346**:343–346.

Tanz, S.K., Castleden, I., Hooper, C.M., Vacher, M., Small, I., and Millar, H.A. (2013). SUBA3: a database for integrating experimentation and prediction to define the SUBcellular location of proteins in Arabidopsis. Nucleic Acids Res. **41**:D1185–D1191.

Tavormina, P., De Coninck, B., Nikonorova, N., De Smet, I., and Cammue, B.P.A. (2015). The plant peptidome: an expanding repertoire of structural features and biological functions. Plant Cell **27**:2095–2118.

Thieme, C.J., Rojas-Triana, M., Stecyk, E., Schudoma, C., Zhang, W., Yang, L., Miñambres, M., Walther, D., Schulze, W.X., Paz-Ares, J., et al. (2015). Endogenous Arabidopsis messenger RNAs transported to distant tissues. Native Plants **1**:15025.

Thimm, O., Bläsing, O., Gibon, Y., Nagel, A., Meyer, S., Krüger, P., Selbig, J., Müller, L.A., Rhee, S.Y., and Stitt, M. (2004). MAPMAN: a user-driven tool to display genomics data sets onto diagrams of metabolic pathways and other biological processes. Plant J. **37**:914–939.

Tyanova, S., Temu, T., Sinitcyn, P., Carlson, A., Hein, M.Y., Geiger, T., Mann, M., and Cox, J. (2016). The Perseus computational platform for comprehensive analysis of (prote)omics data. Nat. Methods **13**:731–740.

Vandeleur, R.K., Sullivan, W., Athman, A., Jordans, C., Gilliham, M., Kaiser, B.N., and Tyerman, S.D. (2014). Rapid shoot-to-root signalling regulates root hydraulic conductivity via aquaporins. Plant Cell Environ. **37**:520–538.

Vercammen, D., van de Cotte, B., De Jaeger, G., Eeckhout, D., Casteels, P., Vandepoele, K., Vandenberghe, I., Van Beeumen, J., Inzé, D., and Van Breusegem, F. (2004). Type II metacaspases Atmc4 and Atmc9 of Arabidopsis thaliana cleave substrates after arginine and lysine. J. Biol. Chem. **279**:45329–45336.

Wang, L., Einig, E., Almeida-Trapp, M., Albert, M., Fliegmann, J., Mithöfer, A., Kalbacher, H., and Felix, G. (2018). The systemin receptor SYR1 enhances resistance of tomato against herbivorous insects. Native Plants **4**:152–156.

Wang, Z.-Y., Seto, H., Fujioka, S., Yoshida, S., and Chory, J. (2001). BRI1 is a critical component of a plasma-membrane receptor for plant steroids. Nature **410**:380–383.

Winter, D., Vinegar, B., Nahal, H., Ammar, R., Wilson, G.V., and Provart, N.J. (2007). An "electronic fluorescent pictograph" browser for exploring and analyzing large-scale biological data sets. PLoS One **2**:e718.

Witte, C.P., Noël, L.D., Gielbert, J., Parker, J.E., and Romeis, T. (2004). Rapid one-step protein purification from plant material using the eight-amino acid StrepII epitope. Plant Mol. Biol. **55**:135–147.

Wu, X., Liu, T., Zhang, Y., Duan, F., Neuhäuser, B., Ludewig, U., Schulze, W.X., and Yuan, L. (2019a). Ammonium and nitrate regulate NH4+ uptake activity of Arabidopsis ammonium transporter AtAMT1;3 via phosphorylation at multiple C-terminal sites. J. Exp. Bot. **70**:4919–4930.

Wu, X.N., Sanchez-Rodriguez, C., Pertl-Obermeyer, H., Obermeyer, G., and Schulze, W.X. (2013). Sucrose-induced receptor kinase SIRK1 regulates a plasma membrane aquaporin in Arabidopsis. Mol. Cell. Proteomics **12**:2856–2873.

Wu, X.N., Chu, L., Xi, L., Pertl-Obermeyer, H., Li, Z., Sklodowski, K., Sanchez-Rodriguez, C., Obermeyer, G., and Schulze, W.X. (2019b). Sucrose-induced receptor kinase 1 is modulated by an interacting kinase with short extracellular domain. Mol. Cell. Proteomics **18**:1556–1571.

Wu, X.N., Xi, L., Pertl-Obermeyer, H., Li, Z., Chu, L.C., and Schulze, W.X. (2017). Highly efficient single-step enrichment of low abundance phosphopeptides from plant membrane preparations. Front. Plant Sci. **8**:1673.

Xi, L., Wu, X.N., Gilbert, M., and Schulze, W.X. (2019). Classification and interactions of LRR receptors and Co-receptors within the Arabidopsis plasma membrane - an Overview. Front. Plant Sci. **10**:472.

Yamaguchi, Y., Huffaker, A., Bryan, A.C., Tax, F.E., and Ryan, C.A. (2010). PEPR2 is a second receptor for the Pep1 and Pep2 peptides and contributes to defense responses in Arabidopsis. Plant Cell **22**:508–522.

Zhang, H., Han, Z., Song, W., and Chai, J. (2016a). Structural insight into recognition of plant peptide hormones by receptors. Mol. Plant **9**:1454–1463.

Zhang, H., Lin, X., Han, Z., Qu, L.J., and Chai, J. (2016b). Crystal structure of PXY-TDIF complex reveals a conserved recognition mechanism among CLE peptide-receptor pairs. Cell Res. **26**:543–555.

Zhang, H., Lin, X., Han, Z., Wang, J., Qu, L.J., and Chai, J. (2016c). SERK family receptor-like kinases function as Co-receptors with PXY for plant vascular development. Mol. Plant **9**:1406–1414.

Zulawski, M., Schulze, G., Braginets, R., Hartmann, S., and Schulze, W.X. (2014). The Arabidopsis Kinome: phylogeny and evolutionary insights into functional diversification. BMC Genom. **15**:548.

Molecular Plant, Volume *15*

Supplemental information

PEP7 acts as a peptide ligand for the receptor kinase SIRK1 to regulate aquaporin-mediated water influx and lateral root growth

Jiahui Wang, Lin Xi, Xu Na Wu, Stefanie König, Leander Rohr, Theresia Neumann, Jan Weber, Klaus Harter, and Waltraud X. Schulze

Supplementary Materials

PEP7 acts as a peptide ligand for the receptor kinase SIRK1 to regulate aquaporin-mediated water influx and lateral root growth

Jiahui Wang [1]*, Lin Xi [1]*, Xu Na Wu [1,2], Stefanie König [1], Leander Rohr [3], Theresia Neumann [1], Jan Weber [1], Klaus Harter [3], Waltraud X. Schulze [1]+

*equal contribution

[1] Department of Plant Systems Biology, University of Hohenheim, 70593 Stuttgart, Germany

[2] School of Life Science, Center for Life Sciences, Yunnan University, 650091 Kunming, People's Republic of China

[3] Center for Plant Molecular Biology, University of Tübingen, 72076 Tübingen, Germany

+ Address of correspondence:

Prof. Dr. Waltraud Schulze

University of Hohenheim

Department of Plant Systems Biology

70593 Stuttgart

Email: wschulze@uni-hohenheim.de

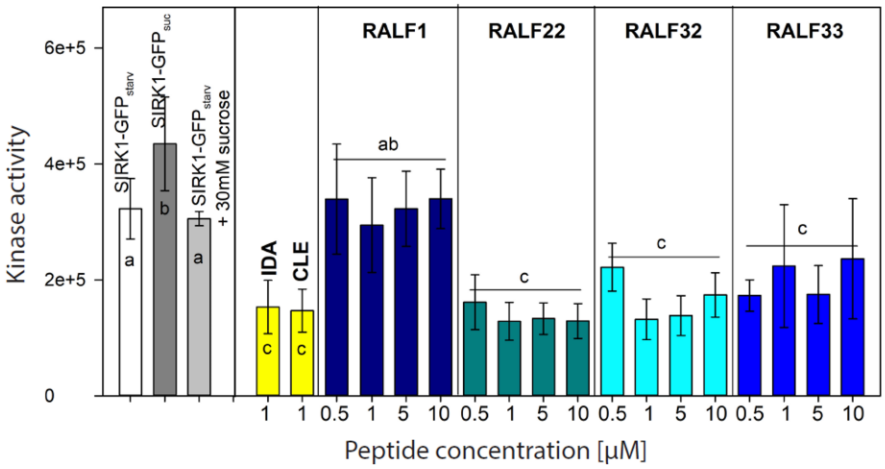

Figure S1: Kinase assay activity assay for SIRK1-GFP enriched from sucrose-starved roots by exposure to different unrelated signaling peptides. IDA and CLE were used as negative controls. RALF peptides were supplied at different concentrations. Averages of three independent assays are shown with standard deviation. Asterisks indicate significant differences to SIRK1-GFP under sucrose starvation (white bar). Note: RALF peptides were added as solubilized synthetic peptides, their internal disulphide bonding structure thus remains unclear (Moussu et al., 2020).

Moussu, S., Broyart, C., Santos-Fernandez, G., Augustin, S., Wehrle, S., Grossniklaus, U., and Santiago, J. (2020). Structural basis for recognition of RALF peptides by LRX proteins during pollen tube growth. Proceedings of the National Academy of Sciences of the United States of America 117:7494-7503.

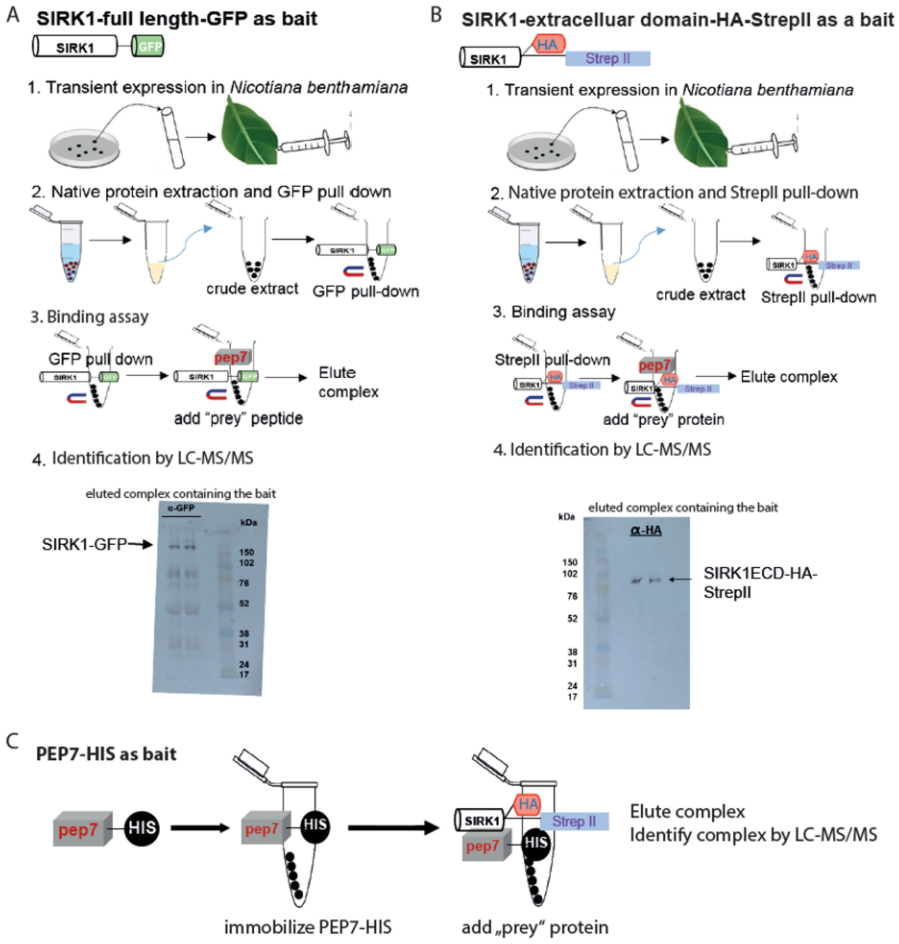

Figure S2: Co-immunoprecipitation workflows to test the interaction of SIRK1 and PEP7. (**A**) Immobilization of SIRK1-GFP to interact with free PEP7. (**B**) Immobilized SIRK1 extracellular domain to interact with free PEP7. (**C**) Immobilized PEP7-HIS6 to interact with SIRK1-GFP, SIRK1 extracellular domain, or native SIRK1 purified from roots. Inserted protein gel blots show the detection of the bait. Interacting proteins were identified by LC-MS/MS.

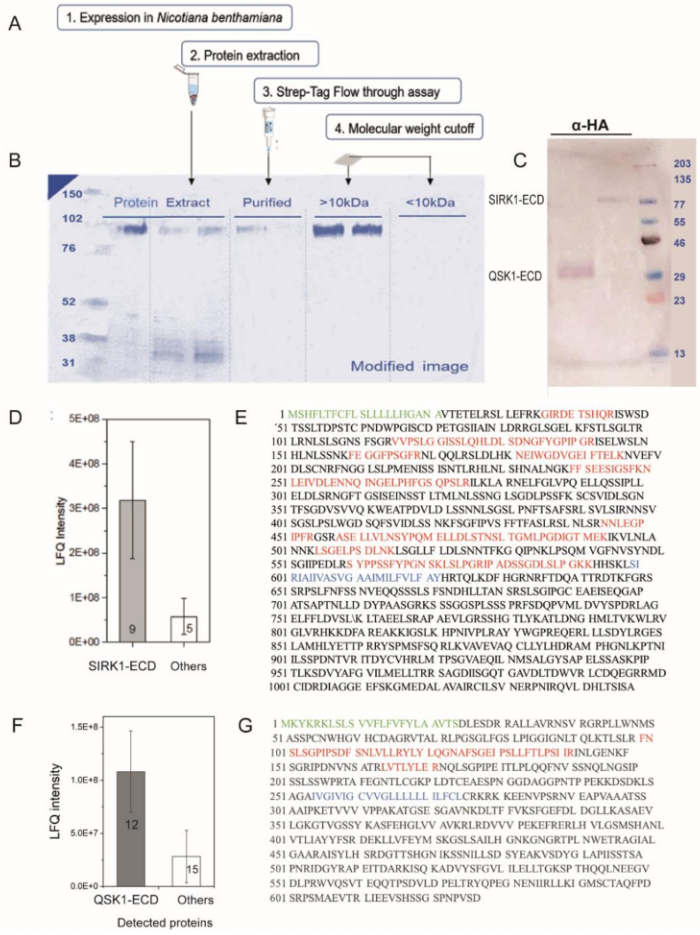

Figure S3: Purification and identification of SIRK1-ECD and QSK1-ECD (**A**) Purification steps of SIRK1-ECD. (**B**) SDS-PAGE analysis of fractions after purifications. (**C**) Western blot of StrepII purified fraction by HA antibody. (**D**) LFQ intensity comparison of tryptic digest peptides from final purified SIRK1-ECD. Nine of the fourteen peptides identified belong to SIRK1, and their summed LFQ intensity was approximately 6-fold higher than the summed LFQ intensity of all the other identified peptides. (**E**) Tryptic digest peptides mass fingerprint analysis of purified SIRK1-ECD. (**F**) LFQ intensity comparison of tryptic digest peptides from final purified QSK1-ECD. (**G**) Tryptic digest peptides mass fingerprint analysis of purified QSK1-ECD. The sequence of full length SIRK1 and QSK1 is shown with signal peptide in green and the transmembrane domain in blue. All identified peptides from the sample were shown in red. All identified SIRK1 peptides cover only the extracellular domain of SIRK1, so does QSK1. Taken together, the purified SIRK1-ECD was considered to meet quality criteria for fluorescent labelling and MST assays.

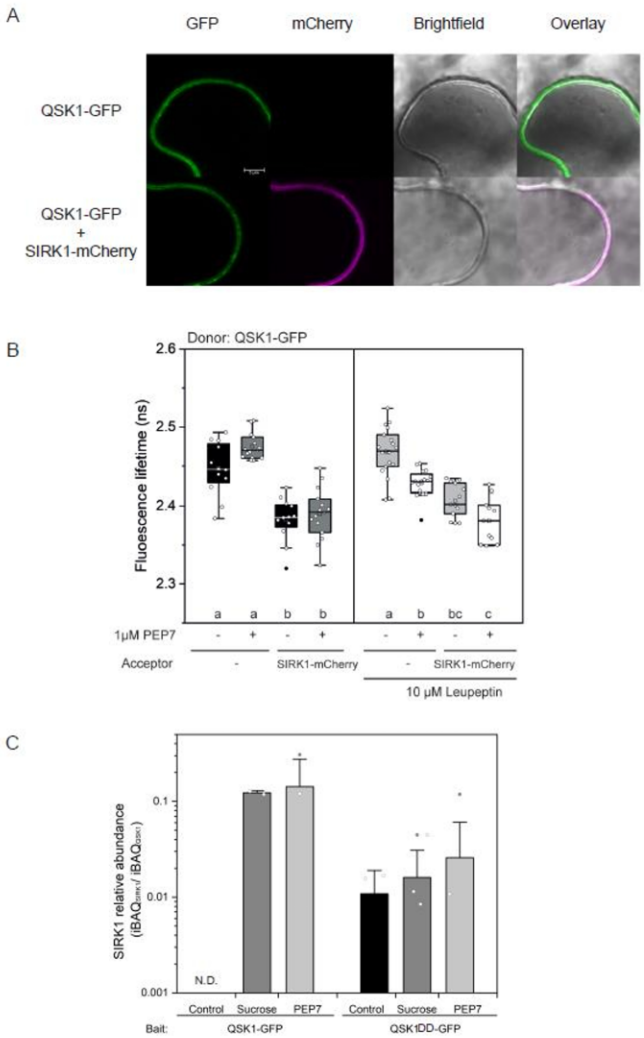

Figure S4: FRET-FLIM of SIRK1 and QSK1 in presence and absence of PEP7. (**A**) Representative confocal images show co-localization of SIRK1 and QSK1 with or without infiltration of 1 µM PEP7. Constructs were transiently transformed in *N. benthamiana* leaf cells. Scale bars indicate 5 µm. (**B**) FRET-FLIM reveals spatial proximity of SIRK1 and QSK1 in presence and absence of proteinase inhibitor leupeptin. For each of measurements, n ≥ 7. Statistical differences in FLT were analysed using a two-way ANNOVA followed by Dunn-Sidak multiple comparison test. Small letters indicate significantly different means at $p<0.05$. The centre line indicates the median, the bounds of the box show the 25th and the 75th percentiles, and the whiskers indicate 1.5 × IQR. (**C**) Bait-normalized ion intensities of SIRK1 detected in pull-down of SIRK1 with QSK1-GFP or phosphomimic QSK1DD-GFP upon stimulation with sucrose or PEP7 in root tissue. Bars indicate averages of three pull-downs with standard deviation. Open circles indicate original values of replicates. "N.D.": not detected.

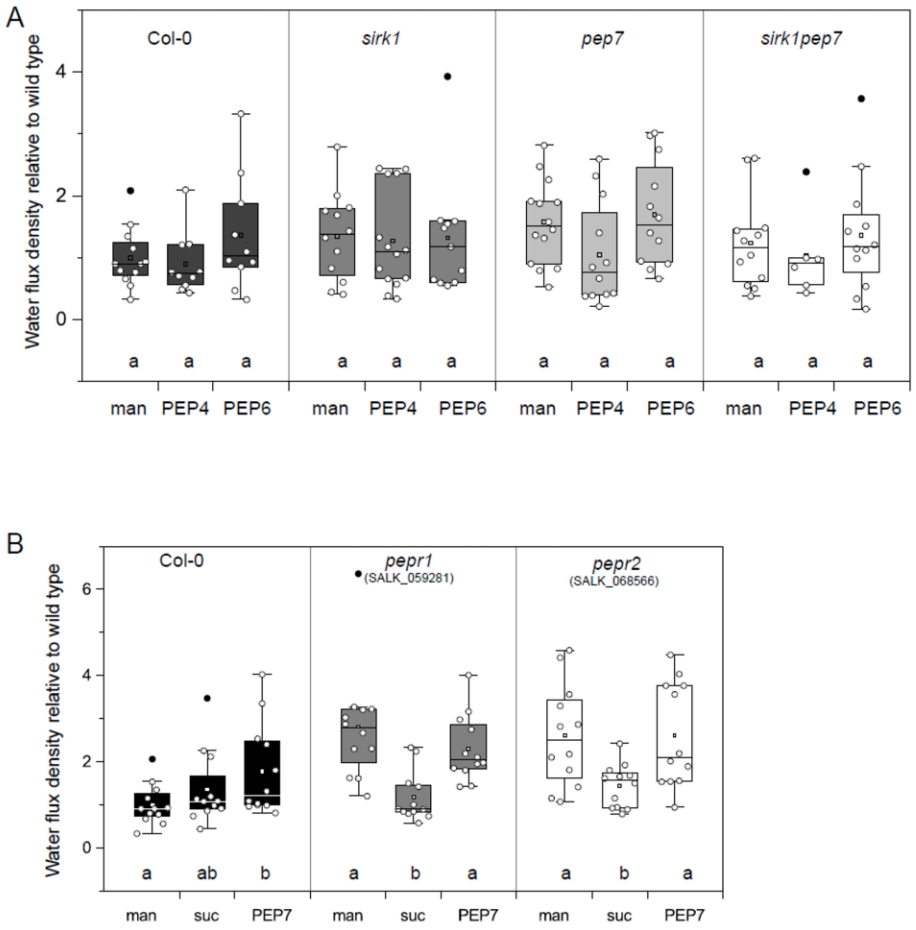

Figure S5: Protoplast swelling assays control treatments. (**A**) Water influx rates relative to wild type mannitol treatment of protoplasts with and without supply of PEP4 and PEP6. (**B**) Water influx rates relative to wild type for pepr1 and pepr2 under mannitol, sucrose and PEP7 treatment. In all panels, boxplots show the median and upper/lower 25th percentile. White dots represent individual measurements. Man, mannitol. Small letters indicate significant differences ($p<0.05$) between treatments as determined by Oneway ANOVA with Holm-Sidak correction.

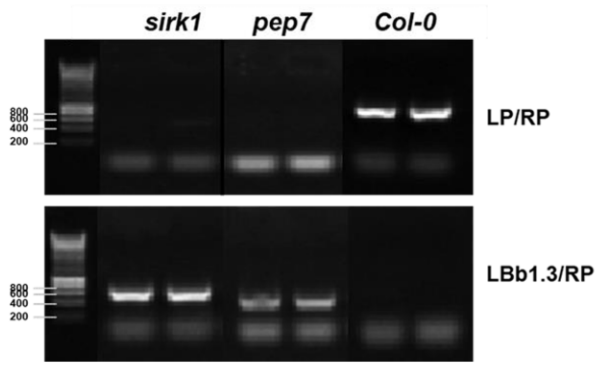

Figure S6: Identification of double mutant of *sirk1pep7* as a result of crossing single mutants *sirk1* (SALK_125543) and *pep7* (SALK_025824).

Supplementary Tables

Supplementary Table 1: Overview of the proteins identified in tryptic and non-tryptic samples in fractions F1, F2 and F3.

Supplementary Table 2: 1076 common Interaction partners of SIRK1 under different treatments.

Supplementary Table 3: List of identified phosphopeptides from which the heatmap in Figure 4 was generated.

Supplementary Table 4: Overview of the buffers used in the protoplast swelling assays.

Perfusion buffer	**Fixed components of Osmotic solutions**		**Non-fixed components of Treatment solutions**			
	Solute with varying concentrations	Solutes of constant concentration	Control	Sucrose	PEP7	PEP6
High osmolarity (300mM) solution	270mM Mannitol	10mM MES, pH 5.8 10mM $CaCl_2$ 10mM KCl	30mM Mannitol	30mM Sucrose	30mM Mannitol containing 1µM PEP7	30mM Mannitol containing 1µM PEP6
Low osmolarity (150mM) solution	120mM Mannitol	10mM MES, pH 5.8 10mM $CaCl_2$ 10mM KCl	30mM Mannitol	30mM Sucrose	30mM Mannitol containing 1µM PEP7	30mM Mannitol containing 1µM PEP6

Note: Sucrose and mannitol produce same osmotic pressure (approximately 1.15 mOsmol kg^{-1} of 1mM osmolyte), measured with a cryoscopic osmometer (Osmomat 030, Gonotec, Berlin, Germany)

Three-Fluorophore FRET Enables the Analysis of Ternary Protein Association in Living Plant Cells

by Glöckner N., zur Oven-Krockhaus S., Rohr L., Wackenhut F., Burmeister M., Wanke F., Holzwart E., Meixner A. J., Wolf S., Harter K. (2022)

in *Plants (Basel)*

doi: https://doi.org/10.3390%2Fplants11192630

Accepted

plants

MDPI

Article

Three-Fluorophore FRET Enables the Analysis of Ternary Protein Association in Living Plant Cells

Nina Glöckner [1], Sven zur Oven-Krockhaus [1,2], Leander Rohr [1], Frank Wackenhut [2], Moritz Burmeister [2], Friederike Wanke [1], Eleonore Holzwart [3], Alfred J. Meixner [2], Sebastian Wolf [1,3] and Klaus Harter [1,*]

[1] Center for Plant Molecular Biology (ZMBP), University of Tübingen, 72076 Tübingen, Germany
[2] Institute for Physical & Theoretical Chemistry, University of Tübingen, 72076 Tübingen, Germany
[3] Centre for Organismal Studies (COS), University of Heidelberg, 69117 Heidelberg, Germany
* Correspondence: klaus.harter@zmbp.uni-tuebingen.de; Tel.: +49-(0)-7071-2972605

Abstract: Protein-protein interaction studies provide valuable insights into cellular signaling. Brassinosteroid (BR) signaling is initiated by the hormone-binding receptor Brassinosteroid Insensitive 1 (BRI1) and its co-receptor BRI1 Associated Kinase 1 (BAK1). BRI1 and BAK1 were shown to interact independently with the Receptor-Like Protein 44 (RLP44), which is implicated in BRI1/BAK1-dependent cell wall integrity perception. To demonstrate the proposed complex formation of BRI1, BAK1 and RLP44, we established three-fluorophore intensity-based spectral Förster resonance energy transfer (FRET) and FRET-fluorescence lifetime imaging microscopy (FLIM) for living plant cells. Our evidence indicates that RLP44, BRI1 and BAK1 form a ternary complex in a distinct plasma membrane nanodomain. In contrast, although the immune receptor Flagellin Sensing 2 (FLS2) also forms a heteromer with BAK1, the FLS2/BAK1 complexes are localized to other nanodomains. In conclusion, both three-fluorophore FRET approaches provide a feasible basis for studying the in vivo interaction and sub-compartmentalization of proteins in great detail.

Keywords: protein-protein interaction; plasma membrane; nanodomains; spectral Förster resonance energy transfer (FRET); FRET-fluorescence lifetime imaging microscopy (FRET-FLIM)

Citation: Glöckner, N.; zur Oven-Krockhaus, S.; Rohr, L.; Wackenhut, F.; Burmeister, M.; Wanke, F.; Holzwart, E.; Meixner, A.J.; Wolf, S.; Harter, K. Three-Fluorophore FRET Enables the Analysis of Ternary Protein Association in Living Plant Cells. *Plants* **2022**, *11*, 2630. https://doi.org/10.3390/plants11192630

Academic Editor: Rongmin Zhao

Received: 5 September 2022
Accepted: 24 September 2022
Published: 6 October 2022

1. Introduction

Integration of different signaling cues at the cellular level is essential for the survival of any organism. In plants, for instance, mechanical damage to the cell wall causes attenuation of cellular growth response while resources are redistributed to repair processes. With the advent of high- and super-resolution microscopy techniques, the discovery of protein localization in nanodomains and the spatial organization of receptors and accompanying proteins (e.g., co-receptors) in the plasma membrane (PM) have come into focus. This has prompted new questions regarding the extent to which the constituents of a given signaling complex or nanodomain are integrated or are disintegrated upon signal perception.

A well-understood pathway in plants is the brassinosteroid (BR) hormone signal transduction, which is mediated by the PM-resident receptor kinase Brassinosteroid Insensitive 1 (BRI1) and its co-receptor BRI1 Associated Kinase 1 (BAK1). The binding of BR to BRI1's extracellular domain increases its interaction with BAK1 and a re-arrangement of proteins in the complex, eventually leading to the auto- and trans-phosphorylation of their Ser/Thr-kinase domains [1,2]. These PM-resident events result in the differential regulation of BR-responsive genes through a nucleo-cytoplasmic signaling cascade [3–6] and the activation of PM-resident P-type proton pumps [7,8].

Receptor-Like Protein 44 (RLP44) was previously described to play a role in cell wall integrity sensing via modulation of BRI1/BAK1-dependent signaling [9] as well as to interact with BRI1 and BAK1 [9,10]. This suggests that RLP44 directly affects the activity of the BRI1/BAK1 complex upon input from the cell wall, as a scaffold protein for the establishment of a specific BRI1/BAK1 complex in the PM [2].

To test the hypothesis of ternary RLP44/BRI1/BAK1 complex formation, we first wanted to establish a three-fluorophore, intensity-based spectral Förster resonance energy transfer (FRET) as well as -fluorescence lifetime imaging microscopy (FRET-FLIM) technique in plant cells. FRET is the non-radiative energy transfer from a donor to an acceptor fluorophore by dipole-dipole interaction, which is only possible over small distances and depends on the relative dipole moment orientation of the donor and acceptor fluorophores [11]. FRET manifests itself by an alteration of the donor and acceptor fluorescence intensities, but also decreases the donor´s excited state lifetime due to the additional relaxation path from the donor to the acceptor [12]. In contrast to two-fluorophore FRET, an intermediate acceptor fluorophore is included in the energy transfer pathway of three-fluorophore FRET. As the plant cell wall cannot be penetrated by organic dyes, our approach depends solely on genetically encoded fluorophores. Here, we exemplary choose monomeric Turquoise 2 (mTRQ2) as donor, monomeric Venus (mVEN) as the first acceptor and monomeric red fluorescence protein 1 (mRFP) as the second acceptor.

Based on theoretical calculations we experimentally show by intensity-based spectral FRET and FRET-FLIM that RLP44, BRI1 and BAK1 are unified in a ternary complex that likely forms in a distinct nanodomain in the PM. This nanodomain is spatially clearly distinct from the FLS2/BAK1 complex-containing nanodomain. In addition, we propose FRET-FLIM to be always better than intensity-based FRET for the analysis of ternary protein complex formation and relative proximity estimates in plant cells.

2. Results

2.1. Physicochemical Properties of the Used Fluorophores

As the selected fluorophores substantially influence the quality of the FRET data, we screened a variety of fluorophores for their suitability in our approach. As a result, all of the used genetically encoded fluorophores were monomeric, minimizing false-positive FRET originating from aggregation. mTRQ2 was used as donor. It has numerous advantages including a long, mono-exponential fluorescence lifetime (FLT) [13] and the spectral overlap of mTRQ2 emission with the absorbance of the first acceptor mVEN is high, yielding a large Förster distance R_0 [14–16]. The second acceptor is mRFP, which has a large spectral overlap with the first acceptor/second donor mVEN. The maturation time of the fluorophores is also a crucial factor for the FRET efficiency (E_{FRET}) [17,18]. In our three-fluorophore system, both mVEN and mRFP have faster maturation times than mTRQ2, ensuring favorable FRET conditions (more details about the fluorophores in Table S1).

2.2. Calculated Properties of the mTRQ2/mVEN/mRFP Three-Fluorophore FRET System

To determine the operational FRET range for the chosen fluorophores, the corresponding Förster distances (R_0) were calculated (Table 1) as well as the distance corresponding to 10% FRET efficiency ($r_{10\%}$). This last parameter best illustrates the measurement limit for FRET that can be realized with standard FRET microscopy measurements. For the complex energy flow in a three-fluorophore setting, $r_{10\%}$ was calculated for the mTRQ2/mRFP pair, adding mVEN as intermediate acceptor. According to the absorption and emission spectra of the used fluorophores (Figure 1a), the emission of mTRQ2 shows a significant spectral overlap with the absorption spectra of both mVEN and mRFP (Figure 1a). Furthermore, the emission spectrum of mVEN substantially overlaps with the absorption spectrum of mRFP, enabling energy transfer from mTRQ2 to mVEN, mVEN to mRFP and mTRQ2 to mRFP. R_0 was calculated with n = 1.4 and κ^2 = 2/3 according to [19], using the spectra and photophysical data from the original publications (Table S2). The resulting Förster distances R_0 were 5.7 nm for the mTRQ2/mVEN, 5.2 nm for the mVEN/mRFP and 5.1 nm for the mTRQ2/mRFP pair (Table 1, Figure 1b). Evidently, the same trend is observed for $r_{10\%}$, which is highest for the mTRQ2/mVEN pair and lowest for the mTRQ2/mRFP pair (Table 1, Figure 1b). In addition, FRET was calculated not to be limited to sequential energy transfer from mTRQ2 via mVEN to mRFP but also from mTRQ2 to mRFP directly (Table 1, Figure 1c).

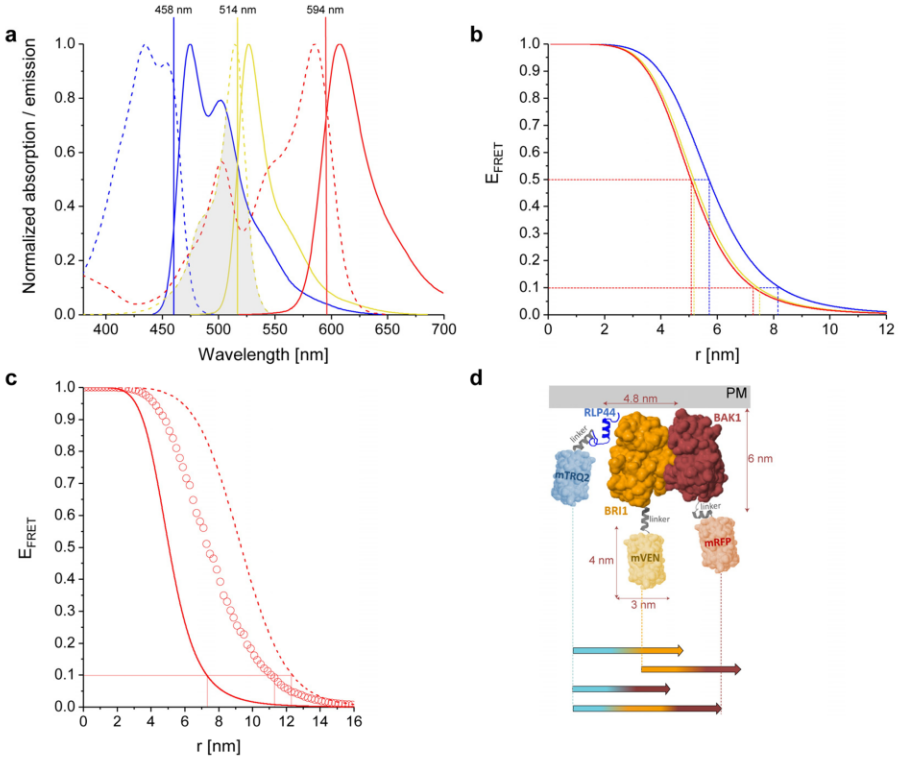

Figure 1. Spectroscopic and FRET properties of the used fluorophores and dimensions of the analyzed RLP44-mTRQ2, BAK1-mVEN and BRI1-mRFP fusion proteins. (**a**) Normalized absorption (dotted lines) and emission (solid lines) spectra of mTRQ2 (blue), mVEN (yellow) and mRFP (red). mTRQ2 is donor to both mVEN as acceptor 1 as well as mRFP as acceptor 2; mVEN is also donor to mRFP. The shaded area corresponds to the spectral overlap between donor emission and acceptor absorption, shown here exemplary for the mTRQ2/mVEN FRET pair. The laser lines for excitation of mTRQ2 (blue), mVEN (yellow) and mRFP (red) are marked as vertical lines at their respective wavelength positions. (**b**) FRET efficiencies (E_{FRET}) for the distances (r) between donor and acceptor fluorophores for mTRQ2-mVEN (blue), mVEN-mRFP (yellow) and mTRQ2-mRFP (red). The Förster distances R_0 at E_{FRET} = 50% as well as the distances that correspond to E_{FRET} = 10% ($r_{10\%}$) for each pair are marked with dashed lines in the respective color. (**c**) E_{FRET} in dependence of distance r between mTRQ2 and mRFP without (solid line) and with intermediate mVEN located either equidistantly (dashed line) or variably (circles) between mTRQ2 and mRFP. For the latter, mVEN was placed at 1000 random positions for each mTRQ2/mRFP distance, averaging over the resulting E_{FRET} values. The $r_{10\%}$ distances are marked with red lines. (**d**) Composite image of the cytoplasmic domains of RLP44 (blue), BRI1 (orange) and BAK1 (brown) fused to the 15 amino acid-long Gateway®-linker to either mTRQ2 (light blue), mVEN (light yellow) or mRFP (light red). The structures of the cytoplasmic domains of BAK1, BRI1 and the fluorophores are shown as solvent-accessible surface models, while the model structures of the cytoplasmic domain of RLP44 and the three Gateway®-linkers (grey) were predicted with PEP-FOLD3 and depicted as cartoons. The orientation of the kinase domains of BRI1 and BAK1 to each other was designed according to a molecular docking analysis in orientation to the PM [20]. The colored arrows below the structures show the $r_{10\%}$ distances for all FRET pairs and the three-chromophore FRET cascade with mVEN inserted at random positions, calculated for a donor to acceptor complex ratio of 1:1. The precise values for b, c and d are listed in Table 1.

Table 1. FRET combinations (1st column), their Förster distances (R_0) (2nd column) and fluorophore distances that correspond to 10% FRET efficiency ($r_{10\%}$), calculated for a linear arrangement with one acceptor (3rd column) in range of each corresponding donor (see also Supplemental Table S2).

FRET Combinations	R_0 [nm]	$r_{10\%}$ [nm], D:A = 1:1
mTRQ2-mVEN	5.7	8.2
mVEN-mRFP	5.2	7.4
mTRQ2-mRFP	5.1	7.3
mTRQ2-mVEN-mRFP (middle position)	-	12.4
mTRQ2-mVEN-mRFP (random position)	-	11.1

For large distances between mTRQ2 and mRFP no direct FRET is expected to be possible. Therefore, the introduction of the intermediate acceptor mVEN could increase the dynamic range between mTRQ2 and mRFP. To estimate this long-range effect, we investigated how the presence of mVEN affects the energy transfer to mRFP in such a FRET cascade [21] and calculated an increase for $r_{10\%}$ from 8.2 nm to 12.4 nm (Figure 1c, Table 1), which is in agreement with the increase in effective FRET distance reported previously [22]. However, the authors of [22] fixed the fluorophore positions along a DNA helix with equidistant separation between the fluorophores. In multimeric protein complexes, however, neither the complex geometry nor the exact position of the attached fluorophores are usually known. Therefore, we additionally calculated an averaged $r_{10\%}$ value when mVEN is inserted at random positions between mTRQ2 and mRFP. In this more realistic representation of our dynamic plant system, we found a slightly smaller increase of $r_{10\%}$ from 8.2 nm to 11.1 nm (Figure 1c, Table 1). This is by far large enough to be able to detect long-range interactions with our three-fluorophore FRET approach.

2.3. Structural Simulation of the Arrangement of the Fluorophore-Tagged Proteins for the Estimation of the FRET Range

To assess how the maximum dynamic range of about 11.1 nm relates to the size of our proteins of interest, we arranged the cytoplasmic domains of RLP44, BRI1 and BAK1 fused to the respective fluorophores and the calculated $r_{10\%}$ values between mTRQ2, mVEN and mRFP in scale in a graph (Figure 1d). As the structures of the fluorophores and the cytoplasmic domains of BRI1 and BAK1 are available, a solvent-accessible surface representation was generated to estimate the protein sizes [23–25]. The orientation of the BRI1 and BAK1 kinase domains to each other was depicted according to the highest probability after a molecular docking analysis [20]. The structures of RLP44´s cytoplasmic domain and the Gateway®-linkers were not available and predicted with PEP-FOLD3 [26] (for details see Section 4). The stoichiometry-adjusted $r_{10\%}$ values for all FRET pairs are between 7.3 and 8.2 nm (Table 1) and therefore could span the distance of two kinase domains, which have diameters of about 4.8 nm (Figure 1d). Most importantly, while RLP44-mTRQ2 and BAK1-mRFP are too far apart for FRET in this exemplary linear arrangement, three-fluorophore FRET from RLP44-mTRQ2 via BRI1-mVEN to BAK1-mRFP is able to span this distance (Figure 1d). The same is expected for a RLP44-mTRQ2/BAK1-mVEN/BRI1-mRFP arrangement.

2.4. Calculation of Cross-Excitation and Bleed-Through in Intensity-Based Spectral FRET Measurements

The vast majority of investigations in animal cells have assessed three-fluorophore FRET with intensity-based methods, specifically by quantitative acquisition of spectra, using predominantly organic dyes. Therefore, we decided to first assess the ternary complex formation for the selected fusion proteins in plant cells with this method.

Regardless of the stoichiometry of the complexes, the expression levels of the fluorophore-fused proteins have a large influence on the spectra of intensity-based FRET, due to cross-excitation and bleed-through. This is demonstrated in the simulated emission

spectra of Figure 2, calculated for a complex stoichiometry of 1:1:1 and a linear arrangement of mTRQ2, mVEN and mRFP placing mVEN at equal distance to the other two fluorophores. With this fluorophore ratio, inter-fluorophore distances above 10 nm (no FRET) and an excitation wavelength of 458 nm, an intensity peak at around 525 nm was calculated to appear due to cross-excitation (Figure 2a, top). With inter-fluorophore distances of 7 nm (Figure 2a, middle) and 5 nm (Figure 2a, bottom), the energy transfer from mTRQ2 to mVEN and mRFP became apparent in the simulated spectra, as the relative mTRQ2 intensity peak decreased, while the mVEN and mRFP peaks increased. The theoretical bleed-through and cross-excitation depend strongly on the donor-to-acceptor ratio of the fluorophores (Figure S2b and Supplementary Materials). Importantly, the bleed-through and cross-excitation effects have a larger influence on the apparent mVEN signal than FRET itself: Already a ratio of 1:2 for mTRQ2/mVEN results in a peak of the fluorescence intensity at around 525 nm similar to that calculated for an inter-fluorophore distance of 7 nm (compare Figure 2a, middle and Figure 2b, top). However, the different mRFP intensity progression was well observable (compare Figure 2a with 2b). This underscores the necessity for a careful calibration of the fusion protein amounts. Therefore, the bleed-through and cross-excitation are always quantified in the presented absorption and emission spectra as well as in the confocal images (see Supplementary Materials).

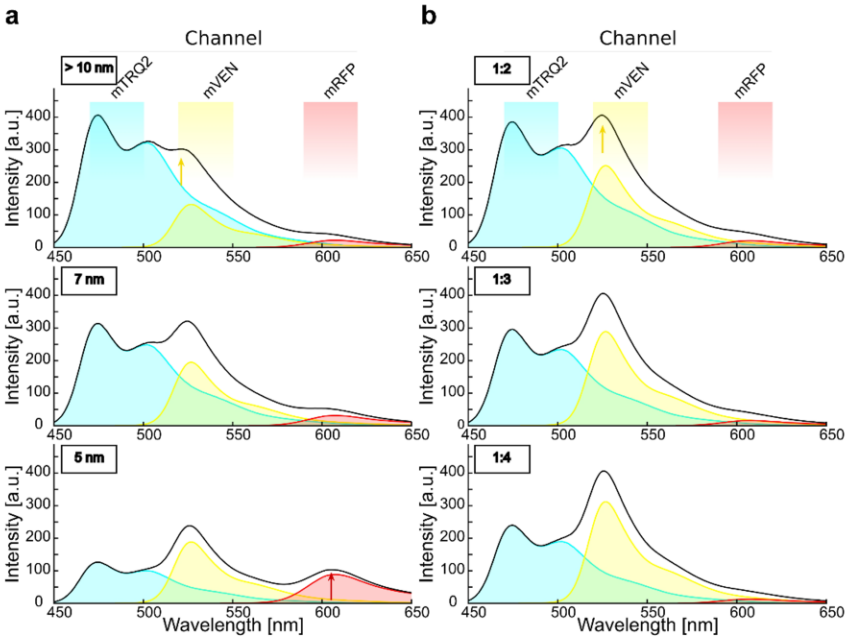

Figure 2. Simulation of emission spectra reveals the crucial impact of relative fluorophore quantities for intensity-based spectral FRET in a three-chromophore arrangement. (**a**) Simulation of the spectra that result from excitation of mTRQ2 with 458 nm for a mTRQ2/mVEN/mRFP stoichiometry of 1:1:1 and in a linear arrangement while placing mVEN at an equal distance from the other two fluorophores. The emission spectra of mTRQ (blue area), mVEN (yellow area) and mRFP (red area) and their combined spectrum (black line) are calculated. The respective emission detector channels are depicted above the plots. With inter-fluorophore distances larger than 10 nm, FRET is negligible (**top**), but cross-excitation

of mVEN (yellow arrow) is apparent. For inter-fluorophore distances of 7 nm (**middle**) and 5 nm (**bottom**), FRET lowers the emission intensity of mTRQ2, while the intensity peaks increases around the emission of mVEN at 525 nm and of mRFP at about 610 nm (red arrow) increase. (**b**) Spectra simulation as in (**a**), but without consideration of FRET, calculated for different mTRQ2/mVEN fluorophore ratios. With rising mTRQ2/mVEN ratios of 1:2 (**top**), 1:3 (**middle**) and 1:4 (**bottom**), the intensity peak of mVEN (yellow arrow) increases. Thus, a mTRQ2/mVEN ratio of 1:2 ((**b**), top) results in a similar spectral shape than with equimolar fluorophores subjected to FRET at a distance of 7 nm ((**a**), middle).

2.5. Experimental Determination of Cross-Excitation and Bleed-Through in Plant Cells

It was previously shown that BRI1/BAK1, RLP44/BRI1 and RLP44/BAK1 form heteromers in plant cells [9,10,27]. In contrast, the PM-localized immune response mediating Flagellin Sensing 2 (FLS2) receptor does not interact with RLP44 [28,29] and was selected as a negative control in the further analyses. The spectra were acquired in transiently transformed *Nicotiana benthamiana* epidermal leaf cells. All fusion proteins localized to the PM (Figure S1). The procedure of spectra acquisition from the regions of interest in the PM is described in detail in Supplementary Materials and Figure S6.

The fluorescence emission spectra of the three fusion constructs (RLP44-mTRQ2, FLS2-mVEN and BAK1-mRFP) were analyzed separately under excitation at 458 nm, whereby only FLS2-mVEN showed a significant amount of cross-excitation (Figure 3a). The quantification of the fluorescence emission of RLP44-mTRQ2 after excitation at 458 nm is a measure of its protein level, manifesting an average intensity of 120 arbitrary units (a.u.) (Figure 3a,b). It was reflected in an emission peak intensity of 120 a.u. in the spectrum (Figure 3a). A relative high accumulation level of FLS2-mVEN with an average intensity of 200 a.u. after excitation at 514 nm (Figure 3b) caused a much smaller background signal of 8 a.u. in the spectrum after excitation with light of 458 nm (Figure 3a). The excitation of BAK1-mRFP with light of 561 nm gave an average intensity of 110 a.u. (Figure 3b) but did not result in a distinct peak in the emission spectrum after excitation with light of 458 nm (Figure 3a). Thus, the different accumulation levels of the fusion proteins led to the same shape of the fluorescence emission spectra but with variations in the peak intensities (Figure S2).

2.6. Intensity-Based FRET Analysis of Dual Protein-Protein Interactions

First, we assessed FRET from the mTRQ2 to the mVEN fusion proteins. Since our simulations indicate that the amount of the fusion proteins has a larger influence on the shape of the spectra than FRET itself, a correction for the relative proteins levels was imperative. Therefore, it was always necessary to compare the spectra with the same donor-to-acceptor ratios of RLP44-mTRQ2/BRI1-mVEN with that of RLP44-mTRQ2/FLS2-mVEN. To this end, each recorded spectrum was subjected to spectral unmixing to determine the relative proportions of mTRQ2 and mVEN (Supplementary Materials; Figure S6). Then, the spectral unmixing information was combined with the respective estimates of fusion protein levels. To do so, each channel was imaged with sequential excitation before acquisition of the spectra (excitation with only 458 nm, then only 514 nm, lastly only 561 nm).

In the spectra with an identical donor-to-acceptor sample ratio, the peak intensity value at about 525 nm was higher for the RLP44-mTRQ2/BRI1-mVEN than for the RLP44-mTRQ2/FLS2-mVEN sample (Figure 3c). The integration of the spectral unmixing results and donor-to-acceptor ratios revealed that the proportion of mVEN emission in the spectra of the RLP44-mTRQ2/BRI1-mVEN sample differed significantly from that of the RLP44-mTRQ2/FLS2-mVEN sample (Figure 3d). This was also true for donor-to-acceptor ratios of approximately 1:10 and 1:4 (Figure 3d). In conclusion, FRET from RLP44-mTRQ2 to BRI1-mVEN was observed when compared with the non-FRET RLP44-mTRQ2/FLS2-mVEN control pair.

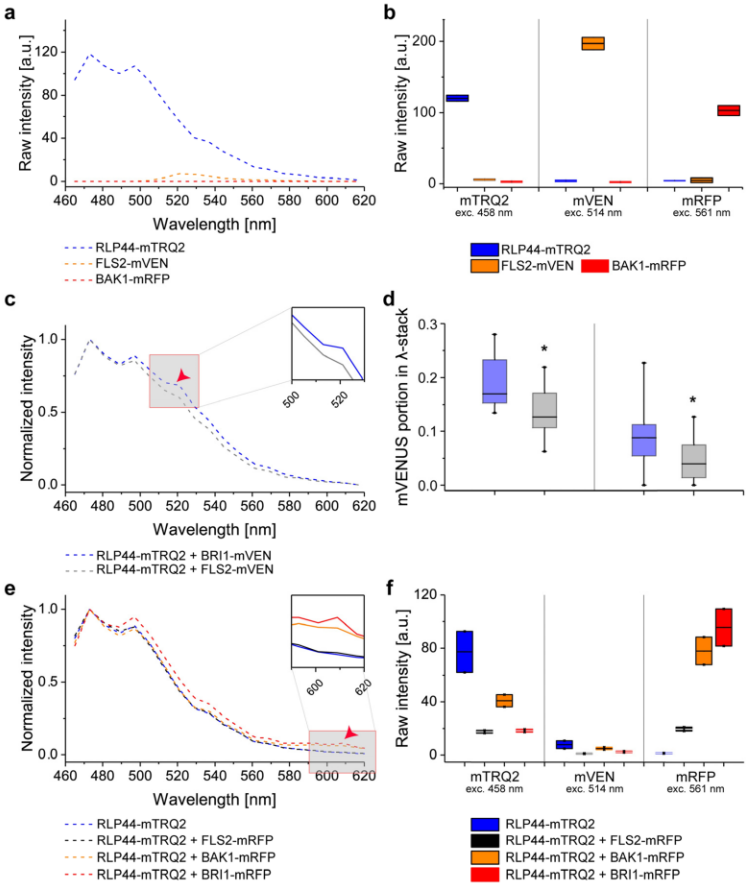

Figure 3. Interaction of RLP44 with BAK1 and BRI1 is detectable in the plasma membrane of *N. benthamiana* epidermal leaf cells by intensity-based spectral FRET. (**a**) Wavelength-dependent intensity of fluorescence emission after irradiation of the cells with 458 nm light for RLP44-mTRQ2 (blue), FLS2-mVEN (orange) and BAK1-mRFP (red). (**b**) Emission intensity after irradiation with light of different wavelengths in the mTRQ2 (left, 458 nm), mVEN (middle, 514 nm) and mRFP channels (right, 561 nm) from 8-bit images for RLP44-mTRQ2 (blue), FLS2-mVEN (orange) and BAK1-mRFP (red) after correction for spectral bleed-through. (**c**) Wavelength-dependent normalized fluorescence emission for RLP44-mTRQ2 co-expressed with BRI1-mVEN (blue) or with FLS2-mVEN (grey). For both spectra, the average donor-to-acceptor ratio was around 1:4 (0.26). The FRET-relevant wavelength area is as an inset and the occurrence of FRET from RLP44-mTRQ2 to BRI1-mVEN is indicated by a red arrow head. The data are presented as the mean ($n \geq 13$). (**d**) Protein-dependent, relative mVEN emission signal after irradiation of the cells with light of 458 nm light. Fusion protein ratios of about 1:4 (left) and 1:10 (right) of the RLP44-mTRQ2/BRI1-mVEN pair (blue) and RLP44-TRQ2/FLS2-mVEN pair (grey) are shown. Significant changes [$n = 7$ (left), $n = 12$ (right)] in a two-sided 2-sample t-test with $p < 0.05$ are indicated by asterisks. (**e**) Wavelength-dependent normalized fluorescence emission after irradiation of the cells with 458 nm light for RLP44-mTRQ2 alone (blue), RLP44-mTRQ/FLS2-mRFP (black), RLP44-mTRQ/BAK1-mRFP (orange) and RLP44-mTRQ/BRI1-mRFP (red). The FRET-relevant wavelength area is highlighted in an enlarged section and the occurrence of FRET fromRLP44-mTRQ2 to BAK1-mRFP or BRI1-mRFP is indicated by a red arrow head. (**f**) Emission intensity after irradiation

of the cells with light of different wavelength in the mTRQ2 (left), mVEN (middle) and mRFP channel (right) from 8-bit images for of RLP44-mTRQ2 (blue), RLP44-mTRQ/FLS2-mRFP (black), RLP44-mTRQ/BAK1-mRFP (orange) and RLP44-mTRQ/BRI1-mRFP (red). For further details see (**b**). For the statistical evaluation see Section 4. Boxplots in (**b**) and (**f**) represent the measured data with the average as a solid black line and the box limits are the mean +/− standard deviation. The boxplot in (**d**) represents all data with the median as a solid black line within the box that is restricted by the first quartile (25%; lower end) and the third quartile (75%; upper end). Whiskers show the minimum and maximum of the measurements, respectively.

We next tested, whether an energy transfer from the mTRQ2 to mRFP fusion proteins was at all possible. No significant increase of the emission at around 610 nm was detected compared to the donor alone control for the co-accumulation of RLP44-mTRQ2 with FLS2-mRFP, (Figure 3e). In contrast, co-accumulation of RLP44-mTRQ2 with BAK1-mRFP or BRI1-mRFP led to a significant increase in the emission at around 610 nm compared to the control (Figure 3e). The fluorescence intensity ratio for the mTRQ2 and mRFP was 1:1 for the RLP44-mTRQ2/FLS2-mRFP pair (Figure 3f), whereas for RLP44-mTRQ2/BRI1-mRFP and RLP44-mTRQ2/BAK1-mRFP it was 1:2 and 1:5 respectively, i.e., higher than in the RLP44-mTRQ2/FLS2-mRFP control (Figure 3f). After correction for the different fusion protein amounts, spectrally detectable FRET clearly was observed from RLP44-mTRQ2 to BAK1-mRFP and to BRI1-mRFP but not to FLS2-mRFP.

2.7. Intensity-Based FRET Analysis of Ternary Protein Complex Formation

When RLP44, BRI1 and BAK1 form a ternary protein complex, the average distance between RLP44 and BAK1 might be altered by the presence of BRI1. For example, BRI1 may be located between RLP44 and BAK1, increasing the distance between them. Also the total number of RLP44/BAK1 pairs may be reduced, as additional pairs such as RLP44/BRI1 or BAK1/BRI1 can be formed [30].

To test this possibility, we expressed BRI1 with a non-fluorescent HA-tag (BRI1-HA) in tobacco cells (Figure S3). Co-expression of BRI1-HA did not change the intensity of the RLP44-mTRQ2 spectrum (compare Figures 4a and 3a). As described above, co-accumulation of RLP44-mTRQ2 with BAK1-mRFP yielded a FRET-induced emission peak at around 610 nm (Figure 4a). This peak was no longer present when BRI1-HA was co-expressed with RLP44-mTRQ2 and BAK1-mRFP (Figure 4a). In contrast, the co-expression of RLP44-mTRQ2/FLS2-mVEN/BRI1-mRFP retained the intensity peak at around 610 nm (Figure S4). Thus, the addition of BRI1-HA increased the average distance between RLP44-mTRQ2 and BAK1-mRFP or led to alterations in the fluorophore-tagged protein levels. As the latter was not the case (Figure 4b), our results demonstrate that the distance between RLP44-mTRQ2 and BAK1-mRFP did indeed change upon BRI1-HA co-accumulation. When BRI1-mVEN was co-expressed instead of BRI1-HA, the emission peak at around 610 nm reappeared (Figure 4c,d). At the same time, energy transfer from mVEN to mRFP was detected, as the emission peak of mVEN at 525 nm strongly decreased in the RLP44-mTRQ2/BRI1-mVEN/BAK1-mRFP sample in comparison with the RLP44-mTRQ2/BRI1-mVEN sample which was not observed in the FLS2 control samples (Figure 4a,c). Although the influence of cross-excitation of mVEN and subsequent FRET directly to mRFP could not be excluded entirely, this effect is negligible, as no energy transfer from mVEN to mRFP was observed for the RLP44/FLS2/FLS2 sample (Figure S4). Likewise, the analysis of the different protein combinations did not change the donor-to-acceptor ratios significantly (Figure 4d). In conclusion, the appearance of the emission peak at around 610 nm, which was accompanied by the parallel reduction of the emission at around 525 nm, fulfils the criteria for three-chromophore FRET from RLP44-mTRQ2 via BRI1-mVEN to BAK1-mRFP. In corroboration, the energy transfer described above was also observed when the acceptor fluorophores were exchanged (Figure S4).

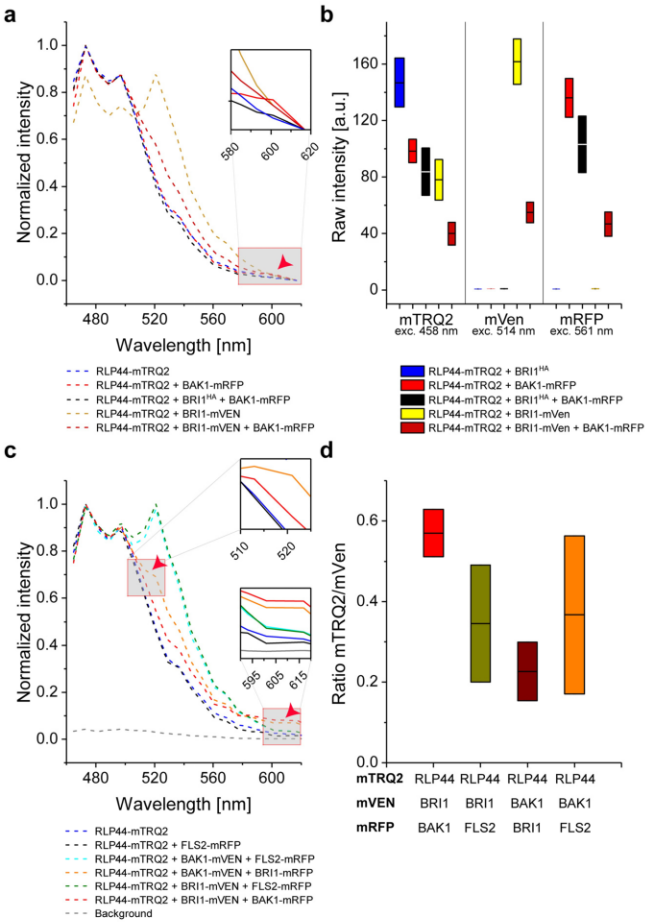

Figure 4. The formation of a ternary complex consisting of RLP44, BAK1 and BRI1, but not FLS2, is detectable in the plasma membrane of *N. benthamiana* epidermal leaf cells by intensity-based spectral FRET. (**a**) Wavelength-dependent normalized fluorescence emission after irradiation of the cells with 458 nm light for RLP44-mTRQ2 alone (blue) or co-expressed with either BAK1-mRFP (light red) or HA-tagged BRI1 ($BRI1^{HA}$) and BAK1-mRFP (black) or BRI1-mVEN (bronze) or BRI1-mVEN and BAK1-mRFP (dark red). The FRET-relevant wavelength area is highlighted in the inset image. The occurrence of FRET from mTRQ2 to mRFP is indicated by a red arrowhead. (**b**) Emission intensity after irradiation of the cells with light of different wavelengths in the mTRQ2 (left, 458 nm), mVEN (middle, 514 nm) and mRFP channels (right, 561 nm) from 8-bit images for RLP44-mTRQ2 co-expressed with either $BRI1^{HA}$ (blue), BAK1-mRFP (light red), $BRI1^{HA}$ and BAK1-mRFP (black), BRI1-mVEN (yellow) or BRI1-mVEN and BAK1-mRFP (dark red). (**c**) Wavelength-dependent normalized fluorescence emission after irradiation of the cells with 458 nm light for the expression of RLP44-mTRQ alone (blue) or co-expression with either BRI1-mVEN and BAK1-mRFP (red) or BAK1-mVEN and BRI1-mRFP (orange) or BRI1-mVEN and FLS2-mRFP (green) or BAK1-mVEN and FLS2-mRFP (cyan) or with FLS2-mRFP (black). The FRET-relevant wavelength areas are highlighted in enlarged sections. The occurrence of FRET from mTRQ2 to mRFP around 610 nm and the FRET-caused decrease of the mVEN signal around 525 nm are indicated by red arrowheads. The cell´s background emission of the cells is shown as dashed grey line. (**d**) Fluorescence emission ratio after irradiation of the cells

with light of different wavelength in the mTRQ2 channel (**left**), mVEN channel (**middle**) and mRFP channel (**right**) from 8-bit images for RLP44-mTRQ2 co-expressed with $BRI1^{HA}$ and BAK1-mRFP (black), BRI1-mVEN (yellow) and BRI1-mVEN and BAK1-mRFP (dark red). See (**b**) for further details. The boxplots in (**b**) and (**d**) represent all data with the average (here equivalent to the median) as a solid black line within the box that is restricted by +/− standard deviation. For the statistical evaluation see Section 4.

In conclusion, our data convincingly demonstrate that FRET from mTRQ2 via mVEN to mRFP specifically occurred for the RLP44/BRI1/BAK1 and RLP44/BAK1/BRI1 combinations, but not for the RLP44/BAK1/FLS2 combination. This indicates that RLP44, BRI1 and BAK1 form a specific ternary complex and/or are arranged in very close spatial proximity (5.7 to 13.7 nm) in the PM specifically. The successful establishment of intensity-based three-fluorophore FRET now prompted us to test whether the complex formation would also be reflected in FLIM measurements.

2.8. Measurement of In Vivo RLP44/BRI1/BAK1 Ternary Complex Formation by FRET-FLIM

When studying three-way interactions with intensity-based spectral methods, the concentration ratio between donor and acceptor molecules is of major importance, as spectral bleed-through and cross-excitation mimics potential FRET. In contrast, when monitoring the fluorescence lifetime (FLT) of the donor by FLIM, no such careful and labor-intensive calibrations are required [7,31]. We therefore tested, whether the complex formation and spatial arrangement of RLP44, BRI1 and BAK1 can also be monitored and confirmed by changes in the FLT of mTRQ2.

We determined an average FLT of about 3.99 ns for RLP44-mTRQ2 (Figure 5a) as reported before [13,15]. Interestingly, a significant decrease in the FLT is observed for the co-accumulation of RLP44-mTRQ2 with BRI1 fused to either mVEN (3.54 ns) or mRFP (3.60 ns) or with BAK1-mRFP (3.54 ns), indicating FRET from RLP44-mTRQ2 to BRI1-mVEN, BRI1-mRFP or BAK1-mRFP (Figure 5a). This constitutes the lower FLT limit that is expected when only heterodimers are present in the PM. Serving as a negative control, the co-expression of FLS2-mVEN (3.70 ns) or FLS2-mRFP (3.90 ns) with RLP44-mTRQ2 did not cause a significant decrease in mTRQ2´s FLT (Figure 5a,b). Furthermore, the co-accumulation of FLS-mRFP with RLP44-mTRQ2 and BRI1-mVEN did not further reduce the FLT of RLP44-mTRQ2 (3.60 ns) compared to the condition, where FLS2-mRFP is not present (Figure 5a). In contrast, the presence of BAK1-mRFP together with RLP44-mTRQ2 and BRI1-mVEN led to a significant further decrease in the FLT of RLP44-mTRQ2 to 3.40 ns, that is beyond the aforementioned values for the RLP44-mTRQ2/BRI1-mVEN heteromers of 3.54 ns (Figure 5a). This is only explainable by the existence of an additional FRET pathway that becomes possible if RLP44, BAK1 and BRI1 have formed a ternary complex. When 10 nM brassinolide (BL), an active brassinosteroid, was applied to the cells, no alteration in the FLT of RLP44-mTRQ2 was observed (Figure 5c). It was previously shown that FRET-FLIM is, in principle, independent of the donor concentration [32]. However, the relative amount of acceptor in comparison to the donor fluorophores (the donor-to-acceptor ratio) may influence the FLT of the donor [21,33]. Therefore, we investigated, whether this effect influences the FLT values obtained using different fluorescent protein ratios. As only the ratio of RLP44-mTRQ2/FLS2-mRFP and RLP44-mTRQ2/BAK1-mRFP exhibited a measurable difference within the RLP44-mTRQ2/BRI1-mVEN/FLS2-mRFP and the RLP44-mTRQ2/BRI1-mVEN/BAK1-mRFP in the three-fluorophore arrangements, differences in expression strength of the fusion proteins were not a major factor influencing the FLT of RLP44-mTRQ2 (Figure S5).

In summary, we were able to confirm the ternary complex formation of RLP44, BAK1 and BRI1 by three-fluorophore FRET-FLIM in living plant cells. Furthermore, the FRET-FLIM approach is clearly superior to the intensity-based FRET approach, because the former is easier to implement and less prone to errors.

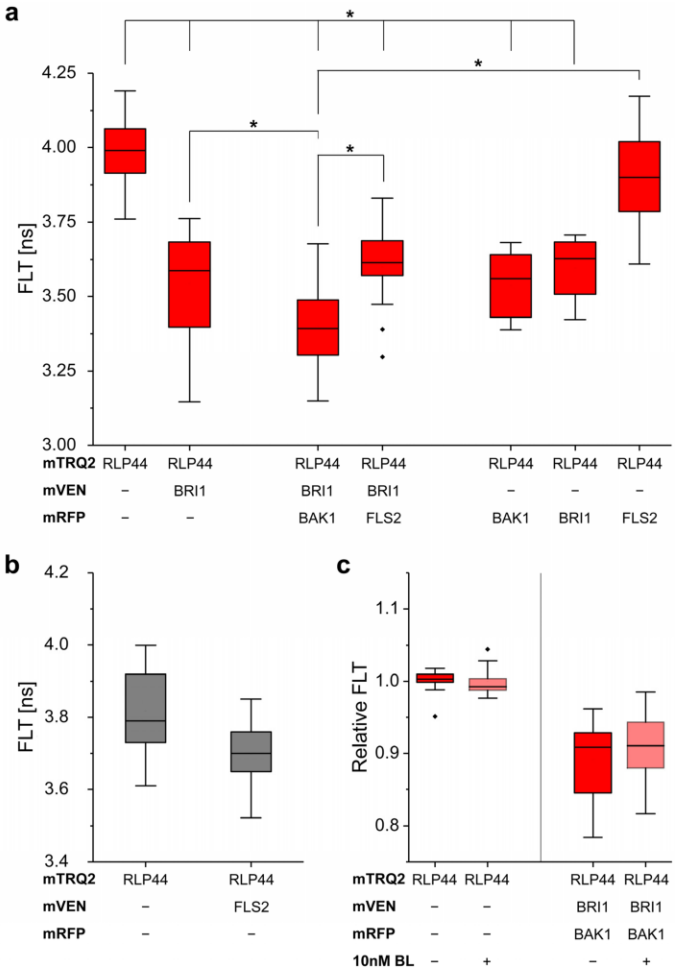

Figure 5. FRET-FLIM enables quantitative three-fluorophore protein-protein interaction and proximity analyses in *N. benthamiana* leaf cells. (**a**) Fluorescence lifetime (FLT) of RLP44-mTRQ2 after pulsed excitation of the cells with 440 nm light in the presence of the indicated mVEN and mRFP fusion proteins. (**b**) FLT of RLP44-mTRQ2 alone or in the presence of FLS2-mVEN. Data presentation as in (**a**). (**c**), Relative FLT of RLP44-mTRQ2 alone or in the presence of the indicated fusion proteins without (dark red) and with application of 10 nM brassinolide (BL) (light red). The average FLT of RLP44-mTRQ2 in the absence of BL was set to 1. The boxplots represent all data with the median as a solid black line within the box that is restricted by the first quartile (25%; lower end) and the third quartile (75%; upper end). Whiskers show the minimum and maximum value of the data, respectively, that are not defined as outlier (1.5 times interquartile range). Outliers are indicated as black diamonds. Statistical evaluations were performed by ANOVA followed by Tukey-Kramer HSD *post hoc* test. The black asterisk indicate statistically significant differences ($p \leq 0.005$).

3. Discussion

Many studies in the non-plant field have independently established fluorophore sets for studying binary protein-protein interactions and complex formation in the cellular

context [34]. Here we present a three-fluorophore intensity-based FRET and a FRET-FLIM approach with the genetically encoded fluorophores mTRQ2, mVEN and mRFP in plant cells. The use of a blue, yellow and red fluorophore was the preferred application for three-fluorophore FRET studies, as it provides a good compromise between large Förster distances due to high spectral overlap and sufficient spectral separation for independent detection. A comparative study on available fluorophores in non-plant cells revealed that mTRQ2, YPet and mCherry is the most promising combination for three-fluorophore FRET [34]. However, YPet is not yet adapted for use in plant cells yet. In addition, even though mVEN is not as bright as YPet, it is a monomer [35], which is essential for FRET-based interaction studies. We reasoned that the slightly lower brightness of mVEN is less of a concern than the potential tendency of other fluorophores to form aggregates at high local concentrations in confined domains, which can be expected when they are fused to PM-resident proteins [35,36]. High brightness fluorophores, such as Ruby2 or TagRFPs, are outperformed by mCherry as it compensates its low brightness with its fast maturation rate [37]. The maturation time of mRFP, however, is also relatively short, which makes it an appropriate acceptor fluorophore as well. Until now, no study was able to circumvent direct FRET between the donor and the 2nd acceptor for genetically encoded fluorophores [21,37–41]. Therefore, extensive corrections for the crosstalk of the fluorophores are required in intensity-based FRET. While organic dyes might have provided better photophysical properties, their application in plant cells is challenging as the cell wall interferes with in vivo labelling. Even in animal cells, the different labelling efficiencies of organic dyes are challenging for three-fluorophore FRET, as the correction for directly excited acceptor fluorescence proves to be problematic [32,42,43].

As of yet, only one single study has tried to estimate the dynamic range of the distances between three fluorophores present in their set [22]. We think that a realistic estimation of the variability and restrictions of a three-fluorophore system is important for the interpretation of FRET data. For example, the general rule of thumb for reliable FRET measurements below 10 nm may be imprecise or incorrect. Here, we calculated adapted distance limits, taking several factors into account: First, the spatial arrangement of the fluorophores in a three-fluorophore setting and secondly, the possibility for multiple acceptors per donor for higher complex stoichiometries. Indeed, for an ideal linear arrangement of the fluorophores mTRQ2, mVEN and mRFP, FRET measurements can cover distances of up to 11.1 nm. This implies that FRET in membranes could not only occur between proteins within one and the same complex or domain, but might also be possible between proteins located in spatially distinct but adjacent domains (Figure 6).

When assuming that the primary donor is located between the 1st and 2nd acceptor in a ternary complex, the likelihood of energy transfer from the donor via acceptor 1 to the acceptor 2 decreases, as the distance between acceptors 1 and 2 increases. These spatial arrangements should be considered when applying intensity-based FRET measurements. Furthermore, in this context it is also recommended in this context to exchange at least one of the fluorophores between the fusion proteins, as it was done here. For classical donor-based FRET-FLIM, the differences in spatial organization may not be detectable, as no information is available on where the energy is transferred to. In principle, such spatial information can also be obtained using more sophisticated FRET-FLIM approaches, like when mVEN is used as donor by excitation with another laser. In any case, FLIM-based FRET measurements have the advantage of a higher sensitivity and require less processing, as the signal-to-noise ratio in intensity-based FRET measurements becomes worse after unmixing and sensitized emission calculations.

Since the PM is a compartment confined to two dimensions, the protein density is comparatively higher than in the three-dimensional case. In particular, membrane receptors tend to form complexes with higher stoichiometries, meaning that a donor can be surrounded by several acceptors, which can increase the apparent FRET efficiency. This can mask the principally linear relationship between E_{FRET} and the affinity properties of the interacting fusion proteins. Therefore, no conclusions can be drawn about their affinity

within a ternary complex and only limited information can be obtained about the absolute distances between the three fluorophores.

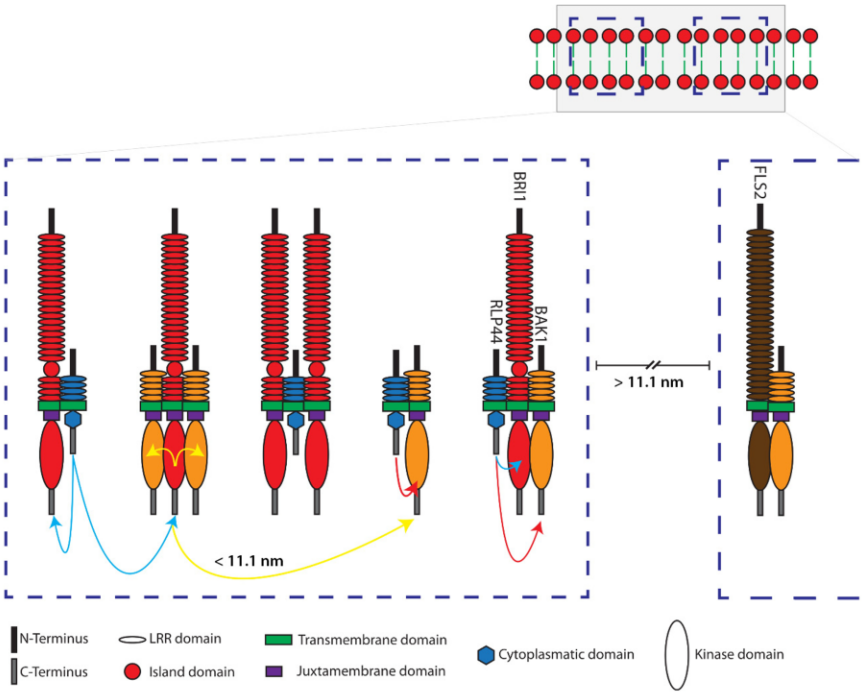

Figure 6. Model of the ternary interactions and spatial distances of RLP44, BRI1, BAK1 and FLS2 in defined nanodomains located in the plasma membrane of plant cells, as determined by three-fluorophore, intensity-based spectral FRET or FRET-FLIM. Shown are two distinct schematic nanodomains (blue dashed squares in the top corner) in the plasma membrane. The left nanodomain in the enlargement consists of RLP44-mTRQ2 (blue), BRI1-mVEN (red) and BAK1-RFP (orange)—without the fluorophores and not in scale. The formation of different complexes is demonstrated by FRET between mTRQ2 and mVEN by blue, mVEN and mRFP by yellow and mTRQ2 and mRFP by red arrows. FRET is also possible between the fusion proteins of differently composed complexes, if they are in a distance of $\leq$11.1 nm (representative yellow arrow). Due to the absence of FRET, for instance, the BAK1-mVEN/FLS2-mRFP (brown) complex must be at least 11.1 nm separated from the nanodomain, that contains the RLP44 related complexes, which is very likely part of an independent nanodomain (right side in the enlargement).

It was previously unclear whether RLP44 interacts with both BRI1 and BAK1 simultaneously. In this study, we applied intensity-based FRET and FRET-FLIM to probe that RLP44 is specifically located in close proximity (below 11.1 nm) to both BRI1 and BAK1 in vivo. In the radius of 11.1 nm, the three proteins can form trimers and/or be arranged as intermediate complexes (Figure 6). Application of 10 nM BL to the cells did not change the FRET characteristics in the spatial RLP44-mTRQ2/BRI1-mVEN/BAK1-mRFP arrangement in the PM. This indicates that the RLP44/BAK1/BRI1 nanodomain is pre-formed in the PM in the absence of BL and none of the proteins appears to leave the nanodomain upon binding of BL to BRI1 to a significant amount.

According to our intensity-based FRET and FRET-FLIM data, FLS2 interacts with neither BRI1 nor RLP44, which is in agreement with recent BiFC studies [30]. Remarkably,

the spatial distance between FLS2 and the RLP44-BAK1, RLP44-BRI1 and the RLP44-BRI1-BAK1 heteromers must be larger than 11.1 nm. This indicates that FLS2 is localized in nanodomains that are spatially distinct from the RLP44-consisting ones. Taking into account the around 20-fold better nanometer accuracy of FRET, our approach decisively proves previous results, indicated by variable angle epifluorescence microscopy (VAEM) which has a physical resolution limit of roughly 250 to 300 nm [29,31].

In summary, using the example of three selected chromophores, we show that three-fluorophore intensity-based FRET and three-fluorophore FRET-FLIM are suitable techniques for analyzing the interaction and relative proximity of different proteins in the PM of living plant cells. Furthermore, by applying the presented calculations and experimental approaches, it is possible to infer spatially distinct complexes and/or nanodomains in the PM that are different in their protein composition.

Although the two approaches are complementary, we strongly recommend the FRET-FLIM approach rather than intensity-based, spectral FRET for ternary protein interaction and proximity analyses, as the latter is particularly vulnerable to changes in the donor-to-acceptor ratio and other technical restrictions.

4. Material and Methods

4.1. Plasmid Construction

The cDNA sequence of the gene of interest without stop codon was brought into pDONR221-P3P2 (donor) or pDONR221-P1P4 (first acceptor) or pENTR™/D-TOPO® (second acceptor) as described by guidelines in the Gateway manual (Life Technologies, Schwerte, Germany) with primers listed in Supplemental Table S3. The coding sequence of BRI1 and BAK1 was brought in the pENTR-D-TOPO previously [7,8]. For the generation of BRI1-HA, primer previously published were used [9] to bring CDS of BRI1 in pDONR207 and an LR with pGWB14 was performed. The LR into pB7RWG2 (RFP) [44] and the 2in1 FRET vector pFRETtv-2in1-CC [15] was performed as described previously [15,45].

4.2. Localization and FRET-FLIM Studies

Transformation of *N. benthamiana* was performed as described by [15,46], omitting the washing step with sterile water. For transformations with multiple constructs, an OD_{600} of 0.1 was set and mixed 1:1:1 with silencing inhibitor p19. Plants were watered and left at ambient conditions (24 °C) with the lid on top and imaged two days past transformation with an SP8 confocal laser scanning microscope (CLSM) (Leica Microsystems GmbH, Wetzlar, Germany) with LAS AF and SymPhoTime software (Picoquant GmbH, Berlin, Germany) using a 63×/1.20 water immersion objective [46,47]. Data were derived from measurements of the lower epidermis, avoiding guard cells and stomata, with at least two biological replicates, comprising in average 20 data points and 11 data points for mTRQ2—mRFP controls. Localization and quantification were performed with a minimum 3-fold line average for mTRQ2, mVEN and mRFP with the Argon laser set to 2% and excitations of 458 nm 40%, 514 nm 20% and 594 nm or 561 nm 30% and emission detection with 465–505 nm 400% on HyD, 525–565 nm 400% on SMD HyD and 605–650 nm 300% on SMD HyD, respectively.

FLIM measurements were performed with a 440 nm pulsed laser (LDH-P-C-470, Picoquant GmbH, Berlin, Germany) with 40 MHz repetition rate at a reduced scanning speed, yielding, with an image resolution of 256 × 256, a pixel dwell time of ~20 µs. The maximal count rate was set to ~2000 cps. Measurements were stopped when the brightest pixel had a photon count of 500. Only measurements with an even intensity distribution at the PM were included. The corresponding emission was detected with HyD SMD from 455 nm to 505 nm by time-correlated single-photon counting using a PicoHarp 300 module or a TimeHarp 260 module (PicoQuant GmbH, Berlin, Germany). The calculation of FLTs was performed by iterative reconvolution, i.e., the instrument response function was convolved with an exponential test functions to minimize the error with regard to the original TCSPC histograms in an iterative process. While the donor-

only samples were fitted with mono-exponential decay functions, the energy transfer to fluorophores in the other samples resulted in additional decay rates. These histograms necessitated biexponential fitting functions, from which the fluorescent lifetime was derived by intensity weighted averaging. For the fastFLIM measurements, the maximal count rate was increased.

4.3. Acquisition of λ-Stacks (Spectra)

Expression of relevant fluorophores were checked via fluorescence level prior λ-stack acquisition. For λ-stacks, both sequential excitation and simultaneous excitation was used as mentioned in Results and an average of at least 6 ROIs of the PM with different expression levels of at least two biological replicates. At the Leica SP8 microscope, excitation at 458 nm 80% was used with SMD HyD ~250%, measuring 460–625 nm with Δ7.5 nm and 256 × 256 px resolution, a pixel dwell time of ~20 µs and three-fold line accumulation. At the Zeiss LSM880 (Carl Zeiss AG, Oberkochen, Germany) excitation at 485 nm with 30%, NF458, 800 V of airy-scan detectors were used, measuring 460–650 nm or 560–650 nm with Δ4.5 nm and 256 × 256 px resolution, speed 2, digital gain set to 2, pinhole set to 14.25 airy units and a three-fold line accumulation. If over-all expression was very high, then for all samples measured that day line average was taken instead. For additional information see Supplementary Material and Figure S6.

4.4. Protein Structures and Sizes

The intracellular domain of BRI1 (5LPW) and BAK1 (3TL8) as well as the fluorophore barrels were exported from the Protein Data Base (PDB). As viewer, Jmol: an open-source Java viewer for chemical structures in 3D [48] with solvent accessible depiction was chosen and protein colors were changed. The secondary structure of linkers and the intracellular RLP44 domain was predicted with PEP-FOLD 3.5 [26], de-novo prediction, with standard settings and always model no1 (of 10) was used. Amino acid sequences were HPTFLYKVGQLLGTS for the donor-linker, NPAFLYKVVSRLGTS for the acceptor-linker, KGGRADPAFLYKVVIS for the second acceptor linker and CLWLRITEKKIVEEEGKISQSMPDY for $RLP44_{Cyto}$. The size of intracellular domains was calculated from the known distance of the alpha-barrel secondary structure, which is Δ5.4 Å from turn-to-turn and 4 Å inner diameter.

4.5. Statistics

With one exception, each measurement was performed in at least three biological replicates. Each biological replica in turn included at least 3 individual recordings. In the exception, 2 biological replicates were performed, each containing 3 individual recordings. Images and plots were generated with Microsoft Excel v1809, SAS JMP 14 or MATLAB [49], also using these programs for calculation of average, standard error (SE) and standard deviation (SD). To test for homogeneity of variance, Levene's test ($p < 0.05$) was employed and statistical significance for non-parametric distributions was calculated by a two-tailed, all-pair Kruskal-Wallis test followed by a Steel-Dwass *post hoc* correction using SAS JMP version 14.0.0 [50]. For small sample numbers in Figure 3d the 2-sample *t*-test was chosen [51].

Supplementary Materials: The following supporting information can be downloaded at: https://www.mdpi.com/article/10.3390/plants11192630/s1, They contain additional information to the Theoretical background, Calculations for FRET cascades, Cross-talk during imaging, Supplementary tables (Tables S1–S3) and Supplementary figures (Figures S1–S6). Ref. [52–57] are cited in the supplementary materials.

Author Contributions: N.G., A.J.M. and K.H. conceived the project. N.G., S.z.O.-K., F.W. (Friederike Wanke) and K.H. designed the study. N.G., S.z.O.-K., M.B., F.W. (Friederike Wanke) and E.H. performed the experiments. N.G., S.z.O.-K. and L.R. conducted the mathematical and statistical analyses. N.G., S.z.O.-K., L.R., F.W. (Frank Wackenhut) and F.W. (Friederike Wanke) analyzed the data. F.W. (Friederike Wanke) helped with the confocal experiments. F.W. (Frank Wackenhut), A.J.M.,

K.H. and S.W. provided experimental materials and intellectual input. N.G., S.z.O.-K., L.R. and K.H. wrote the paper. All authors have read and agreed to the published version of the manuscript.

Funding: Research in our laboratories was supported by the German Research Foundation (DFG) with grants to S.z.O.-K. (CRC 1101-Z02), to S.W. (WO 1660/6-1, WO 1660/6-2), to K.H. (HA 2146/22-1; HA 2146/22-2), to A.J.M. and F.W. (Frank Wackenhut) (ME 1600/13-3) and to K.H. and A.J.M. (CRC 1101-D02).

Data Availability Statement: All data supporting the findings of the study are present in the main text and/or the Supplementary Materials. Source data are provided with this paper. All MATLAB code for the calculation of the values in Table 1 and the spectral unmixing is available at https://github.com/svenzok/3F-FRET (accessed on 23 September 2022).

Acknowledgments: The authors would like to thank F. Fässler for critical reading and the native speakers F. de Courcy and K. Berendzen for English proofreading the manuscript.

Conflicts of Interest: The authors declare no conflict of interest.

References

1. Gou, X.; Li, J. Paired Receptor and Coreceptor Kinases Perceive Extracellular Signals to Control Plant Development. *Plant Physiol.* **2020**, *182*, 1667–1681. [CrossRef]
2. Wolf, S. Deviating from the Beaten Track: New Twists in Brassinosteroid Receptor Function. *Int. J. Mol. Sci.* **2020**, *21*, 1561. [CrossRef]
3. Yin, Y.; Vafeados, D.; Tao, Y.; Yoshida, S.; Asami, T.; Chory, J. A new class of transcription factors mediates brassinosteroid-regulated gene expression in *Arabidopsis*. *Cell* **2005**, *120*, 249–259. [CrossRef]
4. Vert, G.; Chory, J. Downstream nuclear events in brassinosteroid signalling. *Nature* **2006**, *441*, 96–100. [CrossRef] [PubMed]
5. Mora-García, S.; Vert, G.; Yin, Y.; Caño-Delgado, A.; Cheong, H.; Chory, J. Nuclear protein phosphatases with Kelch-repeat domains modulate the response to brassinosteroids in *Arabidopsis*. *Genes Dev.* **2004**, *18*, 448–460. [CrossRef] [PubMed]
6. Zhu, J.-Y.; Li, Y.; Cao, D.-M.; Yang, H.; Oh, E.; Bi, Y.; Zhu, S.; Wang, Z.-Y. The F-box Protein KIB1 Mediates Brassinosteroid-Induced Inactivation and Degradation of GSK3-like Kinases in *Arabidopsis*. *Mol. Cell* **2017**, *66*, 648–657.e4. [CrossRef] [PubMed]
7. Caesar, K.; Elgass, K.; Chen, Z.; Huppenberger, P.; Witthöft, J.; Schleifenbaum, F.; Blatt, M.R.; Oecking, C.; Harter, K. A fast brassinolide-regulated response pathway in the plasma membrane of *Arabidopsis thaliana*. *Plant J.* **2011**, *66*, 528–540. [CrossRef] [PubMed]
8. Witthöft, J.; Caesar, K.; Elgass, K.; Huppenberger, P.; Kilian, J.; Schleifenbaum, F.; Oecking, C.; Harter, K. The activation of the *Arabidopsis* P-ATPase 1 by the brassinosteroid receptor BRI1 is independent of threonine 948 phosphorylation. *Plant Signal. Behav.* **2011**, *6*, 1063–1066. [CrossRef]
9. Wolf, S.; van der Does, D.; Ladwig, F.; Sticht, C.; Kolbeck, A.; Schürholz, A.-K.; Augustin, S.; Keinath, N.; Rausch, T.; Greiner, S.; et al. A receptor-like protein mediates the response to pectin modification by activating brassinosteroid signaling. *Proc. Natl. Acad. Sci. USA* **2014**, *111*, 15261–15266. [CrossRef]
10. Holzwart, E.; Huerta, A.I.; Glöckner, N.; Gómez, B.G.; Wanke, F.; Augustin, S.; Askani, J.C.; Schürholz, A.-K.; Harter, K.; Wolf, S. BRI1 controls vascular cell fate in the *Arabidopsis* root through RLP44 and phytosulfokine signaling. *Proc. Natl. Acad. Sci. USA* **2018**, *115*, 11838–11843. [CrossRef] [PubMed]
11. Förster, T. Zwischenmolekulare Energiewanderung und Fluoreszenz. *Ann. Phys.* **1948**, *437*, 55–75. [CrossRef]
12. Noomnarm, U.; Clegg, R.M. Fluorescence lifetimes: Fundamentals and interpretations. *Photosynth. Res.* **2009**, *101*, 181–194. [CrossRef] [PubMed]
13. Goedhart, J.; von Stetten, D.; Noirclerc-Savoye, M.; Lelimousin, M.; Joosen, L.; Hink, M.A.; Van Weeren, L.; Gadella, T.W.J., Jr.; Royant, A. Structure-guided evolution of cyan fluorescent proteins towards a quantum yield of 93%. *Nat. Commun.* **2012**, *3*, 751. [CrossRef] [PubMed]
14. Müller, S.M.; Galliardt, H.; Schneider, J.; Barisas, B.G.; Seidel, T. Quantification of Förster resonance energy transfer by monitoring sensitized emission in living plant cells. *Front. Plant Sci.* **2013**, *4*, 413. [CrossRef]
15. Hecker, A.; Wallmeroth, N.; Peter, S.; Blatt, M.R.; Harter, K.; Grefen, C. Binary 2in1 Vectors Improve in Planta (Co)localization and Dynamic Protein Interaction Studies. *Plant Physiol.* **2015**, *168*, 776–787. [CrossRef]
16. Martin, K.J.; McGhee, E.J.; Schwarz, J.P.; Drysdale, M.; Brachmann, S.M.; Stucke, V.; Sansom, O.J.; Anderson, K.I. Accepting from the best donor; analysis of long-lifetime donor fluorescent protein pairings to optimise dynamic FLIM-based FRET experiments. *PLoS ONE* **2018**, *13*, e0183585. [CrossRef] [PubMed]
17. Miyawaki, A.; Tsien, R.Y. *Cell Biology and Physiology*; Thorner, J., Ed.; Academic Press: San Diego, MA, USA, 2000; pp. 472–500.
18. Nagai, T.; Ibata, K.; Park, E.S.; Kubota, M.; Mikoshiba, K.; Miyawaki, A. A variant of yellow fluorescent protein with fast and efficient maturation for cell-biological applications. *Nat. Biotechnol.* **2002**, *20*, 87–90. [CrossRef]
19. Wouters, F.S. *Förster Resonance Energy Transfer and Fluorescence Lifetime Imaging*; Wiley-VCH: Weinheim, Germany, 2017.
20. Großeholz, R.; Feldman-Salit, A.; Wanke, F.; Schulze, S.; Glöckner, N.; Kemmerling, B.; Harter, K.; Kummer, U. Specifying the role of BAK1-interacting receptor-like kinase 3 in brassinosteroid signaling. *J. Integr. Plant Biol.* **2019**, *62*, 456–469. [CrossRef]
21. Sun, Y.; Wallrabe, H.; Booker, C.F.; Day, R.N.; Periasamy, A. Three-color spectral FRET microscopy localizes three interacting proteins in living cells. *Biophys. J.* **2010**, *99*, 1274–1283. [CrossRef] [PubMed]

22. Haustein, E.; Jahnz, M.; Schwille, P. Triple FRET: A tool for studying long-range molecular interactions. *ChemPhysChem* **2003**, *4*, 745–748. [CrossRef] [PubMed]
23. Rekas, A.; Alattia, J.-R.; Nagai, T.; Miyawaki, A.; Ikura, M. Crystal structure of venus, a yellow fluorescent protein with improved maturation and reduced environmental sensitivity. *J. Biol. Chem.* **2002**, *277*, 50573–50578. [CrossRef] [PubMed]
24. Yan, L.; Ma, Y.; Liu, D.; Wei, X.; Sun, Y.; Chen, X.; Zhao, H.; Zhou, J.; Wang, Z.-Y.; Shui, W.; et al. Structural basis for the impact of phosphorylation on the activation of plant receptor-like kinase BAK1. *Cell Res.* **2012**, *22*, 1304–1308. [CrossRef] [PubMed]
25. Bojar, D.; Martinez, J.; Santiago, J.; Rybin, V.; Bayliss, R.; Hothorn, M. Crystal structures of the phosphorylated BRI1 kinase domain and implications for brassinosteroid signal initiation. *Plant J.* **2014**, *78*, 31–43. [CrossRef] [PubMed]
26. Lamiable, A.; Thévenet, P.; Rey, J.; Vavrusa, M.; Derreumaux, P.; Tufféry, P. PEP-FOLD3: Fasterde novo structure prediction for linear peptides in solution and in complex. *Nucleic Acids Res.* **2016**, *44*, W449–W454. [CrossRef]
27. Nam, K.H.; Li, J. BRI1/BAK1, a Receptor Kinase Pair Mediating Brassinosteroid Signaling. *Cell* **2002**, *110*, 203–212. [CrossRef]
28. Gómez, B.G.; Holzwart, E.; Shi, C.; Lozano-Durán, R.; Wolf, S. Phosphorylation-dependent routing of RLP44 towards brassinosteroid or phytosulfokine signalling. *J. Cell Sci.* **2021**, *134*, jcs259134. [CrossRef]
29. Bücherl, C.A.; Jarsch, I.K.; Schudoma, C.; Segonzac, C.; Mbengue, M.; Robatzek, S.; MacLean, D.; Ott, T.; Zipfel, C. Plant immune and growth receptors share common signalling components but localise to distinct plasma membrane nanodomains. *eLife* **2017**, *6*, e25114. [CrossRef]
30. Galperin, E.; Verkhusha, V.; Sorkin, A. Three-chromophore FRET microscopy to analyze multiprotein interactions in living cells. *Nat. Chem. Biol.* **2004**, *1*, 209–217. [CrossRef]
31. Hochreiter, B.; Pardo-Garcia, A.P.; Schmid, J.A. Fluorescent proteins as genetically encoded FRET biosensors in life sciences. *Sensors* **2015**, *15*, 26281–26314. [CrossRef]
32. Becker, W. Fluorescence lifetime imaging-techniques and applications. *J. Microsc.* **2012**, *247*, 119–136. [CrossRef]
33. Bunt, G.; Wouters, F.S. FRET from single to multiplexed signaling events. *Biophys. Rev.* **2017**, *9*, 119–129. [CrossRef] [PubMed]
34. Scott, B.L.; Hoppe, A.D. Optimizing fluorescent protein trios for 3-Way FRET imaging of protein interactions in living cells. *Sci. Rep.* **2015**, *5*, 10270. [CrossRef] [PubMed]
35. Bajar, B.T.; Wang, E.S.; Zhang, S.; Lin, M.Z.; Chu, J. A Guide to Fluorescent Protein FRET Pairs. *Sensors* **2016**, *16*, 1488. [CrossRef] [PubMed]
36. Miyawaki, A. Development of probes for cellular functions using fluorescent proteins and fluorescence resonance energy transfer. *Annu. Rev. Biochem.* **2011**, *80*, 357–373. [CrossRef] [PubMed]
37. Hoppe, A.D.; Scott, B.L.; Welliver, T.P.; Straight, S.W.; Swanson, J.A. N-way FRET microscopy of multiple protein-protein interactions in live cells. *PLoS ONE* **2013**, *8*, e64760. [CrossRef]
38. He, L.; Wu, X.; Simone, J.; Hewgill, D.; Lipsky, P.E. Determination of tumor necrosis factor receptor-associated factor trimerization in living cells by CFP-YFP-mRFP FRET detected by flow cytometry. *Nucleic Acids Res.* **2005**, *33*, e61. [CrossRef]
39. Kuo, H.-L.; Ho, P.-C.; Huang, S.-S.; Chang, N.-S. Chasing the signaling run by tri-molecular time-lapse FRET microscopy. *Cell Death Discov.* **2018**, *4*, 1–9. [CrossRef]
40. Pauker, M.H.; Hassan, N.; Noy, E.; Reicher, B.; Barda-Saad, M. Studying the dynamics of SLP-76, Nck, and Vav1 multimolecular complex formation in live human cells with triple-color FRET. *Sci. Signal.* **2012**, *5*, rs3. [CrossRef]
41. Wallrabe, H.; Cai, Y.; Sun, Y.; Periasamy, A.; Luzes, R.; Fang, X.; Kan, H.-M.; Cameron, L.-C.; Schafer, D.A.; Bloom, G.S. IQGAP1 interactome analysis by in vitro reconstitution and live cell 3-color FRET microscopy. *Cytoskeleton* **2013**, *70*, 819–836. [CrossRef]
42. Fábián, Á.; Horváth, G.; Vámosi, G.; Vereb, G.; Szöllősi, J. TripleFRET measurements in flow cytometry. *Cytom. Part A J. Int. Soc. Anal. Cytol.* **2013**, *83*, 375–385. [CrossRef]
43. Fazekas, Z.; Petrás, M.; Fábián, Á.; Pályi-Krekk, Z.; Nagy, P.; Damjanovich, S.; Vereb, G.; Szöllősi, J. Two-sided fluorescence resonance energy transfer for assessing molecular interactions of up to three distinct species in confocal microscopy. *Cytom. Part A J. Int. Soc. Anal. Cytol.* **2008**, *73*, 209–219. [CrossRef] [PubMed]
44. Karimi, M.; Inzé, D.; Depicker, A. GATEWAY™ vectors for Agrobacterium-mediated plant transformation. *Trends Plant Sci.* **2002**, *7*, 193–195. [CrossRef]
45. Grefen, C.; Blatt, M.R. A 2in1 cloning system enables ratiometric bimolecular fluorescence complementation (rBiFC). *BioTechniques* **2012**, *53*, 311–314. [CrossRef]
46. Ladwig, F.; Dahlke, R.I.; Stührwohldt, N.; Hartmann, J.; Harter, K.; Sauter, M. Phytosulfokine Regulates Growth in *Arabidopsis* through a Response Module at the Plasma Membrane That Includes CYCLIC NUCLEOTIDE-GATED CHANNEL17, H^+-ATPase, and BAK1. *Plant Cell* **2015**, *27*, 1718–1729. [CrossRef] [PubMed]
47. Mohrholz, A.; Sun, H.; Glöckner, N.; Hummel, S.; Kolukisaoglu, Ü.; Schneeberger, K.; Harter, K. The striking flower-in-flower phenotype of *Arabidopsis* thaliana Nossen (No-0) is caused by a novel LEAFY allele. *Plants* **2019**, *8*, 599. [CrossRef]
48. Jmol: An Open-Source Java Viewer for Chemical Structures in 3D. Available online: http://www.jmol.org/ (accessed on 23 September 2022).
49. MATLAB. *9.8.0.1417392 (R2020a)*; The MathWorks Inc.: Natick, MA, USA, 2020.
50. Ohmi, Y.; Ise, W.; Harazono, A.; Takakura, D.; Fukuyama, H.; Baba, Y.; Narazaki, M.; Shoda, H.; Takahashi, N.; Ohkawa, Y.; et al. Sialylation converts arthritogenic IgG into inhibitors of collagen-induced arthritis. *Nat. Commun.* **2016**, *7*, 11205. [CrossRef] [PubMed]
51. de Winter, J.C.F. Using the Student's "*t*"-Test with Extremely Small Sample Sizes. *Pract. Assess. Res. Eval.* **2013**, *18*, 10.

52. Balleza, E.; Kim, J.M.; Cluzel, P. Systematic characterization of maturation time of fluorescent proteins in living cells. *Nat. Methods* **2018**, *15*, 47–51. [CrossRef]
53. Campbell, R.E.; Tour, O.; Palmer, A.E.; Steinbach, P.A.; Baird, G.S.; Zacharias, D.A.; Tsien, R.Y. A Monomeric Red Fluorescent Protein. *Proceedings of the National Academy of Sciences of the United States of America.* **2002**, *99*, 7877–7882. [CrossRef]
54. Cranfill, P.J.; Sell, B.R.; Baird, M.A.; Allen, J.R.; Lavagnino, Z.; Gruiter, H.M. de; Piston, D.W. Quantitative assessment of fluorescent proteins. *Nat. Methods* **2016**, *13*, 557–562. [CrossRef]
55. Koushik, S.V.; Blank, P.S.; Vogel, S.S. Anomalous surplus energy transfer observed with multiple FRET acceptors. *PloS ONE 4.* **2009**, e8031. [CrossRef]
56. Kremers, G.-J.; Goedhart, J.; van Munster, E.B.; Gadella, T W. J.; JR. Cyan and yellow super fluorescent proteins with improved brightness, protein folding, and FRET Forster radius. *Biochemistry.* **2006**, *45*, 6570–6580. [CrossRef]
57. Liu, J.; Lu, Y. FRET study of a trifluorophore-labeled DNAzyme. *J. Am. Chem. Soc.* **2002**, *124*, 15208–15216. [CrossRef]

Three-fluorophore FRET enables the analysis of ternary protein association in living plant cells

Nina Glöckner[a], Sven zur Oven-Krockhaus[a,b], Leander Rohr[a], Frank Wackenhut[b], Moritz Burmeister[b], Friederike Wanke[a], Eleonore Holzwart[c], Alfred J. Meixner[b], Sebastian Wolf[c] and Klaus Harter[a*]

[a]Center for Plant Molecular Biology, University of Tübingen, Tübingen, Germany
[b]Institute for Physical & Theoretical Chemistry, University of Tübingen, Tübingen, Germany
[c]Centre for Organismal Studies, University of Heidelberg, Heidelberg, Germany

*corresponding author (Email: klaus.harter@zmbp.uni-tuebingen.de)

Supplementary Materials

Supplemental Notes

Theoretical background

The FRET efficiency (E) between a donor (D) and an acceptor (A) fluorophore is given by

$$E = \frac{R_0^6}{R_0^6 + r^6}, \quad (1)$$

with r as the distance between donor and acceptor and R_0 as the distance for 50 % energy transfer (Förster distance):

$$R_0\ (nm) = 0.02108 \cdot (\kappa^2 \cdot n^{-4} \cdot QY_D \cdot J)^{1/6}, \quad (2)$$

with κ^2 as the dipole orientation factor, n as the refractive index of the medium, QY_D as the quantum yield of the donor and J as the spectral overlap between donor emission and acceptor absorption:

$$J = \varepsilon_A \frac{\int f_D(\lambda) f_A(\lambda) \lambda^4 d\lambda}{\int f_D(\lambda)\, d\lambda}, \quad (3)$$

with ε_A as the molar attenuation coefficient of the acceptor at the peak absorption wavelength, λ as the wavelength in nm, f_D and f_A as the normalized donor emission and acceptor absorption spectra, respectively.

As evident in equation (2), the dipole orientation factor κ^2 has a strong influence on the calculated R_0 and thus E:

$$\kappa^2 = cos^2\, \omega\, (1 + 3cos^2\theta). \quad (4)$$

Here, ω is the angle between the electric field vector of D at the location of A and the absorption dipole orientation of A and θ is the angle between the emission dipole of D and the separation vector of D-A (Lakowicz 2006).

For the standard assumption of κ^2 = 2/3 to be true, the rotational diffusion of a fluorophore has to be faster than the fluorescence lifetime (FLT) of D (Müller et al. 2013; Hink et al. 2002). However, this may not be true for genetically-encoded fluorescent proteins used in FRET studies for several reasons: (i) The fluorophore barrel is large and has a rotational correlation time of about 20–30 ns, whereas the FLT is in a range of 1–4 ns (Vogel et al., 2012). (ii) The fluorophores are attached to the proteins of interest with a flexible linker (Chen et al. 2013; van Rosmalen et al. 2017; George and Heringa 2002; Chen et al. 2013). In previous studies, a linker length of 15 amino acids was assumed to allow free rotation of the fluorophore, even though this may not be fully true (Ujlaky-Nagy et al. 2018; Szöllosi et al. 2006; Shrestha et al.

201). But as no better options are available, the standard assumption is used. This introduces an error due to different fluorophore orientations. Hink et al. (2002) proposed to use κ^2 = 0.476, which is the value of the orientation factor for a rigid, randomized ensemble of D-A pairs (Steinberg 1971). This effectively reduces the calculated Förster distance. It does not eliminate the possibility of specifically existent deviations due to fixed protein arrangements, e.g., preventing FRET or other spatial arrangements. It is important to keep in mind that the FRET efficiency does not correspond to fixed real distances (Müller et al. 2013): The presence of FRET always means that they are in close proximity, but how close exactly can rarely be precisely determined, especially in live-cell imaging. The distance r that is accessible through FRET-measurements is in average between 0.5 $R_0 \leq r \leq 1.5\ R_0$ (Gadella 2009; Müller et al. 2013). Most FRET pairs have Förster distances between 4 and 7 ns (Bajar et al. 2016; Mastop et al. 2017). As a rule of thumb, FRET is restricted to distances below 10 nm. The absence of FRET does not necessarily mean that the proteins of interest are not in close proximity or do not interact, e.g., due to unfavorable fluorophore attachment positions. Three-fluorophore FRET-FLIM, in turn, has the same limitations.

Calculations for FRET cascades

We define a cascading, linear three-chromophore FRET system

$$1 — 2 — 3$$

with 3 as the most redshifted fluorophore. When 2 acts as the donor, the spectral overlap of 2's emission spectrum with 1's absorption spectrum is negligible. The FRET efficiency for the path 2 ⟶ 3 can, therefore, be calculated with (1) as follows:

$$E_{23} = \frac{R_{0}^{6}{}_{23}}{R_{0}^{6}{}_{23} + r^{6}{}_{23}}. \qquad (5)$$

When 1 acts as the donor, two paths are possible:

1 ⟶ 2 ⟶ 3 (energy transfer to 3 via 2) or

1 ⟶ 3 (direct energy transfer to 3).

The energy can follow either path, so the energy transfer possibility for 1 ⟶ 2 is diminished by the energy transfer possibility for 1 ⟶ 3 and vice versa. This decrease can be expressed in terms of the fluorophore's quantum yield, using the following equations by Liu & Lu (2002). For 1 ⟶ 2:

$$\Delta QY_{12} = \frac{R_{0_{13}}^6}{R_{0_{13}}^6 + r^6{}_{13}} \tag{6}$$

R_0 to the power of 6 contains QY as a multiplicator (cf. (2)), so the lost fraction of QY can be implemented in R_0 as follows:

$$R_{0_{12}}^6{}' = R_{0_{12}}^6 \cdot (1 - \Delta QY_{12}) = R_{0_{12}}^6 \cdot \left(1 - \frac{R_{0_{13}}^6}{R_{0_{13}}^6 + r^6{}_{13}}\right), \tag{7}$$

with $R_{0_{12}}^6{}'$ and $R_{0_{12}}^6$ as the Förster distance of $1 \longrightarrow 2$, when 3 is present or absent, respectively.

This adjusted Förster distance now replaces the numerator in (1):

$$E_{12} = \frac{R_{0_{12}}^6{}'}{R_{0_{12}}^6 + r^6{}_{12}} \tag{8}$$

Combining and simplifying (6) and (7):

$$E_{12} = \frac{\left(R_{0_{12}} \cdot r_{13}\right)^6}{\left(R_{0_{12}} \cdot r_{13}\right)^6 + \left(R_{0_{13}} \cdot r_{12}\right)^6 + (r_{12} \cdot r_{13})^6} \tag{9}$$

A similar result can be acquired for $1 \longrightarrow 3$:

$$E_{13} = \frac{\left(R_{0_{13}} \cdot r_{12}\right)^6}{\left(R_{0_{13}} \cdot r_{12}\right)^6 + \left(R_{0_{12}} \cdot r_{13}\right)^6 + (r_{12} \cdot r_{13})^6} \tag{10}$$

The overall FRET efficiency for the above $1 \longrightarrow 2 \longrightarrow 3$ FRET cascade can now be estimated, using (5), (9) and (10):

$$E_{casc.} = E_{12} \cdot E_{23} + E_{13} \tag{11}$$

We acknowledge that this linear FRET cascade approach neglects, e.g., the arrangement 2 — 1 — 3. The truth will be much more complicated, including complex geometric arrangements of the fluorophores, enabling a multitude of possible energy transfer pathways that will not be solved easily without performing extensive numerical simulations. However, this set of equations and the derived results illustrate how a third fluorophore changes the FRET working parameters and how important it is to consider the actual biological situation – in this example, the analysis of protein complexes in the

plasma membrane, which is of great common interest in the life science community. Although these theoretical considerations can only be simplified approximations, they impressively show that FRET interaction assays can, under certain conditions, cover much larger distances than generally expected, making this method viable for a much broader range of analyses.

Cross-talk during imaging

Cross-talk in the form of spectral bleed through (bt) and cross-excitation (ce) was present for our fluorophores. To account for this, the bt and ce was assessed from normalized absorption and emission spectra and quantified by imaging single-fluorophore expressing *N. benthamiana* plants.

Excitation at 458 nm lead to a relative absorption of 91% for mTRQ2 and a cross-excitation of 8% for mVEN and 3% for mRFP (Fig. 1A purple, vertical line). Excitation at 514 nm for mVEN yielded a relative absorption of 99% and a cross-excitation of mRFP of 20% (Fig. 1A green line). mRFP was excited with 561 nm with a relative absorption of 61% (Fig. 1A orange line). Spectral bleed-through was present from mTRQ2 to mVEN and from mVEN to mRFP: When detecting mVEN with a bandwidth from 525 to 565 nm, 35% of the signal originates from mTRQ2 (Fig. S2, Table S2). Detection of mRFP between 605 and 650 nm included 6% of mVEN emission (Fig. S2, Table S2). When quantifying the FI, also the molecular brightness of a fluorophore, detection settings such as detector gain and laser strength are influencing the amount of bleed-through and cross-talk. Thus, we calculated the coefficients from imaging single-labelled samples with sequential excitation (Table S2). Measured bt and ce from mTRQ2 to the yellow and red channel was higher than calculated, as higher laser settings were used to excite mTRQ2. Measured ce from mVEN to the red channel was in the same order of magnitude as calculated. As the molecular brightness of mVEN is relatively high (Table S1), the bt to the red channel was higher than calculated (Table S2), even with reduced laser power for 514 nm compared to the 458 nm and 561 nm laser lines (see Material and methods).

Process of spectral unmixing based on λ-stacks

For λ-stacks, the emission of the sample is recorded in several narrow spectral regions one after the other. Figure S 6b shows such a λ-stack with an excitation wavelength of 458 nm comprising 21 images, each assigned to a spectral region (here with a spectral width of 8 nm). The total detected intensity over all wavelength ranges can be obtained by summing the intensities per pixel along the λ-stack, resulting in an overview image as shown in Figure 6a. Using such an overview image, regions of interest (ROIs) can now be selected. All pixel intensities within a ROI are summed per wavelength range to extract the corresponding spectra (Fig. S6c), where each wavelength range is represented by its central wavelength.

Linear spectral unmixing aims to find a linear combination of the component spectra of mTRQ2, mVEN, and mRFP that best approximates the measured spectrum, pointing to the relative fractions of the fluorophores that were present in the sample. An exemplary graphical representation of the unmixing result can be found in Figure S6d. FRET efficiency calculations can be based on these fractions according to the formulas above, also considering cross-excitation and spectral bleed-through. MATLAB scripts for the corresponding calculations are available at https://github.com/svenzok/3F-FRET. Spectral unmixing with ROIs is based on low pixel numbers and/or intensities. Accordingly, for statistically robust results, great care must be taken to randomize ROI selection and to analyze a reasonable number of biological replicates.

Supplementary Tables

Table S1. Parameters of fluorophores in this study
Quantum yield (QY), Molar attenuation coefficient (ε) at the absorbance maximum, Brightness as the product QY·ε, Maturation half-time at 37°C in E. coli (t_{50}), Photostability as half-time of bleaching under laser scanning illumination with 80 µW ($t_{½}$), pH stability (pK_a) and proportion of monomeric state. For comparison: EGFP features a brightness of 33.6 $mM^{-1}cm^{-1}$, a bleaching half-time of 159.7 s and a pK_a of 6.0.

	QY	ε [mM^{-1} cm^{-1}]	Brightness [mM^{-1} cm^{-1}]	Maturation half-time t_{50} [min]	Photostability $t_{½}$ [s]	pH stability pK_a	monomer [%]
mTRQ2	0.93	30	27.9	33.5	71.7	3.1	93.8
	(Goedhart et al. 2012; Cranfill et al. 2016; Balleza et al. 2018)						
mVEN	0.64	105	67.2	17.6	26.5	5.5	83.9
	(Kremers et al. 2006; Cranfill et al. 2016; Balleza et al. 2018)						
mRFP	0.25	44	11.0	21.9	26.3	4.5	95.8
	(Campbell et al. 2002; Cranfill et al. 2016; Balleza et al. 2018)						

Table S2. Coefficients for spectral bleed-through (bt) and cross-excitation (ce)
The bt and ce coefficients with standard error (SE) for relevant laser lines were both measured in images when only the relevant fluorophore was expressed (D:A1:A2) and additionally calculated based on normalized spectra.

	bleed-through (bt)			cross-excitation (ce)		
	1 >> 2	1 >> 3	2 >> 3	1 >> 2	1 >> 3	2 >> 3
Average false/true signal	0.41	0.04	0.14	0.11	0.03	0.16
SE	0.01	0.001	0.02	0.01	0.01	0.01
Ratio D:A1:A2	1:0:0	1:0:0	0:1:0	0:1:0	0:0:1	0:0:1
Excitation laser [nm]	458	458	514	458	458	514
Calculated false/true signal	0.35	0.01	0.06	0.08	0.03	0.2

Table S3. List of primers.

GOI – vector	Forward primer 5‘ » 3‘	Reverse primer 5‘ » 3‘
RLP44 - pDONR221-P3P2	GGGGACAACTTTGTATAATAAAGTTGtaA TGACAAGGAGTCACCGGTTAC	GGGGACCACTTTGTACAAGAAAGCTGGG TtGTAATCAGGCATAGATTGAC
BRI1 - pDONR221-P1P4	GGGGACAAGTTTGTACAAAAAAGCAGGC TtaATGAAGACTTTTTCAAGCTTCTT	GGGGACAACTTTGTATAGAAAAGTTGGG TGTAATTTTCCTTCAGGAACTTCTT
FLS2 - pDONR221-P1P4	GGGGACAAGTTTGTACAAAAAAGCAGGC TtaATGAAGTTACTCTCAAAGAC	GGGGACAACTTTGTATAGAAAAGTTGGG TGAACTTCTCGATCCTCGTTACG
FLS2 - pDONR207	GGGGACAAGTTTGTACAAAAAAGCAGGC TtaATGAAGTTACT	GGGGACCACTTTGTACAAGAAAGCTGGG TgAACTTCTCGATCCT

Supplementary Figures

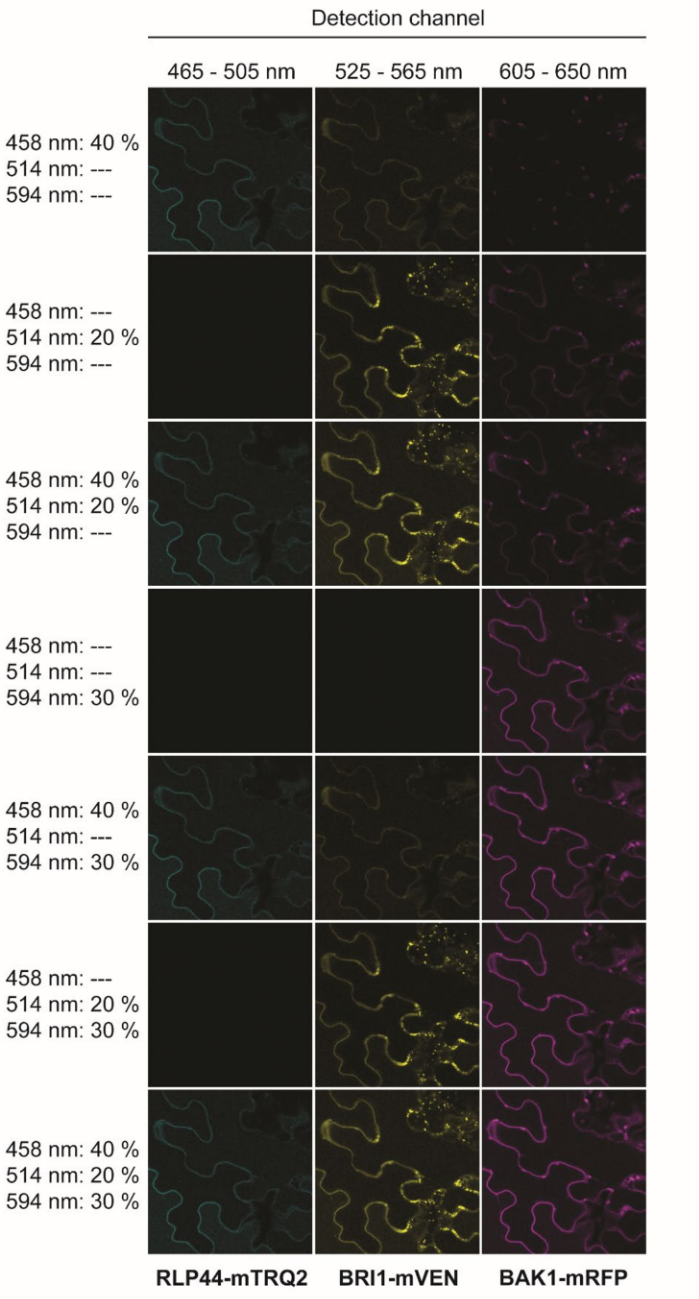

Figure S1. RLP44-mTRQ2, BRI1-mVEN and BAK1-mRFP are expressed together **in** *N. benthamiana* epidermal leaf cells.

Representative confocal images of the fluorescence intensity in the mTRQ2 channel, the mVEN channel and the mRFP channel are exemplary shown for the combination of RLP44-mTRQ2, BRI1-mVEN and BAK1-mRFP two days after transient transformation of *N. benthamiana* leaf cells. The excitation wavelengths and the relative laser intensities are depicted to the left. The blue channel for detection of RLP44-mTRQ was 465-505 nm, the yellow channel for detection of BRI1-mVEN was 525-565 nm and the red channel for detection of mRFP was 605-650 nm. The scale bar represents 20 µm. In general, before the acquisition of spectra or the fluorescence intensities, the expression of each fusion construct was determined by sequential excitation, meaning that one laser line was switched on at a time.

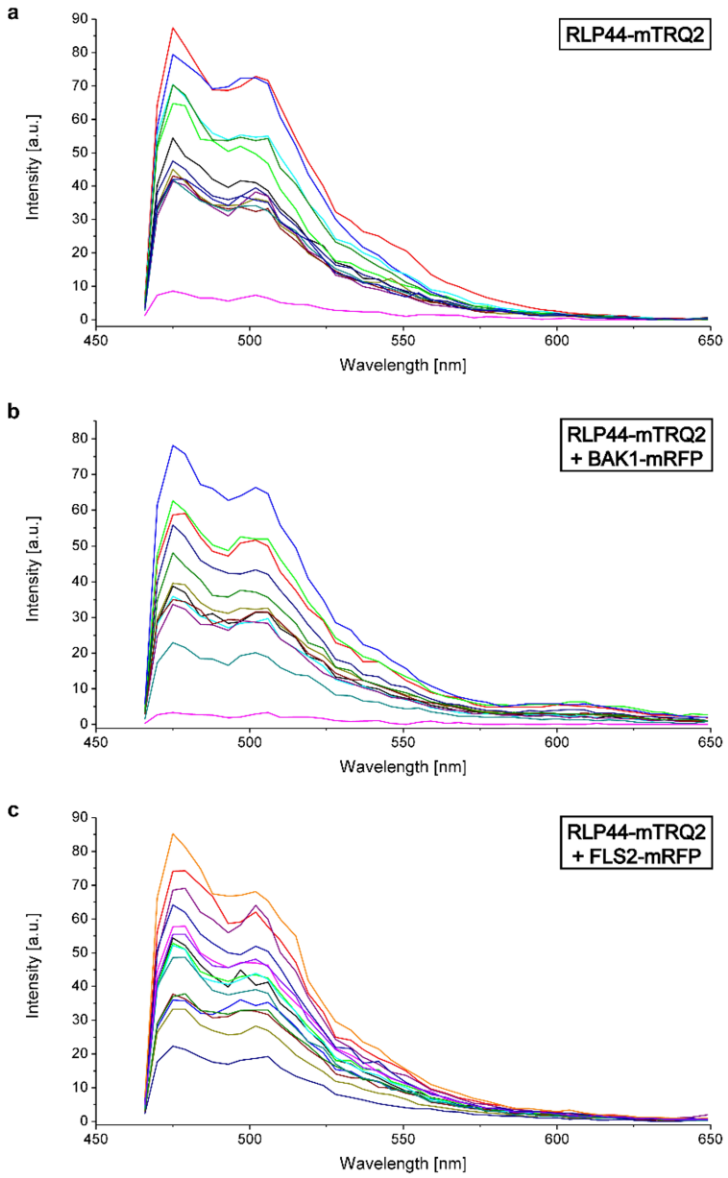

Figure S2. Wavelength-dependent intensity measurements reveal different fusion protein expression levels for different plasma membrane regions in transiently transformed N. benthamiana epidermal leaf cells.

The wavelength-dependent raw intensity of 13 different regions of interest, each, in the plasma membrane of *N. benthamiana* leaf cells after excitation with light of 458 nm is depicted for RLP44-mTRQ2 alone (**a**), the RLP44-mTRQ2 + FLS2-mRFP (**b**) and RLP44-mTRQ2 + FLS2-mRFP pair (**c**).

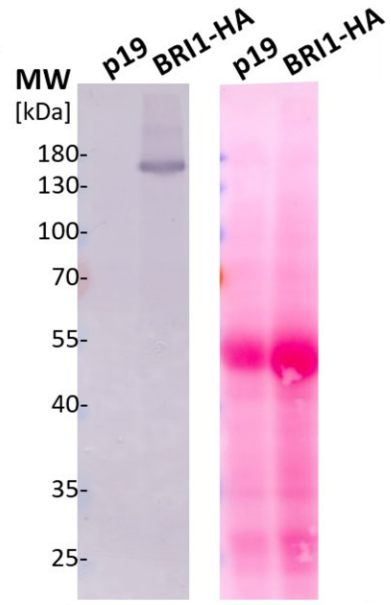

Figure S3. BRI1HA is expressed in transiently transformed N. benthamiana leaf cells.
Western blot (left) and the total protein on the transfer membrane, stained with Ponceau S (right) of *N. benthamiana* leaf extracts prepared two days after transformation with either the silencing inhibitor plasmid p19 (control) or with p19 and a plasmid coding for $BRI1^{HA}$. $BRI1^{HA}$ was detected with an HA antibody. The protein size markers are shown to the left.

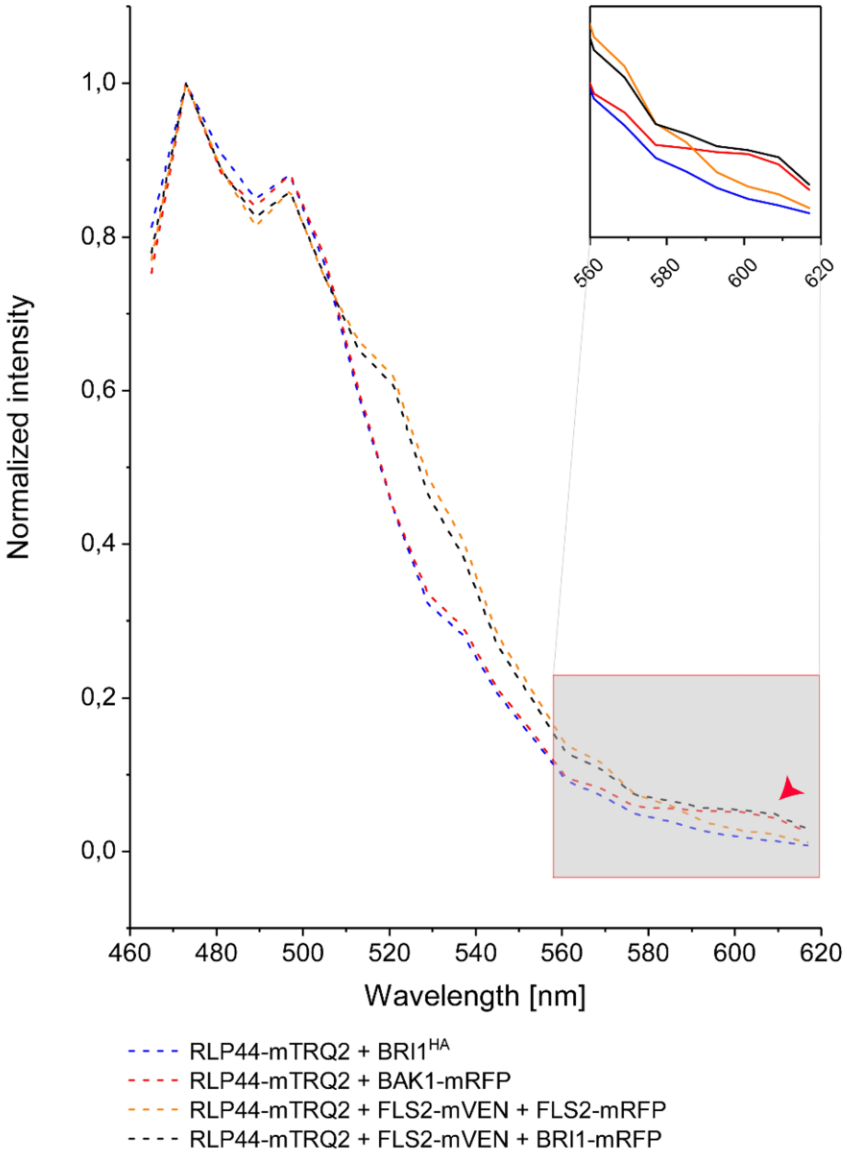

Figure S4. FLS2 does not interfere with the RLP44-related interactions (extension to Fig. 4). Wavelength-dependent normalized fluorescence emission after irradiation of the *N. benthamiana* leaf cells with 485 nm light for the co-expression of RLP44-mTRQ2 with $BRI1^{HA}$ (blue) or with BAK1-mRFP (red) or FLS2-mVEN and FLS2-mRFP (orange) or FLS2-mVEN and BRI1-mRFP4 (black). The FRET-relevant wavelength area is highlighted in the enlarged section. The occurrence of FRET from mTRQ2 to mRFP is indicated by a red arrow head.

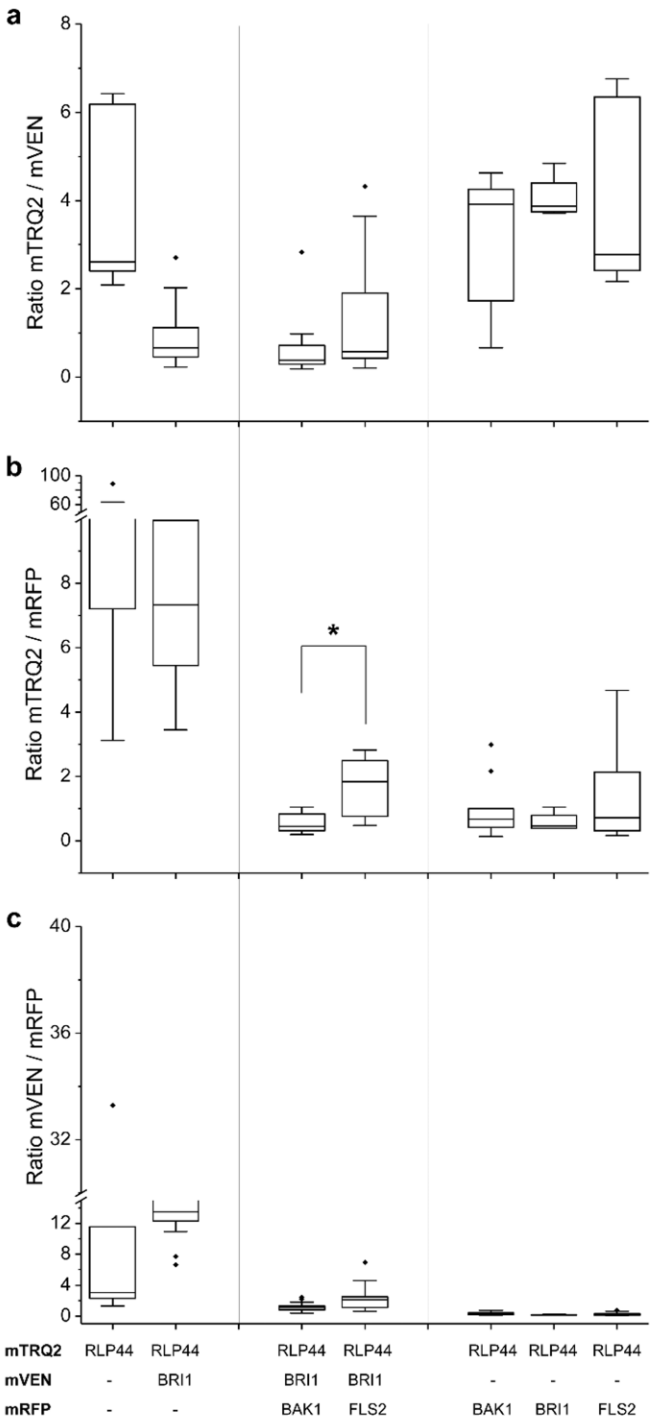
a
Ratio mTRQ2 / mVEN
8
6
4
2
0
b
Ratio mTRQ2 / mRFP
100
60
8
6
4
2
0
*
c
Ratio mVEN / mRFP
40
36
32
12
8
4
0
mTRQ2 RLP44 RLP44 RLP44 RLP44 RLP44 RLP44 RLP44
mVEN - BRI1 BRI1 BRI1 - - -
mRFP - - BAK1 FLS2 BAK1 BRI1 FLS2

Figure S5. The overall donor to acceptor ratios is not significantly different in the protein fusion arrangements of the FRET-FLIM analysis.
Fluorescence emission ratios for the mTRQ2/mVEN fusion protein pairs (**a**), the mTRQ2/mRFP fusion protein pairs (**b**) and mVEN/mRFP fusion protein pairs (**c**) are shown. Data points were left-right scattered (*black dots*) and combined with boxplot information, permitting outliers.
The ratios for mTRQ2/mVEN, mTRQ2/mRFP and mVEN/mRFP were tested for significant differences with a two-tailed, all-pair Kruskal-Wallis test followed by a Steel-Dwass *post hoc* correction. The asterisks marks a significant difference ($p < 0.05$) in the donor-to-acceptor ratios, which was the mTRQ2/mRFP ratio in the RLP44-mRFP4/BRI1-mVEN/BAK1-mRFP and the RLP44-mTRQ2/BRI1-mVEN/FLS2-mRFP arrangements. The boxplots represent all data with the median as a solid line within the box that is restricted by the first quartile (25 %; lower end) and the third quartile (75 %; upper end). The whiskers show the minimum and maximum value of the data, respectively, that are not defined as outliers (1.5 times the interquartile range). Outliers are indicated as black diamonds.

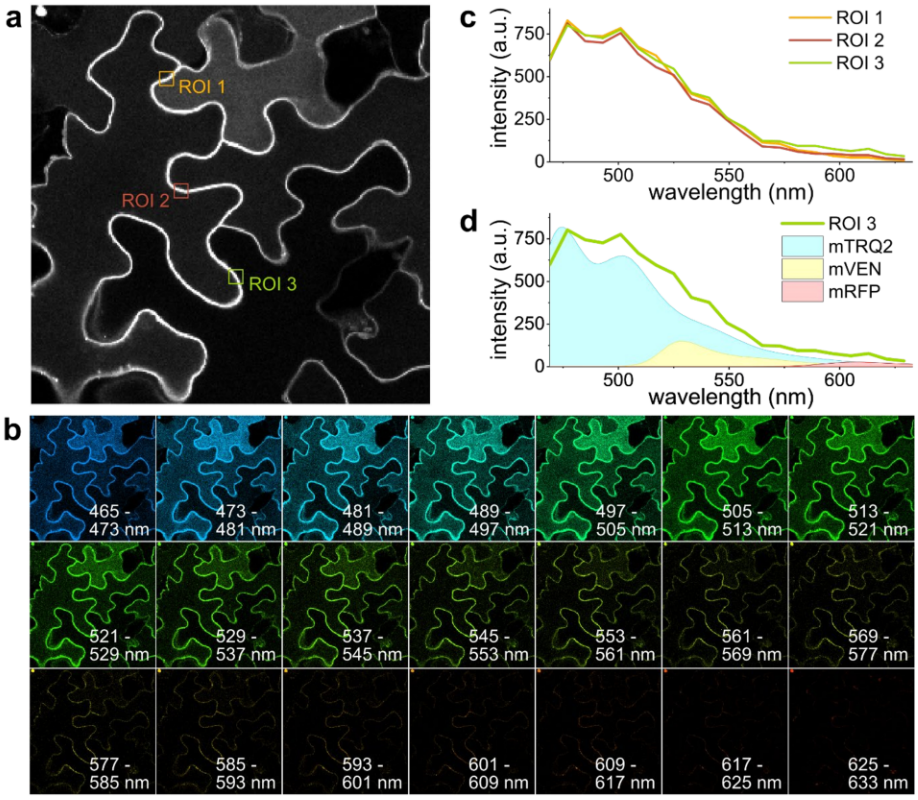

Figure S6. Example of spectral unmixing process based on λ-stacks.
Overview image **(a)** with randomly selected regions of interest (ROI 1-3) of the plasma membrane for cells expressing RLP44-mTRQ2, BAK1-mVEN and BRI1-mRFP. Each frame of the λ-stack **(b)** corresponds to an emission wavelength range, imaged consecutively under constant 458 nm excitation. Intensity summation over all wavelength ranges results in image **(a)**. Spectra **(c)** for each ROI are extracted by summing all pixel intensities of the specified ROI for each wavelength range, resulting in 21 discrete values for each ROI. The x-axis represents the respective center of each wavelength range. Spectral unmixing **(d)** is shown as a graphical representation for ROI 3 (green line). Unmixing describes the process of finding a linear combination of normalized mTRQ2 (blue), mVEN (yellow) and mRFP (red) spectra that best approximates the measured data.

References

Balleza, E., Kim, J. M., & Cluzel, P. (2018). Systematic characterization of maturation time of fluorescent proteins in living cells. *Nature Methods*, *15*(1), 47–51. https://doi.org/10.1038/nmeth.4509.

Bunt, G. & Wouters, F. S. (2017). FRET from single to multiplexed signaling events. *Biophysical reviews 9*, 119–129; 10.1007/s12551-017-0252-z.

Campbell, R. E., Tour, O., Palmer, A. E., Steinbach, P. A., Baird, G. S., Zacharias, D. A., & Tsien, R. Y. (2002). A monomeric red fluorescent protein. *Proceedings of the National Academy of Sciences of the United States of America*, *99*(12), 7877–7882. https://doi.org/10.1073/pnas.082243699

Cranfill, P. J., Sell, B. R., Baird, M. A., Allen, J. R., Lavagnino, Z., Gruiter, H. M. de, . . . Piston, D. W. (2016). Quantitative assessment of fluorescent proteins. *Nature Methods*, *13*(7), 557–562. https://doi.org/10.1038/nmeth.3891

Goedhart, J., Stetten, D. v., Noirclerc-Savoye, M., Lelimousin, M., Joosen, L., Hink, M. A., . . . Royant, A. (2012). Structure-guided evolution of cyan fluorescent proteins towards a quantum yield of 93%. *Nature Communications*, *3*, 751. https://doi.org/10.1038/ncomms1738

Koushik, S. V., Blank, P. S. & Vogel, S. S. (2009). Anomalous surplus energy transfer observed with multiple FRET acceptors. *PloS One 4*, e8031; 10.1371/journal.pone.0008031.

Kremers, G.-J., Goedhart, J., van Munster, E. B., & Gadella, T. W. J., JR. (2006). Cyan and yellow super fluorescent proteins with improved brightness, protein folding, and FRET Forster radius. *Biochemistry*, *45*(21), 6570–6580. https://doi.org/10.1021/bi0516273.

Liu, J., Lu, Y. (2002). FRET study of a trifluorophore-labeled DNAzyme. *J. Am. Chem. Soc., 124*(51), 15208-15216. https://pubs.acs.org/doi/10.1021/ja027647z.

Nagai, T., Ibata, K., Park, E. S., Kubota, M., Mikoshiba, K., & Miyawaki, A. (2002). A variant of yellow fluorescent protein with fast and efficient maturation for cell-biological applications. *Nature Biotechnology*, *20*(1), 87–90. https://doi.org/10.1038/nbt0102-87

Scott, B. L., & Hoppe, A. D. (2015). Optimizing fluorescent protein trios for 3-Way FRET imaging of protein interactions in living cells. *Scientific Reports*, *5*, 10270 EP -. https://doi.org/10.1038/srep10270

Computational modeling and quantitative physiology reveal central parameters for brassinosteroid-regulated early cell physiological processes linked to elongation growth of the *Arabidopsis* root

by Großeholz R., Wanke F., Rohr L., Glöckner N., Rausch L., Scholl S., Scacchi E., Spazierer A. J., Shabala L., Shabala S., Schumacher K., Kummer U., Harter K. (2022)

in *Elife*

doi: https://doi.org/10.7554/elife.73031

Accepted

eLife RESEARCH ARTICLE

Computational modeling and quantitative physiology reveal central parameters for brassinosteroid-regulated early cell physiological processes linked to elongation growth of the *Arabidopsis* root

Ruth Großeholz[1,2*†], Friederike Wanke[3†], Leander Rohr[3], Nina Glöckner[3], Luiselotte Rausch[3], Stefan Scholl[1], Emanuele Scacchi[3,4], Amelie-Jette Spazierer[3], Lana Shabala[5], Sergey Shabala[5,6], Karin Schumacher[1], Ursula Kummer[1,2‡], Klaus Harter[3*‡]

[1]Centre for Organismal Studies, Heidelberg University, Heidelberg, Germany; [2]BioQuant, Heidelberg University, Heidelberg, Germany; [3]Center for Molecular Biology of Plants, University of Tubingen, Tübingen, Germany; [4]Department of Ecological and biological Science, Tuscia University, Viterbo, Italy; [5]Tasmanian Institute for Agriculture, University of Tasmania, Hobart, Australia; [6]International Research Centre for Environmental Membrane Biology, Foshan University, Foshan, China

***For correspondence:** ruth.grosseholz@bioquant.uni-heidelberg.de (RG); klaus.harter@zmbp.uni-tuebingen.de (KH)

†These authors contributed equally to this work
‡These authors also contributed equally to this work

Competing interest: The authors declare that no competing interests exist.

Funding: See page 19

Preprinted: 14 April 2021
Received: 13 August 2021
Accepted: 03 September 2022
Published: 07 September 2022

Reviewing Editor: Krzysztof Wabnik, CBGP Centro de Biotecnologia y Genomica de Plantas UPM-INIA, Spain

Abstract Brassinosteroids (BR) are key hormonal regulators of plant development. However, whereas the individual components of BR perception and signaling are well characterized experimentally, the question of how they can act and whether they are sufficient to carry out the critical function of cellular elongation remains open. Here, we combined computational modeling with quantitative cell physiology to understand the dynamics of the plasma membrane (PM)-localized BR response pathway during the initiation of cellular responses in the epidermis of the *Arabidopsis* root tip that are be linked to cell elongation. The model, consisting of ordinary differential equations, comprises the BR-induced hyperpolarization of the PM, the acidification of the apoplast and subsequent cell wall swelling. We demonstrate that the competence of the root epidermal cells for the BR response predominantly depends on the amount and activity of H^+-ATPases in the PM. The model further predicts that an influx of cations is required to compensate for the shift of positive charges caused by the apoplastic acidification. A potassium channel was subsequently identified and experimentally characterized, fulfilling this function. Thus, we established the landscape of components and parameters for physiological processes potentially linked to cell elongation, a central process in plant development.

Editor's evaluation

The manuscript by Grosseholz et al. addresses a so far much overlooked aspect in plant hormone signalling systems, namely how components primarily identified by genetic means jointly regulate plant root physiology. The authors demonstrate a relevant effect of Brassinosteroid signalling on the control of root cell elongation in Arabidopsis. They used an elegant combination of (electro)

physiology, computer modelling and confocal microscopy to reveal molecular candidates linking BR perception to fine-tuning of cell elongation through ion fluxes.

Introduction

Brassinosteroids (BRs) are plant steroid hormones that regulate a great variety of physiological and developmental processes including elongation growth as well as environmental adaptations (***Müssig et al., 2002***; ***Clouse, 2002***; ***Lv and Li, 2020***; ***Wolf, 2020***). To achieve this, BR signal transduction is closely linked with a multitude of other signaling pathways (***Lv and Li, 2020***).

The canonical sequence of BR perception and signal transduction, which also leads to cell elongation, is mediated by the plasma membrane (PM)-resident, nanoscale-organized receptor kinase brassinosteroid-insensitive 1 (BRI1) and its co-receptor BRI1-activating kinase 1 (BAK1) as central elements (***Bücherl et al., 2013***; ***Bücherl et al., 2017***; ***Lv and Li, 2020***; ***Wolf, 2020***). The binding of BR to the receptor's extracellular domain results in the re-arrangement of several BRI1-associated proteins. This involves the release of inhibitory mechanisms that include BRI1 kinase inhibitor 1 (BKI1) and BAK1-interacting receptor like kinase 3 (BIR3) and leads to the stabilization of BRI1/BAK1 association followed by a variety of auto- and trans-phosphorylation events of their cytoplasmic domains. This cascade of events eventually results in the establishment of the fully active BRI1 receptor complex (***Bücherl et al., 2013***; ***Bücherl et al., 2017***).

Once the active complex is established, the BR response is proposed to divide into two distinct downstream pathways to trigger molecular and physiological processes, which can be linked to cell elongation and differ in their kinetic properties (***Clouse, 2002***; ***Clouse, 2011***; ***Vukašinović et al., 2021***): A long-term (hours to days) gene regulatory pathway leading to extensive transcriptional reprogramming that is realized *via* the kinase Brassinosteroid Insensitive 2 (BIN2), the key transcription factors brassinazole resistant 1 (BZR1) and BR insensitive EMS suppressor 1 (BES1). The gene regulatory pathway is linked to cell wall remodeling as well as the extent and correct timing of anisotropic cell growth (***Lv and Li, 2020***; ***Fridman et al., 2021***; ***Graeff et al., 2021***). Physiological work in the past already suggested the second, short-term pathway is proposed to occur in PM-resident, nano-organized BRI1 complexes (***Cerana et al., 1983***; ***Cerana et al., 1984***; ***Romani et al., 1983***; ***Mandava, 1988***). The response takes place in a matter of a few minutes and leads to the upregulation of the major proton pumping ATPases (AHA1, AHA2) (***Figure 1***; ***Elgass et al., 2009***; ***Caesar et al., 2011***). The activation of AHAs involves their interaction with BRI1 and BAK1, is BRI1 kinase activity-dependent (***Caesar et al., 2011***; ***Ladwig et al., 2015***) and occurs very likely via rapid phosphorylation (within 5 min) of threonine and serine residues in the AHAs' large cytoplasmic domain (***Lin et al., 2015***; ***Witthöft et al., 2011***). The BR-enhanced activity of AHAs induces the acidification of the apoplastic space, hyperpolarization of the PM's membrane potential (E_m) and cell wall swelling within 10 min after BR application (***Elgass et al., 2009***; ***Caesar et al., 2011***; ***Witthöft et al., 2011***; ***Witthöft and Harter, 2011***). The functional link between these BR-regulated cellular responses and AHA activity was proven by the inhibition or constitutive activation of the pump, leading either to the blocking of the reactions or their activation in the absence of BR (***Caesar et al., 2011***).

The cell wall swelling, thus the incorporation of water in the wall matrix, is mediated by the loosening of the walls rigidity *via* the activation of acidic pH-dependent, apoplast-resident enzymes regulating wall extensibility (***Cosgrove, 2000***). According to the acid-growth theory (***Hager, 2003***), the low pH-induced enzymatic loosening of the cell wall, often paralleled by the accumulation of osmotically active substances inside the cell, causes a water potential difference between the extracellular space and the protoplast, the uptake of water and eventually the onset of cell elongation (***Palmgren et al., 2009***; ***Regenberg et al., 1995***; ***Baekgaard et al., 2005***; ***Phyo et al., 2019***). This sequence of short- and long-term signaling and reaction pathways allows for instance root cells in the elongation zone (EZ) to grow four times their size in the meristematic zone (MZ) with a growth rate of up to 0.7 µm min^{-1}(***Fasano et al., 2001***; ***Verbelen et al., 2006***). Comparable growth rates were reported for hypocotyl cells of dark-grown *Arabidopsis* seedlings upon application of BR (***Minami et al., 2019***).

While the activation of the pathway is well understood qualitatively, the information on the inactivation of the pathway is currently still sparse. The receptor BRI1 autophosphorylates at the residue S891, which inhibits the receptor activity (***Oh et al., 2012***). However, the time-scale of this phosphorylation is very slow, as it increases over the course of 12 h after stimulation with BR. The dephosphorylation

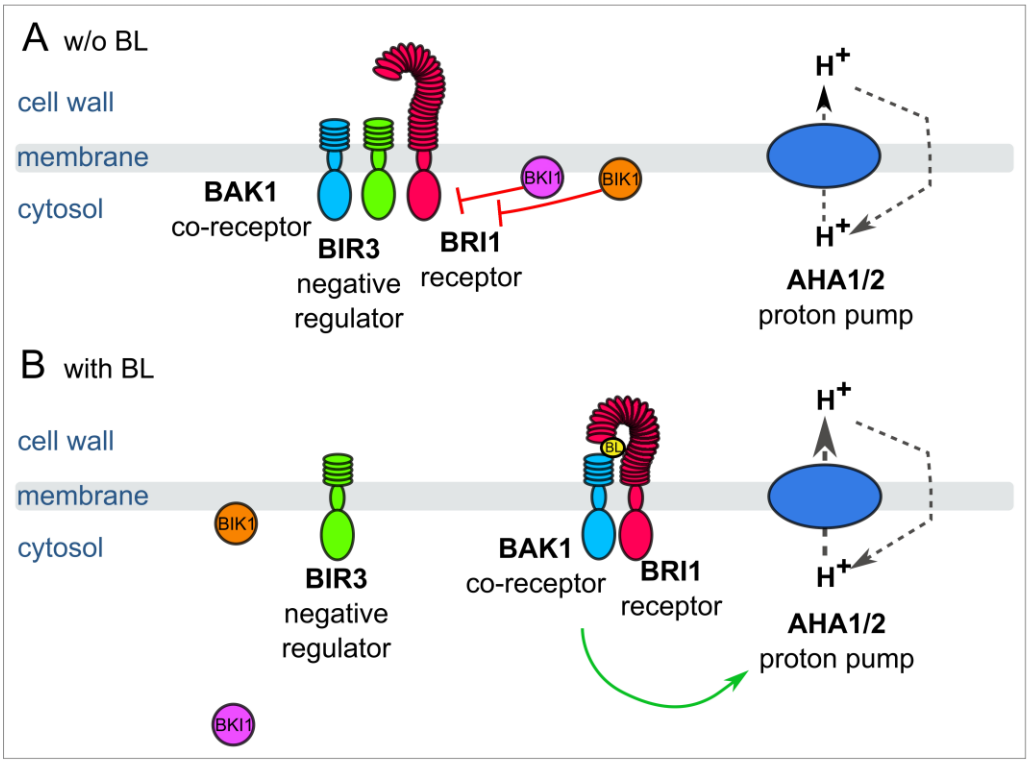

Figure 1. Schematic overview of the key constituents and processes of the plasma membrane-associated fast BR response pathway initiating early steps in cell elongation, here represented by brassinolide (BL). (**A**) Inactive state: Co-localizing in a preformed nano-orgnaized complex, the inhibitors BKI1, BIK1 and BIR3 suppresses the activity of BRI1 in the absence of BL keeping the activity of H^+-ATPases AHA1 and 2 at basic levels. By interaction with BAK1, BIR3 blocks the access of the co-receptor to BRI1. (**B**) Active state: Upon BL-binding to the receptor, the inhibitory mechanisms of BKI1, BIK1 and BIR3 on BRI1 and BAK1 are released causing the formation of the active BRI1/BAK1 complex. The complex enhances the AHA activity resulting in cell wall acidification, plasma membrane hyperpolarization and eventually onset of cell elongation. These key constituents and qualitatively described processes were used for the initial establishment of the computational model at cellular.

of this site is even slower, as residual phosphorylations can be detected 5 days after inhibiting BR synthesis using brassinazole (***Oh et al., 2012***).

Despite the qualitative knowledge on the constituents, the BR perception and the canonical signaling events, the dynamics of the system as a whole have yet to be examined quantitatively in detail (***Sankar et al., 2011***; ***van Esse et al., 2013a***; ***van Esse et al., 2012***; ***van Esse et al., 2013b***; ***Allen and Ptashnyk, 2017***). Therefore, we employed computational modeling in combination with quantitative experimental data on the fast BR response pathway in the PM, focusing on the epidermal cells of the *Arabidopsis* root tip as the epidermis limits the rate of elongation (***Hacham et al., 2011***). The root tip is an excellent model system for such a combined study because cells there first undergo a phase of cell division in the MZ followed by a phase of growth in the EZ. The boundary from the MZ to the EZ is represented by the transition zone (TZ). The formation of the TZ is characterized by the cytokinin-induced expression of the *AHA1* and *AHA2* genes as a precondition for cell elongation in the EZ (***Pacifici et al., 2018***). However, BR is involved in the control of both cell division and cell elongation in the different zones, apparently also adding to the specific functional competence and behavior of the cells along the axis of the root tip.

However, the molecular determinants and processes establishing this competence and their link to the cytokinin-caused gradient of growth competence are poorly understood in terms of their quantitative dynamics. This lack of knowledge virtually provokes the implementation of computational modeling.

While computational modeling has been used frequently in biomedical research since the early 2000 s, its application to the plant field has started more recently (***Hübner et al., 2011***; ***Holzheu and Kummer, 2020***). Here, the growth and development of the root tip has been of particular interest (***Bruex et al., 2012***; ***Muraro et al., 2016***; ***Di Mambro et al., 2017***; ***Rutten and Ten Tusscher, 2019***; ***Salvi et al., 2020***; ***Rutten and Ten Tusscher, 2021***). Further computational studies in plants include the modeling of auxin signaling (***Vernoux et al., 2011***) and transport pattern (***Band et al., 2014***), and parts of the BR signaling (***Sankar et al., 2011***; ***van Esse et al., 2013a***; ***van Esse et al., 2012***; ***van Esse et al., 2013b***; ***Allen and Ptashnyk, 2017***). For instance, the modeling approach by van Esse et al. analyzed the link between the BR dose, gene expression and growth behavior in both the *Arabidopsis* root and shoot (***van Esse et al., 2013a***; ***van Esse et al., 2012***; ***van Esse et al., 2013b***). However, none of the previous modeling approaches has been able to truly quantitatively depict cellular responses, make clear predictions about the cellular behavior, limiting constituents or processes.

In our study, we were able to determine how the constituents of the PM-resident fast BR response pathway work together and identified its rate-limiting elements applying an ordinary differential equations (ODE) approach. Substantiated by wet lab experiments, our computational approach led to a detailed kinetic model that describes the rapid cellular response and offers an explanation for the initiation of BR controlled differential growth behavior of the root cells on the basis of the differential AHA accumulation and activity. Furthermore, the model predicts the existence of a cation influx across the PM that is crucial for the apoplastic acidification and E_m hyperpolarization, which was subsequently narrowed down experimentally. Lastly, the model shows how the extent of the BR response can be fine-tuned by the level of the BIR3 inhibitor. Our model proposes that the specific composition of the PM-resident nano-organized BRI1 complexes determines the competence of the root cells to initiate elongation in response to BR.

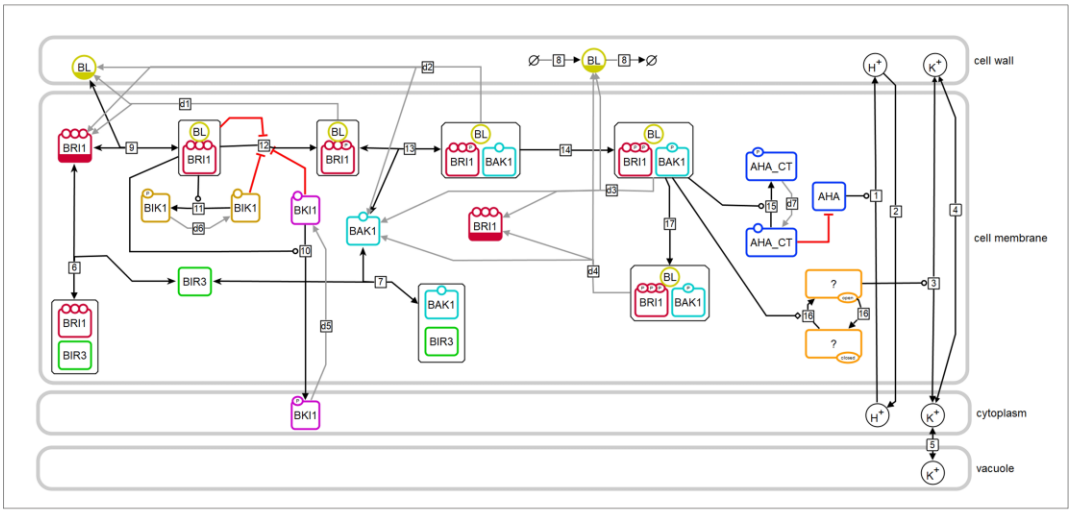

Figure 2. Model structure of the fast BR response pathway of *Arabidopsis thaliana*. Compartments are indicated by grey boxes. Smaller molecules are indicated by circles, proteins by rectangles. Potential sites for protein modifications are indicated by the small circles on the boundaries of the rectangles. Reactions, including substrates and products, are indicated by the arrows, with the reaction numbers noted in the small box. Reactions, which are required for the model to return to the initial state, are drawn in grey. A bar at the bottom of the circle or rectangle indicates that this entity appears more than once in the scheme.

Results

A mathematical model of the fast BR response

To analyze the important steps and factors of the cell-specific, fast BR response in the root tip, we developed a detailed mathematical model consisting of ODEs (***Figure 2***). The model comprises four cell compartments: the cytosol, the cell wall and the vacuole as three-dimensional compartments as well as the PM as a two-dimensional compartment. The explicit inclusion of the PM as two-dimensional compartment was prompted by the fact that most components of the BR perception and initial processes are located in the membrane and the relevance of the membrane as a scaling factor in this kind of system (***Holzheu et al., 2021***). The compartment sizes were set such that the model initially describes the behavior of a single epidermis cell in the early EZ of the *Arabidopsis* root (***Wilma van Esse et al., 2011***) (see ***Appendix 1—table 1***).

The model captures the important components and steps of the fast BR response pathway focusing on protein interactions and post-translational modifications. We decided against the inclusion of data, which are derived from the genetic manipulation of component amounts or activity or are based on long-term incubation of BR biosynthesis inhibitors such as brassinazole. This kind of manipulation or long-term treatment are expected to have considerable effects on the physiological and developmental properties of the plant as a whole. The model is set up in a way that an equilibrium state was reached before the system is stimulated with the hormone by maintaining the system first without the hormone for 24 hr. In this state, only a few crucial reactions occur and carry a flux (v): the interaction between BIR3 and BAK1 (v_7) and BIR3 and BRI1 (v_6), the proton leak from the cell wall into the cytoplasm (v_2) (***Appendix 1—figure 1***), the basal activity of the ATPases AHA1 and AHA2 (ν_1) and the exchange of monovalent cations (here represented by potassium) between cytoplasm and cell wall (v_4) and cytoplasm and vacuole (v_5). Modeling the basal state as a physiologically plausible steady state ensures that the model describes the inactive state of the BR response pathway accurately and that the interactions of BIR3 with BAK1 and BRI1 are in an equilibrium.

The hormone is added to the model by an event triggered at 24 h. According to the current state of knowledge, this initiates a number of molecular processes in the PM that occur almost simultaneously (***Figure 2***): binding of BL to BRI1 (v_9), the loss of BRI1 inhibition by its C-terminus (v_{12}), the release of BKI1 and BIK1 after phosphorylation (v_{10} and v_{11}, respectively) as well as the release of BIR3 from BAK1, the establishment of the BAK1-BRI1 interaction *via* BR (v_{13}), and the auto- and transphosphorylation of BAK1 and BRI1 (v_{14}). These spatial rearrangements and post-translational modifications result in the active form of the BRI1 receptor complex, which immediately stimulates the activity of H^+-ATPases very likely by phosphorylation (***Lin et al., 2015***) (v_{15}). Further signaling events occur later in time and include differential gene expression (***Lv and Li, 2020***). However, these late events were not considered here for our modeling approach.

The main cell physiological output of this early sequence of events is the acidification of the apoplastic space, the hyperpolarization of the E_m and the swelling of the cell wall. The E_m is calculated based on the net change in charge distribution of protons and potassium across the PM, the specific capacitance of the plasma membrane (***White et al., 1999***) and the membrane surface (***Wilma van Esse et al., 2011***) (see ***Appendix 1—table 1***). However, combining the available information derived from the literature resulted in preliminary model draft that was not able to reproduce the measured experimental data, for instance regarding the E_m hyperpolarization. Without a mechanism to balance out the shift in charge distribution caused by the transported protons, even a modest acidification of the apoplast from a pH of 5.4–5.0 will result in a non-physiological membrane hyperpolarization (***Sondergaard et al., 2004***) (see: Appendix 1 - example calculation of E_m and pH change). Consequently, we postulated a cation influx in the model (here represented by potassium) that starts upon activation of the BRI1 complex (v_{16}) and is driven by the E_m (v_3).

However, in order to accurately model and simulate the fast BR response pathway, we needed more experimental data about the PM-based BRI1 response module. Any remaining unknown model parameters were estimated based on experimental data of the cell wall acidification (this study), E_m hyperpolarization (***Caesar et al., 2011***) and the qualitative overexpression behavior of BIR3 (***Imkampe et al., 2017***). To account for non-identifiable parameters, we investigated the parameter space by computing several independent model parameterizations that describe the experimental data equally well. All computational analyses were run with each model of the resulting ensemble of structurally identical models (n=10) to ascertain consistent results across parameter space.

Quantification of signaling components

One experimental challenge for the refinement of the model was to quantify the central components of the pathway comprising predominantly BRI1, BAK1, BIR3 and AHA in the PM of epidermal cells of the root tip. Initially, we drew our attention on their steady-state transcript levels as they were determined by high-throughput single cell RNA-sequencing (scRNA-Seq) of the different *Arabidopsis* root cell types (***Ma et al., 2020***). Whereas *BRI1* and *BIR3* transcripts accumulated in all cell types of the root more or less equally and did not alter much in their amount during cell development along the root axis, *AHA2* and to lesser extent also *AHA1* transcripts were found predominantly in the epidermal cells and the root cortex (***Figure 3A***). During root development, the *AHA2* transcript amount but not those of *BRI1* and *BIR3* started to increase strongly in the cortex and epidermis cells of the TZ and EZ (***Figure 3B***). This temporal transcript pattern was less prominent for *AHA1* (***Figure 3B***) being in agreement with earlier observation that the *AHA1* promoter is not very active in root epidermis cells. This indicates that *AHA1* does not play a prominent role in the control of cell expansion (***Merlot et al., 2007***). Because its transcript accumulation was already induced by protoplasting, the scRNA-Seq data could not be used for *BAK1* with respect to the temporal expression along the root axis (***Ma et al., 2020***).

On the basis of the scRNA-Seq data we focused our further studies on the in vivo protein quantification of the GFP fusions of BRI1, BAK1, BIR3 and AHA2 in developing epidermal cells along the root tip axis. For the PM of cells of the EZ, the amount of BRI1-GFP was already quantified to around 11 receptor molecules per μm^2 and for BAK1-GFP to 5 co-receptors per μm^2 by ***Wilma van Esse et al., 2011***. To complete this data set, we applied quantitative CLSM for the quantification of BIR3-GFP and AHA2-GFP in the epidermal root cells of published transgenic *Arabidopsis* lines that express the fusion protein under the respective native promoter (***Fuglsang et al., 2014***; ***Imkampe et al., 2017***). As these GFP fusion proteins carry the identical fluorophore version, their fluorescence intensity can be set in relation to the BRI1-GFP intensity and, thus, to the BRI1-GFP receptor amount in the PM. The quantification of GFP fluorescence was performed in 50x50 µm areas at the epidermis along the root tip (an exemplary set of root tip images is shown in ***Appendix 1—figure 2***). The amount of BRI1-GFP and BAK1-GFP did not alter much in the epidermal cells in the MZ and early EZ, as it was reported before (***Figure 3C***; ***Wilma van Esse et al., 2011***). A relative homogeneous fluorescence intensity distribution was also observed for BIR3-GFP that translated to about 17 inhibitor molecules per μm^2 PM area in the MZ and 14 in the early EZ (***Figure 3C***). In contrast, there was a significant gradient of AHA2-GFP fluorescence intensity along the root axis, being comparatively low in the MZ (with 4 AHA2 molecules per μm^2 PM area) but high in the late EZ / maturation zone (with about 10 AHA2 molecules per μm^2 PM area) (***Figure 3C***). A relatively sharp alteration of the AHA2-GFP amount was detected for the TZ (***Figure 3C***). If the amount of AHA2-GFP and BIR3-GFP molecules was set in ratio to the number BRI1-GFP molecules in the PM along the root tip axis, there was no alteration with respect to BIR3 (ratio: about 1.35), but a strong increase regarding AHA2 from 0.28 in the MZ to up to 5 in the late EZ.

Our significantly improved spatio-temporal refinement of previous data (***Pacifici et al., 2018***) by scRNA-Seq and quantitative CLSM demonstrate a coincidence of AHA2 protein accumulation with the onset of growth in the EZ. These results suggest that there may be a regulatory link between AHA2 protein accumulation and probably activity pattern and normal and BR-regulated root growth along the root tip axis. This hypothesis is particularly plausible given that AHA2 interacts physically with BRI1 and BAK1 and is phosphorylated within 5 min upon BR treatment in vivo (***Caesar et al., 2011***; ***Ladwig et al., 2015***; ***Lin et al., 2015***; ***Yuan et al., 2018***).

Modeling predicts the H^+-ATPases being crucial regulators of the extracellular pH in the BR/BRI1 response

To test the hypothesis formulated above, we decided to investigate the functional role of AHA in the context of BR-regulated signaling activity both experimentally and computationally. Here, we first sought to quantify and analyze the response in the EZ. With the key components of the H^+ homeostasis and nano-organized BRI1 complex quantified (see ***Figure 3C***), we were able to tailor the model to represent a single epidermis cell in the EZ. By further using a combination of dose-response data and time-course measurements to fit the remaining unknown model parameters, we then should be able to analyze both the overall response and the temporal dynamics of the BR signaling module.

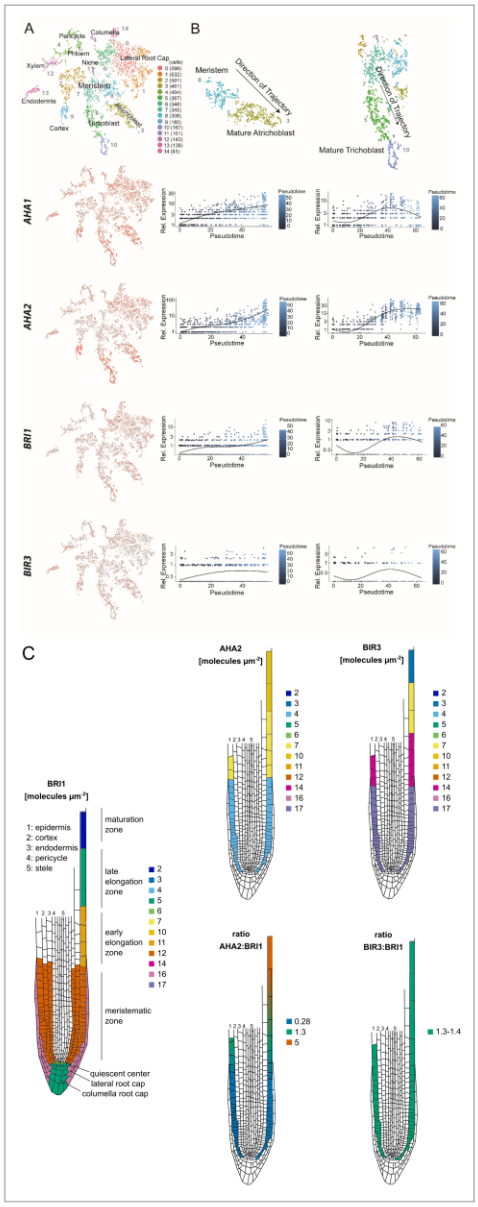

Figure 3. The constituents of the nano-scale organized BRI1 complex are spatio-temporally differentially expressed in the epidermal cells along the *Arabidopsis* root tip axis. (**A**) *AHA1*, *AHA2*, *BIR3* and *BRI1* transcript levels in the different cell types of the *Arabidopsis* root tip derived from scRNA-Seq data (***Ma et al., 2020***). The atrichoblasts and trichoblasts together represent the epidermal cells. (**B**) Developmental trajectories of *AHA1*,

Figure 3 continued on next page

Figure 3 continued

AHA2, BIR3, and *BRI1* transcript accumulation along the root tip (***Ma et al., 2020***). The transition from the MZ to the EZ is at a pseudotime value of around 30. (**C**) Upper panel. Number of the indicated GFP fusion proteins (molecules per μm^2) in the plasma membrane of epidermal cells along the root tip axis. The values for BRI1-GFP and BAK1-GFP were taken from the literature (***Wilma van Esse et al., 2011***). Lower panel. The same but here the ratios of BRI1-GFP/AHA2-GFP and BRI1-GFP/BIR3-GFP molecules in the plasma membrane are given.

To measure the dose-response behavior and the time-course response to BR stimulation experimentally, we relied on the salt 8-hydroxypyrene-1,3,6-trisulfonic acid trisodium (HPTS), a non-invasive dye that incorporates into the plant cell wall and enables the ratiometric fluorescence readout of the pH conditions at cellular resolution (***Barbez et al., 2017***; ***Appendix 1—figure 3***). To determine the apoplastic pH conditions 60 min after brassinolide (BL) application in the EZ, we performed a dose-response analysis. A significant decrease of the apoplastic pH was observed already at a BL concentration of 0.1 nM that continued up to a concentration of 10 nM (***Figure 4A***). Higher concentrations of BL did not further increase the cellular response in the EZ. This behavior is reproduced by the model ensemble (***Figure 4A***).

To capture not only the overall response to BL stimulation in the EZ but also its temporal dynamics, we further performed time-course measurements of the apoplastic pH in response to 10 nM BL using HPTS. Here, we observed a rapid acidification within 10 min after hormone application that is maintained for the remainder of the experiment (***Figure 4B***). This observation was again reproduced by the model ensemble (***Figure 4B***). At the same time, we could also capture the cell wall swelling in the model that has been observed in response to BL application previously (***Elgass et al., 2009***; ***Caesar et al., 2011***; ***Figure 4C***).

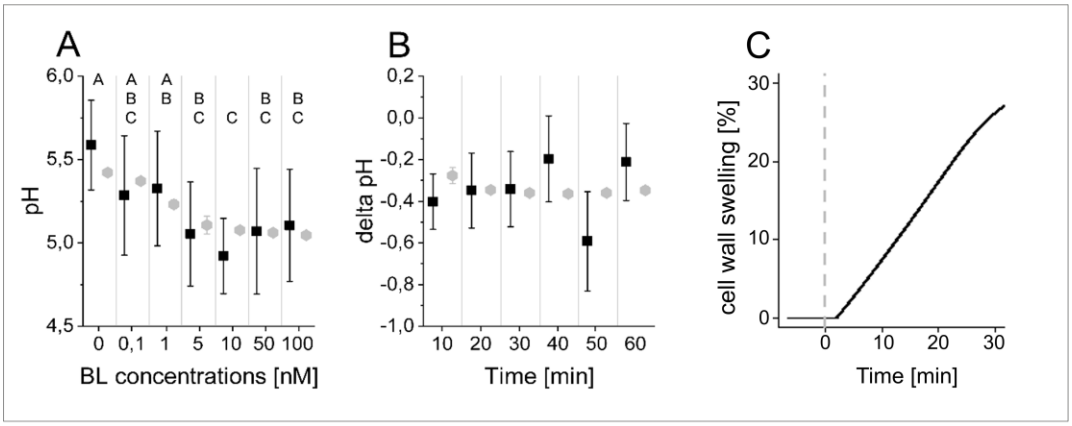

Figure 4. The computational model quantitatively and dynamically captures the sensitivity and kinetics of apoplastic acidification in *Arabidopsis* epidermal cells of the root EZ in response to BL. (**A**) HPTS-staining visualized (black quadrats) and computationally simulated (grey diamonds) dose-response behavior of apoplastic pH. Real or virtual BL incubation was done for 60 min. Error bars represent SD for the experimental data (n≥11) and the simulations of different model parameterizations (n = 10). Statistical evaluations to compare the effect of BL concentrations on experimental data, were performed by an One-way ANOVA followed by a Tukey-HSD post hoc test. Levels not connected by same letter are significantly different. The exact p-values can be found in the corresponding RAW data file. (**B**) HPTS-staining visualized (black quadrats) and computationally simulated (grey diamonds) time-course of apoplastic pH change in response to 10 nM BL. Error bars represent a corrected SD for the experimental data (n≥16) (for calculations see the corresponding RAW data file) and SD for the simulations of different model parameterizations (n = 10). Statistical evaluations on experimental data were performed as described in A. (**C**) Computationally simulated time course of relative wall swelling in response to 10 nM BL. The addition of BL at time 0 is indicated by the vertical dashed line.

The online version of this article includes the following source data for figure 4:

Source data 1. Raw data underlying the representation of the experimental results of ***Figure 4***.

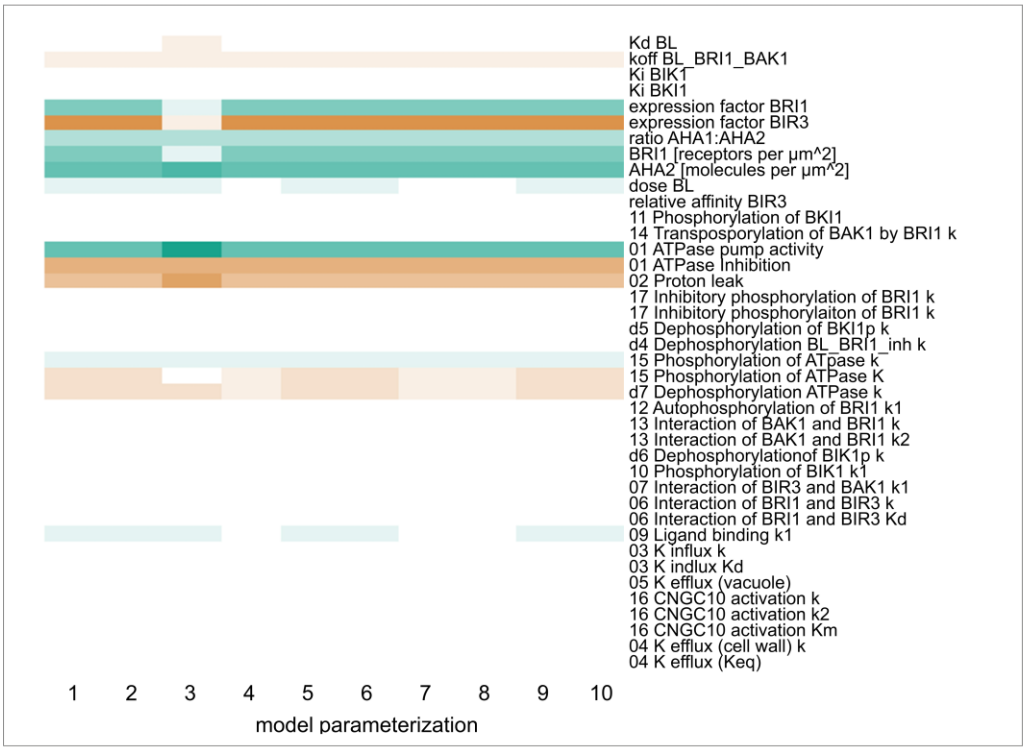

Figure 5. Computational calculation of scaled sensitivities of the cell wall acidification predicts AHA2 activity and molecules in the PM as well as BRI1 expression and molecules in the PM to be the deciding factors for the competence of *Arabidopsis* epidermal root cells to elongate in response to 5 min BL application for all parameterizations of the model. A positive influence is shown in green, a neutral in white and a negative in red, with the color saturation indicating the strength of the influence.

The online version of this article includes the following source data for figure 5:

Source data 1. Raw data underlying the representation of the results.

Using this model ensemble that specifically describes the behavior of a single epidermis cell in the EZ, we analyzed the importance of the individual model components and parameters for the cell physiological response by calculating the scaled sensitivities. In particular, this means that we calculated the relative change of the cell wall acidification in response to relative changes in model parameters while simulating the BR response stimulated with 10 nM BL for 5 min and 60 min. The results of the sensitivity analysis for all model parameterizations (n=10) are summarized in ***Figure 5***, where a positive influence on the BR response is denoted in green, no influence is denoted in white and a negative influence is denoted by red, with the color saturation indicating the strength of the control. Notably, at the beginning of the BR response the initial concentrations of the receptor BRI1 and the proton pumps had a large impact. In addition, parameters influencing proton extrusion such as the degree of inhibition and the pump activity of the ATPases strongly controlled the early BR response across all model parameterizations (***Figure 5***). The sensitivities of the acidification 60 min after BL application in turn showed a greater control of down-regulating elements such as the inhibitory phosphorylation of the receptor (***Appendix 1—figure 4***), although the amount of proton pumps as well as their activity remained impactful. As our previous protein quantification data showed a near constant level of the receptor while the AHA2 levels change notably, this strongly supports the hypothesis that the proton

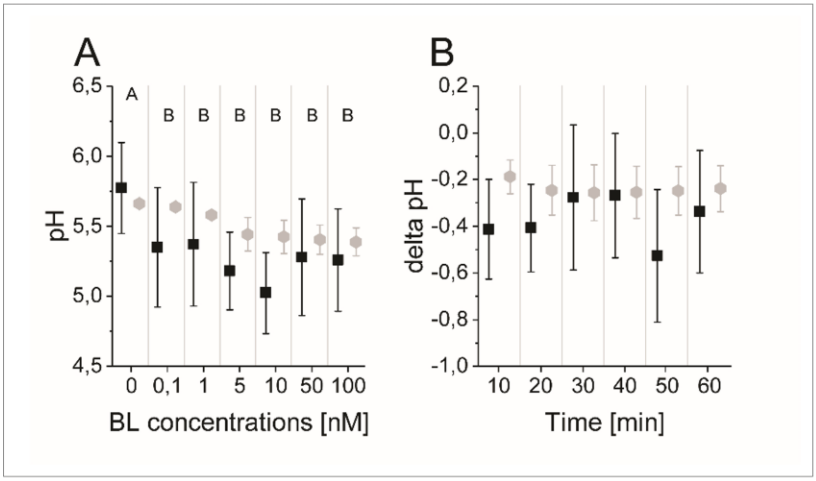

Figure 6. The model quantitatively and dynamically captures the sensitivity and kinetics of apoplastic acidification in *Arabidopsis* epidermal cells of the root MZ in response to BL. (**A**) HPTS-staining visualized (black quadrats) and computationally simulated (grey diamonds) dose-response behavior of apoplastic pH. Real or virtual BL incubation was done for 60 min. Error bars represent SD for the experimental data (n≥11) and the simulations of different model parameterizations (n = 10). Statistical evaluations on experimental data were performed as described in ***Figure 4***. Levels not connected by same letter are significantly different. The exact p-values can be found in the corresponding RAW data file (**B**) HPTS-staining visualized (black quadrats) and computationally simulated (grey diamonds) time-course of apoplastic pH change in response to 10 nM BL. Error bars represent a corrected SD for the experimental data (n≥16) (for calculation see the corresponding RAW data file) and SD for the simulations of different model parameterizations (n = 10). Statistical evaluations on experimental data were performed as described in ***Figure 4***.

The online version of this article includes the following source data for figure 6:

Source data 1. Raw data underlying the representation of the results.

pumps are the key elements that determine the competence of cells to respond to BR stimulation and react with elongation growth.

In consequence, the cells in the MZ should show a higher starting pH and react less strongly to BR stimulation due to the lower expression levels of AHA2. To predict the behavior of an epidermis cell in the MZ, we adjusted the model ensemble to instead represent a single epidermis cell in the MZ in terms of protein concentrations and compartment sizes. This model ensemble shows a higher resting pH and a reduced response to BR stimulation as evident in the dose-response behavior and kinetics properties that was supported in principle experimentally by HPTS visualization (***Figure 6***, ***Appendix 1—figure 5***). However, due to the limitation in the sensitivity of the HPTS method and the biological variability in the different root preparations, the difference in the BL-induced acidification responses between MZ and EZ epidermal cells could not be captured statistically. The modeling approach is therefore advantageous for the prediction of small, cell physiological response differences which are difficult to establish experimentally due to high biological and methodological variability (***Appendix 1—figure 5***). Although the model captures the cellular physiology very well, we cannot entirely exclude the possibility that there is no difference between PH responses in the MZ and EZ cells.

Experimental evaluation confirms the predicted relevance of the H^+-ATPases for the extracellular pH control in the BR/BRI1 response

To confirm the predictions of the model experimentally, we used both HPTS and microelectrode ion flux estimation (MIFE) measurements. MIFE is another non-invasive experimental method in addition to HPTS measurements that allows for contact-free, real-time, electrophysiological measurements of H^+ fluxes at the surface of roots by using an H^+-specific electrode that mainly reflects the ATPase

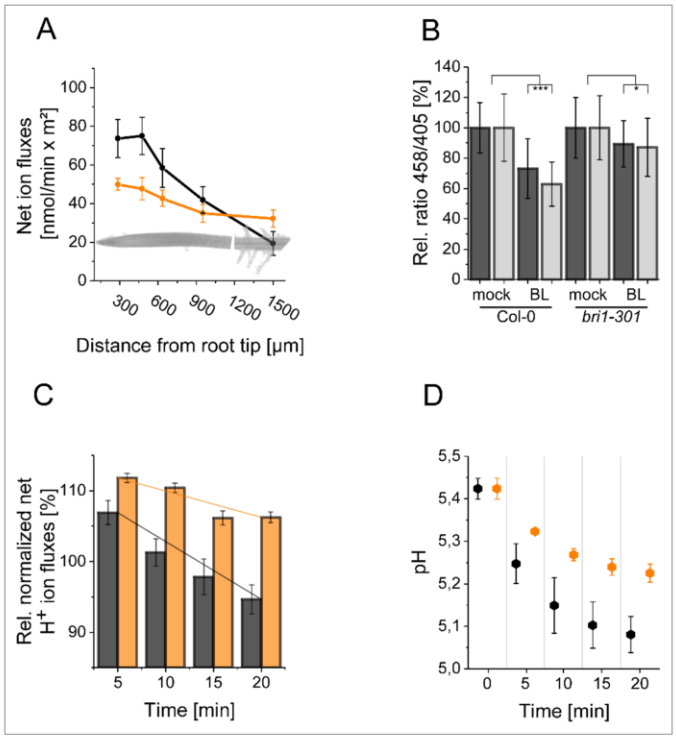

Figure 7. The resting apoplastic pH gradient of epidermal root cells along the axis and its regulation by BR depends on kinase-active BRI1. (**A**) MIFE recording of the H^+ fluxes along the root axis of *Arabidopsis* wild type (black line) and *bri1-301* mutant (orange line) plants. Measurements were performed from 250 µm of the root tip off to the root hair zone. Error bars represent SD (n = 3). (**B**) Comparison of the relative apoplastic pH (ratio 458/405) of epidermal root cells in the MZ (black bars) and EZ (grey bars) of wild type and *bri1-301* mutant plants after 60 min of BL (10 nM) or mock treatment, visualized by HPTS staining. The data derived from the mock treatments of the respective line were set to 100. Error bars represent SD (n≥30). Statistical evaluations were performed by comparing the respective groups separately (e.g. 'Col-0 MZ mock' compared with 'Col-0 MZ BL'). Depending on the distribution of data and other assumptions either a (pooled) Two-Tailed T-Test or a Two-Tailed Wilcoxon Test were applied. The black asterisks indicate statistically significant differences (***: p≤0.001); (*: p≤0.05). The exact p-values can be found in the corresponding RAW data file. (**C**) Relative H^+ fluxes at the EZ of wild type (black bars) and *bri1-301* mutant (orange bars) plants between 5 and 20 min after application of 10 nM BL recorded by MIFE. The flux directly before the addition of BL was set to 100. The increase in net influx after treatment is due to a disturbance of the H^+ conditions at the root surface, which is observed with any treatment. The solid lines illustrate the linear regression. The slope is –0.818 for the wild type and –0.371 for *bri1-301*. Error bars represent SD (n = 3). (**D**) Simulated response to 10 nM BL for the wild type (black) and *bri1-301* mutant (orange), under the assumption that the *bri1-301* mutant is biochemically half as active as the wild type. Error bars represent SD (n=10).

The online version of this article includes the following source data for figure 7:

Source data 1. Raw data underlying the representation of the results.

activity in the underlying tissues (***Newman, 2001***; ***Fuglsang et al., 2014***). Confirming previous results (***Staal et al., 2011***), our MIFE measurements along the *Arabidopsis* root tip revealed a net H^+ influx at the MZ, which then was drastically reduced in the EZ implying higher H^+ ATPase activity in this region (***Figure 7A***). These differential H^+ fluxes translate into a pH gradient along the surface of the root tip with the MZ less acidic and the EZ more acidic (***Staal et al., 2011***). Using HPTS, we substantiated

the MIFE results and confirm the observation of ***Barbez et al., 2017*** that there is an apoplastic pH gradient of the epidermal root cells from the MZ (less acidic) to the EZ (more acidic) (***Appendix 1—figure 3***).

To address the question whether the establishment of the resting pH gradient and the differential changes of the pH conditions upon external BL application depend on fully functional BRI1, we used the *bri1-301* mutant for further HPTS and MIFE measurements. In the *bri1-301* mutant a BRI1 version with a reduced kinase activity is expressed, which causes a weak defective root growth phenotype at ambient temperature (***Lv et al., 2018***; ***Zhang et al., 2018***). This less-pronounced *bri1-301* phenotype allows HPTS and MIFE measurements technically comparable to those of wild type plants. As shown in ***Figure 7B***, the BL-induced changes in the apoplastic pH - here represented in the relative change of 458/405 fluorescence emission ratio - observed for wild type were significantly reduced in the *bri1-301* mutant. The HPTS data were again supported by our MIFE measurements: The wild type cells of the EZ showed an increase in the net H^+ efflux upon application of 10 nM BL, which continued over the measurement period of 20 min, whilst the cells of the *bri1-301* mutant responded much less (***Figure 7C***). Under the assumption that the mutant BRI1-301 receptor is biochemically half as active as wild type BRI1 the model is able to capture the experimentally measured behavior correctly (***Figure 7D***).

In summary, the concordant results of our experimental approaches including those of ***Caesar et al., 2011*** substantiate the prediction of the mathematical model that the enhanced level of H^+-ATPase amount and activity in relation to the number of BRI1 receptors define the BR-regulated apoplastic acidification and linked hyperpolarization of the E_m. Moreover, the maintenance of the pH gradient and H^+-fluxes along the root tip axis and the BL regulation of alterations depend on kinase-active BRI1.

Modeling predicts a cation channel for charge compensation during H^+ export and PM hyperpolarization

The great value of mathematical modeling and prediction is especially demonstrated after we calculated the membrane potential derived from the pH value changes in the apoplastic cell space of the root tip upon BL treatment and compared it with the previously experimentally determined E_m changes (***Caesar et al., 2011***). The calculated E_m change induced by the change in charge distribution due the acidification of the apoplastic space was much stronger than the measured one (***Figure 8A*** and Appendix 1 - example calculation of E_m and pH change based on membrane area, specific membrane capacitance and transported charges): An acidification from pH 5.4 to pH 5.0 in response to 10 nM BL corresponds to an E_m change of approximately 28 mV, as opposed to the experimentally measured 7.2 mV (***Caesar et al., 2011***). As mentioned before (see ***Figure 2***) and according to the prediction of our model, this discrepancy values was eliminated, if an import of monovalent cations such as potassium (K^+), which predominantly contributes to the E_m of the PM in plant cells (***Higinbotham, 1973***), took place in parallel to the ATPase generated H^+ extrusion. Against the background that BAK1 and AHA2 interact with a cation channel of the cyclic nucleotide-gated ion channel (CNGC) family in the phytosulfokine receptor 1-mediated growth response (CNGC17; ***Ladwig et al., 2015***), we searched in the literature and the *Arabidopsis* eFP browser (***Sullivan et al., 2019***) for a CNGC member, which is expressed in the root tip, localizes to the PM and imports monovalent ions, and is functionally linked to cell expansion. Applying these criteria, we identified CNGC10 as a potential candidate. Although to a low extent, CNGC10 is expressed in all cell types of the root tip (***Brady et al., 2007***; ***Jin et al., 2015***; ***Ma et al., 2020***), localizes to the plasma membrane, transports K^+ and is functionally linked to cell expansion (***Borsics et al., 2007***; ***Christopher et al., 2007***; ***Duszyn et al., 2019***). When CNGC10 and its K^+ transport properties derived from the literature above were integrated into our model, the discrepancy between the calculated and measured value was gone (***Figure 8B***). This suggests that the CNGC10-mediated influx of potassium can principally counteract the ATPase-caused efflux of H^+ into the apoplast in the root tip.

To test whether CNGC10 is able to interact with components of the nano-organized BRI1 complexes such as BRI1, BAK1 and AHA2, Förster resonance energy transfer by fluorescence lifetime imaging (FRET-FLIM) analyses in transiently transformed *Nicotiana benthamiana* leaf cells and yeast mating-based split-ubiquitin (mbSUS) assays were performed. The growth of yeast cells on interaction selective media and the reduction of the GFP fluorescence lifetime (FLT) revealed a spatially very close

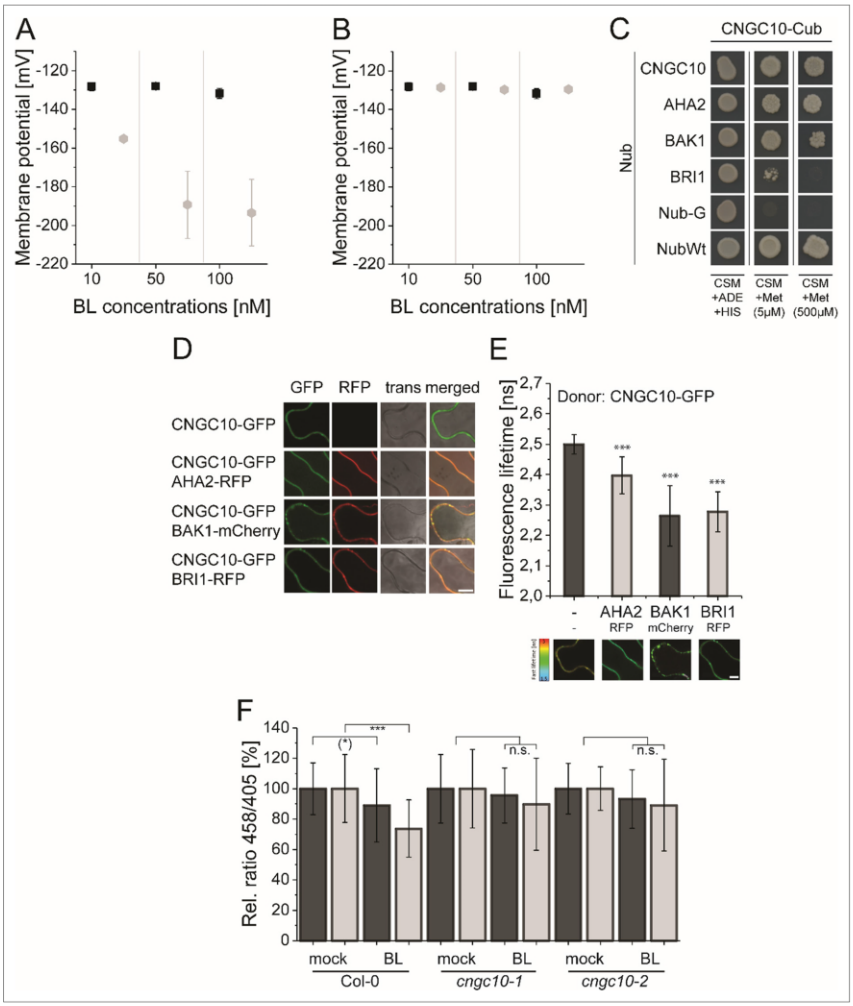

Figure 8. The computational model predicts the existence of a potassium channel, likely to be CNGC10, to maintain the homeostasis of the plasma membrane potential and apoplastic pH in *Arabidopsis* epidermal root cells. (**A**) Modeled E_m in the presence of different BL concentrations without the integration of potassium import (grey diamonds) in comparison to the published experimental data [black quadrats; ***Caesar et al., 2011***] after 20 min of BL treatment. (**B**) Modeled E_m in the presence of different BL concentrations with the integration of the CNGC10 potassium channel (grey diamonds) in comparison to the published experimental data [black quadrats; ***Caesar et al., 2011***]. Error bars in A and B represent SEM (n≥4) in the experimental approach and SD (n = 5) of simulation results of the different model parameterizations. (**C**) CNGC10 forms homomers and interacts with BAK1 and AHA2 in the yeast mating-based split-ubiquitin system. The indicated combinations of Cub and Nub fusion constructs were transformed into yeast cells. Yeast cells were then grown either on media selective for the presence of the plasmids (CSM +Ade, +His) or on interaction selective media with two different concentrations (5 µM, 500 µM) of methionine (CSM +Met). The combination of CNGC10-Cub with Nub-G served as negative and that with NubWT as positive control. (**D**) CNGC10 colocalizes with AHA2, BAK1, and BRI1 in the plasma membrane of plant cells. Representative confocal images of transiently transformed tobacco epidermal leaf cells expressing the indicated fusion proteins. The Scale bars represents 10 µm. (**E**) CNGC10 is spatially closely associated with AHA2, BAK1 and BRI1 in the plasma membrane of plant cells. Fluorescence lifetime imaging microscopy (FLIM) analysis comparing the different Förster resonance energy transfer (FRET) pairs. Top: FLIM measurements of transiently transformed tobacco epidermal leaf cells

Figure 8 continued on next page

Figure 8 continued

expressing the CNGC10-GFP donor fusion with the indicated RFP or mCherry acceptor fusions. Error bars indicate SD (n≥20). Statistical evaluations were performed by a Kruskal-Wallis Test followed by Steel-Dwass post hoc test. The black asterisks indicate statistically significant differences (***: $P \leq 0.0001$). Bottom: Heat maps of representative plasma membrane areas used for FLIM measurements. The donor lifetimes of CNGC10 are color-coded according the scale at the left. The scale bar represents 7 µm. (**F**) Comparison of the relative apoplastic pH (ratio 458/405) of epidermal root cells in the MZ (black bars) and EZ (grey bars) of wild type and two independent *cngc10* mutant lines after 60 min of BL (10 nM) or mock treatment, visualized by HPTS staining. The data derived from the mock treatments of the respective line were set to 100. Error bars represent SD (n≥27). Statistical evaluations were performed as described in ***Figure 7B***. The black asterisks indicate statistically significant differences (***: p≤0.0001); ((*): p = 0.0603; borderline p-value); n.s.: not significant. The exact p-values can be found in the corresponding RAW data file.

The online version of this article includes the following source data for figure 8:

Source data 1. Raw data underlying the representation of the results.

association (below 13 nm; ***Glöckner et al., 2020***) and interaction, respectively, of CNGC10 with BRI1, BAK1, and AHA2 (***Figure 8C–E***). To test whether CNGC10 functions in the fast BR response pathway, we analyzed the BL-induced apoplastic pH change in two independent *cngc10* loss-of-function lines (***Jin et al., 2015***; ***Borsics et al., 2007***) compared to the corresponding wild type (Col-0). In contrast to the wild type both mutants did not acidify the apoplast of the cells in the MZ and EZ upon application of 10 nM BL (***Figure 8F***). These data indicate that CNGC10 is the major K^+ channel to maintain the E_m homeostasis of the PM during BL-induced apoplastic acidification primarily in the EZ and appears to be an additional constituent of the elongation growth-related, nano-scale organized BRI1 complexes.

Discussion

BRs fulfill a central role in regulating plant physiology, growth and development as well as adaption to the environment (***Lv and Li, 2020***). A prominent example for a BR function is the rapid initiation of the (epidermal) cell growth in the EZ but not in the MZ of the *Arabidopsis* root tip (***Lv and Li, 2020***). Evidently, the hormone acts on an already existing functional competence of the root cells that, according to our experimental data, cannot be attributed to the absence of the BRI1/BAK1 perception system but must have other reasons. ***Pavelescu et al., 2018*** proposed that BRI1 signaling in the MZ is sufficient for root growth. More recent, complementary data show the highest BR concentration in the EZ, where it overlaps with BR/BRI1 signaling maxima with respect to cell elongation (***Vukašinović et al., 2021***). This observation implicates BRI1-dependent BR perception and signaling in the regulation of cell elongation in the EZ as well. Moreover, although the main molecular determinants of BR perception and signaling are known, the processes leading to this competence and its realization towards, in this case, elongation were so far not well understood.

By an iterative combination of computational modeling and wet lab experiments, we addressed this question by analyzing the dynamics of the PM-resident fast BR response pathway as a whole. The model's predictions of the crucial constituents in the nano-organized BRI1 complexes were experimentally verified, thereby determining the deciding and regulating elements for the signaling output. Using a detailed kinetic model on the basis of ODEs, we could analyze the interplay of the signaling components and the system as a whole: We captured the dynamics of the apoplastic acidification and E_m hyperpolarization without BR and in response to the hormone. In addition, we showed that the rapidity and degree of the apoplast acidification in response to BR application is determined largely by the amount and activity of the ATPase AHA2 in the PM of the epidermal root cells. Furthermore, the model predicted that an influx of cations is required in order to explain both the pH and E_m changes of the PM simultaneously. We found that CNGC10 is the responsible cation (potassium) channel. Besides functional evidence, it associates with BRI1, BAK1 and AHA2 in vivo. CNGC10 could therefore be another constituent of nano-organized BRI1 complexes in the PM of root cells.

If we project the measured AHA2 amount and AHA activity, and the apoplastic pH of epidermal cells along the axis of the root tip, we observe that they both increase and decrease, respectively, with the beginning of the EZ and strongly correlate with the competence to grow upon BL application. Proposed by the computational model, AHA2 appear to be the rate-limiting factor for the cells' competence to respond to BR by short-term cell physiological responses and eventually elongation. This gradient of AHA2 expression implies that the BR implements on an already existing, functional competence of the cells along the root axis that cannot be attributed to the absence of

the BRI1/BAK1 perception system. The competence to respond to the hormone is rather reflected by a gradient of AHA2 accumulation and probably differential AHA2 incorporation into nano-organized BRI1 complexes along the root axis. As reported previously, the establishment of the AHA2 accumulation along the root axis is achieved by the interplay of cytokinin and auxin activity during root development (**Pacifici et al., 2018**). This agrees with the suggestion of our model that the cells of the MZ should exhibit elongation growth if AHA2 is ectopically expressed and thus acidification enhanced. This is actually the case: Inducible expression of AHA2 enhances the length of MZ cells but in parallel reduces MZ cell number during root development (**Pacifici et al., 2018**). Another competence pattern was recently reported to be the differential local BR biosynthesis along the root axis (**Vukašinović et al., 2021**): While BRs are present throughout the root, the expression of BR synthesis enzymes is highest in the EZ. Remarkably, the additional application of exogenous BR in high concentration causes the elongation of MZ cells and decrease in MZ cell number (**Vukašinović et al., 2021**), copying the phenotype caused by the inducible expression of AHA2 in the MZ zone (**Pacifici et al., 2018**). This suggests that two different competence pattern, BR biosynthesis and accumulation of AHAs, superimpose along the root axis. Whether the differential expression of BR synthetic genes along the root axis is also controlled by the interplay of cytokinin and auxin, has to be analyzed in the future.

The final output of the cell elongation appears to require the sequence of short-term (within minutes) and long-term response mechanisms (from several hours to days). According to our modelling and experimental data as well as published results, short-term molecular and cell physiological responses to BR are predominantly linked to the rapid activation of AHAs very likely by their phosphorylation at two residues in the large cytoplasmic loop (Ser315 and Thr328 in AHA2) within 5 min (**Lin et al., 2015**), followed by the acidification of the apoplastic space detectable within 10 min (shown here), hyperpolarization of the PM detectable within 10 min (**Elgass et al., 2009**; **Caesar et al., 2011**) and wall swelling detectable within 20 min (**Elgass et al., 2009**; **Caesar et al., 2011**). Based on the acid growth theory, these AHA activity-related responses are the prerequisite for the onset of cell elongation (**Cosgrove, 2000**; **Hager, 2003**). Therefore, we propose that the ongoing of the BR-regulated elongation growth, that involves altered gene expression later in time, is not possible if the initial rapid processes do not occur adequately. The BR-mediated control of the H^+ ATPase and, thus, the E_m concerns not only elongation growth.

The E_m is also central for adaptive responses to a broad range of abiotic cues and for developmental processes. Our observations therefore suggest that the regulation of H^+ ATPase might contribute to the versatile functions of BR in many of these processes (**Lv and Li, 2020**; **Wolf, 2020**).

The BR-induced cell physiological processes occurring in the minute range appear to require higher hormone concentrations (around 1–10 nM) compared to those for long-term root growth and (other) gene expression-related processes in the range of hours or days (0.1–0.25 nM; **Chaiwanon and Wang, 2015**; **Vukašinović et al., 2021**). This discrepancy can have different reasons: Firstly, the physiologically effective concentration in the root tissue after short-time BL treatment is not known to us. Due to the short time for diffusion into the root, it may well be that the BL concentration at the target tissues is lower than the externally applied one. Secondly, it cannot be excluded that the continuous growth of seedlings on media containing very low BR concentrations induces the accumulation of BR itself or other growth-promoting hormones in the long-term, for instance by the enhanced expression of their biosynthetic genes. Interestingly, the short-term sequence of events in the *Arabidopsis* root tip is significantly faster and requires lower BL amounts than the AHA activation during cell elongation in the *Arabidopsis* hypocotyl. There, phosphorylation of AHAs at the penultimate threonine (Thr947 in AHA2) is detectable 60 min after BL application at the earliest and at BL concentration of at least 100 nM (**Minami et al., 2019**). Furthermore, the phosphorylation of the penultimate threonine in AHAs appears not to be required for at least the BL-induced E_m hyperpolarization in tobacco leaf cells 30 min after application of 10 nM BL (**Witthöft et al., 2011**). Moreover, the enhanced phosphorylation of the AHAs' penultimate Thr by BR - measured 2 hr after application of 1 µM BL - involves the interaction of SAUR15 with BRI1 (**Li et al., 2022**). It is therefore tempting to speculate that a cascade of different phosphorylation events might be involved in the temporal regulation of AHA activity in different plant organs.

As discussed above, we propose an increased number of AHA2-containing nano-organized BRI1 complexes or an enhanced proportion of AHA2 therein from the MZ to the EZ cells. Varying the composition of nano-organized receptor complexes along a developmental gradient is an elegant way

to achieve cell- and tissue-specific responses to a given cue, when the number of available perception, signaling and output elements is limited. This principle seems to be realized in various BRI1-mediated functions. For example, the BRI1-dependent regulation of the vascular cell fate in the MZ of the root or the BRI1-mediated cross-tissue control of the cell wall homeostasis require nano-organized BRI1 complexes that contain at least additionally RLP44 (**Wolf et al., 2014**; **Holzwart et al., 2018**). Moreover, RLP44-containing BRI1/BAK1 nanoclusters are spatially distinct from for instance FLS2/BAK1 nanoclusters (**Glöckner et al., 2020**).

The availability of a sophisticated model also enables in silico genetics that simplify the understanding of complex regulatory processes and their sometimes non-intuitive effects on the functional outputs. This is illustrated by the example of the negative regulator BIR3 that prevents the interaction of BAK1 and BRI1 in the absence of the hormone thereby suppressing BR signaling (**Imkampe et al., 2017**; **Großeholz et al., 2020**). Our computational model not only represents the previously published BR activity of the growth-related phenotypes of the *Arabidopsis bir3* mutant and BIR3-overexpressing plants but also allows predictions about the dose-dependent fine-tuning of BIR3 on BR/BRI1/BAK1-related functions (see **Appendix 1—figure 6**). Such in silico genetic and physiological approaches can be used to determine the functional and regulatory significance of other components of the fast BR response pathway as shown for AHA2 and the prediction of a cation channel for charge compensation. Thus, computational modeling facilitates the prioritization of the components of a perception and signaling system whose function should first be tested experimentally.

In summary, the recurrent application of computational modeling and subsequent wet lab experiments provided a novel in-depth and quantitative view of the initial cell physiological processes, regulatory networks and information processing leading to a minimal molecular and biochemical framework linked to BR-regulated elongation growth along the axis of the root tip. This approach can in principle be applied for the analysis of every signal perception and transduction process as long as a minimal set of elements and quantitative data are available or experimentally accessible, as has been demonstrated for example in the in-depth analysis of the PLT-auxin network during root zonation development in *Arabidopsis thaliana* (**Salvi et al., 2020**; **Rutten and Ten Tusscher, 2021**).

The ongoing challenge will now be to establish a model of anisotropic elongation growth along all tissues of the root tip, as it was initiated for the description of BR-regulated radial growth of the root MS (**Fridman et al., 2021**). At the cellular level, the further aim is to expand and refine the model by the integration of the data of the potentially BR-modified composition, assembly and dynamics of the nano-organized BRI1 complexes in the PM obtained by sophisticated super-resolution microscopy and in vivo FRET studies (**Glöckner et al., 2020**).

Methods and materials

Experimental methods

Plant material

Seeds of the *Arabidopsis* mutants and lines expressing the different fusion proteins were surface sterilized and placed on ½ Murashige and Skoog (MS) medium plates with 1% phytoagar and 1% sucrose followed by stratification at 4 ° C in the dark for 2 days. Afterwards the plants were grown in growth chambers at 20 ° C under long day conditions (16 hr light/8 hr dark) for 5 days. The transgenic *Arabidopsis* lines (Col-0 ecotype) contained either a *pBRI1:BRI1-GFP* (wild type background; **Friedrichsen et al., 2000**), a *pAHA2:AHA2-GFP* (*aha2-4* mutant background; **Fuglsang et al., 2014**) or a *pBIR3:BIR3-GFP* construct (*bir3-2* background; **Imkampe et al., 2017**). The *Arabidopsis bri1-301* mutant (Col-0) was described in detail previously (**Lv et al., 2018**; **Zhang et al., 2018** and references therein). The previously described *Arabidopsis cngc10-1* and *cngc10-2* mutants (Col-0) (**Jin et al., 2015**; **Borsics et al., 2007**) were obtained from the Nottingham stock center (SALK_015952, SALK_071112).

Confocal imaging

Quantification of the GFP signal on five days old seedlings was performed by confocal laser scanning microscopy (CLSM) on a SP8 laser scanning microscope (Leica Microsystems GmbH) with HyD detectors and a HC PL APOCS2 63 x/1.20 WATER objective. Detection range was set to 500 nm – 540 nm with 400 V gain and line averaging of 4. An adequate laser power for the 488 nm laser was applied

to avoid the saturation of the signal and to ensure a dynamic range across the expression levels of the different transgenic plants. The identical excitation and detection settings were used for all image quantifications. In six imaging sessions, ten straight lying root tips were imaged in the following way: The root tip was placed to the left border of a 1024x512 pixel image. The images for the quantification were taken in a way that 4–5 lanes of epidermal cells were in focus. Fluorescence intensity was quantified with a 50x50 µm region of interest (ROI) in Fiji/Image J. The ROI had to be completely filled by the fluorescence signal, hence "too high" z-layer-images, not filling the ROI completely, were excluded. Also, not completely straight-lying roots were excluded, so that a total of 40 measurements per transgenic plant line were finally used. As readout the Integrated Intensity Feature of Fiji, summing up the intensity of all pixels in a ROI, was used. For statistics, all measurements of 40 roots of at least three plant lines were combined.

Microelectrode ion flux estimation (MIFE) measurement

For MIFE measurements, 5-day-old seedlings were grown as described but in continuous light. Experiments were performed as described by ***Fuglsang et al., 2014***. The seedlings were equilibrated in bath medium (0.1 mM $CaCl_2$, 0.5 mM KCl, pH 5.8) for 2 h before the measurements. Only seedlings without proton oscillations were used. At time point 0.1 nM BL was added. The bathing solution was mixed two times by carefully pipetting up and down after addition of BL. The proximal position of the electrode (near the root) and the distal position (far from the root) were swapped compared to the previous study (***Fuglsang et al., 2014***). Consequently, a decrease in values represents proton efflux and an increase represents proton influx in our measurements.

8-Hydroxypyrene-1,3,6-trisulfonic acid trisodium salt (HPTS) measurement

For root apoplastic pH measurements, plates containing ½ MS agar media pH 5.7 without buffer, 1 mM HPTS dye, and the respective treatments were used. Five-day-old *Arabidopsis* seedlings were transferred onto the media and treated for 60 min with HPTS prior to imaging. For shorter treatments, seedlings were prestained with HPTS and subsequently treated according to the indications. For imaging, the plants on the media were flipped into a nunc imaging chamber (Ibidi 80286), the roots being close to the chamber bottom and covered by the media. Ratiometric imaging was conducted at an inverted Zeiss LSM880 confocal scanning microscope. The 405 nm and 458 nm laser were used at 0.2% and 100% intensity respectively, a PMT detector range from 495 to 535 nm was used and line sequential scans were performed. The detector gain was set at 1200. For imaging, a 40 x water immersion objective was used. The evaluation of ratio in the resulting images was determined following the workflow described by ***Barbez et al., 2017***. For calibration curve measurements, ½MS agar media supplemented with 10 mM MES were adjusted to the desired pH and roots of 5-day-old seedlings were analyzed as described above.

Mating-based split-ubiquitin system (mbSUS) measurements

For the mbSUS the coding sequences of *CNGC10*, *AHA2*, *BAK1* and *BRI1* were either fused to the sequences coding for the C-terminal part of ubiquitin (Cub) or the N-terminal part of ubiquitin (Nub). Namely, the plasmids pMetYC (Cub) and pXNubA22 (Nub) were used (***Grefen et al., 2009***). pNubWt-Xgate (***Obrdlik et al., 2004***) and the empty pXNubA22 vector served as positive and negative control, respectively. The experiments were performed as described by ***Grefen, 2014*** with some modifications: After dropping the mated yeasts on yeast extract peptone dextrose (YPD) plates they were scratched off with pipette tips, resuspended in 100 µl H_2O and 5 µl were transferred to complete supplement mixture (CSM)-Leu -Trp -Ura -Met plates. The growth assay was performed with adjusted optical density of the yeast cultures in one dilution. Here, vector selective plates (CSM-Leu -Trp -Ura -Met) or interaction selective plates (CSM-Leu -Trp -Ura -Met, -Ade, -His) with 5 µM and 500 µM methionine were used. The growth of the yeast was documented after 72 hr of incubation at 28 °C.

FRET-FLIM analysis

For FRET-FLIM analysis, the coding sequences were expressed as C-terminal fluorophore fusions, using pH7FWG2 (GFP), pB7RWG2 (RFP), or pABind-mCherry (***Karimi et al., 2002***; ***Bleckmann et al., 2010***). These binary vectors and *p19* as gene silencing suppressor were transformed into *Agrobacterium tumefaciens* strain GV3101 and infiltrated into *Nicotiana benthamiana* leaves. The

measurements were performed 2–3 days after infiltration using an SP8 laser scanning microscope (Leica Microsystems GmbH) with LAS AF and SymPhoTime (PicoQuant) software as described (***Veerabagu et al., 2012***). Before performing the FRET-FLIM measurement, the presence of the fluorophores was imaged by using 488 nm or 561 nm lasers for GFP or RFP excitation, respectively. The fluorescence lifetime τ [ns] of either the donor only expressing cells or the cells expressing the indicated combinations was measured with a pulsed laser as an excitation light source with 470 nm and a repetition rate of 40 MHz (PicoQuant Sepia Multichannel Picosecond Diode Laser, PicoQuant Timeharp 260 TCSPC Module and Picosecond Event Timer). The acquisition was performed until 500 photons in the brightest pixel were reached. To obtain the GFP fluorescence lifetime, data processing was performed with SymPhoTime software and bi-exponential curve fitting and correction for the instrument response function.

Statistics

All statistical evaluations were performed with SAS JMP 14. The applied tests are indicated within the respective figure texts. Detailed information about the statistics evaluations can be found in the RAW data files.

Computational methods

Model setup

The model consisting of ordinary differential equations was constructed in COPASI (***Hoops et al., 2006***; ***Mendes et al., 2009***) 4.30, build 240, running on a 64-bit machine with Windows 8. Reactions were defined as mass action or Michaelis Menten kinetics where appropriate (see ***Appendix 1—table 3***). Compartment sizes and parameters were defined based on experimental data if possible (***Appendix 1—Tables 1 and 3***). Unknown parameters were determined by parameter estimation. The schematic of the model was drawn using VANTED (***Junker et al., 2006***) and adheres to the Systems Biology Standard of Graphical Notation (SBGN) (***Novère et al., 2009***).

Parametrization

All unknown model parameters, where no or only a range of experimental information were available, were estimated. To account for parameter non-identifiabilities, we generated 10 independent parameter sets by randomly sampling the starting parameter values before running the parameter estimation. Each parameter estimation run was set up using the particle swarm algorithm as implemented in COPASI 4.30 (***Hoops et al., 2006***), using 5,000 generations with a swarm size of 50 individual parameter combinations. The parameter estimation was repeated until the resulting solution had a χ^2 around 10.45.

Model analyses

The time-course simulations were run deterministically using the LSODA algorithm as implemented in COPASI. The simulations of the *bri1-301* mutant were run by setting all rate constants of phosphorylation reactions catalyzed by BRI1 to ½ the original value. The relevant reactions were r_{10}, r_{11}, r_{12}, r_{14}, r_{15}, and r_{16}. The impact of different BIR3 concentrations was analyzed using the parameter scan task in COPASI to simulate the time course of the pH over the time frame of 20 min. The scaled sensitivities of the extracellular pH change in response to changes in model parameters were calculated as $scaled\ sensitivity = \frac{ln(delta\ pH)}{ln(P_i)}$ at 5 min and 60 min. Results were plotted using R (***R CoreTeam, 2020***).

Acknowledgements

The research in our laboratories is supported by the German Research Foundation (DFG) with grants to KH, KS and UK (CRC 1101-A02/D02) and grants for scientific equipment (INST 37/819–1 FUGG, INST 37/965–1 FUGG, INST 37/991–1 FUGG, INST 37/992–1 FUGG). We also thank the Schmeil Foundation and the Joachim Herz Stiftung for their support of RG. In addition, we are grateful for the support by Tom Denyer, ZMBP - University of Tübingen, for his help in the interpretation of the scRNA-Seq data.

Additional information

Funding

Funder	Grant reference number	Author
Deutsche Forschungsgemeinschaft	CRC 1101	Karin Schumacher
Deutsche Forschungsgemeinschaft	INST 37/819- 594 1 FUGG	Klaus Harter
Schmeil Stiftung	RG	Ruth Großeholz
Joachim Herz Stiftung	RG	Ruth Großeholz
Deutsche Forschungsgemeinschaft	INST 37/965-1 FUGG	Klaus Harter
Deutsche Forschungsgemeinschaft	INST 37/991-1 FUGG	Klaus Harter
Deutsche Forschungsgemeinschaft	INST 37/992-1 FUGG	Klaus Harter

The funders had no role in study design, data collection and interpretation, or the decision to submit the work for publication.

Author contributions

Ruth Großeholz, Conceptualization, Data curation, Software, Formal analysis, Funding acquisition, Validation, Investigation, Visualization, Methodology, Writing – original draft, Writing – review and editing; Friederike Wanke, Conceptualization, Data curation, Formal analysis, Supervision, Validation, Investigation, Visualization, Methodology, Writing – original draft, Writing – review and editing; Leander Rohr, Formal analysis, Validation, Investigation, Visualization, Methodology, Writing – review and editing; Nina Glöckner, Conceptualization, Data curation, Formal analysis, Validation, Investigation, Visualization, Methodology, Writing – original draft, Writing – review and editing; Luiselotte Rausch, Data curation, Formal analysis, Investigation, Visualization; Stefan Scholl, Data curation, Formal analysis, Validation, Visualization, Methodology; Emanuele Scacchi, Conceptualization, Supervision, Validation, Methodology, Writing – review and editing; Amelie-Jette Spazierer, Data curation, Validation, Investigation; Lana Shabala, Resources, Formal analysis, Supervision, Methodology; Sergey Shabala, Resources, Formal analysis, Supervision, Validation, Visualization, Methodology, Writing – review and editing; Karin Schumacher, Conceptualization, Formal analysis, Supervision, Funding acquisition, Methodology; Ursula Kummer, Conceptualization, Software, Formal analysis, Supervision, Funding acquisition, Validation, Investigation, Methodology, Project administration, Writing – review and editing; Klaus Harter, Conceptualization, Resources, Formal analysis, Supervision, Funding acquisition, Validation, Investigation, Methodology, Writing – original draft, Project administration, Writing – review and editing

Author ORCIDs

Leander Rohr http://orcid.org/0000-0003-4592-4197
Karin Schumacher http://orcid.org/0000-0001-6484-8105
Klaus Harter http://orcid.org/0000-0002-2150-6970

Decision letter and Author response

Decision letter https://doi.org/10.7554/eLife.73031.sa1
Author response https://doi.org/10.7554/eLife.73031.sa2

Additional files

Supplementary files

- Appendix 1—figure 1—source data 1. Raw data underlying the representation of the results.
- Appendix 1—figure 4—source data 1. Raw data underlying the representation of the results.
- Appendix 1—figure 5—source data 1. Raw data underlying the representation of the results.

- Appendix 1—figure 6—source data 1. Raw data underlying the representation of the results.
- Transparent reporting form

Data availability

All data generated and analysed during this study are included in the manuscript and Appendix 1. Raw and metadata are provided for Figures 4, 5, 6, 7 and 8 as well as for Appendix 1 Figures 2, 3, 4 and 6. Figure 1 represents scheme of early BRI1 signaling and Figure 2 the scheme of the used model structure. Predominantly published scRNA-Seq data were used for Figure 3. Modelling codes are available in Appendix 1 - model information.

The following previously published dataset was used:

Author(s)	Year	Dataset title	Dataset URL	Database and Identifier
Denyer T, Ma X, Klesen S, Scacchi E, Nieselt K, Timmermans MC	2019	Spatiotemporal development trajectories in the Arabidopsis root revealed using high-throughput single-cell RNA sequencing	https://www.ncbi.nlm.nih.gov/geo/query/acc.cgi?acc=GSE123818	NCBI Gene Expression Omnibus, GSE123818

References

Allen HR, Ptashnyk M. 2017. Mathematical modelling and analysis of the brassinosteroid and gibberellin signalling pathways and their interactions. *Journal of Theoretical Biology* **432**:109–131. DOI: https://doi.org/10.1016/j.jtbi.2017.08.013, PMID: 28818467

Baekgaard L, Fuglsang AT, Palmgren MG. 2005. Regulation of plant plasma membrane H+- and ca2+-atpases by terminal domains. *Journal of Bioenergetics and Biomembranes* **37**:369–374. DOI: https://doi.org/10.1007/s10863-005-9473-0, PMID: 16691467

Bairoch A, Apweiler R, Wu CH, Barker WC, Boeckmann B, Ferro S, Gasteiger E, Huang H, Lopez R, Magrane M, Martin MJ, Natale DA, O'Donovan C, Redaschi N, Yeh LSL. 2005. The universal protein resource (uniprot). *Nucleic Acids Research* **33**:D154–D159. DOI: https://doi.org/10.1093/nar/gki070, PMID: 15608167

Band LR, Wells DM, Fozard JA, Ghetiu T, French AP, Pound MP, Wilson MH, Yu L, Li W, Hijazi HI, Oh J, Pearce SP, Perez-Amador MA, Yun J, Kramer E, Alonso JM, Godin C, Vernoux T, Hodgman TC, Pridmore TP, et al. 2014. Systems analysis of auxin transport in the arabidopsis root apex. *The Plant Cell* **26**:862–875. DOI: https://doi.org/10.1105/tpc.113.119495, PMID: 24632533

Barbez E, Dünser K, Gaidora A, Lendl T, Busch W. 2017. Auxin steers root cell expansion via apoplastic ph regulation in *Arabidopsis thaliana*. *PNAS* **114**:E4884–E4893. DOI: https://doi.org/10.1073/pnas.1613499114, PMID: 28559333

Bleckmann A, Weidtkamp-Peters S, Seidel CAM, Simon R. 2010. Stem cell signaling in arabidopsis requires CRN to localize CLV2 to the plasma membrane. *PLANT PHYSIOLOGY* **152**:166–176. DOI: https://doi.org/10.1104/pp.109.149930, PMID: 19933383

Borsics T, Webb D, Andeme-Ondzighi C, Staehelin LA, Christopher DA. 2007. The cyclic nucleotide-gated calmodulin-binding channel atcngc10 localizes to the plasma membrane and influences numerous growth responses and starch accumulation in *Arabidopsis thaliana*. *Planta* **225**:563–573. DOI: https://doi.org/10.1007/s00425-006-0372-3, PMID: 16944199

Brady SM, Orlando DA, Lee JY, Wang JY, Koch J, Dinneny JR, Mace D, Ohler U, Benfey PN. 2007. A high-resolution root spatiotemporal map reveals dominant expression patterns. Science **318**:801–806. DOI: https://doi.org/10.1126/science.1146265, PMID: 17975066

Bruex A, Kainkaryam RM, Wieckowski Y, Kang YH, Bernhardt C, Xia Y, Zheng X, Wang JY, Lee MM, Benfey P, Woolf PJ, Schiefelbein J. 2012. A gene regulatory network for root epidermis cell differentiation in arabidopsis. *PLOS Genetics* **8**:e1002446. DOI: https://doi.org/10.1371/journal.pgen.1002446, PMID: 22253603

Bücherl CA, van Esse GW, Kruis A, Luchtenberg J, Westphal AH, Aker J, van Hoek A, Albrecht C, Borst JW, de Vries SC. 2013. Visualization of bri1 and bak1(serk3) membrane receptor heterooligomers during brassinosteroid signaling. *Plant Physiology* **162**:1911–1925. DOI: https://doi.org/10.1104/pp.113.220152, PMID: 23796795

Bücherl CA, Jarsch IK, Schudoma C, Segonzac C, Mbengue M, Robatzek S, MacLean D, Ott T, Zipfel C. 2017. Plant immune and growth receptors share common signalling components but localise to distinct plasma membrane nanodomains. *eLife* **6**:e25114. DOI: https://doi.org/10.7554/eLife.25114, PMID: 28262094

Caesar K, Elgass K, Chen Z, Huppenberger P, Witthöft J, Schleifenbaum F, Blatt MR, Oecking C, Harter K. 2011. A fast brassinolide-regulated response pathway in the plasma membrane of *Arabidopsis thaliana*. *The Plant Journal* **66**:528–540. DOI: https://doi.org/10.1111/j.1365-313X.2011.04510.x, PMID: 21255166

Cerana R, Bonetti A, Marre MT, Romani G, Lado P, Marre E. 1983. Effects of a brassinosteroid on growth and electrogenic proton extrusion in azuki bean epicotyls. *Physiologia Plantarum* **59**:23–27. DOI: https://doi.org/10.1111/j.1399-3054.1983.tb06565.x

Cerana R, Lado P, Anastasia M, Ciuffreda P, Allevi P. 1984. Regulating effects of brassino steroids and of sterols on growth and h+ secretion in maize roots. *Zeitschrift Für Pflanzenphysiologie* **114**:221–225. DOI: https://doi.org/10.1016/S0044-328X(84)80014-8
Chaiwanon J, Wang ZY. 2015. Spatiotemporal brassinosteroid signaling and antagonism with auxin pattern stem cell dynamics in arabidopsis roots. *Current Biology* **25**:1031–1042. DOI: https://doi.org/10.1016/j.cub.2015.02.046, PMID: 25866388
Christopher DA, Borsics T, Yuen CY, Ullmer W, Andème-Ondzighi C, Andres MA, Kang BH, Staehelin LA. 2007. The cyclic nucleotide gated cation channel atcngc10 traffics from the ER via golgi vesicles to the plasma membrane of arabidopsis root and leaf cells. *BMC Plant Biology* **7**:48. DOI: https://doi.org/10.1186/1471-2229-7-48, PMID: 17877833
Clouse SD. 2002. Brassinosteroid signal transduction: clarifying the pathway from ligand perception to gene expression. *Molecular Cell* **10**:973–982. DOI: https://doi.org/10.1016/s1097-2765(02)00744-x, PMID: 12453407
Clouse SD. 2011. Brassinosteroid signal transduction: from receptor kinase activation to transcriptional networks regulating plant development. *The Plant Cell* **23**:1219–1230. DOI: https://doi.org/10.1105/tpc.111.084475, PMID: 21505068
Cosgrove DJ. 2000. Loosening of plant cell walls by expansins. *Nature* **407**:321–326. DOI: https://doi.org/10.1038/35030000, PMID: 11014181
Degtyarenko K, de Matos P, Ennis M, Hastings J, Zbinden M, McNaught A, Alcántara R, Darsow M, Guedj M, Ashburner M. 2008. ChEBI: a database and ontology for chemical entities of biological interest. *Nucleic Acids Research* **36**:D344–D350. DOI: https://doi.org/10.1093/nar/gkm791, PMID: 17932057
Di Mambro R, De Ruvo M, Pacifici E, Salvi E, Sozzani R, Benfey PN, Busch W, Novak O, Ljung K, Di Paola L, Marée AFM, Costantino P, Grieneisen VA, Sabatini S. 2017. Auxin minimum triggers the developmental switch from cell division to cell differentiation in the arabidopsis root. *PNAS* **114**:E7641–E7649. DOI: https://doi.org/10.1073/pnas.1705833114, PMID: 28831001
Duszyn M, Świeżawska B, Szmidt-Jaworska A, Jaworski K. 2019. Cyclic nucleotide gated channels (cngcs) in plant signalling-current knowledge and perspectives. *Journal of Plant Physiology* **241**:153035. DOI: https://doi.org/10.1016/j.jplph.2019.153035, PMID: 31491601
Elgass K, Caesar K, Schleifenbaum F, Stierhof YD, Meixner AJ, Harter K. 2009. Novel application of fluorescence lifetime and fluorescence microscopy enables quantitative access to subcellular dynamics in plant cells. *PLOS ONE* **4**:e5716. DOI: https://doi.org/10.1371/journal.pone.0005716, PMID: 19492078
Fasano JM, Swanson SJ, Blancaflor EB, Dowd PE, Kao TH, Gilroy S. 2001. Changes in root cap ph are required for the gravity response of the arabidopsis root. *The Plant Cell* **13**:907–921. DOI: https://doi.org/10.1105/tpc.13.4.907, PMID: 11283344
Fridman Y, Strauss S, Horev G, Ackerman-Lavert M, Reiner-Benaim A, Lane B, Smith RS, Savaldi-Goldstein S. 2021. The root meristem is shaped by brassinosteroid control of cell geometry. *Nature Plants* **7**:1475–1484. DOI: https://doi.org/10.1038/s41477-021-01014-9, PMID: 34782771
Friedrichsen DM, Joazeiro CA, Li J, Hunter T, Chory J. 2000. Brassinosteroid-insensitive-1 is a ubiquitously expressed leucine-rich repeat receptor serine/threonine kinase. *PLANT PHYSIOLOGY* **123**:1247–1256. DOI: https://doi.org/10.1104/pp.123.4.1247, PMID: 10938344
Fuglsang AT, Kristensen A, Cuin TA, Schulze WX, Persson J, Thuesen KH, Ytting CK, Oehlenschlæger CB, Mahmood K, Sondergaard TE, Shabala S, Palmgren MG. 2014. Receptor kinase-mediated control of primary active proton pumping at the plasma membrane. *The Plant Journal* **80**:951–964. DOI: https://doi.org/10.1111/tpj.12680, PMID: 25267325
Glöckner N, Oven-Krockhaus S z., Rohr L, Wackenhut F, Burmeister M, Wanke F, Holzwart E, Meixner AJ, Wolf S, Harter K. 2020. Three-Fluorophore FRET Enables the Analysis of Ternary Protein Association in Living Plant Cells. bioRxiv DOI: https://doi.org/10.1101/722124
Graeff M, Rana S, Wendrich JR, Dorier J, Eekhout T, Aliaga Fandino AC, Guex N, Bassel GW, De Rybel B, Hardtke CS. 2021. A single-cell morpho-transcriptomic map of brassinosteroid action in the arabidopsis root. *Molecular Plant* **14**:1985–1999. DOI: https://doi.org/10.1016/j.molp.2021.07.021, PMID: 34358681
Grefen C, Obrdlik P, Harter K. 2009. *Plant Signal Transduction*. Berlin, Germany: Springer.
Grefen C. 2014. *Arabidopsis Protocols*. Berlin, Germany: Springer.
Großeholz R, Feldman-Salit A, Wanke F, Schulze S, Glöckner N, Kemmerling B, Harter K, Kummer U. 2020. Specifying the role of BAK1-interacting receptor-like kinase 3 in brassinosteroid signaling. *Journal of Integrative Plant Biology* **62**:456–469. DOI: https://doi.org/10.1111/jipb.12803, PMID: 30912278
Hacham Y, Holland N, Butterfield C, Ubeda-Tomas S, Bennett MJ, Chory J, Savaldi-Goldstein S. 2011. Brassinosteroid perception in the epidermis controls root meristem size. *Development* **138**:839–848. DOI: https://doi.org/10.1242/dev.061804, PMID: 21270053
Hager A. 2003. Role of the plasma membrane h+-atpase in auxin-induced elongation growth: historical and new aspects. *Journal of Plant Research* **116**:483–505. DOI: https://doi.org/10.1007/s10265-003-0110-x, PMID: 12937999
Higinbotham N. 1973. Electropotentials of plant cells. *Annual Review of Plant Physiology* **24**:25–46. DOI: https://doi.org/10.1146/annurev.pp.24.060173.000325
Hohmann U, Santiago J, Nicolet J, Olsson V, Spiga FM, Hothorn LA, Butenko MA, Hothorn M. 2018. Mechanistic basis for the activation of plant membrane receptor kinases by SERK-family coreceptors. *PNAS* **115**:3488–3493. DOI: https://doi.org/10.1073/pnas.1714972115, PMID: 29531026

Holzheu P, Kummer U. 2020. Computational systems biology of cellular processes in *Arabidopsis thaliana*: an overview. *Cellular and Molecular Life Sciences* **77**:433–440. DOI: https://doi.org/10.1007/s00018-019-03379-9, PMID: 31768604

Holzheu P, Großeholz R, Kummer U. 2021. Impact of explicit area scaling on kinetic models involving multiple compartments. *BMC Bioinformatics* **22**:1–12. DOI: https://doi.org/10.1186/s12859-020-03913-8, PMID: 33430767

Holzwart E, Huerta AI, Glöckner N, Garnelo Gómez B, Wanke F, Augustin S, Askani JC, Schürholz AK, Harter K, Wolf S. 2018. BRI1 controls vascular cell fate in the arabidopsis root through rlp44 and phytosulfokine signaling. *PNAS* **115**:11838–11843. DOI: https://doi.org/10.1073/pnas.1814434115, PMID: 30377268

Hoops S, Sahle S, Gauges R, Lee C, Pahle J, Simus N, Singhal M, Xu L, Mendes P, Kummer U. 2006. COPASI--a complex pathway simulator. *Bioinformatics* **22**:3067–3074. DOI: https://doi.org/10.1093/bioinformatics/btl485, PMID: 17032683

Hübner K, Sahle S, Kummer U. 2011. Applications and trends in systems biology in biochemistry. *The FEBS Journal* **278**:2767–2857. DOI: https://doi.org/10.1111/j.1742-4658.2011.08217.x, PMID: 21707921

Imkampe J, Halter T, Huang S, Schulze S, Mazzotta S, Schmidt N, Manstretta R, Postel S, Wierzba M, Yang Y, van Dongen WMAM, Stahl M, Zipfel C, Goshe MB, Clouse S, de Vries SC, Tax F, Wang X, Kemmerling B. 2017. The arabidopsis leucine-rich repeat receptor kinase BIR3 negatively regulates BAK1 receptor complex formation and stabilizes BAK1. *The Plant Cell* **29**:2285–2303. DOI: https://doi.org/10.1105/tpc.17.00376, PMID: 28842532

Jin Y, Jing W, Zhang Q, Zhang W. 2015. Cyclic nucleotide gated channel 10 negatively regulates salt tolerance by mediating na+ transport in arabidopsis. *Journal of Plant Research* **128**:211–220. DOI: https://doi.org/10.1007/s10265-014-0679-2, PMID: 25416933

Junker BH, Klukas C, Schreiber F. 2006. VANTED: A system for advanced data analysis and visualization in the context of biological networks. *BMC Bioinformatics* **7**:109. DOI: https://doi.org/10.1186/1471-2105-7-109, PMID: 16519817

Karimi M, Inzé D, Depicker A. 2002. GATEWAY vectors for agrobacterium-mediated plant transformation. *Trends in Plant Science* **7**:193–195. DOI: https://doi.org/10.1016/s1360-1385(02)02251-3, PMID: 11992820

Kinoshita T, Caño-Delgado A, Seto H, Hiranuma S, Fujioka S, Yoshida S, Chory J. 2005. Binding of brassinosteroids to the extracellular domain of plant receptor kinase BRI1. *Nature* **433**:167–171. DOI: https://doi.org/10.1038/nature03227, PMID: 15650741

Ladwig F, Dahlke RI, Stührwohldt N, Hartmann J, Harter K, Sauter M. 2015. Phytosulfokine regulates growth in arabidopsis through a response module at the plasma membrane that includes CYCLIC NUCLEOTIDE-GATED CHANNEL17, H+-atpase, and BAK1. *The Plant Cell* **27**:1718–1729. DOI: https://doi.org/10.1105/tpc.15.00306, PMID: 26071421

Li M, Liu C, Hepworth SR, Ma C, Li H, Li J, Wang SM, Yin H. 2022. SAUR15 interaction with bri1 activates plasma membrane h+-atpase to promote organ development of arabidopsis. *Plant Physiology* **189**:2454–2466. DOI: https://doi.org/10.1093/plphys/kiac194, PMID: 35511168

Lin LL, Hsu CL, Hu CW, Ko SY, Hsieh HL, Huang HC, Juan HF. 2015. Integrating phosphoproteomics and bioinformatics to study brassinosteroid-regulated phosphorylation dynamics in arabidopsis. *BMC Genomics* **16**:1–17. DOI: https://doi.org/10.1186/s12864-015-1753-4, PMID: 26187819

Lv M, Li M, Chen W, Wang Y, Sun C, Yin H, He K, Li J. 2018. Thermal-enhanced bri1-301 instability reveals a plasma membrane protein quality control system in plants. *Frontiers in Plant Science* **9**:1620. DOI: https://doi.org/10.3389/fpls.2018.01620, PMID: 30459799

Lv M, Li J. 2020. Molecular mechanisms of brassinosteroid-mediated responses to changing environments in *arabidopsis International Journal of Molecular Sciences* **21**:E2737. DOI: https://doi.org/10.3390/ijms21082737, PMID: 32326491

Ma X, Denyer T, Timmermans MCP. 2020. PscB: A browser to explore plant single cell rna-sequencing data sets. *Plant Physiology* **183**:464–467. DOI: https://doi.org/10.1104/pp.20.00250, PMID: 32209591

Maathuis F, Sanders D. 1993. Energization of potassium uptake in *Arabidopsis thaliana*. *Planta* **191**:302–307. DOI: https://doi.org/10.1007/BF00195686

Mandava NB. 1988. Plant growth-promoting brassinosteroids. *Annual Review of Plant Physiology and Plant Molecular Biology* **39**:23–52. DOI: https://doi.org/10.1146/annurev.pp.39.060188.000323

Mendes P, Hoops S, Sahle S, Gauges R, Dada J, Kummer U. 2009. *Systems Biology*. Berlin, Germany: Springer.

Merlot S, Leonhardt N, Fenzi F, Valon C, Costa M, Piette L, Vavasseur A, Genty B, Boivin K, Müller A, Giraudat J, Leung J. 2007. Constitutive activation of a plasma membrane h(+)-atpase prevents abscisic acid-mediated stomatal closure. *The EMBO Journal* **26**:3216–3226. DOI: https://doi.org/10.1038/sj.emboj.7601750, PMID: 17557075

Minami A, Takahashi K, Inoue S-I, Tada Y, Kinoshita T. 2019. Brassinosteroid induces phosphorylation of the plasma membrane h+-atpase during hypocotyl elongation in *Arabidopsis thaliana*. *Plant & Cell Physiology* **60**:935–944. DOI: https://doi.org/10.1093/pcp/pcz005, PMID: 30649552

Muraro D, Larrieu A, Lucas M, Chopard J, Byrne H, Godin C, King J. 2016. A multi-scale model of the interplay between cell signalling and hormone transport in specifying the root meristem of *Arabidopsis thaliana*. *Journal of Theoretical Biology* **404**:182–205. DOI: https://doi.org/10.1016/j.jtbi.2016.04.036, PMID: 27157127

Müssig C, Fischer S, Altmann T. 2002. Brassinosteroid-regulated gene expression. *Plant Physiology* **129**:1241–1251. DOI: https://doi.org/10.1104/pp.011003, PMID: 12114578

Newman IA. 2001. Ion transport in roots: measurement of fluxes using ion-selective microelectrodes to characterize transporter function. *Plant, Cell & Environment* **24**:1–14. DOI: https://doi.org/10.1046/j.1365-3040.2001.00661.x, PMID: 11762438

Novère NL, Hucka M, Mi H, Moodie S, Schreiber F, Sorokin A, Demir E, Wegner K, Aladjem MI, Wimalaratne SM, Bergman FT, Gauges R, Ghazal P, Kawaji H, Li L, Matsuoka Y, Villéger A, Boyd SE, Calzone L, Courtot M, et al. 2009. The systems biology graphical notation. *Nature Biotechnology* **27**:735–741. DOI: https://doi.org/10.1038/nbt.1558, PMID: 19668183

Obrdlik P, El-Bakkoury M, Hamacher T, Cappellaro C, Vilarino C, Fleischer C, Ellerbrok H, Kamuzinzi R, Ledent V, Blaudez D, Sanders D, Revuelta JL, Boles E, André B, Frommer WB. 2004. K+ channel interactions detected by a genetic system optimized for systematic studies of membrane protein interactions. *PNAS* **101**:12242–12247. DOI: https://doi.org/10.1073/pnas.0404467101, PMID: 15299147

Oh MH, Wang X, Clouse SD, Huber SC. 2012. Deactivation of the arabidopsis brassinosteroid INSENSITIVE 1BRASSINOSTEROID INSENSITIVE 1 (BRI1) receptor kinase by autophosphorylation within the glycine-rich loop. *PNAS* **109**:327–332. DOI: https://doi.org/10.1073/pnas.1108321109, PMID: 22184234

Pacifici E, Di Mambro R, Dello Ioio R, Costantino P, Sabatini S. 2018. Acidic cell elongation drives cell differentiation in the *arabidopsis* root. *The EMBO Journal* **37**:e99134. DOI: https://doi.org/10.15252/embj.201899134, PMID: 30012836

Palmgren MG, Sommarin M, Serrano R, Larsson C. 2009. Identification of an autoinhibitory domain in the C-terminal region of the plant plasma membrane H(+)-atpase. *Journal of Biological Chemistry* **266**:20470–20475. DOI: https://doi.org/10.1016/S0021-9258(18)54948-6

Pavelescu I, Vilarrasa-Blasi J, Planas-Riverola A, González-García M-P, Caño-Delgado AI, Ibañes M. 2018. A sizer model for cell differentiation in *Arabidopsis thaliana* root growth. *Molecular Systems Biology* **14**:e7687. DOI: https://doi.org/10.15252/msb.20177687, PMID: 29321184

Phyo P, Gu Y, Hong M. 2019. Impact of acidic ph on plant cell wall polysaccharide structure and dynamics: insights into the mechanism of acid growth in plants from solid-state NMR. *Cellulose* **26**:291–304. DOI: https://doi.org/10.1007/s10570-018-2094-7

R CoreTeam. 2020. R: A Language and Environment for Statistical Computing. Vienna, Austria: R Foundation for Statistical Computing.

Regenberg B, Villalba JM, Lanfermeijer FC, Palmgren MG. 1995. C-terminal deletion analysis of plant plasma membrane H(+)-atpase: yeast as a model system for solute transport across the plant plasma membrane. *The Plant Cell* **7**:1655–1666. DOI: https://doi.org/10.1105/tpc.7.10.1655, PMID: 7580256

Romani G, Marrie MT, Bonetti A, Cerana R, Lado P, Marre E. 1983. Effects of a brassinosteroid on growth and electrogenic proton extrusion in maize root segments. *Physiologia Plantarum* **59**:528–532. DOI: https://doi.org/10.1111/j.1399-3054.1983.tb06275.x

Rutten JP, Ten Tusscher K. 2019. In silico roots: room for growth. *Trends in Plant Science* **24**:250–262. DOI: https://doi.org/10.1016/j.tplants.2018.11.005, PMID: 30665820

Rutten JP, Ten Tusscher KH. 2021. Bootstrapping and pinning down the root meristem; the auxin-plt-arr network unites robustness and sensitivity in meristem growth control. *International Journal of Molecular Sciences* **22**:4731. DOI: https://doi.org/10.3390/ijms22094731, PMID: 33946960

Salvi E, Rutten JP, Di Mambro R, Polverari L, Licursi V, Negri R, Dello Ioio R, Sabatini S, Ten Tusscher K. 2020. A self-organized plt/auxin/arr-b network controls the dynamics of root zonation development in *Arabidopsis thaliana*. *Developmental Cell* **53**:431–443.. DOI: https://doi.org/10.1016/j.devcel.2020.04.004, PMID: 32386600

Sankar M, Osmont KS, Rolcik J, Gujas B, Tarkowska D, Strnad M, Xenarios I, Hardtke CS. 2011. A qualitative continuous model of cellular auxin and brassinosteroid signaling and their crosstalk. *Bioinformatics* **27**:1404–1412. DOI: https://doi.org/10.1093/bioinformatics/btr158, PMID: 21450717

Sondergaard TE, Schulz A, Palmgren MG. 2004. Energization of transport processes in plants. Roles of the plasma membrane h+-atpase. *Plant Physiology* **136**:2475–2482. DOI: https://doi.org/10.1104/pp.104.048231, PMID: 15375204

Staal M, De Cnodder T, Simon D, Vandenbussche F, Van der Straeten D, Verbelen J-P, Elzenga T, Vissenberg K. 2011. Apoplastic alkalinization is instrumental for the inhibition of cell elongation in the arabidopsis root by the ethylene precursor 1-aminocyclopropane-1-carboxylic acid. *Plant Physiology* **155**:2049–2055. DOI: https://doi.org/10.1104/pp.110.168476, PMID: 21282405

Sullivan A, Purohit PK, Freese NH, Pasha A, Esteban E, Waese J, Wu A, Chen M, Chin CY, Song R, Watharkar SR, Chan AP, Krishnakumar V, Vaughn MW, Town C, Loraine AE, Provart NJ. 2019. An "efp-seq browser" for visualizing and exploring rna sequencing data. *The Plant Journal* **100**:641–654. DOI: https://doi.org/10.1111/tpj.14468, PMID: 31350781

van Esse GW, van Mourik S, Stigter H, ten Hove CA, Molenaar J, de Vries SC. 2012. A mathematical model for brassinosteroid insensitive1-mediated signaling in root growth and hypocotyl elongation. *Plant Physiology* **160**:523–532. DOI: https://doi.org/10.1104/pp.112.200105, PMID: 22802611

van Esse GW, Harter K, de Vries SC. 2013a. Computational modelling of the BRI1 receptor system. *Plant, Cell & Environment* **36**:1728–1737. DOI: https://doi.org/10.1111/pce.12077, PMID: 23421559

van Esse W, van Mourik S, Albrecht C, van Leeuwen J, de Vries S. 2013b. A mathematical model for the coreceptors somatic embryogenesis receptor-like kinase1 and somatic embryogenesis receptor-like kinase3 in brassinosteroid insensitive1-mediated signaling. *Plant Physiology* **163**:1472–1481. DOI: https://doi.org/10.1104/pp.113.222034, PMID: 24072582

Veerabagu M, Elgass K, Kirchler T, Huppenberger P, Harter K, Chaban C, Mira-Rodado V. 2012. The arabidopsis B-type response regulator 18 homomerizes and positively regulates cytokinin responses. *The Plant Journal* **72**:721–731. DOI: https://doi.org/10.1111/j.1365-313X.2012.05101.x, PMID: 22775331

Verbelen J-P, De Cnodder T, Le J, Vissenberg K, Baluska F. 2006. The root apex of *Arabidopsis thaliana* consists of four distinct zones of growth activities: meristematic zone, transition zone, fast elongation zone and growth terminating zone. *Plant Signaling & Behavior* **1**:296–304. DOI: https://doi.org/10.4161/psb.1.6.3511, PMID: 19517000

Vernoux T, Brunoud G, Farcot E, Morin V, Van den Daele H, Legrand J, Oliva M, Das P, Larrieu A, Wells D, Guédon Y, Armitage L, Picard F, Guyomarc'h S, Cellier C, Parry G, Koumproglou R, Doonan JH, Estelle M, Godin C, et al. 2011. The auxin signalling network translates dynamic input into robust patterning at the shoot apex. *Molecular Systems Biology* **7**:508. DOI: https://doi.org/10.1038/msb.2011.39, PMID: 21734647

Vukašinović N, Wang Y, Vanhoutte I, Fendrych M, Guo B, Kvasnica M, Jiroutová P, Oklestkova J, Strnad M, Russinova E. 2021. Local brassinosteroid biosynthesis enables optimal root growth. *Nature Plants* **7**:619–632. DOI: https://doi.org/10.1038/s41477-021-00917-x, PMID: 34007032

Wang ZY, Seto H, Fujioka S, Yoshida S, Chory J. 2001. BRI1 is a critical component of a plasma-membrane receptor for plant steroids. *Nature* **410**:380–383. DOI: https://doi.org/10.1038/35066597, PMID: 11268216

Wang J, Jiang J, Wang J, Chen L, Fan S-L, Wu J-W, Wang X, Wang Z-X. 2014. Structural insights into the negative regulation of BRI1 signaling by BRI1-interacting protein BKI1. *Cell Research* **24**:1328–1341. DOI: https://doi.org/10.1038/cr.2014.132, PMID: 25331450

White PJ, Biskup B, Elzenga JTM, Homann U, Thiel G, Wissing F, Maathuis FJM. 1999. Advanced patch-clamp techniques and single-channel analysis. *Journal of Experimental Botany* **50**:1037–1054. DOI: https://doi.org/10.1093/jxb/50.Special_Issue.1037

Wilma van Esse G, Westphal AH, Surendran RP, Albrecht C, van Veen B, Borst JW, de Vries SC. 2011. Quantification of the brassinosteroid insensitive1 receptor in planta. *Plant Physiology* **156**:1691–1700. DOI: https://doi.org/10.1104/pp.111.179309, PMID: 21617031

Winter D, Vinegar B, Nahal H, Ammar R, Wilson GV, Provart NJ. 2007. An "electronic fluorescent pictograph" browser for exploring and analyzing large-scale biological data sets. *PLOS ONE* **2**:e718. DOI: https://doi.org/10.1371/journal.pone.0000718, PMID: 17684564

Witthöft J, Caesar K, Elgass K, Huppenberger P, Kilian J, Schleifenbaum F, Oecking C, Harter K. 2011. The activation of the arabidopsis P-atpase 1 by the brassinosteroid receptor BRI1 is independent of threonine 948 phosphorylation. *Plant Signaling & Behavior* **6**:1063–1066. DOI: https://doi.org/10.4161/psb.6.7.15650, PMID: 21617383

Witthöft J, Harter K. 2011. Latest news on arabidopsis brassinosteroid perception and signaling. *Frontiers in Plant Science* **2**:58. DOI: https://doi.org/10.3389/fpls.2011.00058, PMID: 22639599

Wolf S, van der Does D, Ladwig F, Sticht C, Kolbeck A, Schürholz AK, Augustin S, Keinath N, Rausch T, Greiner S, Schumacher K, Harter K, Zipfel C, Höfte H. 2014. A receptor-like protein mediates the response to pectin modification by activating brassinosteroid signaling. *PNAS* **111**:15261–15266. DOI: https://doi.org/10.1073/pnas.1322979111, PMID: 25288746

Wolf S. 2020. Deviating from the beaten track: new twists in brassinosteroid receptor function. *International Journal of Molecular Sciences* **21**:E1561. DOI: https://doi.org/10.3390/ijms21051561, PMID: 32106564

Yuan W, Li Y, Li L, Siao W, Zhang Q, Zhang Y, Liu J, Xu W, Miao R. 2018. BR-insensitive1 regulates hydrotropic response by interacting with plasma membrane h^+-atpases in arabidopsis. *Plant Signaling & Behavior* **13**:e1486147. DOI: https://doi.org/10.1080/15592324.2018.1486147, PMID: 30067914

Zhang X, Zhou L, Qin Y, Chen Y, Liu X, Wang M, Mao J, Zhang J, He Z, Liu L, Li J. 2018. A temperature-sensitive misfolded bri1-301 receptor requires its kinase activity to promote growth. *Plant Physiology* **178**:1704–1719. DOI: https://doi.org/10.1104/pp.18.00452, PMID: 30333151

Appendix 1

Model information

Throughout this section we will indicate to concentrations using [], e.g. $[BRI1]$. Proteins or ions, which can appear in different compartments will have the respective compartment indicated in the subscript, e.g. $[H^+_{out}]$. Compartment volumes will be indicated by V, surface areas by A, with the compartment name indicated in the subscript. Time-dependent volumes or global quantities are indicated by (t), e.g. $cell\,wall\,thickness(t)$.

Compartments

The computational model was set up to describe the behavior of one epidermis cell in the *Arabidopsis thaliana* root. Initially, the compartment sizes and concentrations of model species were set such that the model describes an epidermis cell in the early elongation zone (EZ). All unknown parameters were estimated based on the pathway's behavior in this root zone. To verify the model behavior we changed the setting to now describe an epidermis cell in the meristematic zone (MZ) and predicted the time-course and dose-response behavior.

The compartments were defined so that the cytosol, membrane area and vacuole (as well as the vacuolar area) are fixed. The cell wall volume on the other hand is defined as the product of the membrane area and the cell wall thickness. The (initial) sizes for all compartments are listed in ***Appendix 1—table 1***.

As one of the responses to BR signaling is the swelling of the cell wall, both cell wall thickness and volume are time-dependent and change according to the acidification of the cell wall:

$$V_{cell\,wall}(t) = A_{cell\,surface} \cdot cell\,wall\,thickness(t)$$

The cell wall thickness itself is calculated by an ODE using the current value and the instability caused by the acidification: $\frac{d(cell\,wall\,thickness)}{dt} = scaling\,factor \cdot cell\,wall\,instability(t) \cdot cell\,wall\,thickness(t) \cdot stimulation$

The cell wall instability is calculated based on the current level of acidification and limited by how close the cell wall thickness is to the maximally allowed value:

$$cell\,wall\,instability(t) = stimulation \cdot \frac{1}{1+e^{-0.001\left([H^+_{out}]-1.2\cdot proton\,readout\right)}} \cdot \left(1 - \frac{1}{1+e^{-10^7\cdot\left(Cell\,wall\,thickness(t)-5.0\cdot10^{-6}\right)}}\right)$$

Altogether this allows the model to capture not only the pH and Em change after BR stimulation but also the early cell morphological change of cell wall swelling in preparation of cell elongation.

Appendix 1—table 1. Overview of model compartments and (initial) sizes for both MZ and early EZ.
[a] calculated by multiplying the membrane area with the cell wall thickness (***Wilma van Esse et al., 2011***; ***Caesar et al., 2011***). [b] estimated volume based on cell dimensions and cellular volume (***Wilma van Esse et al., 2011***). [c] estimated surface area, included as scaling factor in the global quantities.

Root zone	Compartment	Size
Meristematic zone	cytosol	8.47×10^{-13} dm^3
	membrane	7.67×10^{-8} dm^2
	cell wall[a]	3.03×10^{-13} dm^3
	vacuole	NA
	vacuolar surface	NA
Early elongation zone	cytosol	2.271×10^{-12} dm^3
	membrane	2.098×10^{-7} dm^2
	cell wall[a]	8.2871×10^{-13} dm^3

Appendix 1—table 1 Continued on next page

Appendix 1—table 1 Continued

Root zone	Compartment	Size
	vacuole[b]	2.352×10^{-12} dm^3
	vacuolar surface[c]	1.087×10^{-7} dm^2

Overview of model components

Appendix 1—table 2. Protein are specified by the Uniprot identifier (***Bairoch et al., 2005***) and the corresponding gene ID.
For ions and chemical compounds, the ChEBI (Chemical Entities of Biological Interest ***Degtyarenko et al., 2008***) identifier is used instead. The initial concentrations of all un-phosphorylated species and complexes between proteins were set to 0 pM.

Species	Uniprot ID /	Gene ID	Initial	Source
	ChEBI ID		Concentration	
BRI1	O22476	At4g39400	0.182 633 pM	***Wilma van Esse et al., 2011***
BAK1	Q94F62	At4g33430	0.099 632 pM	***Wilma van Esse et al., 2011***
BIR3			0.237 423 11 pM	this study
AHA*			0.232 442 pM	$[AHA1] + [AHA2]$
AHA1	P20649	At2g18960	0.116 221 pM	assumption:$\frac{AHA1}{AHA2} \approx \frac{1}{1}$
				mRNA data (eFP Browser)
				Winter et al., 2007
AHA2	P19456	At4g30190	0.116 221 pM	this study
AHA CT*	C-terminus		0.232 442 pM	assumed to be
	of AHAs			$[AHA1] + [AHA2]$
BKI1	Q9FMZ0	At5g42750	0.219 16 pM	assumption:$1.2 \cdot [BRI1]_{t=0}$
BIK1	O48814	At2g39660	0.219 16 pM	assumption:$1.2 \cdot [BRI1]_{t=0}$
CNGC10	Q9LNJ0	At1g01340	0.1 pM	
H^+_{in}	24636	-	63 000 pM	
H^+out	24636	-	fitted to data	
K^+out	29103	-	9.8425×10^9 pM	½ MS medium
K^+_{in}	29103	-	8.4×10^{10} pM	***Maathuis and Sanders, 1993***
K^+_{vac}	29103	-	8.4×10^{10} pM	assumed to be identical to K^+_{in}
BL	28277	-	*dose*	see experimental setup

*To avoid overly complicating the model we have summarized the pump activity of $AHA1$ and $AHA2$ into one reaction that is mediated by AHA, which is defined as the sum of $[AHA1]$ and $[AHA2]$. Similarly, regulatory function of the C-terminal regions of the AHAs is mediated by the unphosphorylated form of the C-terminus AHA CT, which represents the C-terminal regions of both $AHA1$ and $AHA2$.

Ordinary differential equations

The differential equations of the model are composed of the individual rate laws of the biochemical and interaction reactions considered for the model (***Figure 2***). Unless otherwise indicated, reaction rates (indicated by "k") and affinities (indicated by "K") are defined locally for that particular reaction. The index of the reaction (r_i) and of the respective rate law (v_i) are identical to the numbers in the model scheme (***Figure 2***).

Overview of reactions

Appendix 1—table 3. Overview of model reactions, including the reaction number (ID), the general type of rate law chosen for the respective reaction as well as available experimental parameter values.

Rate law abbreviations: MA - mass action kinetics, MM - Michaelis-Menten kinetics, CF - constant flux.

ID	Rate law	Parameter	Value	Source
r_{01}	modified MA	K_i	approx. 7.7 — fold for AHA2	*Regenberg et al., 1995*
r_{02}	modified MA	k	$0.84\times10^{-9}\,\mathrm{dm\,s^{-1}}$ to $1.25\times10^{-9}\,\mathrm{dm\,s^{-1}}$	this study
r_{03}	modified MA			
r_{04}	MA			
r_{05}	MA			
r_{06}	MA			
r_{07}	MA			
r_{08}	CF, MA	*dose*	from $0\,\mathrm{nM}$ to $1\times10^{5}\,\mathrm{pM}$	*Caesar et al., 2011* this study
r_{09}	modified MA	K_d	$7.4\times10^{3}\,\mathrm{pM}$ to $5.5\times10^{4}\,\mathrm{pM}$	*Clouse, 2002* *Hohmann et al., 2018*
				Kinoshita et al., 2005
				Wang et al., 2001
		k_{on}	$9.49\times10^{-7}\,\mathrm{pMol^{-1}\,s^{-1}}$	*Hohmann et al., 2018*
r_{10}	modified MM	k	$0.97\,\mathrm{s^{-1}}$	*Wang et al., 2014*
r_{11}	modified MM			
r_{12}	modified MA			
r_{13}	MA			
r_{14}	MA			
r_{15}	MM			
r_{16}	MM			
r_{17}	MM	*time scale*	slow increase over $12\,\mathrm{h}$	*Oh et al., 2012*
r_{d1}	MA			
r_{d2}	MA	max. k_d	$1.05\times10^{-2}\,\mathrm{s^{-1}}$	*Hohmann et al., 2018*
r_{d3}	MA	max. k_d	$1.05\times10^{-2}\,\mathrm{s^{-1}}$	*Hohmann et al., 2018*
r_{d4}	MA	*time scale*	residual P_i after $5\,\mathrm{d}$	*Oh et al., 2012*
r_{d5}	MA			
r_{d6}	MA			
r_{d7}	MA			

Reaction rate laws v_{ID} for all model reactions r_{ID}

$$
\begin{aligned}
r_{01}: \quad & v_{01} = A_{cell\ surface} \cdot k_{01} \cdot [AHA] \cdot [H^+_{in}] \cdot \frac{[AHA]}{[AHA]+Inhibition_{AHA\ CT} \cdot [AHA\ CT]} \\
r_{02}: \quad & v_{02} = A_{cell\ surface} \cdot k_{02} \cdot ([H^+_{out}] - [H^+_{in}]) \\
r_{03}: \quad & v_{03} = A_{cell\ surface} \cdot (k_{03} \cdot [K^+_{in}] - k_{03} \cdot K_{eq} \cdot [K^+_{out}]) \\
r_{04}: \quad & v_{04} = k_{04} \cdot A_{cell\ surface} \cdot [CNGC10_{open}] \cdot \frac{[K^+_{out}]}{K_d} \cdot \left(\frac{E_m}{-0.59} - 1\right) \\
r_{05}: \quad & v_{05} = A_{vacuole} \cdot k_{05} \cdot ([K^+_{in}] - [K^+_{vac}]) \\
r_{06}: \quad & v_{06} = A_{cell\ surface} \cdot (k_{06} \cdot [BIR3] \cdot [BRI1] - k_{06} \cdot K_D \cdot [BIR3\ BRI1]) \\
r_{07}: \quad & v_{07} = A_{cell\ surface} \cdot (k_{07} \cdot [BIR3] \cdot [BAK1] - k_{07} \cdot K_D \cdot [BIR3\ BAK1]) \\
r_{08}: \quad & v_{08} = V_{cell\ wall} \cdot (k_{08} \cdot dose \cdot stimulation - k_{08} \cdot [BL]) \\
r_{09}: \quad & v_{09} = A_{cell\ surface} \cdot (k_{on} \cdot [BL] \cdot [BRI1] - k_{off} \cdot [BRI1\ BL]) \\
r_{10}: \quad & v_{10} = A_{cell\ surface} \cdot k_{10} \cdot [BRI1\ BL] \cdot \frac{[BKI1]}{(K_{i,BKI1}+[BKI1]) \cdot (1+\frac{[BKI1]}{K_{i,BKI1}}) \cdot (1+\frac{[BIK1]}{K_{i,BIK1}})} \\
r_{11}: \quad & v_{11} = A_{cell\ surface} \cdot k_{11} \cdot [BRI1\ BL] \cdot \frac{[BIK1]}{(K_{i,BIK1}+[BIK1]) \cdot (1+\frac{[BKI1]}{K_{i,BKI1}}) \cdot (1+\frac{[BIK1]}{K_{i,BIK1}})} \\
r_{12}: \quad & v_{12} = A_{cell\ surface} \cdot k_{12} \cdot [BRI1\ BL] \cdot \frac{[1]}{(1+\frac{[BKI1]}{K_{i,BKI1}}) \cdot (1+\frac{[BIK1]}{K_{i,BIK1}})} \\
r_{13}: \quad & v_{13} = A_{cell\ surface} \cdot (k_{13} \cdot [BRI1p\ BL] \cdot [BAK1] - k_{off} \cdot [BAK1\ BRI1p\ BL]) \\
r_{14}: \quad & v_{14} = A_{cell\ surface} \cdot k_{14} \cdot [BAK1\ BRI1p\ BL] \\
r_{15}: \quad & v_{15} = A_{cell\ surface} \cdot k_{15} \cdot [BAK1p\ BRI1pp\ BL] \cdot \frac{[AHA\ CT]}{[AHA\ CT]+K} \\
r_{16}: \quad & v_{16} = A_{cell\ surface} \cdot \left(k_{16} \cdot [BAK1p\ BRI1pp\ BL] \cdot \frac{[CNGC10_{closed}]}{K_M+[CNGC10_{closed}]} - k_{-16} \cdot [CNGC10_{open}]\right) \\
r_{d1}: \quad & v_{d1} = A_{cell\ surface} \cdot k_{off} \cdot [BRI1p\ BL] \\
r_{d2}: \quad & v_{d2} = A_{cell\ surface} \cdot k_{off2} \cdot [BAK1\ BRI1p\ BL] \\
r_{d3}: \quad & v_{d3} = A_{cell\ surface} \cdot k_{off2} \cdot [BAK1p\ BRI1pp\ BL] \\
r_{d4}: \quad & v_{d4} = A_{cell\ surface} \cdot k_{off3} \cdot [BAK1p\ BRI1inact\ BL] \\
r_{d5}: \quad & v_{d5} = A_{cell\ surface} \cdot k_{d5} \cdot [BKI1pY211] \\
r_{d6}: \quad & v_{d6} = A_{cell\ surface} \cdot k_{d6} \cdot [BIK1p] \\
r_{d7}: \quad & v_{d7} = A_{cell\ surface} \cdot k_{d7} \cdot [AHA\ CTp]
\end{aligned}
\tag{1}
$$

Model ODEs

$$
\begin{aligned}
\frac{d([BRI1]\cdot A_{cell\ surface})}{dt} &= -v_{09} + v_{d1} + v_{d2} + v_{d3} + v_{d4} \\
\frac{d([BL]\cdot A_{cell\ surface})}{dt} &= -v_{09} + v_{d1} + v_{d2} + v_{d3} + v_{d4} + v_{08} \\
\frac{d([BKI1pY211]\cdot V_{cytosol})}{dt} &= +v_{10} - v_{d5} \\
\frac{d([BKI1]*A_{cell\ surface})}{dt} &= -v_{10} + v_{d5} \\
\frac{d([AHA\ CTp]\cdot A_{cell\ surface})}{dt} &= +v_{15} - v_{d7} \\
\frac{d([AHA\ CT]\cdot A_{cell\ surface})}{dt} &= -v_{15} + v_{d7} \\
\frac{d([BAK1]\cdot A_{cell\ surface})}{dt} &= -v_{07} - v_{13} + v_{d2} + v_{d3} + v_{d4} \\
\frac{d([BAK1\ BRI1p\ BL]\cdot A_{cell\ surface})}{dt} &= +v_{13} - v_{d2} - v_{14} \\
\frac{d([BAK1p\ BRI1pp\ BL]\cdot A_{cell\ surface})}{dt} &= +v_{14} - v_{17} - v_{d3} \\
\frac{d([BAK1p\ BRI1inact\ BL]\cdot A_{cell\ surface})}{dt} &= +v_{17} - v_{d4} \\
\frac{d([BIK1]\cdot A_{cell\ surface})}{dt} &= -v_{11} + v_{d6} \\
\frac{d([BIK1p]\cdot A_{cell\ surface})}{dt} &= +v_{11} - v_{d6} \\
\frac{d([BRI1\ BL]\cdot A_{cell\ surface})}{dt} &= +v_{09} - v_{12} \\
\frac{d([BRI1p\ BL]\cdot A_{cell\ surface})}{dt} &= +v_{12} - v_{13} - v_{d1} \\
\frac{d([BIR3]\cdot A_{cell\ surface})}{dt} &= -v_{07} - v_{06} \\
\frac{d([BIR3\ BAK1]\cdot A_{cell\ surface})}{dt} &= +v_{07} \\
\frac{d([BIR3\ BRI1]\cdot A_{cell\ surface})}{dt} &= +v_{06} \\
\frac{d([H^+_{out}]\cdot V_{cell\ wall})}{dt} &= +v_{01} - v_{02} \\
\frac{d([CNGC10_{open}]\cdot A_{cell\ surface})}{dt} &= +v_{16} \\
\frac{d([CNGC10_{closed}]\cdot A_{cell\ surface})}{dt} &= +v_{16} \\
\frac{d([K^+_{in}]\cdot V_{cell})}{dt} &= +v_{04} + v_{03} - v_{05} \\
\frac{d([K^+_{vac}]\cdot V_{vacuole})}{dt} &= +v_{05}
\end{aligned}
\tag{2}
$$

Global quantities

The computational model also comprises a number of global quantities that are important for the model setup and analysis. First, the net change in charge distribution and in the membrane potential are calculated as global quantities. The net change in charge distribution is calculated based on the change in intracellular potassium amount (K^+_{in}) and in the extracellular proton amount (H^+_{out}), the Faraday constant F and a scaling factor from $pmol$ to mol:

$$\Delta Q(t) = (([K^+_{in}] - [K^+_{in,t=0}]) \cdot V_{cell} - ([H^+_{out}] - [H^+_{out,0}]) \cdot V_{cell\ wall(t)}) \cdot F \cdot factor_{pmol\ to\ mol}$$
$$with:\ F = 96485.33212 C\,mol^{-1}$$

The corresponding membrane potential change ΔE_m is then calculated based on the change in charge distribution ΔQ, the specific membrane capacitance and the membrane area.

$$\triangle E_m(t) = \frac{net\ charge\ distribution\ change\ \triangle Q(t)}{specific\ capacitance * membrane\ area}$$

The membrane potential itself as then computed based on the initial value and the calculated membrane potential change:

$$E_m(t) = E_{m,\,t=0} + \triangle E_m(t)$$

Expression factors for BIR3 and BRI1

Factors representing the expression level of BIR3 and BRI1. 1 represents the normal expression level, 100 represents the overexpression level. These factors are used to simulate the behavior of the overexpression phenotypes.

Global model parameters

A number of model parameters were defined as global quantities: the affinity and dissociation rate of BL from BRI1 (K_d and $k_{off\,BL}$, respectively), the dissociation rate of BL from BRI1 and BAK1 ($k_{off\,BL\,BRI1\,BAK1}$), the affinity between BIR3 and BAK1 as $K_{d\,BIR3\,BAK1} = rel\,affinity\,BIR3 \dot{K}_{d\,BIR3\,BRI1}$ (with $rel\,affinity\,BIR3 < 1$), and the inhibitory constants for BIK1 and BKI1 (as $K_{i\,BKI1}$ and $K_{i\,BIK1}$, respectively).

Events

Stimulation

Trigger: $Model\,Time > 86400\,s$

Target: Global quantity $stimulation\,transient\,value$ is set to 1 from the initial value of 0.

pH measurements using pHusion

A. thaliana seedlings stably expressing SYP122-pHusion were treated with with 500 µM orthovanadate and the pH was measured after 30 min and 60 min based on the fluorescent ratio of mRFP and eGFP in the EZ. The measurements were conducted for n=30 seedlings. Plants treated with MS medium were taken as control, outliers were set to pH 8.

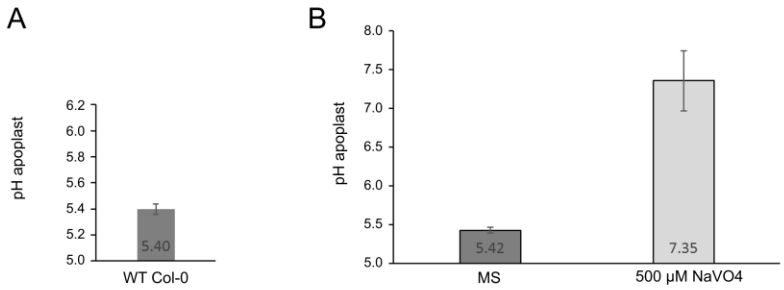

Appendix 1—figure 1. Measurement of the proton leak flux from the cell wall using SYP122-pHusion. (**A**) Resting pH in the EZ of the WT Col-0. Error bars represent SD (n=3). (**B**) pH after 1 h of treatment with $500\,\mathrm{M}$ orthovanadate compared to control (MS). Error bars represent SD (n=30). The proton leak was estimated based on the pH difference and the average size of an epidermis cell in the mid EZ (***Wilma van Esse et al., 2011***).

The online version of this article includes the following source data for appendix 1—figure 1:

- **Appendix 1—figure 1—source data 1.** Raw data underlying the representation of the results.

Example calculation of E_m and pH change

pH 5.4 → 5.0

$$\triangle[H^+]: \quad 10^{-5.0}M - 10^{-5.4}M = 1 \cdot 10^{-5} - 3.16 \cdot 10^{-6}M = 6.019 \cdot 10^{-6}M$$

$$\triangle nH^+: \quad 6.019 \cdot 10^{-6}M \cdot 8.2892 \cdot 10^{-13}l = 4.99 \cdot 10^{-18}mol$$

$$\triangle Q: \quad 4.99 \cdot 10^{-18}mol \cdot 96485.33212 \frac{C}{mol} = 4.81 \cdot 10^{-13}C$$

$$\triangle E_m: \quad \frac{4.81 \cdot 10^{-13}C}{0.0081 \cdot 2.098 \cdot 10^{-9}m^2} = 2.83 \cdot 10^{-2}V = 28.3mV$$

Computational modeling enables the in silico analysis of BIR3 function

To further demonstrate the importance of modeling for the understanding of a cell physiological process, we investigated the function of the inhibitor BIR3 in the activity modulation of the nano-organized BRI1 complexes in more detail in silico. The basis for the focus on BIR3 were the observations by ***Imkampe et al., 2017*** regarding the activity of the BR signaling in BIR3 as well as BIR3 and BRI1 overexpressing plant in the parameter estimation and the proof of the graduated interaction of the cytplasmic domains of BIR3 with BAK1 and BRI1 (***Großeholz et al., 2020***): The pathway should be

inactive (=no acidification), when BIR3 is overexpressed, whilst the additional overexpression of BRI1 should restore the signaling activity to approximately normal levels. As shown in figure S14 A, the model was actually able to describe and represent the BR activity of the respective growth-related experimentally measured phenotypes of *Arabidopsis* plants with altered BIR3 levels (***Imkampe et al., 2017***). The accuracy of the model allowed us to investigate the behavior of different BIR3 expression levels in comparison to wild type level in the root by analyzing the pH change 20 min after stimulation with 10 nM BL. As shown in the resulting expression-response curve (Fig. S14 B), the overall response decreased with increasing concentrations of BIR3 for all model parameterizations. The model therefore suggests that it is possible for the plant to fine-tune the signaling output by adjusting the protein level of the negative regulator BIR3. Again using the model, we also analyzed the dynamics of the overall pH response at different BIR3 accumulation levels, namely in the absence of BIR3, the wild type protein amount of around 13 BIR3 molecules μm^{-2} PM and a 10- and 100-fold overaccumulation of BIR3. Here, the actual time-course behavior of the acidification varies between the different model parameterizations as the span of possible values deviated from the average pH response for the BIR3 expression (Fig. S14 C). Depending on the parameterization, it was possible for the model to either show a strong activation that tapered off or a more gradual response over the time- frame of an hour. However, for most model parameterizations, a 10-fold overexpression of BIR3 is sufficient to inactivate the BRI1 signaling module confirming the importance of the regulation by BIR3. In summary, the modeling reveals insights into the quantitative properties of the considered cell physiological process with an accuracy that is very difficult to assess experimentally.

Supporting figures

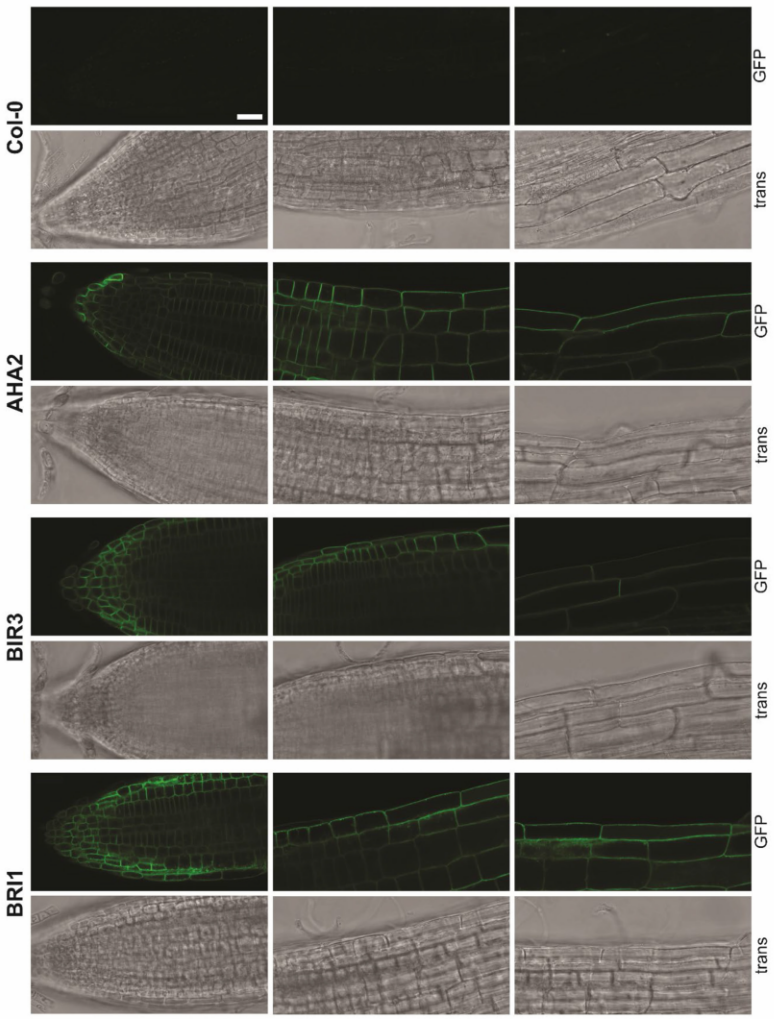

Appendix 1—figure 2. Exemplary images of the localization of fusions proteins. Localization along the root axis. Shown is the localization of AHA2-GFP, BIR3-GFP and BRI1-GFP, expressed under the respective native promoter in the respective mutant background (5-days-old seedlings). Col-0 (top) served as control. From top to bottom: GFP channel; transmitted light (trans). As reported before the amount of BRI1-GFP did not alter much (see ***Figure 3C***; ***van Esse et al., 2012***). In addition, for BIR3-GFP a homogenous fluorescence was observed, as well (see ***Figure 3C***). In contrast, there was a gradient of AHA2-GFP fluorescence intensity along the root axis, being comparatively low in the meristematic zone (MZ) but high in the elongation zone (EZ) / maturation zone (see ***Figure 3C***). Images were taken with a SP8 laser scanning microscope (Leica Microsystems GmbH) under the use of the HC PL APO CS2 63 x/1.20 WATER objective. For all images, the same settings were used: Argon Laser: 30%. For GFP excitation: 488 nm laser line (with adequate laser power to avoid saturation of the signal). GFP

Appendix 1—figure 2 continued on next page

Appendix 1—figure 2 continued
fluorescence was detected by an HyD detector between 500 nm – 550 nm (190 V gain, –0.01 offset). PMT Trans was used to detect transmitted light (217 V gain, offset off). By an XY-dimension of 1024x512 px and a scan speed of 200 Hz, the zoom factor was 0.75. For better visibility, the intensity values were adjusted as followed: 0–75 (AHA2) for GFP channel and 0–85 for all transmitted light channels. Scale bar represents 25 µm and applies to all partial images.

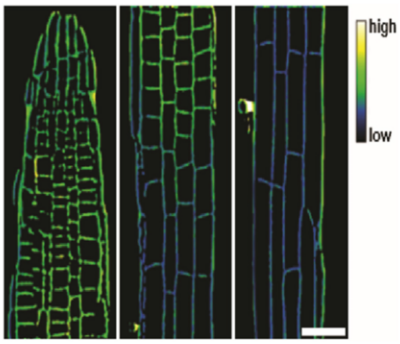

Appendix 1—figure 3. Representative image of the apoplastic pH of epidermal cells along the root axis of wild type *Arabidopsis* using HPTS-staining starting with the meristematic zone (MZ, left) over the transition zone (TZ, middle) to the elongation zone (EZ, right). The scale bar represents 25 µm and applies to all partial images.

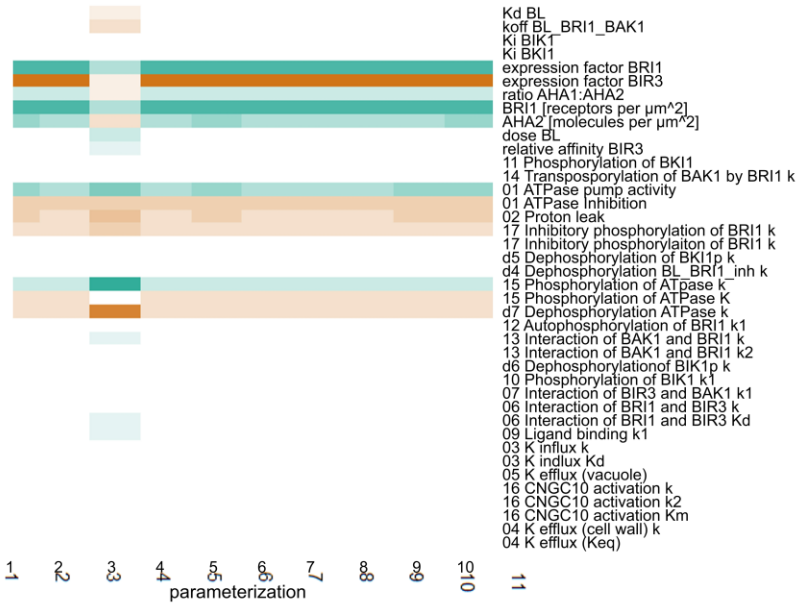

Appendix 1—figure 4. Scaled sensitivities of the pH change 60 min after stimulation with 10 nM BL in response to changes in the parameter and global quantities values. Color code: red - negative control, white - no influence, green - positive control. Color saturation indicates strength of the influence.

The online version of this article includes the following source data for appendix 1—figure 4:

- **Appendix 1—figure 4—source data 1.** Raw data underlying the representation of the results.

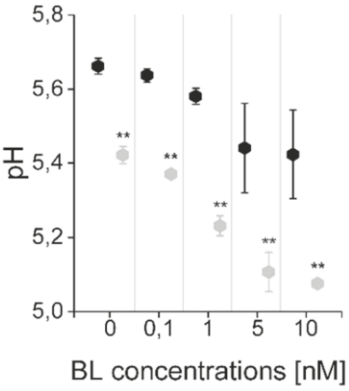

Appendix 1—figure 5. The computational model captures the differences in the sensitivity of apoplastic acidification between the root epidermal cells of the meristematic zone (MZ) and elongation zone (EZ) in response to BL. Black diamonds represent MZ and grey diamonds EZ. Virtual BL incubation of different concentration was

Appendix 1—figure 5 continued on next page

Appendix 1—figure 5 continued

done for 60 min. Error bars represent SD for the simulations of different model parameterizations (n=10). Statistical evaluations were performed by comparing the respective groups separately (e.g. '0 nM MZ' compared with '0 nM EZ'). For all comparisons a Two-Tailed Wilcoxon Test was applied. The black asterisks indicate statistically significant differences (**: p≤0.01). The exact p-values can be found in the attached RAW data file. The EZ cells showed a lower resting apoplastic pH and a stronger concentration-dependent response than MZ cells.

The online version of this article includes the following source data for appendix 1—figure 5:

- **Appendix 1—figure 5—source data 1.** Raw data underlying the representation of the results.

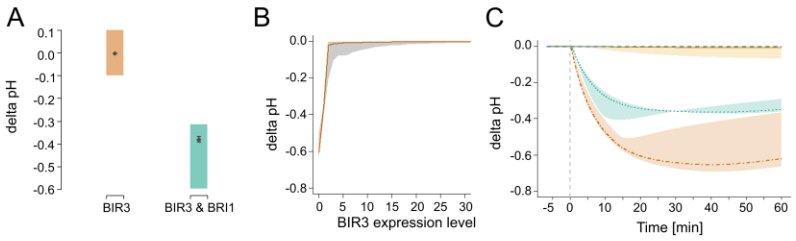

Appendix 1—figure 6. In silico analysis of the functional role of the negative regulator BIR3 on BL-regulated apoplastic acidification. (**A**) Modelled qualitative acidification output of plants overexpressing BIR3 and BIR3 & BRI1, respectively. The colored area represents the pH response targeted during parameter estimation, which was approximated by the activity of BR signaling indicated by the plant phenotypes (***Imkampe et al., 2017***). (**B**) BIR3-Expression-response curve. Shown is the pH change 20 min after stimulation with 10 nM BL at different BIR3 expression levels ranging from 0- (loss-of-function mutant) to 30-times the normal expression level of the wild type. The entire range of simulated responses is indicated by the shaded area, the averaged response of all models is denoted by the line. (**C**) Exemplary time-course simulations of the pH change at 0 (loss-of-function mutant, orange), 1- (wild type expression, green), 10- (yellow), and 100-fold (blue) expression of BIR3 upon virtual application of 10 nM BL. Shown is the average pH response for the respective BIR3 expression level with the span between minimal and maximal values indicated by the colored area. The virtual addition of BL at time 0 is indicated by the vertical dashed line.

The online version of this article includes the following source data for appendix 1—figure 6:

- **Appendix 1—figure 6—source data 1.** Raw data underlying the representation of the results.